UNIVERSITY OF SHEFFIELD
Department of Civil and Structural Engineering

SIMULATION OF THE STRUCTURAL BEHAVIOUR OF STEEL-FRAMED BUILDINGS IN FIRE.

by Colin Gareth Bailey

A thesis submitted in partial fulfilment of the requirements for the Degree of Doctor of Philosophy.

July, 95

SUMMARY.

A three-dimensional finite element computer program has been developed which can predict the behaviour of steel-framed buildings, including the supported floor system, in any specified fire scenario. The developed software provides a more realistic prediction of structural behaviour at elevated temperatures, than is possible with models which are limited to frame analysis, since the building structure is considered as a more complete entity. Confidence in the software is strengthened by comparison with test results to the extent that different structural and fire scenarios may in future be investigated very cheaply. This could lead to a better understanding of the behaviour of steel-framed structures during fires and to more rational approaches to specification of fire protection requirements, which are currently rather expensive in terms of material and fixing costs.

The steel beam-column members are represented by one-dimensional two-noded elements which incorporate both material and geometrical non-linearities. These can model three-dimensional steel member behaviour including lateral-torsional buckling. Temperature gradients can be specified through the steel cross-section and also along its length. Spring elements, of zero length, have been introduced to represent semi-rigid joints. These degrade in stiffness and strength with rise in temperature and are represented by any specified moment-rotation-temperature relationship. Unloading from an inelastic state has been modelled for both the steel members and connections, allowing the behaviour of the frame during the cooling phase of a fire to be investigated. This will enable the repairability of the frame to be assessed after a fire has occurred. The flooring system is represented by shell finite elements, which are linear elastic and include thermal strains, although the temperature distribution through the slab's thickness must be assumed uniform. A simplified method of representing cracking in the concrete has been introduced by placing a limit on its maximum bending stress. The node position of the steel one-dimensional finite elements can be displaced to allow connection to the two-dimensional shell elements at a common point. This allows composite action between the beam and supported slab to be modelled.

Comparison has been made between computer simulations and fire tests on the full-scale test frame at Cardington. It has been shown that modelling isolated members is highly unrealistic. However models which incorporate a significant amount of the structure surrounding the heated zone, including the membrane action of the flooring system, perform far better when compared to actual tests. These comparisons indicate that the future development of design methods for fire safety of structures needs to be steered away from its traditional emphasis on isolated member behaviour, and towards considering the interaction of the whole building structure with the aim of avoiding disproportionate collapse.

TABLE OF CONTENTS.

LIST OF FIGURES.

LIST OF TABLES.

NOTATION.

(Only the general notations used during this thesis are presented here. Symbols which have only been used once and are of a more specific nature have been explained clearly when they arise in the text)

A	Arbitrary point.
A, B, n	Temperature-dependent factors shown in Table 3.01.
B	Strain-displacement matrix.
b_r^t	Transformed thickness of the segment.
b_r	Original thickness of the segment.
C	Generalised stress-strain matrix.
C_s	Specific heat of steel.
E_{20}	Young's Modulus of the material at 20°C
E_t	Tangent modulus of the material.
f	Shear force.
F	Vector of externally applied nodal force.
G	Shear modulus.
h	Shape functions.
H_w	Matrix of shape functions.
I_y, I_x..*etc*..	Cross-sectional properties.
J	Jacobian operator.
K	Local stiffness
[K]	Tangent stiffness matrix.
k_s	Thermal conductivity of steel.
l	Member length.
M_f	Applied moment at the fire limit state.
M_p	Plastic moment.
M_{cr}	Elastic critical moment.
m,n,...etc.	Stress resultants.
O	Arbitrary point on the centroidal axis.
P	Elastic critical load.
P_y	Yield stress.
{Q}	External nodal forces (local coordinates).
{q}	Nodal displacements (local coordinates).
R	External nodal forces (global coordinates)
R	Load ratio.
r_1,r_2, r_n	Sampling points.
T	Temperature.

TOL	Tolerance limit.
TSV	Torsional moment due to St.Venant shear stress.
t_s	Steel temperature.
$\hat{u}$	Vector of displacements at nodal positions.
$\overline{\hat{u}}$	Identity matrix.
X, Y, Z, θ	Global coordinates.
x, y, z, θ	Local coordinates.
W	Virtual work.
$\tilde{w}$	Sectorial coordinate.
α	Weighting factor.
Δ	Prefixed to other term, denotes an increment.
δ	Prefixed to other term, denotes virtual variation.
∂	Denotes partial differentiation.
ε	Strain.
σ, τ	Stress.
σ_{20}	Stress at 20°C.
μ_0	Degree of utilisation.
θ	Rotation.
$\{\phi\}$	Cubic shape functions.
γ	Shear strains.
ψ	Unbalanced forces of equation 5.25.
η	Imperfection parameter.
λ	Slenderness ratio.
Π	Potential energy.
{ }	Denotes a column vector.
$\langle\ \rangle$	Denotes a row vector.
[ ]	Denotes a matrix.
$[\ ]^{-1}$	Denotes a matrix inverse.
$\|\ \|_2$	Denotes a norm vector.
Σ	Denotes a summation.
d	Denotes ordinary differentiation.
'	Denotes differentiation with respect to the single argument.
"	Denotes second derivative with respect to single argument.

ACKNOWLEDGEMENT.

The author expresses his thanks to Dr. I.W. Burgess for his supervision, and also the advice and comments provided by Dr. R.J. Plank, during this research project.

From October 1992 to April 1994, financial support was provided from the University of Sheffield and British Steel. From April 1994 the research was sponsored by the Engineering and Physical Sciences Research Council of Great Britain. This support is gratefully acknowledged.

DECLARATION.

Except where specific reference has been made to the work of others, this thesis is the result of the my own work. No part of it has been submitted to any University for a degree, diploma, or other qualification.

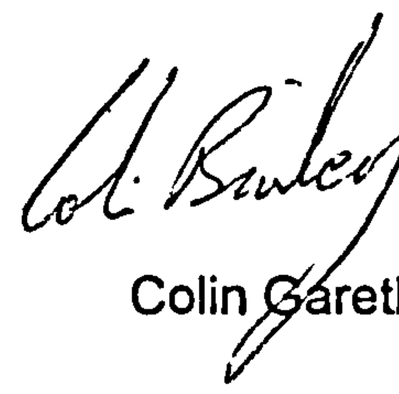

Colin Gareth Bailey.

1.0: INTRODUCTION.

In the U.K. steel is the one of the most popular materials used in construction, with 57% of multi-storey buildings and 90-95% of single-storey factories and warehouses being constructed in steel during the 1991-1992 period[1]. The main advantages of steel construction are fast erection sequences and lighter structures which allow longer spans and smaller foundations. However, compared to other materials used to frame single-storey and multi-storey structures, steel has a high thermal conductivity value and therefore rises in temperature, thus losing strength and stiffness, at a much faster rate. Recognising this as a disadvantage when considering the choice of material for structural frames, the steel industry has invested much research into the use of new protective materials and design methods. The aim of this is to reduce both the protective material costs and also the impact of application of the protection on the construction programme.

Regulatory requirements state that all habitable buildings require a minimum degree of fire resistance to fulfil two main objectives;

- to ensure life safety,
- to minimise property or financial loss.

The Building Regulations[2] are generally concerned with the former objective while insurance companies are concerned with both. , Safe evacuation by early detection, smoke clearing equipment and reduced travel distances to fire protected stairs are classed as typical life safety measures. Fire protection in the form of passive measures by structural protection and containment, or active measures by sprinklers are more commonly associated with property protection. However, the Building Regulations are not only based on the minimum time expected for complete evacuation of the building (which can be relatively short, typically 30 minutes). The safety of fire fighters, risk of structural collapse and fire spread are also of concern. Therefore the minimum time periods which are specified in the Building Regulations are dependent on:

1. the type of building;
2. the height of building or compartment;
3. the floor area of building or compartment;
4. the cubic capacity of building or compartment.

The time periods are specified as 1/2, 1, 2, 3, or 4 hours. These times are not allowable escape times for occupants or survival times for the structure, but a simple convenient way of grading different categories of building.

The passive fire protection measures of containment and structural protection are particularly attractive to legislative authorities since they are 'fail safe' methods compared to active measures. For steel-framed buildings, the most familiar and traditional method of applying structural fire protection is to use some form of insulating material. This keeps the steel at a sufficiently low temperature to retain enough strength and stiffness during the regulatory stated period of fire resistance. Originally the maximum permitted value of steel temperature (approximately 550°C[3]) was based on steel losing its design safety margin on strength at this temperature value. Although this philosophy fits well with permissible-stress design codes such as BS449[4] it is extremely simplified in the way it considers the behaviour of steel members in fire. It assumes that members are uniformly heated, fully stressed at ambient temperature, and also ignores the fact that stress-strain curves become highly curvilinear at elevated temperatures with continuing strength at increasing strains. Recent design codes BS5950 Part 8[5] and EC3 Part 1.2,[6] which are based on fire engineering methods, allow designers to treat fire as one of the basic limit states. The design methods incorporate non-uniform heating (created by partial protection either inherent in the structure or purposely added), true load levels and actual stress-strain characteristics of steel at elevated temperatures. Coupled with the structural response, fire engineering methods are also concerned with predicting the actual rate of temperature rise in the steel members. This is dependent on its location, thickness and exposed surface area, together with the heating rate and maximum temperature of the atmosphere inside the compartment. Prediction of this internal atmospheric heating rate and maximum temperature depends on the severity of the fire, which is governed by the amount of combustible material in the compartment (fire load), type and surface area of the fuel, ventilation, size and configuration of the compartment.

Adopting a more rational approach to the fire performance of steel structures can greatly reduce the amount of fire protection required. In some cases such as sports halls, airport and railway terminals, where fire loads are low, a fire engineering approach can demonstrate that no protection is required to the steel members. At the present time the majority of designs using fire engineering concepts are concerned with achieving a certain period of fire resistance in a standard fire test as defined in BS476 Part 20[7] or ISO834[8]. Within these tests the element should be subjected to stress levels of a similar nature and magnitude to those likely to be encountered in practice. However using standard furnaces usually limits members to 4.0 metres in length for beams and 3.0 metres in height for columns. The test arrangements for both beams and columns are shown in Figs. 1.02 and 1.03.

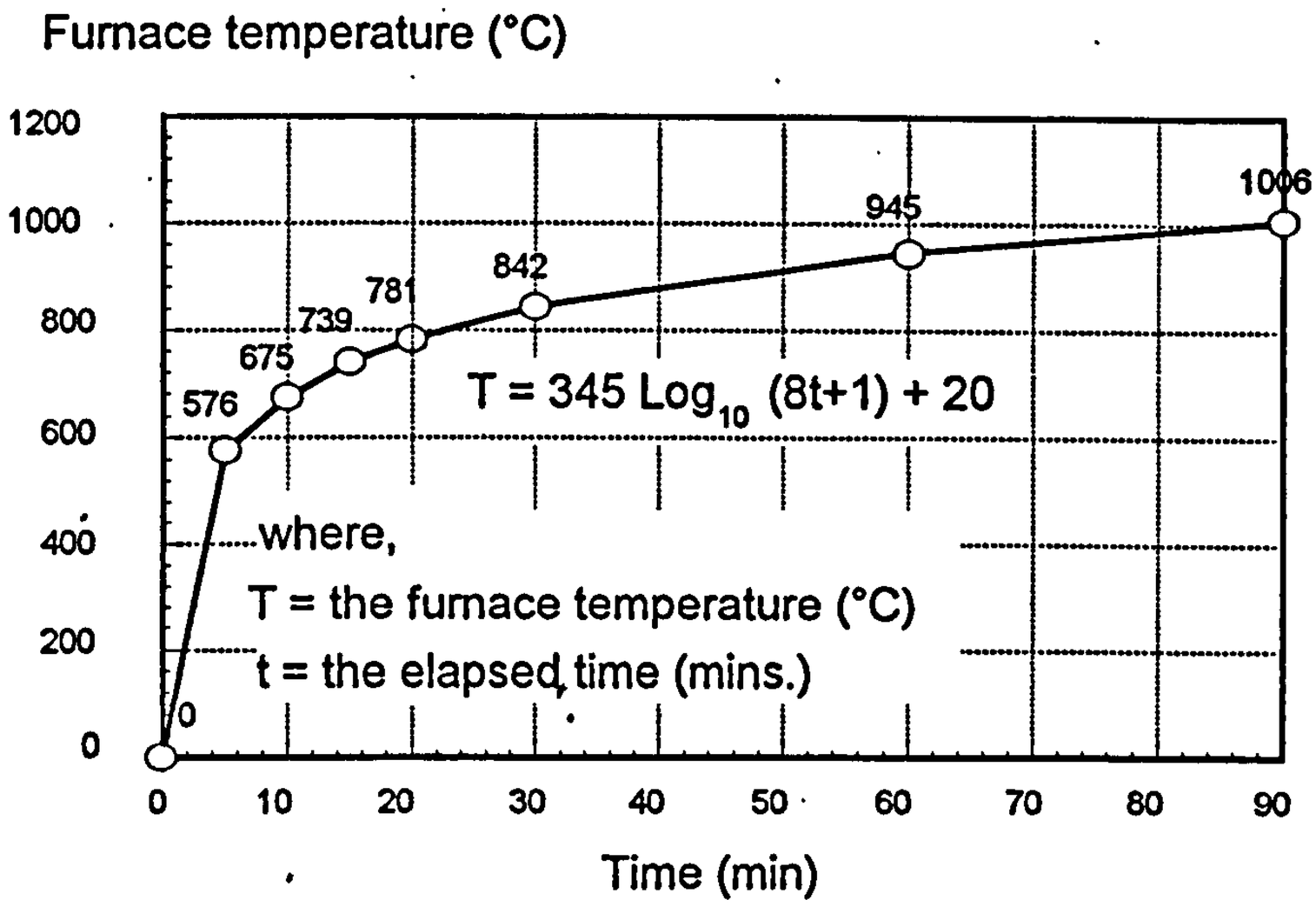

Fig. 1.01: Temperature-time relationship in a standard fire test.

To allow comparisons between different fire tests a standard time-temperature relationship is specified, as shown in Fig. 1.01. This standard fire curve is only used to allow comparison between tests, since fires differ depending on the size and nature of the fire load, degree of ventilation and the size and shape of the compartment. The performance criteria for the fire test are insulation, integrity and load-bearing capacity. Insulation and integrity deal mainly with non-structural fire protection materials and are therefore not considered here. For load-carrying capacity the structural failure of beams is considered to occur when either the deflection rate reaches $L^2/9000d$ (where L is the beam span and d is the beam depth) for deflections greater than $L/30$, or a maximum deflection of $L/20$ is reached. For columns failure is considered to occur when the applied load cannot be supported. Concerns have been expressed over the interpretation of the results and limitations of the standard test, and some of these are listed below.

1. The behaviour of members subjected to the standard time-temperature curves may not be the same for other fire scenarios encountered.
2. Tests on isolated members ignore the effect of restraint from the rest of the structure, which could either be cold or also heated.
3. The cost of tests is extremely high, so that the effect of the member's cross-sectional size, span (which is controlled by the furnace size) restraint, and structural configuration cannot economically be investigated fully.

Results from standard fire tests[9] together with knowledge of steel properties at elevated temperatures (discussed in section 1.1) have allowed development of the

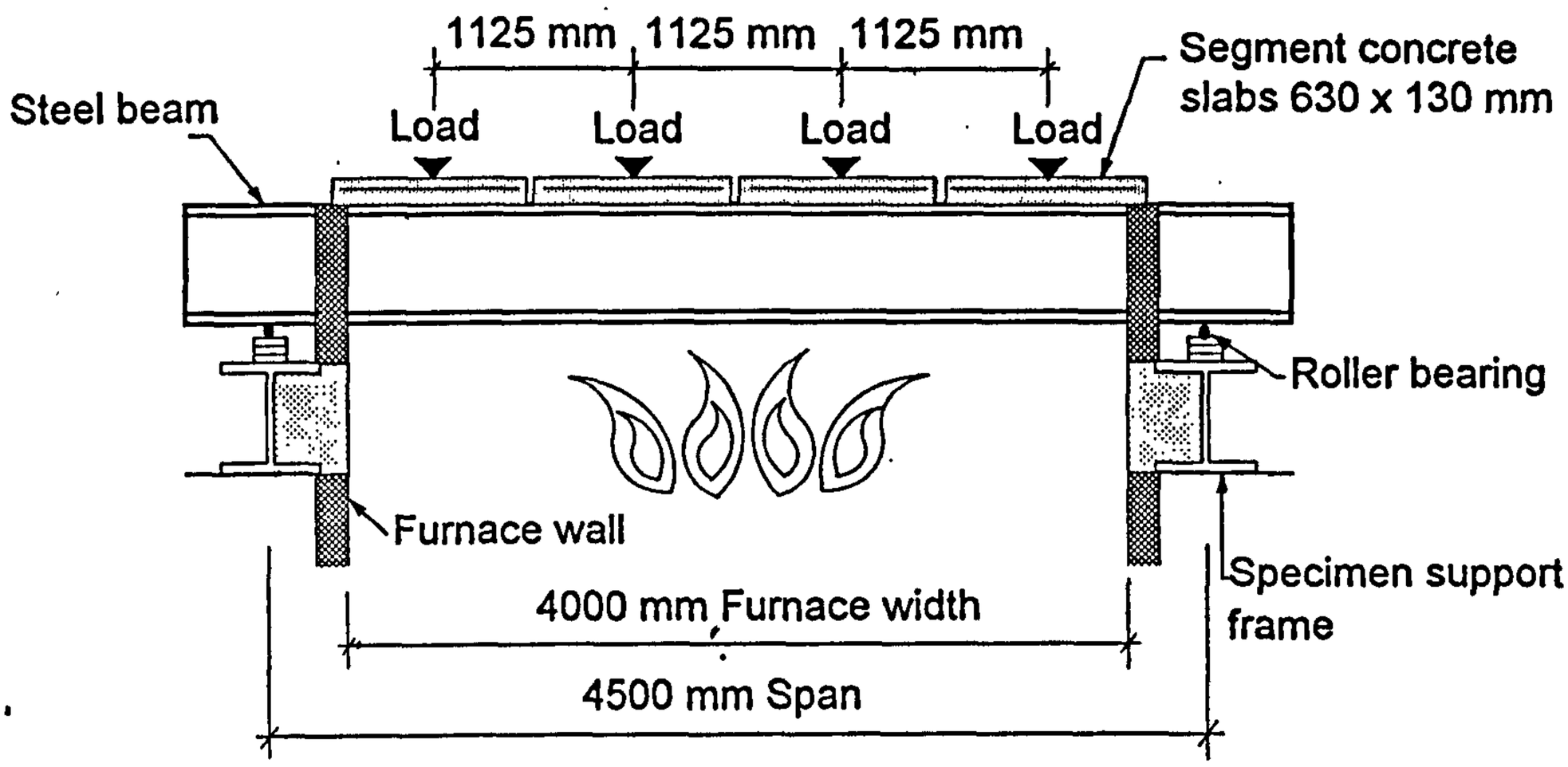

Fig. 1.02 Test arrangement for simple beams.

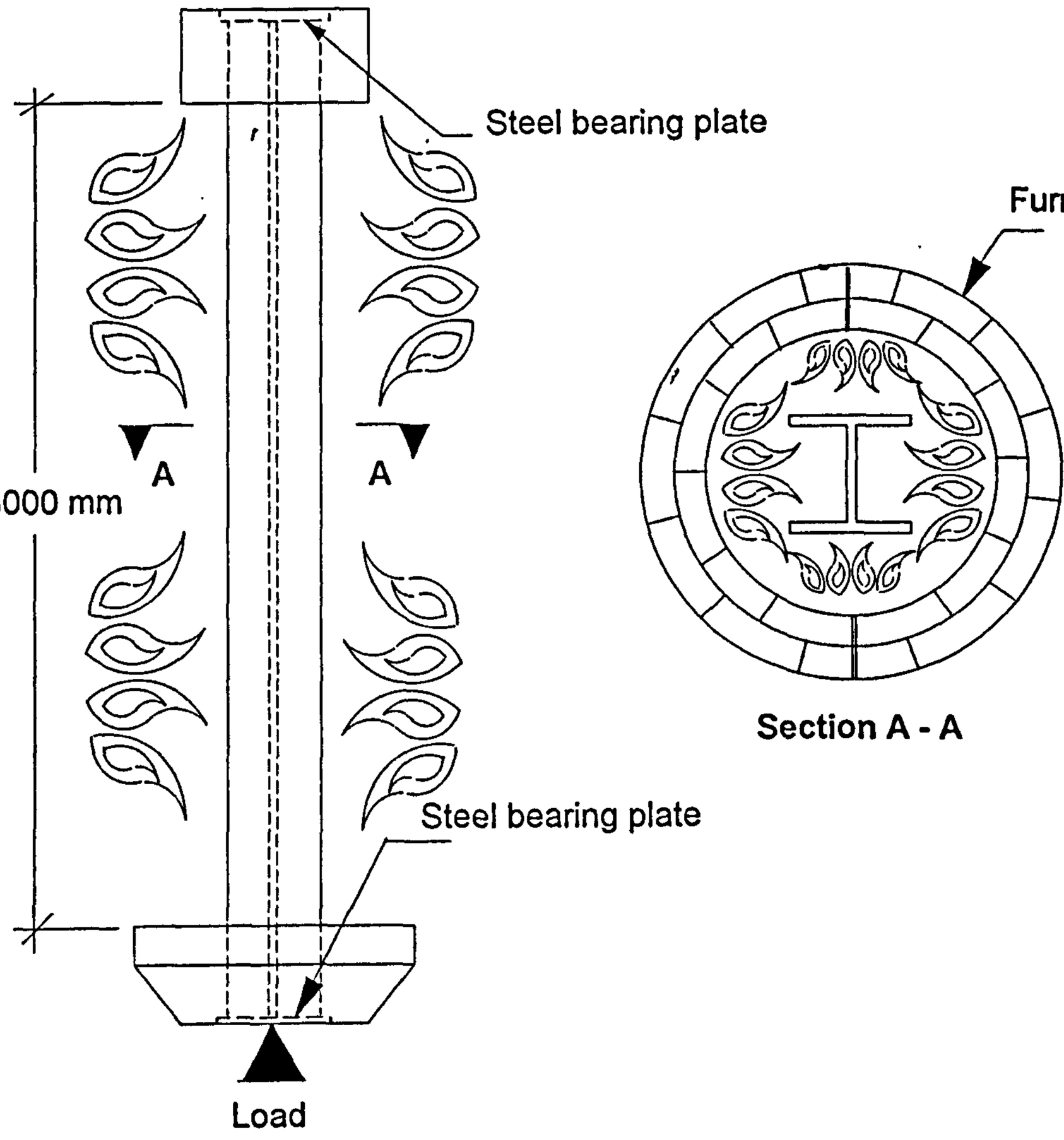

Fig 1.03: Test arrangement for simple columns.

recent codes BS5950 Part 8[5] and EC3 Part 1.2[6]. However these codes are limited in that they consider isolated member design only. Due to the safety requirement of compartmentation, which consists of division of the structure into compartments to contain fire and smoke as shown in Fig. 1.04, all buildings will normally be subjected to localised fires. This will create a zone of heated structural members which is surrounded by the rest of the full-strength cold structure, the extent of which depends on the position of the fire compartment in relation to the whole building arrangement. The effects of the surrounding structure on the heated compartment are twofold. Firstly the restraint against thermal expansion will increase the axial forces in heated members, causing possible column instability at lower temperatures than are suggested by predictions which ignore such continuity. The second effect, which is beneficial, consists of the strength of the structure around and above the heated area which can provide support to the weakening members, even to the extent of re-routing the load paths so that collapse is avoided.

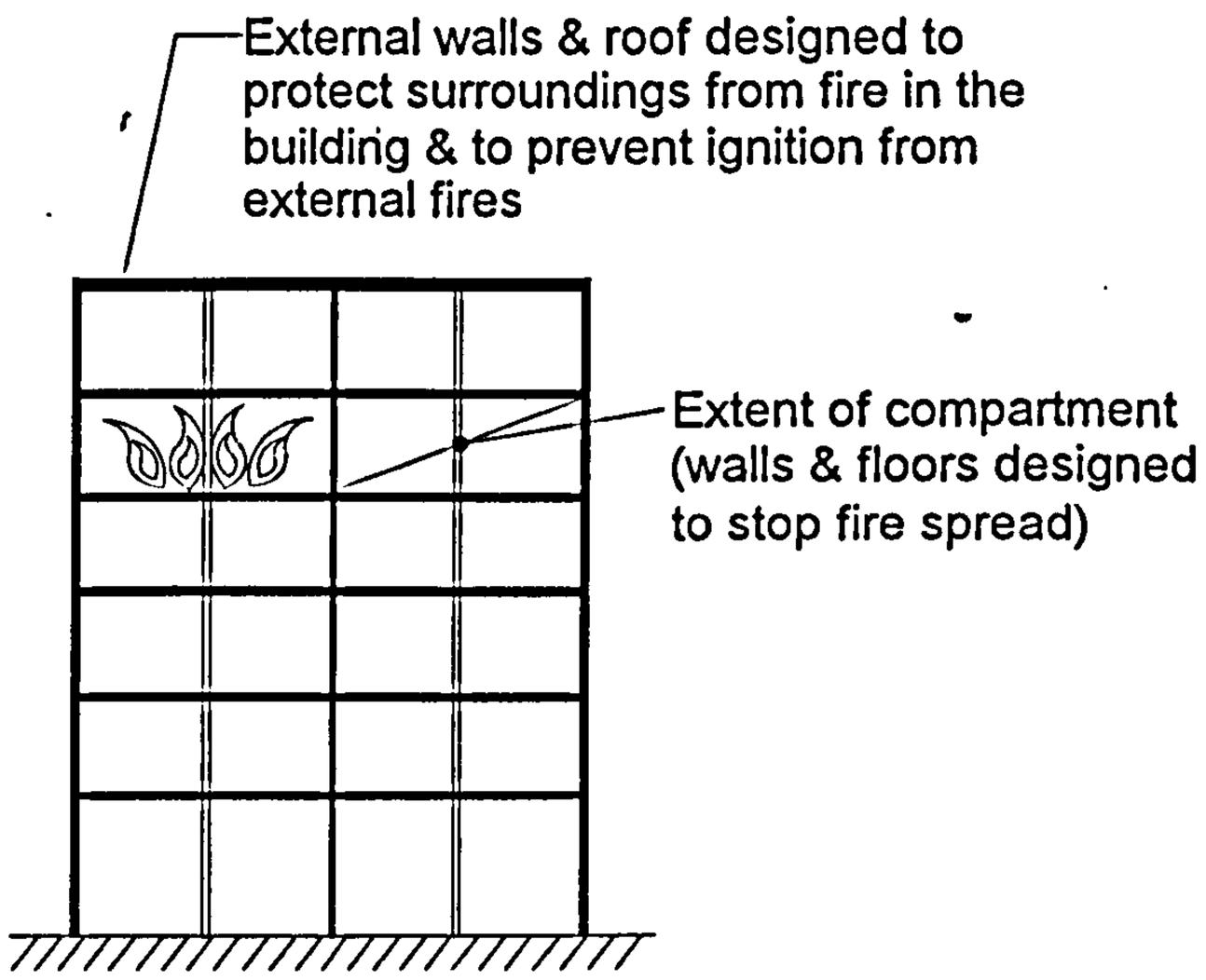

Fig. 1.04: Structural fire containment.

1.1: MATERIAL PROPERTIES.

Strength, deformation, thermal expansion, specific heat and thermal conductivity are all properties of steel which are temperature-dependent. Steel begins to lose strength at temperatures above 300°C and continues to weaken at an approximately steady rate until about 800°C. The degradation of the small residual strength remaining above this temperature continues, but at a slower rate until melting is reached at approximately 1500°C. The British Steel stress-strain data[10] (which is embodied

within BS5950 Part 8) for grade 43 steel, is shown in Fig. 1.05, and throughout the research published here a Ramberg-Osgood type of equation[11] was used to represent this data.

The stress-strain behaviour of steel at elevated temperatures is dependent on the rate of heating, due to a component of deformation arising from creep at temperatures above 450°C. Since creep is time-dependent and very complicated to incorporate in design methods, research has been conducted into the different heating rates likely to be encountered in actual buildings[10]. It has been concluded that if a linear rise of temperature to a limit of 600°C is assumed, together with a range of failure periods between 30 and 120 minutes, then the heating rates fall into the range of 5 to 20°C per minute. Therefore if the heating rates for small-scale tests are kept within these limits then the results obtained will be representative of the behaviour of steel in large-scale tests. The British Steel data presented in Fig. 1.05 is consistent with a heating rate of 10°C per minute.

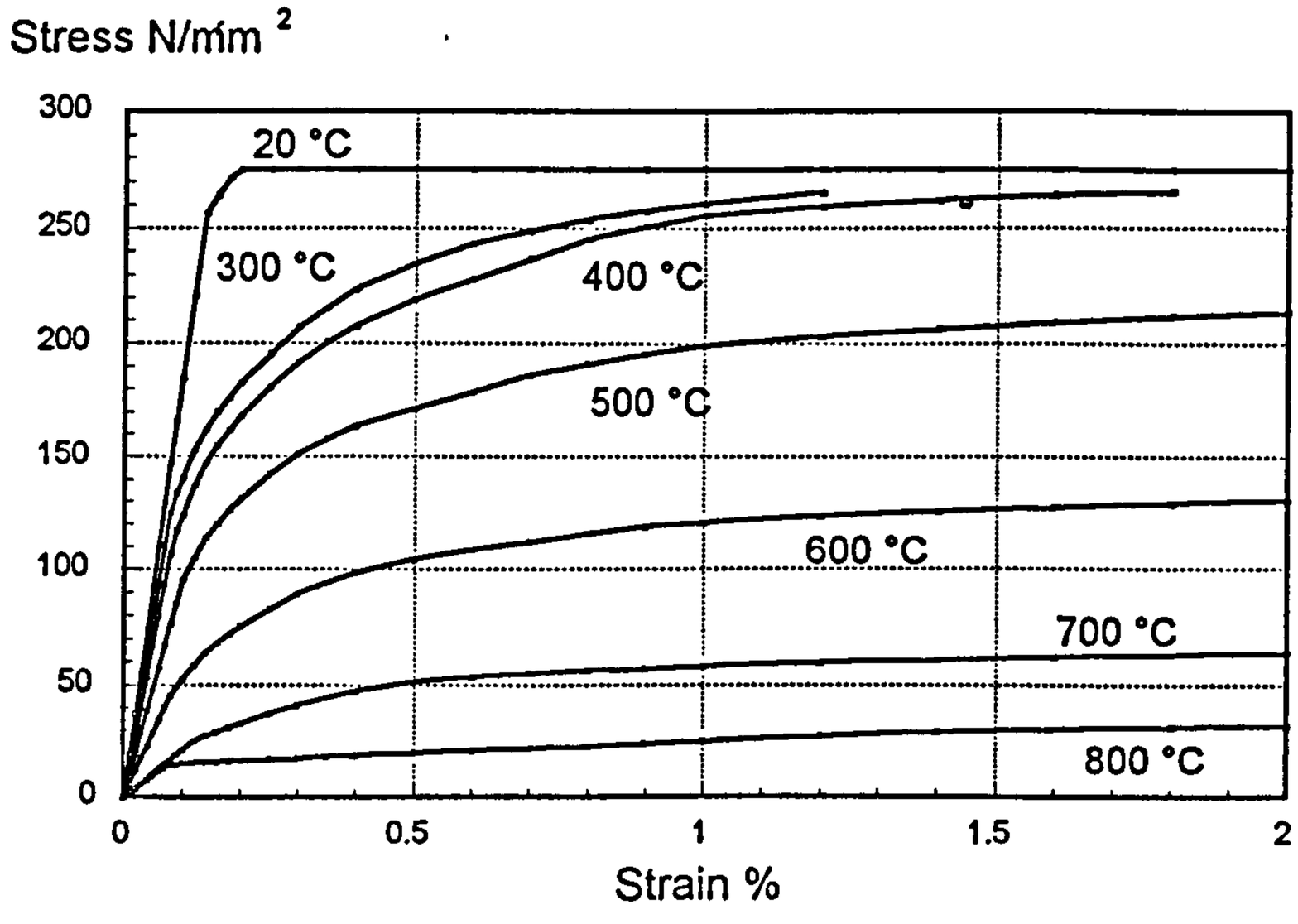

Fig. 1.05: Stress-strain data for grade 43 steel at elevated temperatures.

There are two methods of tensile testing to determine stress-strain characteristics at elevated temperatures.

- Isothermal (or steady-state) tests, which have traditionally been used for mechanical engineering applications, consist of applying a constant temperature to the tensile test specimen and inducing strain at a steady rate which will produce a stress-strain curve for a given constant temperature.

- Anisothermal (or transient) tests consist of applying a constant load to the tensile test specimen and increasing its temperature by pre-determined amounts. The resulting strains are measured, with the effect of thermal strains being deduced after obtaining results from unloaded specimens subjected to the same temperature conditions. Stress-stain curves at particular temperatures are obtained by interpolation from a family of curves at different stresses.

Kirby and Preston[12] reviewed both methods of testing and concluded that anisothermal tests indicate lower strengths but can be claimed to be more realistic.

Apart from the rate of heating and type of test, considerable debate also exists about the strain values at which the residual strength of steel should be measured when strength reduction factors are specified in the design codes. Strength reduction factors are defined in this context as the residual strength of steel at a particular temperature, relative to the basic yield strength at room temperature. For mild steels at ambient temperature the yield strain is traditionally defined as the value consistent with a yield stress plateau. However at elevated temperatures there is a gradual increase in strength with increasing strain. BS5950 Part 8 adopts a strain limit of 1.5% for beams and 0.5% for columns, whereas EC3 Part 1.2 adopts a strain limit of 2.0% for all members. The strength reduction factors relating to specific strain limits are shown in Fig. 1.06

The thermal of expansion of steel increases with temperature until 725°C when the material undergoes a phase-change in crystal structure, with a marked change in the expansion characteristics as the steel absorbs energy and adopts a denser internal structure. The thermal expansion used throughout this research is consistent with EC3 Part 1.2 and is given by,

$$\frac{\Delta l}{l} = -2.416 \times 10^{-4} + 1.2 \times 10^{-5} \times t + 0.4 \times 10^{-8} (t_s)^2 \qquad (1.01)$$

for $20°C \le t_s \le 750°C$

and,

$$\frac{\Delta l}{l} = 11.0 \times 10^{-3} \qquad (1.02)$$

for $750°C < t_s \le 860°C$

and,

$$\frac{\Delta l}{l} = -6.2 \times 10^{-3} + 2.0 \times 10^{-5} \times t_s \qquad (1.03)$$

for $860°C < t_s \le 1200°C$

where,

l = length at room temperature of the steel member,

Δl = temperature induced-elongation of the steel member,

t_s = steel temperature.

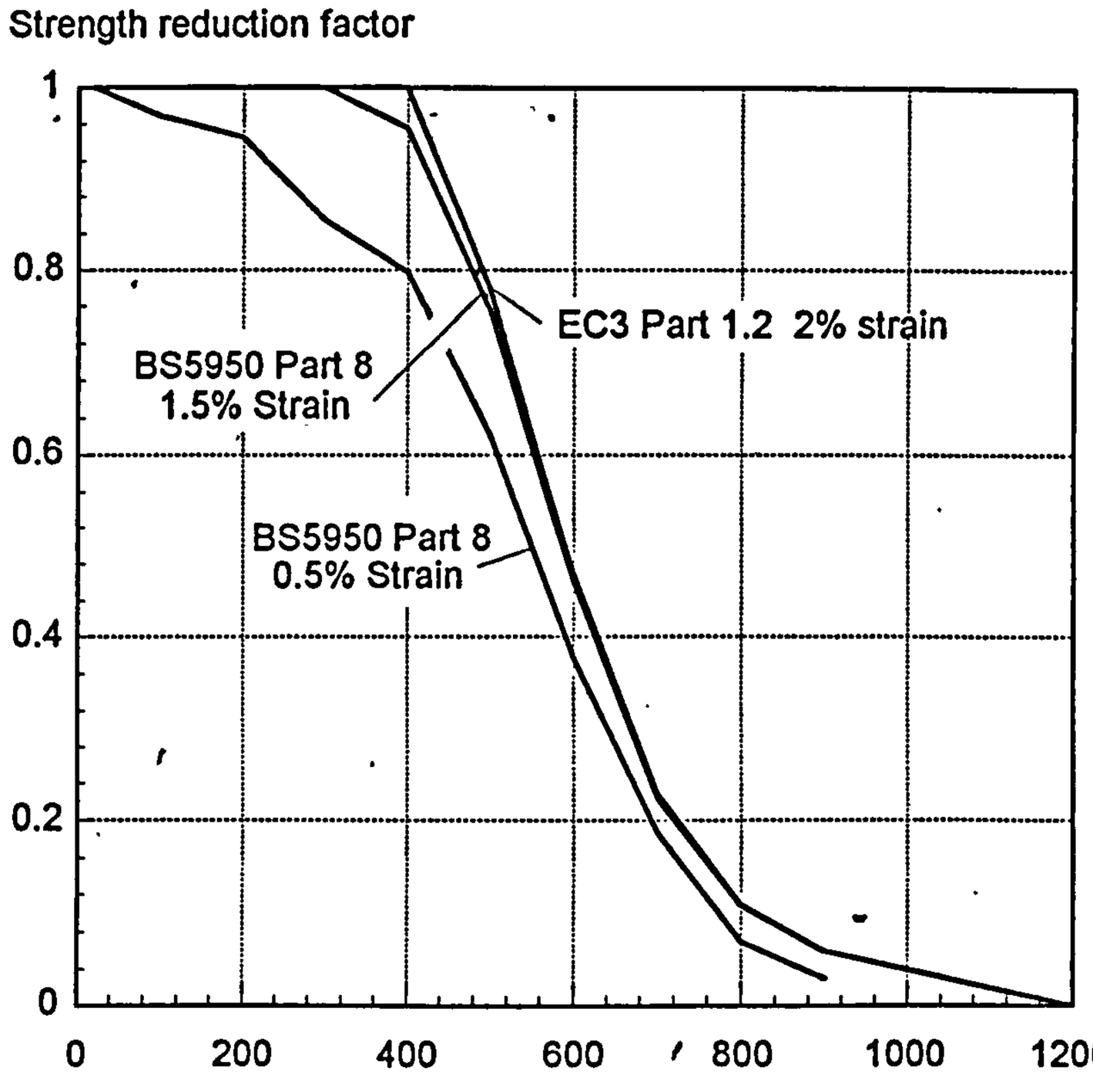

Fig. 1.06: Strength reduction factors for structural steel at elevated temperatures.

The specific heat of steel is defined as the heat stored (in Joules) in a unit mass of steel for 1°C temperature rise. Generally a constant value of 520J/(kg°C) may be assumed for the specific heat of steel, or more accurately up to temperatures of 725°C the following equation may be used[10]:

$$C_s = 0.47 + 2.0x10^{-4} t_s + 38.0x10^{-8} t_s^2 \qquad (kJ/kg^\circ C) \qquad (1.04)$$

where,

C_s = specific heat of steel,

t_s = temperature of steel.

Above 725°C the specific heat of steel rises rapidly due to the changes in its internal lattice structure.

Thermal conductivity is defined as the amount of heat in unit time (in Watts) which passes through a unit cross-sectional area of material for a unit temperature gradient. For steel this value is very high, being 50 times greater than concrete and 500 times greater than vermiculite-cement (which is used as a typical fire protection material). The thermal conductivity of steel can be taken as 37.5 W/m°C or more accurately as[10],

$$k_s = 52.57 - 1.541\times10^{-2}t_s - 2.155\times10^{-5}t_s^2 \qquad (W/m°C) \qquad (1.05)$$

where,
K_s = thermal conductivity of steel,
t_s = temperature of steel.

Poisson's ratio and the density of steel are almost temperature-independent and are taken as 0.3 and 7850 kg/m³ respectively.

1.2: STRUCTURAL COMPUTER MODELLING.

Due to the high cost and physical limitations of furnace testing, it was identified at a very early stage that reliable analytical models were required as a cost effective method of obtaining a comprehensive knowledge of the factors which affect members' response. Development of modelling techniques, together with limited fire tests on simple frameworks[13], also highlighted the need to consider restraining effects which are encountered in actual steel-framed buildings.

One of the earliest analyses of steel members in fire was presented by Witteveen[14] in 1967. He estimated the collapse temperatures of steel beams using a plastic analysis with temperature-dependent yield stresses. Uniform temperature and free thermal expansion were assumed. In 1972 Marchant[15] presented an elastic-perfectly plastic method for the analysis of frames. Degradation of both the elastic modulus and yield stress were included, together with the capability of including a linear temperature variation through the cross-section and the effects of thermal expansion. Also in 1972 Knight[16] produced a beam analysis assuming elastic-perfectly plastic stress-strain characteristics which degraded with temperature. Within his work he highlighted the significant effect of design stress levels at various temperatures, and of restraint against thermal expansion, on the predicted failure temperatures of beams. In 1973 Ossenbruggen, Aggarwal and Culver[17,18,19] presented a method of analysing axially loaded steel columns, subjected to thermal gradients through the cross-section and along the length, using Newmark's numerical integration method. Their adopted

stress-strain curves were elastic-perfectly plastic and had been proposed by Brockenbrough[20]. Cheng and Mak[21], in 1975, developed a finite element program for the analysis of plane steel frames in fire. Elastic-perfectly plastic stress-strain characteristics were assumed and also thermal creep deformations were included. Based on the same theory but using different material properties and thermal characterises, Furumura and Shinohara[22] investigated the behaviour of protected isolated columns. A simplified analytical method for beams and beam-columns at elevated temperatures was presented by Kruppa[23] in 1979. This method assumed elastic-perfectly plastic stress-strain characteristics and compared the ultimate stress at ambient temperature with the stress at an assumed temperature under a given load.

In 1981 Iding and Bresler[24] developed a computer program called FASBUSII (Fire Analysis of Steel BUilding Systems), which modelled both the steel frame and the flooring system. They adopted a finite element method, with the frame being represented by one-dimensional 2-noded elements and the flooring system being represented by two-dimensional 3-noded plate elements. Bi-linear stress-strain curves for steel were assumed and considerable variation of material properties and temperature through the members could be modelled. The first finite element analysis of plane frames subjected to fire to include geometrical non-linearity was developed by Jain and Rao[25] in 1983. The ability to model creep deformations was also included within their analysis. Non-linear material properties of steel at elevated temperatures were included within the finite element method by Baba and Nagura in 1985[26]. The material properties were derived from experimental results, and from their analyses it was concluded that non-linear material behaviour could not be ignored.

In 1987 a computer model called CEFICOSS[27] (Computer Engineering of FIre design of COmposite and Steel Structures) was developed jointly by ARBED-Research, Luxembourg and Franssen at The University of Liege, Belgium. The analysis uses beam-column finite elements and is capable of analysing two-dimensional semi-rigid composite frames. The computer model can also carry out the thermal analysis of the steel members using a finite difference method. The model has recently been extended by Franssen to include three-dimensional behaviour of frames, but at present no published data is available on this area of work. Also in 1987, Sharples[28] developed a program called ELTEMP. This was based on an original geometrically non-linear spread-of-yield program called INSTAF, written by El-Zanaty and Murray[29] in order to study the two-dimensional behaviour of steel frames at ambient

temperature. Sharples used the program to investigate the behaviour of columns subjected to thermal gradients through their cross-section, eccentric loading and any initial out-of-straightness.

Olawale,[30,31] in 1988, developed a finite strip method for the analysis of perfect isolated columns in fire. This analysis was based on small-deflection theory and considered residual stresses, load eccentricity and local buckling. The developed program was used to obtain solutions for a wide range of perfect columns. A secant stiffness approach for the analysis of flexural members was developed by El-Rimawi[32,33] in 1989, using a Ramberg-Osgood representation of the stress-strain data presented in BS5950 Part 8. This program was quickly extended to analyse two-dimensional composite frames with semi-rigid joints.

Following the work by Sharples, Saab[34,35] also extended the program INSTAF to include elevated temperature material properties. He used his program to investigate the behaviour of plane non-sway and sway frames in fire conditions, assuming various heating and protection schemes. Recently a three-dimensional semi-rigid composite frame analysis called FAUST (Fire And Ultimate load analysis of STructures), has been developed at City University, London. The model was developed by Jeyarupalingam and Virdi[36] and was an extension of the numerical method developed by Virdi *et al* [37] for the inelastic analysis of columns at ambient temperature. The method is based on establishing an equilibrium deflected shape using the moment-thrust-curvature relation for each increment of load, time or temperature. At the Building Research Establishment, Wang *et al* [38] have developed a computer model capable of analysing three-dimensional semi-rigid composite steel frames at elevated temperatures. Recently Wang extended the program to include shell elements to represent floor slabs, but at the present time very little published reporting is available on this work.

The developments conducted by Saab to the original program INSTAF have further been extended by Najjar[39,40] to include three-dimensional behaviour of steel members at elevated temperatures, which also incorporates warping characteristics. Najjar's program is capable of analysing rigidly jointed three-dimensional bare steel frames. Within his formulation every effort was made to retain higher-order terms, resulting in a very accurate treatment of geometric non-linearity, together with the capacity to allow for considerable variation in cross-sectional properties. The research work presented here is based on an extension of Najjar's computer model, and is discussed in Chapter 2.

2.0 THE DEVELOPMENT OF THE FINITE ELEMENT MODEL.

The finite element model adopted was originally based on a frame program embodying geometrical non-linearity and spread-of-yield, written by El-Zanaty and Murray,[29] in order to study the two-dimensional behaviour of steel frames at ambient temperature. This program was extended first by Saab[34,35] to include elevated temperature effects, and more recently by Najjar[39,40] to analyse three-dimensional bare steel frame behaviour. At each development stage extensive validation was carried out and documented. This validation showed that the model is very accurate for large-deflection problems, both at ambient and elevated temperatures. The research work presented here is based on an extension of Najjar's program, to include the following capabilities.

1. The introduction of spring elements to represent semi-rigid connection characteristics, which degrade at elevated temperatures. The ability to model the unloading characteristics of these connections has also been included.
2. The facility to place the nodal point at any position on or outside the cross-section, which allows external loads to be placed at any position relative to the beam's centroid. This facility will also allow the connection of two-dimensional shell elements to one-dimensional beam elements.
3. An extension of the formulation to include flexural shear forces, which allows lateral-torsional buckling at ambient and elevated temperatures to be modelled.
4. The inclusion of shell elements to represent the continuous floor slab.
5. A proper treatment of strain reversal in cooling.

These extensions constitute the major analytical developments and will be discussed in more detail in the relevant chapters. The formulation of the model up to the completion of Najjar's research is not repeated here (although extensions to the formulation are shown in relevant chapters). Instead a summary is presented which explains the physical mechanics of the model.

The beam-columns are represented by 2-noded one-dimensional line elements. Each node has eight degrees of freedom in local coordinates, which transform into 11 degrees of freedom in global coordinates, as shown in Fig. 2.01.

As with any finite element solution of continuum problems, the physical beam length is separated into imaginary (finite) elements connected at nodal points. The reference axis (and thus the nodal positions) is placed at the centroid of the section, which is

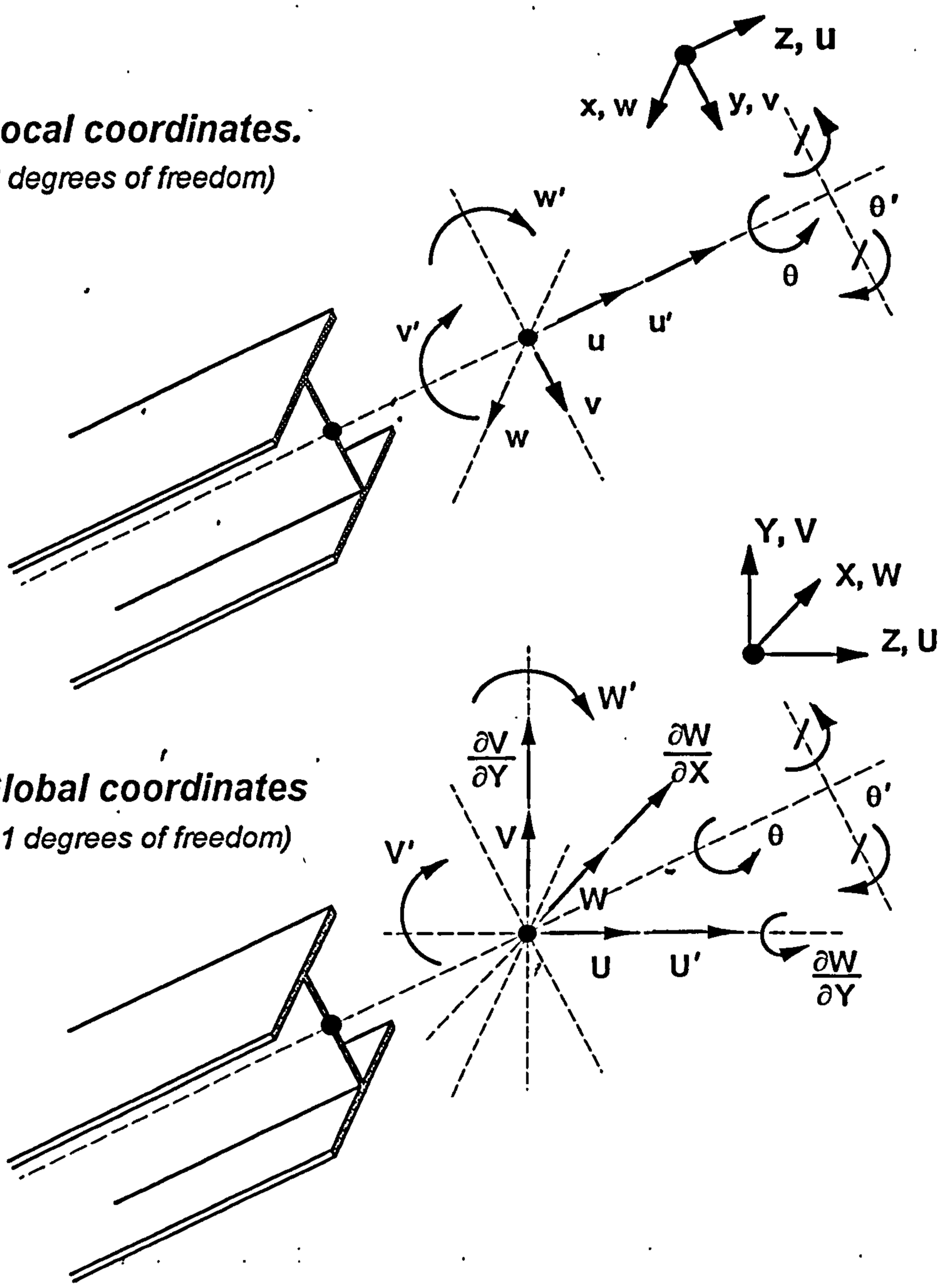

Fig 2.01: Degrees of freedom in local and global coordinates.

calculated at ambient temperature and remains static. The displacements of the nodal points are the basic unknown parameters of the problem. By adopting the displacement field finite element procedure[42], which is easier to implement than the stress field, interpolation (shape) functions are used to define uniquely the displacement of the reference axis within an element bounded by nodal points. This model uses standard cubic polynomial interpolation functions[42]. Since the displacement can be defined at any point on the cross-section within an element, the state of strain can also be obtained by using a large displacement-strain equation[43].

This equation will introduce, by retaining higher order terms, non-linear geometrical behaviour within the formulation. Applying the constitutive properties of steel the state of stress throughout the member can be calculated, together with the boundary (nodal) stresses. As with typical discrete structural analysis, equilibrium is enforced between boundary stresses and the externally applied loads.

The simplest method of enforcing equilibrium at nodal points is to use the Principle of Virtual Work, as shown in equation (2.01)

$$\delta W = \int_V \sigma_z \, \delta\varepsilon_z \, dv - \langle Q \rangle \{\delta q\} = 0 \qquad (2.01)$$

where,

σ_z = axial stress,

$\delta\varepsilon_z$ = virtual axial strain (corresponding to the imposed virtual displacements),

$\langle Q \rangle$ = row vector of external loads,

$\{\delta q\}$ = column vector of imposed virtual displacements.

Following the standard finite element procedure[41,42] equation (2.01) results in the standard stiffness relationship of,

$$[K] \{q\} = \{Q\}$$

where,

$[K]$ = tangent stiffness matrix,

$\{q\}$ = vector of nodal displacements,

$\{Q\}$ = vector of nodal forces.

For a non-linear analysis (iterative process) the above equation becomes[43],

$$[K] \{\Delta q\} = \{\Delta Q\} \qquad (2.02)$$

where,

$\{\Delta q\}$ = vector of incremental nodal displacements,

$\{\Delta Q\}$ = vector of out-of-balance nodal forces.

As can be seen from the virtual work equation a volume integration of the element is required. The numerical method adopted is Gaussian Integration[41,44], which evaluates first the integral over the cross-sectional area (using simple numerical methods) at

sampling (Gauss) points, and with the use of weighting factors completes the calculation of internal work by integrating along the length of the element. The position of the Gauss points, together with the corresponding weighting factors, will give the maximum accuracy of the integration possible with the number of sampling points used. Within this model four Gauss points are used for each element, and the position of these points along the length of the beam together with the weighting factors can be obtained from any good numerical text book[41,44].

Integration over the cross-section results in stress resultants, which can be obtained from sectional properties, or more easily for inelastic cases by direct numerical integration of the stresses. To allow a considerable variation of stress through the cross-section, displacements and strains are defined at 13 points (splitting the section into 12 segments) as shown in Fig. 2.02.

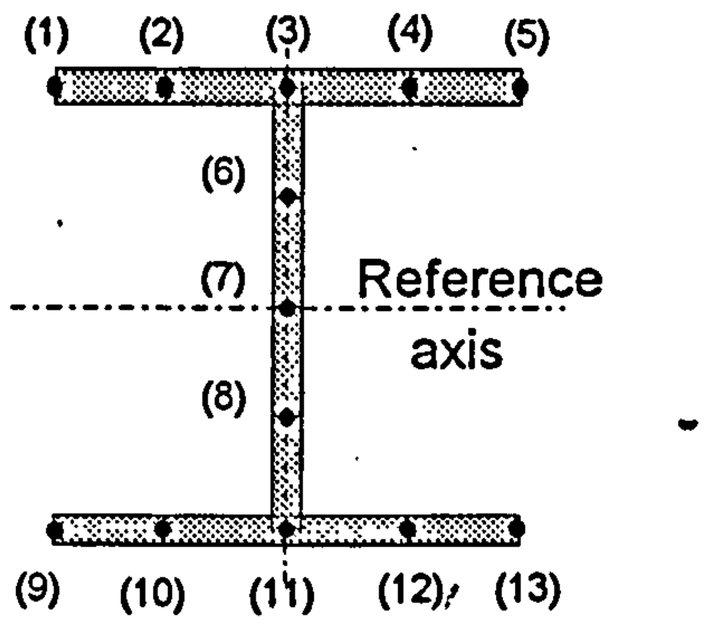

Fig. 2.02: Positions on the cross-section at which displacements, strains and stresses are defined.

Since an iterative method (Newton-Raphson) is required due to non-linearities, the incremental stress resultants are required for the formulation of the tangent stiffness matrix. The calculation of these values requires the sectional and sectorial[45,46] (warping) properties, which are calculated numerically in relation to the reference axis.

Material non-linearity enters the formulation via the constitutive model, relating strain to stress and also specifying the tangent modulus of the material at a specific strain value. To calculate the sectional and sectorial properties, taking into account material non-linearity, the transformed section concept was used[47]. This method transforms the thickness of each of the twelve segments, shown in Fig. 2.02, based on the average tangent modulus of the material within the segment, thus creating an equivalent elastic cross-section. This is shown more clearly in equation (2.03).

$$b_r^t = \frac{E_t\, b_r}{E} \qquad (2.03)$$

where,

b_r^t = transformed thickness of the segment,

E_t = average tangent modulus of the material within the segment,

b_r = original thickness of the segment,

E = original Young's Modulus of the material within the segment.

One of the assumptions adopted within the formulation is the requirement of placing external loads at nodal positions only. It was found in the validation of inelastic behaviour carried out by El-Zanaty and Murray[29] that the spread of yield in the proximity of nodal areas was not reflected in the element tangent stiffness, due to the distribution of the four Gauss points used in the numerical integration. It was found that better results were obtained by subdividing the member into three elements, with the central element being 80% of the length of the member. This results in the two outer elements having four Gauss points which are clustered near the nodal position causing inelastic strains to be incorporated within the element stiffness matrix when they occur. An element stiffness matrix is then formed by applying a static condensation scheme to eliminate the internal degrees of freedom created by this sub-division. The element stiffness matrix is then transformed from local to global coordinates, and using the direct stiffness method the contribution from the element is included within the structural stiffness matrix. The above procedure is basically automating the requirement of refining the size of the elements in areas of high stress gradients. However care is still required (as with all finite element models) by the user when defining the element layout, especially in areas where these high stress gradients are expected.

Since the model is highly non-linear an iterative process is required to obtain equilibrium. The basic Newton-Raphson method has been used and is summarised below.

1. With reference to Fig. 2.03 consider the analysis at 20 °C. At the first iteration the total displacements throughout the structure are zero, resulting in zero internal forces and an elastic stiffness matrix based on the sectional properties.
2. The equation,
   $$\{\Delta q\} = [K]^{-1}\{\Delta Q\} \qquad (2.04)$$
   is solved, where $\{\Delta Q\}$ is the vector of out-of-balance forces, which for the first iteration at 20 °C corresponds to the external loads.

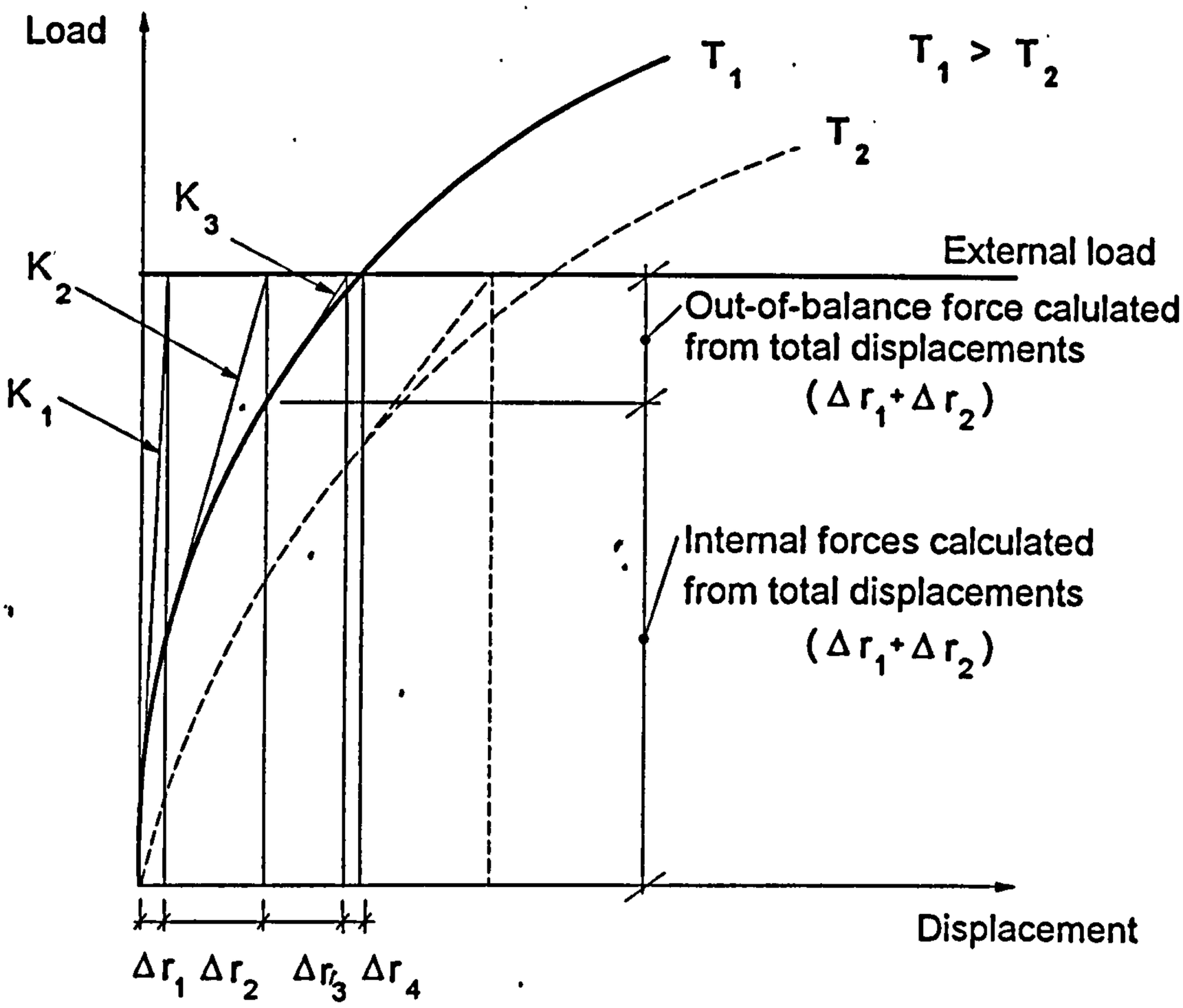

K_1 = elastic stiffness matrix.

K_2 = stiffness matrix calculated from total displacements (Δr_1)

K_3 = stiffness matrix calculated from total displacements ($\Delta r_1 + \Delta r_2$)

Fig. 2.03: Newton-Raphson procedure.

3. The incremental displacements are added to the total displacements, defining the state of strain throughout the member. The out-of-balance forces are calculated together with the tangent stiffness matrix. Equation (2.04) is once again solved for incremental displacements. These are then added to the total displacements and the process repeated until the incremental displacements and unbalanced forces are small enough.

The same procedure is adopted when the temperature of the section increases, except for the inclusion of thermal effects which are explained below. It should be noted that the displacements calculated from the previous analysis at equilibrium are used as a 'starting point' for the solution sequence.

For ease of explanation of the inclusion of thermal effects into the model consider the example of a simply supported beam, which could either be unrestrained or restrained against axial movement and has a point load at mid-span. Consider first the

unrestrained case. At ambient temperature the iterative structural analysis is carried out and at equilibrium the total displacements are obtained. With the external load on the beam remaining constant the temperature is increased in a pre-determined fashion, which for this example is assumed to be represented by the profile shown in Fig. 2.04.

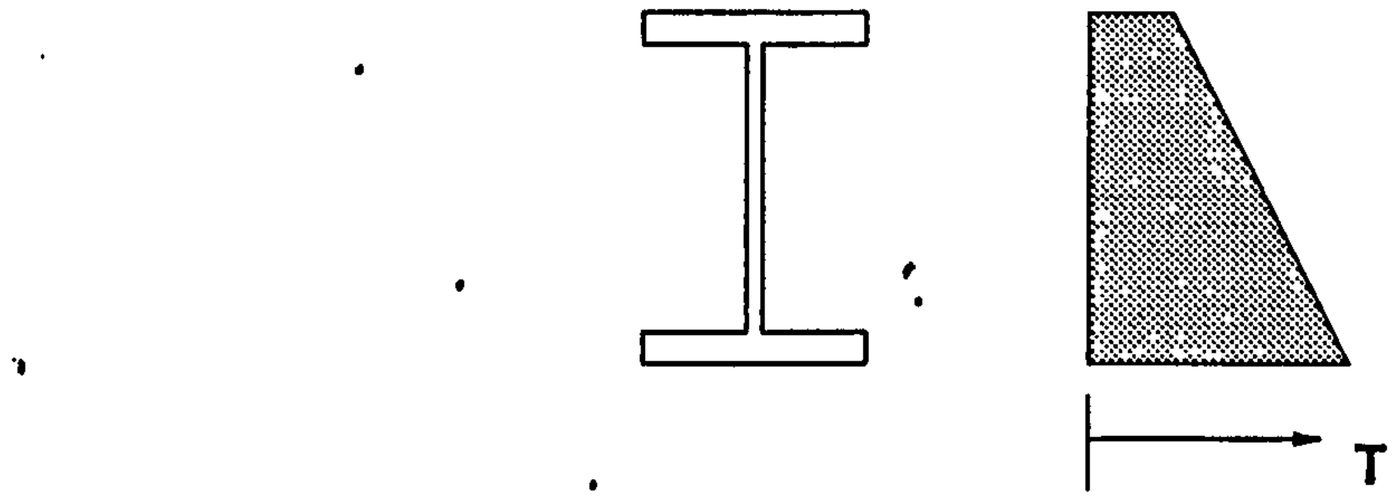

Fig. 2.04: Temperature profile adopted.

For the first iteration of the analysis carried out at this stated temperature profile, the total displacements (obtained from the previous analysis) are used to define the state of strain throughout the member. Thermal strains are calculated, based on the temperature profile and added as mechanical strains of the opposite sign, as shown in Fig. 2.05.

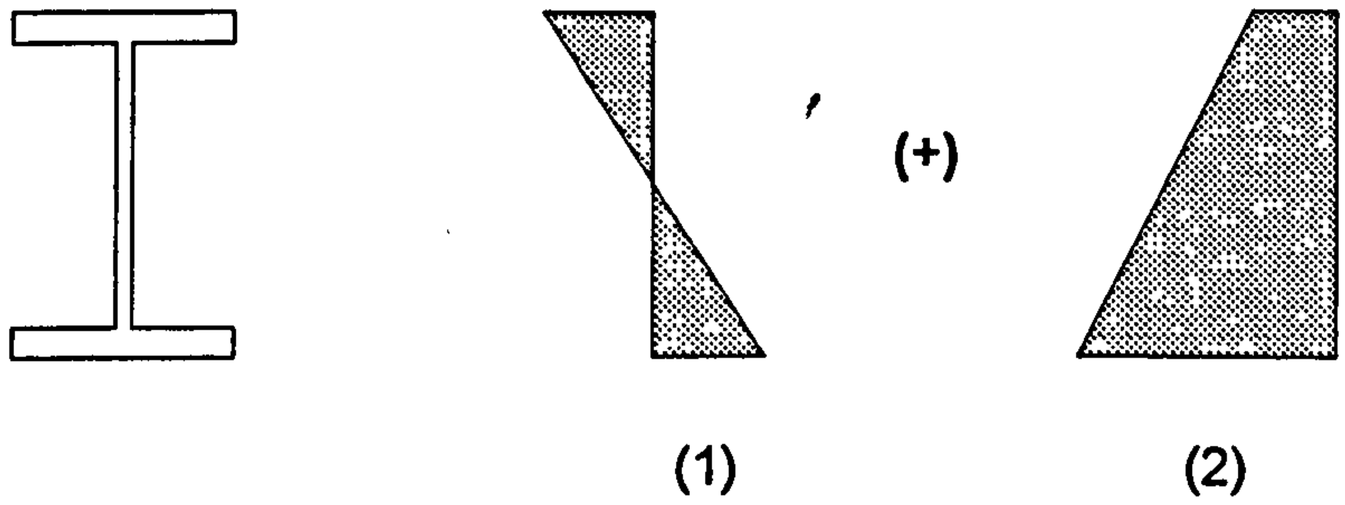

(1). Strain profile based on the displacements calculated from the previous analysis.
(2) Strain profile (of the opposite sign) caused by thermal effects.

Fig. 2.05: The addition of thermal strains on the first iteration.

Now the unbalanced force is calculated from,

$$\{\Delta Q\} = \{Q_{applied} - Q_{internal} - Q_{thermal}\} \qquad (2.05)$$

and solving equation (2.04) produces incremental displacements which include thermally induced displacements. The sign of thermally induced axial displacements will change to the correct one (expansion) due to the negative sign of the unbalanced

thermal forces. These incremental displacements are added to the total displacements which are then used to define the state of strain in the next iteration. Therefore for equilibrium of internal and external forces to occur the thermal strains must be removed from the state of strain calculated from the total displacements (which include thermally induced displacements) in successive iterations. For the restrained case the same procedure is followed, except that, in the first iteration, when thermal strains are added as mechanical strains the resulting displacements are prevented by the relevant boundary conditions. On successive iterations, when thermal strains are removed from the strain state (calculated based on total displacements) internal thermal forces are induced into the member.

For the next increase in temperature (say from T_2 to T_3) the same procedure explained above is followed. On the first iteration for the analysis at temperature T_3 the total state of strain is calculated from the total displacements obtained from the previous analysis at temperature T_2 which contain any free thermal displacements. The thermal strains resulting from T_2 are removed from the total strains, leaving only mechanical strains. The incremental thermal strains resulting from the rise in temperature from T_2 to T_3 are then added (as before) as mechanical strains of the opposite sign. This results in calculation of the incremental displacements which will include the additional thermally induced displacements caused by the rise in temperature from T_2 to T_3. These incremental displacements are added to the total displacements, which now include the total thermal displacements, and so thermal strains must be removed on successive iterations to ensure equilibrium. As explained above, if the beam is restrained the thermal displacements are prevented thus removing thermal strains on successive iterations results in internal thermal forces.

2.1: IDENTIFICATION OF STRUCTURAL FAILURE BY THE COMPUTER MODEL.

2.11: CONVERGENCE CRITERIA.

Two convergence criteria based on incremental displacements and out-of-balance forces are used within the model to check if the numerical solution has been obtained within specified tolerances, so that the iterative process can be terminated. The first convergence criterion consists of a check on the incremental displacements, which should become progressively smaller as the iterations increase and the true solution is approached. This displacement convergence criterion is given [41,43,48] by,

$$\frac{\|\Delta q\|_2}{\|q+\Delta q\|_2} \leq TOL \qquad (2.06)$$

where, $\|\Delta q\|_2$ is the norm vector of the incremental displacements given by,

$$\|\Delta q\|_2 = \left(\sum_{i=1}^{n}\{q_i\}^2\right)^{1/2} \qquad (2.07)$$

Note that n is the number of elements in the vector, which corresponds to the number of degrees-of-freedom, and $\|q+\Delta q\|_2$ is the norm vector of total displacements, (updated for each iteration) given by,

$$\|q+\Delta q\|_2 = \left(\sum_{i=1}^{n}(\{q_i\}+\{\Delta q_i\})^2\right)^{1/2} \qquad (2.08)$$

and 'TOL' is the tolerance specified.

The second criterion consists of a check on convergence of the out-of-balance forces which is given [41,43,48] by,

$$\frac{\|\{Q_{external}\}-\{Q_{internal}\}\|_2}{\|\{Q_{external}\}\|_2} \leq TOL \qquad (2.09)$$

where, $\|\{Q_{external}\}-\{Q_{internal}\}\|_2$ is the norm vector of the out-of-balance forces given by,

$$\|\{Q_{external}\}-\{Q_{internal}\}\|_2 = \left(\sum_{I=1}^{n}(\{Q_{I(external)}\}-\{Q_{I(Internal)}\})^2\right)^{1/2} \qquad (2.10)$$

and $\|\{Q_{external}\}\|_2$ is the norm vector of the externally applied forces, given by,

$$\|Q_{external}\|_2 = \left(\sum_{I=1}^{n}\{Q_{I(external)}\}^2\right)^{1/2}$$

Care is required when specifying the tolerance limits in using the above convergence criteria. If the tolerance is too loose inaccurate results are obtained, whereas if the tolerance is too tight numerous extra iterations are carried out to obtain an unjustifiable increase in numerical accuracy for a process which is inherently approximate.

2.12: TERMINATION OF THE MODEL DUE TO IDENTIFICATION OF STRUCTURAL FAILURE.

For each iteration the linear equation (2.02) has to be solved for incremental displacements, which is carried out using Gaussian Elimination. Each step of the Gaussian Elimination can be physically interpreted as the relaxation of a constraint on the structure[41], where the constraint at any step corresponds to a degree of freedom being eliminated. Therefore the remaining coefficient matrix at any stage is the

stiffness matrix of the structure with the constraints corresponding to the eliminated equations relaxed. If any of the diagonal terms of this remaining matrix are negative, the structure must be unstable. Thus the program is terminated if a negative number appears on the leading diagonal of the stiffness matrix, and the critical value, which in this case is in terms of temperature, is assumed to be reached. To ensure that the correct failure point is achieved calculation of the stiffness matrix must be correct and small changes in temperature must be adopted near the failure point.

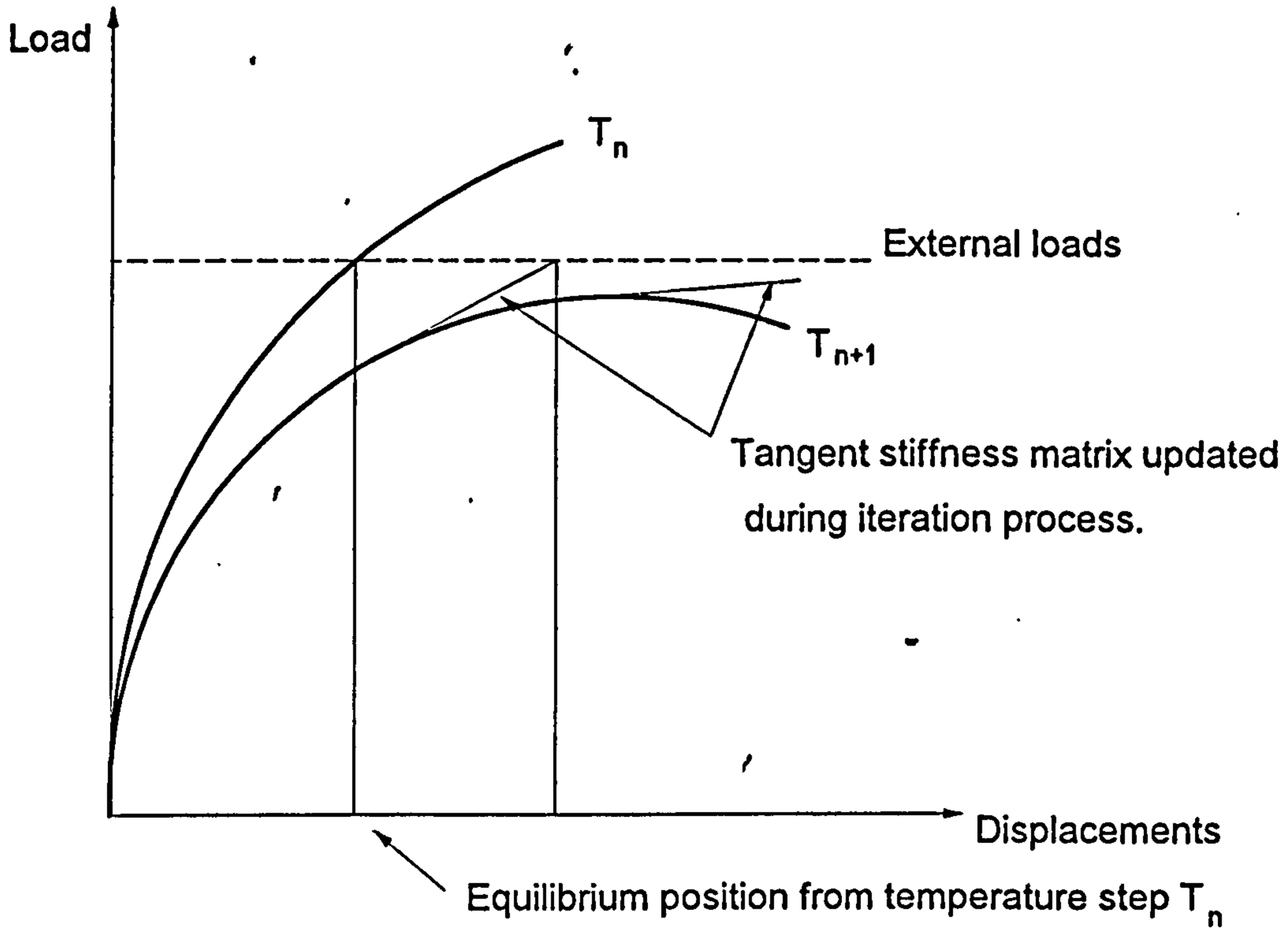

Fig. 2.06: Newton-Raphson procedure in the proximity of structural failure.

An automatic procedure is implemented within the model to refine the incremental increase in temperature when the structural failure point is approached. This procedure is required to ensure that 'true' failure is identified, and that termination of the analysis due to numerical failure (which could be caused by a large increase in temperature) is not encountered. From the start of the analysis the temperature is increased in increments specified by the user (usually 50-100°C). At some stage the program will indicate a negative number on the diagonal of the stiffness matrix. This is shown in Fig. 2.06 as occurring at temperature T_{n+1}. However since a more accurate prediction of failure temperature (within the approximations of the model) is required, and to ensure that numerical instability does not occur at temperature T_{n+1}, the incremental increase of temperature from the last recorded equilibrium position at T_n is reduced to 10% of the original increment. The analysis then continues from T_n

until a negative number once again appears on the diagonal of the stiffness matrix. If numerical instability originally occurred at T_{n+1} then the analysis will continue past this temperature using the reduced increment. The process of returning to the last recorded equilibrium position and reducing the temperature increment to 10 % is repeated each time failure occurs, until the temperature increment is equal to or less than 0.1°C.

2.13: EXTENSION OF THE MODEL TO INCLUDE THE MODIFIED NEWTON-RAPHSON ITERATIVE TECHNIQUE.

An alternative iterative technique based on the Modified Newton-Raphson method was included within the model by the author. The basic modified method consists of using the stiffness matrix calculated during the first iteration of the analysis for all successive iterations until equilibrium is reached, as shown in Fig. 2.07. Using this technique, termination of the analysis occurs by divergence of either the out-of-balance forces or the incremental displacements. Although savings in computational terms are achieved by the need to calculate the stiffness matrix only once, the number of iterations required by this method to reach equilibrium is greatly increased. The advantage of the modified version of the method is that, as the limit point in the force-displacement relationship is approached, the 'zone of attraction' for equilibrium is frequently increased[43].

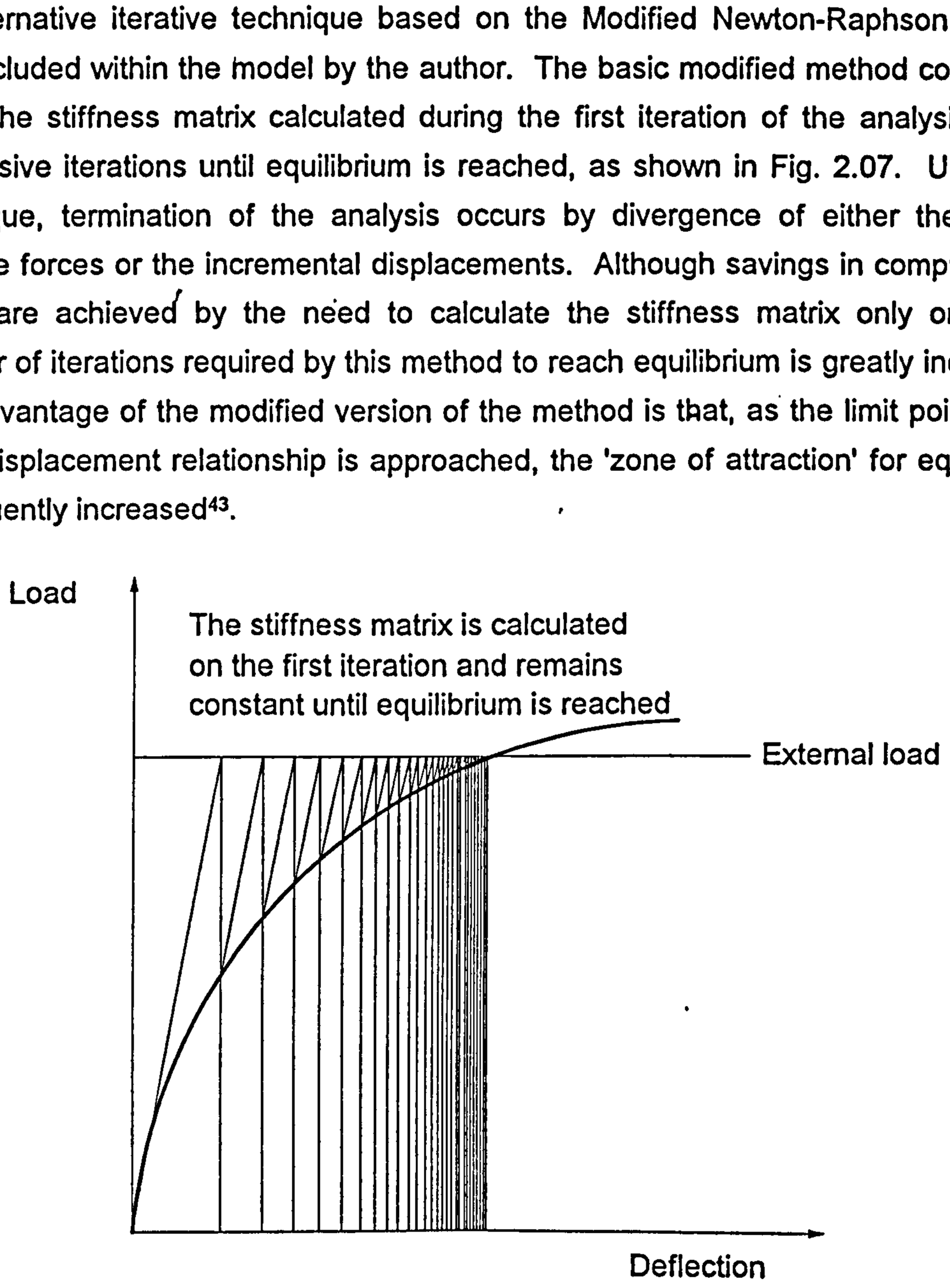

Fig. 2.07: Modified Newton-Raphson procedure.

Following the standard procedure of the Modified Newton-Raphson method the stiffness matrix calculated on the first iteration of each analysis for a stated temperature profile should be kept constant until either equilibrium or failure, identified by divergence, occurs. However within the model the stiffness matrix calculated during the first iteration is based on total displacements which include any incremental displacements induced by thermal effects. It was therefore proposed to continue to calculate the stiffness matrix on the second iteration (where these thermal effects are removed) and then keep this constant throughout the analysis. A possible alternative to overcome the problem of thermal effects when using this iterative method is to keep the stiffness matrix calculated on the first iteration at ambient temperature (which is the elastic stiffness matrix) constant throughout the rise in temperature. However it was found that, due to the high non-linearities typically encountered in elevated temperature analyses of structures, the number of iterations needed to reach equilibrium became very large and impractical even for small structural problems. It was therefore decided to abandon this option and limit the method to keeping the stiffness matrix calculated on the second iteration constant, for each analysis during the rise in temperature.

2.14: COMPARISON OF NEWTON-RAPHSON PROCEDURES.

To compare the two methods of solution the pin-ended strut shown in Fig. 2.08 was analysed. The strut was subjected to a load ratio of 0.6 (in terms of BS5950, Part 1[49]), and had an initial imperfection of length/1000 at mid-height in both positive directions of the displacement axes.

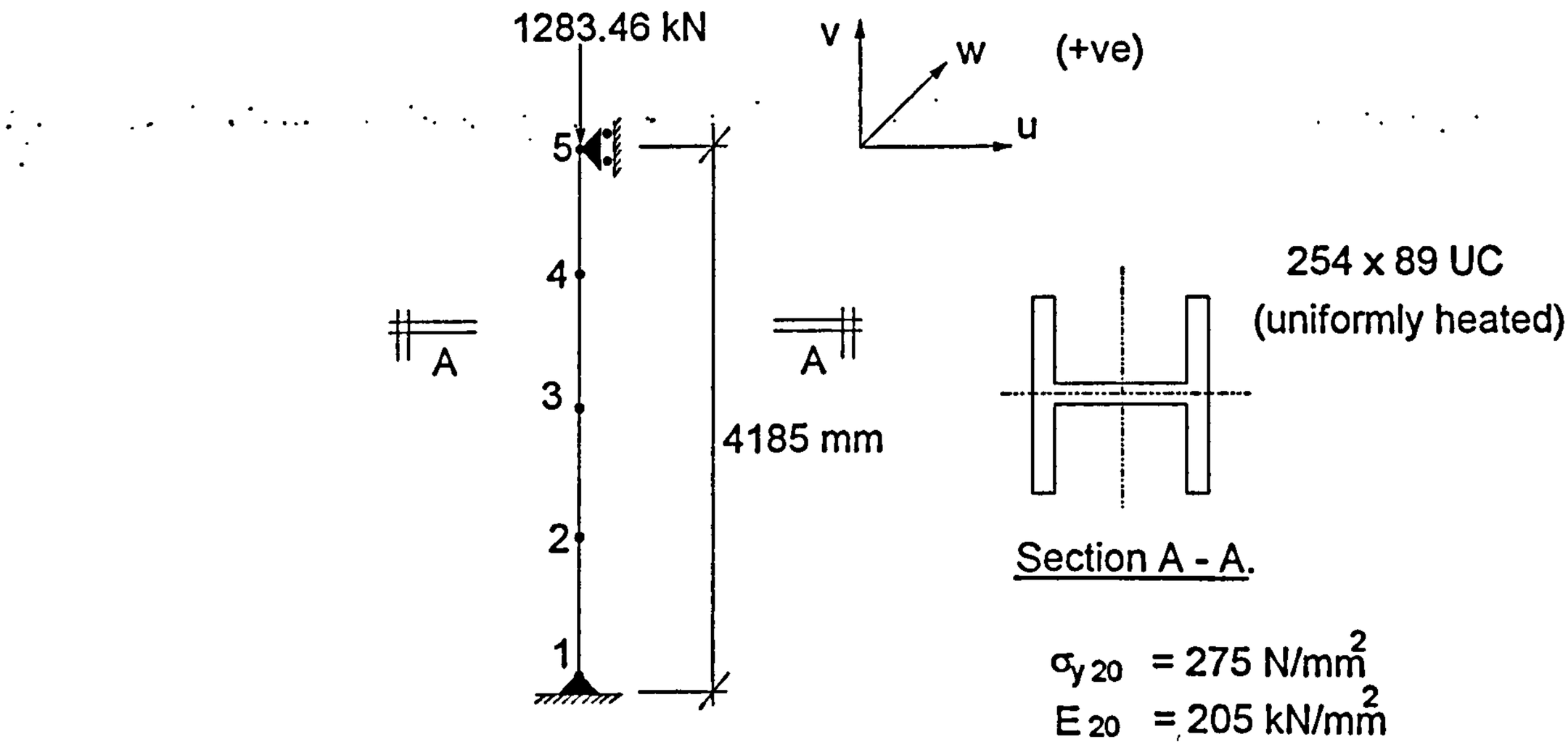

Fig. 2.08: Example used to compare the Modified and original Newton-Raphson methods.

The strut was uniformly heated with an initial incremental increase in temperature of 50°C. The results are presented in tabular form to show the progress of the analyses as the failure point is approached.

Temp.	PROGRAM					
	Newton Raphson			Modified Newton-Raphson		
°C	Iterations	Δv_5	Δw_3	Iterations	Δv_5	Δw_3
20	4	-2.31	1.19	4	-2.31	1.19
50	3	-0.76	1.19	3	-0.76	1.19
100	3	1.87	1.19	3	1.87	1.19
150	3	4.50	1.25	3	4.50	1.25
200	3	7.20	1.31	3	7.20	1.31
250	3	9.97	1.39	3	9.97	1.39
300	4	12.77	1.77	4	12.77	1.77
350	5	15.47	3.03	6	15.47	3.03
400	5	18.38	3.59	6	18.38	3.59
450	9	20.32	11.95	12	20.32	11.95
500	'Failed'			'Failed'		
455	10	20.17	16.68	13	20.17	16.68
460						
455.5	8	20.11	17.70	9	20.11	17.70
456.0	12	20.00	19.27	14	20.00	19.27
456.5	'Failed'			'Failed'		
456.05	10	19.98	19.51	11	19.98	19.51
456.10	12	19.96	19.78	12	19.96	19.78
456.15	13	19.93	20.10	14	19.93	20.10
456.20	17	19.89	20.52	18	19.89	20.52
456.25	44	19.82	21.34	55	19.82	21.34
456.30	'Failed'			'Failed'		

Within the table of results the following notation is adopted,
Δv_5 = displacement in the 'v' direction at node 5,
Δw_3 = displacement in the 'w' direction at node 3.

Table 2.01: Results from the Modified and original Newton-Raphson iterative techniques used when analysing the example in Fig. 2.08.

As can be seen from the results presented both programs, using different iterative techniques, produced exactly the same results. As expected the Modified Newton-

Raphson method used more iterations as the failure (limit) point was approached. The mode of failure for the above example consists of out-of-plane buckling, which is highlighted in Table 2.01 by a rapid increase in the rate of out-of-plane displacement as the failure point is approached.

In the methods of solution presented within this chapter, collapse of the structure is assumed when failure of the iterative solution process occurs. In the case of the Newton-Raphson method this occurs when the stiffness matrix develops a negative number on the diagonal during the Gaussian Elimination procedure. For the Modified Newton-Raphson method failure is identified when divergence of the out-of-balance forces or incremental displacements occur. Every effort has been made, using these methods, to ensure that these collapse loads correspond to the limit points on the load-displacement curve for the structure in question. This is achieved by continually refining the increment in temperature profile as the limit point is approached.

However the only unquestionable method of ensuring that the limit point has been achieved, and that premature structural instability has not occurred due to failure of the iterative process, is to continue the analysis past the limit point. Numerous techniques (the most common are the Arc-Length methods[50]) have been developed at ambient temperature to allow the analysis to continue beyond a limit point. Development of such techniques to allow elevated temperature analysis beyond instability is out of the scope of this Ph.D. project.

3.0: THE INFLUENCE OF STEEL CONNECTIONS ON FRAME BEHAVIOUR AT ELEVATED TEMPERATURES.

Rigid, semi-rigid or simple design methods can be used when analysing steel frame buildings[49]. The rigid design method assumes that the connection stiffness is sufficient to maintain full slope continuity between adjoining members, with full transfer of moment across the connection. This method is used typically for the design of single-storey portal frames and in-situ concrete frames, but due to the cost of ensuring rigid connections the method is not usually employed in the design of multi-storey steel framed buildings. In the semi-rigid design method the true flexural behaviour of the connection is considered, which is represented by the relationship between the moment transmitted by the connection and the relative rotation between adjoining members. Considerable research has been performed[51,52,53,54,55] at ambient temperature into the structural characteristics of different connection details, and their effect on frame behaviour. In a typical multi-storey building the main steel-to-steel connections encountered are beam-to-column flange (major axis), beam-to-column web (minor axis), and beam-to-beam. The physical type of connection can vary, with the most commonly used being extended, flush and partial end-plates, fin plates and web cleats. The actual behaviour of each type of connection will depend on the plate thickness, bolt or/and weld arrangement and the sizes of the connecting members. Therefore due to the large assortment of connections which can be used, together with the increase in complication of the analysis, practising engineers tend to ignore this method of design. In the simple design method pinned connections are assumed to resist shear only with lateral stability being obtained by vertical bracing or concrete shear walls. Multi-storey buildings tend to be designed using this method due to its simplicity.

A reserve of strength and stiffness in simply designed multi-storey buildings will be provided by the actual flexural rigidity of the connections, which can be utilised when analysing frame behaviour in fire conditions. The failure temperatures of beams (defined in terms of a limit on deflection or rate of deflection[7]) will be increased, as shown in Fig. 3.01, by the rigidity of the connections provided that the adjoining members can withstand the transfer of moment. Previously published research[56,57] has stated that no evidence exists at elevated temperatures that connections are the weak link in the design of frames, and although additional forces may develop in the connection caused by the restraint to thermal expansion, premature failure of the connection is not expected. This is mainly due to connections being at a lower temperature than the surrounding members due to the 'massivity' of the plates and

bolts. Although the author agrees with these observations on the performance of connections during the fire, questions must be asked about the behaviour during cooling. If a beam which is restrained from thermal expansion begins to cool, from an inelastic state, it will pull on the surrounding structure inducing high tensile forces which could cause the bolts in the connections to snap. This type of behaviour will be more important in an end-plate type of connection, as observed at the first fire test conducted on the eight-storey test frame at Cardington. Documentation on this test is confidential and unavailable at this time. A more detailed investigation on the behaviour of frames during the cooling phase will be presented in Chapter 7. To allow the influence of the behaviour of connections in simply designed frames to be studied (until the cooling phase is reached in a fire) the model was extended to incorporate spring elements, which can represent the characteristics of any specific connection.

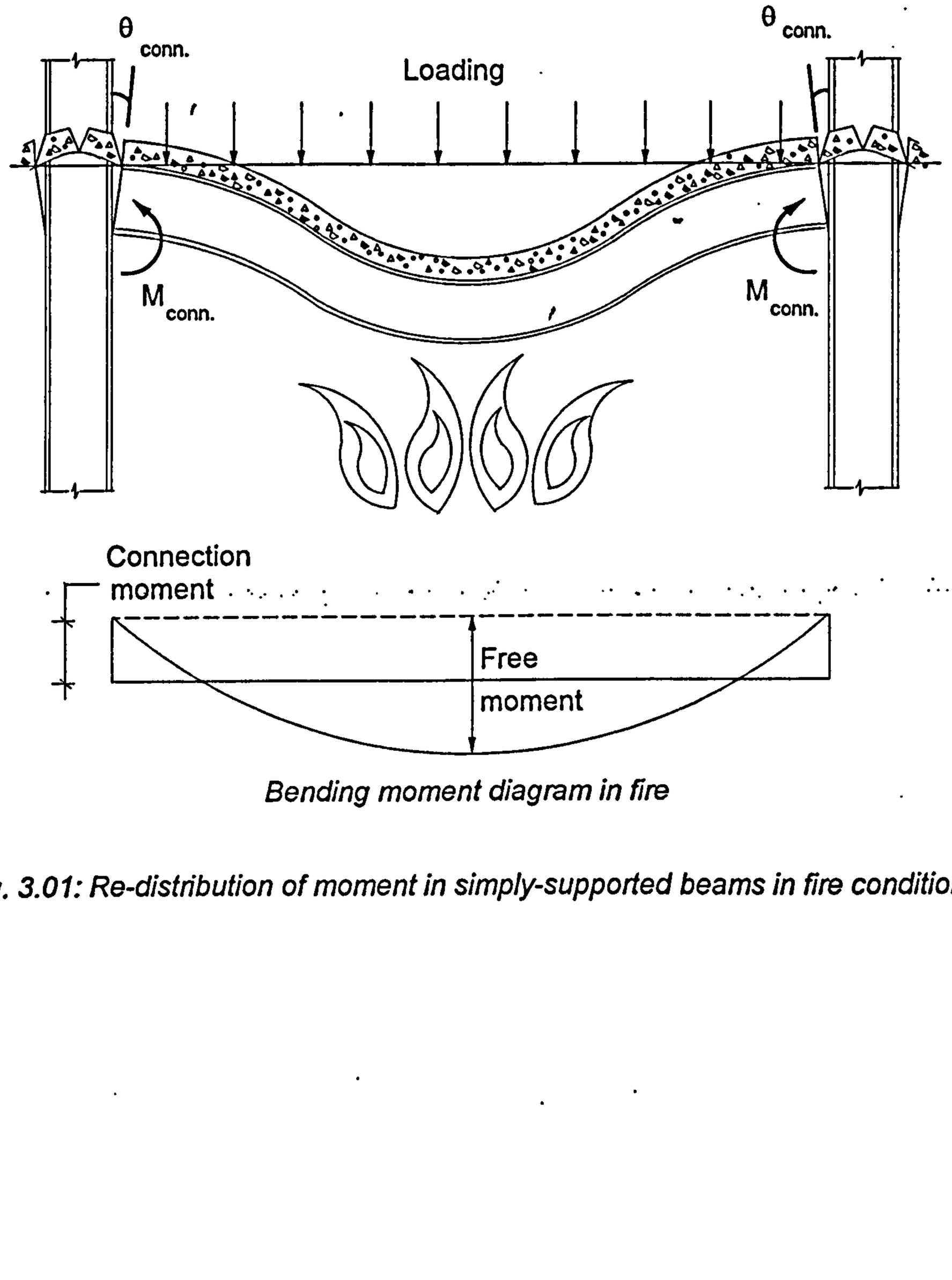

Bending moment diagram in fire

Fig. 3.01: Re-distribution of moment in simply-supported beams in fire conditions.

3.1: DEVELOPMENT AND INCLUSION OF SPRING ELEMENTS INTO THE MODEL

To allow the characteristics of semi-rigid connections to be modelled a two-noded spring element of zero length, with eight degrees of freedom in local coordinates (as shown in Fig. 3.02) was included within the model. Using the standard transformation matrix within the model, the spring element will have eleven degrees of freedom in global coordinates corresponding to the existing beam-column element, which is shown in Fig. 2.01.

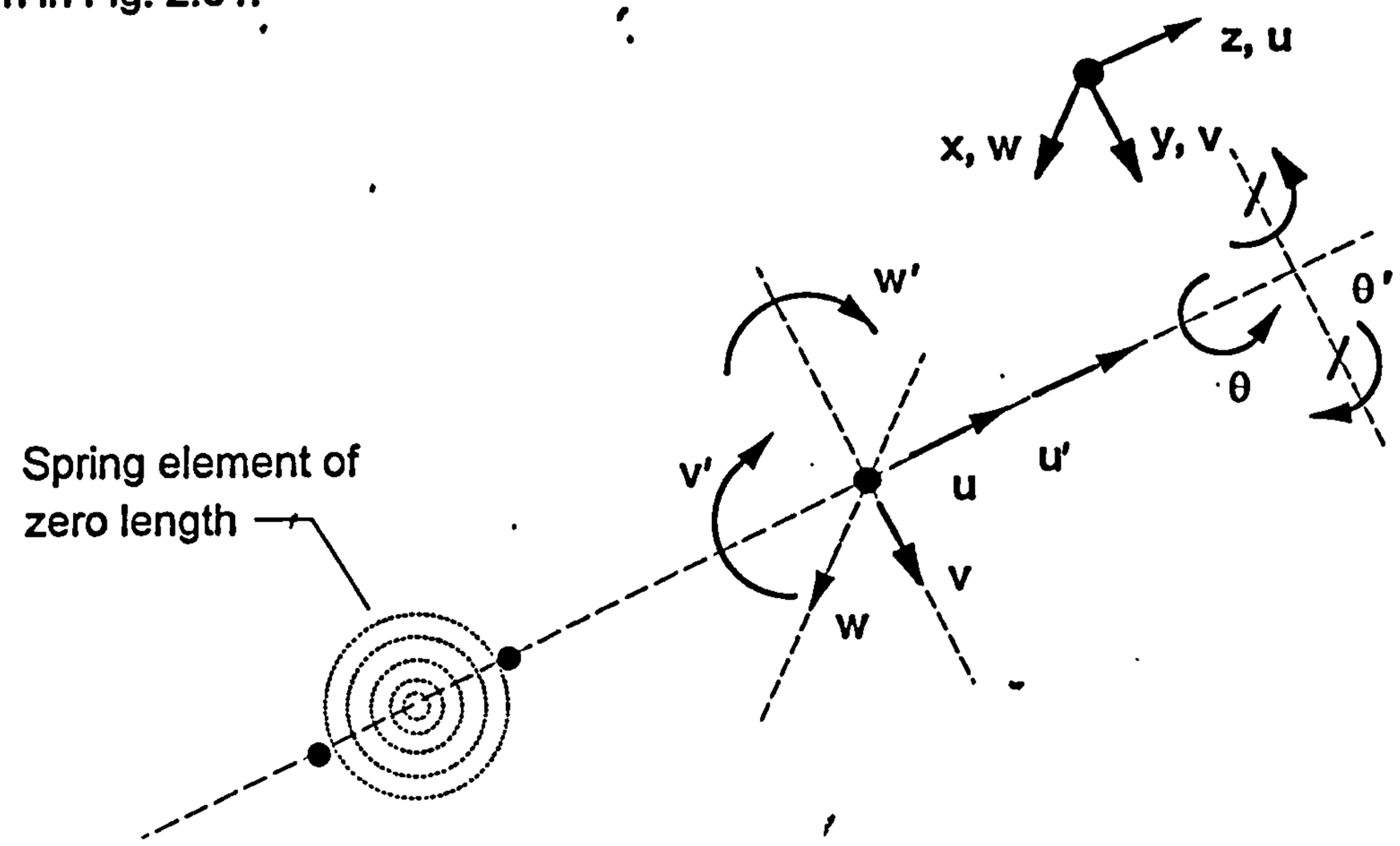

Fig. 3.02: Degrees of freedom for the spring element in local coordinates.

The spring element is very versatile and can be placed at any position within the frame since in-plane, out-of-plane, torsion, warping and translational displacements are represented. The eight degrees of freedom (in local coordinates) were modelled independently creating a stiffness matrix as shown in Fig. 3.03. Each of the degrees of freedom can be represented by an independently specified moment-rotation (or force-displacement) relationship.

3.2: MODELLING SEMI-RIGID CONNECTIONS AT ELEVATED TEMPERATURES.

To model the behaviour of semi-rigid frames in fire, the moment-rotation characteristics of the connections at various temperatures need to be known. Although a vast collection of experimental data exists for joint characteristics at

$$
\begin{bmatrix}
K_u & 0 & 0 & 0 & 0 & 0 & 0 & 0 & -K_u & 0 & 0 & 0 & 0 & 0 & 0 & 0 \\
0 & K'_u & 0 & 0 & 0 & 0 & 0 & 0 & 0 & -K'_u & 0 & 0 & 0 & 0 & 0 & 0 \\
0 & 0 & K_v & 0 & 0 & 0 & 0 & 0 & 0 & 0 & -K_v & 0 & 0 & 0 & 0 & 0 \\
0 & 0 & 0 & K'_v & 0 & 0 & 0 & 0 & 0 & 0 & 0 & -K'_v & 0 & 0 & 0 & 0 \\
0 & 0 & 0 & 0 & K_w & 0 & 0 & 0 & 0 & 0 & 0 & 0 & -K_w & 0 & 0 & 0 \\
0 & 0 & 0 & 0 & 0 & K'_w & 0 & 0 & 0 & 0 & 0 & 0 & 0 & -K'_w & 0 & 0 \\
0 & 0 & 0 & 0 & 0 & 0 & K_\theta & 0 & 0 & 0 & 0 & 0 & 0 & 0 & -K_\theta & 0 \\
0 & 0 & 0 & 0 & 0 & 0 & 0 & K'_\theta & 0 & 0 & 0 & 0 & 0 & 0 & 0 & -K'_\theta \\
-K_u & 0 & 0 & 0 & 0 & 0 & 0 & 0 & K_u & 0 & 0 & 0 & 0 & 0 & 0 & 0 \\
0 & -K'_u & 0 & 0 & 0 & 0 & 0 & 0 & 0 & K'_u & 0 & 0 & 0 & 0 & 0 & 0 \\
0 & 0 & -K_v & 0 & 0 & 0 & 0 & 0 & 0 & 0 & K_v & 0 & 0 & 0 & 0 & 0 \\
0 & 0 & 0 & -K'_v & 0 & 0 & 0 & 0 & 0 & 0 & 0 & K'_v & 0 & 0 & 0 & 0 \\
0 & 0 & 0 & 0 & -K_w & 0 & 0 & 0 & 0 & 0 & 0 & 0 & K_w & 0 & 0 & 0 \\
0 & 0 & 0 & 0 & 0 & -K'_w & 0 & 0 & 0 & 0 & 0 & 0 & 0 & K'_w & 0 & 0 \\
0 & 0 & 0 & 0 & 0 & 0 & -K_\theta & 0 & 0 & 0 & 0 & 0 & 0 & 0 & K_\theta & 0 \\
0 & 0 & 0 & 0 & 0 & 0 & 0 & -K'_\theta & 0 & 0 & 0 & 0 & 0 & 0 & 0 & K'_\theta
\end{bmatrix}
\cdot
\begin{Bmatrix}
u_i \\ u'_i \\ v_i \\ v'_i \\ w_i \\ w'_i \\ \theta_i \\ \theta'_i \\ u_j \\ u'_j \\ v_j \\ v'_j \\ w_j \\ w'_j \\ \theta_j \\ \theta'_j
\end{Bmatrix}
=
\begin{Bmatrix}
U_i \\ U'_i \\ V_i \\ M_{y_i} \\ W_i \\ M_{x_i} \\ M_{z_i} \\ M_{b_i} \\ U_j \\ U'_j \\ V_j \\ M_{y_j} \\ W_j \\ M_{x_j} \\ M_{z_j} \\ M_{b_j}
\end{Bmatrix}
$$

Fig. 3.03: Stiffness matrix for a spring element in local coordinates.

ambient temperature[58,59], very little has been published for high-temperature behaviour. However a series of twelve tests was conducted by the Steel Construction Institute and British Steel[57] to investigate the behaviour of a range of typical connection types in fire. The tests were carried out on small cruciform assemblies of column (203x203x52UC) and beam (305x165x40UB) stubs, and heated according to the standard fire curve[7]. Equal moments were applied to the connections by a symmetrical arrangement of loads, which remained constant during the test, with the rotation being measured at various temperatures. The results produced were in a simplified form,[57] largely for use by structural designers. Since only one test per joint configuration was conducted it was impossible to obtain a family of moment-rotation-temperature curves for any single connection. To obtain these curves a significant number of fire tests would have to be conducted on similar joint configurations at different load levels . However preliminary research has been conducted by El-Rimawi *et al* [60] into the influence of semi-rigid connections, using a two-dimensional frame analysis program called NARR2[32]. To allow this preliminary investigation postulated moment-rotation-temperature curves were constructed from the available data on one of these tests, which consisted of an extended end-plate connecting the beam to the flange of the column (major axis). These curves are reproduced in Fig. 3.04 and are represented by a Ramberg-Osgood type of expression given by,

$$\theta_r = \frac{M}{A} + 0.01\left(\frac{M}{B}\right)^n \qquad (3.01)$$

where,

$\theta_r =$ relative rotation (rads/1000),

$M =$ moment (kNm),

$A, B, n =$ temperature-dependent factors shown in Table 3.01.

At any arbitrary rotation the moment can be obtained from equation (3.01) by applying an iterative technique. The tangent stiffness can be evaluated by differentiating M with respect to θ producing,

$$\frac{dM}{d\theta} = \frac{1}{\frac{1}{A} + 0.01\left(\frac{M}{B}\right)^{n-1}\frac{1}{B}} \qquad (3.02)$$

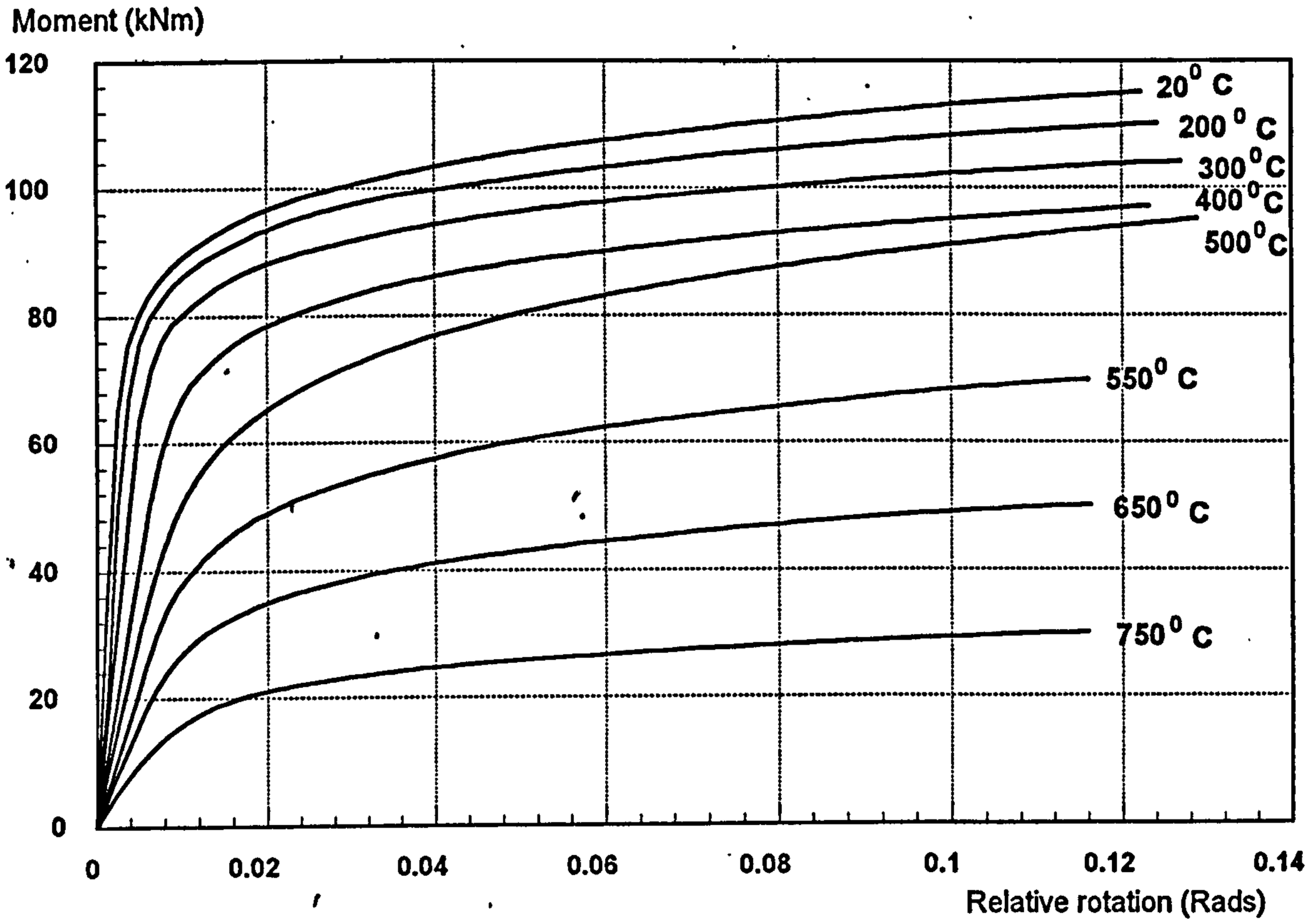

Fig. 3.04: Postulated moment-rotation curves at increasing temperature based on an extended end-plate connection used in one of the tests conducted by Steel Construction Institute and British Steel[57].

Temperature. range.	Equation parameters.		
	A	B	n
< = 50	28.75	49.33	11.08
100	24.38	50.71	11.45
150	22.5	49.36	11.56
200	19.5	51.61	12.40
250	15.9	49.73	11.93
300	13.0	50.85	13.11
350	10.0	46.19	12.11
400	8.13	41.79	11.06
450	7.10	34.19	9.06
500	6.00	23.49	6.68
550	4.50	17.62	6.68
950 = > T = > 600	{(900-T)/350}x4.5	{(900-T)/350}x17.6	6.68

Table 3.01: Temperature-dependent factors for an extended end-plate connection used in one of the tests conducted by Steel Construction Institute and British Steel.

The above characteristics can be used to model in-plane bending only. Since axial and shearing displacements are considered small compared to rotations infinite stiffnesses are assumed between the nodes of the spring element for these degrees of freedom. Very little information has been published about out-of-plane, torsional and warping deformations, and although the program is capable of modelling all these connection characteristics the studies conducted here are limited to two-dimensional behaviour.

3.3: VALIDATION OF THE INCLUSION OF SEMI-RIGID CONNECTIONS INTO THE MODEL.

The plane frame shown in Fig. 3.05 was modelled at elevated temperatures and compared against the results produced by the existing program NARR2[60], which has been extensively validated against experimental results and other computer models. All the members shown in Fig. 3.05, which are grade 43 steel, were uniformly heated at the same rate, except the connections which were assumed to be at 0.7 times the temperature of the bottom flange of the connecting beam. Moment-rotation-temperature characteristics were created in this example by scaling down both the stiffness and strength of the extended end-plate, whose characteristics are shown in Table 3.01, by 50%. This involved scaling down the factors A and B shown in equation (3.01). The vertical deflection of node 6 (centre of the beam) and node 3 (head of the column) are shown in Fig. 3.06, and indicate a very good correlation between the two models.

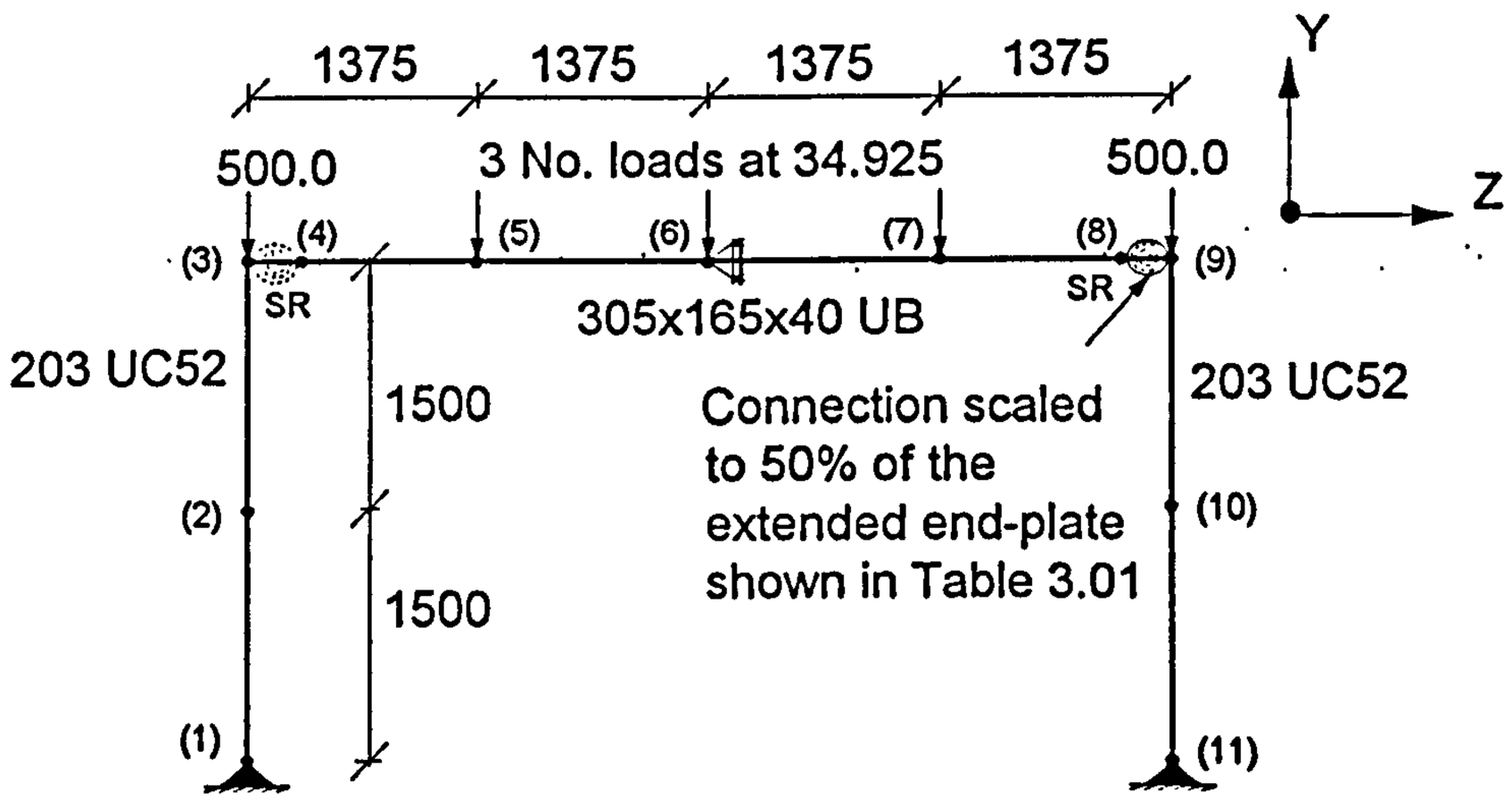

All loads are in kNm. All dimensions are in mm

SR represents semi-rigid connection.

All members are heated uniformly and at the same rate.

σ_{y20} = 275 N/mm^2 E_{20} = 205 kN/mm^2

Fig. 3.05: Example used to validate the model against NAAR2.

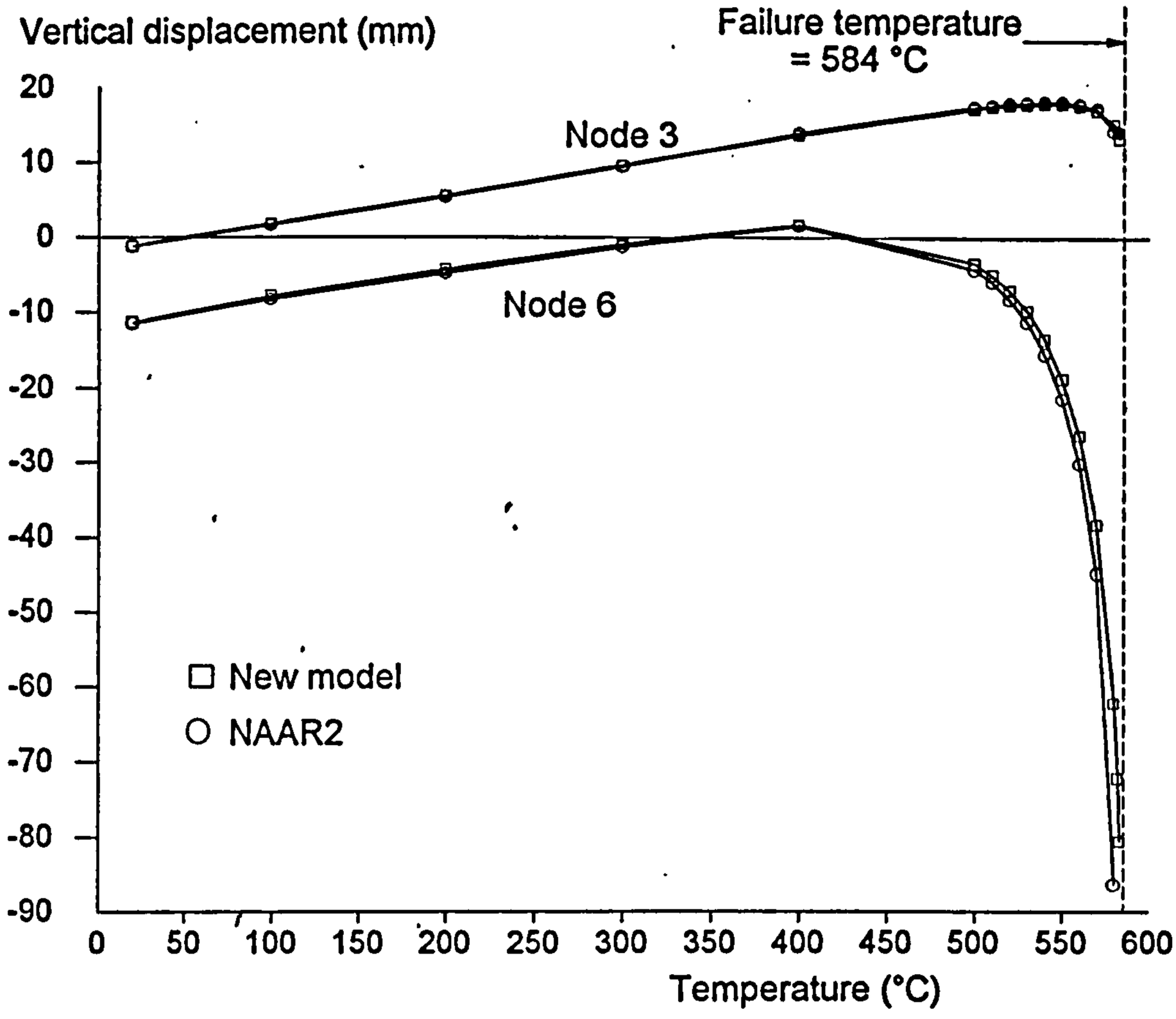

Fig. 3.06: Comparison between the new model and NARR2 programs for the example shown in Fig. 3.05.

Apart from very similar results being obtained from the two models Fig. 3.06 indicates, by a sudden decrease in vertical displacement at node 3, that failure was mainly due to the column. To demonstrate that this failure was caused by in-plane buckling of the column (since only two-dimensional behaviour was modelled) the horizontal displacement of node 2 calculated by the model is shown in Fig. 3.07. It can be seen that the rate of this displacement increases rapidly as the failure temperature of 584°C is approached.

3.4: PRELIMINARY INVESTIGATION INTO THE INFLUENCE OF SEMI-RIGID CONNECTIONS ON ELEMENTS AND SUB-FRAMES AT ELEVATED TEMPERATURES.

3.41: SIMPLE BEAM ELEMENTS.

The beam of size 305x165x40UB and grade 43 steel, shown in Fig. 3.08, was loaded at the quarter points producing a load ratio of 0.6, according to BS5950 Part 1[49]. Different end restraints were considered, consisting of pinned, fully rigid, and 25%, 50%, 75% and 100% scaling of both the stiffness and strength of the extended end-

plate characteristics shown in Table 3.01. The beam is assumed to be uniformly heated, with the temperature in the connection being 0.7 times the beam temperature.

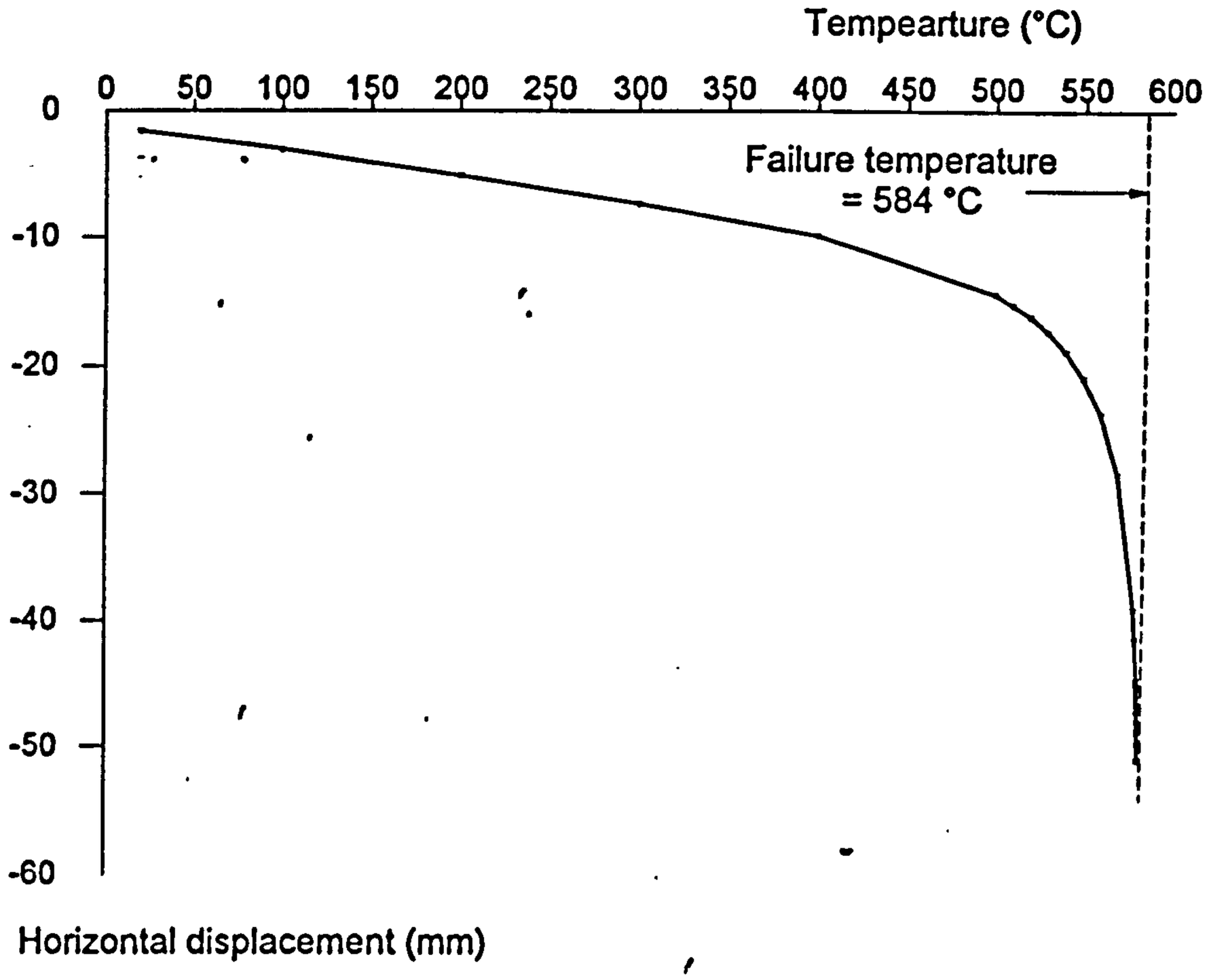

Fig. 3.07: Horizontal displacement at column mid-height.

Since simple element design has been used, the increase in survival time of the beam will be overestimated (except in the pinned case) due to the assumption of infinitely stiff columns. The results of the analysis, together with the specified limiting temperature in BS5950 Part 8[5] for a uniformly heated simply supported beam, are indicated in Fig. 3.08. The model predicts that this failure will occur at a mid-span displacement of span/20, which corresponds to the failure criterion for a standard fire test[7]. It can clearly be seen from the results that the survival time of the beam is increased if the rigidity of the semi-rigid joint, which was not utilised in ambient temperature design, is considered in fire conditions. For this type of connection (based on the extended end-plate) very little difference was indicated between the 75% and 100% rigidities and the fully rigid connection, indicating that the modelled connection is actually fairly rigid.

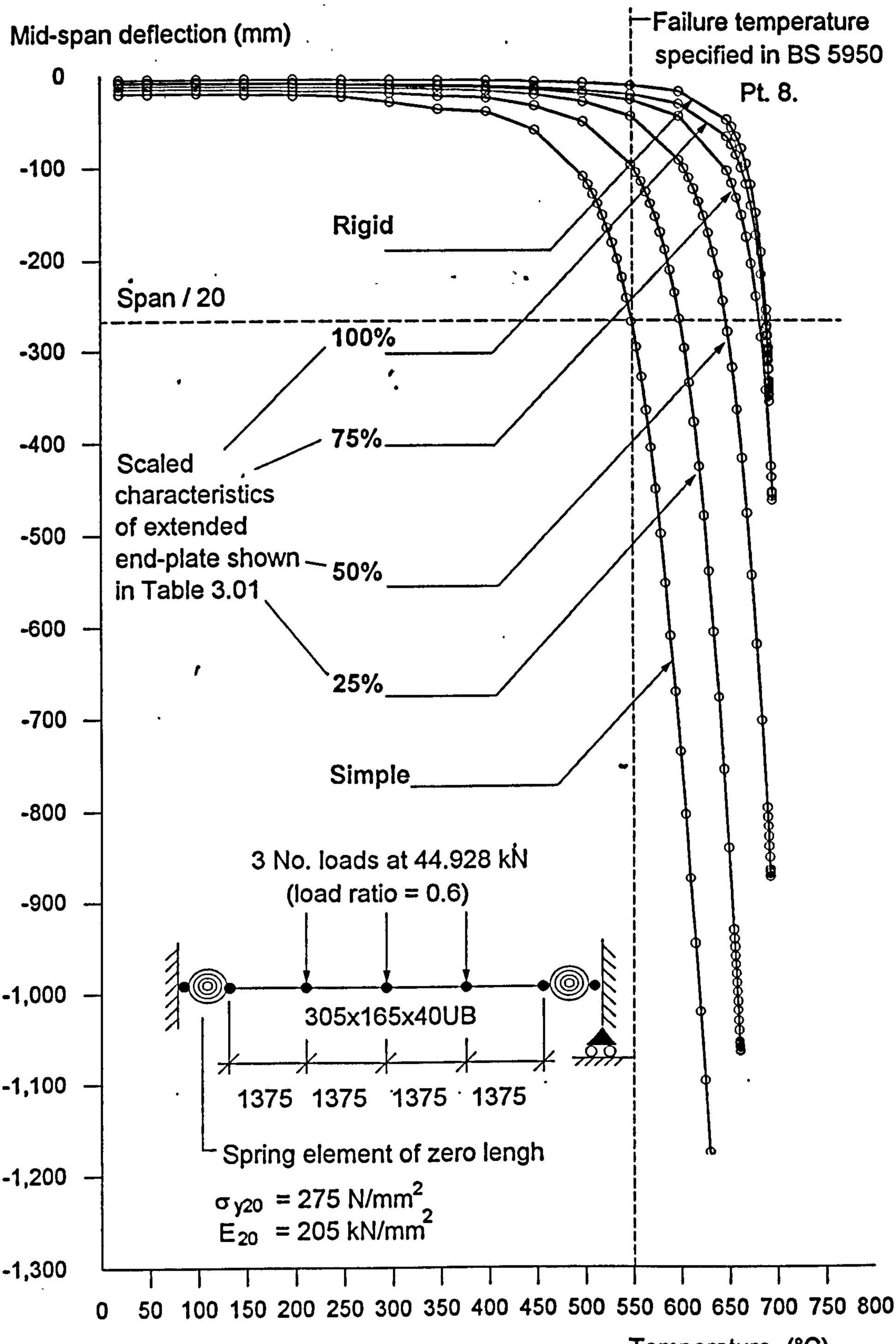

Fig. 3.08: Effect of semi-rigid connections on beams at elevated temperatures.

From the modelling point of view it is of interest to note the recorded displacement just before termination of the analysis, which indicates structural failure. The largest mid-span displacement was recorded for the simple beam, and progressively became smaller as the joint rigidity increased. Since no buckling can occur in this example due to the absence of axial forces and the two-dimensional nature of the analysis, termination will occur by divergence of the out-of-balance forces. For the simple beam, as the temperature increases and the force-displacement relationship becomes very curvilinear the deformations become very large as spread of yield through the cross-section increases. Eventually equilibrium cannot be obtained between internal and external forces when the plastic hinge is complete, causing termination of the analysis. In the indeterminate case of the rigidly connected beam, the mid-span displacements are reduced due to support moments until spread of yield through the cross-section has occurred at a significant number of points along the beam, causing loss of equilibrium between internal and external forces and forming a mechanism.

3.42: Sub-frames.

The previous beam was re-analysed as part of an internal sub-frame, as shown in Fig. 3.09. An axial load was applied to the column which, together with the reactions from the beams, produced a load ratio of 0.3 as defined in BS5950 Part 8[5]. The adjoining beams and their respective connections are assumed to remain cold, together with the columns above. The beam itself and the lower columns were heated uniformly at the same rate, with the connections being heated at 0.7 times this temperature. Exactly the same range of joint rigidities was considered, and the results are shown in Fig. 3.10.

As can be seen from the results, the mid-span displacements for the sub-frame are slightly different from those produced for isolated element design, which are shown in Fig. 3.08. When pinned connections are used in the sub-frame, and if span/20 is adopted as the failure criterion, then the model predicts a lower failure temperature compared to BS5950 Part 8[4], which is based on simple element design. The lower failure temperature calculated for the sub-frame is due to axial forces being induced in the beam, caused by the restraint of the columns against thermal expansion. Although these axial forces are small (a maximum of 5.7 kN was recorded) the magnitude of the displacements, and thus the lever arm to this force, is such that it will increase the overall mid-span displacement.

For the 25% and 50% scaled connection rigidity the failure temperature is increased compared to the pinned connection. If a comparison is made with the isolated beam

analysis, the mid-span displacements are slightly greater (as explained for the pinned case) due to the induction of axial forces into the beam. Above the 50% scale the mid-span deflection does not exceed span/20 and failure was due to the column, which could not support the applied load at the failure temperature. Column failure is due to in-plane buckling (since only two-dimensional analysis is being used) with the lateral displacement at mid-height of the column shown in Fig. 3.11, for the examples where the rigid, 100% and 75% scaled connections were used. This sub-frame analysis shows that even with a very low load ratio on the column (0.3) failure can be initiated either by the beam or column, depending on the rigidity of the connection.

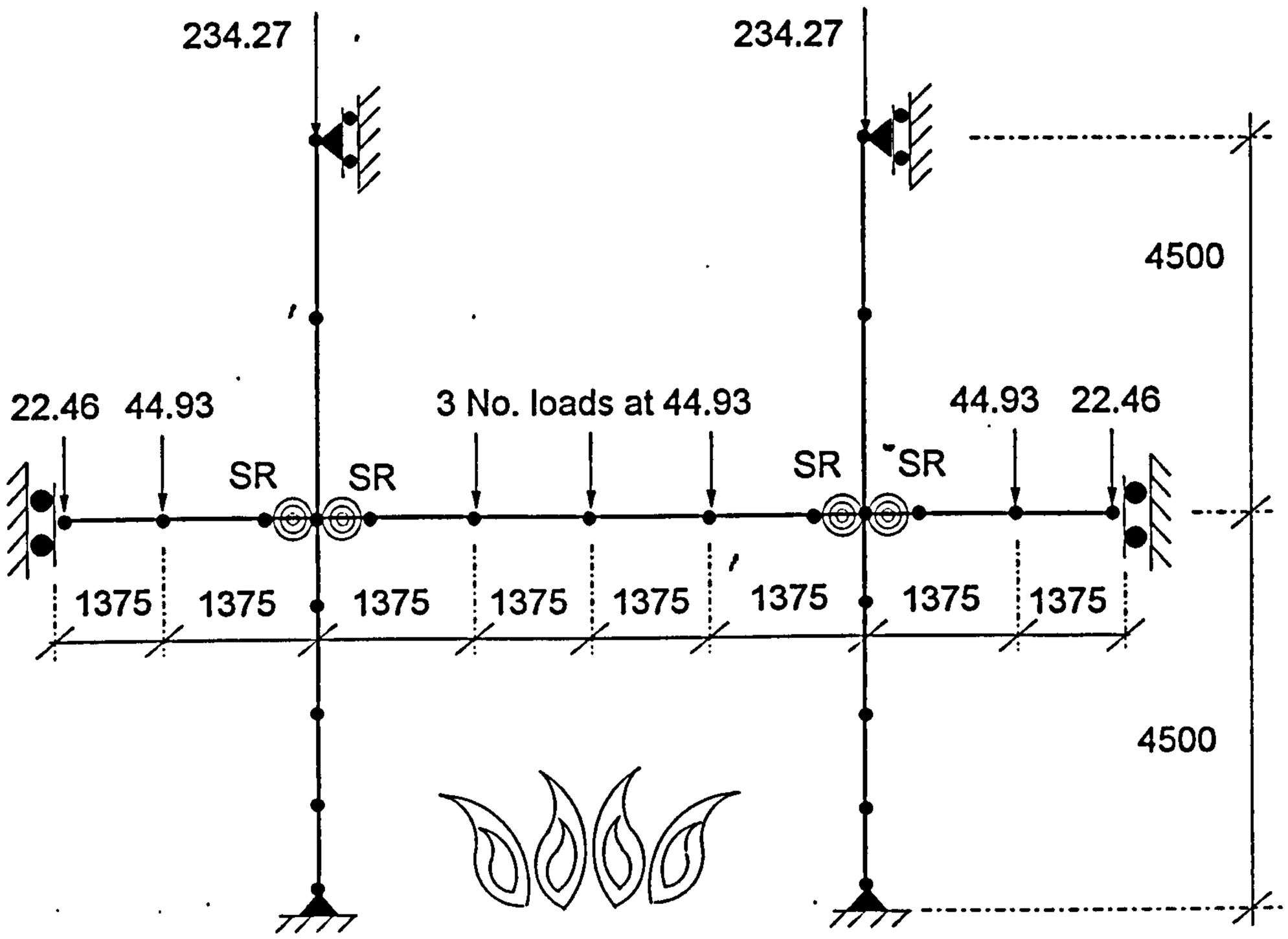

All loads are in kN.
All dimensions are in mm.
All heated members are uniformly heated at the same rate.
SR represents a semi-rigid connection.

Fig. 3.09: Example used to investigate the effect of semi-rigid connections on frame behaviour.

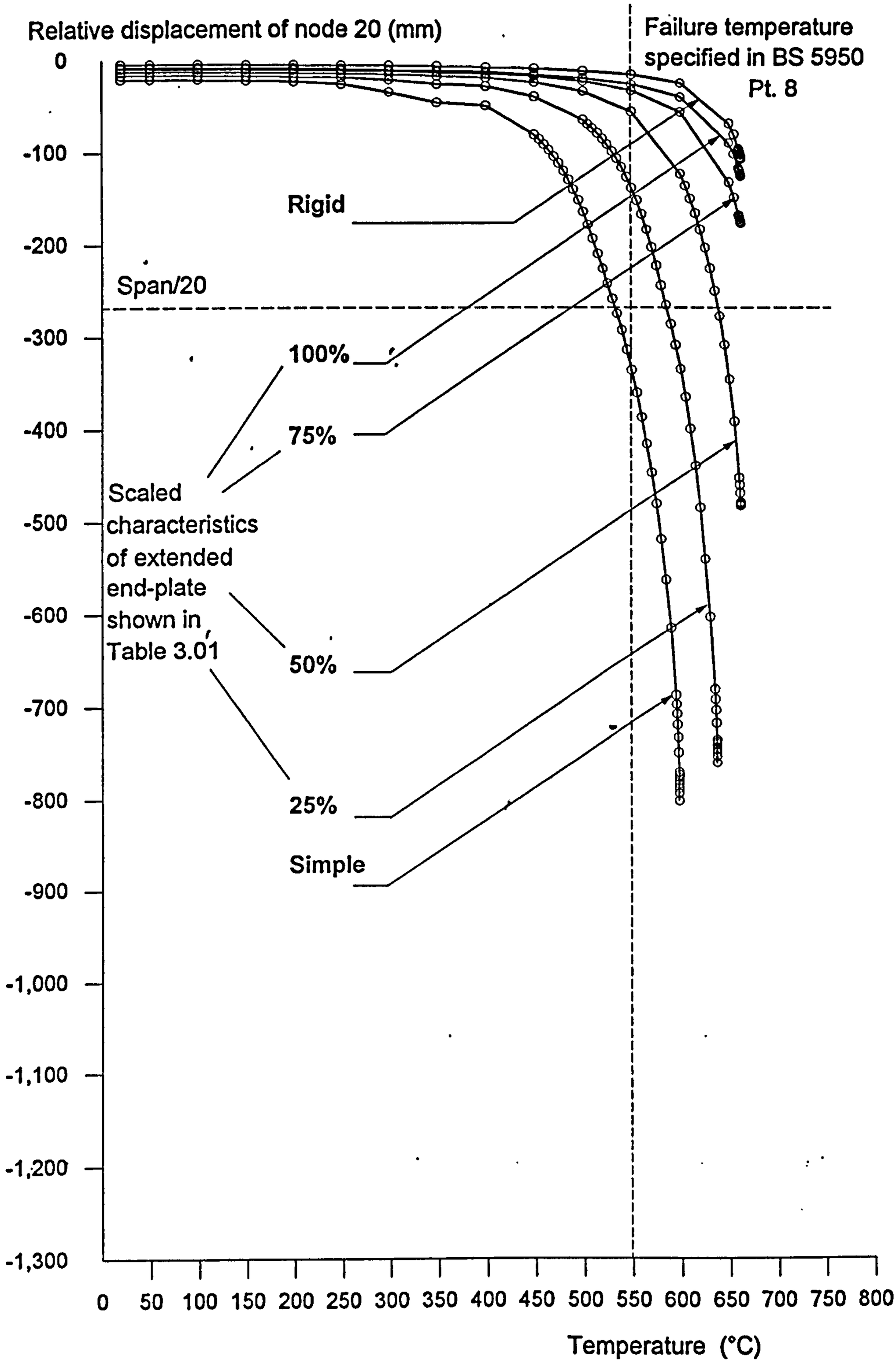

Fig. 3.10: Effect of semi-rigid connections on sub-frames at elevated temperatures.

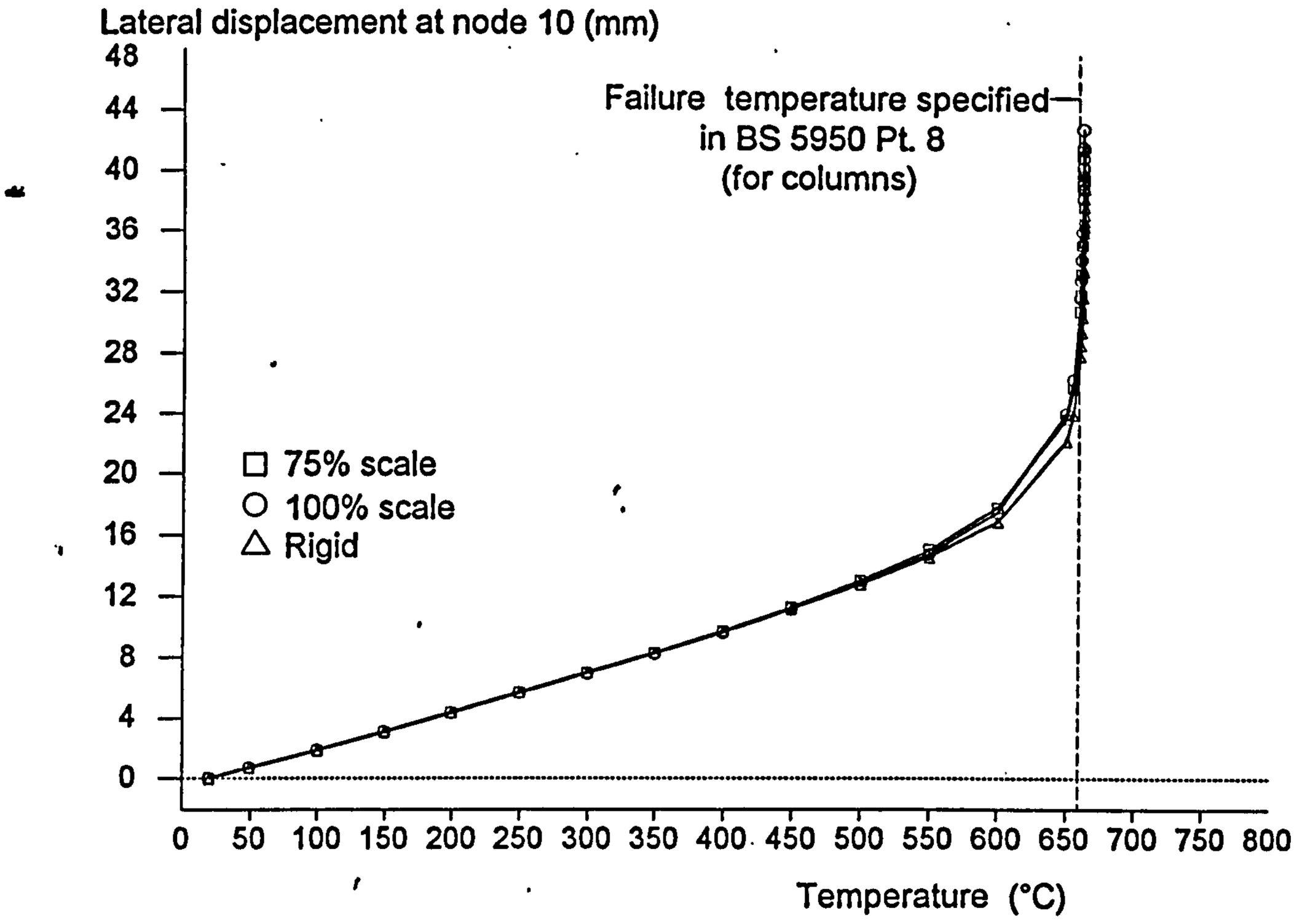

Fig 3.11: Lateral deflection of the columns for the sub-frames using 75%, 100% and rigid connections.

Only a very limited study has been conducted into the effect of semi-rigid connections at elevated temperatures. This is due to the absence of experimental data for connection behaviour during a rise in temperature, which will allow the moment-rotation-temperature characteristics to be specified. The model has been developed so that these characteristics can be implemented very easily when they become available. It has been decided to suspend a comprehensive parametric study until credible moment-rotation-temperature characteristics of a connection are obtained, thus making the exercise worthwhile instead of purely academic.

3.5: MODELLING THE UNLOADING OF SEMI-RIGID CONNECTIONS.

If a connection goes through a relative rotation so that the inelastic phase is entered and then a reversal in relative rotation is experienced, the unloading path separates from the loading path of the moment-rotation relationship. Unloading of connections can occur due to the deflection of columns, as shown in Fig. 3.13, or in the case of sway frames due to the application of lateral loads. If a connection unloads from a

post-yield state then the unloading stiffness is higher than the local tangent stiffness. To allow a preliminary investigation into the unloading behaviour of connections in fire the bilinear unloading curve as shown in Fig. 3.12 was implemented within the computer model. The yield point (M_e) was assumed to occur at the proportional limit of the moment-rotation curve. This curve was based on the work by Gerstle[61,62], who devised unloading curves from experimental observations. A more comprehensive unloading model has been implemented into the program for strain-reversal within a beam-column element, to investigate the steel behaviour during the cooling phase of a fire. This will be discussed in Chapter 7.

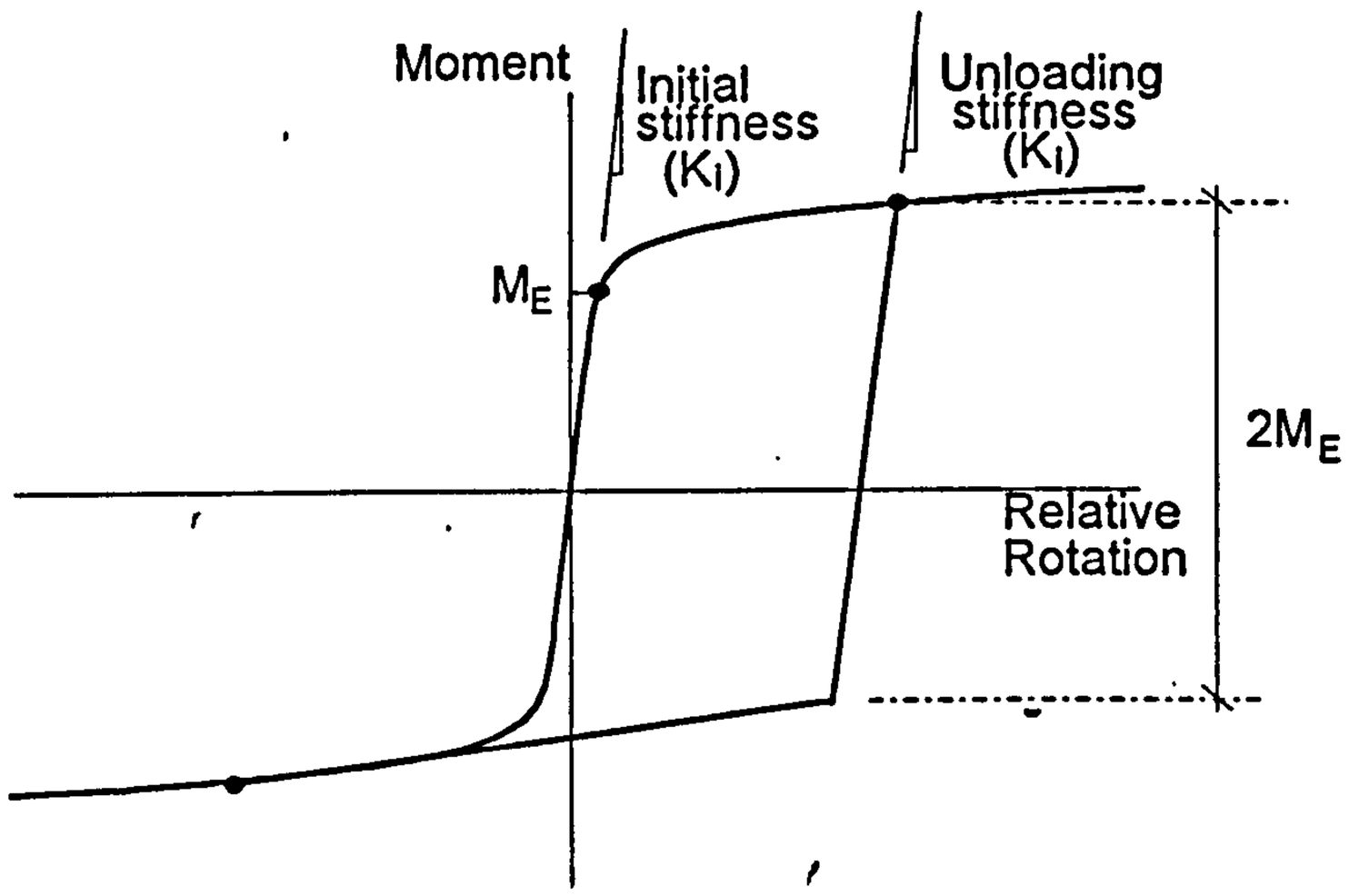

Fig. 3.12: Moment-rotation characteristics for loading and unloading of a connection.

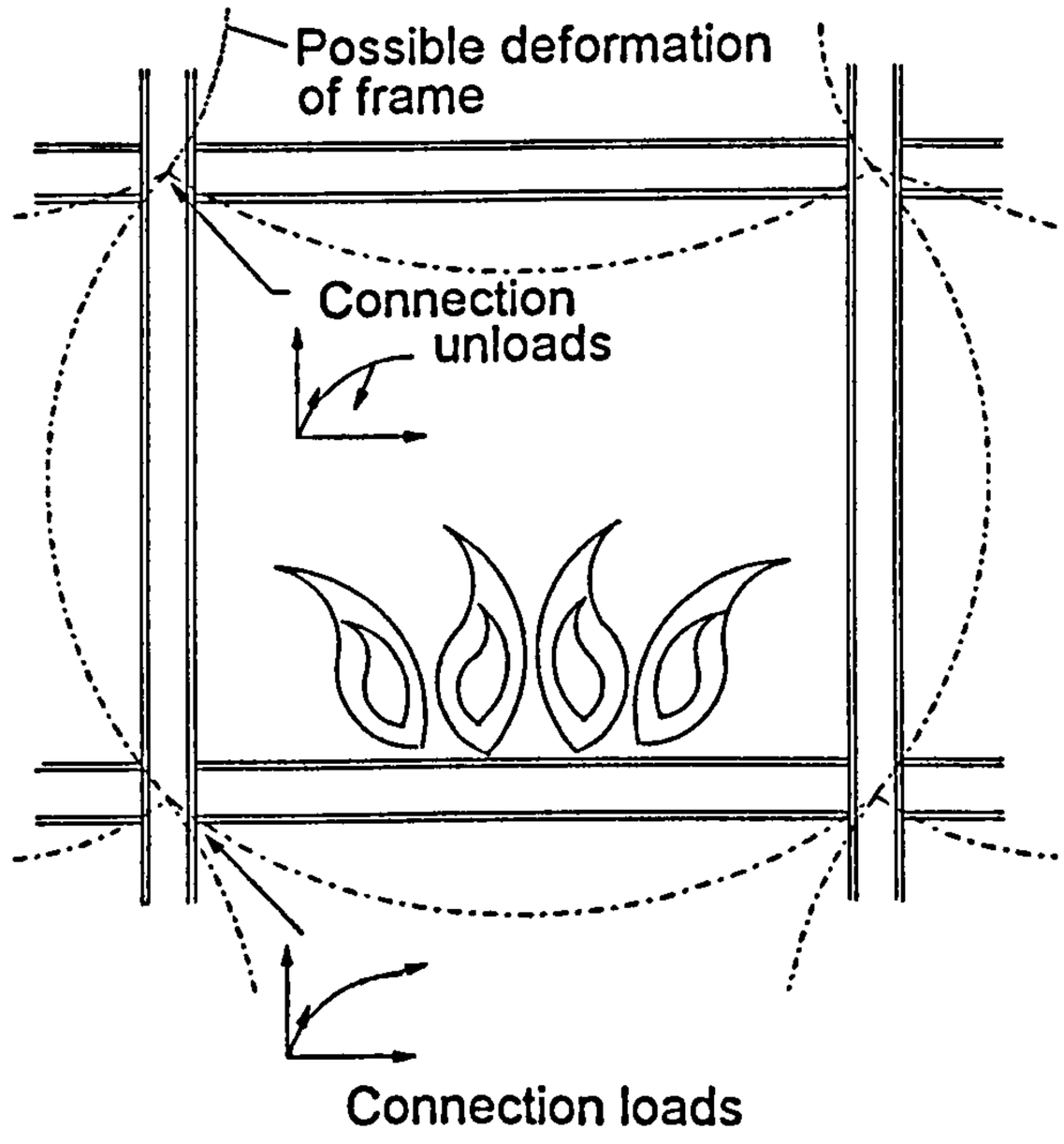

Fig 3.13: Possible deformation of frame causing unloading of connections.

3.6: VALIDATION OF UNLOADING CHARACTERISTICS FOR SEMI-RIGID CONNECTIONS AT AMBIENT TEMPERATURE.

- The program was first verified at ambient temperature, using connections scaled to 25% of the strength and stiffness of the extended end-plate characteristics shown in Table 3.01. A bi-linear representation of the moment-rotation relationship of these characteristics was adopted as shown in Fig. 3.14 to allow manual calculations to be conducted as a check.

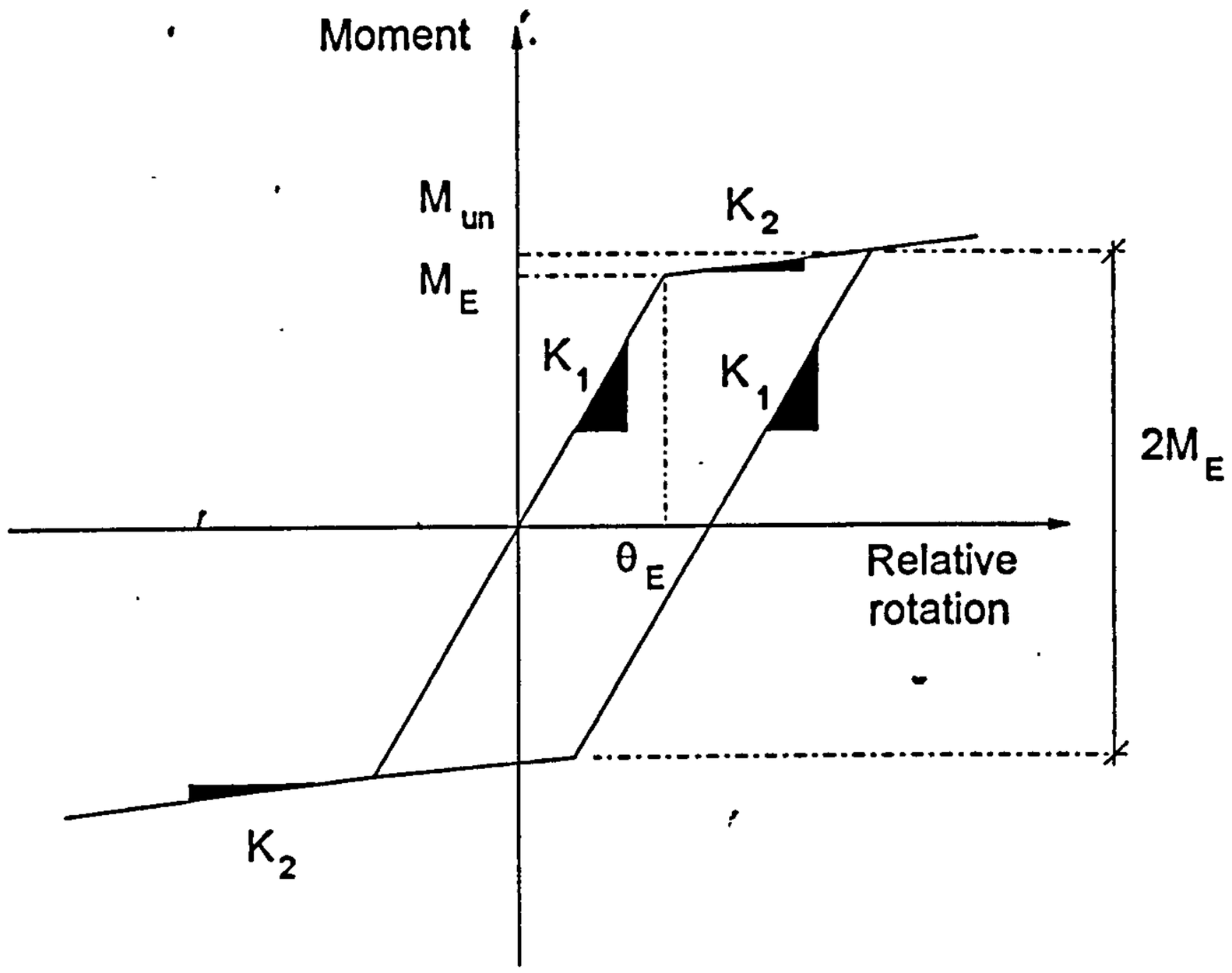

$K_1 = 7.18 \times 10^3$ kNm/rad $K_2 = 43.44$ kNm/rad

$M_E = 24.0$ kNm $\theta_E = 3.34 \times 10^{-3}$ rad

M_{un} = Moment at which unloading begins.

Equation of curve with gradient K_2 is given by, $M=43.44\ (\theta) + 23.76$

Fig. 3.14: Moment-rotation curve for connection used in the T-frame shown in Fig. 3.15.

A two-dimensional T-frame, which incorporated a very slender column as shown in Fig. 3.15, was chosen as a verification example. The 203x203x52UC (grade 43) column had an initial imperfection of L/1000 (12mm) at mid-height. During the analysis the beam loads were applied and remained constant, while the column axial load was increased in increments. It was noted that the left hand connection unloaded, while the right hand connection loaded, as the column axial load increased. Two analyses were conducted, the former adopting an unloading path which retraces the loading path using the tangent stiffness, and the second using an unloading path

with a stiffness equal to the initial stiffness. The corresponding load-deflection relationships for the column are shown in Fig. 3.16. A Southwell plot shown in Fig. 3.17, was also constructed to allow the elastic critical load to be estimated by calculating the reciprocal of the slope of the best fit line.

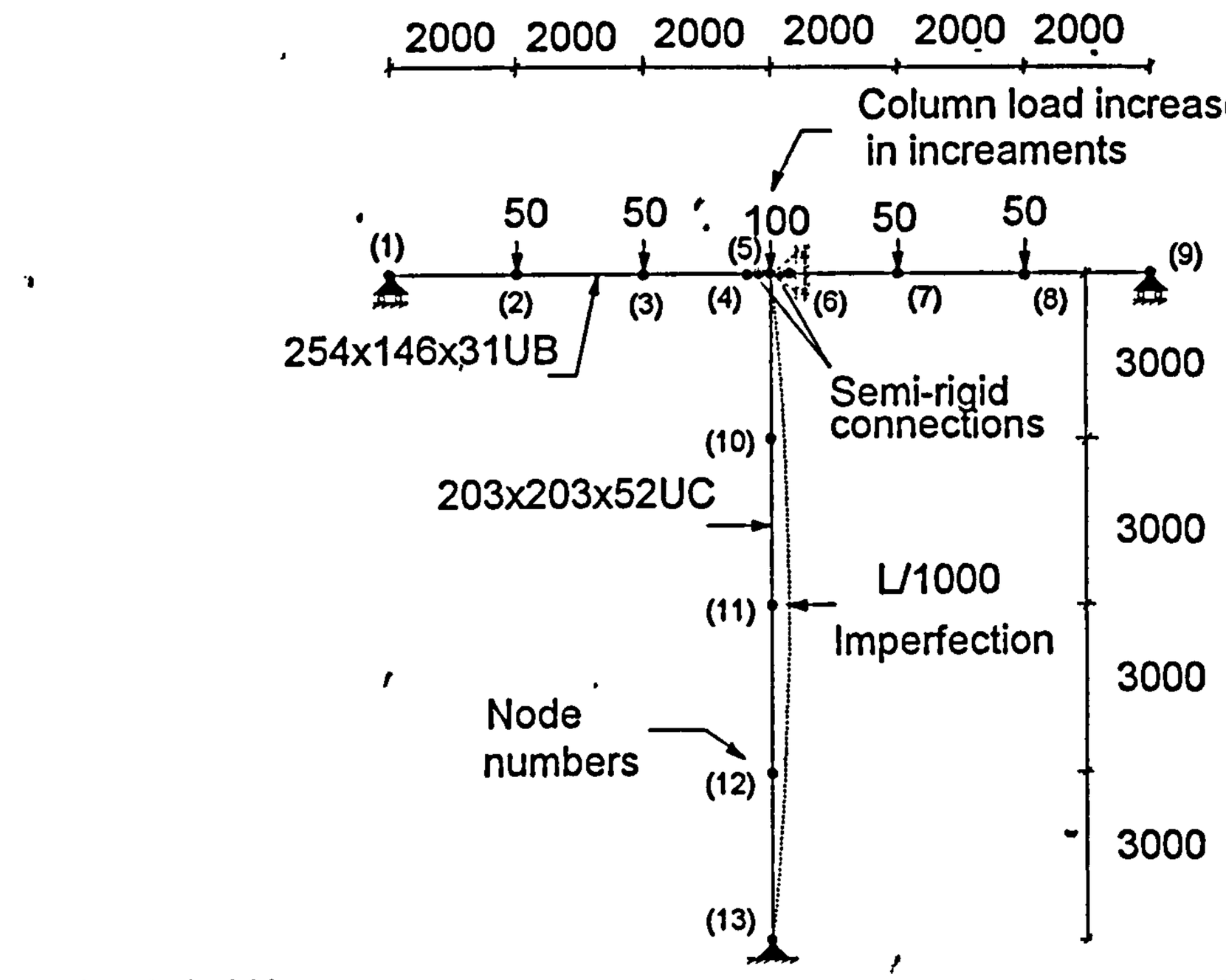

All loads in kN.
All dimensions in mm.
Out-of-plane displacement restrained.
Slenderness ratio of column = 135.

$\sigma_{y20} = 275\ N/mm^2$
$E_{20} = 205\ kN/mm^2$

Fig 3.15: T-Frame used to examine effect of unloading characteristics at ambient temperature.

For the analysis where the unloading path retraces the loading path (non-linear elastic analysis) the elastic critical load was obtained from,

$$elastic\ critical\ load = \frac{1}{slope} = \frac{1}{1.33 \times 10^{-3}} = 750kN$$

For the other analysis where the unloading path had a stiffness equal to the initial stiffness (true unloading analysis), the critical load was obtained from,

$$elastic\ critical\ load = \frac{1}{slope} = \frac{1}{9.4 \times 10^{-4}} = 1064kN$$

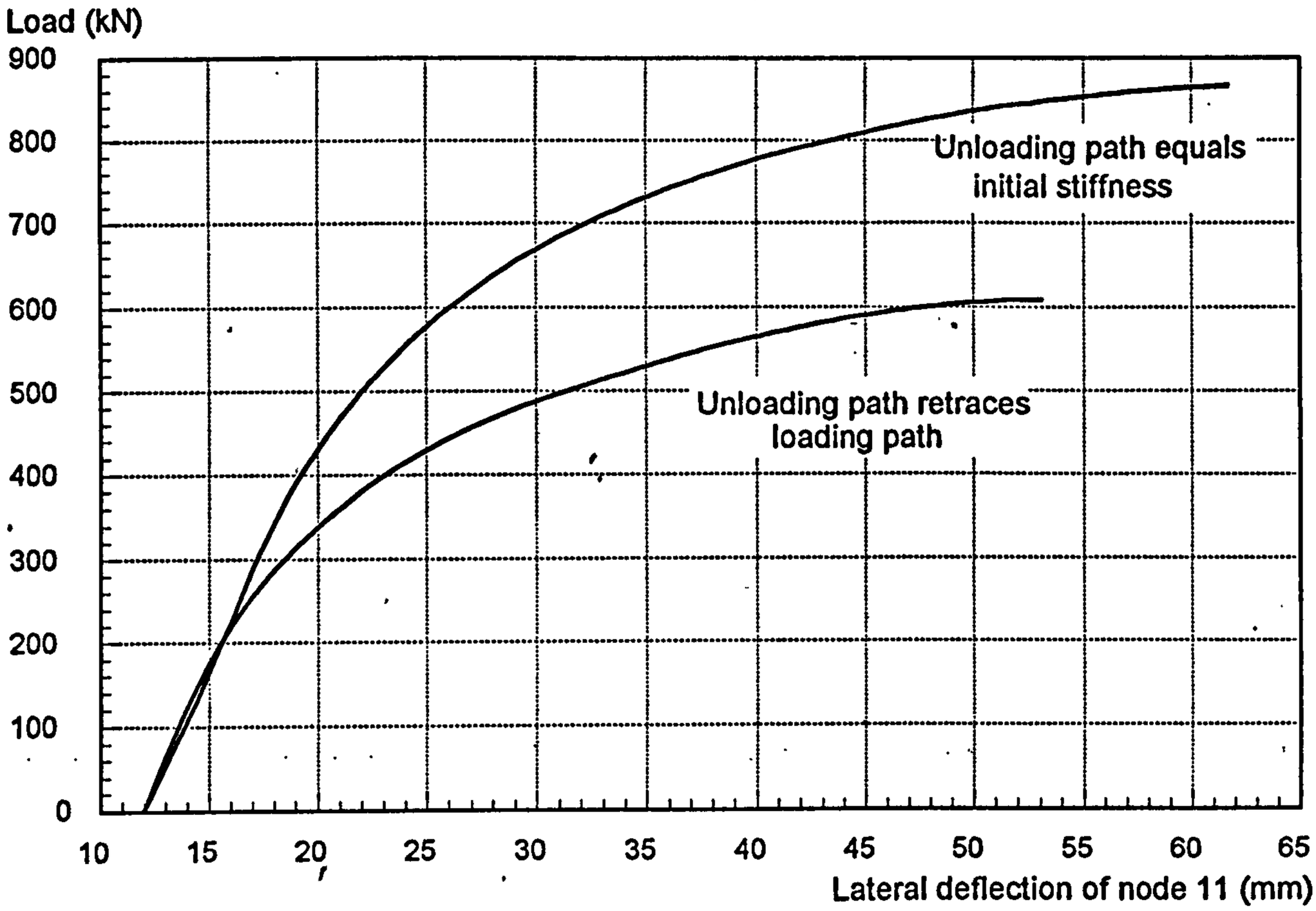

Fig 3.16: Load-lateral deflection relationship for node 11.

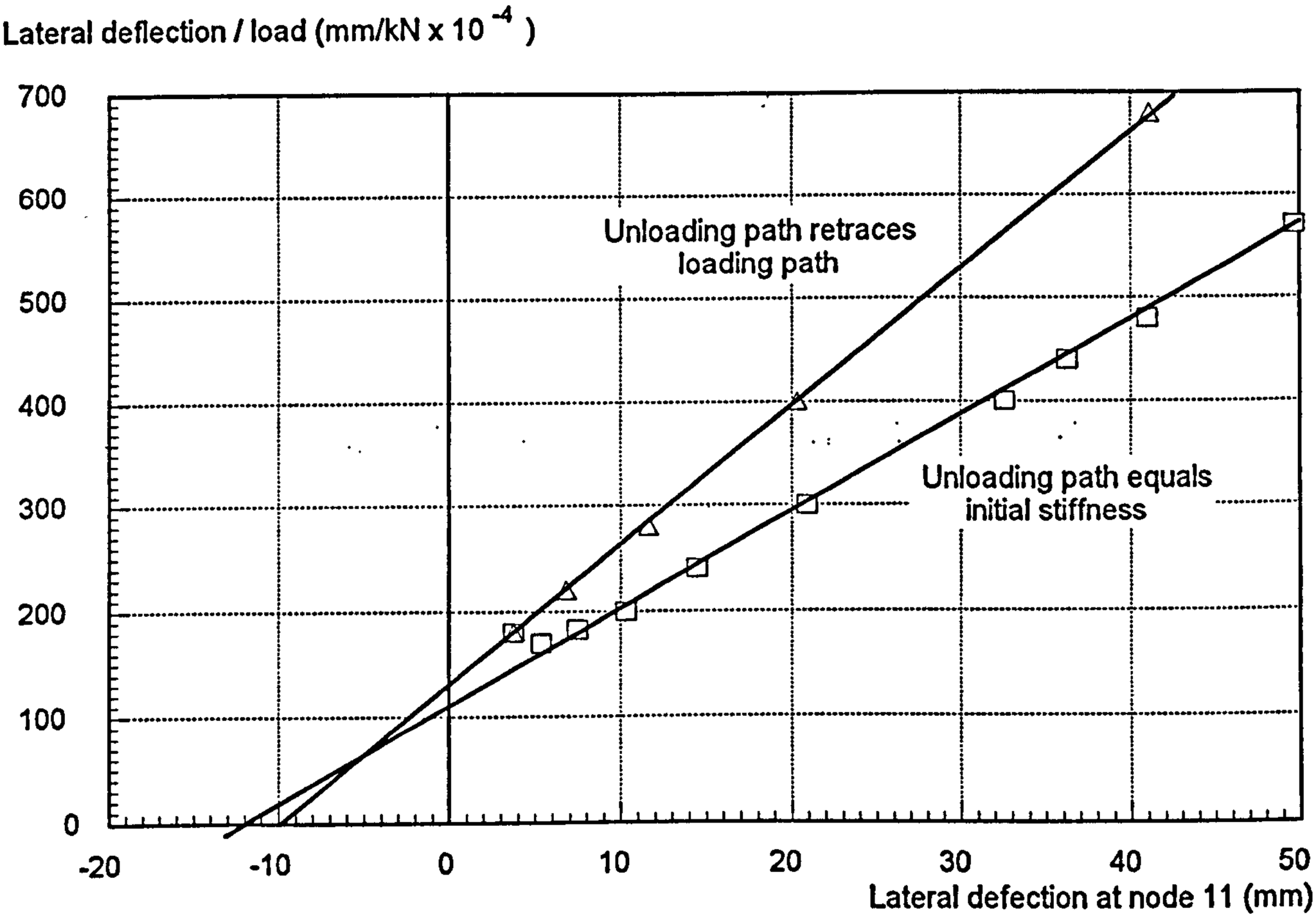

Fig 3.17: Southwell plot to allow the elastic critical load to be calculated from the computer results on the T-frame shown in Fig. 3.15.

To validate the results produced by the model, the same example was analysed manually, utilising the standard formula for the elastic critical load of a perfect column with one end pinned and the other end restrained by a torsional spring, as shown in Fig. 3.18.

Fig. 3.18: Perfect column with one end pinned and one end restrained by a torsional spring.

The elastic critical load is given by the solution of,

$$\tan\left[L\sqrt{\frac{P}{EI}}\right]=L\sqrt{\frac{P}{EI}}\left\{\frac{K}{PL+K}\right\} \qquad (3.03)$$

where,

L = length of column,

P = elastic critical load,

E = Young's modulus,

I = second moment of area,

K = stiffness of the spring.

Consider first, the case when the unloading path retraces the loading path. The value of the stiffness (K) in equation (3.03), includes the contribution from both connections in the post-yield state and also the beams. The beam stiffness is given by,

$$K_{Beam}=\frac{3EI}{L}=\frac{3(205\times10^3\times4440\times10^4)}{6000}=4.55\times10^9 Nmm/rad$$

The stiffness of both connections is given by,

$$K_{Spring}=43.436\times10^6 Nmm/rad$$

Therefore the total stiffness to be substituted into equation (3.03) is calculated from,

$$\therefore K_{Total} = 2\left[\frac{1}{\frac{1}{K_{Beam}} + \frac{1}{K_{Spring}}}\right]$$

$$\therefore K_{Total} = 2\left[\frac{1}{\frac{1}{4.55 \times 10^9} + \frac{1}{43.436 \times 10^6}}\right] = 86.05 \times 10^6 \, Nmm \, / \, rad$$

Substituting the stiffness into equation (3.03) produces,

$$\therefore Tan\left[12000\sqrt{\frac{P}{205 \times 10^3 \times 5260 \times 10^4}}\right] = 12000\sqrt{\frac{P}{205 \times 10^3 \times 5260 \times 10^4}}\left\{\frac{86.05 \times 10^6}{P(12000) + 86.05 \times 10^6}\right\}$$

By applying an iterative procedure an elastic critical load of 753 kN is obtained.

Now consider the case where the unloading stiffness equals the initial stiffness. Since one connection loads and the other unloads, the stiffnesses of the elements are given by,

K_{beam} = 4.551 x 10^9 Nmm/rad,
$K_{connection\ unloading}$ = 7.18 x 10^9 Nmm/rad,
$K_{connection\ loading}$ = 43.436 x 10^6 Nmm/rad.

Therefore the total stiffness is given by,

$$K_{Total} = \left[\frac{1}{\frac{1}{4.55 \times 10^9} + \frac{1}{43.436 \times 10^6}}\right] + \left[\frac{1}{\frac{1}{4.55 \times 10^9} + \frac{1}{7.18 \times 10^9}}\right] = 2.828 \times 10^9 \, Nmm \, / \, rad$$

Substituting into equation (3.03) gives,

$$\therefore Tan\left[12000\sqrt{\frac{P}{205 \times 10^3 \times 5260 \times 10^4}}\right] = 12000\sqrt{\frac{P}{205 \times 10^3 \times 5260 \times 10^4}}\left[\frac{2.828 \times 10^9}{P(12000) + 2.828 \times 10^9}\right]$$

Once again applying an iterative procedure, an elastic critical load of 1050 kN is obtained.

- The results obtained from the manual calculations and the Southwell plots compare very well, and are shown in Table 3.02.

	ELASTIC CRITICAL LOAD	
	Unloading path retraces loading path.	Unloading path equal to initial stiffness
Model results	750 kN	1064 kN
Theoretical results	753 kN	1050 kN

Table 3.02: Comparison between computer model and theoretical elastic critical loads.

3.7: MODELLING THE UNLOADING OF CONNECTIONS IN FRAMES SUBJECTED TO ELEVATED TEMPERATURES.

At ambient temperature the unloading of connections is identified by a reduction in relative rotation, or reversal of the transferred moment. The analysis is usually conducted by applying load increments to the frame and monitoring the relative rotation or moment of the connection. If unloading is identified and the inelastic phase of the connection is reached, then the initial stiffness replaces the instantaneous tangent stiffness.

For an analysis which models a steel frame subjected to increasing temperatures a method of identifying unloading of connections is required which incorporates the reduction in strength of the connection as the temperature rises. The procedure adopted for identifying unloading, as the analysis transfers from one moment-rotation curve to another, for different temperatures, is shown in Fig. 3.19. At ambient temperature the tangent stiffness is used until convergence is obtained. The permanent relative rotation between adjoining members can then be calculated, and this is assumed to be unaffected by temperature variation. This permanent rotation will allow the 'reference point' to be calculated for the next temperature step as shown in Fig. 3.19. The analysis for the increased temperature is carried out using the tangent stiffness, and once convergence is obtained the calculated rotation is compared against the 'reference point'. If this rotation is less than the 'reference

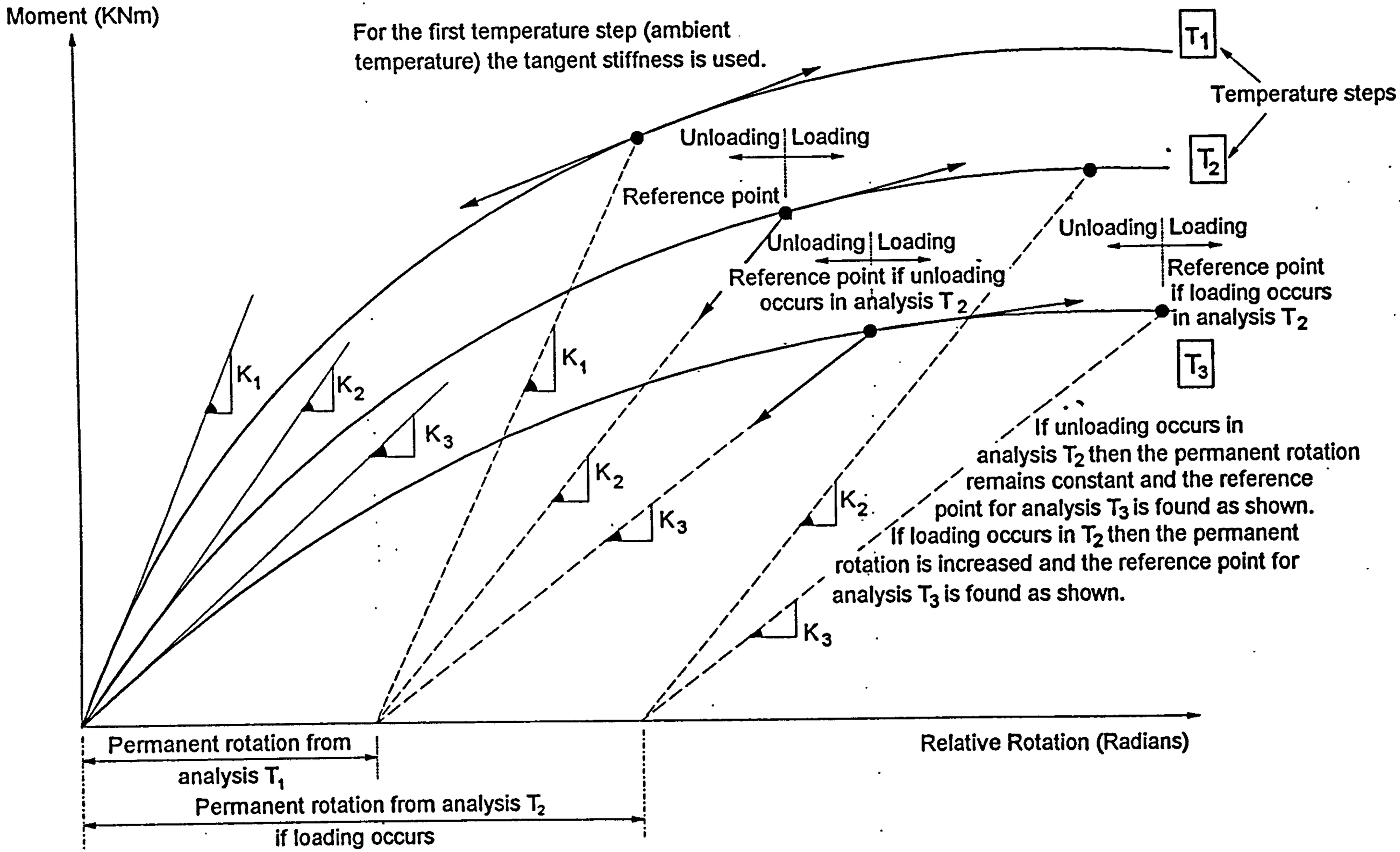

Fig 3.19: Definition of loading and unloading paths during temperature change.

point' unloading is identified and the analysis repeated replacing the tangent stiffness with the initial stiffness for the connections which are unloading. If unloading occurs then the permanent relative rotation remains constant and is used to define the reference point at higher temperatures, but if loading occurs the permanent rotation increases and the new value is used to find the reference point for the next temperature. Although theoretically this method is correct it is numerically inefficient in the sense that the analysis is repeated if unloading is identified. A more comprehensive model which deals with steel member strain reversal was developed, and is discussed in Chapter 7. However for a preliminary study into connection unloading the above method was adopted.

To show the effect of unloading of connections in frames at elevated temperatures the example shown in Fig. 3.20 was analysed. The loads on the beam produced a load ratio of 0.56, designed as simply supported in accordance with BS5950 part 8, with the column axial load being 60% of the load carrying capacity. The connection stiffness and strength was scaled to 25% of the value for an extended end-plate shown in Table 3.01, with the assumption that the inelastic range commences at the proportional limit of the moment-rotation curve. A temperature gradient was assumed for all members, with the inside flanges being heated at twice the rate of the outside flanges. The temperature of the connection was 0.7 times the temperature of the bottom flange of the connecting beam.

Due to the thermal gradient the columns begin to bow towards the fire when the temperature starts to increase. This behaviour together with the load and thermal gradient on the beam causes the connections to load. As the temperature continues to increase the resultant internal axial force of the columns moves towards the area of section whose strength and stiffness is decreasing at a slower rate. Since the application of the axial load on the column remains constant at the original centroid (mid-web) of the cross-section, the eccentricity causes the column to bow in the opposite direction. Beyond 400°C the lateral displacements of the columns reverse direction due to the bowing caused by the increasing eccentricity of load being greater than the bowing caused by the thermal gradient. Above 430°C this behaviour will cause the connections to unload. To observe the frame sensitivity to unloading of connections it was decided to conduct two analyses. For the first analysis the unloading path was assumed to retrace the loading path, and in the second analysis the unloading path was assumed to equal the initial stiffness. The lateral deflections of the column as the temperature rises are shown in Fig. 3.21, for both analyses. As

can be seen, using an increased stiffness for unloading of the connections increased the failure temperature by approximately 25°C.

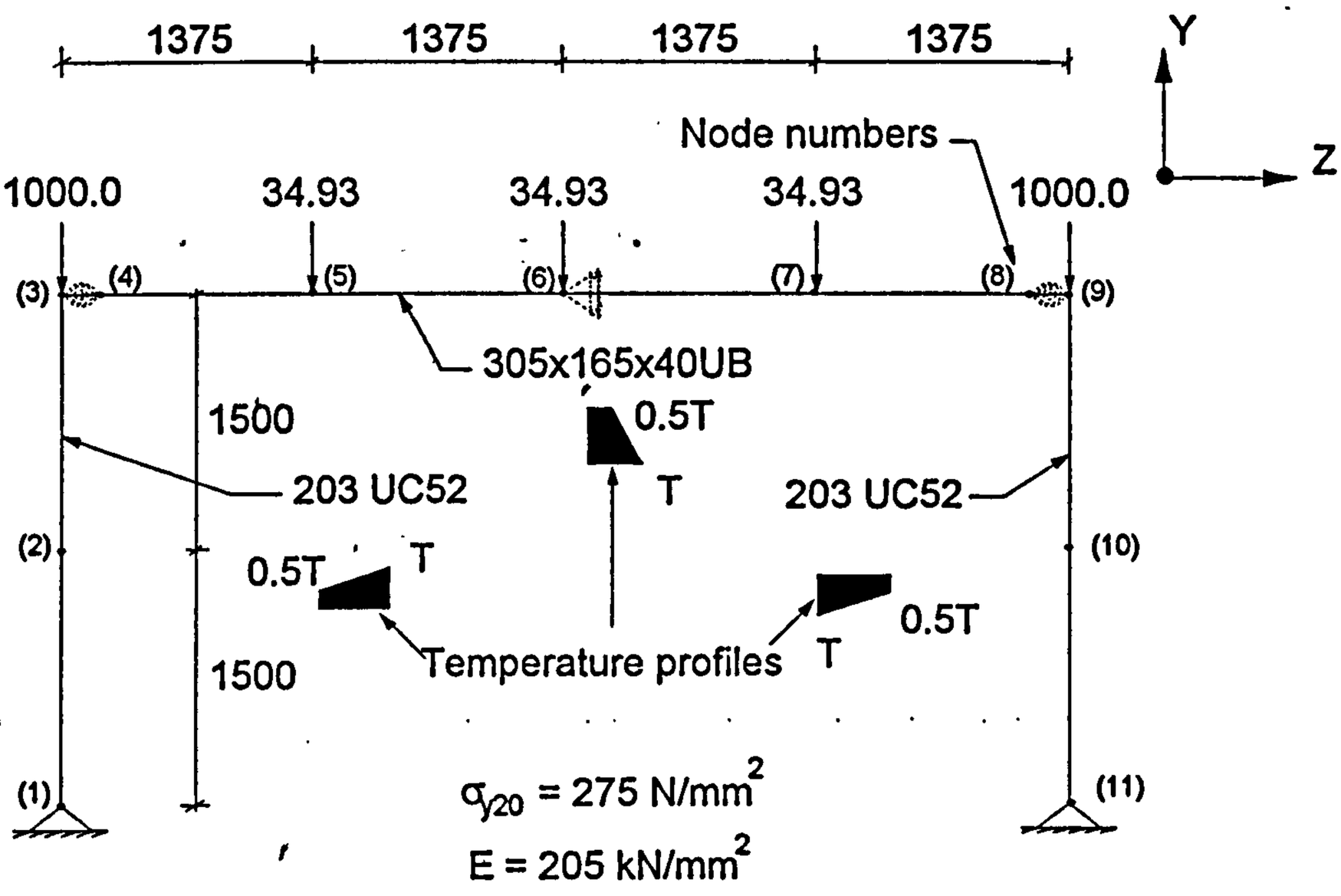

Fig. 3.20: Frame used to indicate the effect of connection unloading

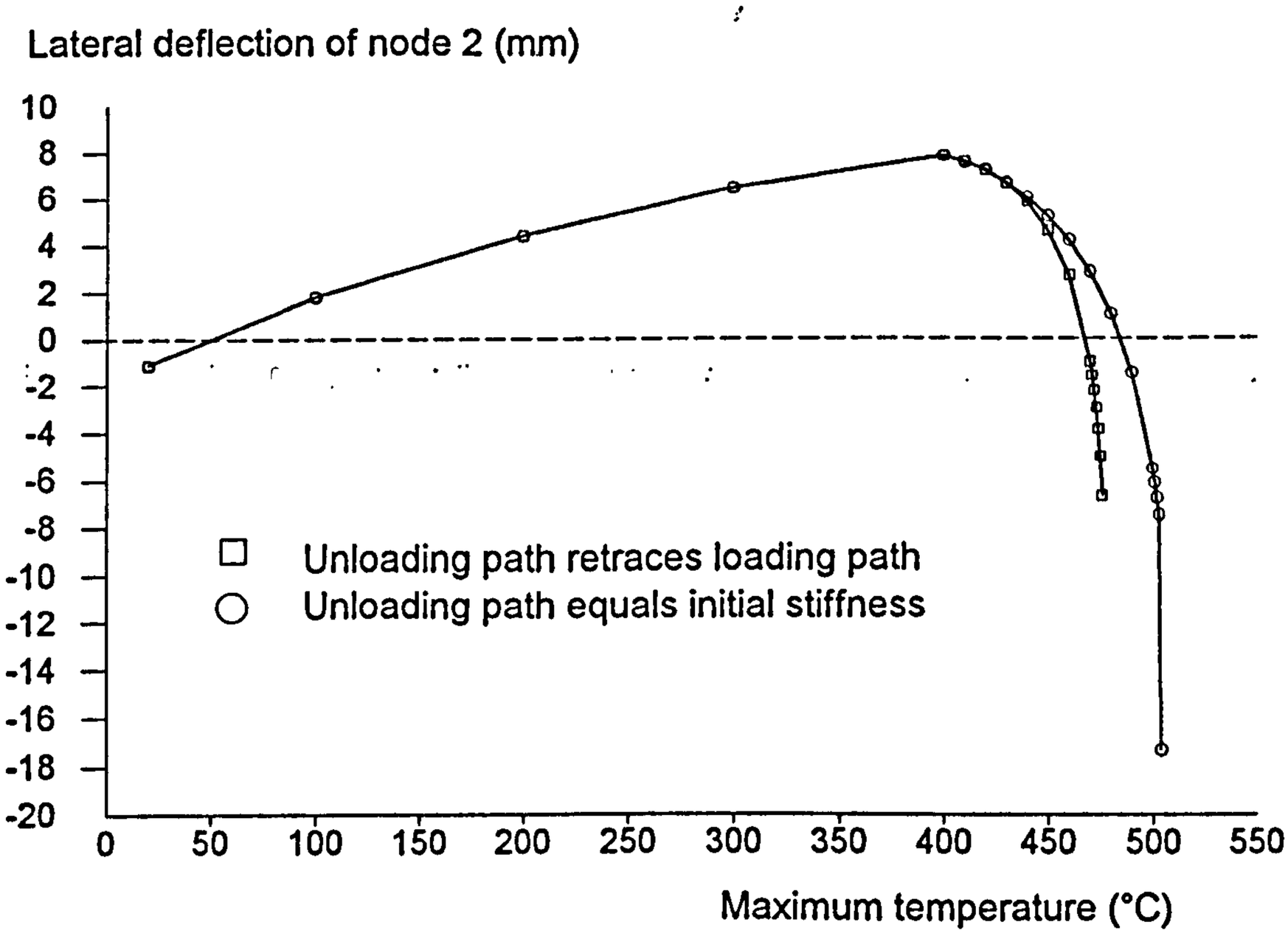

Fig. 3.21: Difference between the lateral deflection of columns when connection unloading is considered.

Since it is impossible to validate the above model against experimental results, when the connection unloads, it was decided to obtain the connection parameters at various temperatures used throughout the analysis, to confirm that the connection behaviour complies with the adopted theory. These parameters are shown in Table 3.03, and graphically in Fig. 3.22.

Connection Temperature (°C)	Relative Rotation (Rads. x10^{-3})	Moment (kNm)	Permanent Rotation (Rads. x10^{-3})	Reference Point (Rads. x10^{-3})
20	4.4	19.6	1.7	
70	15.2	23.4	11.75	4.6
140	27.7	24.3	23.4	15.75
210	39.1	24.8	33.8	28.56
280	50.5	24.5	43.6	40.6
287	51.0	24.3	43.96	50.7
294	51.4	24.2	44.13	51.2
301	51.54	23.97	44.13	51.6
308	51.6	23.4	44.13	51.8
315	51.58	22.5	44.13	52.0
322	51.44	21.4	44.13	52.2
329	51.14	19.7	44.13	52.48
336	50.65	17.7	44.13	52.75
343	49.9	15.0	44.13	53.05
350	48.6	11.2	44.13	53.37

Table 3.03: Connection parameters at various temperatures for the analysis of the frame shown in Fig. 3.20

Not all fire and structural scenarios will induce unloading of connections, and in some cases where unloading occurs the relative angle of rotation will not be large enough to create a significant difference between the tangent and initial stiffness. However should a connection reverse direction due to the frame behaviour then the additional connection stiffness should be incorporated into the analysis to obtain more realistic modelling predictions.

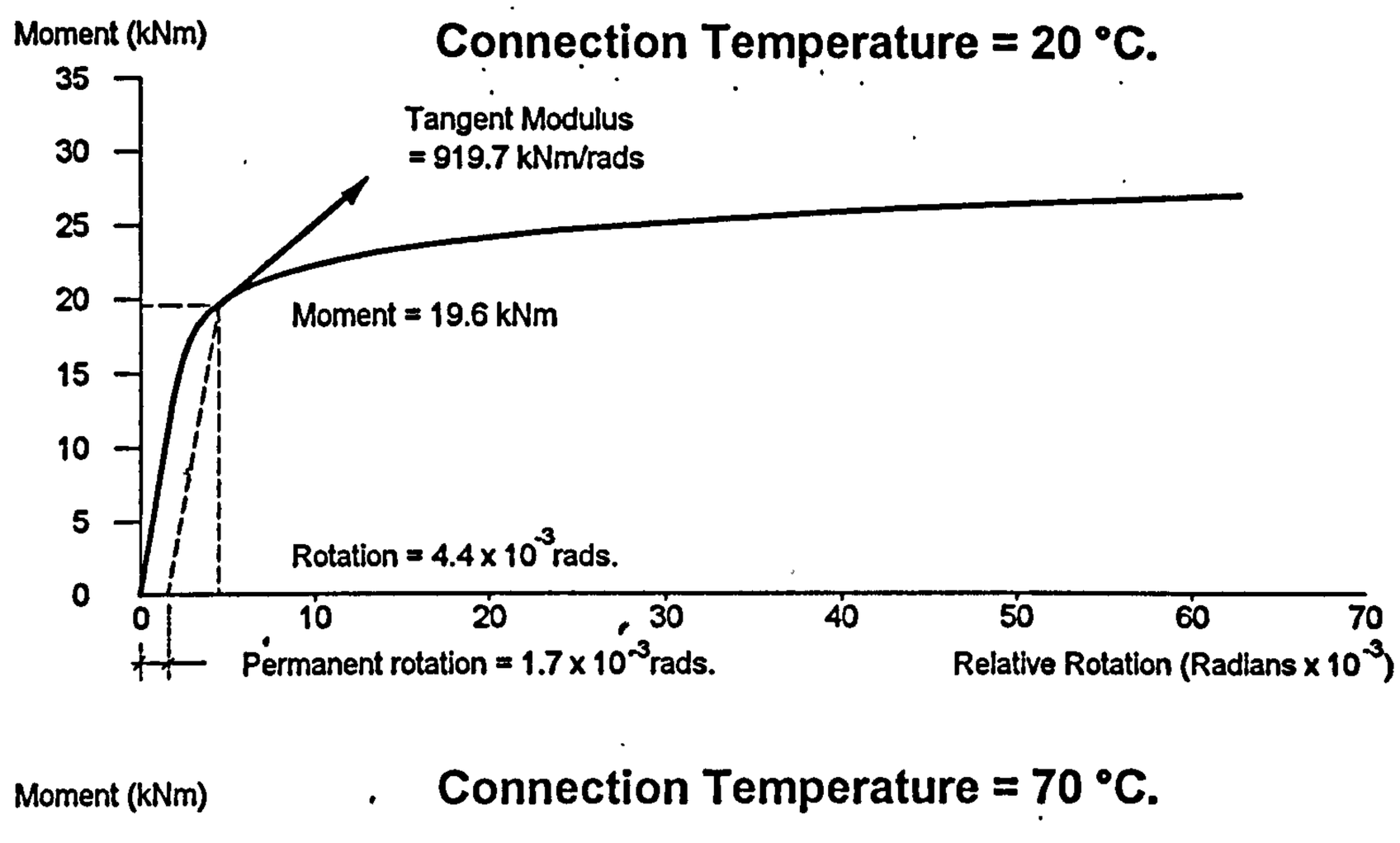

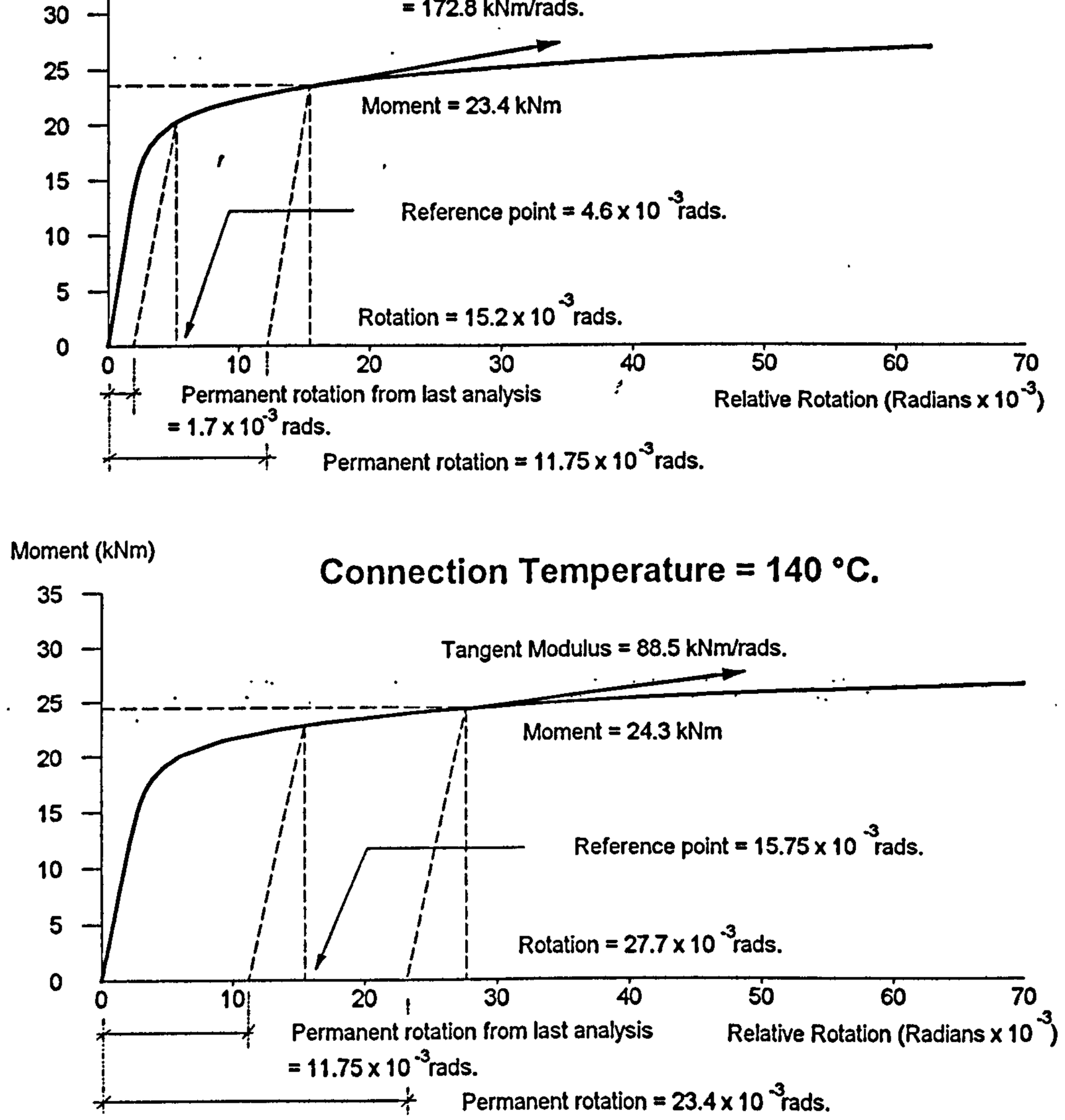

Fig 3.22: Moment-rotation-temperature characteristics of the connection used for the example shown in Fig. 3.20.

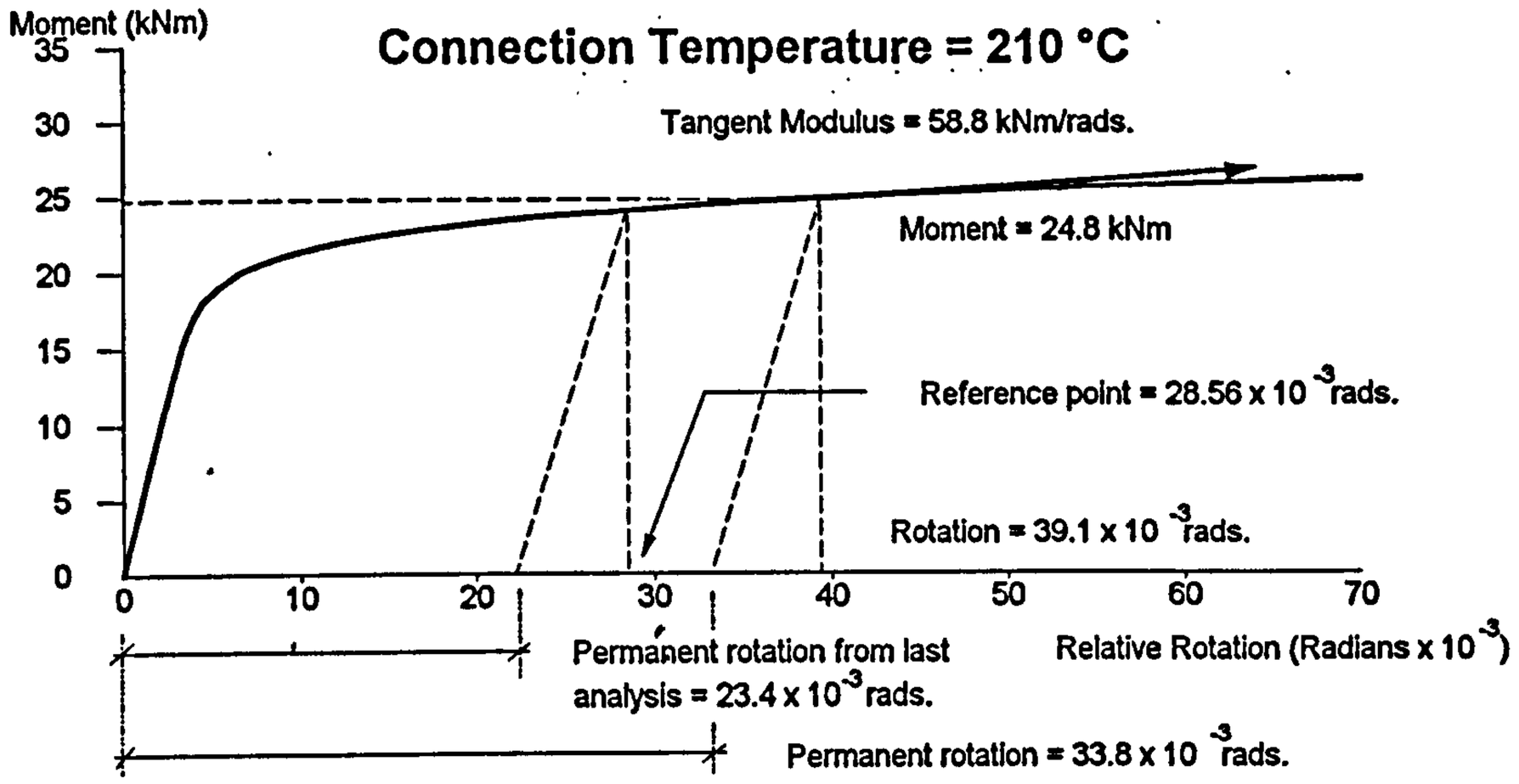

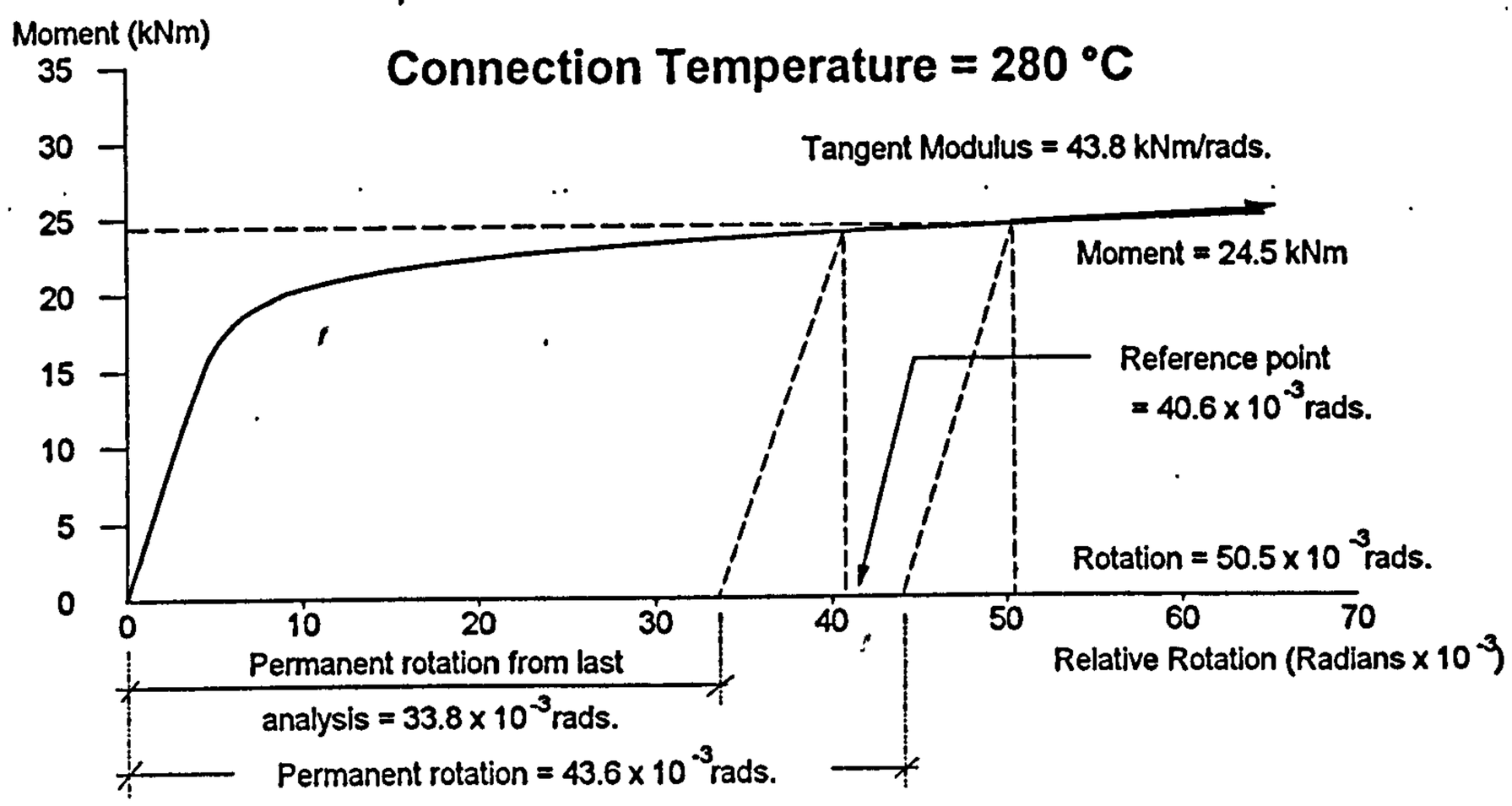

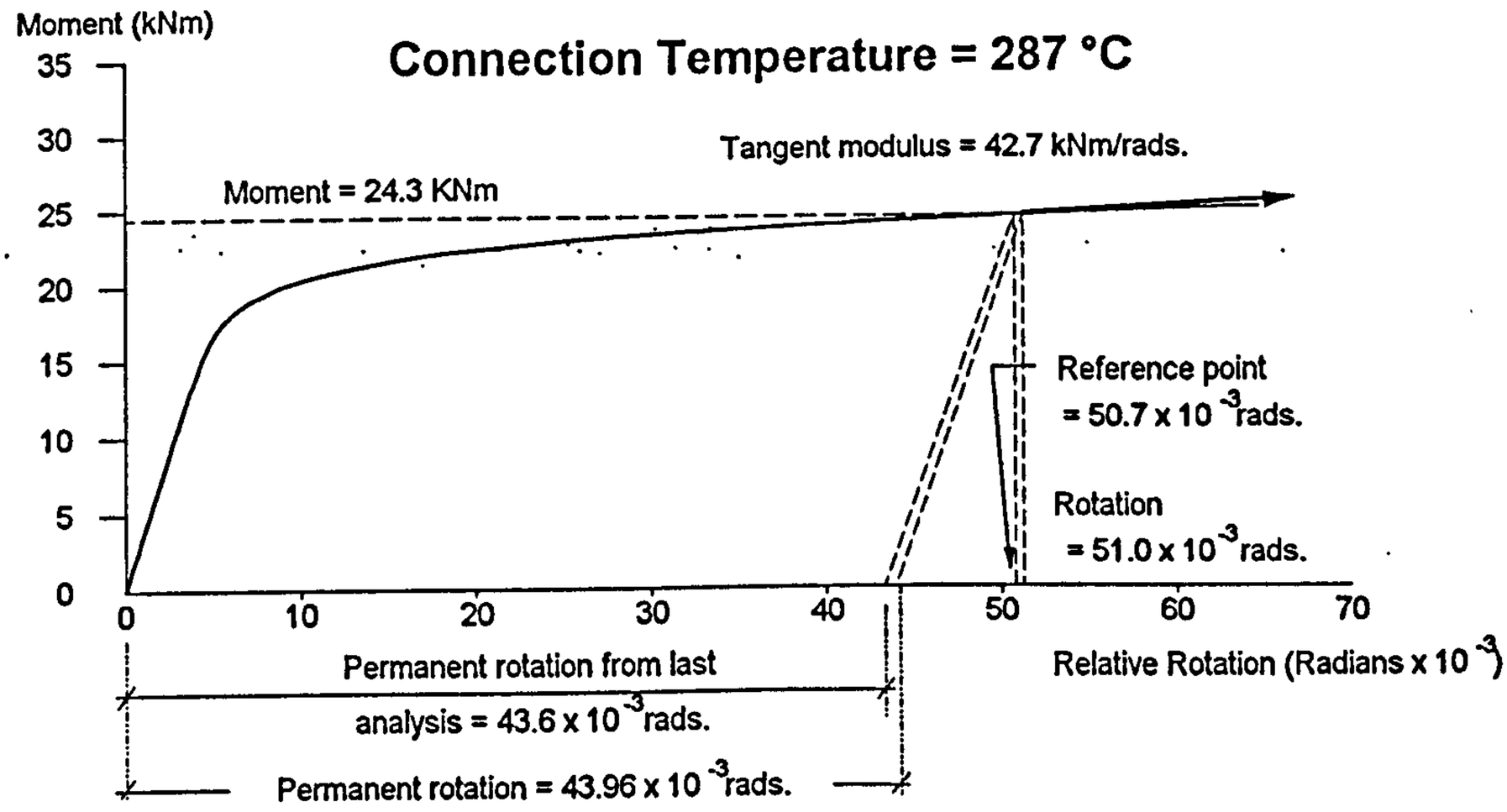

Fig 3.22:(Continued) Moment-rotation-temperature characteristics of the connection used for the example shown in Fig. 3.20.

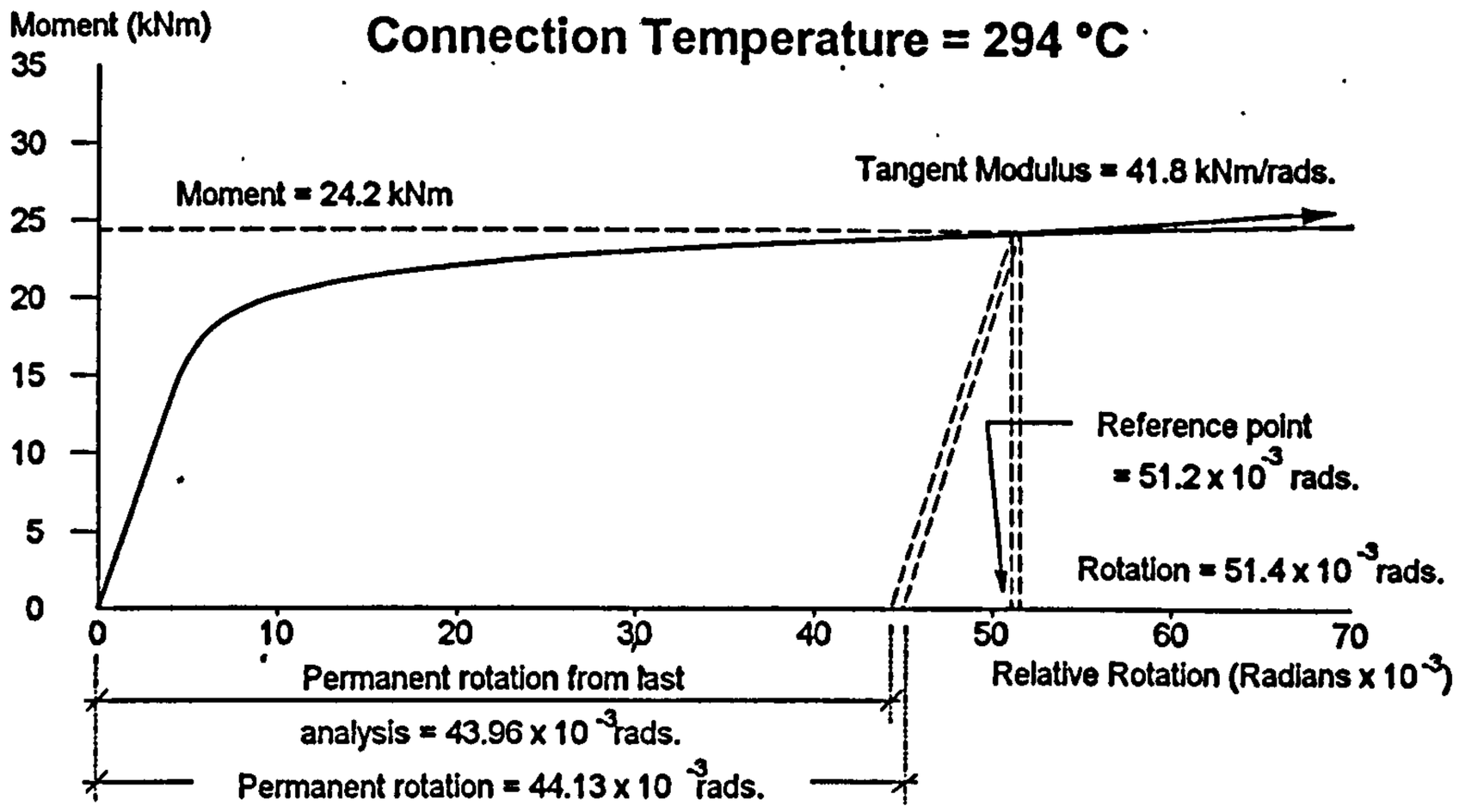

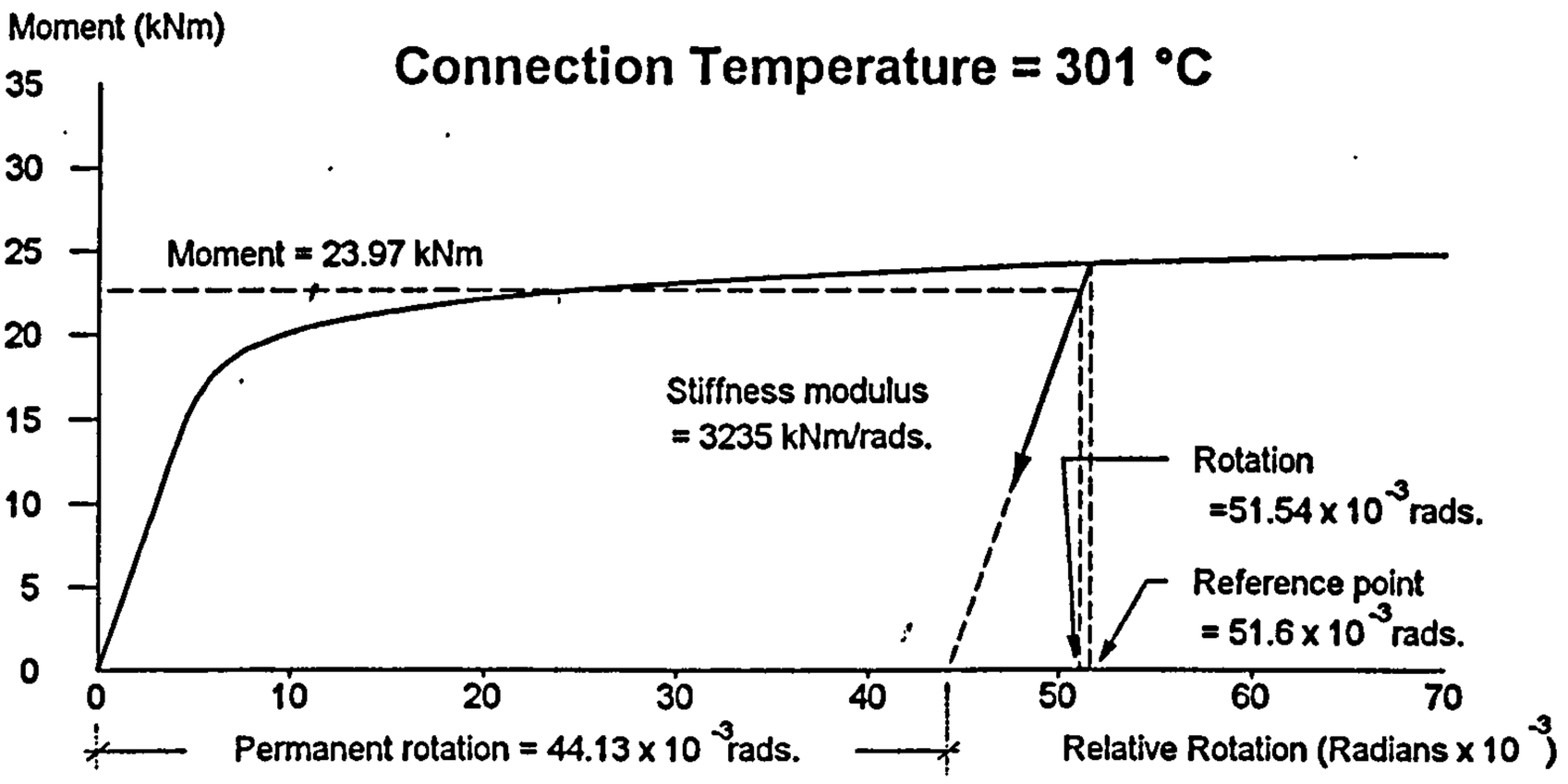

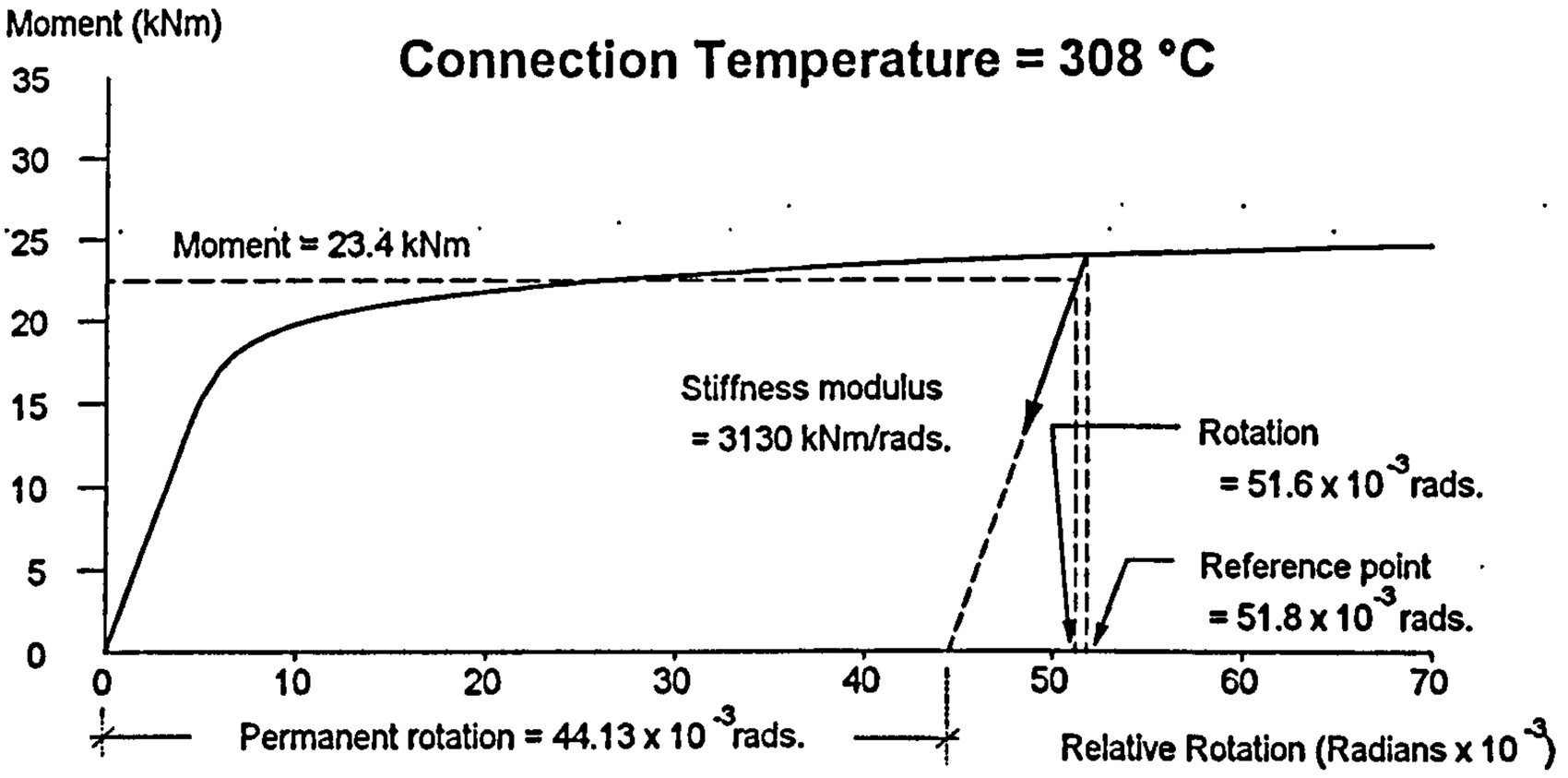

Fig 3.22:(Continued) Moment-rotation-temperature characteristics of the connection used for the example shown in Fig. 3.20.

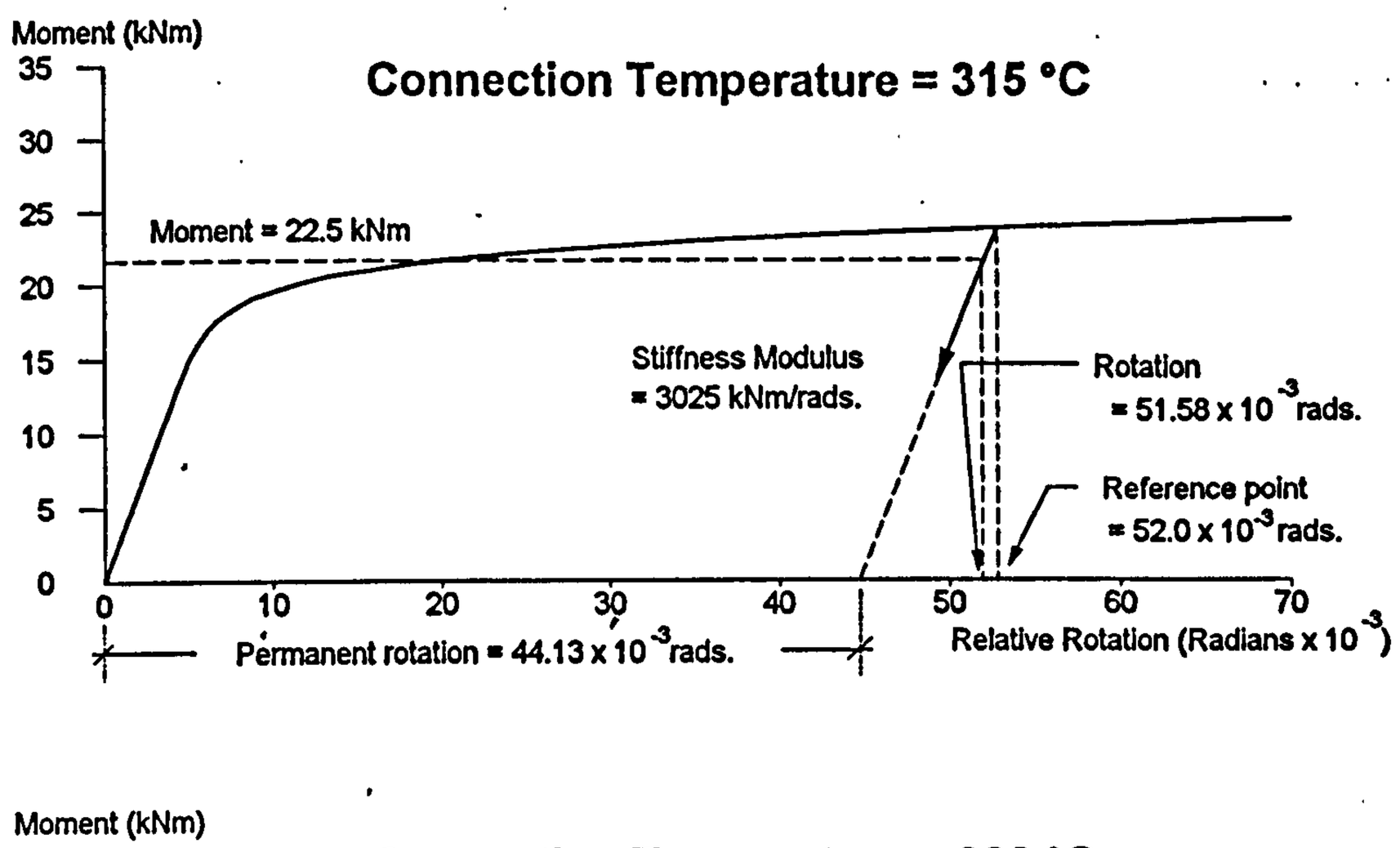

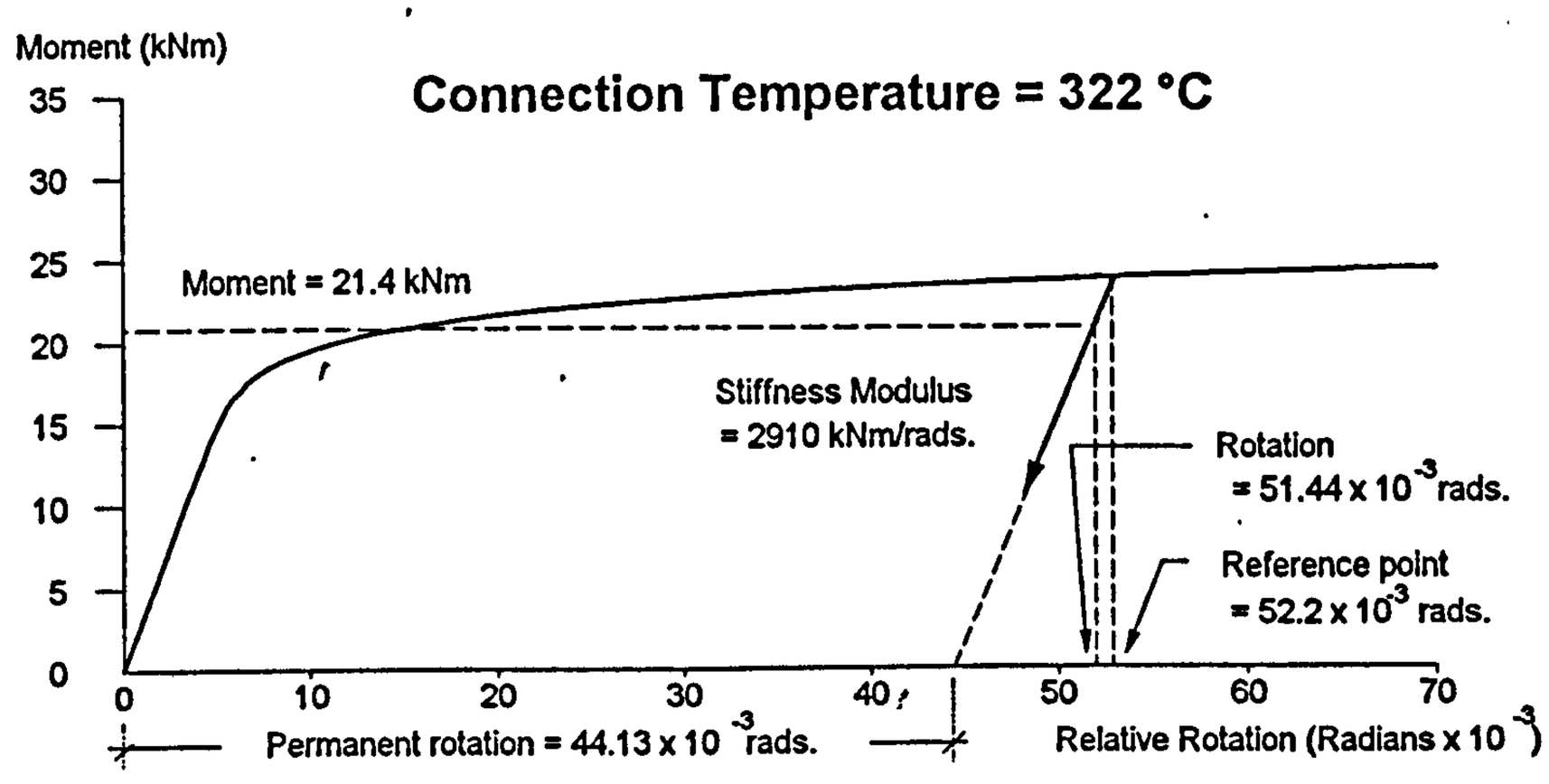

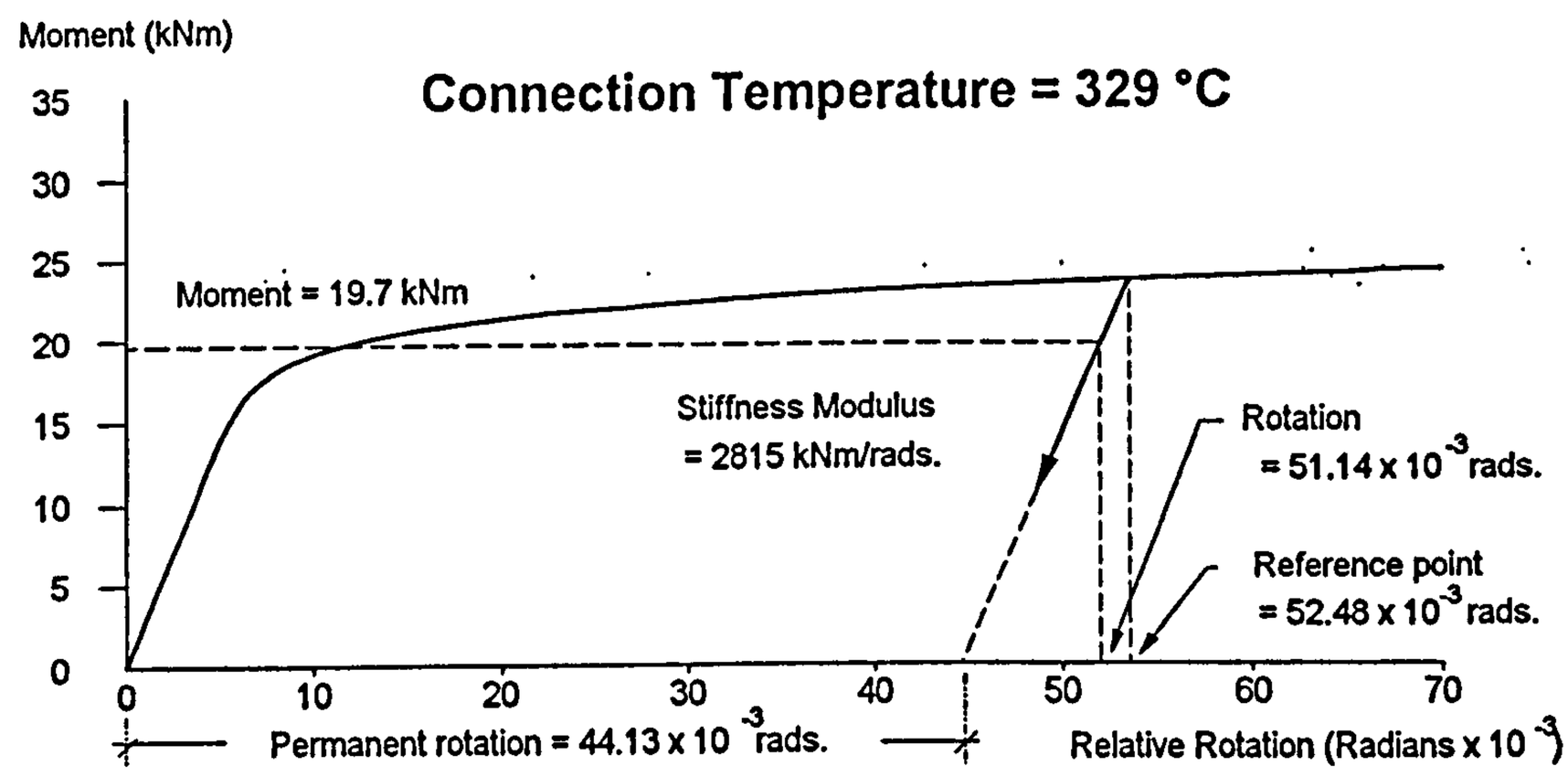

Fig 3.22:(Continued) Moment-rotation-temperature characteristics of the connection used for the example shown in Fig. 3.20.

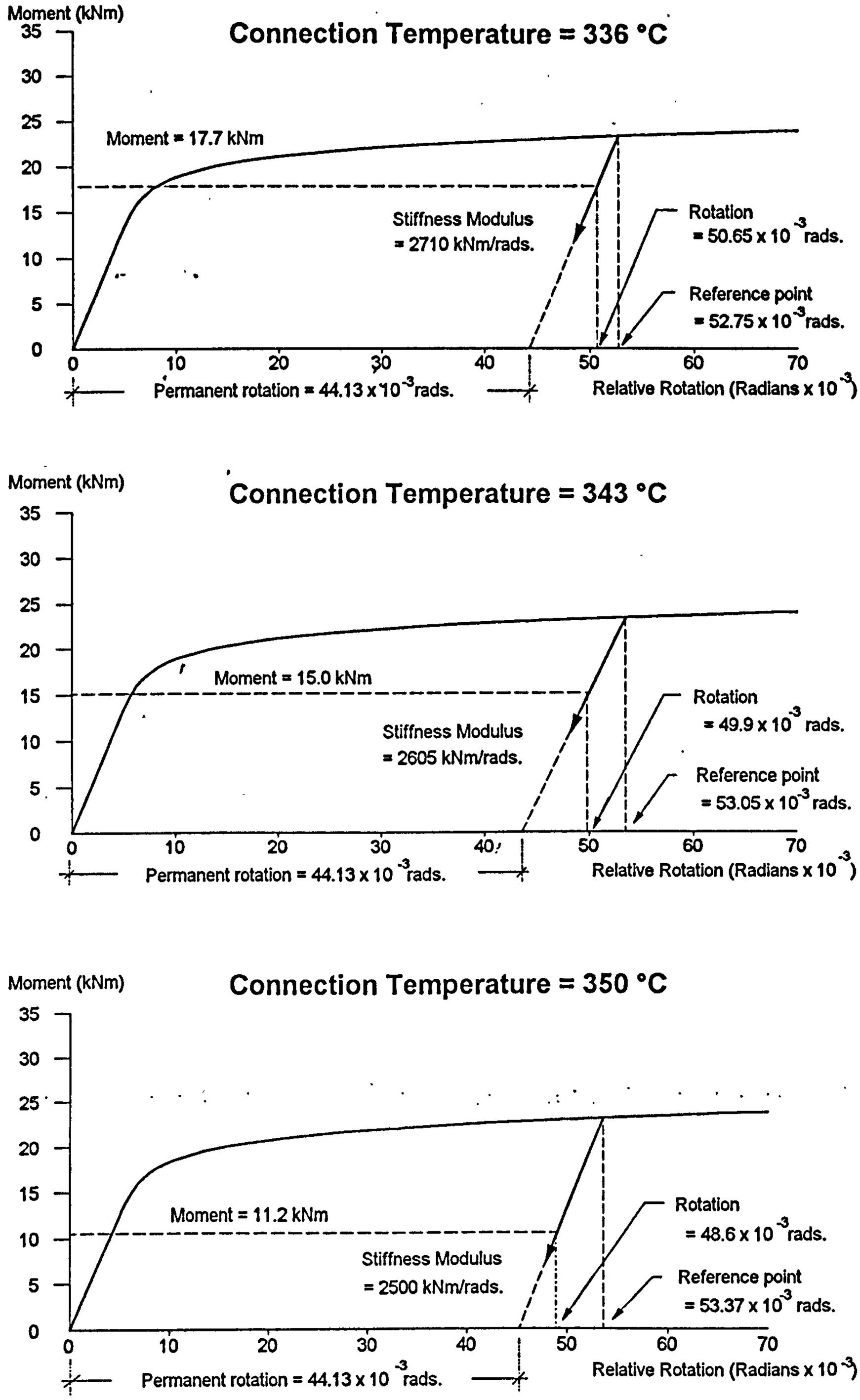

Fig 3.22:(Continued) Moment-rotation-temperature characteristics of the connection used for the example shown in Fig. 3.20.

4.0: RELOCATING THE POSITION OF THE REFERENCE AXIS.

In the previously existing version of the software the reference axis, at which the nodal position is placed, was located at the centroid of the elastic cross-section of the beam-column finite elements. The position is calculated at ambient temperature and remains static during any temperature change. To allow for connection of two-dimensional shell elements to one-dimensional beam elements, allowing representation of a continuous floor slab supported on the top flange of the beam, the facility of placing the reference axis at any position on or outside the cross-section was included within the model.

The formulation of the software, which was originally based on the work by El-Zanaty and Murray[29] and has been recently extended by Najjar[39] to include three-dimensional behaviour, is not repeated here. Instead only the parts of the formulation which are influenced by the extension of the software, to allow the ability of specifying the position of reference axis, are presented below.

Within the formulation the following assumptions apply,

- The element is straight, prismatic and symmetric about the principal axes.
- The plane cross sections of each of the thin-walled flat plates of which the beam-column is composed remain plane after loading.
- The shearing deformation in the mid-surface of the thin-walled plate is extremely small and can be neglected.

The nodal displacements at their specified positions within the structure, which is divided into imaginary finite elements, are the basic unknown parameters of the problem. Displacement of the reference axis within an element is uniquely defined by cubic shape functions and the boundary nodal point displacements. From the displaced reference axis the displacement of any arbitrary point on the cross-section can be defined. This is shown in Fig. 4.01 for an example where the reference axis is positioned on the top flange of the beam. The displacements *u, v, w,* of an arbitrary point *'A'* on the beam cross-section can be expressed in terms of the displacement of the reference axis by the following expressions

$$u = u_0 - \left(y \sin\theta_y + x \sin\theta_x\right) \tag{4.01}$$

$$v = v_0 - y + \left(y \cos\theta_y \cos\theta_z + x \cos\theta_x \sin\theta_z\right) \tag{4.02}$$

$$w = w_0 - x + \left(x \cos\theta_x \cos\theta_z - y \cos\theta_y \sin\theta_z\right) \tag{4.03}$$

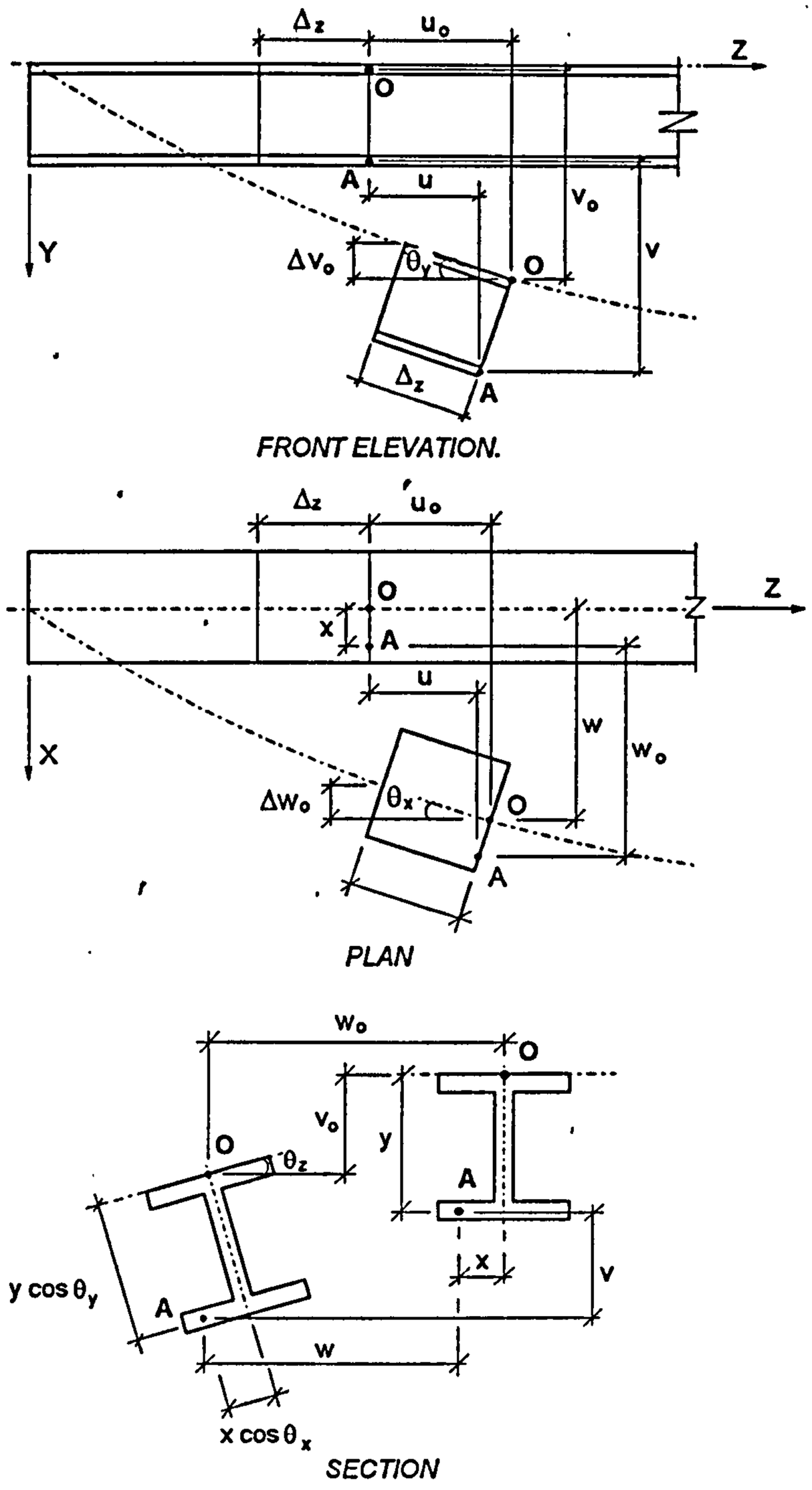

Fig. 4.01: Definition of the displacement of an arbitrary point on the cross-section with respect to the reference axis.

The following assumptions are adopted:

1. The slope of the member about the y-axis is,

$$v_0' = \sin\theta_y \qquad (4.04)$$

and its slope about the x-axis is,

$$w_0' = \sin\theta_x. \qquad (4.05)$$

Although the slopes of the member defined in equations (4.04) and (4.05) should be represented by tangents, the sine assumption allows the derivation[29] to be undertaken

with no additional assumptions or simplifications, except to ignore higher-order terms when they are negligible

2. The twist angle is small, so that

$$\sin\theta_z = \theta_z \tag{4.06}$$

and

$$\cos\theta_z = 1. \tag{4.07}$$

Using the above assumptions, equations (4.01) to (4.03) can be reduced to,

$$u = u_0 - yv_0' - xw_0' \tag{4.08}$$

$$v = v_0 - y + \left(y\cos\theta_y + x\theta_z\cos\theta_z\right) \tag{4.09}$$

$$w = w_o - x + \left(x\cos\theta_x - y\theta_z\cos\theta_y\right) \tag{4.10}$$

Equation (4.08), which represents the axial deformation, is based on Bernoulli's hypothesis which assumes that plane sections remain plane during deformation. However for thin-walled beams the Vlasov hypothesis[63], which takes into account the effect of warping, should be adopted. The extension of equation (4.08) to incorporate the effect of warping produces

$$u = u_0 - yv_0' - xw_0' + \tilde{w}\theta_z \tag{4.11}$$

where,

$\tilde{w}$ = sectorial coordinate of the arbitrary point 'A'.

To illustrate the use of the sectorial coordinate of a symmetrical I-section two examples are presented, one with the reference axis positioned at the centroid and the other with this axis above the cross-section. Calculation of the sectorial coordinate of an arbitrary point A for both cases is defined in Figs. 4.02 and 4.03.

With the displacements defined at any point within the element the state of strain can be obtained from[43]

$$\varepsilon_z = u' + \frac{1}{2}\left\{(u')^2 + (v')^2 + (w')^2\right\} \tag{4.12}$$

Applying the constitutive properties of the material, the state of stress throughout the member can be calculated, together with the boundary (nodal) stresses. As with typical discrete structural analysis, equilibrium is enforced between boundary stresses and the externally applied loads.

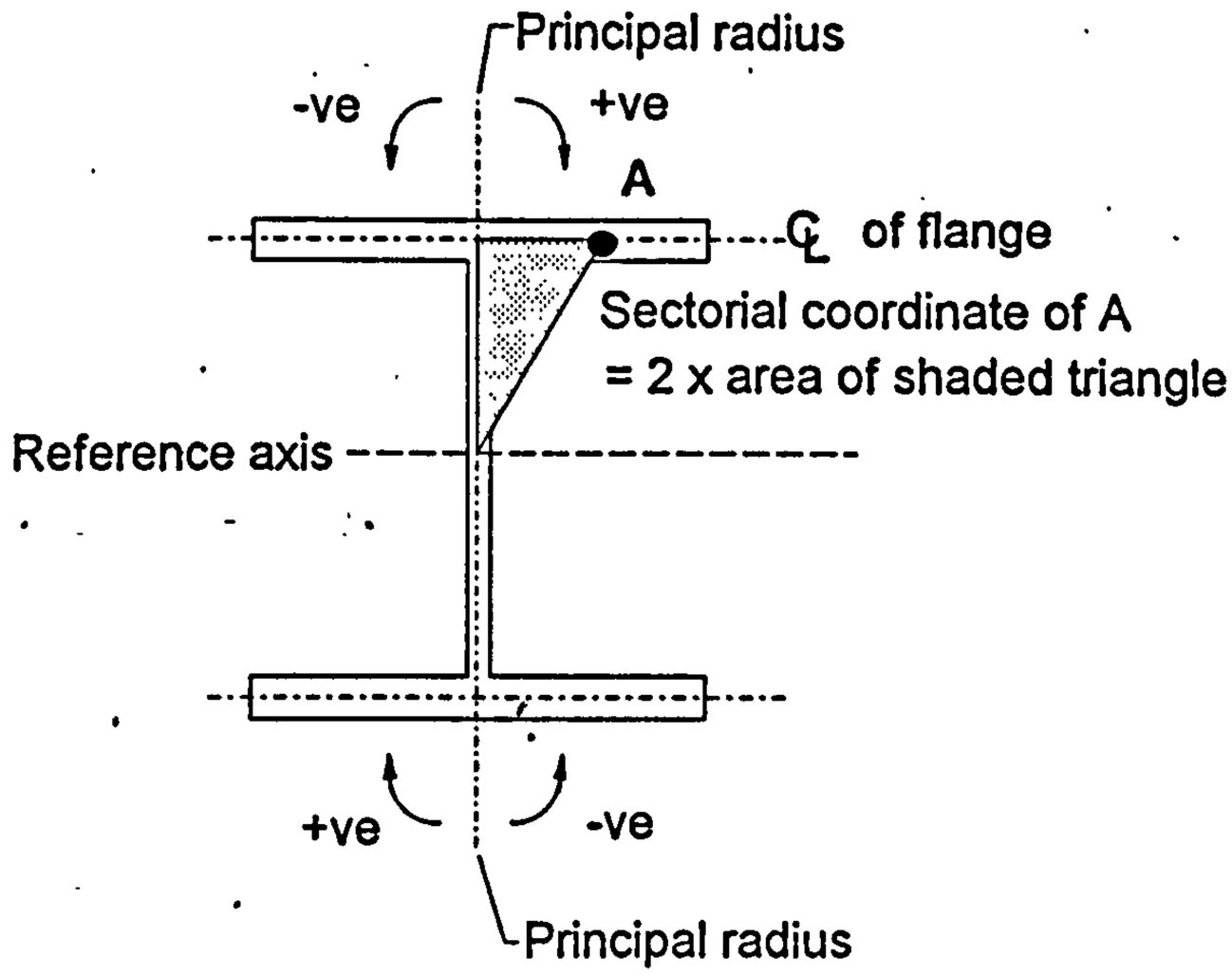

Fig 4.02: Definition of the warping coordinate of an arbitrary point on the cross-section when the reference axis is placed at the centroid.

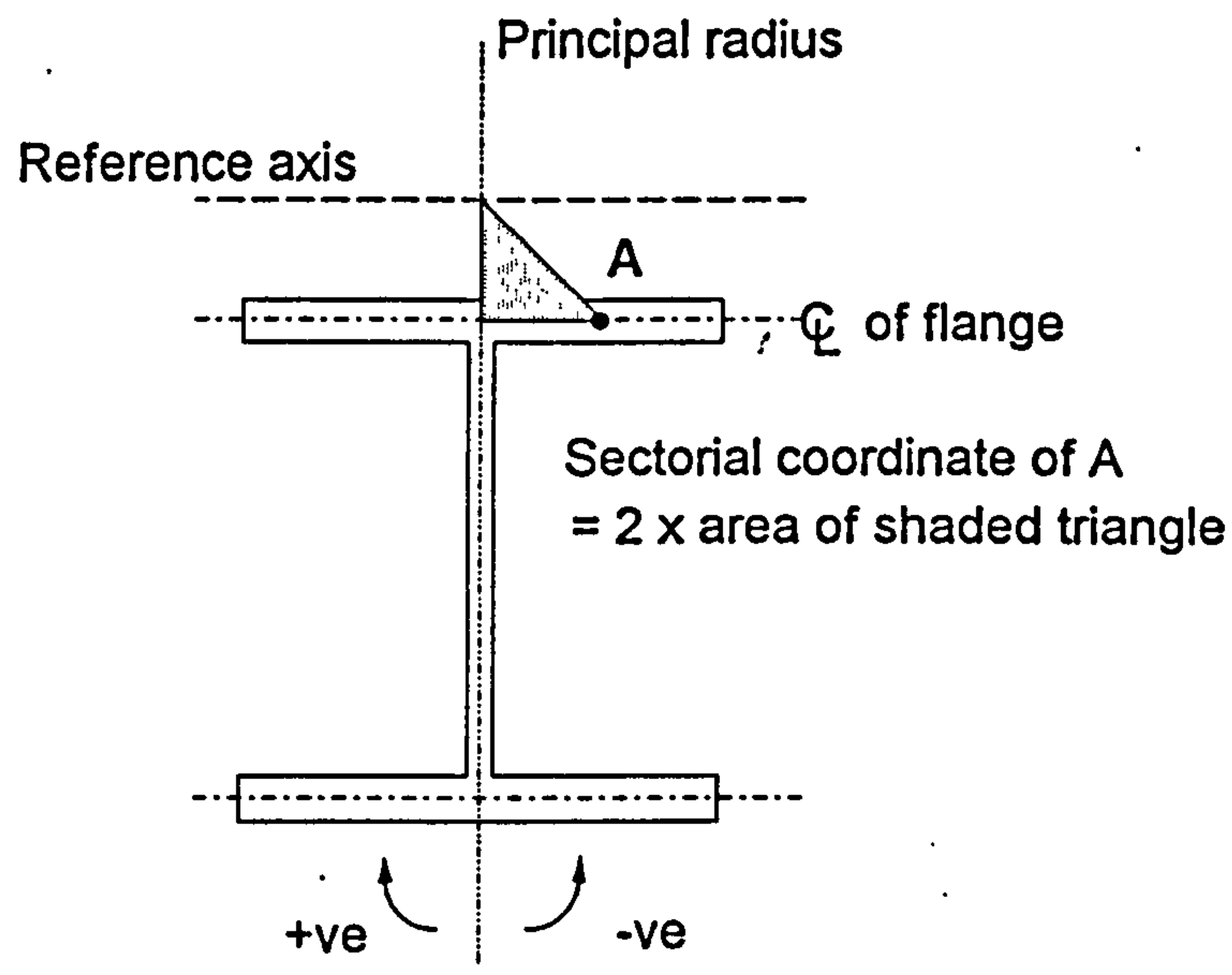

Fig 4.03: Definition of the warping coordinate of an arbitrary point on the cross-section when the reference axis is placed above the cross-section.

The simplest method of enforcing equilibrium at nodal points is to use the Principle of Virtual Work, as shown in equation (4.13)

$$\delta W = \int_V \sigma_z \, \delta\varepsilon_z \, dv - \langle Q \rangle \{\delta q\} = 0 \qquad (4.13)$$

where,

σ_z = axial stress,

$\delta\varepsilon_z$ = virtual axial strain (corresponding to the imposed virtual displacements),

$\langle Q \rangle$ = row vector of external loads,

$\{\delta q\}$ = column vector of imposed virtual displacements.

As discussed in Chapter 2, an integration of stress over the cross-section is conducted. These stress resultants are obtained by numerical integration of the stress defined through the cross-section at Gauss points. This allows numerical integration to be performed along the member. Since incremental stress resultants are required in the formulation of the tangent stiffness matrix, the sectional and sectorial (warping) properties are calculated numerically relative to the reference axis. To take into account inelastic behaviour the transformed section concept[47] is used, as explained in Chapter 2.

To allow a considerable variation of stress through the cross-section, displacements are defined at 13 points thus dividing the section into 12 segments as shown in Fig. 4.04

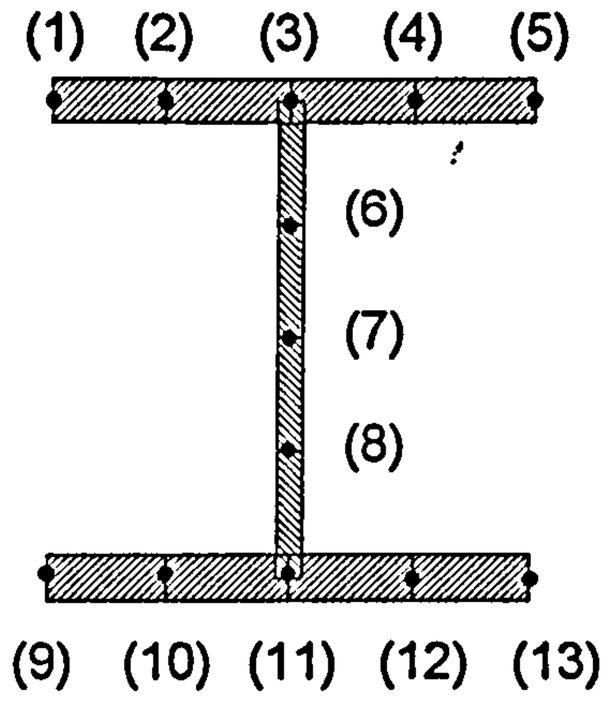

Fig. 4.04: Position on the cross-section at which displacements, strains and stresses are defined.

The required sectional and sectorial properties and stress resultants are specified below, with numerical evaluation of these properties being defined in the formulation by El-Zanaty and Murray[29] and the formulation by Najjar[39]. The definition of these properties remains unchanged (and is therefore ~~are~~ not repeated here) with the only difference occurring due to the displacement of the reference axis about which these properties are calculated.

The sectional properties required are,

$$A = \int_A dA \qquad I_y = \int_A y\,dA$$

$$I_{y2} = \int_A y^2\,dA \qquad I_{y3} = \int_A y^3\,dA$$

$$I_{y4} = \int_A y^4\,dA \qquad I_x = \int_A x\,dA$$

$$I_{x2} = \int_A x^2\,dA \qquad I_{x3} = \int_A x^3 dA$$

$$I_{x4} = \int_A x^4\,dA \qquad I_{xy} = \int_A x\,y\,dA$$

$$I_{x2y} = \int_A x^2 y\,dA \qquad I_{xy2} = \int_A xy^2\,dA$$

$$I_{x2y2} = \int_A x^2 y^2\,dA \qquad I_{x3y} = \int_A x^3 y\,dA$$

$$I_{xy3} = \int_A xy^3\,dA$$

The sectorial properties required are

$$I_\omega = \int_A \omega\,dA \qquad I_{\omega x} = \int_A \omega\,x\,dA$$

$$I_{\omega y} = \int_A \omega\,y\,dA \qquad I_{\omega x2} = \int_A \omega\,x^2\,dA$$

$$I_{\omega y2} = \int_A \omega\,y^2\,dA \qquad I_{\omega 2} = \int_A \omega^2\,dA$$

The stress resultants required are

$$n = \int_A \sigma_z dA \qquad m_x = \int_A \sigma_z y dA$$

$$m_x^{\,2} = \int_A \sigma_z y^2 dA \qquad m_y = \int_A \sigma_z x dA$$

$$m_y^{\,2} = \int_A \sigma_z x^2 dA \qquad m_w = \int_A \sigma_z \tilde{w}\,dA$$

$$m_z = \int_A \sigma_z \left(x^2 + y^2\right) \cdot \theta_z' dA \qquad TSV = \mathrm{G}\mathrm{J}\theta_z'$$

where,

n = axial force,

m_x = bending moment about the x-axis,

$m_x^{\,2}$ = stress resultant calculated, due to the higher order terms within the strain-displacement equation, which represent non-linear effects,

m_y = bending moment about the y-axis,

m_y^2 = stress resultant calculated, due to the higher order terms within the strain-displacement equation, which represent non-linear effects,

m_w = warping moment,

m_z = contribution to the torsional moment due to warping deformations (this is a second-order effect known as the Wagner effect[45]),

TSV = torsional moment due to St.Venant shear stress,

4.1: VALIDATION OF RELOCATION OF REFERENCE AXIS.

Since the original model has been validated for large displacements at ambient and elevated temperatures,[29,39] the extension of the model to allow relocation of the reference axis was compared against the original model with the reference axis positioned at the centroid.

The first example considered was the simply supported beam shown in Fig. 4.05 with a load ratio of 0.5 to BS5950 Part 8[5] and uniformly heated. The original model with the reference axis at the centroid was compared with the new model with the reference axis positioned at the top flange. The vertical displacements for both cases are shown in Fig. 4.07.

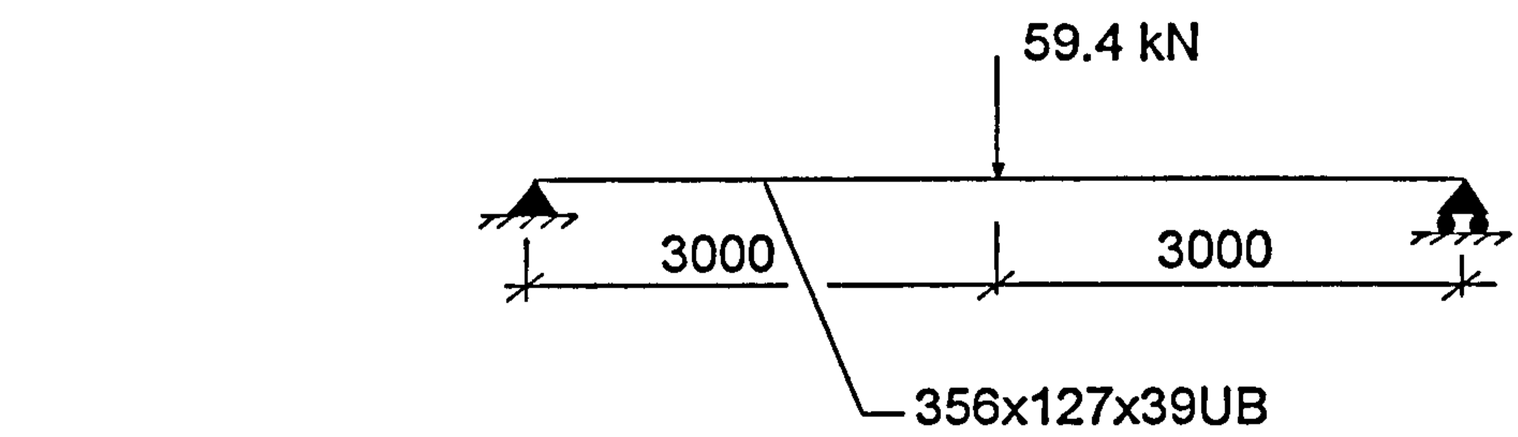

σ_{y20} = 275 N/mm²
E_{20} = 205 kN/mm²

Fig. 4.05: Uniformly heated simply-supported beam used to validate the repositioning of the reference axis.

For the next example a beam with built-in ends with a load ratio of 0.5 to BS5950 Part 8[5], as shown in Fig. 4.06, was uniformly heated. Since full restraint is provided against thermal expansion, the axial forces induced will have a significant effect. The vertical displacements at mid-span are shown in Fig. 4.08 with the values being exactly the same irrespective of the position of the reference axis.

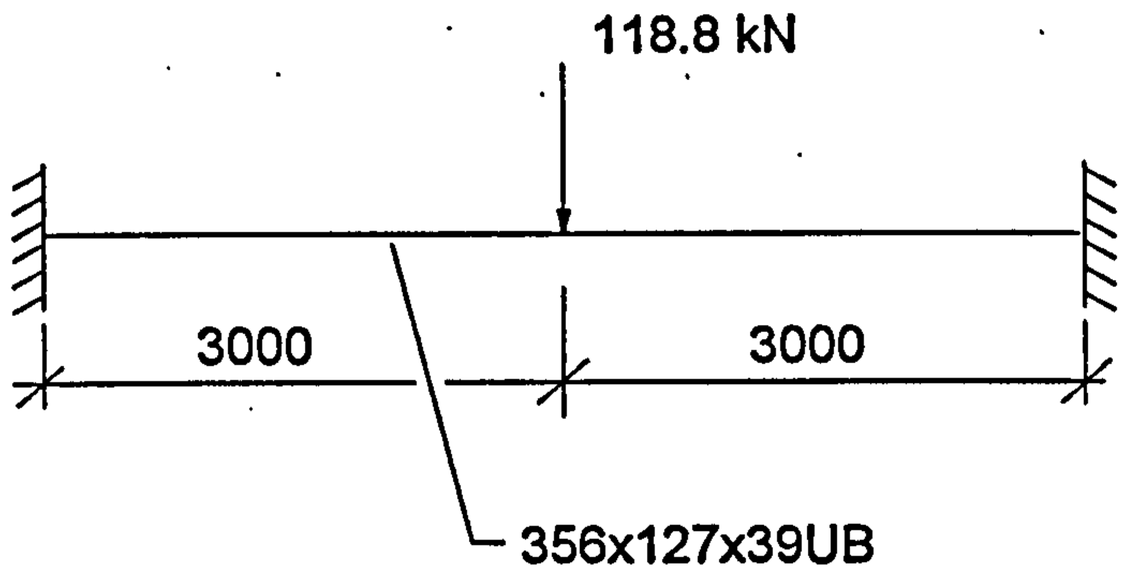

$\sigma_{y20} = 275$ N/mm²
$E_{20} = 205$ kN/mm²

Fig. 4.06: Uniformly heated beam with ends built-in, used to validate the repositioning of the reference axis.

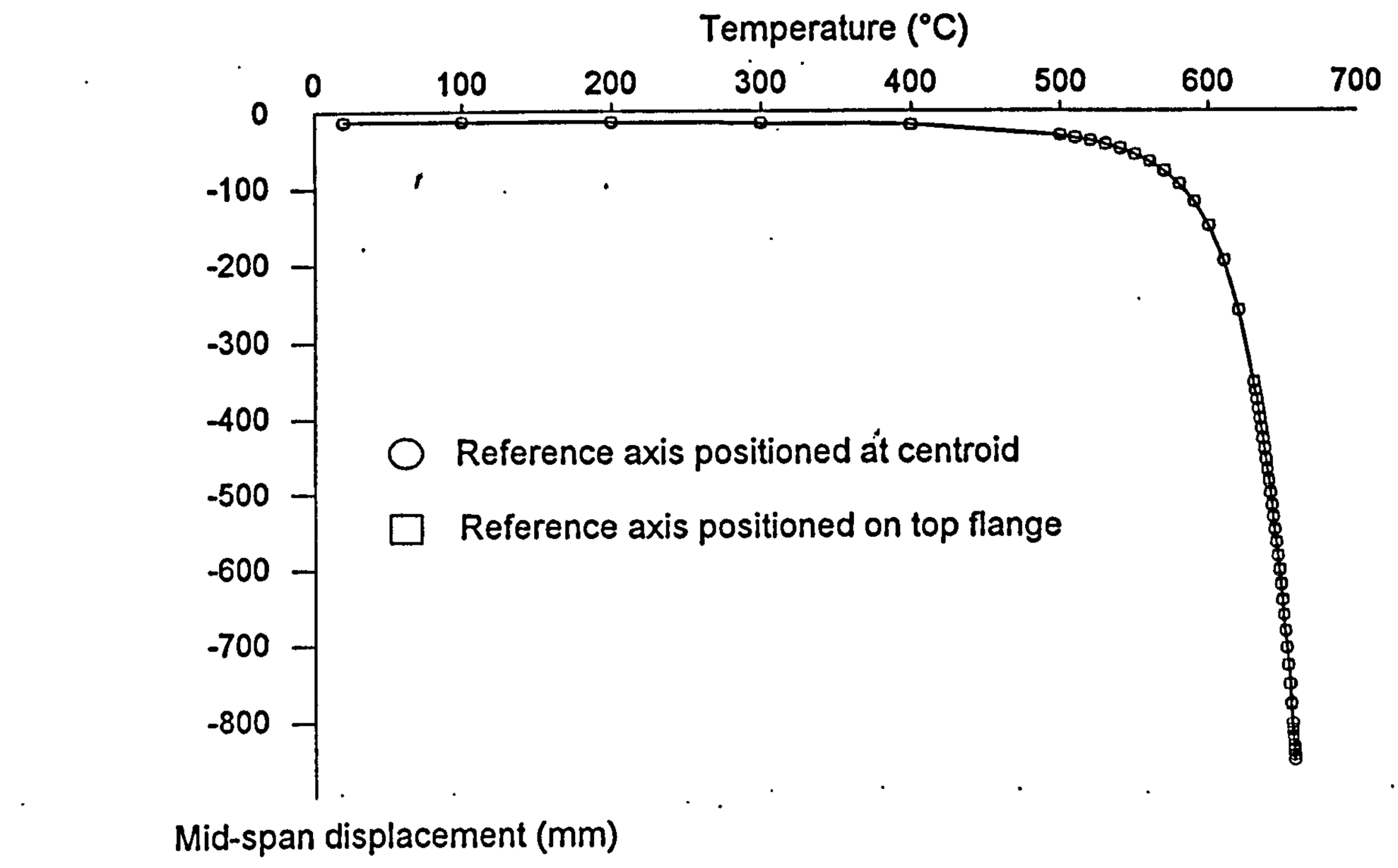

Fig. 4.07: Vertical displacement at mid-span of the simply-supported beam of Fig. 4.05 with the reference axis at the centroid and at the top flange of the cross-section.

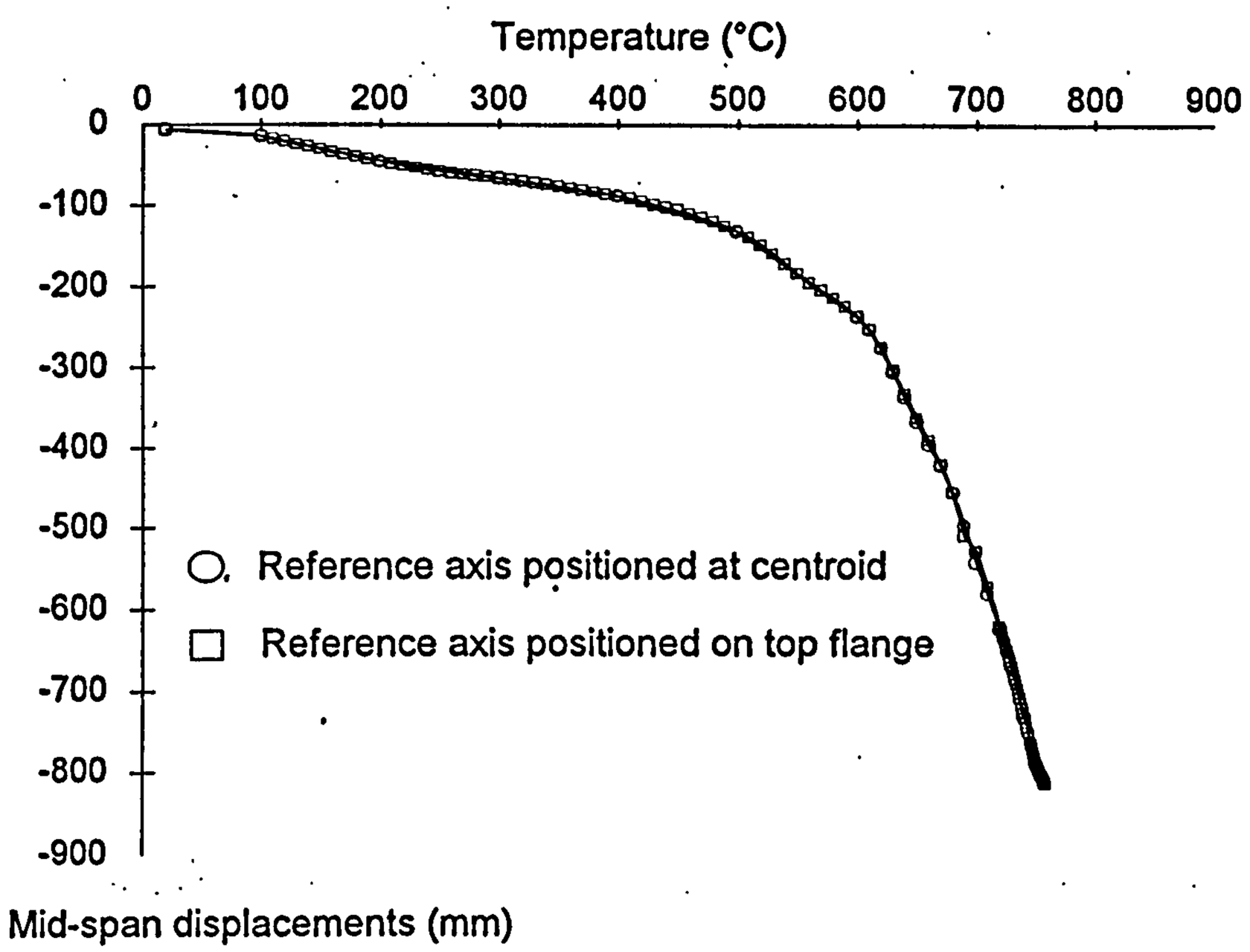

Fig. 4.08: Vertical displacement at mid-span of a beam with ends built-in and the reference axis at the centroid and at the top flange of the cross-section.

Shown in Fig. 4.09 is a comparison between the internal moments for this example, calculated at mid-span for both positions of the reference axis. To allow explanation of these values the axial force is required, as shown in Fig. 4.10. Consider first the case when the reference axis is positioned at the centroid and the moment is calculated at this point. The moment increases until a temperature of 400°C is reached. This is due to the secondary geometrical effect of the vertical displacement and compressive axial forces, acting through the centroid of the cross-section, induced by the restraint to thermal expansion. Beyond 400°C the moment decreases due to a decrease in axial force as shown in Fig. 4.10. The axial force decreases continuously with catenary action being identified before failure, identified by the change in sign of the force. With the reference axis at the top flange and the moment calculated at this position the induced axial forces which act through the centroid have a greater effect on the value of the moment, as shown in Fig. 4.09. This could cause numerical instability problems due to the large changes in moment during the heating scheme. This was experienced in this example above 100°C at which the temperature step size had to be reduced.

Further validation examples are presented in Chapter 5, for the case when simple elastic beams fail by lateral-torsional buckling when the load is placed on the top flange.

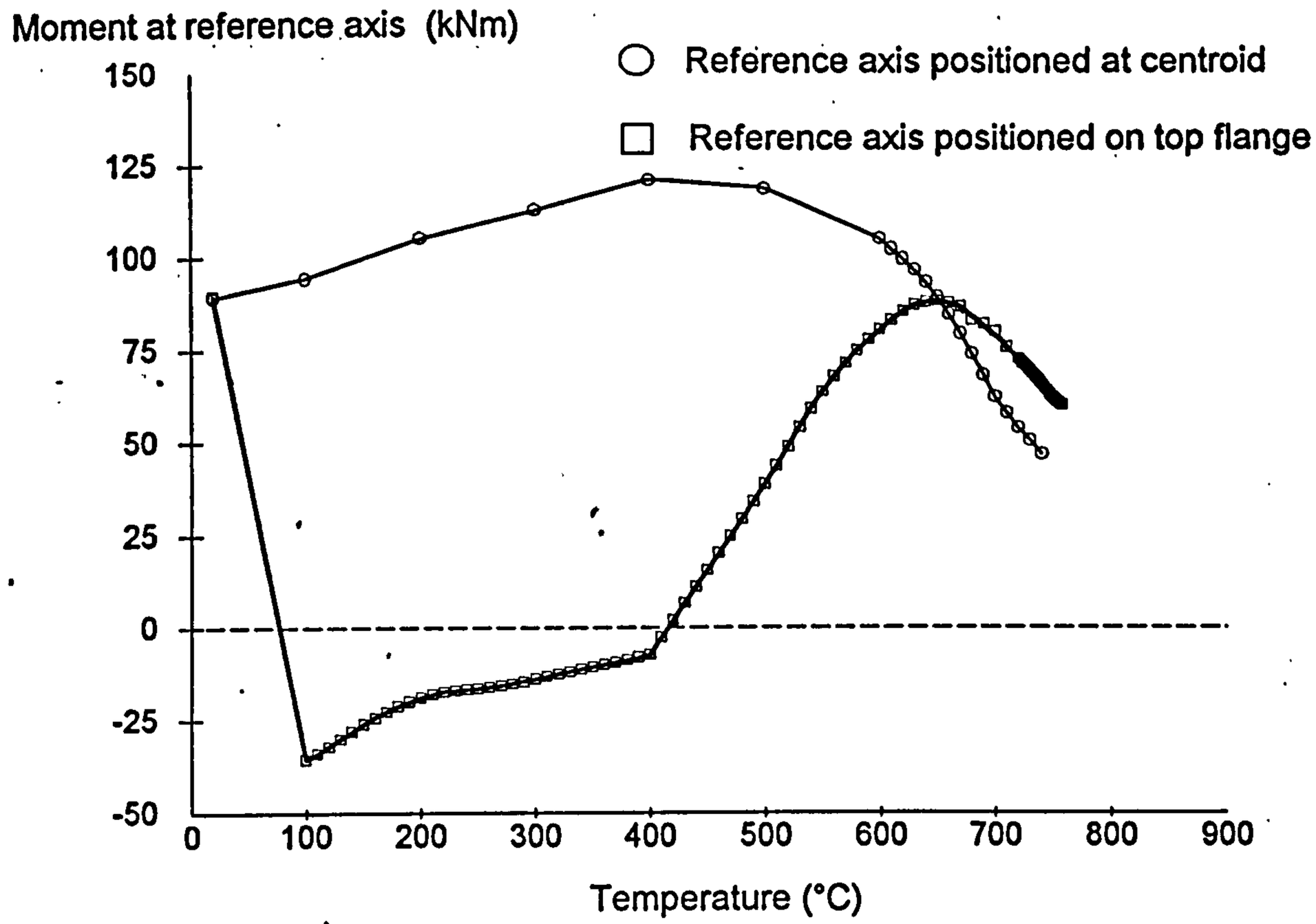

Fig. 4.09: Comparison between moments calculated at mid-span about the reference axis which is positioned at the centroid and at the top flange.

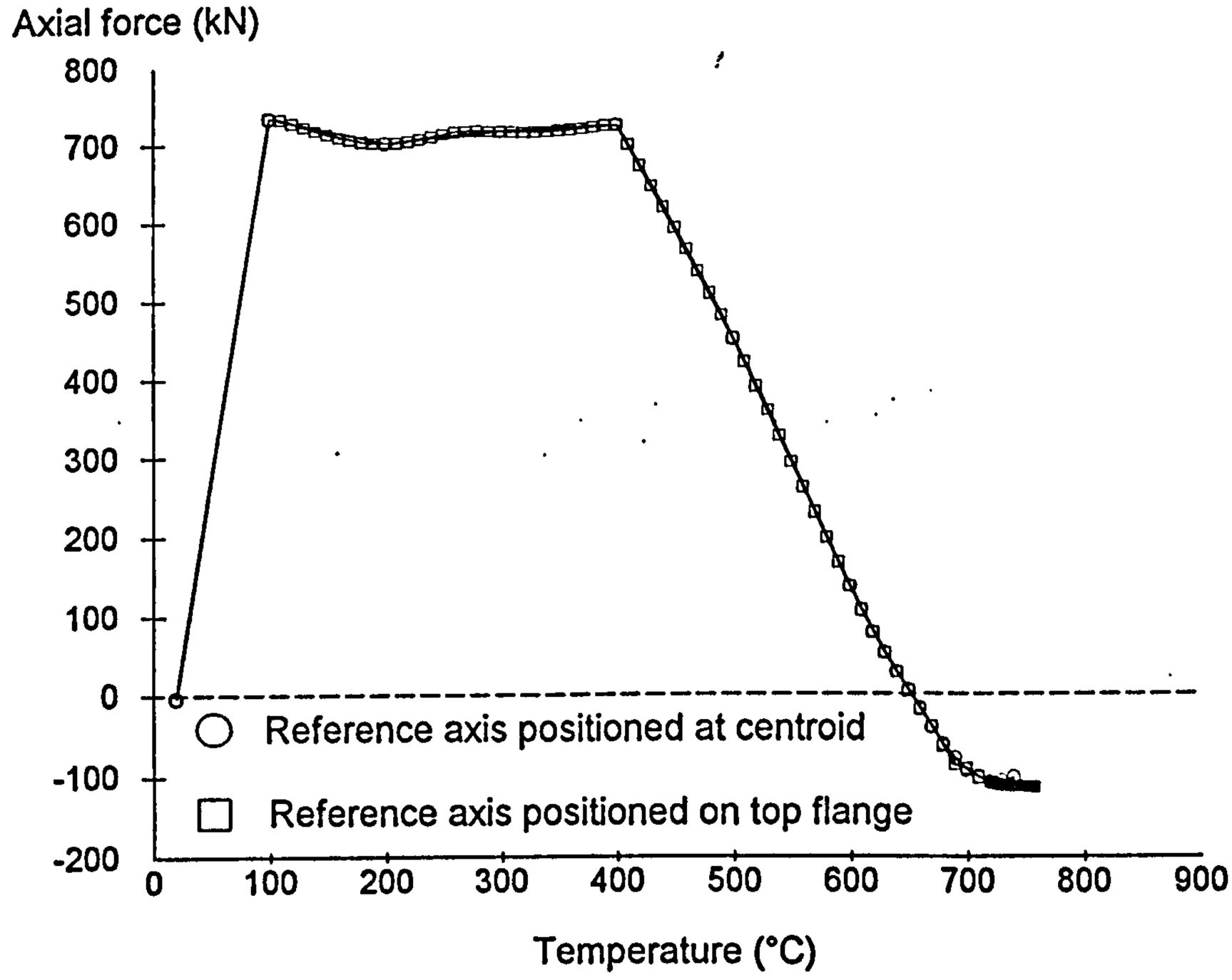

Fig. 4.10: Comparison between axial forces when the reference axis is positioned at the centroid and at the top flange.

5.0: THE LATERAL-TORSIONAL BUCKLING OF UNRESTRAINED STEEL BEAMS IN FIRE.

Beams are structural members which resist applied loads primarily by bending and shearing actions. The bending stresses and deflections of beams usually govern their design, with the bending action occurring in-plane about the major axis provided no twisting of the beam is induced and adequate lateral restraint is present. In the majority of systems used in multi-storey building frames beams are arranged such that the applied loads act through their shear centres, thus eliminating twisting, and adequate lateral restraint to the compression flange is obtained from the supported flooring system. Therefore most steel beams are fabricated from hot-rolled open sections, which are easy to connect on site and have their material efficiently distributed to resist in-plane bending. However these sections are weak in resisting loads which may induce any out-of-plane bending or twisting.

If adequate lateral restraint is not provided and the beam does not have sufficient lateral and torsional stiffness, then the in-plane loads can cause out-of-plane buckling in a combination of lateral deflection and twisting. This form of behaviour is known as lateral-torsional buckling, with the two components being interdependent. This is due to the applied in-plane moment exerting a torsional component about the laterally deflected longitudinal axis, which causes the beam to twist. This twisting action causes the applied in-plane moment to exert a lateral bending component which causes the beam to deflect sideways.

Considering the behaviour of steel beams at elevated temperatures the simplest calculation method presented in BS5950 Part 8[5], is known as the Limiting Temperature Method. In this method the maximum permissible temperature of a member is based on its type, its loading characteristics and load ratio. This method presents little difficulty in implementation, and is clearly the approach which will recommend itself to practising engineers. The development of limiting temperatures in BS5950 Part 8 has been based on a large number of fire tests and supplementary computer model predictions. For members in bending, standard fire tests[9] have been carried out on beams which support concrete or composite floors, the major variables being the applied load, structural configuration and beam size. A more comprehensive experimental study of various parameters which affect the behaviour is not feasible due to the very high cost of structural furnace testing and the size limitations of standard test furnaces. It is not surprising that the beams tested have represented the systems in most common use; floor beams carrying precast slabs on

the top flange or on shelf-angles, slim floors with the slab filling the space between the flanges, and composite beams using metal decking and slabs tied through shear connectors to the top flange. Not only are these systems the most common in current steel building construction, but all have full compression flange restraint, and therefore present no threat to the integrity of the test furnace which might be caused by lateral buckling failure.

In the context of present-day building design at elevated temperatures beams without lateral restraint to the compression flange may be considered as of secondary importance. However in some situations, such as industrial buildings and plant areas, beams may not have continuous lateral restraint. This also applies in some office construction systems, notably the "Parallel Beam Approach"[64] in which the primary (spine) beams are unrestrained and support composite secondary (rib) beams on their top flanges, thus providing service spaces in both directions within the depths of these beams. It is necessary to calculate limiting temperatures for unprotected beams either to determine the required protection thickness or, as part of a fire engineering approach, to set the required section size, load ratio and possibly partial protection. BS5950 Part 8[5] deals with unrestrained beams firstly by using a load ratio based on lateral-torsional buckling failure at ambient temperature, and then by giving limiting temperatures reduced by about 65°C from those for restrained beams. An underlying problem is that the limiting temperatures for beams in furnace testing are based on a definition of failure[7] of a maximum in-plane deflection of span/20, or a maximum rate of deflection when span/30 is exceeded.

To allow an investigation into the accuracy of the design of unrestrained beams presented in the design codes, BS 5950 Part 8[5] and EC3 Part 1.2[6], the computer model was extended to allow lateral-torsional buckling to be predicted at elevated temperatures.

5.1: EXTENSION OF THE COMPUTER MODEL TO ALLOW LATERAL-TORSIONAL BUCKLING.

As explained in Chapter 2 the beam elements model three-dimensional behaviour including warping characteristics. Apart from the twist (which is based on pure and warping shear stresses) the formulation is based on normal stresses, adopting the typical assumption associated with thin-walled sections that shear deformations are negligible and can be ignored. However in lateral-torsional deformation the

geometrical effect of shear forces associated with flexural shear stresses has to be included. Since the shear forces cannot be defined in terms of deformations, due to thin-walled beam assumptions, they are calculated as reactions and are only needed for equilibrium. To indicate the effect of shear forces on unrestrained beams, consider first the case of a simply supported beam loaded with in-plane uniform bending moment as shown in Fig. 5.01. The beam supports prevent both lateral deflection and twist, but the flange ends are free to warp.

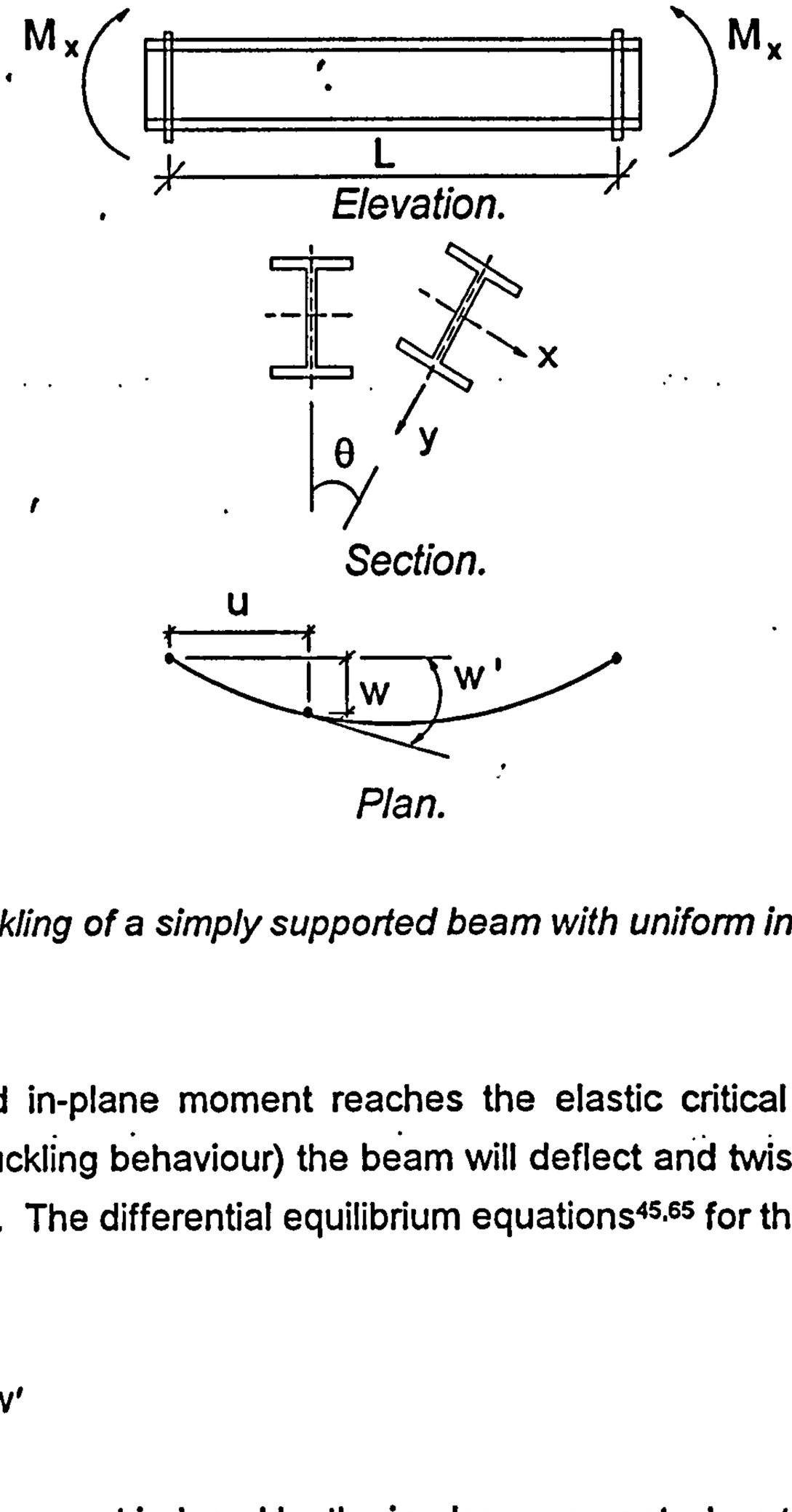

Fig. 5.01: Buckling of a simply supported beam with uniform in-plane moment.

When the applied in-plane moment reaches the elastic critical value (in terms of lateral torsional-buckling behaviour) the beam will deflect and twist into an equilibrium position as shown. The differential equilibrium equations[45,65] for this condition are:

$$-EI_y w'' = M_x \theta \qquad (5.01)$$

$$GJ\theta' - EI_w \theta''' = M_x w' \qquad (5.02)$$

where,

$M_x\theta$ = lateral moment induced by the in-plane moment when the beam twists,

$M_x w'$ = torque induced by the in-plane moment when the beam deflects laterally,

EI_y = minor axis bending stiffness,

GJ = torsional stiffness based on pure torsion,

EI_w = warping stiffness.

Now consider the same beam, but with unequal end moments as shown in Fig. 5.02.

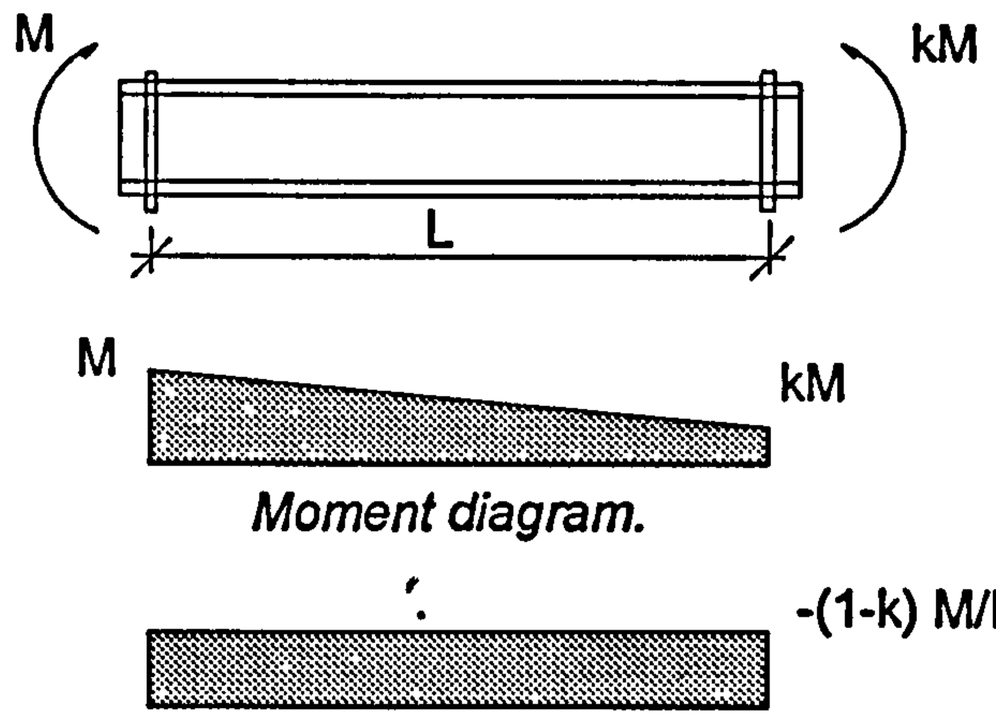

Fig. 5.02: Buckling of a simply supported beam with unequal in-plane moment.

For this condition, the differential equilibrium equations[45,65] of minor axis bending and torsion of the beam in the buckled position are:

$$-EI_y w'' = M_x \theta \qquad (5.03)$$

$$GJ\theta' - EI_w \theta''' = M_x w' - V_y w \qquad (5.04)$$

where,

$V_y w$ = torque induced by the shear force when the beam deflects laterally.

Before extension of the computer model to include flexural shear stresses three examples, which are shown in Fig. 5.03, were analysed. In each example the material was assumed to remain elastic and to be initially unstressed, so that the results could be compared against classical theoretical solutions[66].

The beam was modelled using four elements, and although the model can predict bifurcation loads, it was also decided to subject the beam to various imperfections (consisting of an initial lateral bow and twist) thus allowing a more comprehensive validation to be conducted. The predicted load-lateral deflection relationships are shown, together with a Southwell Plot, in Fig. 5.04 for the case of uniform moment. The elastic critical load of 112 kNm estimated from the Southwell Plot and the computer model prediction of 110 kNm for the bifurcation load of the perfect case, compared very well with the theoretical elastic critical load of 109 kNm, calculated by Timoshenko[66].

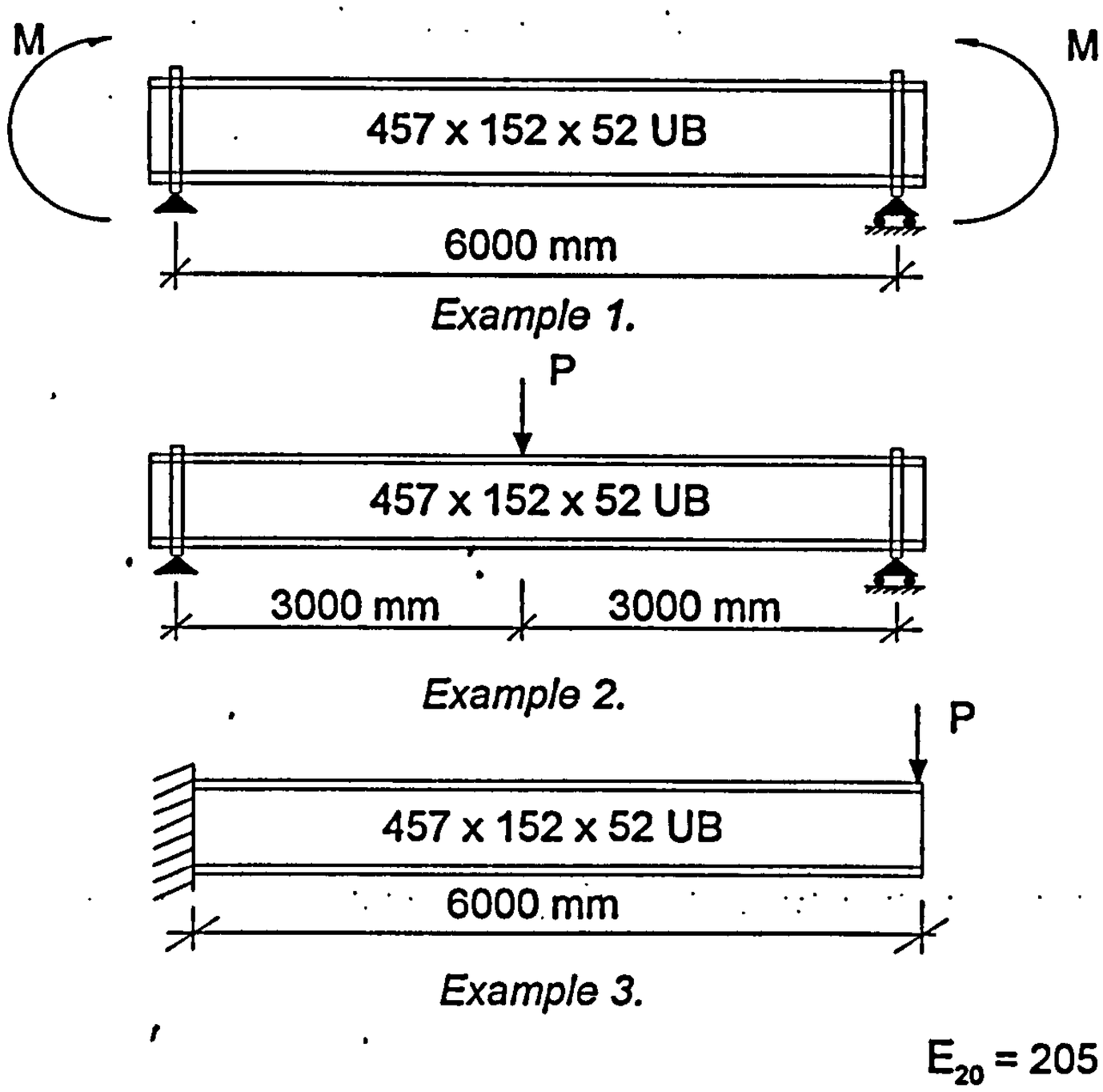

Fig. 5.03: Examples analysed by the computer model before the inclusion of flexural shear stress into the formulation.

The next two examples considered were a simply-supported beam with a point load at mid-span, and a cantilever beam with a point load at the tip, as shown in Fig. 5.03. In both cases the loads were assumed to act through the centroid (also the shear centre) of the cross-section, and are therefore 'neutral' as compared with 'stabilising' or 'destabilising' loads. The two configurations were analysed with various imperfections, and as expected, due to the model ignoring flexural shear stresses, major errors in the prediction of the elastic critical load were encountered. The results from the model overestimated the critical load for the simply supported beam and underestimated the critical load for the cantilever. The different signs of the errors can be explained by considering equation (5.04) and realising that the sign of the moment is different in the two examples. To highlight the magnitude of these errors, the bifurcation loads for both examples are shown in Table 5.01 and compared with the theoretical elastic critical loads calculated by Timoshenko[66].

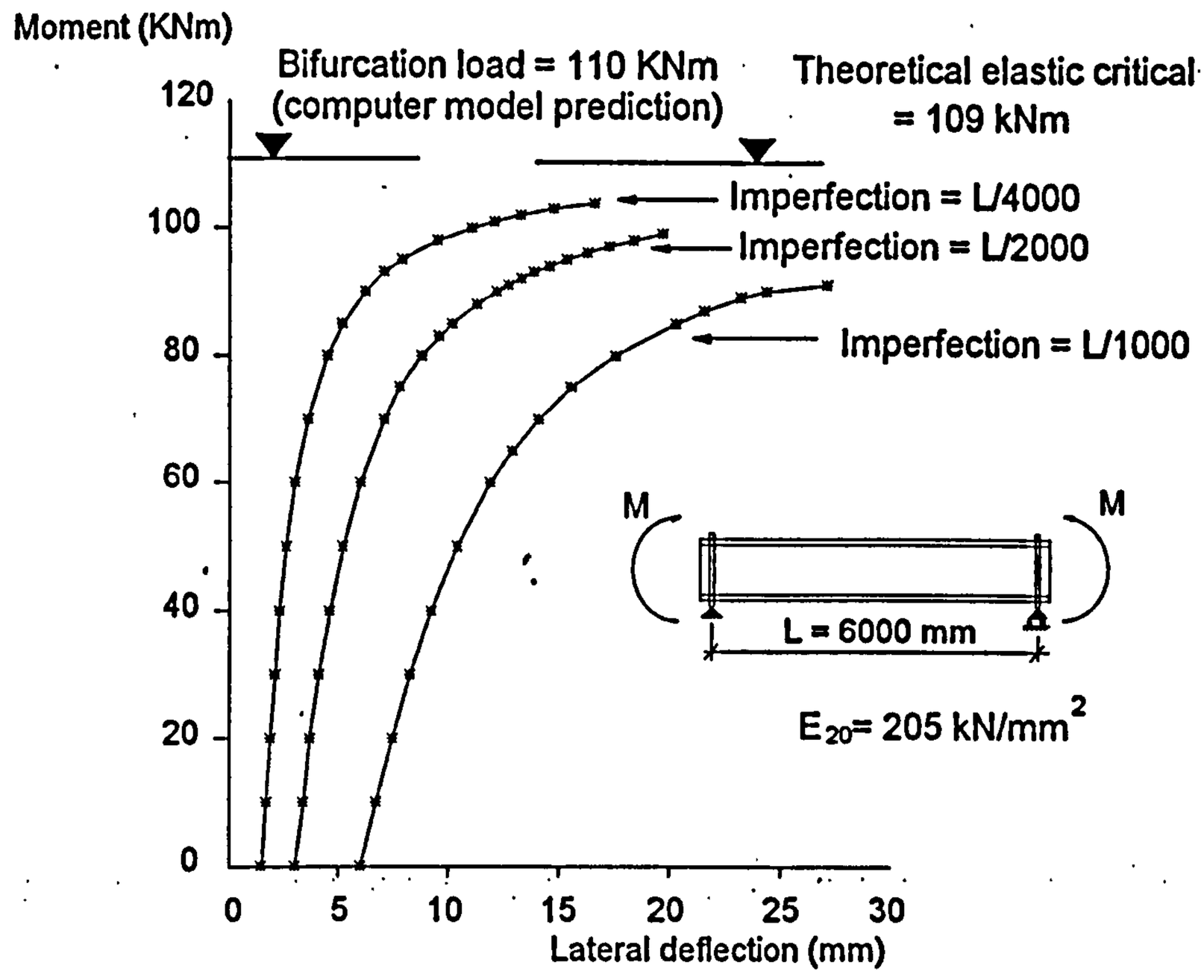

LOAD-LATERAL DEFLECTION RELATIONSHIP FOR THE SIMPLY-SUPPORTED BEAM WITH UNIFORM MOMENT.

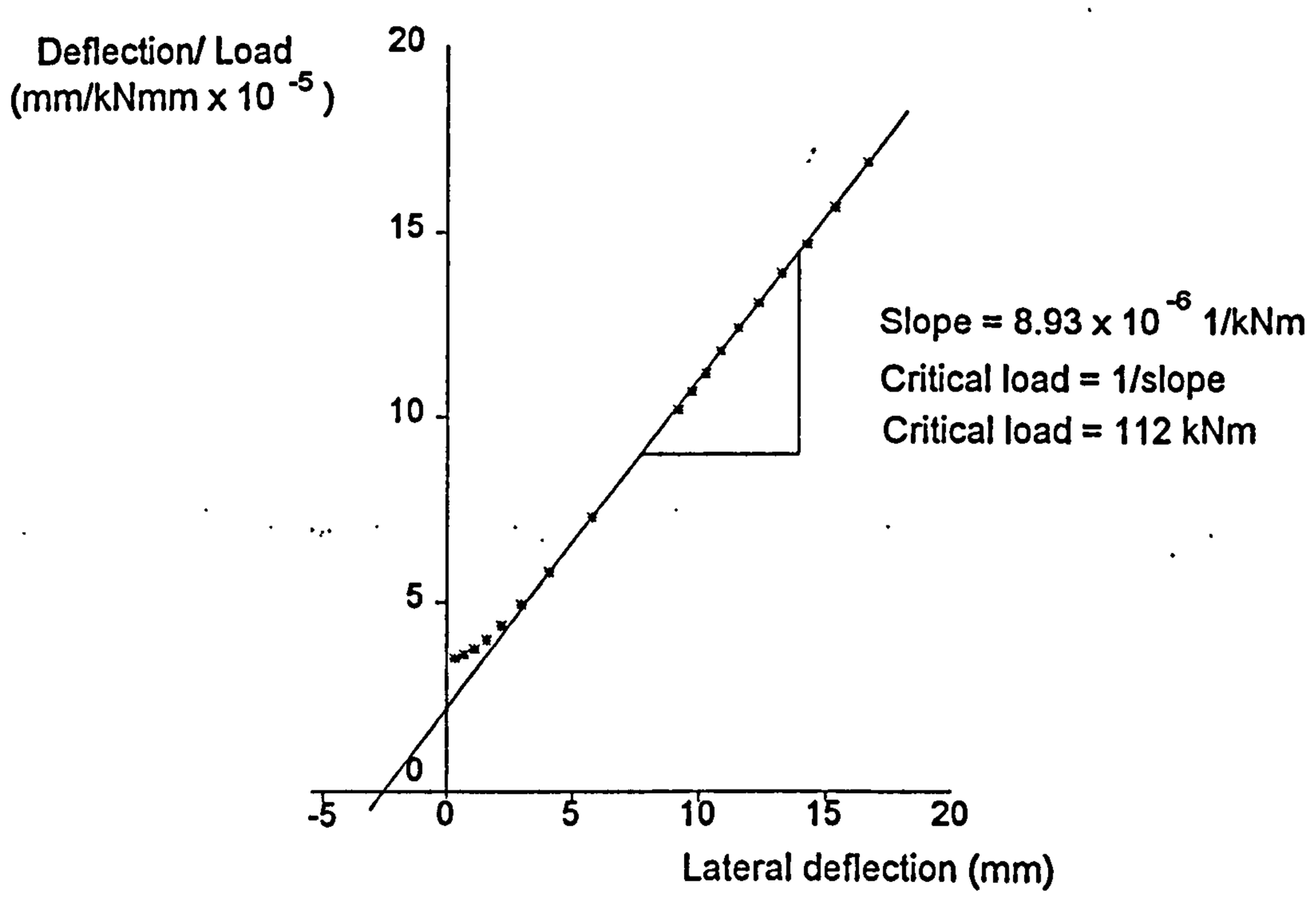

SOUTHWELL PLOT FOR BEAM WITH L/2000 IMPERFECTIONS

Fig. 5.04: Load-lateral displacement relationships and Southwell Plot for a simply-supported beam with uniform moment.

Beam	ELASTIC CRITICAL LOADS (kN)		
	Computer model	Theoretical	% Error
Simply-supported	161	100	+61
Cantilever	22	31.2	-41.8

Table 5.01: Comparison between theoretical solutions and computer model results before the inclusion of flexural shear stresses into the formulation.

These comparisons demonstrate the importance of extending the basic formulation of the beam elements to incorporate flexural shear stresses to allow lateral-torsional buckling to be predicted for any load condition. The formulation was originally based on the work by El-Zanaty and Murray[29] and has been extended recently by Najjar[39] to include three-dimensional behaviour. Najjar's formulation included warping normal and shear stresses together with pure torsional shear stresses. Only those parts of the formulation influenced by the inclusion of flexural shear stresses are shown here.

Considering Fig. 5.05, the displacements *u, v, w,* of an arbitrary point 'A' on the beam cross-section can be expressed in terms of the displacement of the reference axis, which in this case coincides with the centroid of the beam at 20°C, by equations (4.09), (4.10) and (4.11). As explained in Chapter 4 the reference axis can be positioned at any position on or outside the cross-section.

Now the non-linear axial strain-displacement relationship, for an arbitrary point on the cross section is given by[43]

$$\varepsilon_z = u' + \frac{1}{2}\left\{(u')^2 + (v')^2 + (w')^2\right\} \tag{5.05}$$

The non-linear shear strain-displacement relationships are given by[43,45]

$$\gamma_{xz} = \frac{\partial u}{\partial x} + \frac{\partial w}{\partial z} + \left\{\frac{\partial w}{\partial x}\cdot\frac{\partial w}{\partial z} + \frac{\partial v}{\partial x}\cdot\frac{\partial v}{\partial z} + \frac{\partial u}{\partial x}\cdot\frac{\partial u}{\partial z}\right\} \tag{5.06}$$

and,

$$\gamma_{yz} = \frac{\partial u}{\partial y} + \frac{\partial v}{\partial z} + \left\{\frac{\partial w}{\partial y}\cdot\frac{\partial w}{\partial z} + \frac{\partial v}{\partial y}\cdot\frac{\partial v}{\partial z} + \frac{\partial u}{\partial y}\cdot\frac{\partial u}{\partial z}\right\} \tag{5.07}$$

Differentiating equations (4.09), (4.10) and (4.11) produces,

$$u' = u_0' - yv_0'' - xw_0'' + \tilde{w}\theta_z'' \tag{5.08}$$

$$v' = v_0' - y\sin\theta_y \frac{d\theta_y}{dz} - x\theta_z \sin\theta x \frac{d\theta_x}{dz} + x\theta_z' \cos\theta_x \qquad (5.09)$$

$$w' = w_0' - x\sin\theta_x \frac{d\theta_x}{dz} + y\theta_z \sin\theta_y \frac{d\theta_y}{dz} - y\theta_z' \cos\theta_y \qquad (5.10)$$

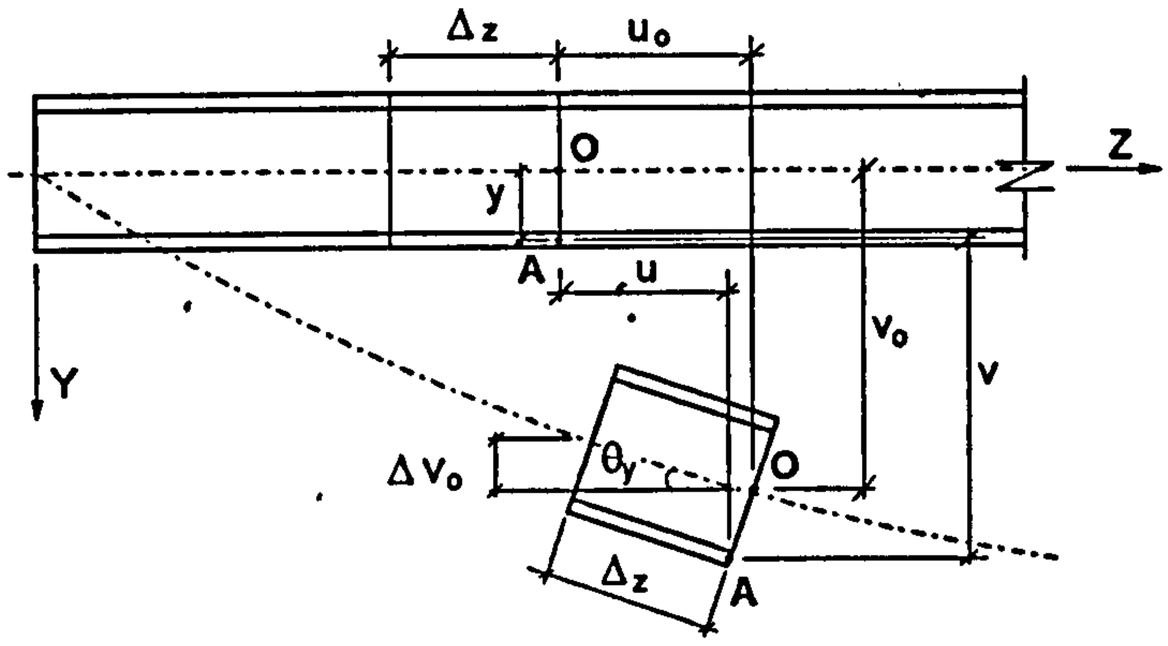

FRONT ELEVATION.

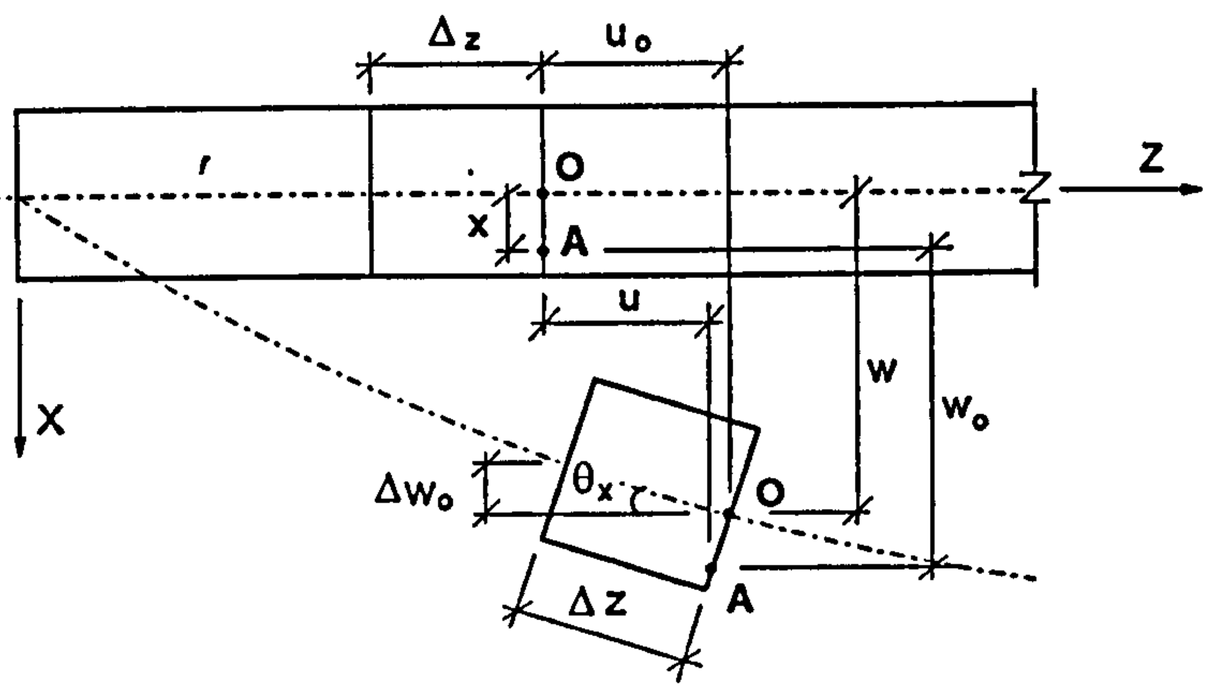

PLAN

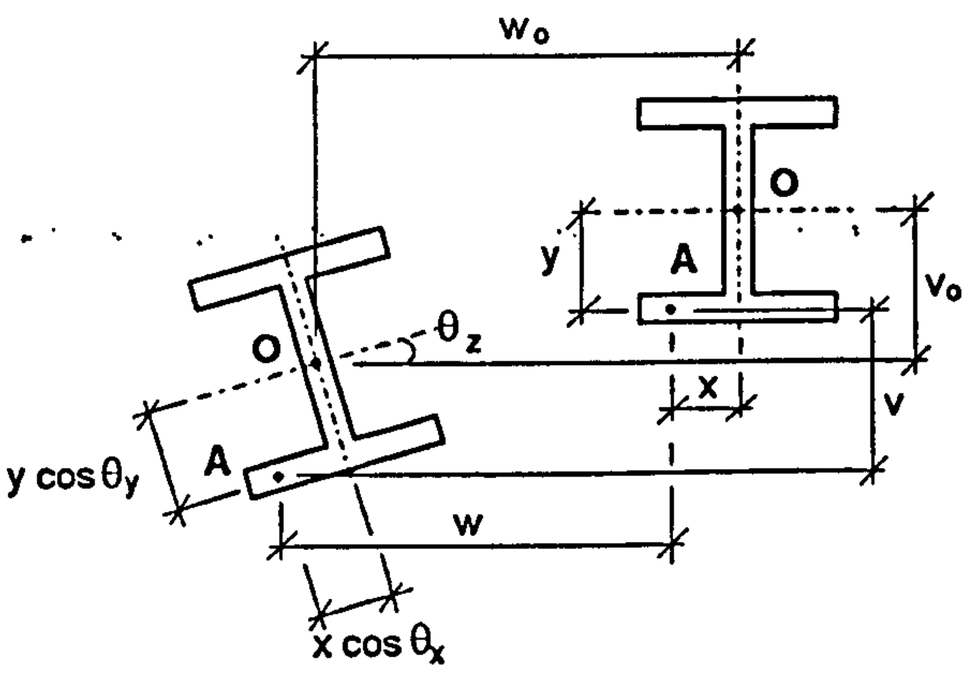

SECTION

Fig. 5.05: Definition of the displacement of an arbitrary point on the cross-section.

From Fig. 5.05, the physical interpretation of v_0' allows $\cos\theta_y$ to be approximated as,

$$\cos\theta_y = \frac{\sqrt{\Delta z^2 - \Delta v^2}}{\Delta z}$$

Since, $$\Delta z = \frac{\Delta v}{v_0'}$$

then,

$$\cos\theta_y = \sqrt{1-(v_0')^2} \qquad (5.11)$$

and similarly the physical interpretation of w_0' allows $\cos\theta_x$ to be approximated as,

$$\cos\theta_x = \sqrt{1-(w_0')^2} \qquad (5.12)$$

To evaluate the terms, $d\theta_y/dz$ and $d\theta_x/dz$, differentiate the equations (4.04) and (4.05) to produce,

$$v_0'' = \cos\theta_y \frac{d\theta_y}{dz} \qquad (5.13)$$

and,

$$w_0'' = \cos\theta_x \frac{d\theta_x}{dz} \qquad (5.14)$$

Rearranging these equations and substituting for $\cos\theta_y$ and $\cos\theta_x$ produces

$$\frac{d\theta_y}{dz} = \frac{v_0''}{\sqrt{1-(v_0')^2}} \qquad (5.15)$$

$$\frac{d\theta_x}{dz} = \frac{w_0''}{\sqrt{1-(w_0')^2}} \qquad (5.16)$$

Substituting equations (5.11), (5.12), (5.15), and (5.16) into equations (5.09) and (5.10) and ignoring higher order terms produces

$$v' = v_0' - \frac{y v_0' v_0''}{\sqrt{1-(v_0')^2}} + x\theta_z' \sqrt{1-(w_0')^2} \qquad (5.17)$$

$$w' = w_0' - \frac{x w_0' w_0''}{\sqrt{1-(w_0')^2}} - y\theta_z' \sqrt{1-(v_0')^2} \qquad (5.18)$$

Therefore the axial strain at any arbitrary point on the cross-section can be expressed in terms of the displacement of the reference axis by substituting equations (5.08), (5.17), and (5.18) into equation (5.05) producing

$$\varepsilon_z = u_0' - yv_0'' - xw_0'' + \tilde{w}\theta_z'' + \frac{1}{2}(u_0')^2 - yu_0'v_0'' - xu_0'w_0'' + \frac{1}{2}(yv_0'')^2 + \frac{1}{2}(xw_0'')^2 + \frac{1}{2}(v_0')^2$$
$$-\frac{yv_0''(v_0')^2}{\sqrt{1-(v_0')^2}} + v_0'x\theta_z'\sqrt{1-(w_0')^2} + \frac{1}{2}y^2\frac{(v_0')^2(v_0'')^2}{1-(v_0')^2} + \frac{1}{2}x^2(\theta_z')^2\left(1-(w_0')^2\right) + \frac{1}{2}(w_0')^2$$
$$-\frac{x(w_0)^2w_0''}{\sqrt{1-(w_0')^2}} - w_0'y\theta_z'\sqrt{1-(v_0')^2} + \frac{1}{2}x^2\frac{(w_0')^2(w_0'')^2}{1-(w_0')^2} + \frac{1}{2}y^2(\theta_z')^2\left(1-(v_0')^2\right) \qquad (5.19)$$

By considering equation (5.06) and (5.07) and ignoring higher order terms the shear strain is given by,

$$\gamma_{xz} = v_0'\theta_z \qquad (5.20)$$

and,

$$\gamma_{yz} = -w_0'\theta_z \qquad (5.21)$$

Applying the Principle of Virtual Work over the length of the beam gives

$$\delta W = \int_V \sigma_z\delta\varepsilon_z + \tau_{xz}\delta\gamma_{xz} + \tau_{yz}\delta\gamma_{yz}dv - \langle Q\rangle\{\delta q\} = 0 \qquad (5.22)$$

where,

σ_z = axial stress,
$\delta\varepsilon_z$ = incremental variation in axial strain,
τ_{xz}, τ_{yz} = shear stress,
$\delta\gamma_{xz}, \delta\gamma_{yz}$ = incremental variation in shear strain,
$\langle Q\rangle$ = row vector of external forces,
$\{\delta q\}$ = column vector of incremental deformations.

The variation in strains can be obtained by differentiating equations (5.19), (5.20), and (5.21) and appreciating that $u_0', v_0', w_0', v_0'', w_0'', \theta_z, \theta_z'$, and θ_z'' may vary independently. Introducing the calculation of the variation in strains into equation (5.22) produces the virtual work relationship of,

$$\delta W = \iint_{I,A}\Big[\sigma_z(1+u_0' - yv_0'' - xw_0'' + \tilde{w}\theta_z'')\delta u_0' + \sigma_z\Bigg(v_0' - \frac{2yv_0'v_0''}{\sqrt{1-(v_0')^2}} - \frac{y(v_0')^3v_0''}{\left(1-(v_0')^2\right)^{3/2}}$$
$$+x\theta_z'\sqrt{1-(w_0')^2} + \frac{y^2v_0'(v_0'')^2}{1-(v_0')^2} + \frac{y^2(v_0')^3(v_0'')^2}{\left(1-(v_0')^2\right)^2} + \frac{yw_0'\theta_z'v_0'}{\sqrt{1-(v_0')^2}} - y^2(\theta_z')^2(v_0')\Bigg)\delta v_0'$$

$$+\tau_{xz}(\theta_z)\delta v_0' + \sigma_z\left(w_0' - \frac{x v_0'\theta_z' w_0'}{\sqrt{1-(w_0')^2}} - x^2(\theta_z')^2 w_0' - \frac{2x w_0' w_0''}{\sqrt{1-(w_0')^2}} - \frac{x(w_0')^3(w_0'')}{\left(1-(w_0')^2\right)^{3/2}} \right.$$

$$\left. + \frac{x^2(w_0')(w_0'')^2}{1-(w_0')^2} + \frac{x^2(w_0')^3(w_0'')^2}{\left(1-(w_0')^2\right)^2} \right)\delta w_0' - \tau_{yz}(\theta_z)\delta w_0$$

$$+\sigma_z\left(-y + y^2 v_0'' - y u_0' - \frac{y(v_0')^2}{\sqrt{1-(v_0')^2}} + \frac{y^2(v_0')^2 v_0''}{1-(v_0')^2} \right)\delta v_0''$$

$$+\sigma_z\left(-x - x u_0'' + x^2 w_0'' - \frac{x(w_0')^2}{\sqrt{1-(w_0')^2}} + \frac{x^2(w_0')^2(w_0'')}{1-(w_0')^2} \right)\delta w_0'' + \left(\tau_{xz} v_0' - \tau_{yz} w_0'\right)\delta\theta_z$$

$$+\sigma_z\left(x v_0'\sqrt{1-(w_0')^2} + x^2(\theta_z')\left(1-(w_0')^2\right) - y w_0'\sqrt{1-(v_0')^2} + y^2(\theta_z')\left(1-(v_0')^2\right) \right)\delta\theta_z'$$

$$\sigma_z(\tilde{w} + u_0'\tilde{w})\delta\theta_z''\Big]\, da\, dz - \langle Q\rangle\{\delta q\} = 0 \qquad (5.23)$$

Defining the stress resultants as,

$$n = \int_A \sigma_z dA \qquad m_x = \int_A \sigma_z y dA$$

$$m_x^{\,2} = \int_A \sigma_z y^2 dA \qquad m_y = \int_A \sigma_z x dA$$

$$m_y^{\,2} = \int_A \sigma_z x^2 dA \qquad m_w = \int_A \sigma_z \tilde{w} dA$$

$$m_z = \int_A \sigma_z\left(x^2 + y^2\right)\cdot\theta_z' dA \qquad TSV = \mathrm{G}\mathrm{J}\theta_z'$$

$$f_x = \int_A \tau_{xz} dA \qquad f_y = \int_A \tau_{yz} dA$$

where,

n = axial force,

m_x = bending moment about the x-axis,

$m_x^{\,2}$ = stress resultant due to the higher order terms within the strain-displacement equation which represent non-linear effects,

m_y = bending moment about the y-axis,

$m_y^{\,2}$ = stress resultant due to the higher order terms within the strain-displacement equation which represent non-linear effects,

m_w = warping moment,

m_z = contribution to the torsional moment due to warping deformations (this is a second-order effect known as the Wagner effect[45]),

TSV = torsional moment due to St.Venant shear stress,

f_x = shear force parallel to the x-axis,
f_y = shear force parallel to the y-axis.

The shear forces required for the above formulation are calculated from the reactions, due to the thin-walled assumption that shear deformations are small and may be neglected.

Using the stress resultants defined above the virtual work equation can be re-written as

$$\int_l \left(a_1\delta u_0' + a_2\delta v_0' + a_3\delta v_0'' + a_4\delta w_0' + a_5\delta w_0'' + a_6\delta\theta_z' + a_7\delta\theta_z'' + a_8\delta\theta_z\right) dz - \langle Q\rangle\{\delta q\} = 0 \tag{5.24}$$

where

$$a_1 = n(1+u_0') - m_x(v_0'') - m_y(w_0'') + m_{\bar{w}}(\theta_z'')$$

$$a_2 = n(v_0') + m_x\left(\frac{w_0'\theta_z'v_0'}{\sqrt{1-(v_0')^2}} - \frac{2v_0'v_0''}{\sqrt{1-(v_0')^2}} - \frac{(v_0')^3v_0''}{\left(1-(v_0')^2\right)^{3/2}}\right) + m_y\left(\theta_z'\sqrt{1-(w_0')^2}\right)$$

$$+m_x{}^2\left(\frac{(v_0')^3(v_0'')^2}{\left(1-(v_0')^2\right)^2} + \frac{v_0'(v_0'')^2}{1-(v_0')^2} - (\theta_z')^2(v_0')\right) + f_x(\theta_z)$$

$$a_3 = -m_x\left(1+u_0' + \frac{(v_0')^2}{\sqrt{1-(v_0')^2}}\right) + m_x{}^2\left(v_0'' + \frac{(v_0')^2(v_0'')}{1-(v_0')^2}\right)$$

$$a_4 = n(w_0') - m_y\left(\frac{v_0'\theta_z'w_0'}{\sqrt{1-(w_0')^2}} + \frac{2w_0'w_0''}{\sqrt{1-(w_0')^2}} + \frac{(w_0')^3(w_0'')}{\left(1-(w_0')^2\right)^{3/2}}\right) - m_x\left(\theta_z'\sqrt{1-(v_0')^2}\right)$$

$$+m_y{}^2\left(\frac{(w_0')(w_0'')^2}{1-(w_0')^2} + \frac{(w_0')^3(w_0'')^2}{\left(1-(w_0')^2\right)^2} - (\theta_z')w_0'\right) - f_y(\theta_z)$$

$$a_5 = -m_y\left(1+u_0' + \frac{(w_0')^2}{\sqrt{1-(w_0')^2}}\right) + m_y^2\left(w_0'' + \frac{(w_0')^2w_0''}{1-(w_0')^2}\right)$$

$$a_6 = -m_x\left(w_0'\sqrt{1-(v_0')^2}\right) + m_y\left(v_0'\sqrt{1-(w_0')^2}\right) + m_y{}^2(\theta_z')\left(1-(w_0')^2\right)$$

$$+m_x{}^2\left(\theta_z'\left(1-(v_0')^2\right)\right) + TSV + \frac{1}{2}m_z(\theta_z')^2$$

$$a_7 = m_w(1+u_0')$$

$$a_8 = f_x(v_0') - f_y(w_0')$$

In order to establish the force-displacement relationship for an element the displacements u_0, v_0, w_0, and θ_0, are written in terms of nodal displacement coordinates q_i where i has a range of N. (N equals the number of local degrees of freedom per node). This allows equation (5.24) to be written as

$$\psi_i = 0 \tag{5.25}$$

where

$$\psi_i = \int_l \left(a_1 \frac{\partial u_0'}{\partial q_i} + a_2 \frac{\partial v_0'}{\partial q_i} + a_3 \frac{\partial v_0''}{\partial q_i} + a_4 \frac{\partial w_0'}{\partial q_i'} + a_5 \frac{\partial w_0''}{\partial q_i} + a_6 \frac{\partial \theta_z'}{\partial q_i} + a_7 \frac{\partial \theta_z''}{\partial q_i} + a_8 \frac{\partial \theta_z}{\partial q_i} \right) dz - Q_i \tag{5.26}$$

Equation (5.26) is non-linear, and if it is not satisfied corrections to q_i may be obtained by applying Newton-Raphson iteration, producing the relationship[43]

$$\Delta\psi_i = \frac{\partial \psi_i}{\partial q_j} \Delta q_j = -\psi_i' \tag{5.27}$$

where j also has a range of N.

Substituting equation (5.26) into (5.27) produces;

$$\int_l \left(\frac{\partial a_1}{\partial q_j}\frac{\partial u_0'}{\partial q_i} + \frac{\partial a_2}{\partial q_j}\frac{\partial v_0'}{\partial q_i} + \frac{\partial a_3}{\partial q_j}\frac{\partial v_0''}{\partial q_i} + \frac{\partial a_4}{\partial q_j}\frac{\partial w_0'}{\partial q_i} + \frac{\partial a_5}{\partial q_j}\frac{\partial w_0''}{\partial q_i} + \frac{\partial a_6}{\partial q_j}\frac{\partial \theta_z'}{\partial q_i} + \frac{\partial a_7}{\partial q_j}\frac{\partial \theta_z''}{\partial q_i} + \frac{\partial a_8}{\partial q_j}\frac{\partial \theta_z}{\partial q_i} \right) dz \cdot \Delta q_i =$$

$$Q_i - \int_l \left(a_1 \frac{\partial u_0'}{\partial q_i} + a_2 \frac{\partial v_0'}{\partial q_i} + a_3 \frac{\partial v_0''}{\partial q_i} + a_4 \frac{\partial w_0'}{\partial q_i} + a_5 \frac{\partial w_0''}{\partial q_i} + a_6 \frac{\partial \theta_z'}{\partial q_i} + a_7 \frac{\partial \theta_z''}{\partial q_i} + a_8 \frac{\partial \theta_z}{\partial q_i} \right) dz \tag{5.28}$$

Once u_0, v_0, w_0, and θ_0 are defined in terms of q's, then equation (5.28) can be evaluated, producing the incremental tangent stiffness matrix $[K_T]$ and the unbalanced load vector $\{\Delta Q\}$. Equation (5.28) can be written symbolically as,

$$[K_T]\{\Delta q\} = \{\Delta Q\} \tag{5.29}$$

where the coefficients of the tangent stiffness matrix are given by

$$(K)_{ij} = \int_l \left(\frac{\partial a_1}{\partial q_j}\frac{\partial u_0'}{\partial q_i} + \frac{\partial a_2}{\partial q_j}\frac{\partial v_0'}{\partial q_i} + \frac{\partial a_3}{\partial q_j}\frac{\partial v_0''}{\partial q_i} + \frac{\partial a_4}{\partial q_j}\frac{\partial w_0'}{\partial q_i} + \frac{\partial a_5}{\partial q_j}\frac{\partial w_0''}{\partial q_i} + \frac{\partial a_6}{\partial q_j}\frac{\partial \theta_z'}{\partial q_i} + \frac{\partial a_7}{\partial q_j}\frac{\partial \theta_z''}{\partial q_i} + \frac{\partial a_8}{\partial q_j}\frac{\partial \theta_z}{\partial q_i} \right) dz \tag{5.30}$$

and the unbalanced force ΔQ_i is given by,

$$\Delta Q_i = Q_i - \int_l \left(a_1\frac{\partial u_0'}{\partial q_i} + a_2\frac{\partial v_0'}{\partial q_i} + a_3\frac{\partial v_0''}{\partial q_i} + a_4\frac{\partial w_0'}{\partial q_i} + a_5\frac{\partial w_0''}{\partial q_i} + a_6\frac{\partial \theta_0'}{\partial q_i} + a_7\frac{\partial \theta_z''}{\partial q_i} + a_8\frac{\partial \theta_z}{\partial q_i} \right) dz \tag{5.31}$$

Equation (5.30) can be written as

$$(K)_{ij} = \int_l \left(e_{1j}\frac{\partial u_0'}{\partial q_i} + e_{2j}\frac{\partial v_0'}{\partial q_i} + e_{3j}\frac{\partial v_0''}{\partial q_i} + e_{4j}\frac{\partial w_0'}{\partial q_i} + e_{5j}\frac{\partial w_0''}{\partial q_i} + e_{6j}\frac{\partial \theta_z'}{\partial q_i} + e_{7j}\frac{\partial \theta_z''}{\partial q_i} + e_{8j}\frac{\partial \theta_z}{\partial q_i} \right) dz \tag{5.32}$$

where e_{1j} to e_{8j} are obtained by differentiating the equations for a_1 to a_8 with respect to q_i, resulting in,

$$e_{1j} = \frac{\partial n}{\partial q_j}(1+u_0') + n\frac{\partial u_0'}{\partial q_j} - \frac{\partial m_x}{\partial q_j}(v_0'') - m_x\frac{\partial v_0''}{\partial q_j} - \frac{\partial m_y}{\partial q_j}(w_0'') - m_y\left(\frac{\partial w_0''}{\partial q_j}\right) + \frac{\partial m_{\tilde{w}}}{\partial q_i}(\theta_z'') + m_{\tilde{w}}\left(\frac{\partial \theta_z''}{\partial q_j}\right)$$

$$e_{2j} = \frac{\partial n}{\partial q_j}(v_0') + n\left(\frac{\partial v_0'}{\partial q_j}\right) + \frac{\partial m_x}{\partial q_j}\left(\frac{w_0'\theta_z'v_0'}{\sqrt{1-(v_0')^2}} - \frac{2v_0'v_0''}{\sqrt{1-(v_0')^2}} - \frac{(v_0')^3v_0''}{\left(1-(v_0')^2\right)^{3/2}}\right)$$

$$+m_x\left(\frac{w_0'\theta_z'}{\sqrt{1-(v_0')^2}} + \frac{w_0'\theta_z'(v_0')^2}{\left(1-(v_0')^2\right)^{3/2}} - \frac{2v_0''}{\sqrt{1-(v_0')^2}} - \frac{2(v_0')^2v_0''}{\left(1-(v_0')^2\right)^{3/2}} - \frac{3(v_0')^2v_0''}{\left(1-(v_0')^2\right)^{3/2}}\right.$$

$$\left.-\frac{3(v_0')^4(v_0'')}{\left(1-(v_0')^2\right)^{5/2}}\right)\frac{\partial v_0'}{\partial q_j} - m_x\left(\frac{2v_0'}{\sqrt{1-(v_0')^2}} + \frac{(v_0')^3}{\left(1-(v_0')^2\right)^{3/2}}\right)\frac{\partial v_0''}{\partial q_j} + m_x\left(\frac{\theta_z'v_0'}{\sqrt{1-(v_0')^2}}\right)\frac{\partial w_0'}{\partial q_j}$$

$$+m_x\left(\frac{w_0'v_0'}{\sqrt{1-(v_0')^2}}\right)\frac{\partial \theta_z'}{\partial q_j} + \frac{\partial m_y}{\partial q_j}\left(\theta_z'\sqrt{1-(w_0')^2}\right) + m_y\left(\sqrt{1-(w_0')^2}\right)\frac{\partial \theta_z'}{\partial q_j}$$

$$-m_y\left(\frac{\theta_z'w_0'}{\sqrt{1-(w_0')}}\right)\frac{\partial w_0'}{\partial q_j} + \frac{\partial m_x{}^2}{\partial q_j}\left(\frac{(v_0')^3(v_0'')^2}{\left(1-(v_0')^2\right)^2} + \frac{v_0'(v_0'')^2}{1-(v_0')^2} - (\theta_z')^2v_0'\right)$$

$$+m_x{}^2\left(\frac{3(v_0')^2(v_0'')^2}{\left(1-(v_0')^2\right)^2}+\frac{4(v_0')^4(v_0'')^2}{\left(1-(v_0')^2\right)^3}+\frac{(v_0'')^2}{1-(v_0')^2}+\frac{2(v_0')^2(v_0'')^2}{\left(1-(v_0')^2\right)^2}-(\theta_z')^2\right)\frac{\partial v_0'}{\partial q_J}$$

$$+m_x{}^2\left(\frac{2(v_0')^3(v_0'')}{\left(1-(v_0')^2\right)^2}+\frac{2v_0'(v_0'')}{1-(v_0')^2}\right)\frac{\partial v_0''}{\partial q_J}-m_x{}^2(2\theta_z'v_0')\frac{\partial \theta_z'}{\partial q_J}+f_x\frac{\partial \theta_z}{\partial q_J}+\frac{\partial f_x}{\partial q_J}(\theta_z)$$

$$e_{3J}=-\frac{\partial m_x}{\partial q_I}\left(1+u_0'+\frac{(v_0')^2}{\sqrt{1-(v_0')^2}}\right)-m_x\left(\frac{\partial u_0'}{\partial q_I}\right)-m_x\left(\frac{2v_0'}{\sqrt{1-(v_0')^2}}+\frac{(v_0')^3}{\left(1-(v_0')^2\right)^{3/2}}\right)\frac{\partial v_0'}{\partial q_I}$$

$$+\frac{\partial m_x{}^2}{\partial q_J}\left(v_0''+\frac{(v_0')^2v_0''}{1-(v_0')^2}\right)+m_x{}^2\left(\frac{2v_0'v_0''}{1-(v_0')^2}+\frac{2(v_0')^3v_0''}{\left(1-(v_0')^2\right)^2}\right)\frac{\partial v_0'}{\partial q_J}$$

$$+m_x{}^2\left(1+\frac{(v_0')^2}{1-(v_0')^2}\right)\frac{\partial v_0''}{\partial q_I}$$

$$e_{4J}=\frac{\partial n}{\partial q_J}(w_0')+n\left(\frac{\partial w_0'}{\partial q_J}\right)-\frac{\partial m_y}{\partial q_J}\left(\frac{v_0'\theta_z'w_0'}{\sqrt{1-(w_0')^2}}+\frac{2w_0'w_0''}{\sqrt{1-(w_0')^2}}+\frac{(w_0')^3(w_0'')}{\left(1-(w_0')^2\right)^{3/2}}\right)$$

$$-m_y\left(\frac{v_0'\theta_z'}{\sqrt{1-(w_0')^2}}+\frac{v_0'\theta_z'(w_0')^2}{\left(1-(w_0')^2\right)^{3/2}}+\frac{2w_0''}{\sqrt{1-(w_0')^2}}+\frac{2(w_0')^2w_0''}{\left(1-(w_0')^2\right)^{3/2}}+\frac{3(w_0')^2w_0''}{\left(1-(w_0')^2\right)^{3/2}}\right.$$

$$\left.+\frac{3(w_0')^4(w_0'')}{\left(1-(w_0')^2\right)^{5/2}}\right)\frac{\partial w_0'}{\partial q_I}-m_y\left(\frac{\theta_z'w_0'}{\sqrt{1-(w_0')^2}}\right)\frac{\partial v_0'}{\partial q_J}-m_y\left(\frac{2w_0'}{\sqrt{1-(w_0')^2}}+\frac{(w_0')^3}{\left(1-(w_0')^2\right)^{3/2}}\right)\frac{\partial w_0''}{\partial q_J}$$

$$-m_y\left(\frac{v_0'w_0'}{\sqrt{1-(w_0')^2}}\right)\frac{\partial \theta_z'}{\partial q_J}-\frac{\partial m_x}{\partial q_J}\left(\theta_z'\sqrt{1-(v_0')^2}\right)-m_x\left(\sqrt{1-(v_0')^2}\right)\frac{\partial \theta_z'}{\partial q_J}$$

$$+m_x\left(\frac{\theta_z'v_0'}{\sqrt{1-(v_0')^2}}\right)\frac{\partial v_0'}{\partial q_J}+\frac{\partial m_y{}^2}{\partial q_J}\left(\frac{w_0'(w_0'')^2}{1-(w_0')^2}+\frac{(w_0')^3(w_0'')^2}{\left(1-(w_0')^2\right)^2}-\theta_z'w_0'\right)$$

$$+m_y{}^2\left(\frac{(w_0'')^2}{1-(w_0')^2}+\frac{2(w_0')^2(w_0'')^2}{\left(1-(w_0')^2\right)^2}+\frac{3(w_0')^2(w_0'')^2}{\left(1-(w_0')^2\right)^2}+\frac{4(w_0')^4(w_0'')^2}{\left(1-(w_0')^2\right)^3}-(\theta_z')^2\right)\frac{\partial w_0'}{\partial q_J}$$

$$+m_y{}^2\left(\frac{2(w_0'')}{1-(w_0')^2}+\frac{2(w_0')^3w_0''}{\left(1-(w_0')^2\right)^2}\right)\frac{\partial w_0''}{\partial q_J}-m_y{}^2(2w_0'\theta_z')\frac{\partial \theta_z'}{\partial q_J}-f_y\frac{\partial \theta_z}{\partial q_J}-\frac{\partial f_y}{\partial q_J}(\theta_z)$$

$$e_{5J}=-\frac{\partial m_y}{\partial q_J}\left(1+u_0'+\frac{(w_0')^2}{\sqrt{1-(w_0')^2}}\right)-m_y\left(\frac{\partial u_0'}{\partial q_J}\right)-m_y\left(\frac{2w_0'}{\sqrt{1-(w_0')^2}}+\frac{(w_0')^3}{\left(1-(w_0')^2\right)^{3/2}}\right)\frac{\partial w_0'}{\partial q_J}$$

$$+\frac{\partial m_y^2}{\partial q_j}\left(w_0''+\frac{(w_0')^2(w_0'')}{1-(w_0')^2}\right)+m_y^2\left(\frac{2w_0'w_0''}{1-(w_0')^2}+\frac{2(w_0')^3(w_0'')}{\left(1-(w_0')^2\right)^2}\right)\frac{\partial w_0'}{\partial q_j}$$

$$+m_y^2\left(1+\frac{(w_0')^2}{1-(w_0')^2}\right)\frac{\partial w_0''}{\partial q_j}$$

$$e_{6j}=-\frac{\partial m_x}{\partial q_j}\left(w_0'\sqrt{1-(v_0')^2}\right)-m_x\left(\sqrt{1-(v_0')^2}\right)\frac{\partial w_0'}{\partial q_j}+m_x\left(\frac{w_0'v_0'}{\sqrt{1-(v_0')^2}}\right)\frac{\partial v_0'}{\partial q_j}$$

$$+\frac{\partial m_y}{\partial q_j}\left(v_0'\sqrt{1-(w_0')^2}\right)+m_y\left(\sqrt{1-(w_0')^2}\right)\frac{\partial v_0'}{\partial q_j}-m_y\left(\frac{v_0'w_0'}{\sqrt{1-(w_0')^2}}\right)\frac{\partial w_0'}{\partial q_j}$$

$$+\frac{\partial m_y^2}{\partial q_j}\left(\theta_z'\left(1-(w_0')^2\right)\right)+m_y^2\left(1-(w_0')^2\right)\frac{\partial \theta_z'}{\partial q_j}-m_y^2(2\theta_z'w_0')\frac{\partial w_0'}{\partial q_j}+\frac{\partial m_x^2}{\partial q_j}\left(\theta_z'\left(1-(v_0')^2\right)\right)$$

$$+m_x^2\left(1-(v_0')^2\right)\frac{\partial \theta_z'}{\partial q_j}-m_x^2(2\theta_z'v_0')\frac{\partial v_0'}{\partial q_j}+GJ\frac{\partial \theta_z'}{\partial q_j}+\frac{1}{2}m_z\left(\frac{\partial \theta_z'}{\partial q_j}\right)^2$$

$$e_{7j}=\frac{\partial m_w}{\partial q_j}(1+u_0')+m_w\left(\frac{\partial u_0'}{\partial q_j}\right)$$

$$e_{8j}=f_x\left(\frac{\partial v_0'}{\partial q_j}\right)-f_y\left(\frac{\partial w_0'}{\partial q_j}\right)+\frac{\partial f_x}{\partial q_j}(v_0')-\frac{\partial f_y}{\partial q_j}(w_0') \qquad (5.33)$$

To allow a numerical solution of the above formulation a finite element model was developed. This consisted of representing displacements at any position within each finite element by shape functions, (also known as interpolating functions), and the generalised displacements at the nodes. Cubic shape functions[42] were adopted within this formulation, allowing the displacements at any point within an element to be obtained from,

$$u_0=\langle\phi\rangle\{\bar{u}\}$$
$$v_0=\langle\phi\rangle\{\bar{v}\}$$
$$w_0=\langle\phi\rangle\{\bar{w}\}$$
$$\theta_0=\langle\phi\rangle\{\bar{\theta}\} \qquad (5.34)$$

where,

$\langle\phi\rangle$ = row vector of standard cubic shape functions,

and

$\{\bar{u}\},\{\bar{v}\},\{\bar{w}\},\{\bar{\theta}\}$ = generalised displacements at the nodes, given by,

$$\langle\bar{u}\rangle=\langle u_i,u_i',u_j,u_j'\rangle$$

$$\langle \bar{v} \rangle = \langle v_i, v_i', v_j, v_j' \rangle$$
$$\langle \bar{w} \rangle = \langle w_i, w_i', w_j, w_j' \rangle$$
$$\langle \bar{\theta} \rangle = \langle \theta_i, \theta_i', \theta_j, \theta_j' \rangle \qquad (5.35)$$

where, i and j are the numbers of the two nodes at either end of the beam element.

The derivatives of the displacements at any point within an element are given by,

$$u_0' = \langle \phi' \rangle \{\bar{u}\}$$
$$v_0' = \langle \phi' \rangle \{\bar{v}\} \qquad v_0'' = \langle \phi'' \rangle \{\bar{v}\}$$
$$w_0' = \langle \phi' \rangle \{\bar{w}\} \qquad w_0'' = \langle \phi'' \rangle \{\bar{w}\}$$
$$\theta_z' = \langle \phi' \rangle \{\bar{\theta}\} \qquad \theta_z'' = \langle \phi'' \rangle \{\bar{\theta}\} \qquad (5.36)$$

Differentiating equation (5.36) with respect to q_l produces

$$\frac{\partial u_0'}{\partial q_l} = \phi_{ql}'$$
$$\frac{\partial v_0'}{\partial q_l} = \phi_{ql}' \qquad \frac{\partial v_0''}{\partial q_l} = \phi_{ql}''$$
$$\frac{\partial w_0'}{\partial q_l} = \phi_{ql}' \qquad \frac{\partial w_0''}{\partial q_l} = \phi_{ql}''$$
$$\frac{\partial \theta_0'}{\partial q_l} = \phi_{ql}' \qquad \frac{\partial \theta''}{\partial q_l} = \phi_{ql}'' \qquad (5.37)$$

where, ϕ_{ql}' and ϕ_{ql}'' are the differentiated shape functions associated with the generalised displacement q_l in $\{\bar{u}\}$,$\{\bar{v}\}$,$\{\bar{w}\}$ or $\{\bar{\theta}\}$ as defined in equation (5.35).

Incorporating the finite element formulation into equation (5.31) allows the unbalanced load vector to be expressed as

$$\Delta Q_l = Q_l - \int_l (a_1 \phi_{ql}') dz \qquad \text{for i = 1 to 4}$$

(this corresponds to displacements $\{\bar{u}\}$) (5.38)

$$\Delta Q_l = Q_l - \int_l (a_2 \phi_{ql}' + a_3 \phi_{ql}'') dz \qquad \text{for i = 5 to 8}$$

(this corresponds to displacements $\{\bar{v}\}$) (5.39)

$$\Delta Q_l = Q_l - \int_l (a_4 \phi_{ql}' + a_5 \phi_{ql}'') dz \qquad \text{for i = 9 to 12}$$

(this corresponds to displacements $\{\bar{w}\}$) (5.40)

$$\Delta Q_i = Q_i - \int_l \left(a_6\phi'_{qi} + a_7\phi''_{qi} + a_8\phi_{qi}\right)dz \qquad \text{for i = 13 to 16}$$

(this corresponds to displacements $\{\bar{\theta}\}$) (5.41)

The above equations can be expressed symbolically as

$$\{\Delta Q\} = \{Q\} - \{Q^R\} \qquad (5.42)$$

where,

$\{Q\}$ = vector of applied loads

and

$\{Q^R\}$ = vector of resisting forces, which can be defined as,

$$\{Q^R\} = \int_l \begin{bmatrix} a_1\{\phi'\} \\ a_2\{\phi'\} + a_3\{\phi''\} \\ a_4\{\phi'\} + a_5\{\phi''\} \\ a_6\{\phi'\} + a_7\{\phi''\} + a_8\{\phi\} \end{bmatrix} dz \qquad (5.43)$$

To evaluate the above vector, Gaussian numerical integration is used. The basic assumption of Gaussian numerical integration is that,

$$\int_b^a \{F(r)\}dr = \alpha_1\{F(r_1)\} + \alpha_2\{F(r_2)\} + \ldots\ldots + \alpha_n\{F(r_n)\} \qquad (5.44)$$

where,

$\{F(r)\}$ = vector/matrix, to be integrated between the limits a and b,

$\alpha_1, \alpha_2, \ldots \alpha_n$ = weighting factors corresponding to the sampling points,

$r_1, r_2, \ldots r_n$ = sampling points, positioned between the limits a and b.

The weighting factors and sampling points are calculated to give maximum accuracy based on the number of points specified. These values can be obtained from most numerical analysis text books[41,44].

Therefore the contribution to the resisting force vector at the k^{th} sampling point can be expressed as

$$\{Q^R\} = \sum_{k=1}^{n} \alpha_k \begin{bmatrix} a_1\{\phi'\} \\ a_2\{\phi'\} + a_3\{\phi''\} \\ a_4\{\phi'\} + a_5\{\phi''\} \\ a_6\{\phi'\} + a_7\{\phi''\} + a_8\{\phi\} \end{bmatrix}_k \qquad (5.45)$$

where *n* is the number of sampling points (Gauss points) along the element. Within this model four sampling points per element are used.

Incorporating the finite element formulation into equation (5.32) allows the stiffness matrix to be expressed as '.

$$(K_T)_{ij} = \int_l e_{1j}\phi'_{qi}\, dz \qquad \text{For i = 1 to 4,}$$

(this corresponds to displacements $\{\bar{u}\}$) (5.46)

$$(K_T)_{ij} = \int_l \left[e_{2j}\phi'_{qi} + e_{3j}\phi''_{qi}\right] dz \qquad \text{for i = 5 to 8,}$$

(this corresponds to displacements $\{\bar{v}\}$) (5.47)

$$(K_T)_{ij} = \int_l \left[e_{4j}\phi'_{qi} + e_{5j}\phi''_{qi}\right] dz \qquad \text{for i = 9 to 12,}$$

(this corresponds to displacements $\{\bar{w}\}$ (5.48)

$$(K_T)_{ij} = \int_l \left[e_{6j}\phi'_{qi} + e_{7j}\phi''_{qi} + e_{8j}\phi_{qi}\right] dz \qquad \text{for i = 13 to 16.}$$

(this corresponds to displacements $\{\bar{\theta}\}$) (5.49)

where $e_{1j}, e_{2j}, \ldots\ldots, e_{8j}$ are defined in equation (5.33). Therefore the j^{th} column can be written as,

$$\{K_T\}_j = \int_l \begin{Bmatrix} e_{1j}\{\phi'\} \\ e_{2j}\{\phi'\} + e_{3j}\{\phi''\} \\ e_{4j}\{\phi'\} + e_{5j}\{\phi''\} \\ e_{6j}\{\phi'\} + e_{7j}\{\phi''\} + e_{8j}\{\phi\} \end{Bmatrix} dz \qquad (5.50)$$

with the full matrix being written as

$$[K_T] = \int_l \begin{bmatrix} \langle e_1\rangle\{\phi'\} \\ \langle e_2\rangle\{\phi'\} + \langle e_3\rangle\{\phi''\} \\ \langle e_4\rangle\{\phi'\} + \langle e_5\rangle\{\phi''\} \\ \langle e_6\rangle\{\phi'\} + \langle e_7\rangle\{\phi''\} + \langle e_8\rangle\{\phi\} \end{bmatrix} dz \qquad (5.51)$$

This can be written symbolically as

$$[K_T]=\begin{bmatrix}[K_1]\\ [K_2]+[K_3]\\ [K_4]+[K_5]\\ [K_6]+[K_7]+[K_8]\end{bmatrix} \tag{5.52}$$

where $[K_1],[K_2],.....,[K_8]$ are 4x16 matrices, which can be defined by incorporating the finite element model into equation (5.33), and using equation (5.51), producing

$$[K_1]=\int_l \left(e_{1j}\phi'_{ql}\right) dz$$

$$=\int_l \phi'\left[(1+u'_0)\left\langle\frac{\partial n}{\partial q}\right\rangle-(v''_0)\left\langle\frac{\partial m_x}{\partial q}\right\rangle-(w''_0)\left\langle\frac{\partial m_y}{\partial q}\right\rangle+n\langle\phi'_1\rangle-m_x\langle\phi''_2\rangle\right.$$

$$\left.-m_y\langle\phi''_3\rangle+m_w\langle\phi''_4\rangle\right] dz \tag{5.53}$$

$$[K_2]=\int_l \left(e_{2j}\phi'_{ql}\right) dz$$

$$=\int_l \phi'\left[(v'_0)\left\langle\frac{\partial n}{\partial q}\right\rangle+\left(\frac{w'_0\theta'_z v'_0}{\sqrt{1-(v'_0)^2}}-\frac{2v'_0v''_0}{\sqrt{1-(v'_0)^2}}-\frac{(v'_0)^3v''_0}{\left(1-(v'_0)^3\right)^{3/2}}\right)\left\langle\frac{\partial m_x}{\partial q}\right\rangle\right.$$

$$+\left(\theta'_z\sqrt{1-(w'_0)^2}\right)\left\langle\frac{\partial m_y}{\partial q}\right\rangle+\left(\frac{(v'_0)^3(v''_0)^2}{\left(1-(v'_0)^2\right)^2}+\frac{v'_0(v''_0)^2}{1-(v'_0)^2}-(\theta'_z)^2v'_0\right)\left\langle\frac{\partial m_x{}^2}{\partial q}\right\rangle$$

$$+(\theta_z)\left\langle\frac{\partial f_x}{\partial q}\right\rangle+n(\phi'_2)+m_x\left(\frac{w'_0\theta'_z}{\sqrt{1-(v'_0)^2}}+\frac{w'_0\theta'_z(v'_0)^2}{\left(1-(v'_0)^2\right)^{3/2}}-\frac{2v''_0}{\sqrt{1-(v'_0)^2}}-\frac{2(v'_0)^2v''_0}{\left(1-(v'_0)^2\right)^{3/2}}\right.$$

$$\left.-\frac{3(v'_0)^2v''_0}{\left(1-(v'_0)^2\right)^{3/2}}-\frac{3(v'_0)^4(v''_0)}{\left(1-(v'_0)^2\right)^{5/2}}\right)\langle\phi'_2\rangle-m_x\left(\frac{2v'_0}{\sqrt{1-(v'_0)^2}}+\frac{(v'_0)^3}{\left(1-(v'_0)^2\right)^{3/2}}\right)\langle\phi''_2\rangle$$

$$+m_x\left(\frac{\theta'_z v'_0}{\sqrt{1-(v'_0)^2}}\right)\langle\phi'_3\rangle+m_x\left(\frac{w'_0v'_0}{\sqrt{1-(v'_0)^2}}\right)\langle\phi'_4\rangle+m_y\left(\sqrt{1-(w'_0)^2}\right)\langle\phi'_4\rangle$$

$$-m_y\left(\frac{\theta'_z w'_0}{\sqrt{1-(w'_0)}}\right)\langle\phi'_4\rangle+m_x{}^2\left(\frac{3(v'_0)^2(v''_0)^2}{\left(1-(v'_0)^2\right)^2}+\frac{4(v'_0)(v''_0)^2}{\left(1-(v'_0)^2\right)^3}+\frac{(v''_0)^2}{1-(v'_0)^2}+\frac{2(v'_0)^2(v''_0)^2}{\left(1-(v'_0)^2\right)^2}\right.$$

$$\left.-(\theta'_z)^2\right)\langle\phi'_2\rangle+m_x{}^2\left(\frac{2(v'_0)^3(v''_0)}{1-(v'_0)^2}+\frac{2v'_0(v''_0)}{1-(v'_0)^2}\right)\langle\phi''_2\rangle-m_x{}^2(2\theta'_z v'_0)\langle\phi'_4\rangle+f_x\langle\phi_4\rangle$$

$$\tag{5.54}$$

$$[K_3]=\int_l \left(e_{3l}\phi''_{ql}\right)dz$$

$$=\int_l \phi''\left[-\left(1+u'_0+\frac{(v'_0)^2}{\sqrt{1-(v'_0)}}\right)\left\langle\frac{\partial m_x}{\partial q}\right\rangle+\left(v''_0+\frac{(v'_0)^2 v''_0}{1-(v'_0)^2}\right)\left\langle\frac{\partial m_x{}^2}{\partial q}\right\rangle-m_x\langle\phi'_1\rangle\right.$$

$$-m_x\left(\frac{2v'_0}{\sqrt{1-(v'_0)^2}}+\frac{2(v'_0)^3 v''_0}{\left(1-(v'_0)^2\right)^2}\right)\langle\phi'_2\rangle+m_x{}^2\left(\frac{2v'_0 v''_0}{1-(v'_0)^2}+\frac{2(v'_0)^3 v''_0}{\left(1-(v'_0)^2\right)^2}\right)\langle\phi'_2\rangle$$

$$\left.+m_x{}^2\left(1+\frac{(v'_0)^2}{1-(v'_0)^2}\right)\langle\phi''_2\rangle\right]dz \qquad (5.55)$$

$$[K_4]=\int_l \left(e_{4l}\phi'_{ql}\right)dz$$

$$\int_l \phi'\left[(w'_0)\left\langle\frac{\partial n}{\partial q}\right\rangle-\left(\frac{v'_0\theta'_z w'_0}{\sqrt{1-(w'_0)^2}}+\frac{2w'_0 w''_0}{\sqrt{1-(w'_0)^2}}+\frac{(w'_0)^3(w''_0)}{\left(1-(w'_0)^2\right)^{3/2}}\right)\left\langle\frac{\partial m_y}{\partial q}\right\rangle\right.$$

$$-\left(\theta'_z\sqrt{1-(v'_0)^2}\right)\left\langle\frac{\partial m_x}{\partial q}\right\rangle+\left(\frac{(w'_0)(w''_0)^2}{1-(w'_0)^2}+\frac{(w'_0)^3(w''_0)^2}{\left(1-(w'_0)^2\right)^2}-(\theta'_z)^2 w'_0\right)\left\langle\frac{\partial m_y{}^2}{\partial q}\right\rangle$$

$$-(\theta_z)\left\langle\frac{\partial f_y}{\partial q}\right\rangle+n\langle\phi'_3\rangle-m_y\left(\frac{v'_0\theta'_z}{\sqrt{1-(w'_0)^2}}+\frac{v'_0\theta'_z(w'_0)^2}{\left(1-(w'_0)^2\right)^{3/2}}+\frac{2w''_0}{\sqrt{1-(w'_0)^2}}+\frac{2(w'_0)^2 w''_0}{\left(1-(w'_0)^2\right)^{3/2}}\right.$$

$$\left.+\frac{3(w'_0)^2 w''_0}{\left(1-(w'_0)^2\right)^{3/2}}+\frac{3(w'_0)^4 w''_0}{\left(1-(w'_0)^2\right)^{5/2}}\right)\langle\phi'_3\rangle-m_y\left(\frac{\theta'_z w'_0}{\sqrt{1-(w'_0)}}\right)\langle\phi'_2\rangle-m_y\left(\frac{2w'_0}{\sqrt{1-(w'_0)^2}}\right.$$

$$\left.+\frac{(w'_0)^3}{\left(1-(w'_0)^2\right)^{3/2}}\right)\langle\phi''_3\rangle-m_y\left(\frac{v'_0 w'_0}{\sqrt{1-(w'_0)^2}}\right)\langle\phi_4\rangle-m_x\left(\sqrt{1-(v'_0)^2}\right)\langle\phi'_4\rangle$$

$$+m_x\left(\frac{\theta'_z v'_0}{\sqrt{1-(v'_0)^2}}\right)\langle\phi'_2\rangle+m_y{}^2\left(\frac{(w''_0)^2}{1-(w'_0)^2}+\frac{2(w'_0)^2(w''_0)^2}{\left(1-(w'_0)^2\right)^2}+\frac{3(w'_0)^2(w''_0)^2}{\left(1-(w'_0)^2\right)^2}\right.$$

$$\left.+\frac{4(w'_0)^4(w''_0)^2}{\left(1-(w'_0)^2\right)^3}-(\theta'_z)^2\right)\langle\phi'_3\rangle+m_y{}^2\left(\frac{2(w''_0)}{1-(w'_0)^2}+\frac{2(w'_0)^3(w''_0)}{\left(1-(w'_0)^2\right)^2}\right)\langle\phi''_3\rangle$$

$$\left.-m_y{}^2(2w'_0\theta'_z)\langle\phi'_4\rangle-f_y\langle\phi_4\rangle\right]dz \qquad (5.56)$$

$$[K_5]=\int_l\left(e_{5j}\phi''_{qi}\right)dz$$

$$=\int_l\phi''\left[-\left(1+u'_0+\frac{(w'_0)^2}{\sqrt{1-(w'_0)^2}}\right)\left\langle\frac{\partial m_y}{\partial q}\right\rangle+\left(w''_0+\frac{(w'_0)^2(w''_0)}{1-(w'_0)^2}\right)\left\langle\frac{\partial m_y^{\,2}}{\partial q}\right\rangle-m_y\langle\phi'_1\rangle\right.$$

$$-m_y\left(\frac{2w'_0}{\sqrt{1-(w'_0)^2}}+\frac{(w'_0)^3}{\left(1-(w'_0)^2\right)^{3/2}}\right)\langle\phi'_3\rangle+m_y^{\,2}\left(\frac{2w'_0w''_0}{1-(w'_0)^2}+\frac{2(w'_0)^3(w''_0)}{\left(1-(w'_0)^2\right)^2}\right)\langle\phi'_3\rangle$$

$$\left.+m_y^{\,2}\left(1+\frac{(w'_0)^2}{1-(w'_0)^2}\right)\langle\phi''_3\rangle\right]dz \qquad (5.57)$$

$$[K_6]=\int_l\left(e_{6j}\phi'_{qi}\right)dz$$

$$=\int_l\phi'\left[-\left(w'_0\sqrt{1-(v'_0)^2}\right)\left\langle\frac{\partial m_x}{\partial q}\right\rangle+\left(v'_0\sqrt{1-(w'_0)^2}\right)\left\langle\frac{\partial m_y}{\partial q}\right\rangle+\left(\theta'_z\left(1-(w'_0)^2\right)\right)\left\langle\frac{\partial m_y^{\,2}}{\partial q}\right\rangle\right.$$

$$+\left(\theta'_z\left(1-(v'_0)^2\right)\right)\left\langle\frac{\partial m_x^{\,2}}{\partial q}\right\rangle-m_x\left(\sqrt{1-(v'_0)^2}\right)\langle\phi'_3\rangle+m_x\left(\frac{w'_0v'_0}{\sqrt{1-(v'_0)^2}}\right)\langle\phi'_2\rangle$$

$$+m_y\left(\sqrt{1-(w'_0)^2}\right)\langle\phi'_2\rangle-m_y\left(\frac{v'_0w'_0}{\sqrt{1-(w'_0)}}\right)\langle\phi'_3\rangle+m_y^{\,2}\left(1-(w'_0)^2\right)\langle\phi'_4\rangle-m_y^{\,2}(2\theta'_zw'_0)\langle\phi'_3\rangle$$

$$\left.+m_x^{\,2}\left(1-(v'_0)^2\right)\langle\phi'_4\rangle-m_x^{\,2}(2\theta'_zv'_0)\langle\phi'_2\rangle+GJ\langle\phi'_4\rangle+m_z(\theta'_4)\right]dz \qquad (5.58)$$

$$[K_7]=\int_l\left(e_{7j}\phi'_{qi}\right)dz$$

$$=\int_l\phi''\left[(1+u'_0)\left\langle\frac{\partial m_w}{\partial q}\right\rangle+m_w\left(\phi'_1\right)\right]dz \qquad (5.59)$$

$$[K_8]=\int_l\left(e_{8j}\phi_{qi}\right)dz$$

$$=\int_l\phi\left[f_x\left(\phi'_2\right)-f_y\left(\phi'_3\right)+(v'_0)\left\langle\frac{\partial f_x}{\partial q}\right\rangle-w'_0\left\langle\frac{\partial f_y}{\partial q}\right\rangle\right]dz \qquad (5.60)$$

In the above formulation of the stiffness matrix, the terms, $\langle\phi'_1\rangle,\langle\phi'_2\rangle,\langle\phi''_2\rangle,\langle\phi'_3\rangle,\langle\phi''_3\rangle,\langle\phi_4\rangle,\langle\phi'_4\rangle$, and $\langle\phi''_4\rangle$ are 1x16 row vectors which are defined as,

$$\langle\phi'_1\rangle = \langle\langle\phi'\rangle\vdots\langle 0\rangle\vdots\langle 0\rangle\vdots\langle 0\rangle\rangle \qquad \langle\phi'_2\rangle = \langle\langle 0\rangle\vdots\langle\phi'\rangle\vdots\langle 0\rangle\vdots\langle 0\rangle\rangle$$
$$\langle\phi''_2\rangle = \langle\langle 0\rangle\vdots\langle\phi''\rangle\vdots\langle 0\rangle\vdots\langle 0\rangle\rangle \qquad \langle\phi'_3\rangle = \langle\langle 0\rangle\vdots\langle 0\rangle\vdots\langle\phi'\rangle\vdots\langle 0\rangle\rangle$$
$$\langle\phi''_3\rangle = \langle\langle 0\rangle\vdots\langle 0\rangle\vdots\langle\phi''\rangle\vdots\langle 0\rangle\rangle \qquad \langle\phi_4\rangle = \langle\langle 0\rangle\vdots\langle 0\rangle\vdots\langle 0\rangle\vdots\langle\phi\rangle\rangle$$
$$\langle\phi'_4\rangle = \langle\langle 0\rangle\vdots\langle 0\rangle\vdots\langle 0\rangle\vdots\langle\phi'\rangle\rangle \qquad \langle\phi''_4\rangle = \langle\langle 0\rangle\vdots\langle 0\rangle\vdots\langle 0\rangle\vdots\langle\phi''\rangle\rangle \tag{5.61}$$

where, $\langle\phi\rangle, \langle\phi'\rangle, \langle\phi''\rangle$ are 1x4 row vectors of cubic shape functions and their derivatives.

Numerical evaluation of stress resultants and their respective derivatives remains unchanged from the previous formulation and is therefore not repeated here. The stress resultants evaluating the shear forces are obtained from the calculated reactions of each member. The derivatives of the shear forces are always zero for each member, due to the assumption that external forces act at nodal points only.

After extending the model formulation to include flexural shear stress examples 2 and 3 shown in Fig. 5.03 were re-analysed. The simply-supported beam, with a point load at mid-span, was modelled using four elements. Although the model can predict bifurcation loads it was also decided to subject the beam to various imperfections, consisting of an initial lateral bow and twist, thus allowing a more comprehensive validation to be conducted. Predicted load-lateral deflection relationships are shown in Fig. 5.06, together with a Southwell Plot of one of these predictions. The elastic critical load of 101.0 kN estimated from the Southwell plot, and the computer model prediction of the perfect bifurcation load of 100.0 kN compared very well with the theoretical load of 100.1 kN, calculated by Timoshenko[66].

The cantilever beam, with a point load at the tip was also modelled using four elements and subjected to various imperfections. The predicted load-lateral deflection relationships corresponding to this beam are shown in Fig. 5.07. The elastic critical load of 30.6 kN estimated from the Southwell Plot, and the computer model prediction of the perfect bifurcation load of 30.0 kN once again compared very well with the theoretical load of 31.17 kN, calculated by Timoshenko[66].

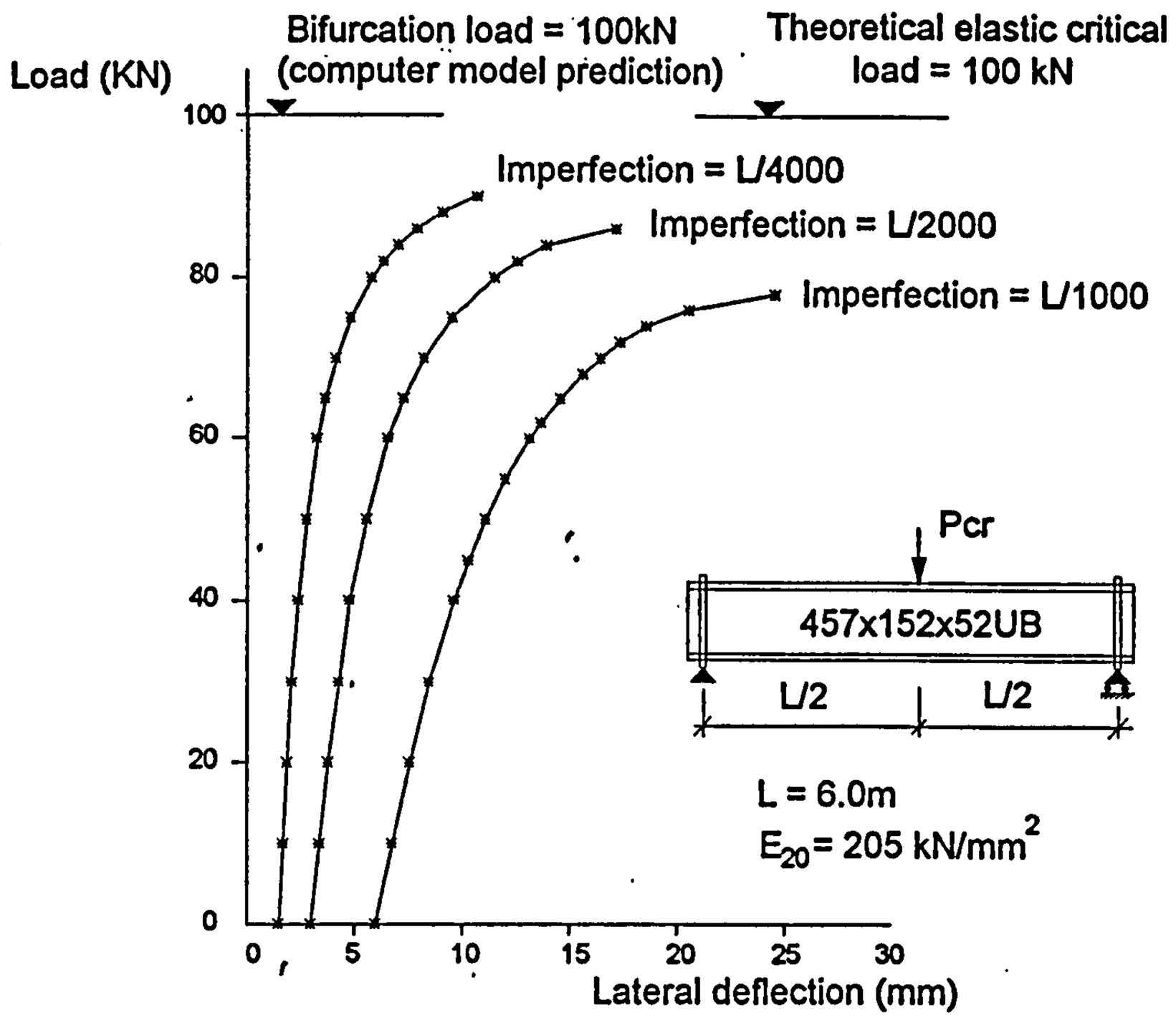

LOAD-LATERAL DEFLECTION RELATIONSHIP FOR SIMPLY-SUPPORTED BEAM WITH A POINT LOAD AT MID-SPAN.

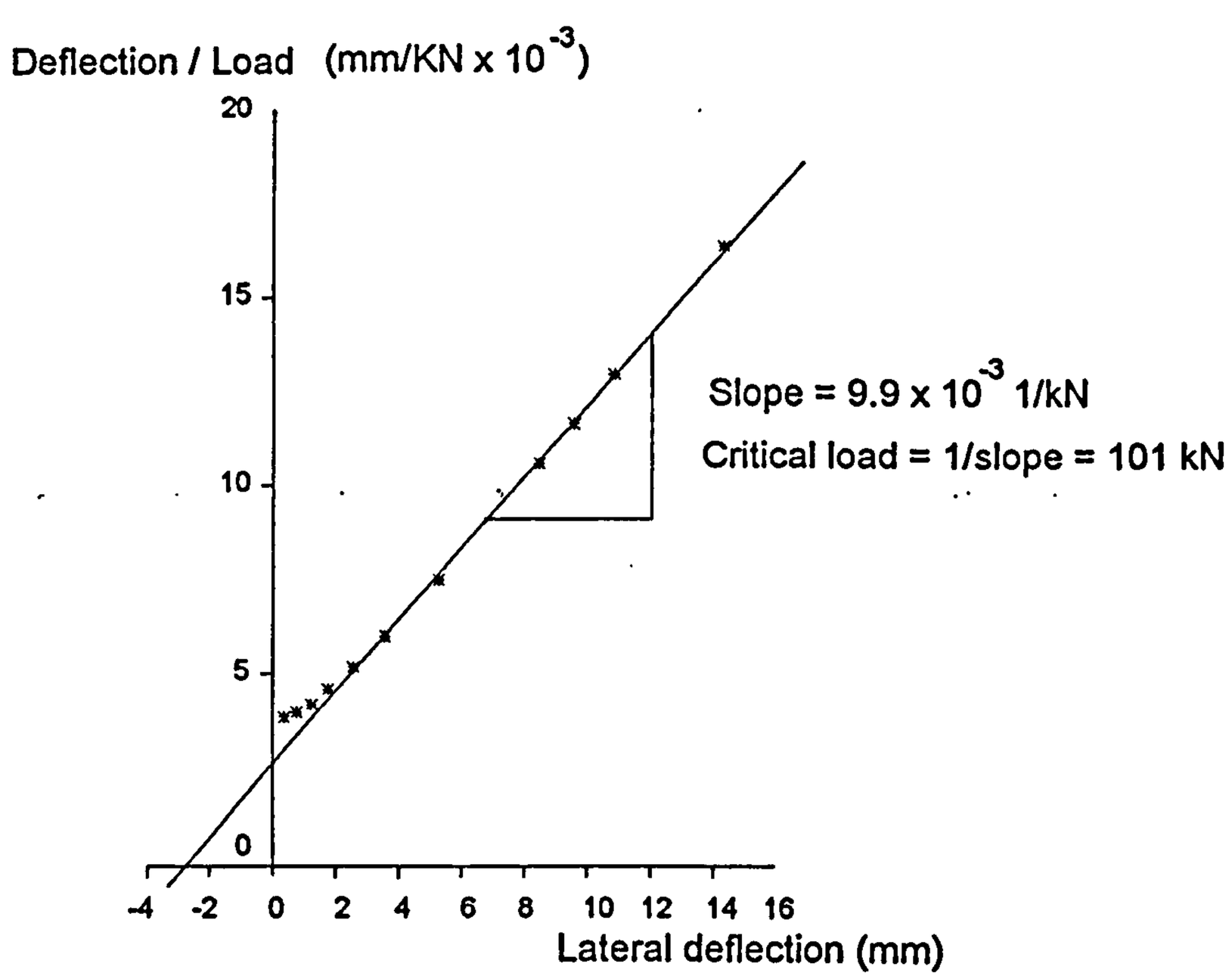

SOUTHWELL PLOT FOR THE BEAM WITH L/2000 IMPERFECTIONS.

Fig. 5.06: Load-lateral displacement relationships and Southwell Plot for a simply-supported beam with a point load at mid-span.

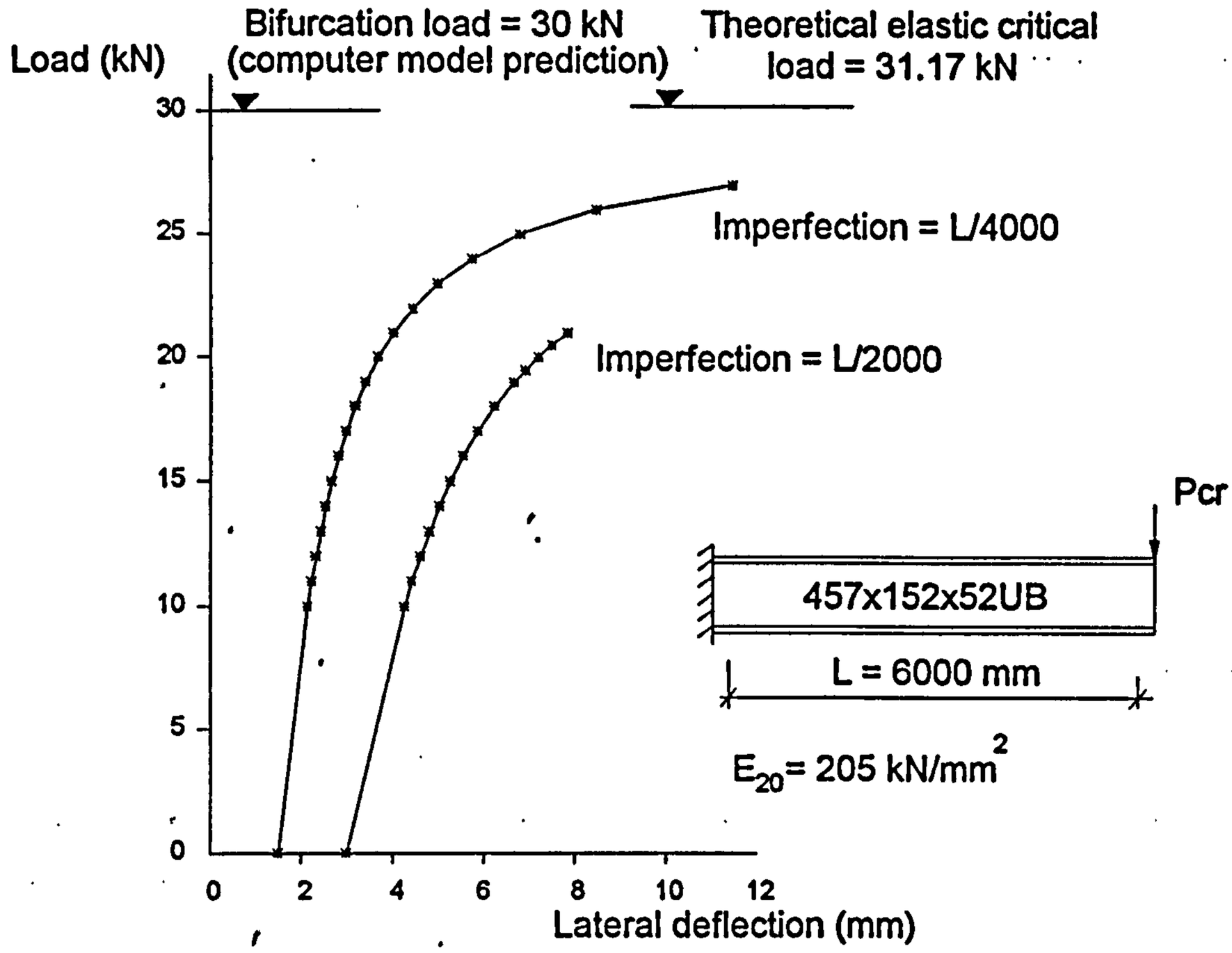

LOAD-LATERAL DEFLECTION RELATIONSHIPS FOR CANTILEVER BEAM WITH A POINT LOAD AT THE TIP.

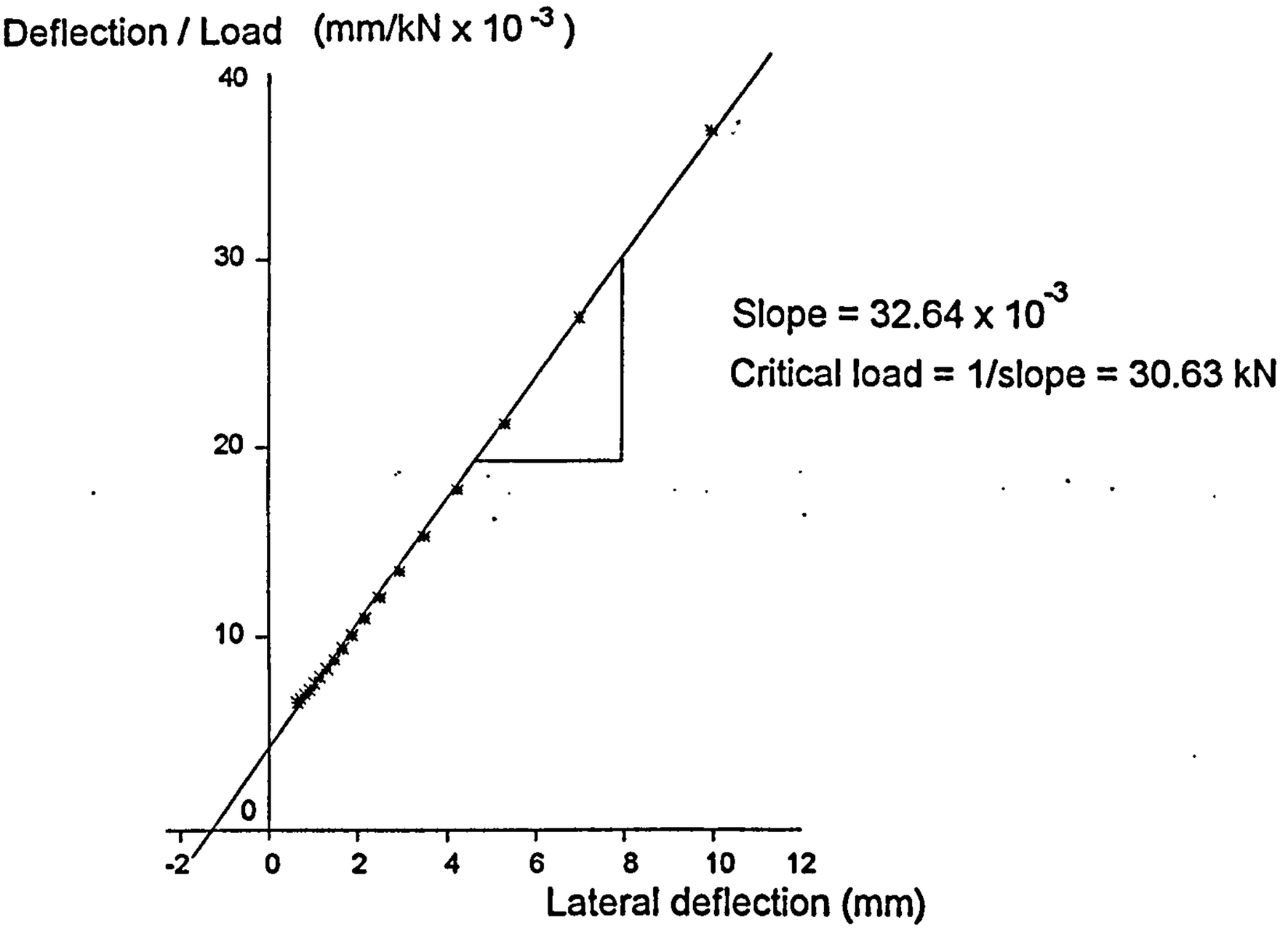

SOUTHWELL PLOT FOR THE CANTILEVER WITH L/4000 IMPERFECTIONS

Fig. 5.07: Load-lateral displacement relationships and Southwell Plot for a cantilever beam with a point load at the tip.

Additional validation of the model was conducted by calculating bifurcation loads and comparing them against theoretical solutions[66]. Simply-supported beams of various sizes and span lengths and a point load at mid-span were considered. The beams was considered to be perfectly straight (since bifurcation loads are required) and modelled using four elements. The predicted elastic critical loads are compared with the theoretical solutions and are shown in Table 5.02

Beam size (UB's)	Span length L (m)	Slenderness ratio $\lambda=l/r_y$	Predicted elastic critical load (kN.)	Theoretical load (kN.)	Error (%)
838x292x176	12.0	203.4	280.80	280.90	0.04
686x254x125	8.0	152.7	394.00	390.41	0.92
533x210x82	8.0	182.7	154.50	154.20	0.19
406x178x54	6.0	155.8	137.00	136.77	0.17
406x140x39	6.0	207.6	55.70	55.35	0.63
305x102x28	6.0	288.5	23.65	23.53	0.51
254x102x28	6.0	270.3	27.00	26.78	0.82

Table 5.02: Comparison between computer model and theoretical solutions for elastic critical loads of a simply-supported beam with a point load at mid-span.

Further validation examples were considered, with the structural configuration being changed to a simply supported beam subjected to a uniformly distributed load. The number of elements used to model each beam was increased from four to eight. This was deemed necessary to allow a reduction in the error caused by the model requirement of representing a uniformly distributed loads as a set of point loads at nodal positions. The beam size, span length, predicted and theoretical elastic critical load for each example are shown in Table 5.03.

Beam size (UB's)	Span length L (m)	Slenderness ratio $\lambda=l/r_y$	Predicted elastic critical load (KN./m)	Theoretical load (kN./m)	Error (%)
838x292x176	14.0	237.3	23.03	23.00	0.13
533x210x82	10.0	228.4	14.98	14.90	0.54
305x102x28	6.0	288.5	6.64	6.53	1.68
406x140x39	6.0	207.6	15.61	15.35	1.69
254x102x28	6.0	270.3	7.60	7.47	1.74

Table 5.03: Comparison between computer model and theoretical solutions for elastic critical loads of a simply-supported beam with uniformly distributed load.

5.11: CONVERGENCE STUDY ON THE PREDICTION OF LATERAL-TORSIONAL BUCKLING.

To investigate the convergence of the model, when predicting lateral-torsional buckling, the simply supported beam with a point load at mid-span as shown in Fig. 5.03 (example 2) was used. The beam was modelled using 2, 4, 8, 16 and 32 elements. The theoretical load, calculated to three decimal places, was found to be 100.099 kN. The results obtained from the model are shown in Table 5.04, with the error being shown graphically in Fig 5.08.

Number of elements	Elastic critical load (computer prediction). (kN)	Error (%)
2	100.141	+0.040
4	99.976	-0.120
8	99.953	-0.140
16	99.951	-0.148
32	99.951	-0.148

Table 5.04: Results of convergence study to predict lateral-torsional buckling.

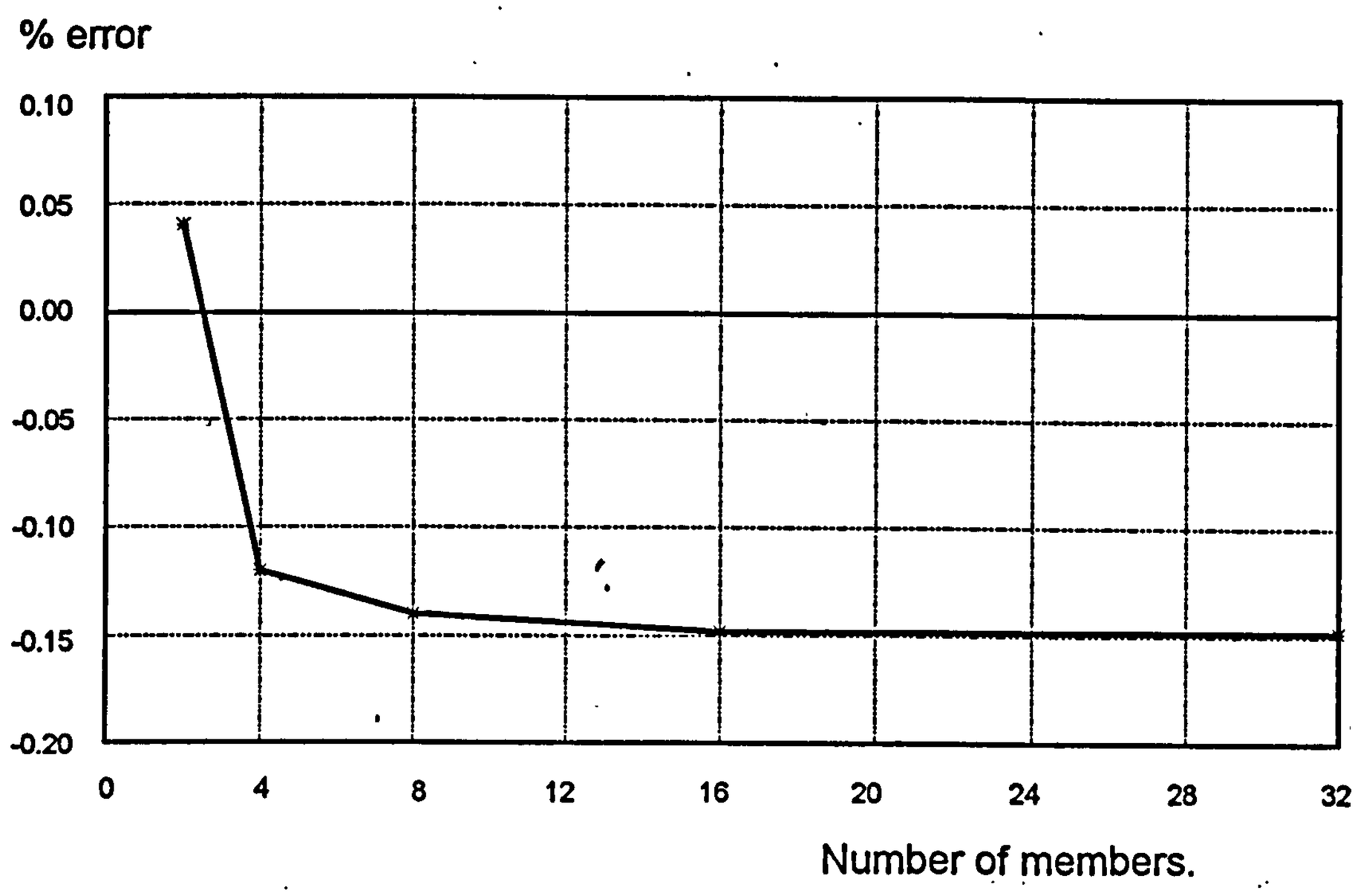

Fig. 5.08: Graphical representation of convergence study into predicting lateral-torsional buckling.

It was found that the model converged towards an answer of 99.951 kN compared to the theoretical load of 100.099 kN giving an error of -0.148%. This error was considered to be acceptable and conservative.

5.12: DESTABILISING LOADS.

As explained in Chapter 4, the model has been extended to allow the reference axis (and thus the nodal positions) to be placed at any point on or outside the cross-section of the beam. With this capability the position of load application, which is at the nodal point on the reference axis, can be varied. As an extra validation for the re-positioning of the reference axis, and to extend the validation for lateral-torsional buckling, the node was placed on the top flange and the examples studied for a simply-supported beam with a point load at mid-span were repeated. The predicted elastic critical loads obtained from the model are shown in Table 5.05 together with a comparison with theoretical solutions[66] for destabilising loads.

Beam size (UB's)	Span length L (m)	Slenderness ratio $\lambda=l/r_y$	Predicted elastic critical load (kN)	Theoretical load (kN)	Error (%)
838x292x176	12.0	203.4	186.425	186.150	0.15
686x254x125	8.0	152.7	257.098	252.098	1.99
533x210x82	8.0	182.7	102.363	102.290	0.07
406x178x54	6.0	155.8	89.635	89.250	0.40
406x140x39	6.0	207.6	36.607	36.715	0.30
305x102x28	6.0	288.5	17.609	17.570	0.22
254x102x28	6.0	270.3	20.936	20.955	0.09

Table 5.05: Comparison between computer model and theoretical solutions for elastic critical loads of a simply-supported beam with a point load at mid-span and positioned on the top flange.

As expected the critical loads are less than the values given in Table 5.02, due to the additional torque induced by the load being applied at the top flange as twisting of the beam occurs . The computer model predictions for destabilising loads compare very well with the theoretical solutions.

5.13: VALIDATION FOR INELASTIC LATERAL-TORSIONAL BUCKLING.

In the previous section, to enable the model to be compared against classical theoretical solutions for elastic critical loads, the beams were assumed to remain elastic, to be initially unstressed and for bifurcation solutions to be perfectly straight.

However some beams can fail by lateral-torsional buckling in the inelastic range, in which some of the material has yielded before buckling commences. The inelastic buckling load will be lower than the corresponding elastic buckling load due to spread of yield within the member. If the beam is stocky enough then nearly the whole cross-section, at its most highly stressed areas, will become inelastic and buckling will not occur before failure due to in-plane bending. Therefore there are three possible modes of failure for an unrestrained beam which are summarised below and are dependent on the slenderness of the beam (represented by the relationship[67] between the plastic moment capacity *Mp*, and the elastic critical moment *Mcr):*

(a) Beams of high slenderness $\left(\sqrt{Mp/Mcr} > 1.1\right)$ which fail by elastic lateral-torsional buckling at *Mcr.*

(b) Beams of intermediate slenderness $\left(1.1 \rangle \sqrt{Mp/Mcr} > 0.4\right)$ for which collapse is by inelastic lateral-torsional buckling, at loads below *Mcr.*

(c) Stocky beams $\left(0.4 > \sqrt{Mp/Mcr}\right)$ which are capable of attaining *Mp* without buckling.

These three conditions are shown schematically in Fig. 5.09.

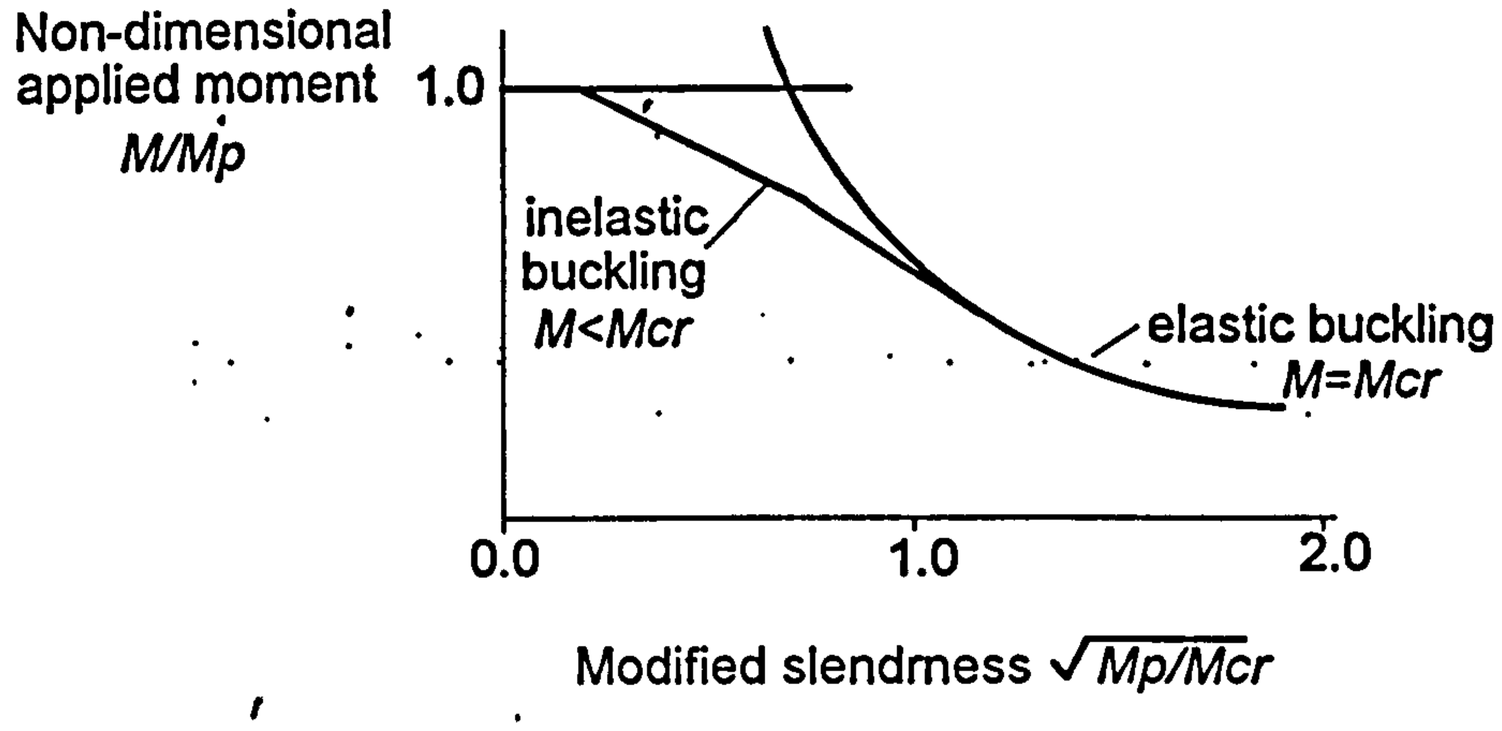

Fig. 5.09: Different modes of failure for unrestrained beams.

Apart from the possibility of significant portions of the beam being inelastic when buckling commences, different forms of imperfection will also need to be considered. These include

(i) geometrical imperfections, such as initial curvature and twist,

(ii) construction tolerances creating eccentricities at the position of the applied load and supports,

(iii) residual stresses,

(iv) variations in material properties.

Design rules use an empirical design curve, which is based on an adjusted Perry-Robertson approach[67,65,49]. This curve uses one type of equivalent imperfection, an initial lateral bow, which allows approximately for all imperfections. The imperfection parameter used to obtain the maximum value of the initial bow is given by,

$$\eta = 0.003\lambda \qquad \text{for BS 449}^{4} \qquad (5.62)$$

and

$$\eta = 0.007(\lambda_{LT} - \lambda_{LO}) \qquad \text{for BS5950 Part 1}^{49} \qquad (5.63)$$

where,

$$\lambda_{LO} = 0.4\left(\frac{\pi^2 E}{P_y}\right)^{\frac{1}{2}} \qquad \text{and} \qquad \lambda_{LT} = nuv\lambda$$

where

λ = slenderness ratio about the minor axis,

and the other symbols are defined in BS 5950 Part 1[49].

Both formulas for the maximum lateral bow at mid-span give very similar solutions.

To validate the model for inelastic lateral torsional buckling a comparison was made with full-scale tests conducted by Kitipornchai and Trahair[68], who also made finite element predictions[69]. The structural configuration consisted of a simply-supported beam, with a point load placed at mid-span at a height of 219mm above the centroid of the beam as shown in Fig. 5.10.

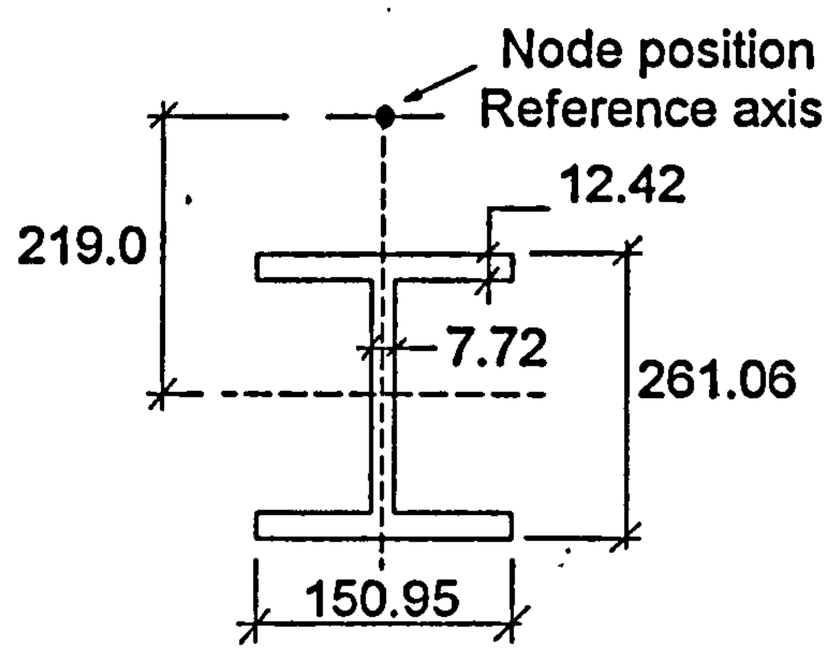

(all dimensions in mm)

Fig. 5.10: Structural configuration for the experiments conducted by Kitipornchai and Trahair[68].

Four tests were carried out on different spans of a single serial size, which produced a range of minor axis slenderness ratio from 68.14 to 170.34. The loading arrangement was such that the resultant applied load remained vertical throughout the test even when the beam deflected laterally and twisted. The support conditions prevented twisting of the beam together with lateral and vertical displacement, but allowed lateral and vertical rotation together with warping. The measured material properties of 203 kN/mm² for Young's modulus and 302.2 N/mm² for the yield stress were used in the analysis. The comparison between experimental and predicted results is shown in Table 5.06. The computer model results compare well with the previous theoretical solutions, with both sets of results being within about 10% of the experimental results. Kitipornchai and Trahair attributed the error between their predicted and experimental results to initial geometrical imperfections. The analyses differ slightly in that initial

residual stresses, for which an assumed pattern was included in the analysis by Kitipornchai and Trahair, were ignored in this work. Within these validation examples all imperfections were assumed to be represented by an equivalent initial out-of-plane bow, calculated by the BS5950 Part 1 assumption (equation 5.74). An inspection of the published lateral displacements during the test suggests that this has underestimated the actual imperfection.

Beam serial size	Beam span (m)	Slenderness ratio $\lambda=l/r_y$	Experimental critical load (kN)	Present analysis (kN)	Kitipornchai & Trahair analysis (kN)
10 UB 29	2.44	68.1	234.96	259.199	252.5
	3.05	85.2	185.12	204.998	198.3
	3.66	102.2	145.07	148.399	152.6
	6.10	170.3	56.96	53.599	55.0

Table 5.06 : Comparison between computer model predictions of inelastic lateral-torsional buckling loads and Kitipornchai and Trahair[68] experimental and computer results.

5.2: THE BEHAVIOUR OF BEAMS AT ELEVATED TEMPERATURES.

In order to set the findings for unrestrained beams into context the prescribed limiting temperatures (failure temperatures), specified in BS5950 Part 8[5], are first compared with analytical results for beams with the compression flange continuously restrained against lateral deflection. Uniform heating is assumed throughout.

5.21: BEAMS WITH CONTINUOUSLY RESTRAINED COMPRESSION FLANGE.

This case has often been analysed, particularly for beams supporting concrete slabs on their top flange with uniformly distributed loading, and it is known that the limiting temperatures given in BS5950 Part 8[5] and EC3 Part 1.2[6] for this three-sided heating (the heat sink effect of the concrete keeps the top flange cooler) are an accurate lower bound. The examples presented here are slightly different in that uniform heating is assumed (since the main investigation is for unrestrained beams) causing the neutral axis to remain static at the section's centroid. Since no buckling can take place the "failure" criterion when in-plane deflection reaches span/20 must be used. Before a study is conducted another validation example (and convergence study) was

conducted by comparing the results for the example shown in Fig. 5.11 against those produced by another model developed by Burgess *et. al* [70]

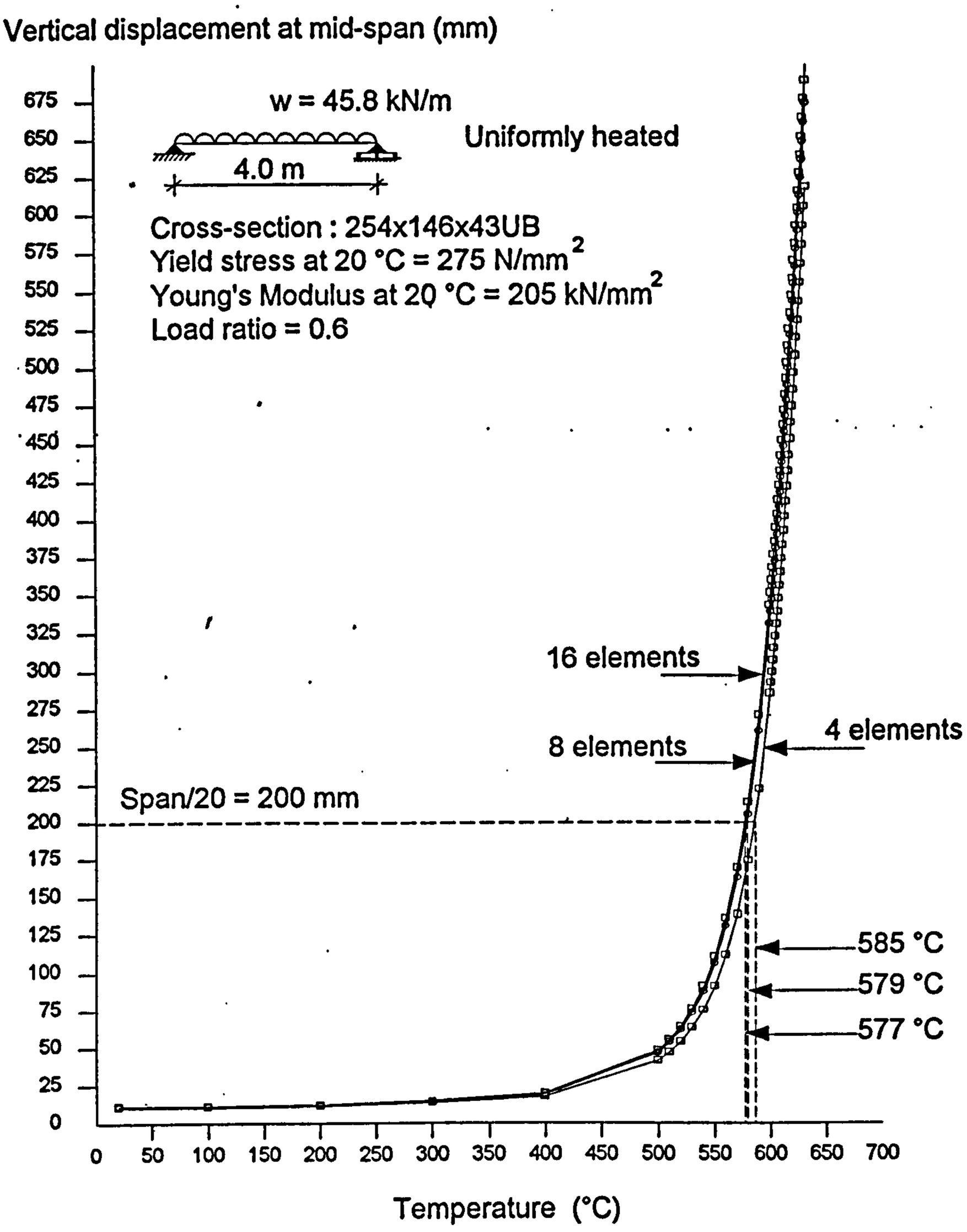

Fig 5.11: Convergence study for a uniformly heated simply-supported beam with uniformly distributed load and continuously restrained compression flange.

The model calculated that a deflection of span/20 is reached at 585°C when four elements were used to model the beam. When the number of elements was increased to 8 and then 16, temperatures of 579°C and 577°C were obtained. The convergence study conducted by increasing the elements was not continued beyond 16 since the results from 8 to 16 elements are very similar. The main difference in the

results is due to the representation of a uniformly distributed load by a series of point loads, since the model is limited to loads being placed at nodal points. Therefore throughout this study all beams are modelled using four elements except for beams with uniformly distributed load for which the number is increased to eight.

The results produced by the model compare very well with the analysis by Burgess *et. al.*[70] who calculated a failure temperature of 575°C. Both analyses predicted higher temperatures than the limiting temperature in BS5950 Part 8, of 555°C.

A more extensive study was conducted to allow a comparison of the predicted limiting temperatures at different load ratios for uniformly loaded beams. A series of different serial sizes and spans were used (as shown in Fig. 5.12) giving different span:depth ratios. To allow a comparison with BS5950 Part 8, the results shown in Fig. 5.12 are presented in terms of limiting (failure) temperature and load ratio defined for restrained beams as

$$R = \frac{M_f}{M_c}$$

where M_f = applied moment at the fire limit state,
M_c = moment capacity about major axis.

It has previously been shown[70] that the span:depth ratio is a controlling parameter for limiting temperatures of restrained beams, and the effect of this parameter is also shown in Fig. 5.12. It can be seen that the limiting temperatures given by BS5950 Part 8[5] are generally conservative compared with the computed results. The yield stress used in design at ambient temperature differs slightly between BS5950 Part 1[49] and EC3 Part 1.1[71], so it is not possible to plot the EC3 Part 1.2[6] limiting temperatures on the same figure since the load ratios have slightly different meanings. However these differences are small and since the relationship between limiting temperature and load ratio is identical in each of the codes it may be said that the use of the limiting temperature method on simple beams with continuous compression flange restraint and uniformly distributed loading is vindicated by these results. Also shown in Fig. 5.12 are computed failure temperatures when the loading pattern is changed to a point load placed at mid-span. These results also vindicate the use of the limiting temperature method for this type of load pattern and structural configuration.

When the form of loading is changed to the most onerous condition of uniform bending it can be seen from Fig. 5.12 that the limiting temperatures lie within the cluster of computed results rather than below them. For the higher span:depth ratios the codes are no longer conservative, although the discrepancies are relatively small

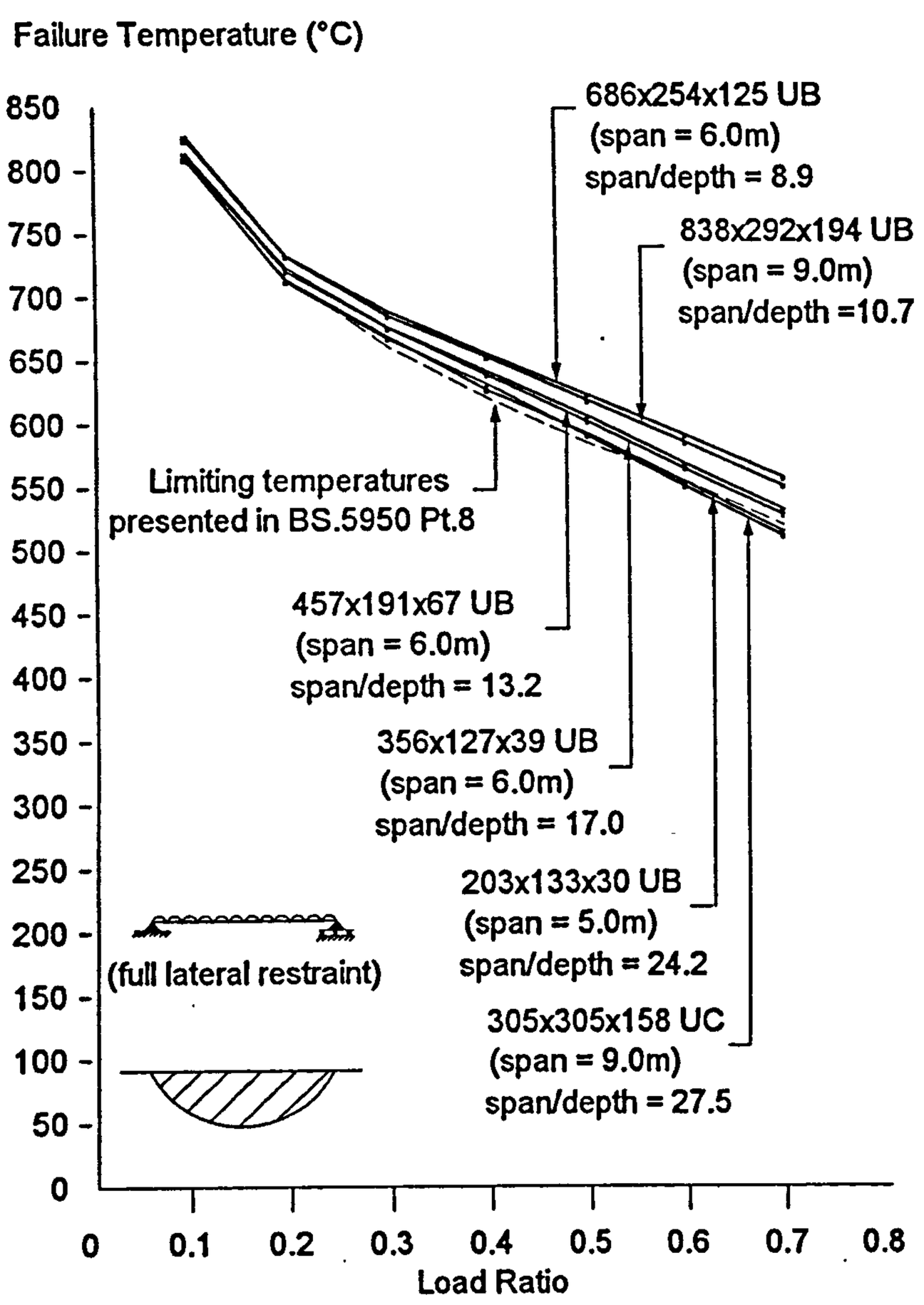

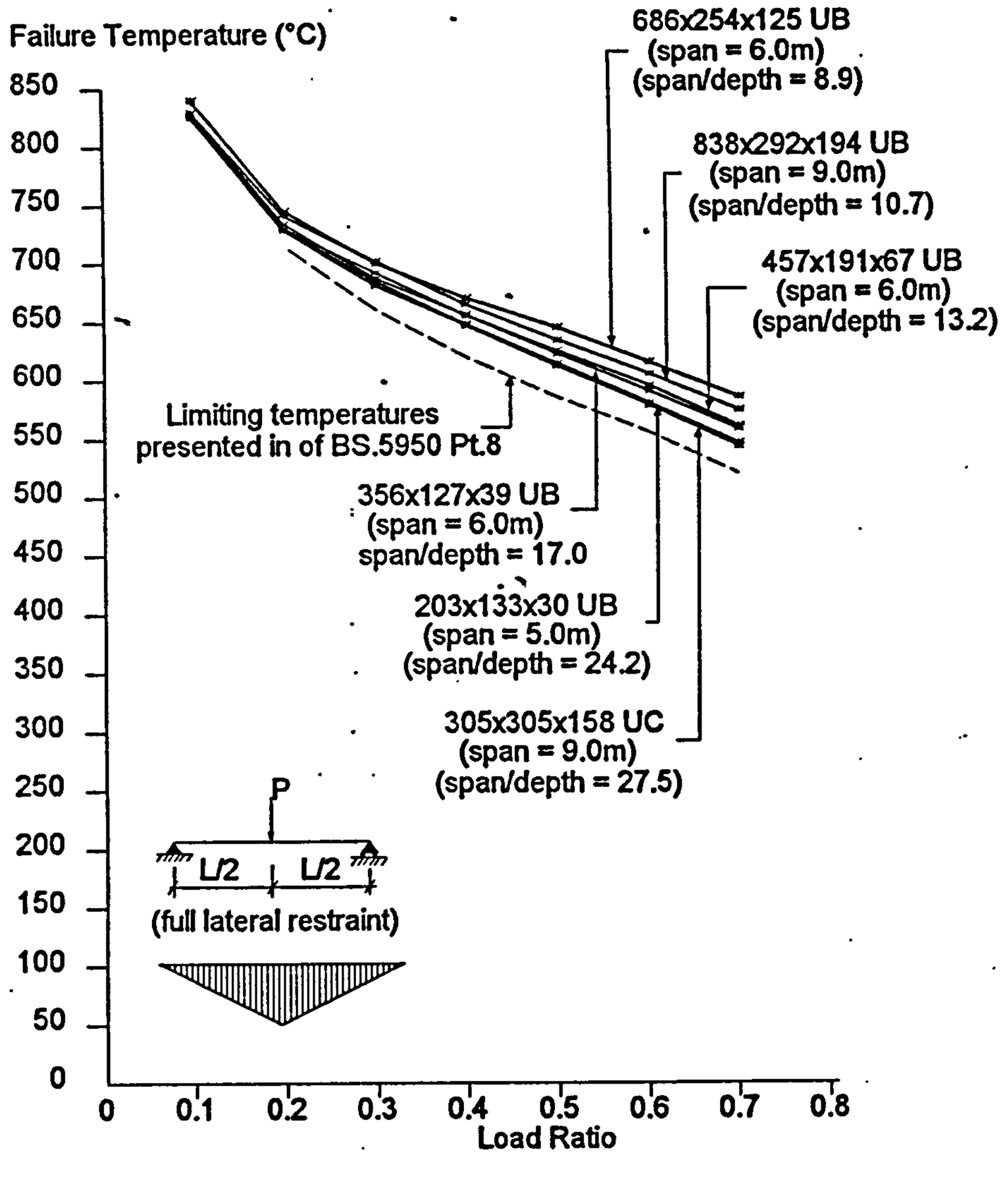

Fig. 5.12: Comparison between limiting temperatures and computer analysis for simple beams with continuously restrained compression flange.

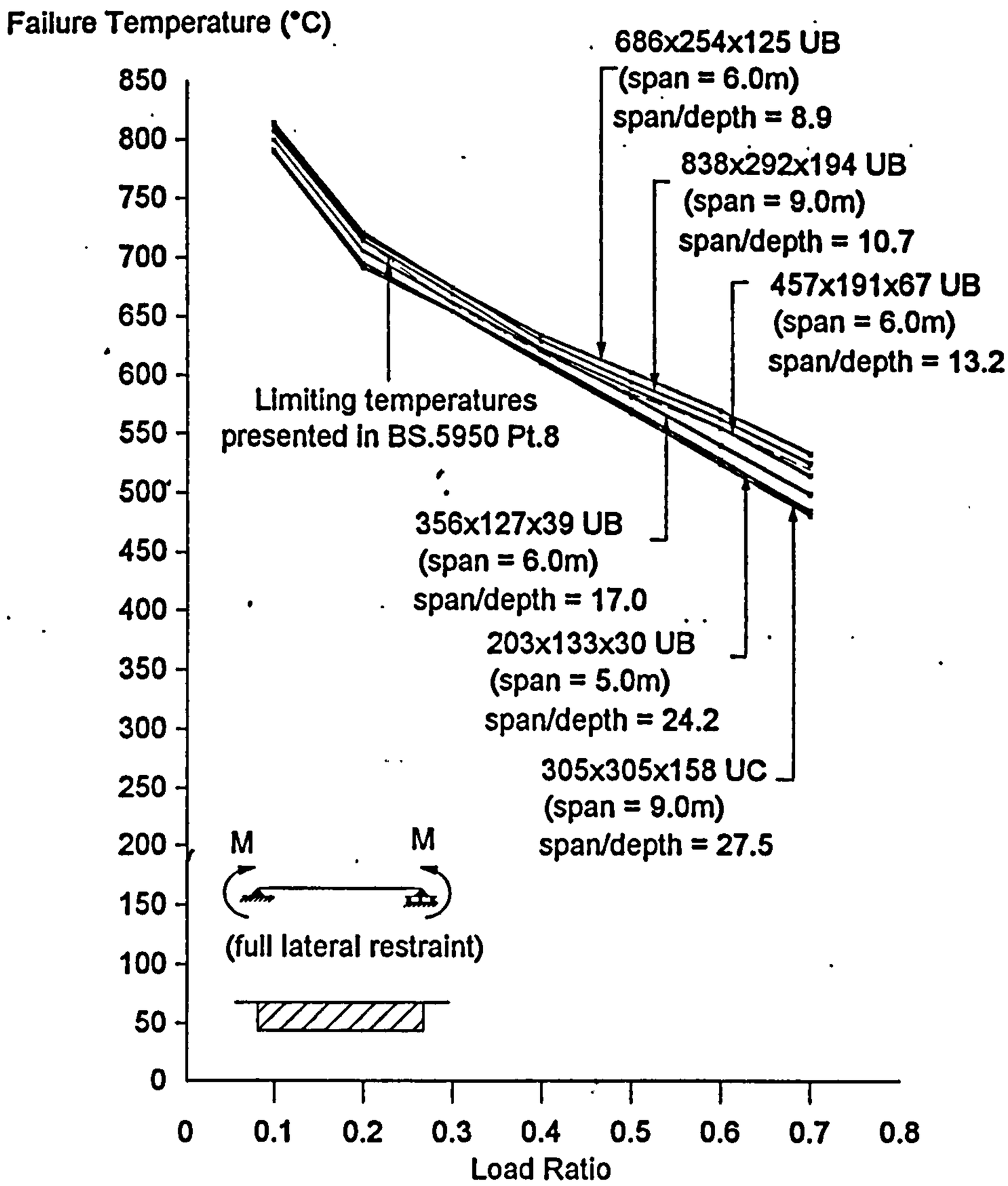

Fig. 5.12: (Continued) Comparison between limiting temperatures and computer analysis for simple beams with continuously restrained compression flange.

and would not imply more than a few minutes reduction in fire survival time. However since regulatory requirements specify survival time in a step-wise manner[2], passing over set thresholds contributes a large increase in regulatory fire protection.

Comparing the load cases presented, the relationship between load ratio and limiting temperature in both Codes is based simply on strength reduction factors[5,6] (which were discussed in Chapter 1). If steel exhibited a sharp yield-point at high temperatures, and if failure was defined by completion of the central plastic hinge, then the use of strength reduction factors would produce a single failure temperature for all simple beams at any given load ratio, without reference to the loading case. However since a deflection criterion is actually used, with stress-strain curves which are curvilinear at high temperatures, some spread of failure temperatures occurs, as can be seen, although this spread should never be very great for restrained beams.

5.22 UNRESTRAINED BEAMS WITH LOAD APPLIED AT THE SHEAR CENTRE.

The model was used to conduct an investigation into the behaviour of uniformly heated, unrestrained simply-supported beams, loaded at the centroid (also the shear centre) of the cross-section. There are several factors which affect the lateral-torsional buckling behaviour of steel I-beams at ambient temperature, including cross-sectional properties; span, support and restraint conditions, and the precise form of loading employed. For any given case the ratio M_b/M_{cx} (in the terminology of BS5950 Part 1[49]) is a convenient measure of the tendency to lateral-torsional buckling, with low values representing slender cases and values approaching 1.0 representing stocky beams where the preferred mode of failure is due to the formation of a plastic hinge. Within this study six different serial sizes were chosen, with spans giving a wide range of values for M_b/M_{cx}, which are shown in the graphical representation of the results presented in Figs. 5.13 and 5.14. Two of the beams, 457x191x67UB and 838x292x194UB were chosen to give exactly the same value of M_b/M_{cx}. In the case of a uniform load an additional beam 914x305x253UB, was analysed which produced a similar M_b/M_{cx} ratio to the beam 305x305x158UC. This was deemed necessary as an additional check for this load case, since a sudden change in gradient was experienced between load ratios of 0.6 and 0.7 (refer Fig. 5.13) when the 305x305x158UC was analysed. The range of the ratio M_b/M_{cx} was chosen so that at ambient temperature both elastic and inelastic lateral-torsional buckling failure modes were represented. The actual value of this ratio varies with the loading arrangement and is shown in the graphical representation of the results. An initial out-of-plane imperfection was assumed which gave an imperfection parameter value of $\eta = 0.003\lambda$. The support conditions allow both flanges to rotate and warp, but prevent twisting about the beam's axis. Thus the effective length of the beam is its actual span, in the absence of intermediate points of restraint.

The results were represented in terms of failure temperature and load ratio, which is defined as

$$R = \frac{mM_f}{M_b} \qquad (5.64)$$

where,

m = equivalent uniform moment factor (=1.0 if the slenderness correction factor n is used in the calculation of M_b),

M_f = applied moment at the fire limit state,

M_b = buckling resistance moment (lateral torsional)

For each condition the value of M_b was obtained from tables of member capacities[72], with the value of n (slenderness correction factor) being obtained from Table 20 in BS5950 Part 1[49]. The loading conditions shown in Figs 5.13 and 5.14 were chosen to give a wide range of bending moment distributions. The most severe case, in terms of its effect on lateral stability is that of uniform moment, for which the slenderness correction factor n is set at 1.0 in BS5950 Part 1. Other less severe patterns of bending moments are considered with the value of the slenderness correction factor highlighting the severity of the bending moment distribution. Each of the six beams was subjected to different loading conditions, and to load ratios of 0.7, 0.6, 0.5, 0.4, 0.3, 0.2, and 0.1. Four elements were found to be adequate to model each beam for all loading conditions, except that of uniformly distributed load for which the element number was increased to eight in order to reduce the error due to the limitation of the model in accepting nodal loads only. The results obtained are shown in Figs. 5.13 and 5.14 in which the limiting temperatures presented in Table 5 of BS5950 Part 8[5] are shown for comparison.

It would be of interest to compare the computed failure temperatures with both BS5950[5] and EC3[6] limiting temperatures. Both design Codes essentially use the same concept of load ratio, with EC3 using a "reduction factor" in its Load Domain calculation and a "degree of utilisation" in the Temperature Domain. For equivalent values of load ratio very similar failure (limiting) temperatures are obtained from the two Codes. However the essential difference in the processes is in calculation of the ambient-temperature buckling resistance moments, with EC3 typically producing higher values. In fire design EC3 Part 1.2 reduces the buckling resistance by dividing it by an "empirical correction factor" of 1.2. Therefore if this reduced buckling resistance moment is the same as that calculated in BS5950 Part 1, then the load ratio defined in both Codes is identical and thus similar failure temperatures are specified. However this is not typically the case, with the values of load ratio from the two Codes being different. Therefore the comparison between the analytical results, BS5950 and EC3 cannot be shown on the same graph. In this study the analysis was compared against BS5950 only, except in the basic case of uniform moment for which comparison was made with both Codes, as shown in Fig. 5.13.

Specimen design calculations of limiting temperature according to both Codes are presented for a simple beam of serial size 686x254x125UB, Grade 43, with 6.0m span and a uniform bending moment of 329.4 kNm at the fire limit state.

(a) Using BS5950 Parts 1[49] and 8[5]

Buckling capacity calculation from Part 1:

Slenderness correction factor	n	= 1.0	[Table 20]
Effective length	L_e	= 6.0 m	[Table 9]
Buckling resistance moment	M_b	= 549 kNm	

Limiting temperature calculation from Part 8:

Equivalent uniform moment factor	m	= 1.0
Applied moment at fire limit state	M_f	= 329.4 kNm
Load ratio	$\dot{R} = \frac{mM_f}{M_b}$	= 0.6
Hence, limiting temperature		= 555°C

(b) Using EC3 Parts 1.1[71] and 1.2[6]

Buckling capacity calculation from Part 1.1:

Since,

Modulus of elasticity	E	= 210,000 N/mm²
Shear modulus	G	= 80769.2 N/mm²
Warping constant	I_w	= 4.79 x 10^{12} mm⁶
Second moment of area about the minor axis	I_z	= 4380x 10^4 mm⁴
Torsion constant	I_t	= 116 x 10^4 mm⁴
Effective length factors	k	= 1.0
	k_w	= 1.0
Load case factor	C_1	= 1.0
Elastic critical moment	$M_{cr} = C_1 \frac{\pi^2 E I_z}{(KL)^2}\left[\left[\frac{k}{k_w}\right]^2 \frac{I_w}{I_z} + \frac{(kL)^2 G I_t}{\pi^2 E I_z}\right]^{0.5}$	
		= 965.2 kNm
Yield stress	f_y	= 275 N/mm² [Table 3.1]
For class 1 section	β_w	= 1.0 [Table 5.3.1]
Normalised slenderness	$\overline{\lambda}_{LT} = \left[\frac{\beta_w W_{ply} f_y}{M_{cr}}\right]^{0.5}$	
		= 1.07

{where W_{PLY} is the plastic section modulus about major axis (Y-Y)}

$$\phi_{LT} = 0.5\left[1 + \alpha_{LT}\left(\overline{\lambda}_{LT} - 0.2\right) + \overline{\lambda}^2{}_{LT}\right]$$

= 1.16

Reduction factor for lateral-torsional buckling

$$X_{LT} = \frac{1}{\phi_{LT} + \left[\phi^2_{LT} - \overline{\lambda}^2_{LT}\right]^{0.5}}$$

$= 0.62$

U.K. partial safety factor $\gamma_{M,1} = 1.05$

Buckling resistance moment $$M_{bRd} = \frac{X_{LT} B_w W_{ply} f_y}{Y_{m1}}$$ [cl. 5.5.2]

$= 649.2$ kNm

Limiting temperature calculation from Part 1.2 (temperature domain):

Design effect of the actions in fire $E_{fi,d} = 329.4$ kNm

Load capacity at time t=0 $R_{fi,d,0} = 649.5 / 1.2 = 541.25$ kNm

{where 1.2 is an empirical correction factor}

Degree of utilisation at time t=0 $\mu_0 = E_{fi,d}/R_{fi,d,0}$

$= 0.61$

Critical (limiting) temperature $$\theta_{a,cr} = 39.19\, ln\left(\frac{1}{0.9674\mu_0^{3.833}} - 1\right) + 482$$

$= 551$ °C

Alternative limiting temperature calculation from Part 1.2 (load domain)

Design buckling resistance at time t $M_{b,fi,t,Rd} = 329.4$ kNm

Reduction factor for yield strength of steel at temperature θ_{max}

$$k_{y,\theta max} = \frac{1.2 M_{b,fi,t,Rd}}{M_{b,Rd}} = 0.609$$

{where 1.2 is an empirical correction factor}

From Table 3.1 $\theta_{max} = 555$ °C.

The limiting temperatures for the above example are similar in both Codes. This was due to the "empirical correction factor" in EC3 Part 1.2 which divides by 1.2 the buckling moment calculated in EC3 Part 1, which in this case gave a value for buckling capacity at time = 0 similar to the buckling capacity given by BS5950 Part 1. This caused the load ratios to be similar and thus gave the same limiting temperatures. However extrapolation from this example may be dangerous, since the discrepancies between the two Codes' calculations of ambient-temperature buckling capacity is rather inconsistent. This is highlighted in Table 5.07 where a comparison is made between the two Codes for the six beams used in this study with uniform moment.

Beam section size	Span (mm)	Lateral-torsional buckling resistance moment (kNm)		% Difference
		BS5950	EC3	
356x127x39UB	6000	44.70	50.28	12.5
457x191x67UB	6000	159.00	183.18	15.2
838x292x194UB	9000	786.00	925.19	17.7
203x133x30UB	5000	39.00	43.60	11.8
686x254x125UB	6000	549.00	647.86	18.0
305x305x158UC	9000	527.00	551.17	4.6

Table 5.07: Comparison between BS5950 Part 1 and EC3 Part 1.1 for the lateral-torsional buckling resistance moment of simple beams under uniform moment.

Although both Codes produced a failure temperature of 555°C this does not compare very well with the analytical prediction of buckling at 487°C. Fig. 5.13 shows the full comparisons between limiting temperatures according to both Codes and the analysis, for all six beams over the full range of load ratios. The essential difference between the two graphs lies in the way in which the load ratios have been calculated. It is interesting to note from the graph in which load ratios are calculated to BS5950 that the beams 457x191x67UB and 838x292x194UB and the beams 305x305x158UC and 914x305x253UB, which have spans set to produce identical M_b/M_{cx} for uniform moment, have identical failure temperatures throughout the range of load ratio.

The predicted failure temperatures for various other loading conditions are shown graphically in Fig. 5.14, but are only compared with BS5950 limiting temperatures. These show a general pattern of results similar to those for uniform moment, except that the range of variation in failure temperatures for various M_b/M_{cx} values is not as high.

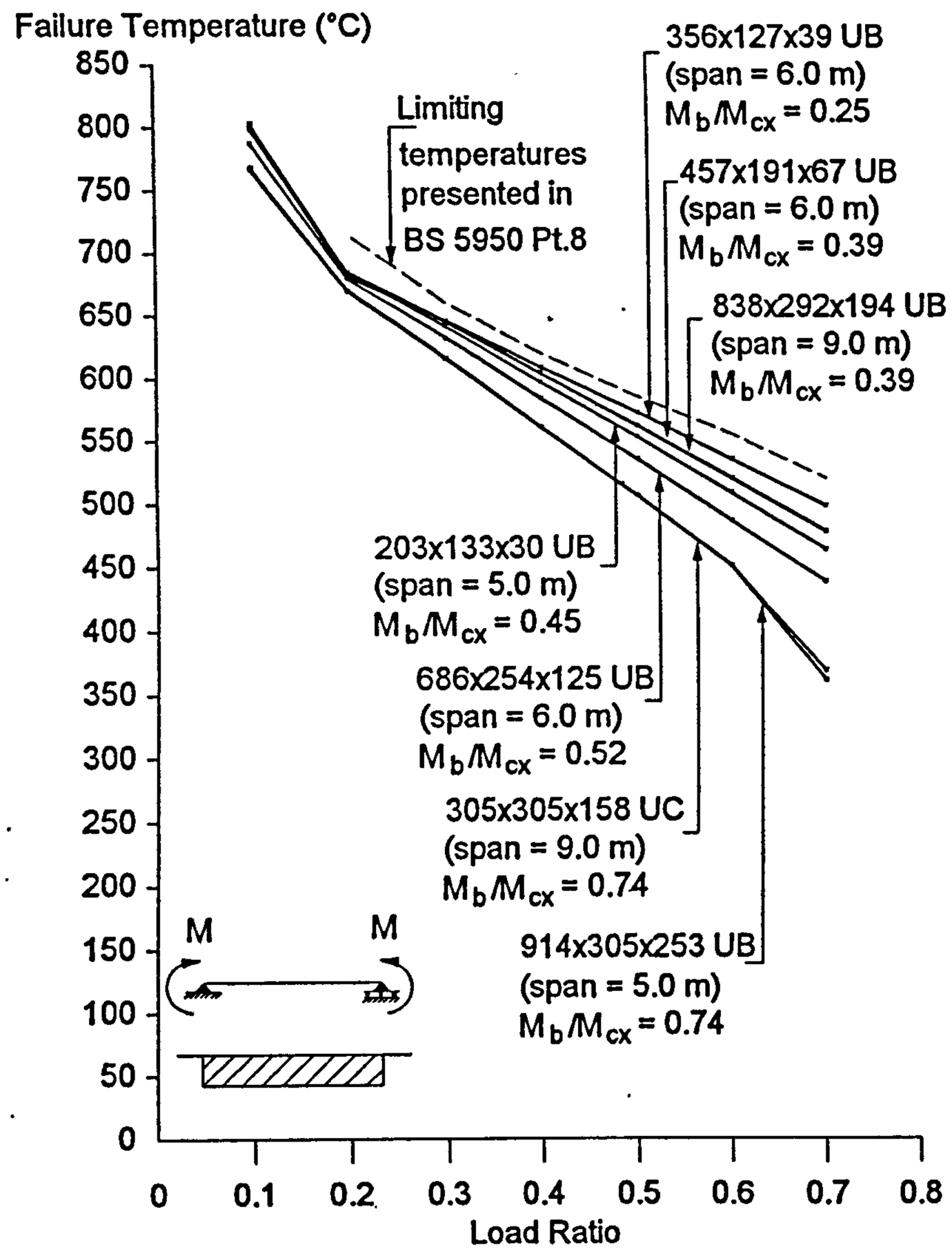

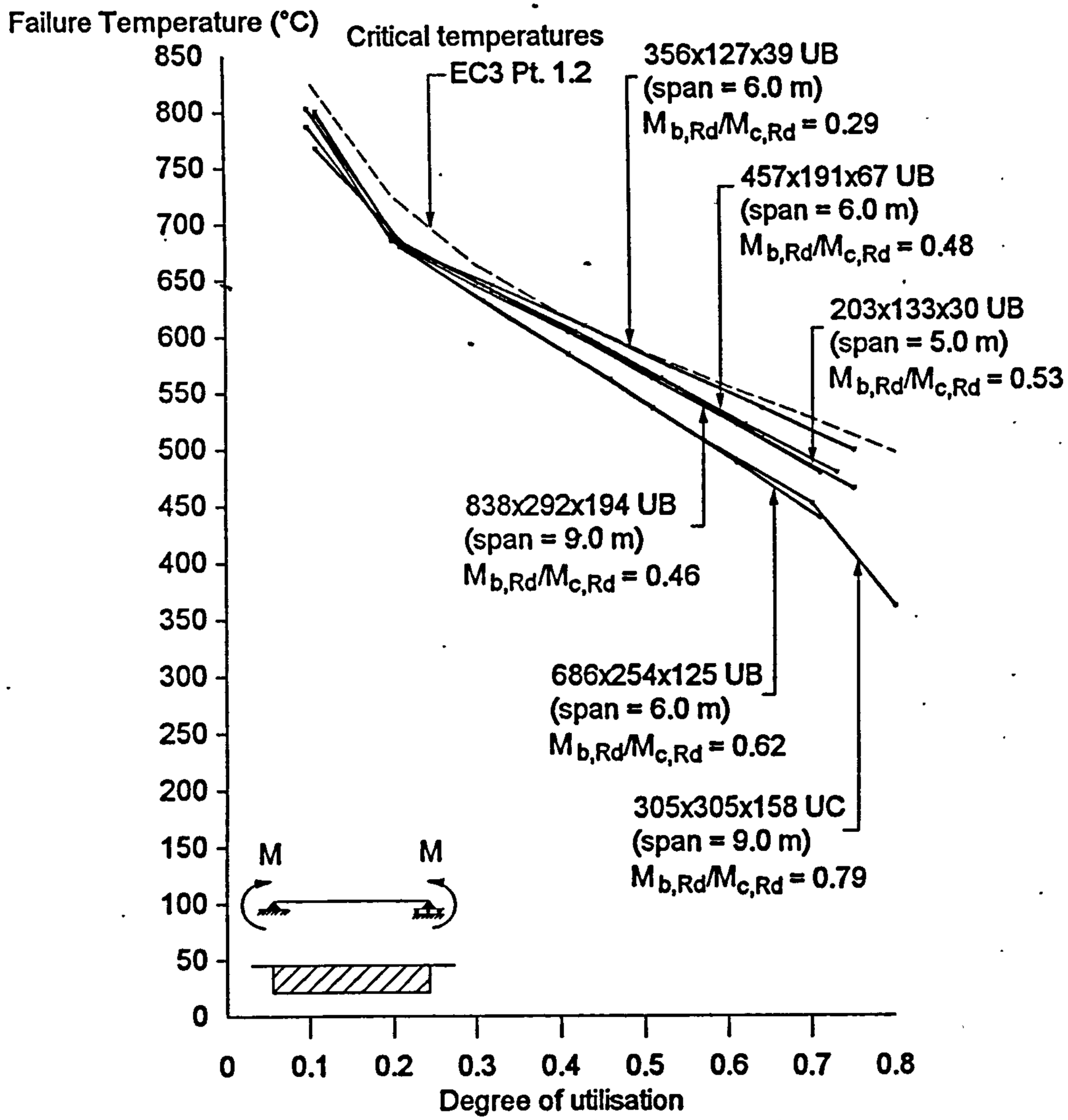

Fig. 5.13: Failure temperatures for unrestrained simply-supported beams with uniform moment; comparison with BS5950 Part 8 and EC3 Part 1.2

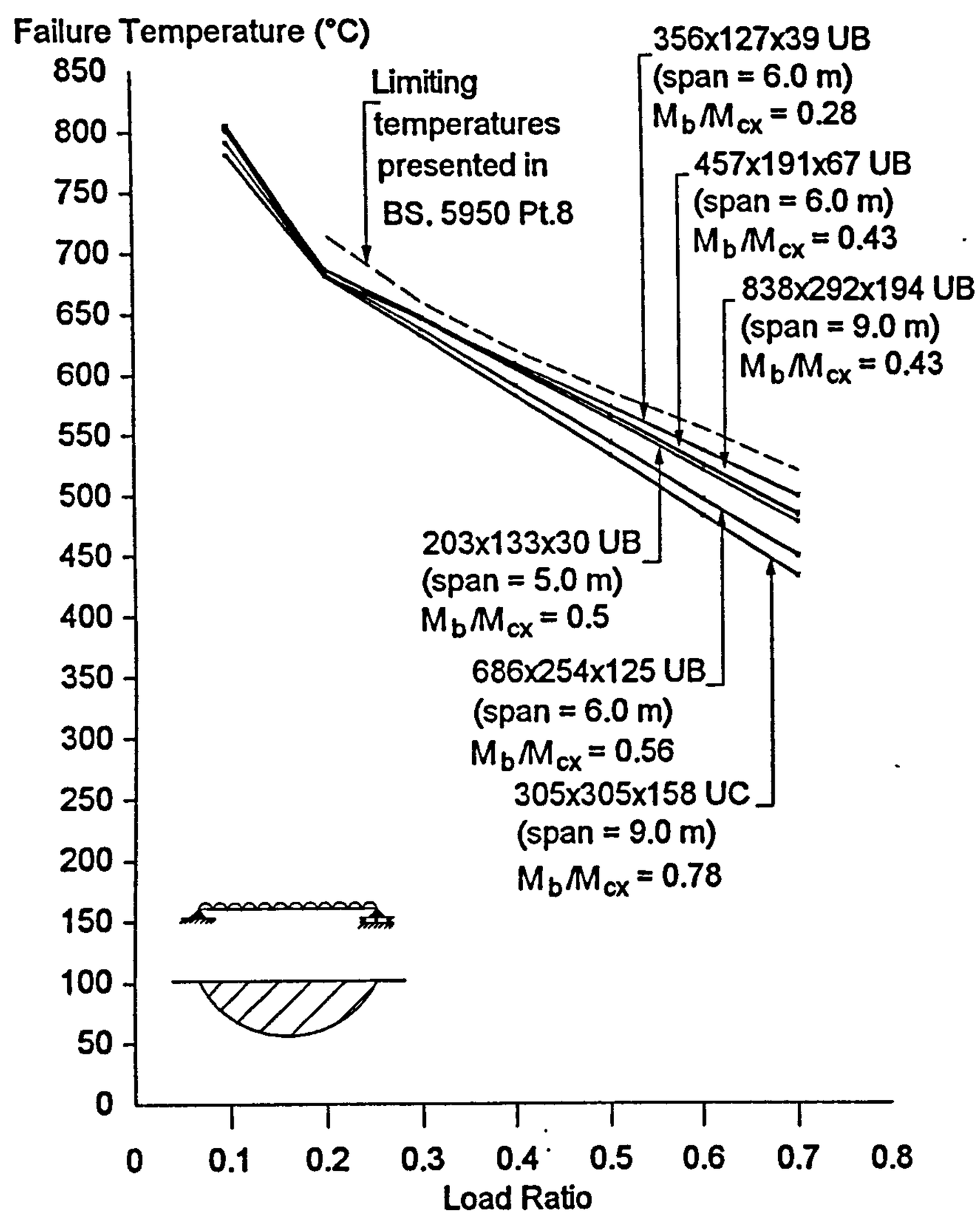

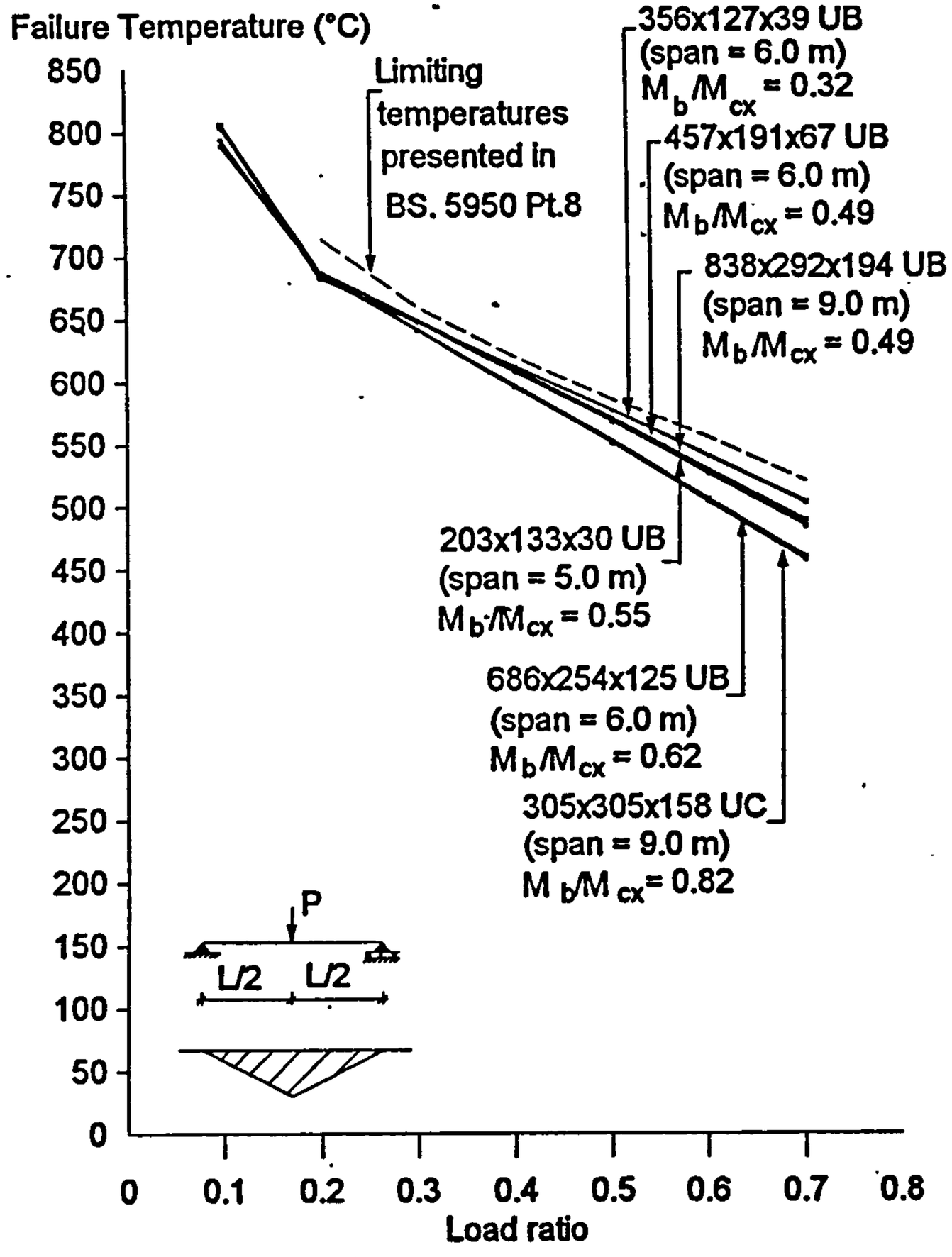

Fig. 5.14: Failure temperatures for unrestrained beams under the loading patterns shown

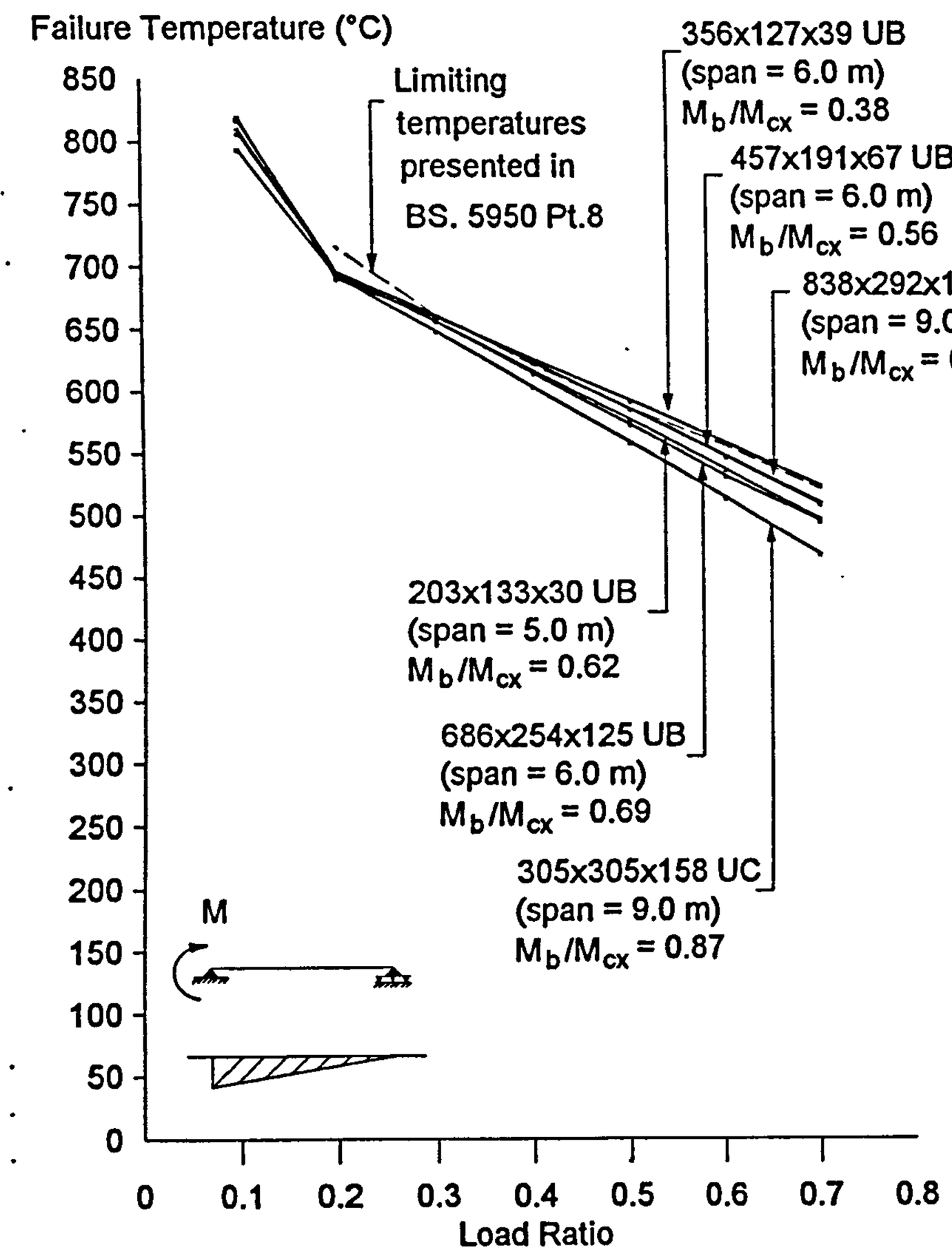

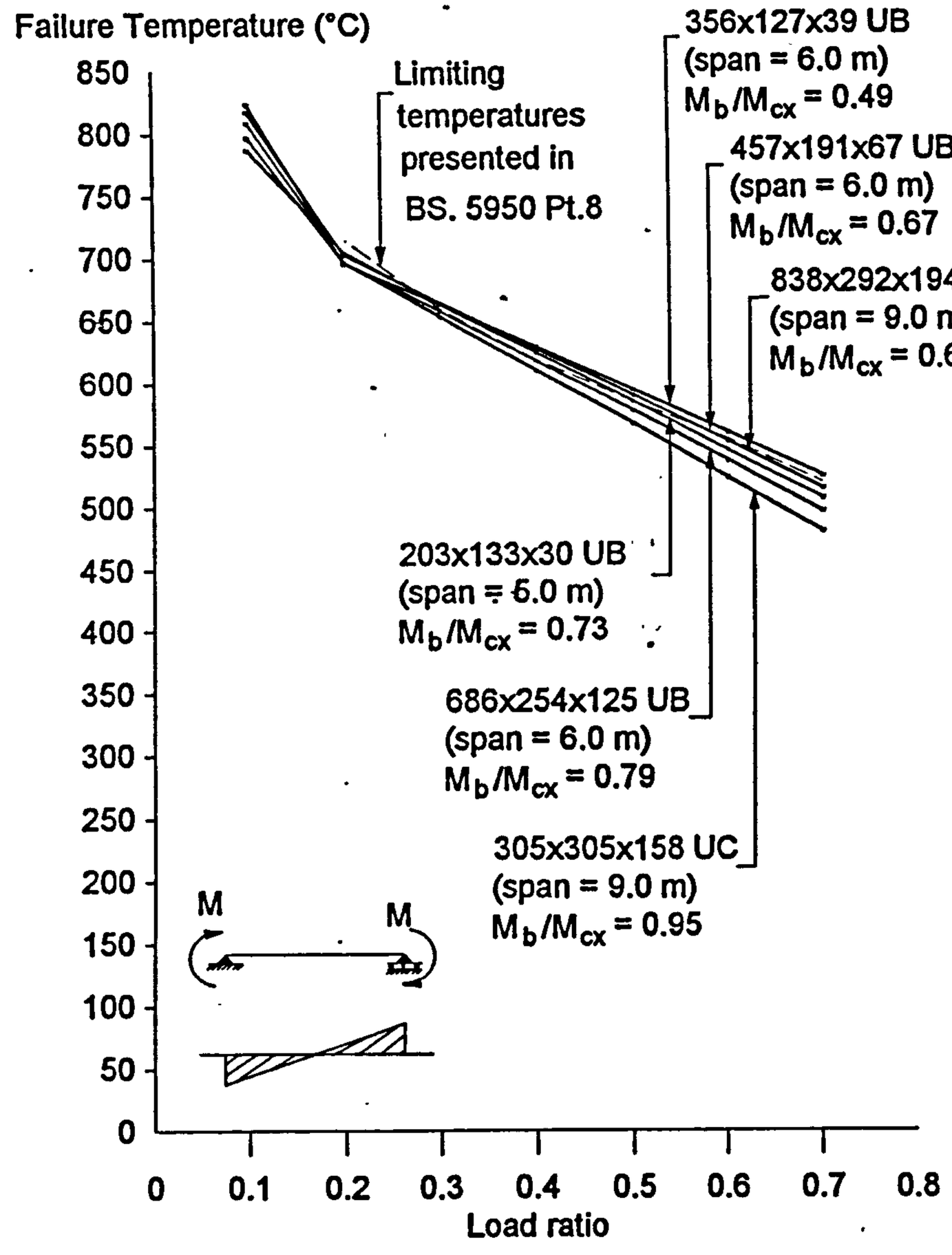

Fig. 5.14: (Continued) Failure temperatures for unrestrained beams under the loading patterns shown

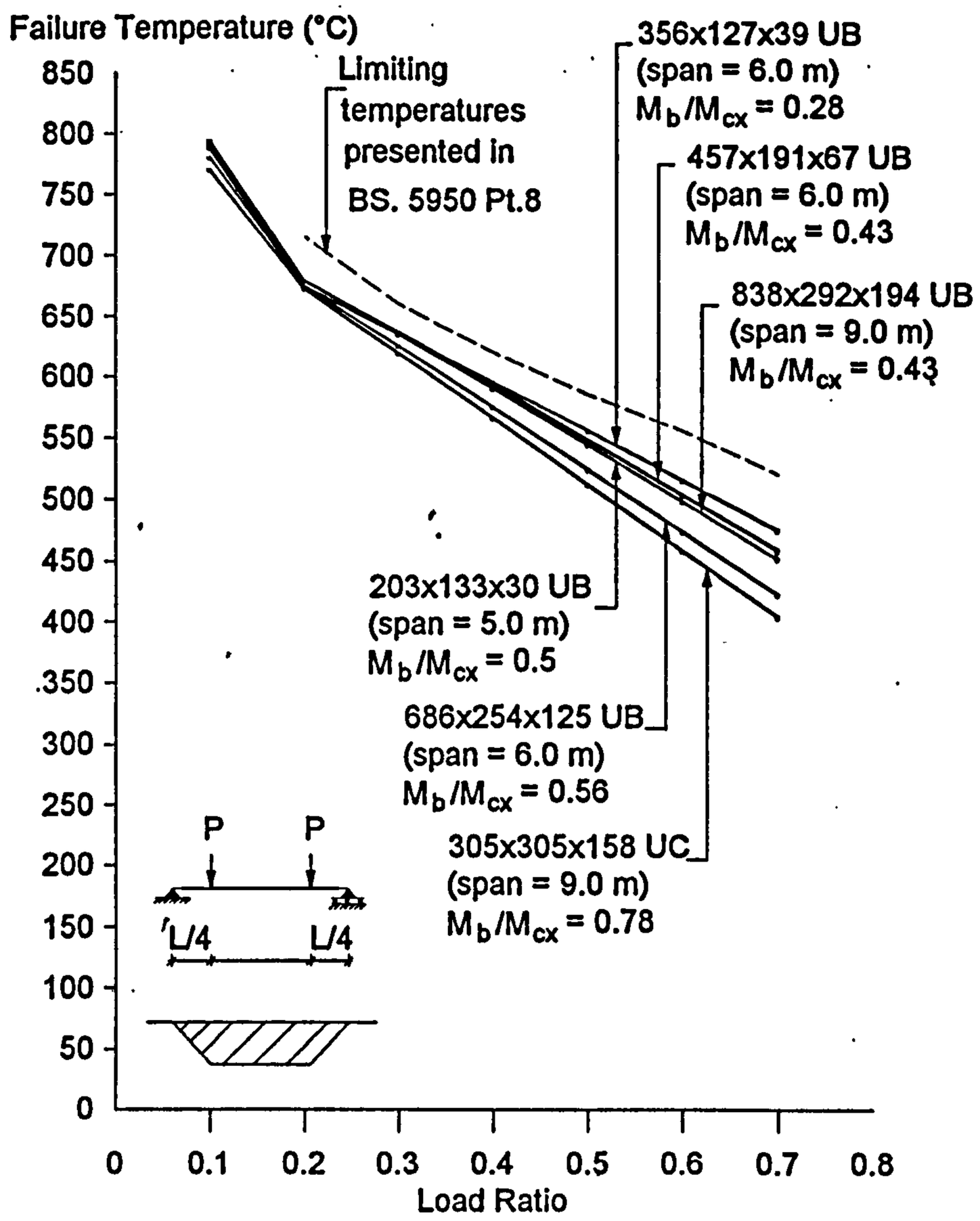

Fig. 5.14: (Continued) Failure temperatures for unrestrained beams under the loading pattern shown

In all the examples studied failure was due to lateral-torsional buckling. It would not be possible (or worthwhile) due to space limitations to produce lateral displacement:temperature relationships for each case. Instead only two examples are presented, both with point loads placed at quarter span (the most "unconservative" comparison with BS5950). The first is 356x127x39UB with a load ratio of 0.7, and it can clearly be seen from Fig. 5.15 that failure is due to lateral-torsional buckling. The second example is 305x305x158UC with a load ratio of 0.5, and once again Fig. 5.16 shows that failure is due to lateral-torsional buckling.

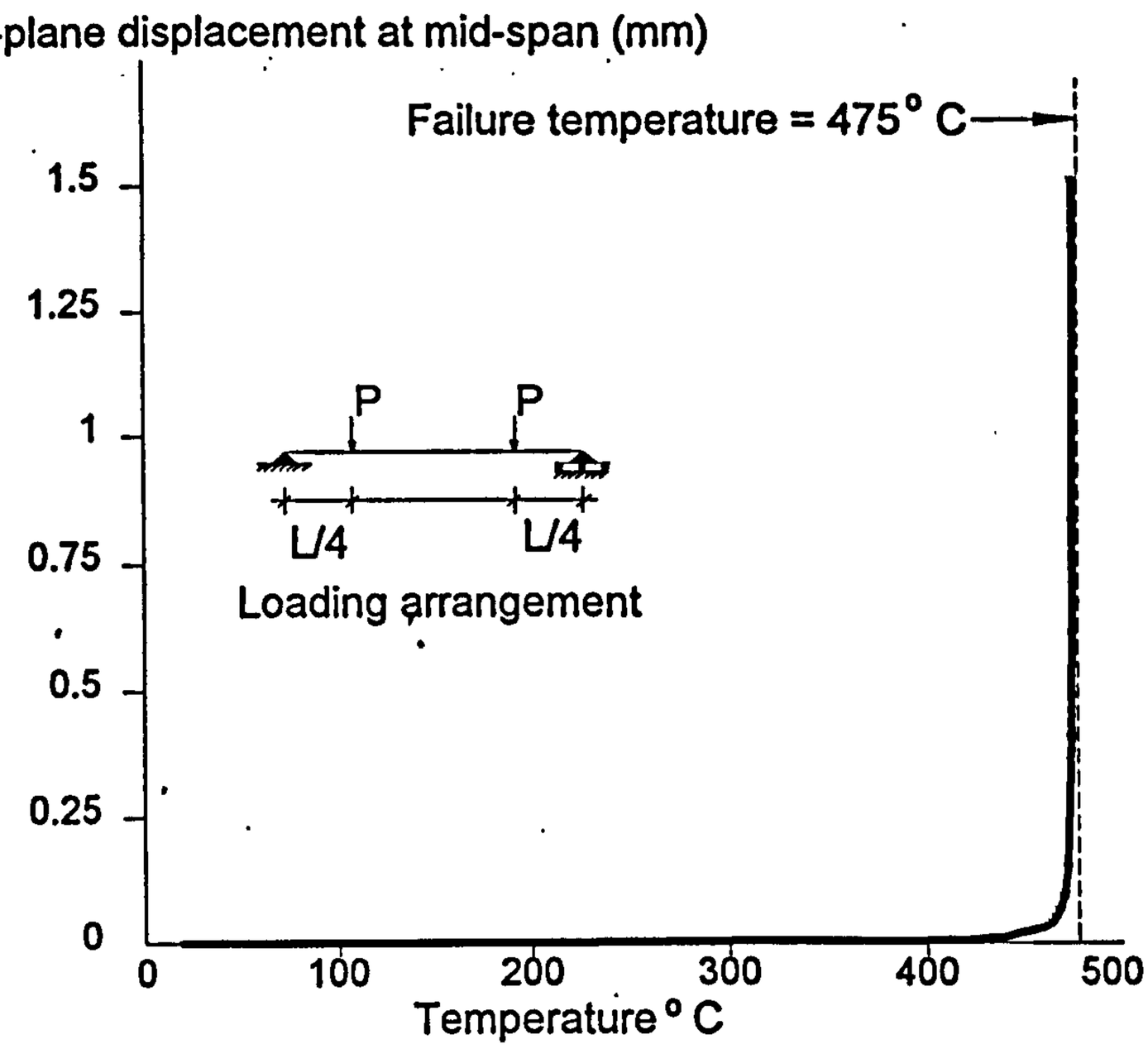

Fig. 5.15: Temperature - lateral displacement relationship for unrestrained 356x127x39UB with load ratio of 0.7 .

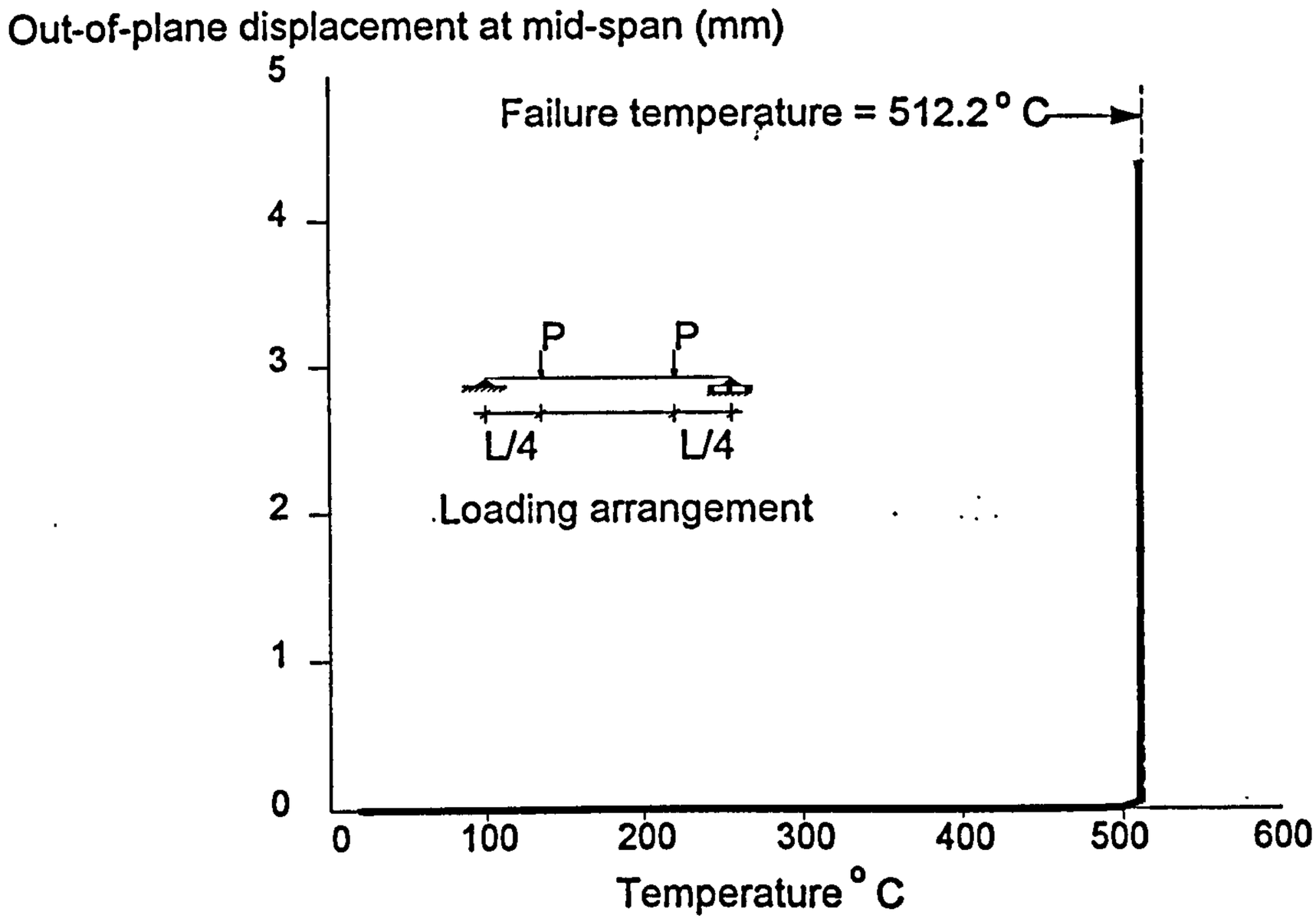

Fig. 5.16: Temperature - lateral displacement relationship for unrestrained 305x305x158UC with load ratio of 0.5.

5.23: UNRESTRAINED BEAMS WITH LOAD APPLIED ABOVE THE SHEAR CENTRE.

The destabilising effect of placing the load on the top flange was considered for the case of a point load at mid-span and an uniformly distributed load. The same six beams were analysed, but with different spans. Once again the 457x191x67UB and 838x292x194UB spans were chosen to give exactly the same value of M_b/M_{cx} to allow a comparison to be made.

As can be seen from the results shown in Fig. 5.17, the failure temperatures are higher compared to the predicted results with the load placed at the shear centre. This is due to the very conservative nature of the BS5950 Part 1[49] design calculation for the ambient-temperature buckling resistance moment under destabilising load. The method uses a slenderness correction factor of 1.0, irrespective of the moment pattern, and also a 'blanket allowance' of an assumed effective length equal to 1.2 times the actual span. Load ratios are therefore artificially increased in these cases. EC3 Part 1.1[71] adopts a more analytical approach to the calculation of ambient-temperature load capacities under destabilising load, in which the height of the load application point is specifically used, and this again produces higher buckling capacities compared to BS5950 Part 1. Considering uniformly distributed load placed on the top flange for the beams used in this study EC3 Part 1.1 increases the lateral-torsional buckling capacity generally by about 20%, except for the Universal Column section for which the increase is only 9%, although this increase is reduced by the use of the "empirical correction factor" of 1.2 in fire design.

5.24: GENERAL OBSERVATIONS OF THE BEHAVIOUR OF UNRESTRAINED BEAMS AT ELEVATED TEMPERATURES.

Taking an overview of the results shown in Figs. 5.13, 5.14 and 5.17 it can be seen that, at least for the higher range of load ratios, the failure temperatures for unrestrained beams with any consistent loading pattern vary with the value of M_b/M_{cx} (or $M_{b,Rd}/M_{c,Rd}$ in the notation of EC3), with instability occurring at progressively lower temperatures as this increases. It may be argued that this is because inelastic buckling loads in general are controlled by tangent modulus values on the local stress-strain curves of the members affected, just prior to instability occurring. The stress-strain curves of steel at elevated temperatures are continuously curvilinear, tending towards zero slope at ultimate stress levels which degrade with rise in

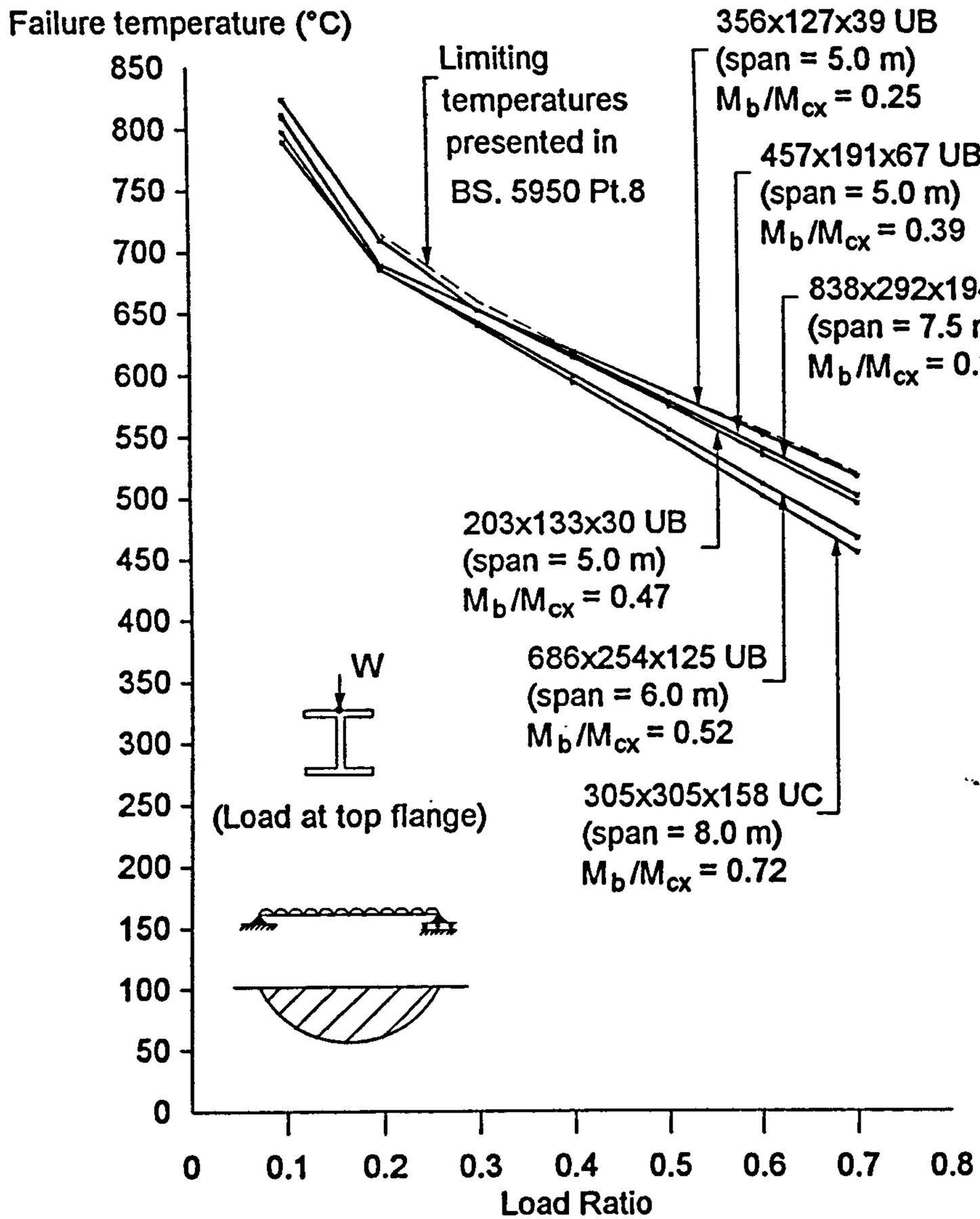

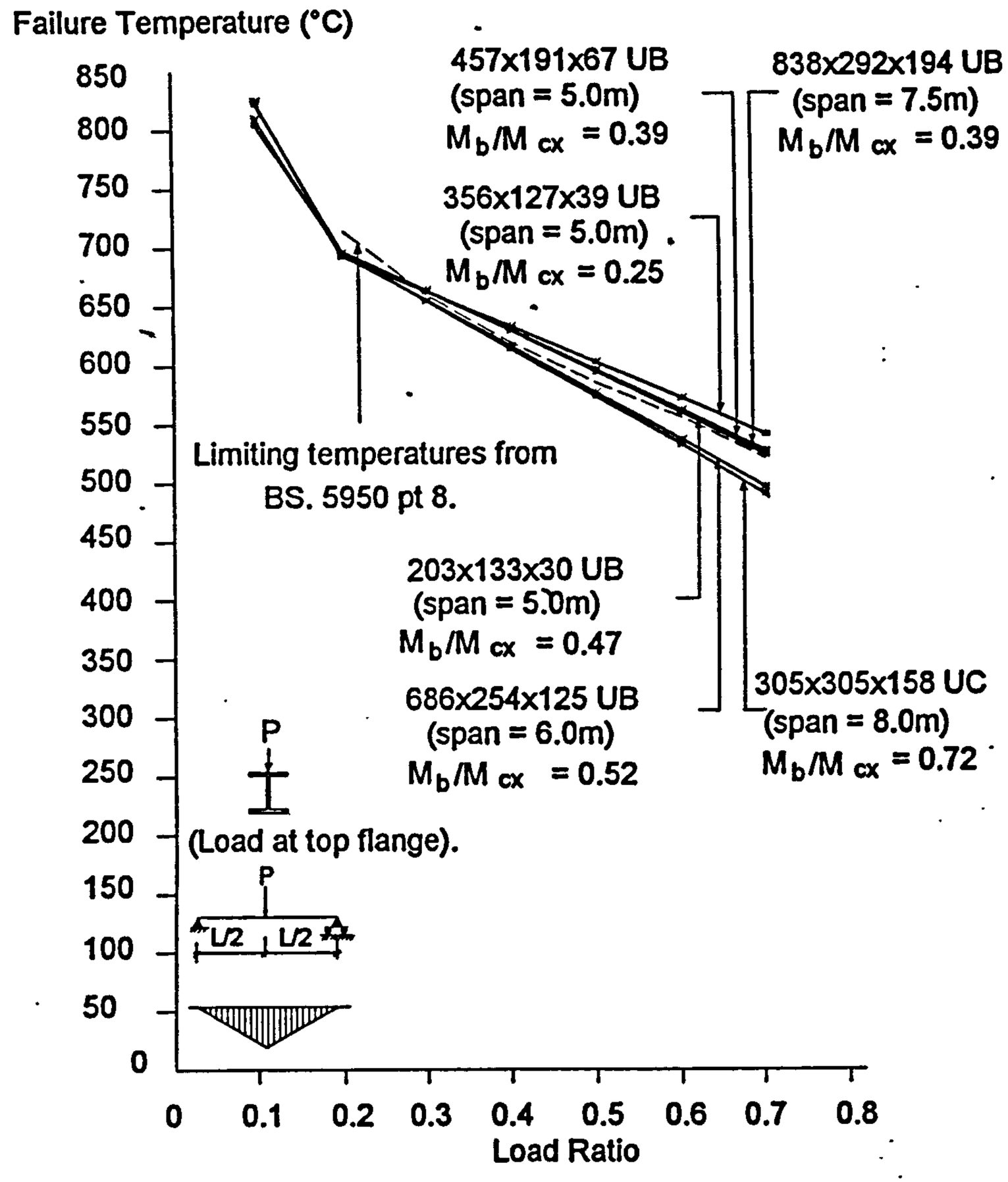

Fig 5.17: Failure temperatures for unrestrained simply-supported beams loaded at the top flange (destabilising position) with the loading patterns shown.

temperature. At any given load ratio a beam with a higher value of M_b/M_{cx} will be more highly stressed than one with a lower value. Its compression flange is therefore subject to a lower tangent modulus in resisting any infinitesimal disturbance and as the temperature rises this tangent modulus rapidly declines. This is shown schematically in Fig. 5.18.

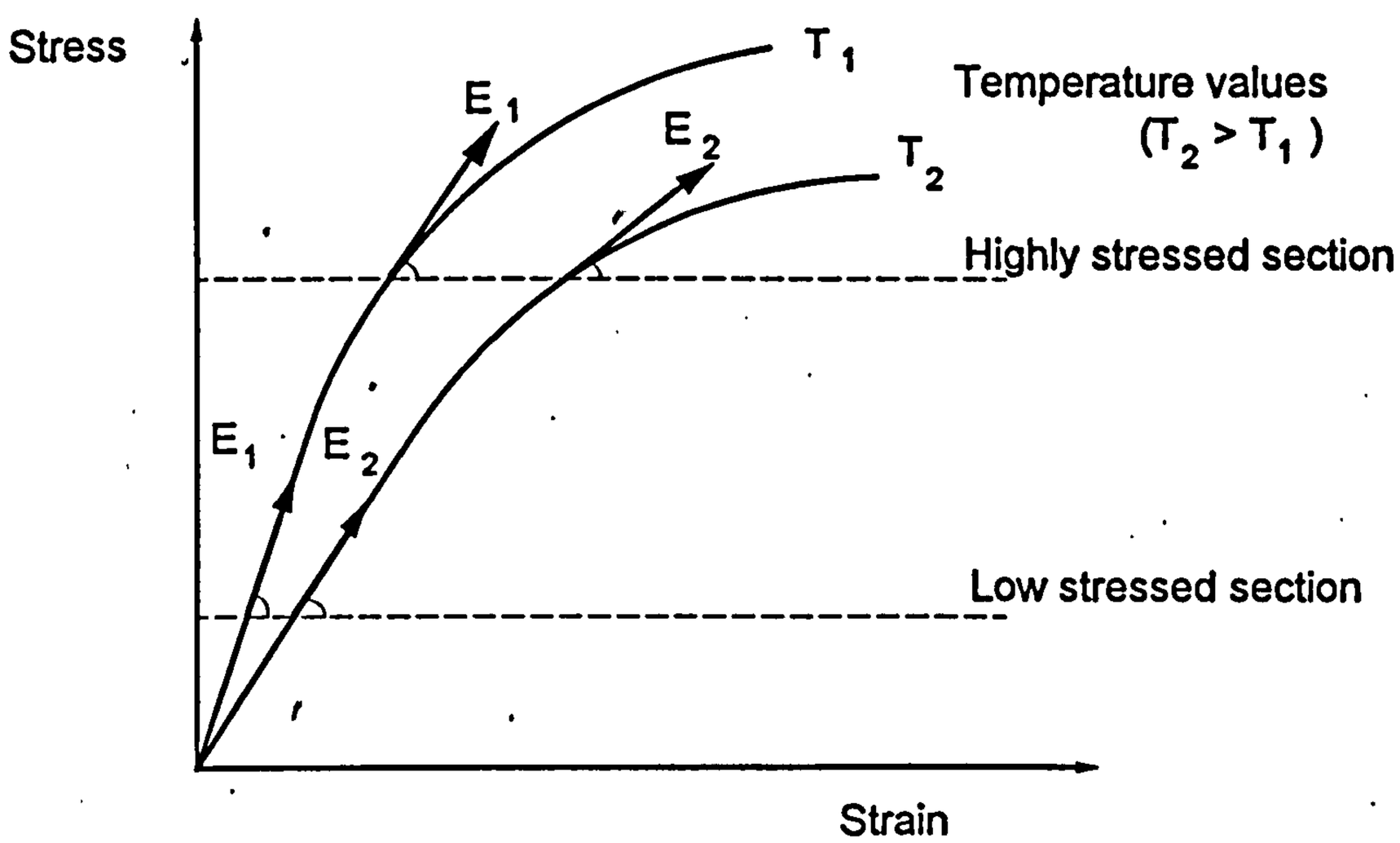

Fig. 5.18: Illustration of the different rates of degradation of tangent modulus with temperature for members at high and low load levels.

As load ratios decrease the failure temperatures of all beams can be seen to converge to a single value depending only on the load ratio. Failure for these cases is essentially by elastic buckling, which takes place when the increase in temperature has reduced the initial (Young's) modulus to a proportion of its original value approximately equal to the load ratio.

An effort was made to rationalise the results presented for lateral-torsional buckling similar to the representation at ambient temperature, which uses an empirically based design curve[49,73], defined by a modified form of the Perry equation. This curve allows the lateral-torsional buckling strength (P_b) to be obtained based on the slenderness value (λ_{LT}) of the beam. The slenderness value considers a beam's geometrical properties, support conditions and (if the *n*-factor method is adopted[49,73]) the arrangement of the applied load. The basic design curve assumes uniform moment between lateral restraints. If a moment gradient is applied to the beam the tendency toward instability would be less severe compared to uniform moment, with the beam being able to withstand a larger peak moment before becoming laterally unstable. To utilise the beneficial effect of moment gradient when using the design curve two

alternative methods are presented. The first, known as the *n*-factor method[49,73], involves modifying the slenderness value by a factor *n*, which produces a value of P_b which reflects the enhanced strength of the beam due to non-uniform moment. The second approach, known as the *m*-factor method[49,73], consists of adjusting the design moment by multiplying the applied maximum moment by a factor *m* (where $m<1$ for a non-uniform moment). By using appropriate values of *n* and *m* both methods will produce the same results. However BS5950 Part 1 restricts the use of the *m*-factor method to beams loaded at points of lateral restraint only.

Considering unrestrained beams at elevated temperatures an effort was made to represent the behaviour for any given load ratio, independent of the loading pattern, based on failure temperature and slenderness of the beam (analogous to the design curve at ambient temperature). However this was not possible due to the different rates of degradation of stiffness for different loading arrangements. For example, considering a beam under uniform moment the stress distribution through the cross-section is the same along the length of the beam, and so the reduction of stiffness due to the rise in temperature is constant along its length. However in the case of a moment gradient the rate of reduction of stiffness in the more highly stressed zones of the beam will be greater than in the zones of low stress, as shown in Fig. 5.18. This can be seen by comparing the case of uniformly distributed load with that of two point loads placed at the quarter points of the span (see Fig. 5.14). Both these loading arrangements produce an *n*-factor of 0.94 and thus have similar buckling capacities at ambient temperature. However the two point loads produce peak moment over the greater length of beam compared to a uniformly distributed load. Since the degradation of stiffness is greater in the zones of higher stress, the beam with the point loads fails at lower temperature. This additional variable of the rate of reduction in stiffness along the beam for different loading conditions will destroy the relationship between failure temperature and slenderness. Therefore, unfortunately, there seems no obvious method of rationalising the results presented for lateral-torsional buckling of beams at elevated temperatures.

6.0: MODELLING FLOOR SLABS USING FLAT SHELL ELEMENTS.

A typical method of forming a flat shell element is to superimpose a plate bending stiffness and a plane stress membrane stiffness, as shown in Fig. 6.01.

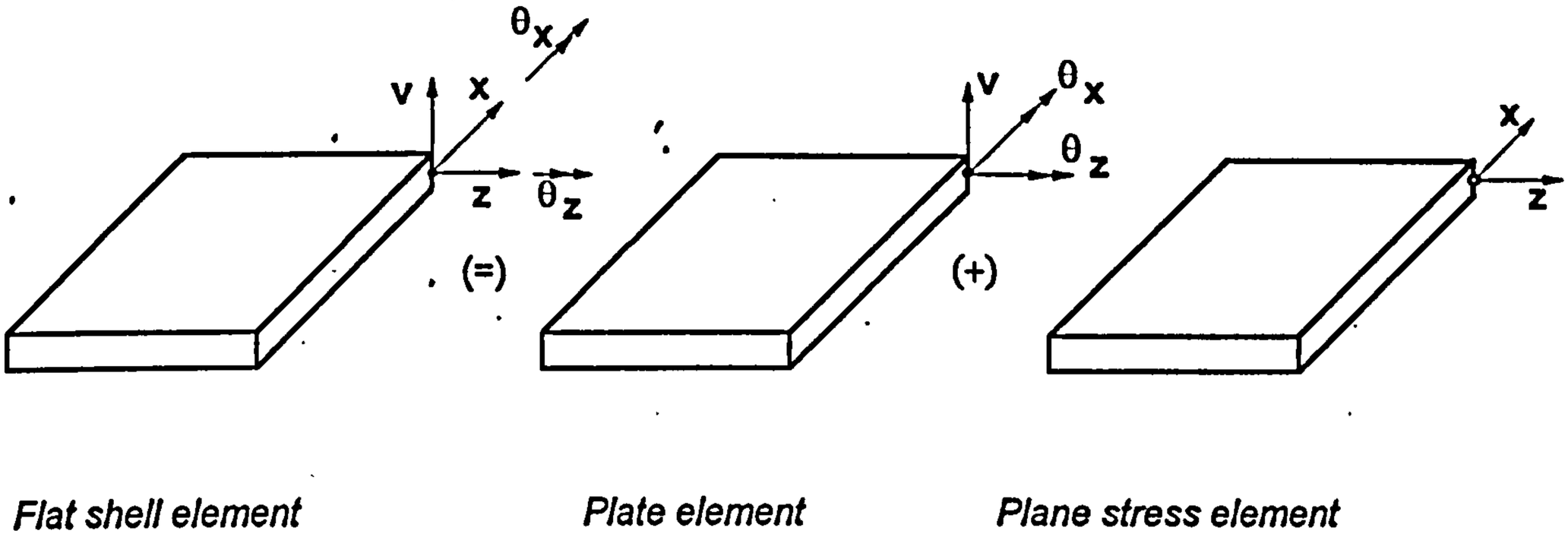

Fig. 6.01: Flat shell element.

6.01 PLATE ELEMENT FORMULATION.

With the plate element formulation the following assumptions are made[41],

1. The stress normal to the surface of the plate is zero.
2. As the plate deforms, material particles which were originally on a straight line normal to the mid-surface of the plate remain on a straight line. In the Kirchhoff (thin plate) theory, shear deformations are neglected and straight lines originally perpendicular to the mid-surface remain perpendicular during deformation. In the Mindlin/Reissner (thick plate) theory, shear deformations are included and therefore lines originally normal to the mid-surface will in general, not remain perpendicular to the mid-surface during deformation.

In the Kirchhoff theory[41,43] the state of plate deformation is represented by a single quantity (v), corresponding to the lateral displacement of the middle plane of the plate. Therefore the generalised strains are represented by the second derivatives of this lateral displacement. To ensure finite values for the strains, the lateral displacement and the slope (first derivative of v) must be continuous between element boundaries. This continuity requirement is known as C_1 continuity[43], and causes mathematical and computational difficulties in defining shape functions to fulfil this criterion for plate elements.

The Mindlin/Reissner theory[41,43] uses different variables to define the lateral displacement and slope, each with independent shape functions. Therefore the generalised strains are represented by the first derivatives of the slope, which means that the slope and lateral displacement must be continuous at the element boundaries. This continuity criterion is referred to as C_0 continuity[43] and is easier to implement than C_1 continuity. However the Mindlin theory can only be used for thin plates if higher-order elements (elements with 9 or 16 nodes) are used. If lower-order elements (elements with 4 nodes) are adopted to model thin plates then the elements become artificially stiff, a phenomenon commonly referred to as shell-locking[41,43]. Various methods have been developed to overcome this problem, consisting of the use of selective or reduced integration, or the use of discrete Kirchhoff theory[74].

However recent research[75] has shown that these approaches can be integrated into a more general formulation which approximates the shear and bending deformations independently (a method known as mixed interpolation). It was therefore decided to adopt the Mindlin/Reissner theory with mixed interpolation so that,

1. any form (i.e. thick and thin) of shell/plate can be modelled.
2. lower-order elements (mainly 4-noded) can be used when modelling thin shells.
3. the formulation can be extended to geometrical and material non-linearities[84].

The basic isoparametric[41] finite element formulation was followed with a relationship existing between displacements at any point within the element and the element nodal displacements, by the use of interpolation (shape) functions[41,42]. These interpolations express the element coordinates and displacements in the form of the natural coordinate system of the element, which has variables r,s and t that each vary from -1 to +1, as shown in Fig. 6.02.

If we consider the general three-dimensional element the coordinate interpolations are,

$$x = \sum_{i=1}^{q} h_i x_i \qquad y = \sum_{i=1}^{q} h_i y_i \qquad z = \sum_{i=1}^{q} h_i z_i \tag{6.01}$$

where,

x, y, z are local the coordinates any point within the element,

$x_i, y_i, z_i \quad (i = 1,2,3,.....,q)$ are the coordinates of the element nodes,

$h_i \quad (i = 1,2,3,.....,q)$ are the shape functions defined in the natural coordinate system[41].

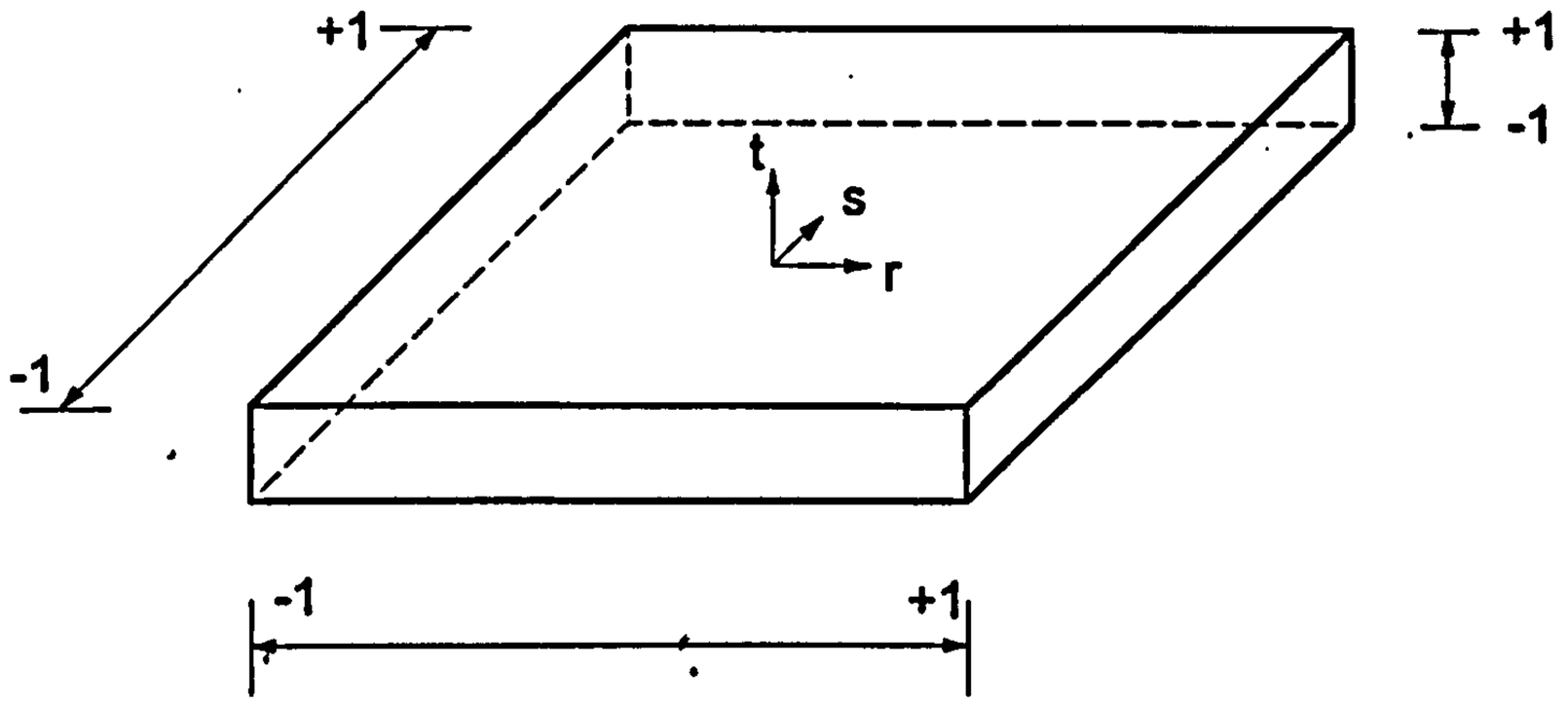

Fig. 6.02: Natural coordinate system of the element.

The element displacements are interpolated in the same way, and are given by,

$$u = \sum_{i=1}^{q} h_i u_i \qquad v = \sum_{i=1}^{q} h_i v_i \qquad w = \sum_{i=1}^{q} h_i w_i \tag{6.02}$$

where,

u,v,w are local element displacements at any point within the element,

$u_i,v_i,w_i \quad (i = 1,2,3,.....,q)$ are the element nodal displacements.

In the formulation of the element stiffness matrix the element strains are required, which are obtained in terms of the derivatives of element displacements with respect to the local coordinates. Since the element displacements are defined in the natural coordinate system, the x,y and z derivatives need to be related to the r,s and t derivatives. Therefore let,

$$x = f_1(r,s,t) \qquad y = f_2(r,s,t) \qquad z = f_3(r,s,t) \tag{6.03}$$

where f_i denotes 'function of'. Also let,

$$r = f_4(x,y,z) \qquad s = f_5(x,y,z) \qquad t = f_6(x,y,z) \tag{6.04}$$

To obtain the derivatives $\partial/\partial x, \partial/\partial y$ and $\partial/\partial z$ the chain rule is used.

$$\frac{\partial}{\partial x} = \frac{\partial}{\partial r}\frac{\partial r}{\partial x} + \frac{\partial}{\partial s}\frac{\partial s}{\partial x} + \frac{\partial}{\partial t}\frac{\partial t}{\partial x} \tag{6.05}$$

with similar expressions for $\partial/\partial y$ and $\partial/\partial z$.

To obtain $\partial/\partial x$, the value $\partial r/\partial x$ is needed which requires the relationship defined in equation (6.04) to be evaluated. However these relationships are generally difficult to establish explicitly, and so the required derivatives are obtained in the following way.

Using the chain rule, the following relationship is formed,

$$\begin{Bmatrix} \frac{\partial}{\partial r} \\ \frac{\partial}{\partial s} \\ \frac{\partial}{\partial t} \end{Bmatrix} = \begin{bmatrix} \frac{\partial x}{\partial r} & \frac{\partial y}{\partial r} & \frac{\partial z}{\partial r} \\ \frac{\partial x}{\partial s} & \frac{\partial y}{\partial s} & \frac{\partial z}{\partial s} \\ \frac{\partial x}{\partial t} & \frac{\partial y}{\partial t} & \frac{\partial z}{\partial t} \end{bmatrix} \begin{Bmatrix} \frac{\partial}{\partial x} \\ \frac{\partial}{\partial y} \\ \frac{\partial}{\partial z} \end{Bmatrix} \tag{6.06}$$

which can be expressed in matrix form as,

$$\frac{\partial}{\partial r} = J\frac{\partial}{\partial x} \tag{6.07}$$

where J is the Jacobian operator, relating the natural coordinate derivatives to the local coordinate derivatives. Since $\partial/\partial x$ is required we obtain,

$$\frac{\partial}{\partial x} = J^{-1}\frac{\partial}{\partial r} \tag{6.08}$$

which requires that the inverse of J exists. This will be the case provided that there is a one-to-one correspondence between the natural and local coordinates of the element. Once the derivatives are obtained the strain-displacement transformation matrix '*B*' can be obtained which allows the strains at any point within the element to be calculated using,

$$\varepsilon = B\hat{u} \tag{6.09}$$

where,

ε = strain vector,

B = strain-displacement matrix,

$\hat{u}$ = vector of displacements at nodal positions.

It should be noted that the formulation presented so far has been for a general three-dimensional element, and will be truncated for the following two-dimensional elements.

Considering a plate element shown in Fig. 6.03, and following the sign convention of the existing model, the displacement components of a point of coordinates x,y,z (assuming small-displacement bending theory) are,

$$u = -y\beta_z(x,y) \qquad w = -y\beta_x(x,y) \qquad v = v(x,y) \tag{6.10}$$

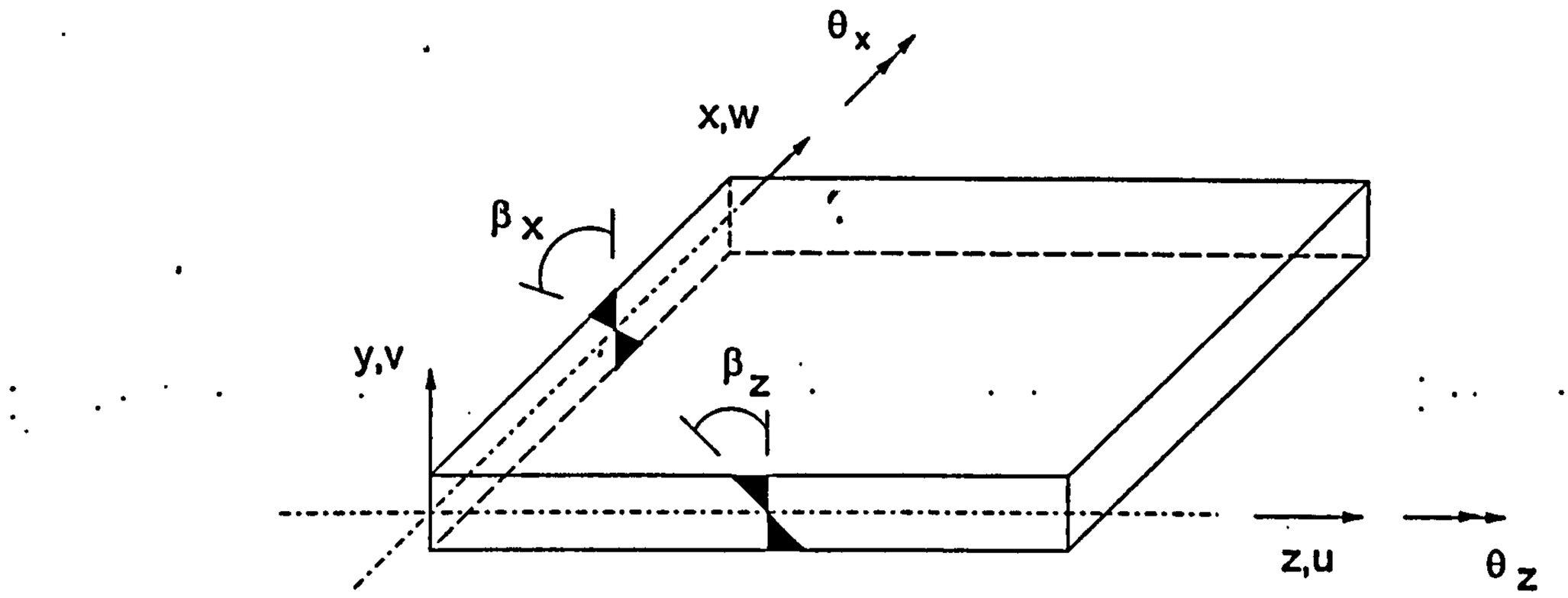

Fig. 6.03: Plate element

The bending strains $\varepsilon_{zz}, \varepsilon_{xx}, \gamma_{zx}$ vary linearly through the plate thickness and are given by the curvatures of the plate, as shown.

$$\begin{Bmatrix} \varepsilon_{zz} \\ \varepsilon_{xx} \\ \gamma_{zx} \end{Bmatrix} = y \begin{Bmatrix} -\dfrac{\partial \beta_z}{\partial z} \\ -\dfrac{\partial \beta_x}{\partial x} \\ -\dfrac{\partial \beta_z}{\partial x} - \dfrac{\partial \beta_x}{\partial z} \end{Bmatrix} \tag{6.11}$$

The transverse shear strains are assumed to be constant through the thickness and are given by,

$$\begin{bmatrix} \gamma_{zy} \\ \gamma_{xy} \end{bmatrix} = \begin{Bmatrix} \dfrac{\partial v}{\partial z} - \beta_z \\ \dfrac{\partial v}{\partial x} - \beta_x \end{Bmatrix} \tag{6.12}$$

Considering an isotropic material, the stress can be obtained from,

$$\begin{Bmatrix}\tau_{zz}\\ \tau_{xx}\\ \tau_{zx}\end{Bmatrix} = y\frac{E}{1-\nu^2}\begin{bmatrix}1 & \nu & 0\\ \nu & 1 & 0\\ 0 & 0 & \frac{1-\nu}{2}\end{bmatrix}\begin{Bmatrix}-\frac{\partial\beta_z}{\partial z}\\ -\frac{\partial\beta_x}{\partial x}\\ -\frac{\partial\beta_z}{\partial z}-\frac{\partial\beta_x}{\partial x}\end{Bmatrix} \tag{6.13}$$

and,

$$\begin{Bmatrix}\tau_{zy}\\ \tau_{xy}\end{Bmatrix} = \frac{E}{2(1+\nu)}\begin{Bmatrix}\frac{\partial v}{\partial z}-\beta_z\\ \frac{\partial v}{\partial x}-\beta_x\end{Bmatrix} \tag{6.14}$$

The expression for the total potential energy (Π), of the plate element is given by,

$$\Pi = \frac{1}{2}\int_A\int_{-h/2}^{h/2}\{\varepsilon_{zz} \quad \varepsilon_{xx} \quad \gamma_{zx}\}\begin{Bmatrix}\tau_{zz}\\ \tau_{xx}\\ \tau_{zx}\end{Bmatrix}dy\,dA + \frac{k}{2}\int_A\int_{-h/2}^{h/2}\{\gamma_{zy} \quad \gamma_{xy}\}\begin{Bmatrix}\tau_{zy}\\ \tau_{xy}\end{Bmatrix}dy\,dA - \int_A wp\,dA \tag{6.15}$$

where, p is equal to the transverse loading per unit area and k is a constant representing the non-uniformity of the shearing stress[72], which is generally set to 5/6.

Substituting equations (6.11) to (6.14) into (6.15) and integrating over the thickness 'y' produces,

$$\Pi = \frac{1}{2}\int_A \kappa^T C_b \kappa\,dA + \frac{1}{2}\int_A \gamma^T C_s \gamma\,dA - \int_A wp\,dA \tag{6.16}$$

where,

$$\kappa = \begin{Bmatrix}-\frac{\partial\beta_z}{\partial z}\\ -\frac{\partial\beta_x}{\partial x}\\ -\frac{\partial\beta_z}{\partial z}-\frac{\partial\beta_x}{\partial x}\end{Bmatrix} \qquad \gamma = \begin{Bmatrix}\frac{\partial v}{\partial z}-\beta_z\\ \frac{\partial v}{\partial x}-\beta_x\end{Bmatrix}$$

$$C_b = \frac{Eh^3}{12(1-\nu^2)}\begin{bmatrix}1 & \nu & 0\\ \nu & 1 & 0\\ 0 & 0 & \frac{1-\nu}{2}\end{bmatrix} \qquad C_s = \frac{Ehk}{2(1+\nu)}\begin{bmatrix}1 & 0\\ 0 & 1\end{bmatrix}$$

Since the normal stress in the plate has been integrated, C_b is the generalised stress-strain matrix relating moments per unit length to bending strains:

$$\begin{Bmatrix} M_{zz} \\ M_{xx} \\ M_{zx} \end{Bmatrix} = C_b \begin{Bmatrix} -\dfrac{\partial \beta_z}{\partial z} \\ -\dfrac{\partial \beta_x}{\partial x} \\ -\dfrac{\partial \beta_z}{\partial z} - \dfrac{\partial \beta_x}{\partial x} \end{Bmatrix}$$

Similarly C_s is the generalised stress-strain matrix relating shear force per unit length to shear strains, i.e.,

$$\begin{Bmatrix} V_{zy} \\ V_{xy} \end{Bmatrix} = C_s \begin{Bmatrix} \gamma_{zy} \\ \gamma_{xy} \end{Bmatrix}$$

For equilibrium, $\delta\Pi=0$; and since C is symmetrical, we obtain from equation (6.16),

$$\int_A \delta\kappa^T C_b \kappa dA + \int_A \delta\gamma^T C_s \gamma \, dA - \int_A \delta w p \, dA = 0 \qquad (6.17)$$

which is the Principle of Virtual Displacements for a plate element based on the Mindlin/Reissner theory[41], with the first two terms representing internal work due to virtual strains (that correspond to the imposed virtual displacements) and the last term representing external work, due to external forces subject to virtual displacements.

In finite element analysis we use[41,42,43],

$$v = \sum_{I=1}^{q} h_I v_I \qquad \beta_z = \sum_{I=1}^{q} h_I \theta_x{}^I \qquad \beta_x = \sum_{I=1}^{q} h_I \theta_z{}^I$$
$$z = \sum_{I=1}^{q} h_I z_I \qquad x = \sum_{I=1}^{q} h_I x_I \qquad (6.18)$$

and adopt the following notation,

$$\kappa(r,s) = B_\kappa \hat{u} \qquad \gamma(r,s) = B_\gamma \hat{u} \qquad v(r,s) = H_w \hat{u} \qquad (6.19)$$

where B_κ and B_γ are generalised strain-displacement matrices, H_w is a matrix of the shape functions and $\hat{u}$ is a matrix of nodal displacements.

Substituting the notation of (6.19) into equation (6.17) and letting the imposed virtual nodal displacements be $\bar{\hat{u}}$ gives,

$$\bar{\hat{u}}^T\left[\int_A B_\kappa^T C_b B_\kappa \, dA + \int_A B_\gamma^T C_s B_\gamma^T \, dA\right]\hat{u} = \bar{\hat{u}}^T \int_A H_w^T p \, dA \qquad (6.20)$$

To solve equation (6.20) for unknown nodal displacements the virtual displacement method of applying a unit virtual displacement in turn at all displacement components is used. Therefore,

$\bar{\hat{u}} = identity\ matrix$

which allows equation (6.20) to be expressed as,

$$K\hat{u} = R \qquad (6.21)$$

where,

$$K = \int_A \left(B_\kappa^T C_b B_\kappa + B_\gamma^T C_s B_\gamma\right) dA \qquad (6.22)$$

and,

$$R = \int_A H_w^T p \, dA \qquad (6.23)$$

Equations (6.22) and (6.23) have to be converted to natural coordinates (r and s), which requires the area differential to be expressed as,

$$dA = \det \mathbf{J} \, dr \, ds \qquad (6.24)$$

Where detJ is the determinant of the Jacobian operator. Therefore equations (6.22) and (6.23) are re-written as,

$$K = \det \mathbf{J} \int_{-1}^{+1} \int_{-1}^{+1} \left(B_\kappa{}^T C_b B_\kappa + B_\gamma{}^T C_s B_\gamma\right) dr \, ds \qquad (6.25)$$

and,

$$R = \det \mathbf{J} \int_{-1}^{+1} \int_{-1}^{+1} H_w^T p \, dr \, ds \qquad (6.26)$$

Since different shape functions are used for bending and shearing deformations, consider first the shape functions used for the bending deformations.

The shape functions are,

$$h_1 = \frac{1}{4}(1+r)(1+s) \qquad h_2 = \frac{1}{4}(1-r)(1+s)$$
$$h_3 = \frac{1}{4}(1-r)(1-s) \qquad h_4 = \frac{1}{4}(1+r)(1-s) \tag{6.27}$$

Therefore the coordinate interpolations are given by,

$$z = \frac{1}{4}(1+r)(1+s)z_1 + \frac{1}{4}(1-r)(1+s)z_2 + \frac{1}{4}(1-r)(1-s)z_3 + \frac{1}{4}(1+r)(1-s)z_4 \tag{6.28}$$

$$x = \frac{1}{4}(1+r)(1+s)x_1 + \frac{1}{4}(1-r)(1+s)x_2 + \frac{1}{4}(1-r)(1-s)x_3 + \frac{1}{4}(1+r)(1-s)x_4 \tag{6.29}$$

and the displacement interpolations are given by,

$$v = \frac{1}{4}(1+r)(1+s)v_1 + \frac{1}{4}(1-r)(1+s)v_2 + \frac{1}{4}(1-r)(1-s)v_3 + \frac{1}{4}(1+r)(1-s)v_4 \tag{6.30}$$

$$\beta_z = \frac{1}{4}(1+r)(1+s)\theta_x^1 + \frac{1}{4}(1-r)(1+s)\theta_x^2 + \frac{1}{4}(1-r)(1-s)\theta_x^3 + \frac{1}{4}(1+r)(1-s)\theta_x^4 \tag{6.31}$$

$$\beta_x = \frac{1}{4}(1+r)(1+s)\theta_y^1 + \frac{1}{4}(1-r)(1+s)\theta_y^2 + \frac{1}{4}(1-r)(1-s)\theta_y^3 + \frac{1}{4}(1+r)(1-s)\theta_y^4 \tag{6.32}$$

To evaluate the displacement derivatives we need to calculate,

$$\begin{Bmatrix} \frac{\partial}{\partial r} \\ \frac{\partial}{\partial s} \end{Bmatrix} = \begin{bmatrix} \frac{\partial z}{\partial r} & \frac{\partial x}{\partial r} \\ \frac{\partial z}{\partial s} & \frac{\partial x}{\partial s} \end{bmatrix} \begin{Bmatrix} \frac{\partial}{\partial z} \\ \frac{\partial}{\partial x} \end{Bmatrix} \tag{6.33}$$

which can be expressed as,

$$\frac{\partial}{\partial r} = \mathrm{J}\frac{\partial}{\partial z} \tag{6.34}$$

Now,

$$\frac{\partial z}{\partial r} = \frac{1}{4}(1+s)z_1 - \frac{1}{4}(1+s)z_2 - \frac{1}{4}(1-s)z_3 + \frac{1}{4}(1-s)z_4 \tag{6.35}$$

$$\frac{\partial z}{\partial s} = \frac{1}{4}(1+r)z_1 + \frac{1}{4}(1-r)z_2 - \frac{1}{4}(1-r)z_3 - \frac{1}{4}(1+r)z_4 \tag{6.36}$$

$$\frac{\partial x}{\partial r}=\frac{1}{4}(1+s)x_1-\frac{1}{4}(1+s)x_2-\frac{1}{4}(1-s)x_3+\frac{1}{4}(1-s)x_4 \tag{6.37}$$

$$\frac{\partial x}{\partial s}=\frac{1}{4}(1+r)x_1+\frac{1}{4}(1-r)x_2-\frac{1}{4}(1-r)x_3-\frac{1}{4}(1+r)x_4 \tag{6.38}$$

Therefore the Jacobian operator can be obtained at any value for r and s ($-1\leq r\leq +1$ and $-1\leq s\leq +1$), which allows the displacement derivatives to be evaluated at any value of r and ś using,

$$\begin{Bmatrix}\frac{\partial}{\partial z}\\ \frac{\partial}{\partial x}\end{Bmatrix}_{at\ r=r_i\ and\ s=s_j}=J_{ij}^{-1}\begin{Bmatrix}\frac{\partial}{\partial r}\\ \frac{\partial}{\partial s}\end{Bmatrix}_{at\ r=r_i\ and\ s=s_j} \tag{6.39}$$

Now,

$$\frac{\partial\beta_z}{\partial r}=\frac{1}{4}(1+s)\theta_x^1-\frac{1}{4}(1+s)\theta_x^2-\frac{1}{4}(1-s)\theta_x^3+\frac{1}{4}(1-s)\theta_x^4 \tag{6.40}$$

$$\frac{\partial\beta_z}{\partial s}=\frac{1}{4}(1+r)\theta_x^1+\frac{1}{4}(1-r)\theta_x^2-\frac{1}{4}(1-r)\theta_x^3-\frac{1}{4}(1+r)\theta_x^4 \tag{6.41}$$

$$\frac{\partial\beta_x}{\partial r}=\frac{1}{4}(1+s)\theta_y^1-\frac{1}{4}(1+s)\theta_y^2-\frac{1}{4}(1-s)\theta_y^3+\frac{1}{4}(1-s)\theta_y^4 \tag{6.42}$$

$$\frac{\partial\beta_x}{\partial s}=\frac{1}{4}(1+r)\theta_y^1+\frac{1}{4}(1-r)\theta_y^2-\frac{1}{4}(1-r)\theta_y^3-\frac{1}{4}(1+r)\theta_y^4 \tag{6.43}$$

Therefore the displacement derivatives are given by,

$$\begin{Bmatrix}-\frac{\partial\beta_z}{\partial z}\\ -\frac{\partial\beta_z}{\partial x}\end{Bmatrix}=\frac{1}{4}J^{-1}\begin{bmatrix}0 & 0 & -(1+s) & 0 & 0 & (1+s) & 0 & 0 & (1-s) & 0 & 0 & -(1-s)\\ 0 & 0 & -(1+r) & 0 & 0 & -(1-r) & 0 & 0 & -(1-r) & 0 & 0 & -(1+r)\end{bmatrix}\{\hat{u}\} \tag{6.44}$$

$$\begin{Bmatrix}-\frac{\partial\beta_x}{\partial z}\\ -\frac{\partial\beta_x}{\partial x}\end{Bmatrix}=\frac{1}{4}J^{-1}\begin{bmatrix}0 & -(1+s) & 0 & 0 & (1+s) & 0 & 0 & (1-s) & 0 & 0 & -(1-s) & 0\\ 0 & -(1+r) & 0 & 0 & -(1-r) & 0 & 0 & (1-r) & 0 & 0 & (1+r) & 0\end{bmatrix}\{\hat{u}\} \tag{6.45}$$

where,

$$\{\hat{u}\}=\begin{pmatrix}v_1 & \theta_z^1 & \theta_x^1 & v_2 & \theta_z^2 & \theta_x^2 & v_3 & \theta_z^3 & \theta_x^3 & v_4 & \theta_z^4 & \theta_x^4\end{pmatrix}^T$$

Therefore from equation (6.19) the generalised strain-displacement B_κ is given by

$$B_\kappa = \frac{1}{4}J^{-1}\begin{bmatrix} 0 & 0 & -(1+s) & 0 & 0 & (1+s) & 0 & 0 & (1-s) & 0 & 0 & -(1-s) \\ 0 & -(1+r) & 0 & 0 & -(1-r) & 0 & 0 & (1-r) & 0 & 0 & (1+r) & 0 \\ 0 & -(1+s) & -(1+r) & 0 & (1+s) & -(1-r) & 0 & (1-s) & -(1-r) & 0 & -(1-s) & -(1+r) \end{bmatrix}$$

(6.46)

To obtain the generalised stress-displacement matrix for shear strains, the derivation by Bathe and Dvorkin[75] was adopted.

Let the shear strains be expressed as,

$$\gamma_{zy} = \gamma_{ry}Sin\beta - \gamma_{sy}Sin\alpha$$
$$\gamma_{xy} = -\gamma_{ry}Cos\beta + \gamma_{sy}Cos\alpha \qquad (6.47)$$

where, α and β are the angles between the r and x-axes, and the s and x-axes respectively. In this formulation, it is assumed that the plate is not originally deformed, therefore,

$$\beta = 90^0 \qquad \alpha = 0^0$$

Using the derivation by Bathe and Dvorkin[75], the following expressions are used,

$$\gamma_{ry} = \frac{\sqrt{\left[(C_z + r\beta_z)^2 + (C_x + r\beta_x)^2\right]}}{8\det J}\left\{(1+s)\left[\frac{v_1 - v_2}{2} + \frac{z_1 - z_2}{4}\left(\theta_x^1 + \theta_x^2\right) - \frac{(x_1 - x_2)}{4}\left(\theta_z^1 + \theta_z^2\right)\right]\right.$$
$$\left.+(1-s)\left[\frac{v_4 - v_3}{2} + \frac{z_4 - z_3}{4}\left(\theta_z^4 + \theta_z^3\right) - \frac{(x_4 - x_3)}{4}\left(\theta_z^4 - \theta_z^3\right)\right]\right\} \qquad (6.48)$$

and,

$$\gamma_{sy} = \frac{\sqrt{\left[(A_z + s\beta_z)^2 + (A_x + s\beta_x)^2\right]}}{8\det J}\left\{(1+r)\left[\frac{v_1 - v_4}{2} + \frac{z_1 - z_4}{4}\left(\theta_x^1 + \theta_x^4\right) - \frac{x_1 - x_4}{4}\left(\theta_z^1 + \theta_z^4\right)\right]\right.$$
$$\left.+(1-r)\left[\frac{v_2 - v_3}{2} + \frac{z_1 - z_3}{4}\left(\theta_x^2 + \theta_x^3\right) - \frac{x_2 - x_3}{4}\left(\theta_z^2 + \theta_z^3\right)\right]\right\} \qquad (6.49)$$

where,

$A_z = z_1 - z_2 - z_3 + z_4$ $\qquad$ $A_x = x_1 - x_2 - x_3 + x_4$

$B_z = z_1 - z_2 + z_3 - z_4$ $\qquad$ $B_x = x_1 - x_2 + x_3 - x_4$

$C_z = z_1 + z_2 - z_3 - z_4$ $\qquad$ $C_x = x_1 + x_2 - x_3 - x_4$

where,

$z_i \quad (i = 1,.....,4)$ are the z-coordinates,

$x_i \quad (i = 1,.....,4)$ are the x-coordinates.

Now,

$\begin{Bmatrix} \gamma_{zy} \\ \gamma_{xy} \end{Bmatrix} = B_\gamma \hat{u}$ and using the notation, $B_\gamma = \begin{Bmatrix} B_{\gamma\, ry} \\ B_{\gamma\, sy} \end{Bmatrix}$

where,

$$B_{\gamma ry} = Tr_1 \left\langle \frac{1}{2}(1+s) \quad \frac{1}{4}(-x_1+x_2)(1+s) \quad \frac{1}{4}(z_1-z_2)(1+s) \quad -\frac{1}{2}(1+s) \right.$$
$$\frac{1}{4}(-x_1+x_2)(1+s) \quad \frac{1}{4}(z_1-z_2)(1+s) \quad -\frac{1}{2}(1-s) \quad \frac{1}{4}(x_4+x_3)(1-s)$$
$$\left. \frac{1}{4}(z_4-z_3)(1-s) \quad \frac{1}{2}(1-s) \quad \frac{1}{4}(-x_4+x_3)(1-s) \quad \frac{1}{4}(z_4-z_3)(1-s) \right\rangle \tag{6.50}$$

with,

$$Tr_1 = \frac{\sqrt{\left[(C_z + r\beta_z)^2 + (C_x + r\beta_x)^2\right]}}{8 \det J}$$

and,

$$B_{\gamma sr} = Tr_2 \left\langle \frac{1}{2}(1+r) \quad \frac{1}{4}(-x_1+x_4)(1+r) \quad \frac{1}{4}(z_1-z_4)(1+r) \quad \frac{1}{2}(1-r) \right.$$
$$\frac{1}{4}(-x_2+x_3)(1-r) \quad \frac{1}{4}(z_2-z_3)(1-r) \quad -\frac{1}{2}(1-r) \quad \frac{1}{4}(-x_2+x_3)(1-r)$$
$$\left. \frac{1}{4}(z_2-z_3)(1-r) \quad -\frac{1}{2}(1+r) \quad \frac{1}{4}(-x_1+x_4)(1+r) \quad \frac{1}{4}(z_1-z_4)(1+r) \right\rangle \tag{6.51}$$

with,

$$Tr_2 = \frac{\sqrt{\left[(A_z + sB_z)^2 + (A_x + sB_x)^2\right]}}{8 \det J}$$

Obtaining the generalised strain-displacement matrices B_x, B_y allows the member stiffness matrix to be obtained from,

$$K = \det J \int_{-1-1}^{+1+1} \int \left(B_x^T C_b B_x + B_y^T C_s B_y \right) dr\, ds \tag{6.52}$$

Gaussian numerical integration[41,44] is used to solve the above equation. Let

$$K = \int_{-1-1}^{+1+1} \int f\, dr\, ds \tag{6.53}$$

where,

$$f = \left(B_x^T C_b B_x + B_y^T C_s B_y \right) \det J$$

Therefore applying numerical integration,

$$K = \sum_{IJ} \alpha_{IJ} f_{IJ} t_{IJ} \tag{6.54}$$

where f_{IJ} is the matrix f evaluated at points r_I and s_J , with t_{IJ} being the thickness at this point and α_{IJ} being a constant known as a weighting factor which depends on the position of r_I and s_I. The position of r_I and s_J together with the value of the weighting factor are such as to give maximum integration accuracy for the number of Gauss points (i.e. r_I and s_J) used. In this formulation 2-point Gauss integration is employed, which means that the matrix f_{IJ} is calculated at four points as shown in Fig. 6.04.

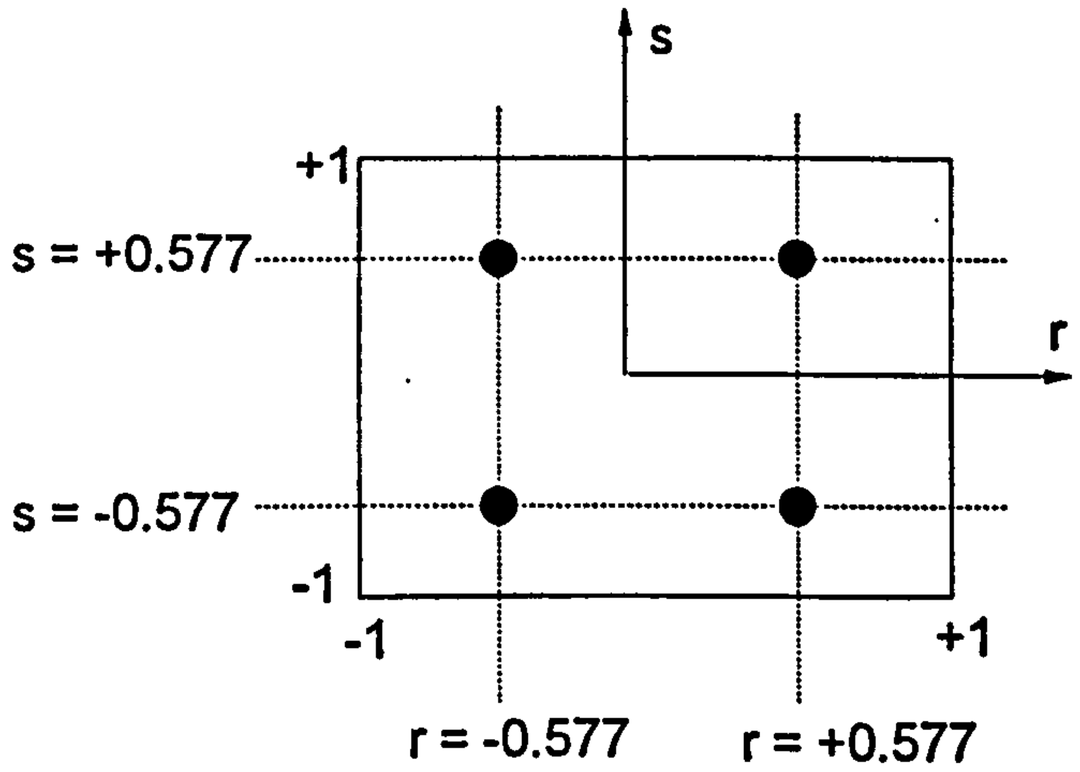

Fig. 6.04: Position of Gauss points in the element.

The weighting factors corresponding to the position of these Gauss points can be obtained from any numerical methods text book[41,44].

6.02 PLANE STRESS FORMULATION.

For the plane stress membrane stiffness consider the element in Fig. 6.05.

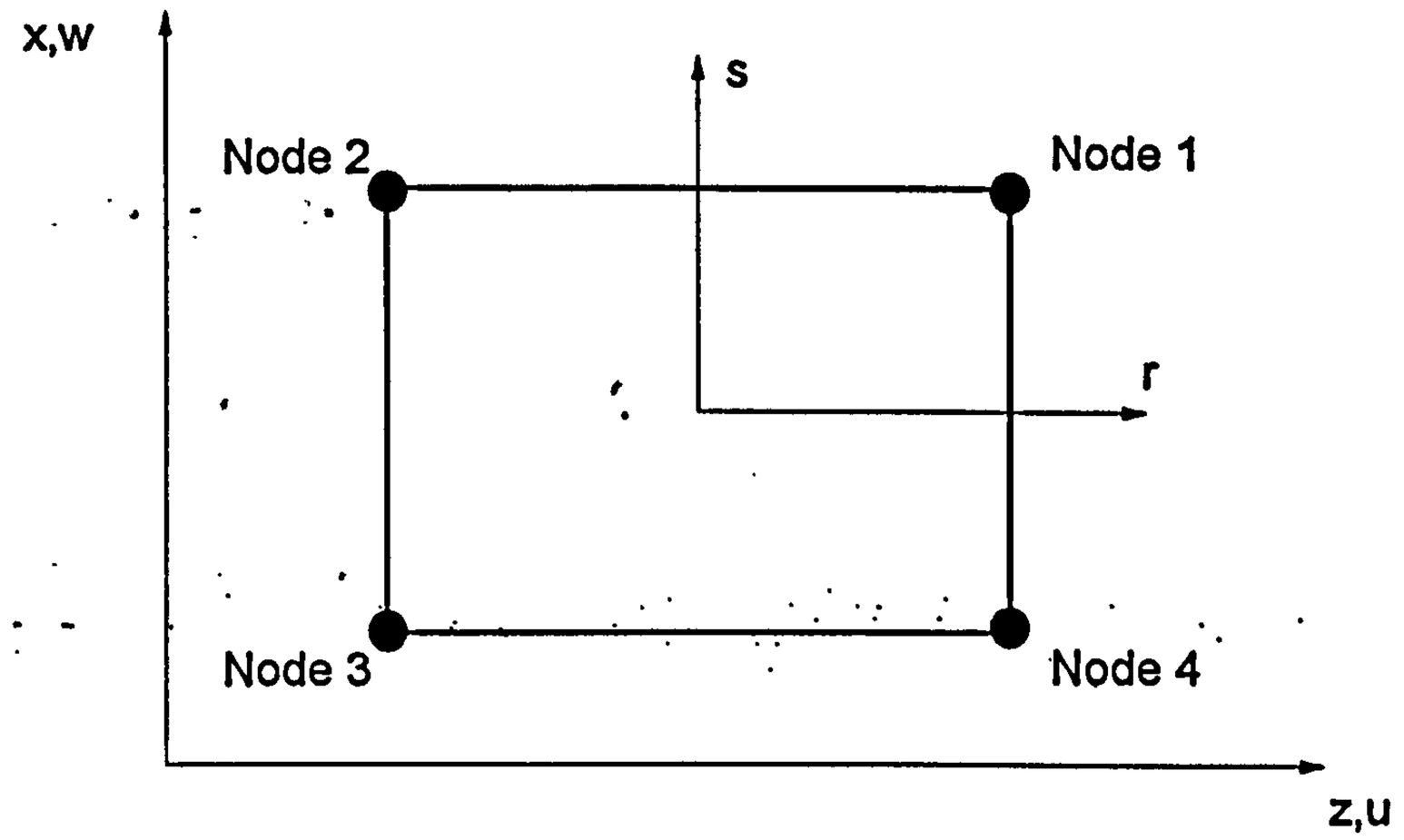

Plan view

Fig 6.05 : Plane stress element.

Similar to the plate formulation the Principle of Virtual Displacements for a plane stress element is given by,

$$\int_A \delta\varepsilon^T \tau dA = \sum_I \delta\hat{u}^{IT} F^I \qquad (6.55)$$

where,

F^I = the concentrated external force at node i,

$\hat{u}^I$ = the nodal displacement at node i.

Using $\varepsilon = B\hat{u}$ and letting the imposed virtual nodal displacements equal $\bar{\hat{u}}$ gives,

$$\bar{\hat{u}}^T \left[\int_A B^T C\, B\, dA \right] \hat{u} = \bar{\hat{u}}^T \{F\} \qquad (6.56)$$

where,

$\{F\}$ = vector of externally applied nodal force.

Using the virtual displacement method of applying a unit virtual displacement in turn to all displacement components causes,

$\hat{\bar{u}} = identity\ matrix$

which allows equation (6.56) to be expressed as,

$$K\hat{u} = F \tag{6.57}$$

where, the stiffness matrix K, is given by,

$$K = \int_A B^T C B \, dA \tag{6.58}$$

Converting this equation to the natural coordinate system (as shown in the derivation of the plate element) produces,

$$K = \det J \int_{-1-1}^{+1+1} \left(B^T C B\right) dr\, ds \tag{6.59}$$

Considering Fig. 6.05, the coordinate and displacement interpolations are given by,

$$x = \sum_{I=1}^{q} h_I x_I \qquad z = \sum_{I=1}^{q} h_I z_I \qquad w = \sum_{I=1}^{q} h_I w_I \qquad u = \sum_{I=1}^{q} h_I u_I \tag{6.60}$$

where,

x and z are the local coordinates at any point within the element,

x_I and z_I are the local coordinates at the i th node,

w and u are the local displacements at any point within the element,

w_I and u_I are the local displacements at the i th node,

h_I are the interpolation functions, which are the same as those used for the plate element, and are shown again below.

$$h_1 = \frac{1}{4}(1+r)(1+s) \qquad h_2 = \frac{1}{4}(1-r)(1+s)$$
$$h_3 = \frac{1}{4}(1-r)(1-s) \qquad h_4 = \frac{1}{4}(1+r)(1-s) \tag{6.61}$$

Therefore the local coordinates at any position within the element are given by,

$$z = \frac{1}{4}(1+r)(1+s)z_1 + \frac{1}{4}(1-r)(1+s)z_2 + \frac{1}{4}(1-r)(1-s)z_3 + \frac{1}{4}(1+r)(1-s)z_4 \tag{6.62}$$

$$x = \frac{1}{4}(1+r)(1+s)x_1 + \frac{1}{4}(1-r)(1+s)x_2 + \frac{1}{4}(1-r)(1-s)x_3 + \frac{1}{4}(1+r)(1-s)x_4 \tag{6.63}$$

and the local displacements at any position within the element are given by,

$$u = \frac{1}{4}(1+r)(1+s)u_1 + \frac{1}{4}(1-r)(1+s)u_2 + \frac{1}{4}(1-r)(1-s)u_3 + \frac{1}{4}(1+r)(1-s)u_4 \tag{6.64}$$

$$w = \frac{1}{4}(1+r)(1+s)w_1 + \frac{1}{4}(1-r)(1+s)w_2 + \frac{1}{4}(1-r)(1-s)w_3 + \frac{1}{4}(1+r)(1-s)w_4 \tag{6.65}$$

The element strains in a plane stress element are given by,

$$\varepsilon = \begin{Bmatrix} \varepsilon_{zz} \\ \varepsilon_{xx} \\ \gamma_{zx} \end{Bmatrix} \quad \text{where,} \quad \varepsilon_{zz} = \frac{\partial u}{\partial z} \qquad \varepsilon_{xx} = \frac{\partial w}{\partial x} \qquad \gamma_{zx} = \frac{\partial u}{\partial x} + \frac{\partial w}{\partial z} \tag{6.66}$$

The displacement derivatives can be evaluated at any value of r and s using,

$$\begin{Bmatrix} \frac{\partial}{\partial z} \\ \frac{\partial}{\partial x} \end{Bmatrix}_{at\ r=r_i\ and\ s=s_j} = \mathbf{J}_{ij}^{-1} \begin{Bmatrix} \frac{\partial}{\partial r} \\ \frac{\partial}{\partial s} \end{Bmatrix}_{at\ r=r_i\ and\ s=s_j} \tag{6.67}$$

The formulation of the Jacobian matrix **J** has been shown in the derivation of the plate element.

Now,

$$\frac{\partial u}{\partial r} = \frac{1}{4}(1+s)u_1 - \frac{1}{4}(1+s)u_2 - \frac{1}{4}(1-s)u_3 + \frac{1}{4}(1-s)u_4 \tag{6.68}$$

$$\frac{\partial u}{\partial s} = \frac{1}{4}(1+r)u_1 + \frac{1}{4}(1-r)u_2 - \frac{1}{4}(1-r)u_3 - \frac{1}{4}(1+r)u_4 \tag{6.69}$$

$$\frac{\partial w}{\partial r} = \frac{1}{4}(1+s)w_1 - \frac{1}{4}(1+s)w_2 - \frac{1}{4}(1-s)w_3 + \frac{1}{4}(1-s)w_4 \tag{6.70}$$

$$\frac{\partial w}{\partial s} = \frac{1}{4}(1+r)w_1 + \frac{1}{4}(1-r)w_2 - \frac{1}{4}(1-r)w_3 - \frac{1}{4}(1+r)w_4 \tag{6.71}$$

Therefore the displacement derivatives are given by,

$$\begin{bmatrix} \frac{\partial u}{\partial z} \\ \frac{\partial u}{\partial x} \end{bmatrix} = \frac{1}{4} J^{-1} \begin{bmatrix} (1+s) & 0 & -(1+s) & 0 & -(1-s) & 0 & (1-s) & 0 \\ (1+r) & 0 & (1-r) & 0 & -(1-r) & 0 & -(1+r) & 0 \end{bmatrix} \{\hat{u}\} \tag{6.72}$$

$$\begin{bmatrix} \frac{\partial w}{\partial z} \\ \frac{\partial w}{\partial x} \end{bmatrix} = \frac{1}{4} J^{-1} \begin{bmatrix} 0 & (1+s) & 0 & -(1+s) & 0 & -(1-s) & 0 & (1-s) \\ 0 & (1+r) & 0 & (1-r) & 0 & -(1-r) & 0 & -(1+r) \end{bmatrix} \{\hat{u}\} \tag{6.73}$$

where,

$$\{\hat{u}\} = \langle z_1 \quad x_1 \quad z_2 \quad x_2 \quad z_3 \quad x_3 \quad z_4 \quad x_4 \rangle^T$$

Therefore using,

$\varepsilon = B\hat{u}$

the strain-displacement matrix B, is given by,

$$B = \frac{1}{4} J^{-1} \begin{bmatrix} (1+s) & 0 & -(1+s) & 0 & -(1-s) & 0 & (1-s) & 0 \\ 0 & (1+r) & 0 & (1-r) & 0 & -(1-r) & 0 & -(1+r) \\ (1+r) & (1+s) & (1-r) & -(1+s) & -(1-r) & -(1-s) & -(1+r) & (1-s) \end{bmatrix} \tag{6.74}$$

Therefore the member stiffness matrix can be formed using,

$$K = \det J \int_{-1-1}^{+1+1} \int \left(B^T C B \right) dr\, ds \tag{6.75}$$

where **C** is the stress-strain matrix given by,

$$C = \frac{E}{1-\nu^2} \begin{bmatrix} 1 & \nu & 0 \\ \nu & 1 & 0 \\ 0 & 0 & \frac{1-\nu}{2} \end{bmatrix} \tag{6.76}$$

Gaussian numerical integration is used to solve for the member stiffness matrix, and the method has been explained previously in the derivation of the plate stiffness matrix.

6.1: CONNECTING BEAM AND SHELL ELEMENTS.

As explained in Chapter 4, the computer program has the ability to position the reference axis, and thus the nodal position of the beam element, at the beam's centroid or at any point on or above the top flange. The shell elements have 4 nodes which are positioned at the mid-height. Therefore the reference axis on the beam element is positioned to coincide with the nodal position of the shell element, as shown in Fig. 6.06. This will ensure compatibility at nodal positions.

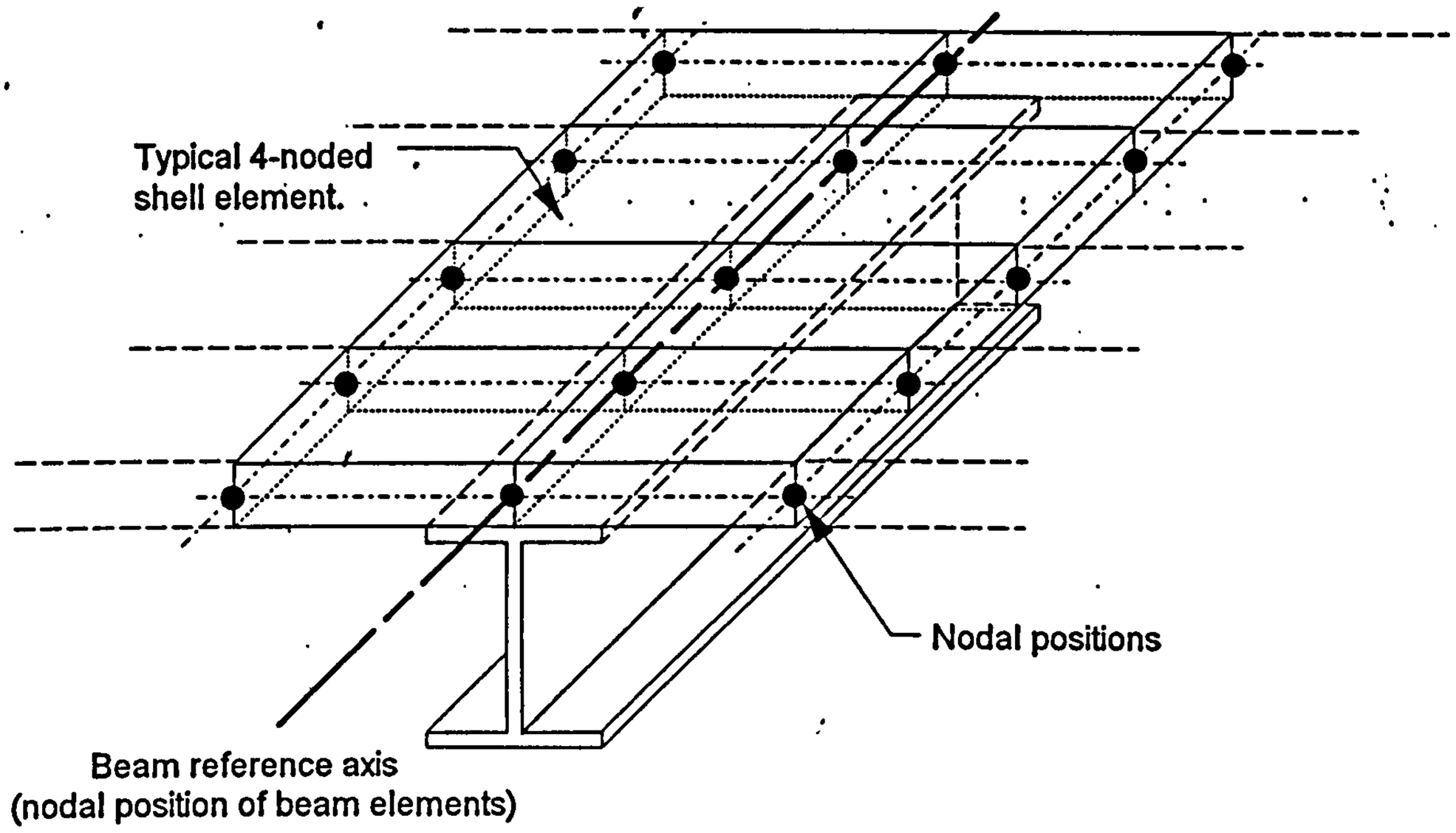

Fig. 6.06: Connection of beam and shell element.

6.2: VALIDATION OF SHELL ELEMENTS.

To validate the plate bending characteristics of the shell element the example of a simply-supported plate shown in Fig. 6.07, was analysed.

The theoretical solution is given by[43,76]

$$\Delta_c = 0.0116\frac{PL^2}{D} \qquad \text{where,} \quad D = \frac{Et^3}{12\left(1-\nu^2\right)} \tag{6.77}$$

$$\text{therefore,} \quad D = \frac{205\times10^3(8.0)^3}{12\left(1-0.3^2\right)} = 9611721.6\,Nmm$$

giving, $$\Delta_c = \frac{0.0116 \times 2.0 \times 10^3 \times 2000^2}{9611721.6} = 9.65 mm$$

For the computer analysis symmetry was utilised, with only a quarter of the plate, with correct boundary conditions, being required to represent the whole plate. A convergence study was carried out and the results are shown in Fig 6.08. It can been seen from these results that as the number of elements increases the computer results converge quickly to the exact solution. It should be noted that even a fairly sparse mesh (n=2) gives an acceptable error of below 1%.

To validate the plane stress membrane characteristics a deep beam analysis was carried out. In elementary beam bending theory, it is assumed that plane sections remain plane during bending, with no account taken of the presence of shear stresses. These shear stresses will cause plane cross-sections to distort during bending, and significantly affect the stresses and displacements of the beam when the depth of the cross-section is a substantial proportion of the length of the beam.

Therefore to validate the membrane characteristics of the shell element the deep beam shown in Fig. 6.09 was analysed. The theoretical solution is given by[77]

$$\Delta_c = \frac{5}{24}\frac{qL^4}{EI}\left[1+\frac{12}{5}\frac{C^2}{L^2}\left(\frac{4}{5}+\frac{\nu}{2}\right)\right] \qquad (6.78)$$

giving,

$$\Delta_c = \frac{5}{24}\frac{500 \times 3000^4}{205 \times 10^3 \times 2.5 \times 10^9}\left[1+\frac{12}{5}\frac{(500)^2}{(3000)^2}\left(\frac{4}{5}+\frac{0.3}{2}\right)\right] = 17.51 mm$$

For the computer model predictions, symmetry was utilised and the mesh layouts adopted are shown in Fig. 6.11. The results of the convergence test are shown in Fig. 6.10. Once again this test shows that as the number of elements are increased the computed results converge towards the exact solution.

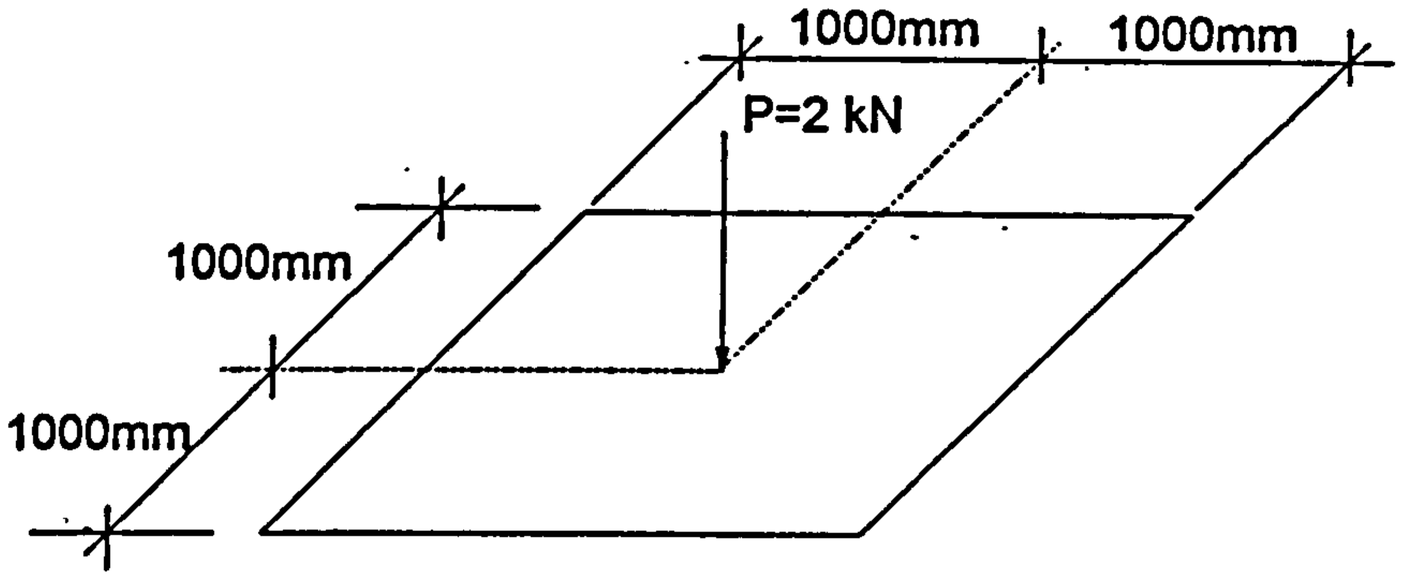

t = 8.0 mm

E = 205 x 10^3 N/mm^2

ν = 0.3

Simply-supported along all four sides.

Fig 6.07: Simply-supported plate.

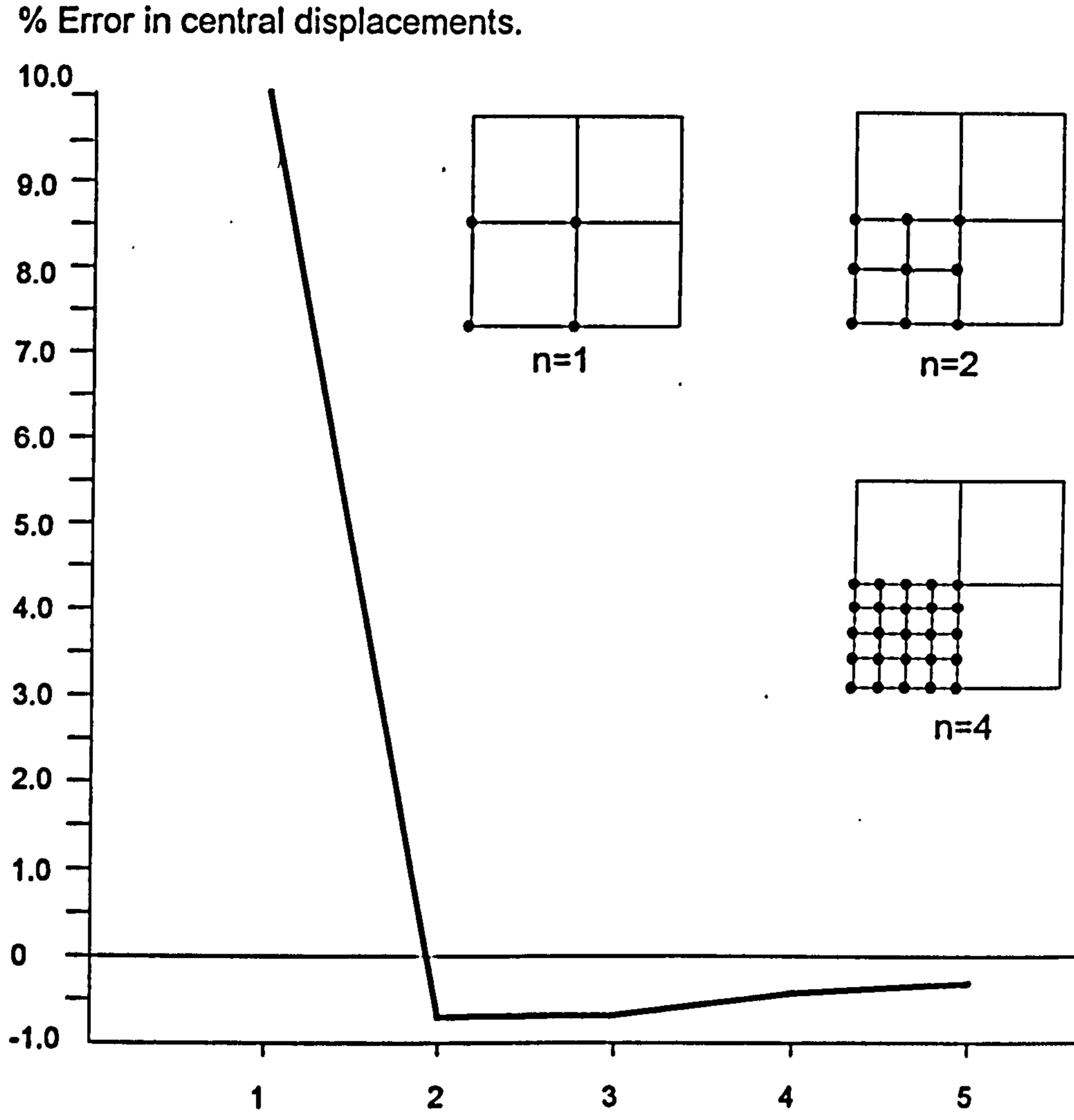

Fig. 6.08: Convergence study for the plate element.

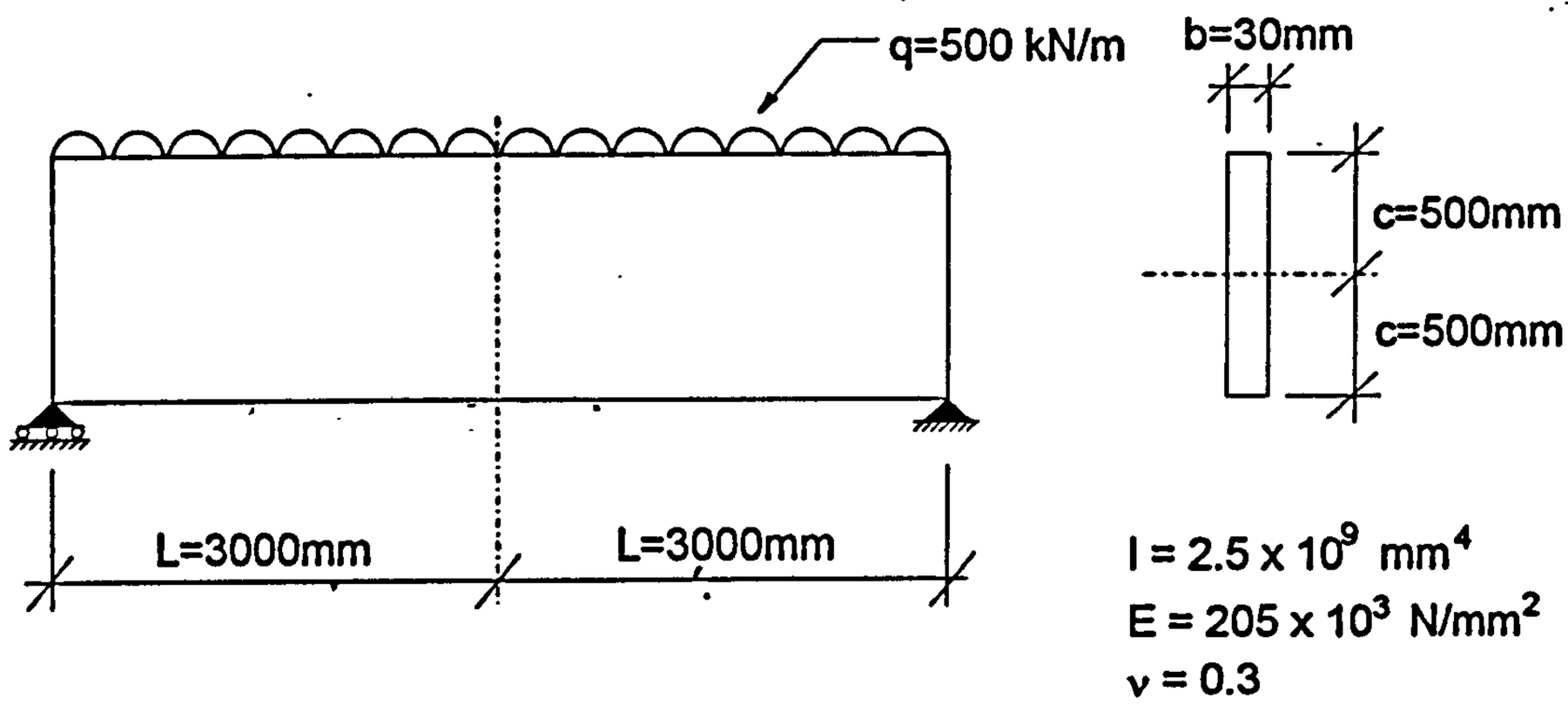

Fig 6.09: Deep beam analysis used to validate plane stress membrane characteristics of the shell element.

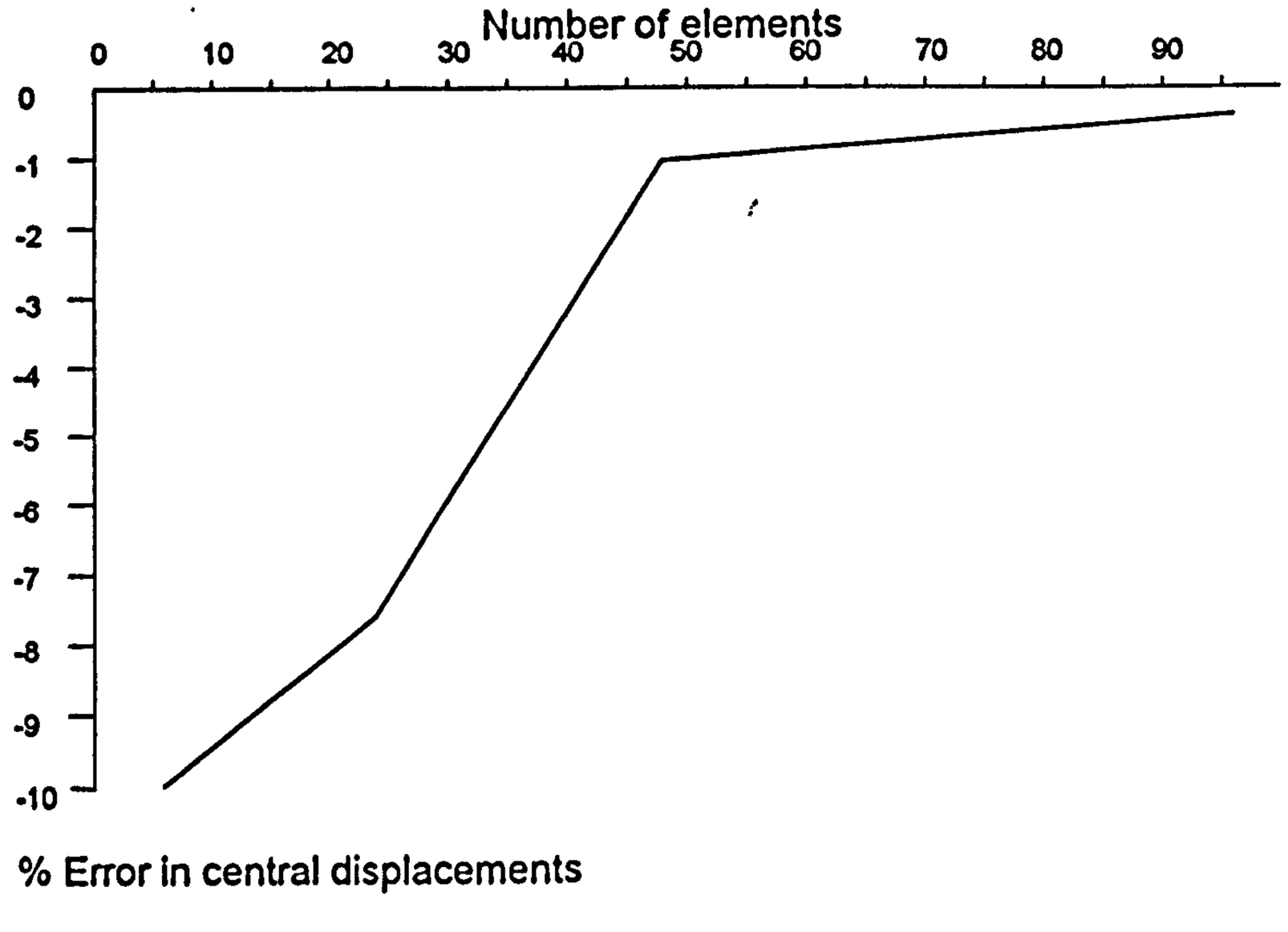

Fig 6.10: Convergence study for the plane stress membrane characteristics of the shell element.

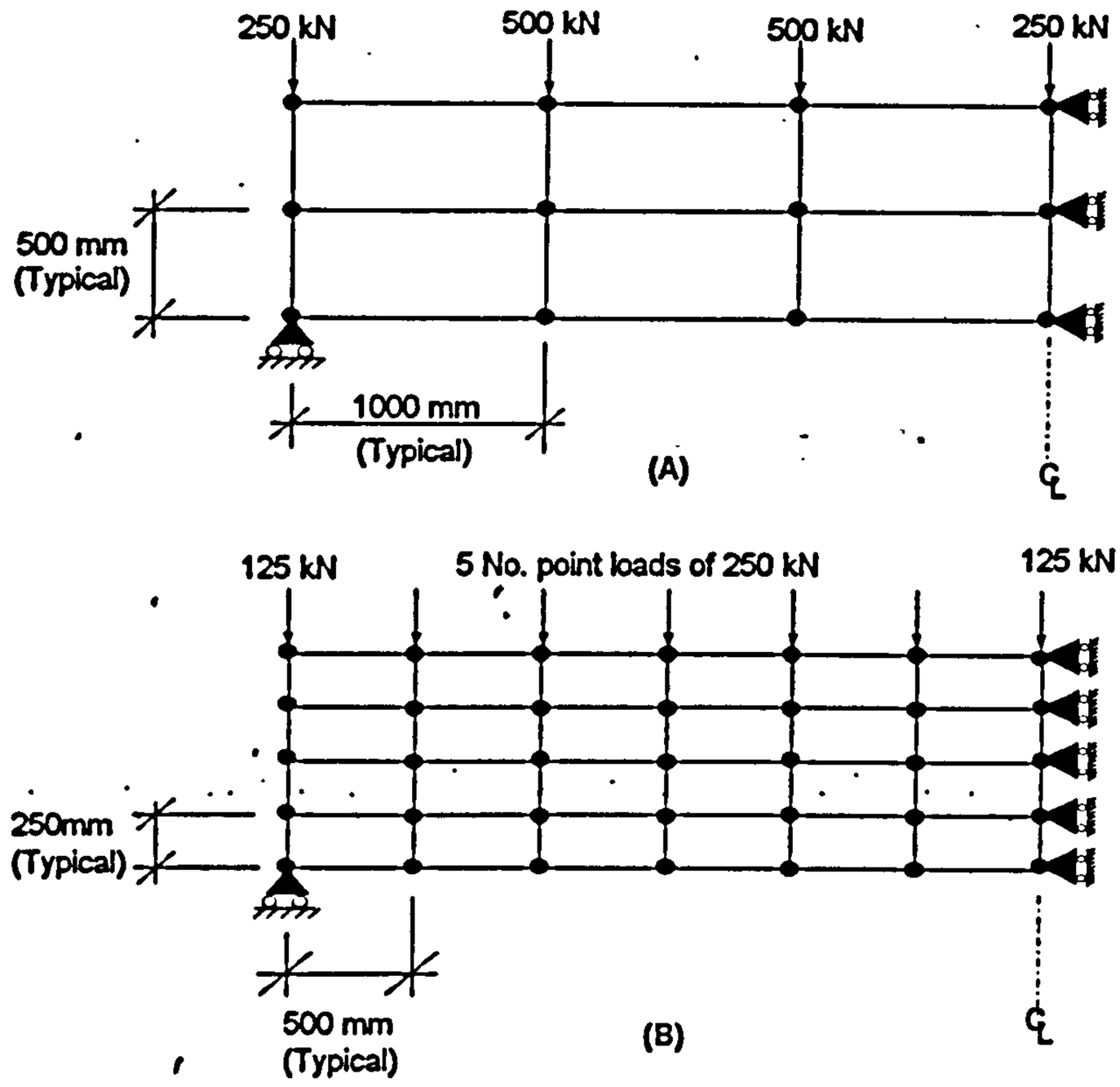

Fig 6.11: Mesh configurations used for convergence study for plane stress characteristics of the shell element.

To validate the program when shell and beam elements are connected, the composite cantilever beam shown in Fig. 6.12 was analysed. A load of 10 kN was placed at the tip, and assuming small displacement theory the theoretical maximum vertical deflection was calculated using the transformed (or equivalent) cross-section approach.

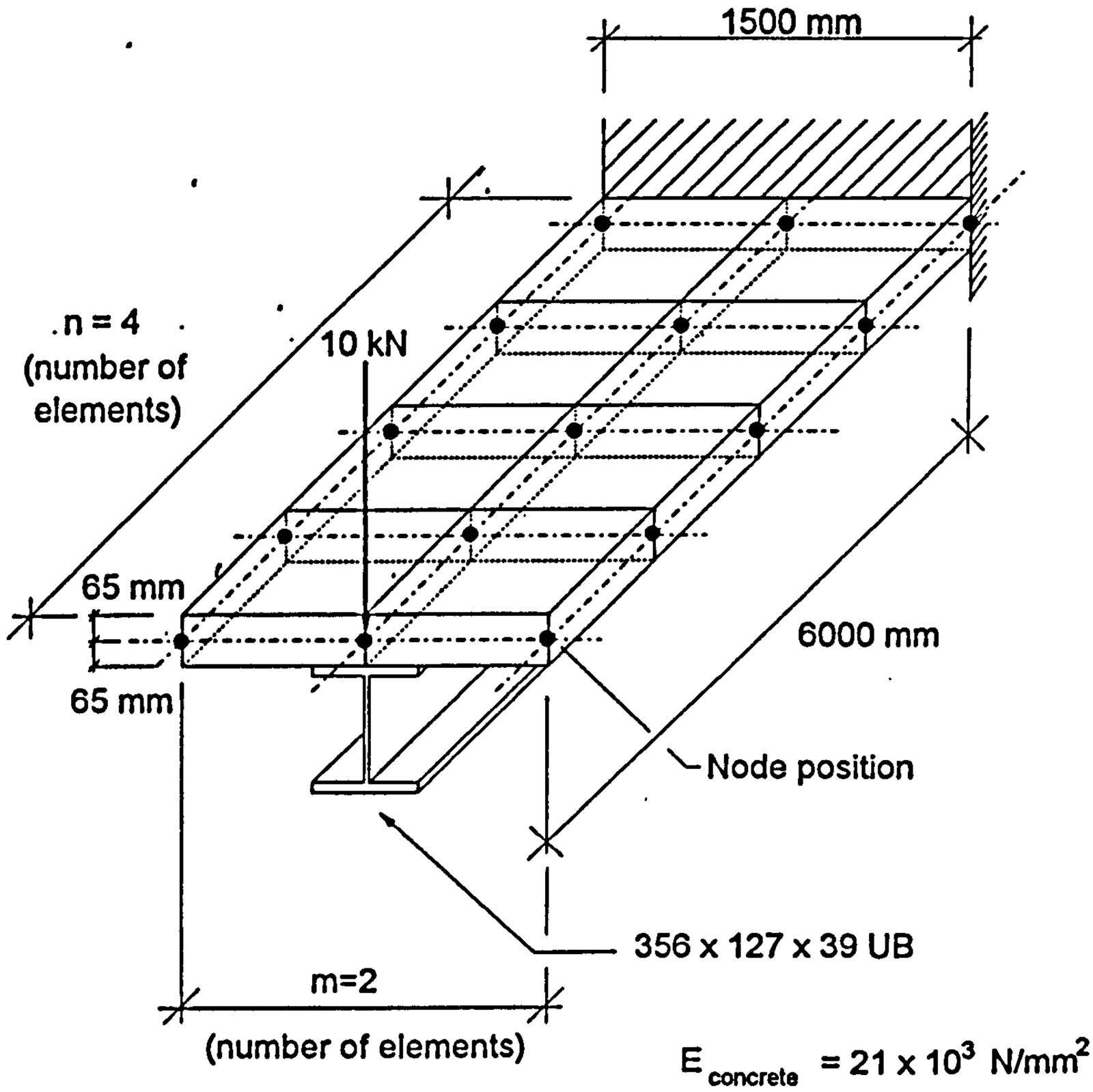

Fig 6.12: Composite cantilever beam used to validate connection between beam and shell elements.

A convergence study was carried out by varying n (the number of shell elements along the beam) and m (the number of shell elements across the beam). The number of beam elements will correspond to n, to ensure continuity at the nodes. The mesh layouts adopted are shown in Fig. 6.13, together with the results of the convergence study. The computed vertical displacement at the tip of the cantilever converges quickly to the value calculated using the transformed cross-section approach, as the beam and shell elements are increased. It can be seen that even with a fairly sparse

mesh comprising of eight shell elements and four beam elements the error in the computed result is only 2.8%.

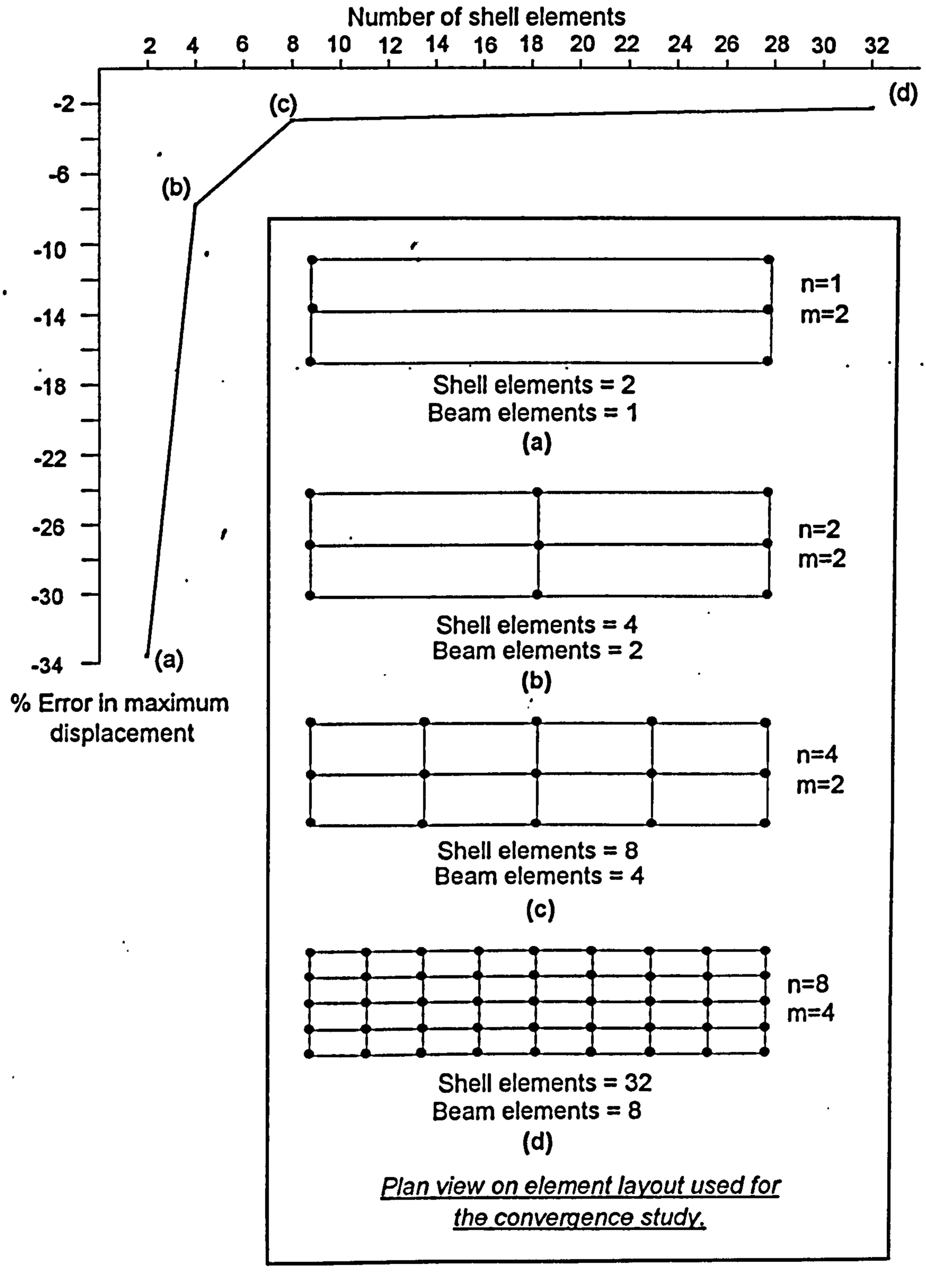

Fig. 6.13: Convergence study for deflection of the composite cantilever beam shown in Fig. 6.12.

6.3: THERMAL CURVATURE OF COMPOSITE BEAMS.

To investigate the effects of thermal bowing the composite cantilever beam, shown in Fig. 6.14 was analysed.

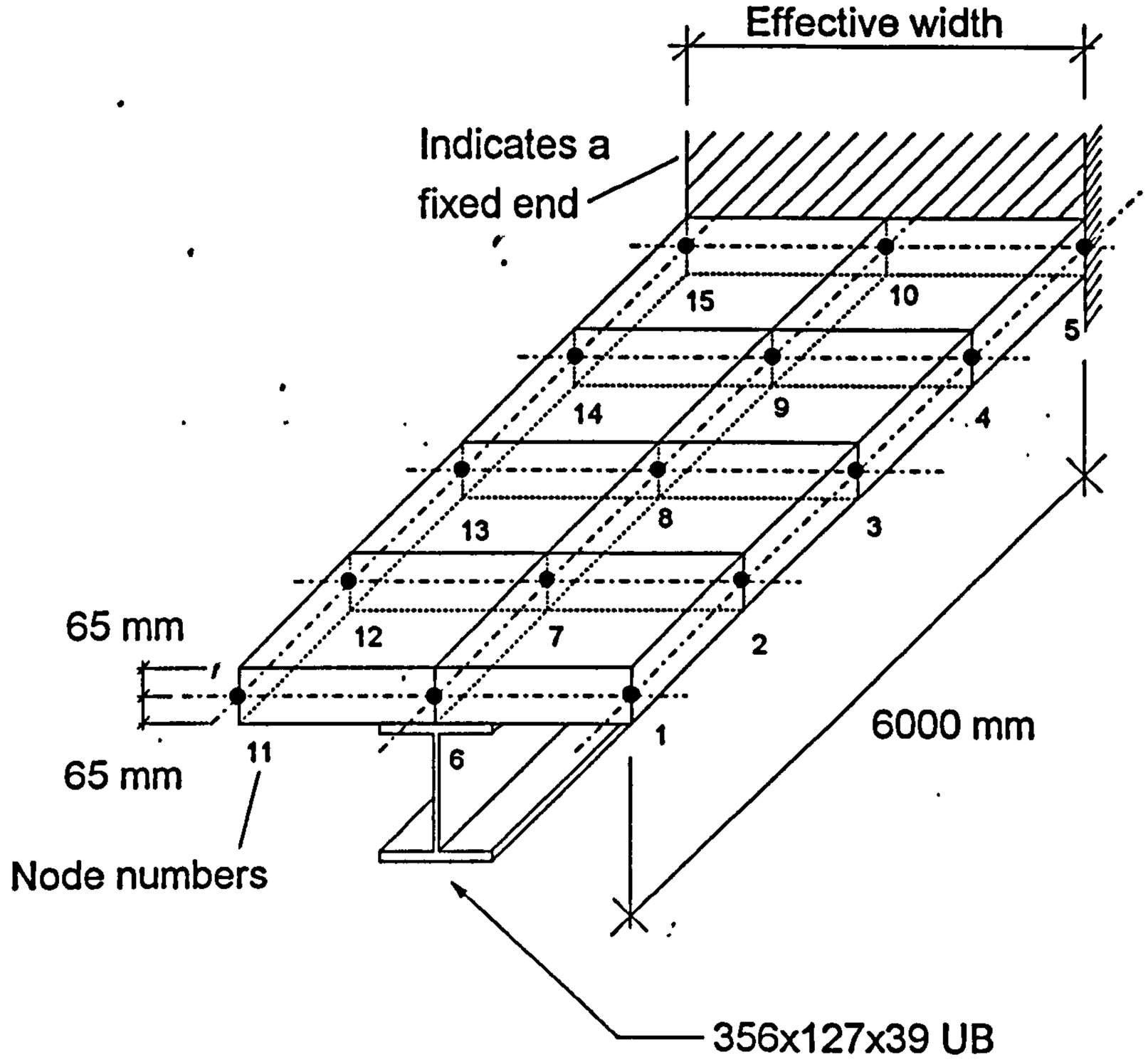

Fig 6.14: Composite cantilever beam used to investigate thermal bowing.

No external load was placed on the structure, with the steel beam being uniformly heated and the concrete slab remaining at ambient temperature. Obviously this example is fictitious since the heat-sink effect of the slab on the temperature profile of the steel beam is ignored, and it is assumed that the concrete slab remains at ambient temperature. These simplifications were adopted to allow validation of the effects of thermal bowing with manual calculations.

The relationship between vertical displacement at the tip and the temperature in the steel, for various effective widths of the slab, is shown in Fig. 6.15.

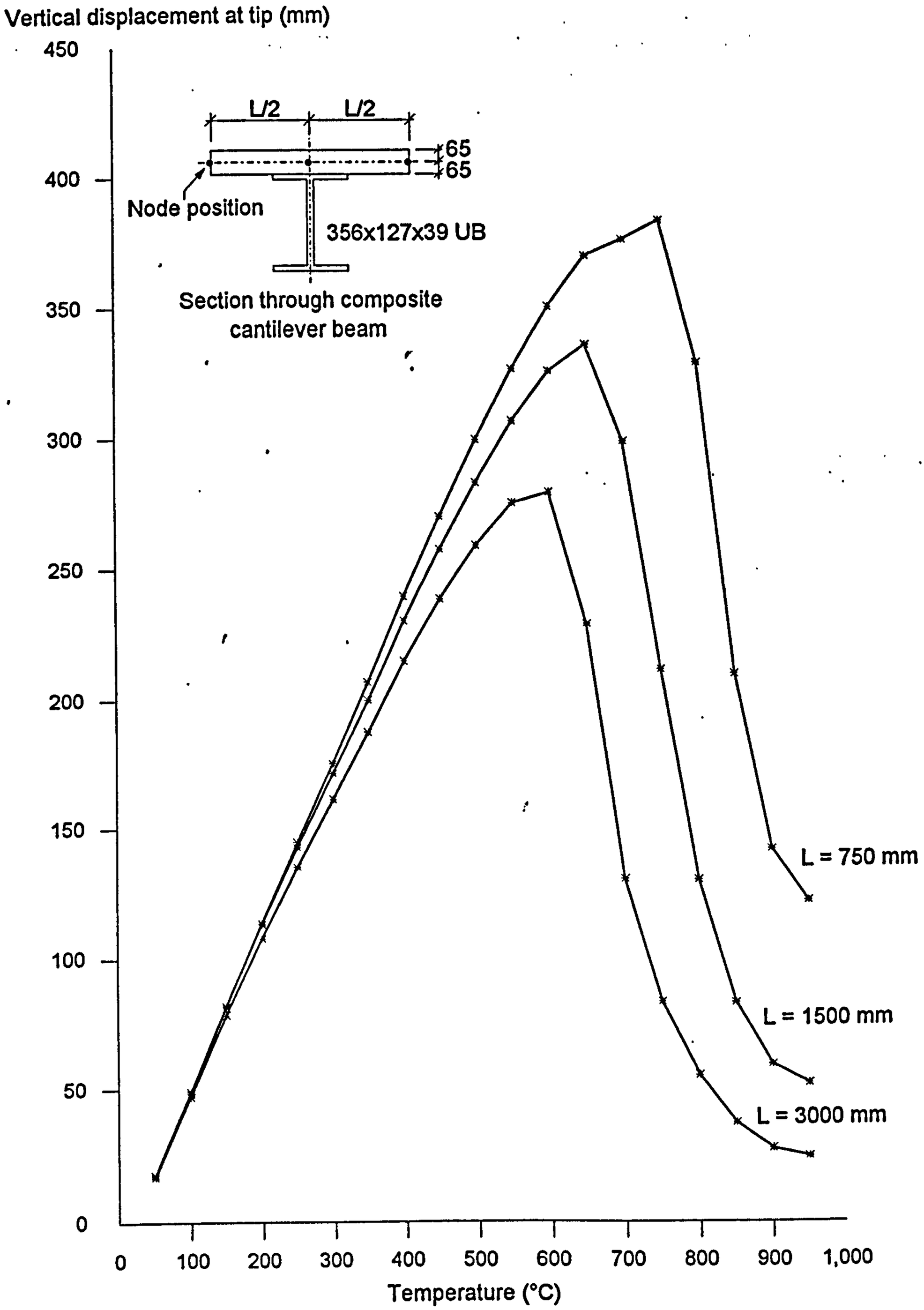

Fig. 6.15: Relationship between thermal bowing and the effective width of the slab.

As can be seen in Fig. 6.15, the vertical displacement at the tip rises upwards to a peak, and then starts to change direction and reduce. To obtain an understanding of

the mechanics of this behaviour, the structural restraint to thermal expansion needs to be considered. When the beam begins to expand, the membrane resistance of the slab causes the structure to bow upwards. This bowing action is resisted by the bending resistance of the slab and beam. At a certain temperature the bending resistance of the slab begins to overcome the compressive resistance of the steel beam, which is decreasing due to softening of the material. This will cause the continuing expansion to compress the steel beam, thus causing the vertical displacement to change direction and reduce.

To prove the above theory the beam with an effective width of 1500mm was re-analysed, with the exception that the axial displacement of the nodes was fully restrained, so that only the bending action of the slab was considered. Five examples of this beam were analysed with varying depths of slab, ranging from 130mm to 0mm. The node height of 65mm above the beam remained constant for all examples with the slab thickness distributed equally about the node. The results are presented in Fig. 6.16, which shows that the greater the slab depth (and therefore the higher the bending stiffness) the lower the temperature at which the vertical displacement reverses direction. When there is no slab (thickness equals 0mm) the vertical displacement at the tip does not reverse direction and is proportional to the thermal expansion of the steel. Because of the simplicity of this example it was possible to check the computer results against manual calculations, which are shown below.

The thermal elongation of steel is given by,

$$\frac{\Delta l}{l} = -2.416\times10^{-4} + 1.2\times10^{-5}\times t_s + 0.4\times10^{-8}(t_s)^2 \qquad \text{when} \quad 20°C \le t_s \le 750°C \qquad (6.79)$$

and,

$$\frac{\Delta l}{l} = 11.0\times10^{-3} \qquad \text{when} \quad 750°C < t_s \le 860°C \qquad (6.80)$$

and,

$$\frac{\Delta l}{l} = -6.2\times10^{-3} + 2.0\times10^{-5}\times t_s \qquad \text{when} \quad 860°C \le t_s \le 1200°C \qquad (6.81)$$

where,

l = length at room temperature of the steel member,

Δl = temperature induced elongation of the steel member,

t_s = steel temperature.

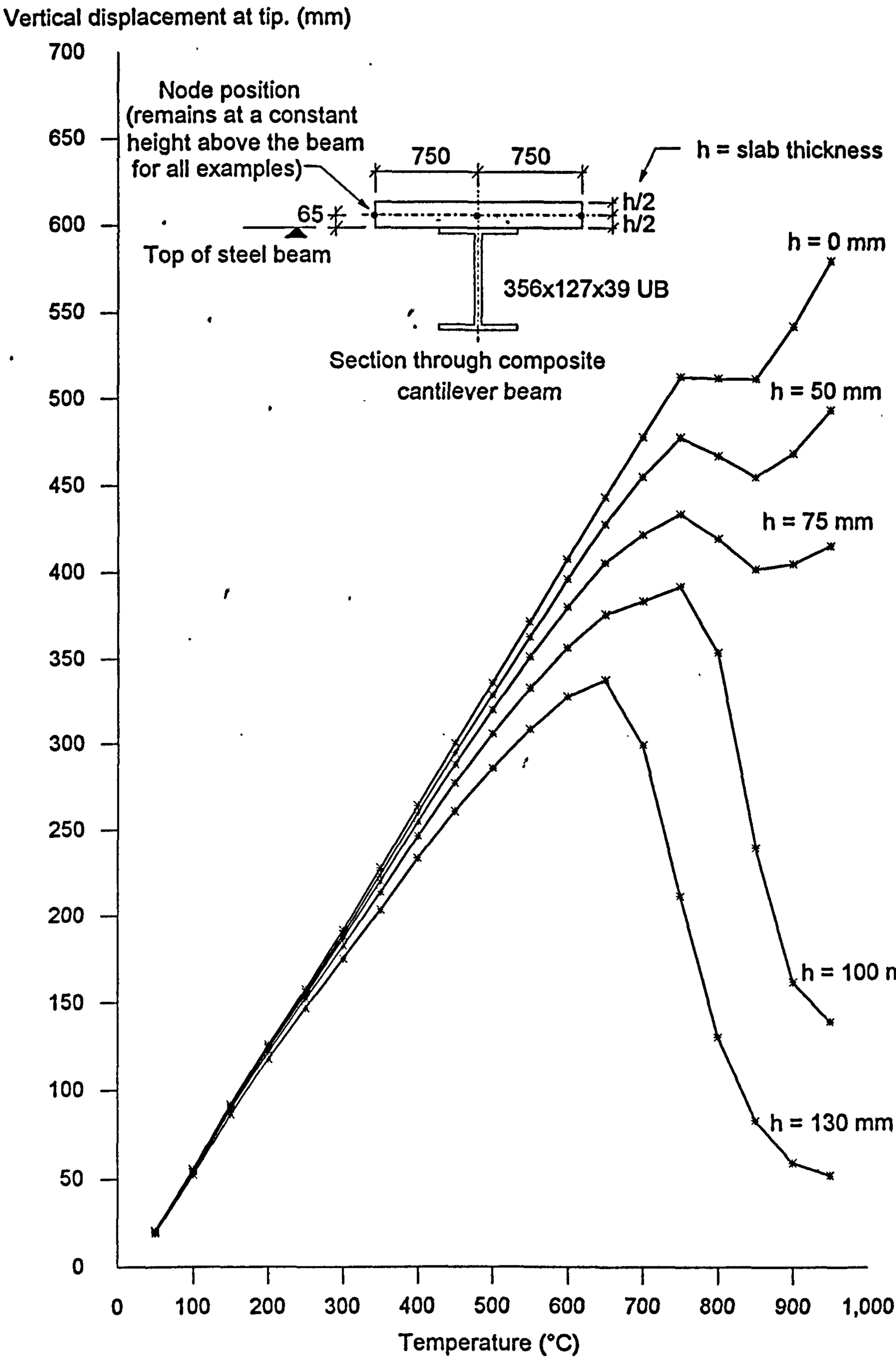

Fig 6.16: Relationship between thermal bowing and the bending stiffness in the slab.

Therefore at 100°C the thermal strain in the steel is given by

$$\varepsilon = -2.416\times10^{-4} + 1.2\times10^{-5}(100) + 0.4\times10^{-8}(100)^2 = 9.98\times10^{-4}$$

the stress can be calculated from

$$\sigma = E\varepsilon = 205\times10^{3}\times9.98\times10^{-4} = 204.7\ N/mm^2$$

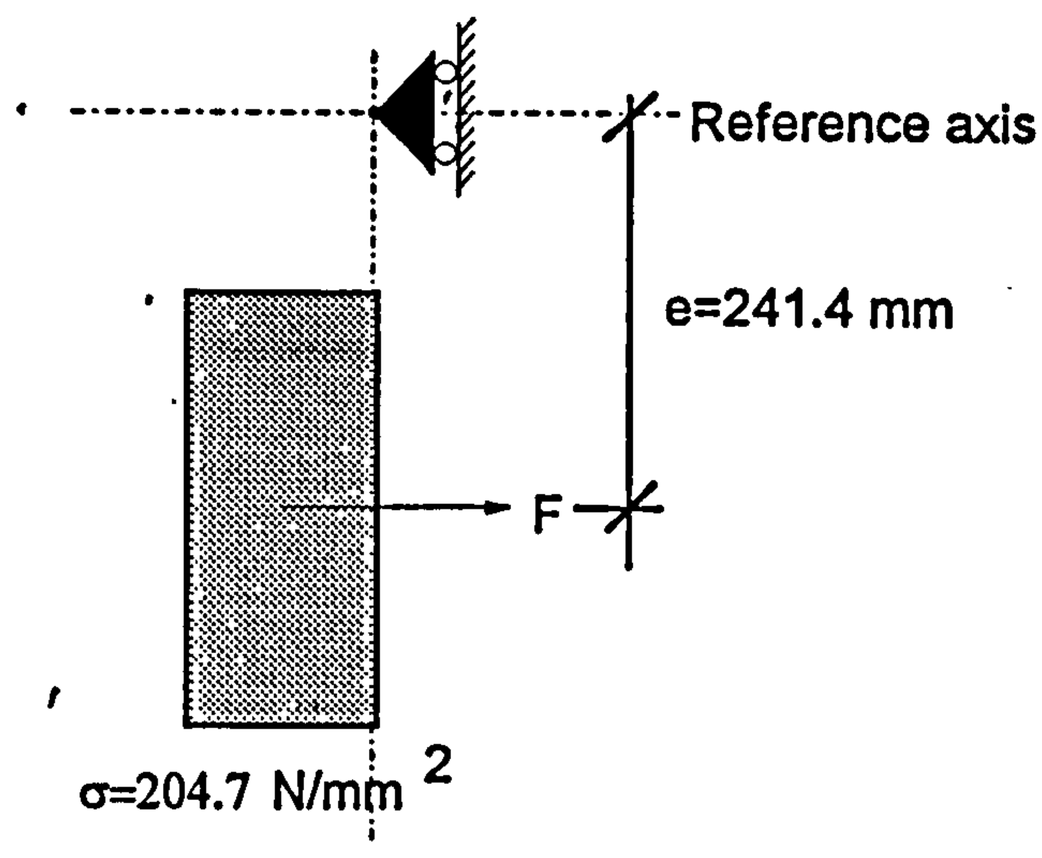

Fig 6.17: Stress block due to a temperature rise of 100° C

Area of cross-section = $49.4\text{x}10^2\ mm^2$

The axial force is given by,

$$F = \sigma A = 204.7\times49.4\times10^{2} = 1011.07\ N$$

The moment is given by (considering Fig. 6.17),

$$M = Fe = 1011.07\times241.4\times10^{3} = 244.07\times10^{6}\ Nmm$$

Now assuming plane sections remain plane, the total strain is given by,

$$\varepsilon = \varepsilon_0 + \frac{1}{R}y \qquad (6.82)$$

where,

ε_0 = normal strain at the reference axis,

$1/R$ = curvature of the reference axis,

y = distance from the reference axis.

since,

$$M = \int \sigma y \, dA \qquad \text{and} \qquad \sigma = E\varepsilon$$

then,

$$M = E\left(\int y \, dA \, \varepsilon_0 + \int y^2 dA \frac{1}{R}\right) \tag{6.83}$$

where,

$\int y \, dA =$ first moment of area about the reference axis,

$\int y^2 dA =$ second moment of area about the reference axis.

now, $\varepsilon_0 = 0$ (axially restrained at reference axis)

and using the parallel axis theorem,

$$\int y^2 dA = 10100 \times 10^4 + \left(49.4 \times 10^2 \times 241.4^2\right) = 388.87 \times 10^6 mm^4$$

therefore, substituting the moment value and second moment of area into equation (6.83), yields a value of curvature of

$$\frac{1}{R} = 3.06 \times 10^{-6}$$

Now,

$$\frac{1}{R} = \frac{dv^2}{dz^2} \tag{6.84}$$

where v and z are identified below,

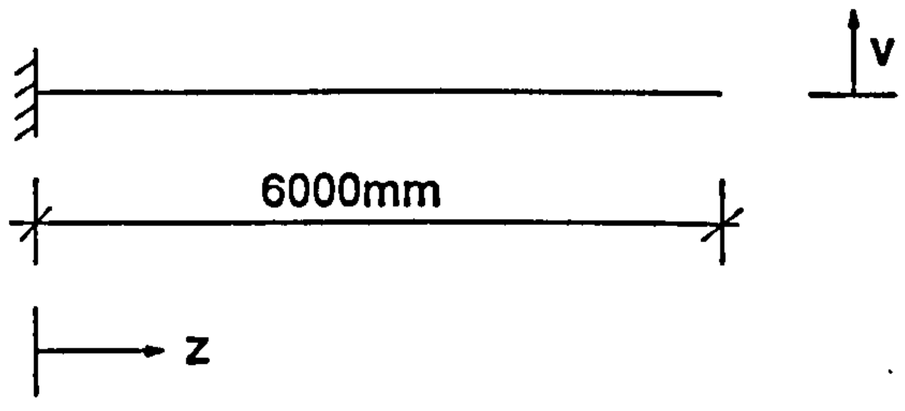

Integrating equation (6.84) produces,

$$\frac{dv}{dz} = -\frac{1}{R}z + A$$

and integrating again produces,

$$v = -\frac{1}{2}\frac{1}{R}z^2 + Az + B$$

where, A and B are constants.
When Z=0, the slope dv/dz and the displacement v are both zero, therefore,

A=0

and

B=0.

which produces,

$$v = -\frac{1}{2}\frac{1}{R}z^2 = -\frac{1}{2} \times 3.06 \times 10^{-6} \times (6000)^2 = 55.12mm$$

this compares very well with the computer model prediction of 55.76mm.

6.4: CALCULATION OF STRESS VALUES IN THE SHELL ELEMENTS.

Once the nodal displacements of the element are known, the stress values at any position within the element can be calculated using[41]

$$\tau = \mathbf{CB}\hat{u} \qquad (6.85)$$

where,

τ = generalised stress,

C = generalised stress-strain matrix,

B = generalised strain-displacement matrix,

$\hat{u}$ = matrix of nodal displacements.

For a displacement field finite element formulation the accuracy of the stress values is dependent on the position at which they are calculated within an element[41]. Provided all convergence criteria are satisfied the displacements across element boundaries are continuous. However in a displacement field formulation the stress values across boundaries are in general not continuous, and in fact the only way to ensure continuity is to base the formulation on a stress field[42]. Previous research[78] has considered the accuracy of predicted stress values in relation to their location within the element for finite element formulations based on the displacement field. Observations conclude that the stress values at the Gauss integration points are the

most accurate. It was therefore decided to calculate these values for each element, (a total of four) and average them to obtain a stress value for the element.

6.5: IMPOSITION OF A MAXIMUM BENDING STRESS ON THE SHELL ELEMENTS.

Connection of the beam element to the shell element at common nodal points causes both the steel beam and concrete floor to act compositely. A spread of yield through the cross-section of the steel beam and also along its length can be modelled. However the formulation for the shell elements so far has assumed that the represented material is isotropic, linear elastic, and has the same properties in compression and tension, although the formulation was developed so that extension to incorporate material non-linearities is possible. As a first development stage towards representing the true behaviour of the concrete floor it was decided to simply apply a limitation on bending stresses, although in reality a limitation on the total stress distribution which includes membrane stresses should be considered. The bending stresses are checked at each iteration, and if the maximum specified stress is exceeded the thickness of the element is reduced, as shown in Fig. 6.18. The maximum stress specified depends on whether the element is in sagging or hogging, with the maximum hogging stress being typically 10% of the value for the maximum sagging stress. After the maximum tensile stress in the hogging regions was recorded in an element all concrete in tension was ignored.

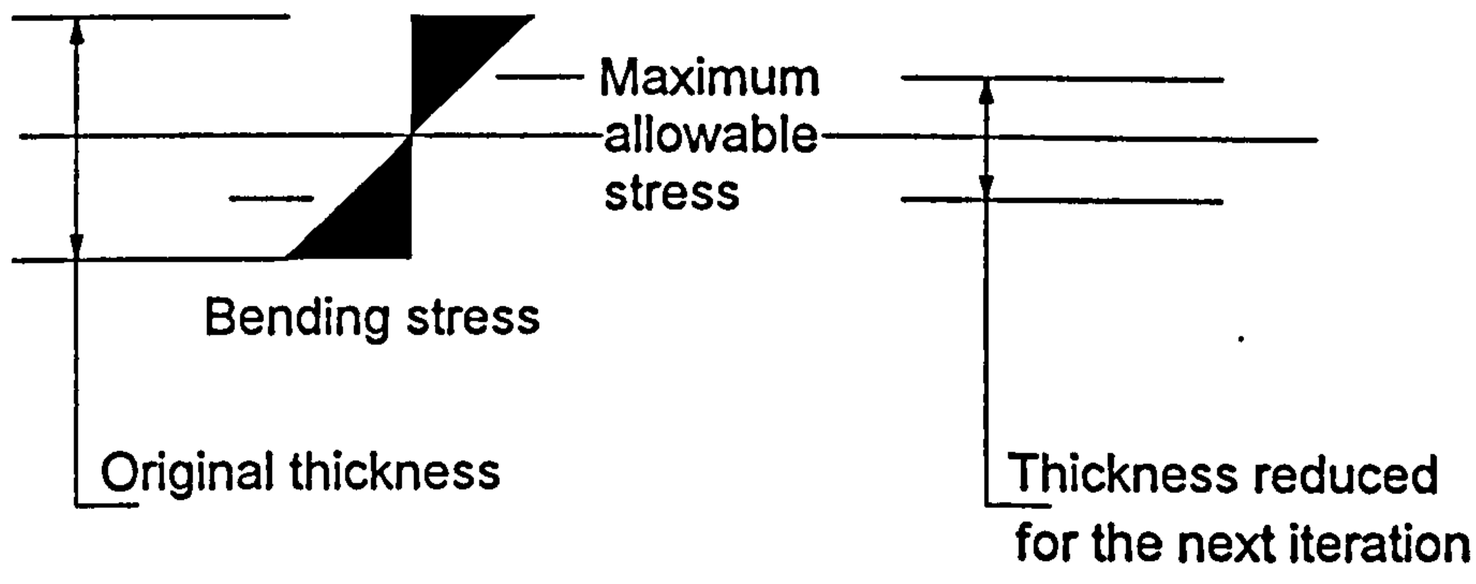

Fig. 6.18: Reduction of slab thickness based on maximum allowable bending stress.

These are clearly considerable simplifications in representing the cracking/crushing behaviour of the slab, and it is worth considering how they affect the realism of the modelling. When the slab spans between beams it is basically in bending and the above method is fairly accurate. The method of dealing with tensile stresses in the concrete slab when spanning perpendicular to the beam is also acceptable (although extremely simplified). However when we consider the slab spanning over and parallel

to a beam, the connection at the nodal points between the beam and shell elements represents a composite element, but the bending stress values in the slab are calculated assuming that the slab acts independently, with its neutral axis at mid-height. In traditional design methods the position of the neutral axis is based on the steel beam and an effective width of the slab. During a fire the neutral axis will change position, moving towards the cooler and thus stronger areas of the cross-section. Although the above simplifications are adopted to represent the concrete slab, the model will give an indication of the importance of the continuous floor slab on the total behaviour of steel framed buildings at elevated temperatures.

6.6: ADDITION OF THERMAL STRAINS.

Since at this stage in the development of the model flat shell elements are used, the temperature distribution through the thickness of the slab must be assumed to be uniform. Thermal strains are incorporated within the model by treating them as initial nodal forces. Therefore extending the Principle of Virtual Displacements for a plane stress element, given in equation (6.55), to include initial nodal forces produces,

$$\int_A \delta\varepsilon^T \tau dA = \sum_I \delta\hat{u}'^T F^I + \int_A \delta\,\varepsilon^T\,\tau^I \qquad (6.86)$$

where,

$\int_A \delta\,\varepsilon^T\,\tau^I$ = external work of the initial stress due to virtual strains, which correspond to the imposed virtual displacements.

Therefore equation (6.56) is extended to,

$$\bar{\hat{u}}^T\left[\int_A B^T C\,B\,dA\right]\hat{u} = \bar{\hat{u}}^T[F] + \bar{\hat{u}}^T\int_A B^T\tau^I\,dA \qquad (6.87)$$

Since $\bar{\hat{u}} = identity\ matrix$, then the initial nodal forces are given by,

$$R_I = \int_A B^T\,\tau^I\,dA \qquad (6.88)$$

where,

$$\tau^I = -\frac{E\alpha}{1-\nu^2}\begin{bmatrix} 1 & \nu & 0 \\ \nu & 1 & 0 \\ 0 & 0 & \frac{1-\nu}{2} \end{bmatrix}\begin{bmatrix} 1 \\ 1 \\ 0 \end{bmatrix}\{\theta - \theta_0\} \qquad (6.89)$$

where,

$\alpha =$ thermal coefficient of expansion,

θ_0 = initial temperature,

θ = temperature.

6.7: VALIDATION OF SHELL ELEMENTS INCORPORATING MAXIMUM ALLOWABLE BENDING STRESS AND THERMAL STRAINS.

Comparison was made between the model and two tests conducted in 1982 (tests 15 and 16 presented in the Compendium of UK standard fire tests[9]) on simply supported composite beams, as shown in Fig. 6.19. The same structural configuration was used for the two tests but different magnitudes of load were applied. The first test had four point loads which produced a maximum stress in the steel beam if no composite action was considered. In the second test the load was increased to produce a maximum stress in the beam, designed to CP117[79], if composite action was taken into account. The temperature profiles in the steel were obtained from the published test results at various times, with the temperature in the concrete assumed to be 10% of the hottest part of the steel. The assumed concrete characteristics (since insufficient information was published) are shown, together with the results, in Figs 6.20, and 6.21.

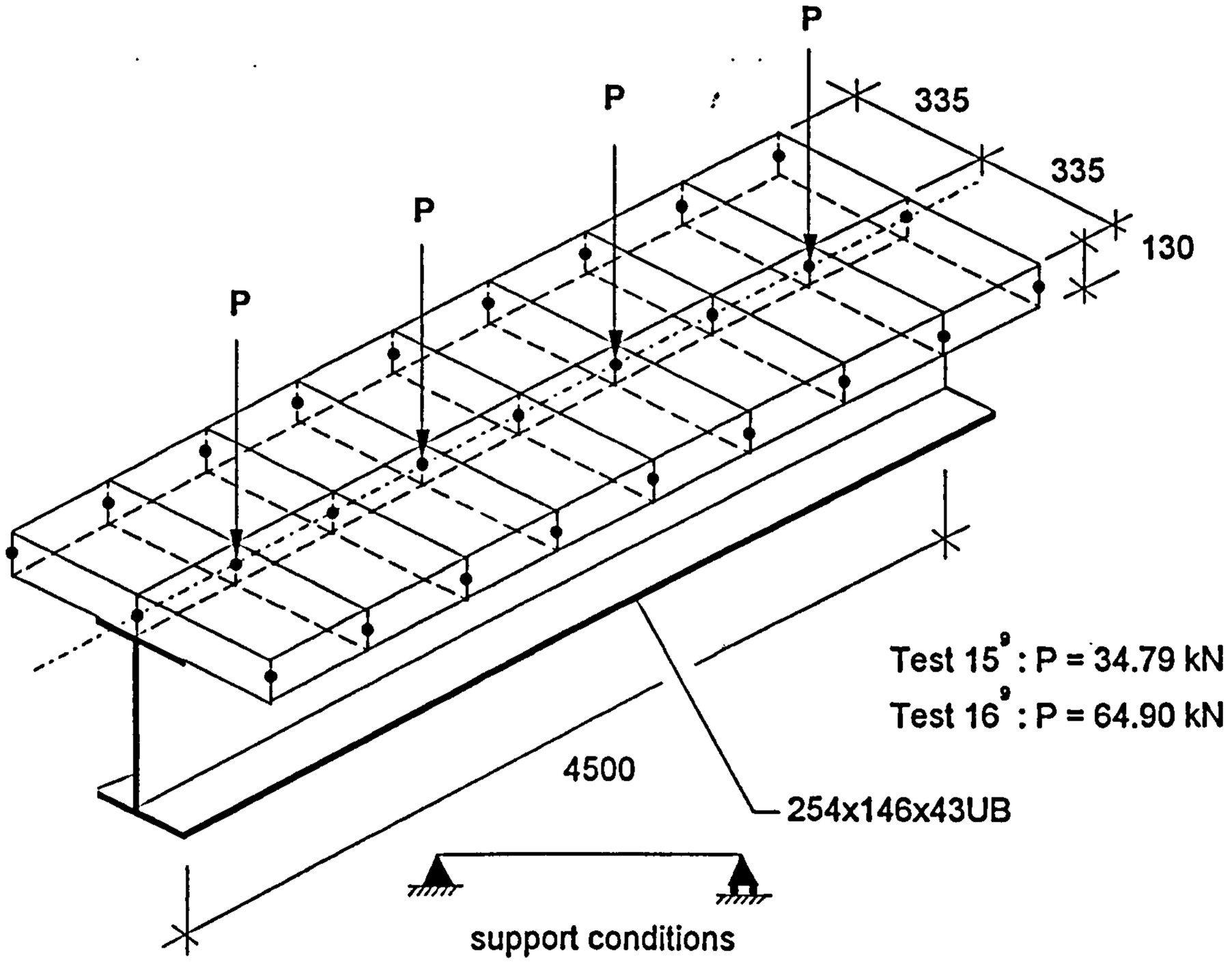

Fig. 6.19: Model of the simply-supported composite beam used in Test 15 and 16 presented in the Compendium of UK standard fire tests.

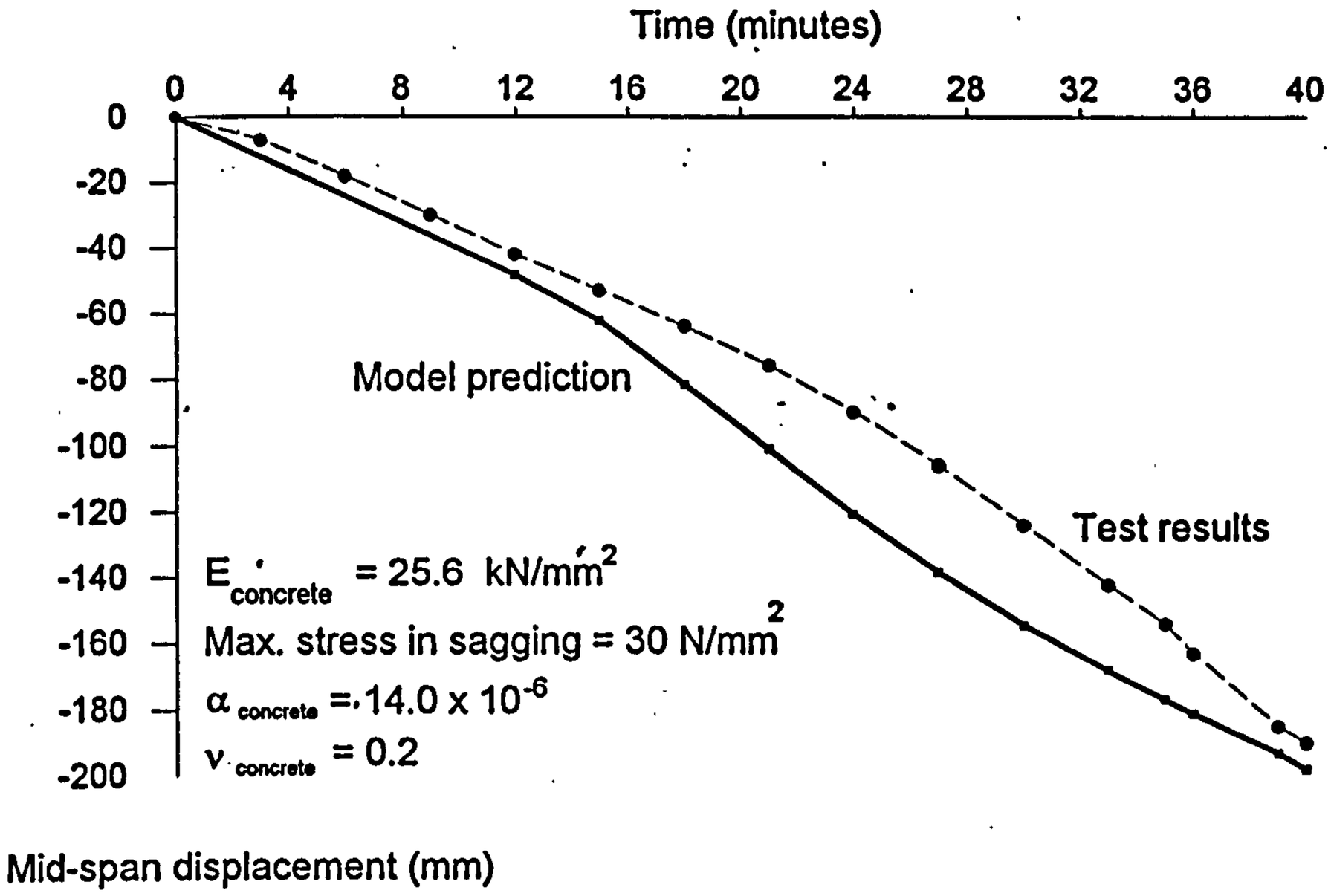

Fig. 6.20: Comparison between the model and test results for test 15.

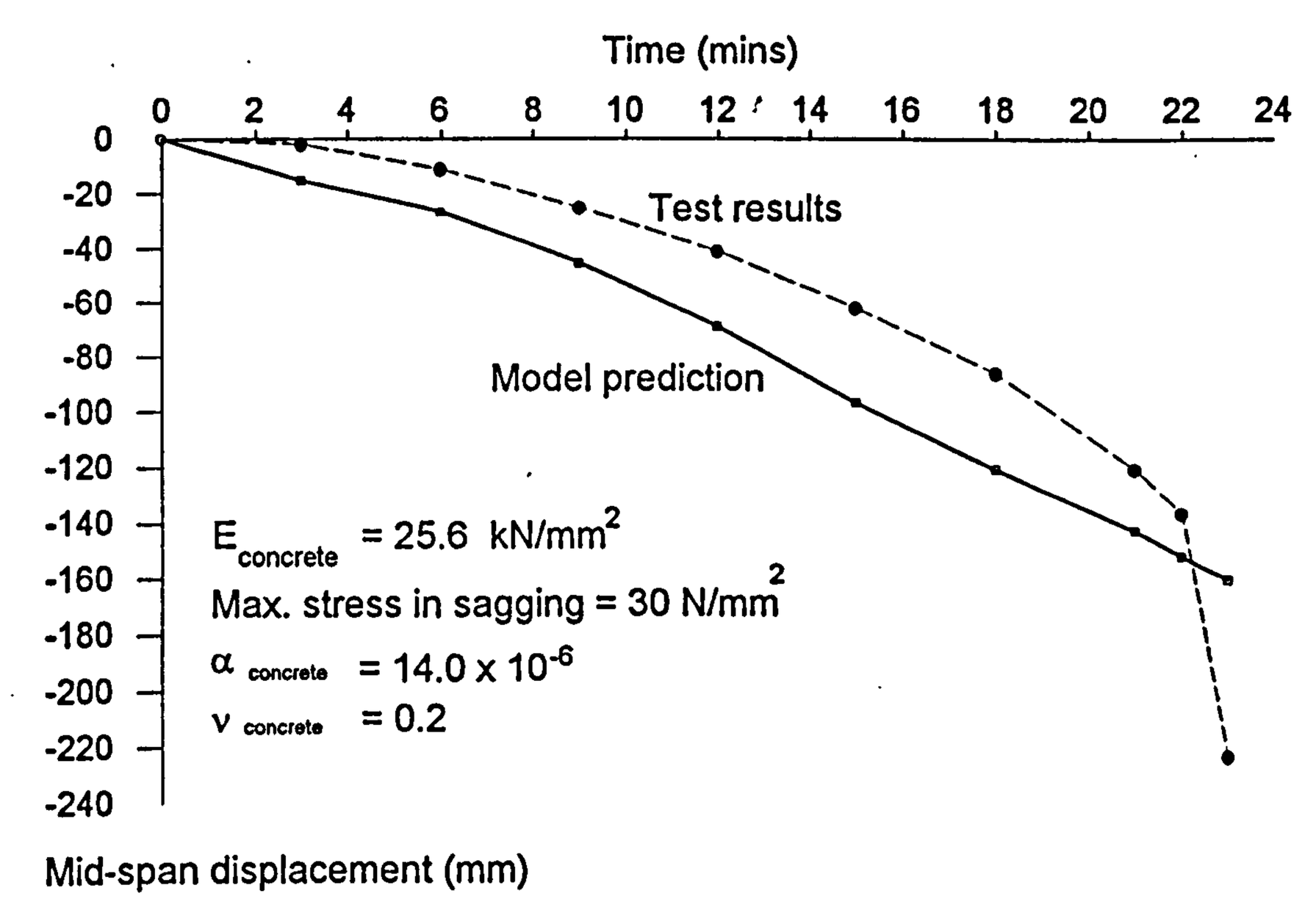

Fig. 6.21: Comparison between the model and test results for test 16.

Apart from the problems with slab assumptions discussed previously, other factors which may influence the correlation between the predictions and the test results are:

1. The beam was assumed to be simply-supported, whereas even the low levels of end-restraint which are often present in tests can have a significant effect.
2. The concrete properties were assumed. A future parametric study will be needed to investigate the effect of varying these properties.
3. The temperature in the concrete is assumed to be uniform and 10% of the value of the hottest part of the steel. The cooler and more uniform the temperature in the concrete, the greater the displacement due to thermal bowing.

It can be seen from the figures that the analysis predicts higher deflections than both sets of test results, apart from the very final stage of Test 16. This has been the case for most attempts to simulate furnace test deflections with different software[11,27], and it does seem that support conditions in furnace tests are affecting the measured results. In addition, the fact that the more highly loaded test appears to deflect less for about 13 minutes must cast some doubt on the reference positions from which deflections were measured. The basic correlation with Test 15 is excellent and, if the datum for Test 16 were adjusted accordingly the agreement is much improved.

Better correlation with the test results could have been obtained by assuming a more logical concrete temperature variation than the constant relationship of 10% of the exposed flange temperature. Such a variation might assume that the gradient of the concrete temperature rise is higher than has been assumed, but with a time-lag behind the steel temperature curve, and with a limit of 100°C. This would tend to reduce the amount of thermal bowing in the intermediate range of the test, but would give a more rapid weakening in the final stages.

The inclusion of shell elements into the model, allowing continuous floor systems to be modelled, will allow an investigation into the full-scale fire tests which are to be conducted on the Cardington frame. These analyses are discussed in Chapter 8.

7.0: THE BEHAVIOUR OF STEEL-FRAMED BUILDINGS DURING THE COOLING PHASE OF A FIRE.

Previous research work has mainly focused on the behaviour of steel-framed buildings up to a maximum temperature. This is either the temperature expected to be reached at the end of a specified time period, or the temperature at which structural failure occurs. Considering the latter in relation to actual buildings, the regulatory requirement of compartmentation[2] (which localises fires) together with the inherent high degree of redundancy in buildings, complete structural collapse is highly unlikely. Therefore it will be necessary to investigate the effect of the cooling phase of a fire on the behaviour of steel-framed buildings, so that once the structure has cooled down its permanent deformations, internal forces, residual strength and repairability can be assessed. Since the cooling phase can cause extensive strain reversal in the steel, its constitutive model will need to be extended to incorporate this.

7.01 STRESS-STRAIN RELATIONSHIP.

The constitutive model used to represent the uniaxial stress-strain relationship is based on a Ramberg-Osgood type of expression[11], given by

$$\varepsilon_T = \frac{\sigma_T}{A_T} + 0.01\left(\frac{\sigma_T}{B_T}\right)^{n_T} \qquad (7.01)$$

where,

ε_T = strain at temperature T,

σ_T = stress at temperature T,

A_T, B_T, and n_T are temperature-dependent constants shown in Table 7.1.

The constants, which are shown in Table 7.1, are based on a yield stress of 250 N/mm² and an elastic modulus of 180 kN/mm² for the steel. If these values are different then the constants are modified by multiplying A_T by a constant *'a'* and B_T by a constant *'b'*, which are given by

$$a = E_{20}/(180 \times 10^3)$$

$$b = \sigma_{y20}/250$$

The steel characteristics are assumed to be identical in tension and compression.

If the calculated strain values remain in the elastic region of the constitutive model and decrease in absolute value, then the loading and unloading paths are coincident. However if a decrease of absolute strain value occurs in the inelastic range then the loading and unloading paths separate, with the unloading path creating a hysteresis loop. Therefore to allow the unloading path to be defined the elastic and inelastic bounds need to be identified.

Temperature range (°C)	A_T	B_T	n_T
20 - 100	180×10^3	$0.00134T^2$ $-0.26T+254.67$	$237-1.58T$
100 - 400	$(194-0.14T)$ $\times1000$	242	$15.3\times10^{-7}\times$ $(400-T)^{3.1}+6$
400-700	$(295.33-$ $0.39333T)\times1000$	$492.667-0.6266T$	6
700-800	$(30.5-0.015T)$ $\times1000$	$306-0.36T$	$0.04T-22$

Table 7.01: Temperature-dependent constants used in the constitutive model of steel.

At elevated temperatures steel does not display a well defined yield point, which causes problems identifying the true elastic and inelastic bounds. It was therefore proposed that the yield point be defined by the 0.1% proof stress, which is shown schematically in Fig. 7.01.

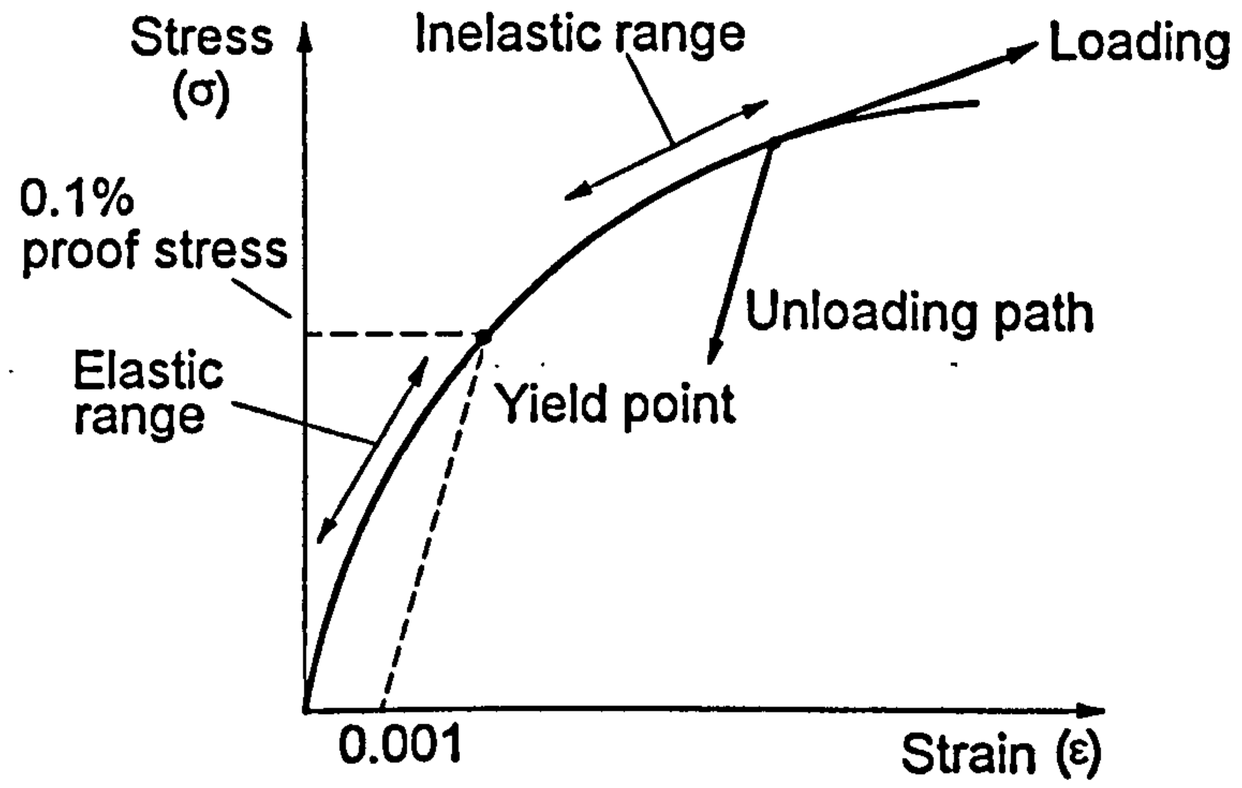

Fig. 7.01. Definition of elastic and inelastic bounds.

7.02: DEFINING THE UNLOADING HYSTERESIS LOOP

Once unloading is identified in the inelastic range the stress-strain path separates from the loading path, forming a hysteresis loop which returns tangentially to a position on the loading curve corresponding to the value of the original point (but of opposite sign) at which the loop left the loading curve (refer to Fig. 7.02). To define the unloading hysteresis loop Massing's hypothesis has been adopted[80], which is widely used for structural metals and corresponds well with observed experimental behaviour at ambient temperature. Massing's rule defines the hysteresis loop in unloading, from a point of strain reversal, '*as a curve which is formed by scaling the loading curve (also known as the skeleton curve) by a factor of 2*'. This is shown schematically in Fig. 7.02.

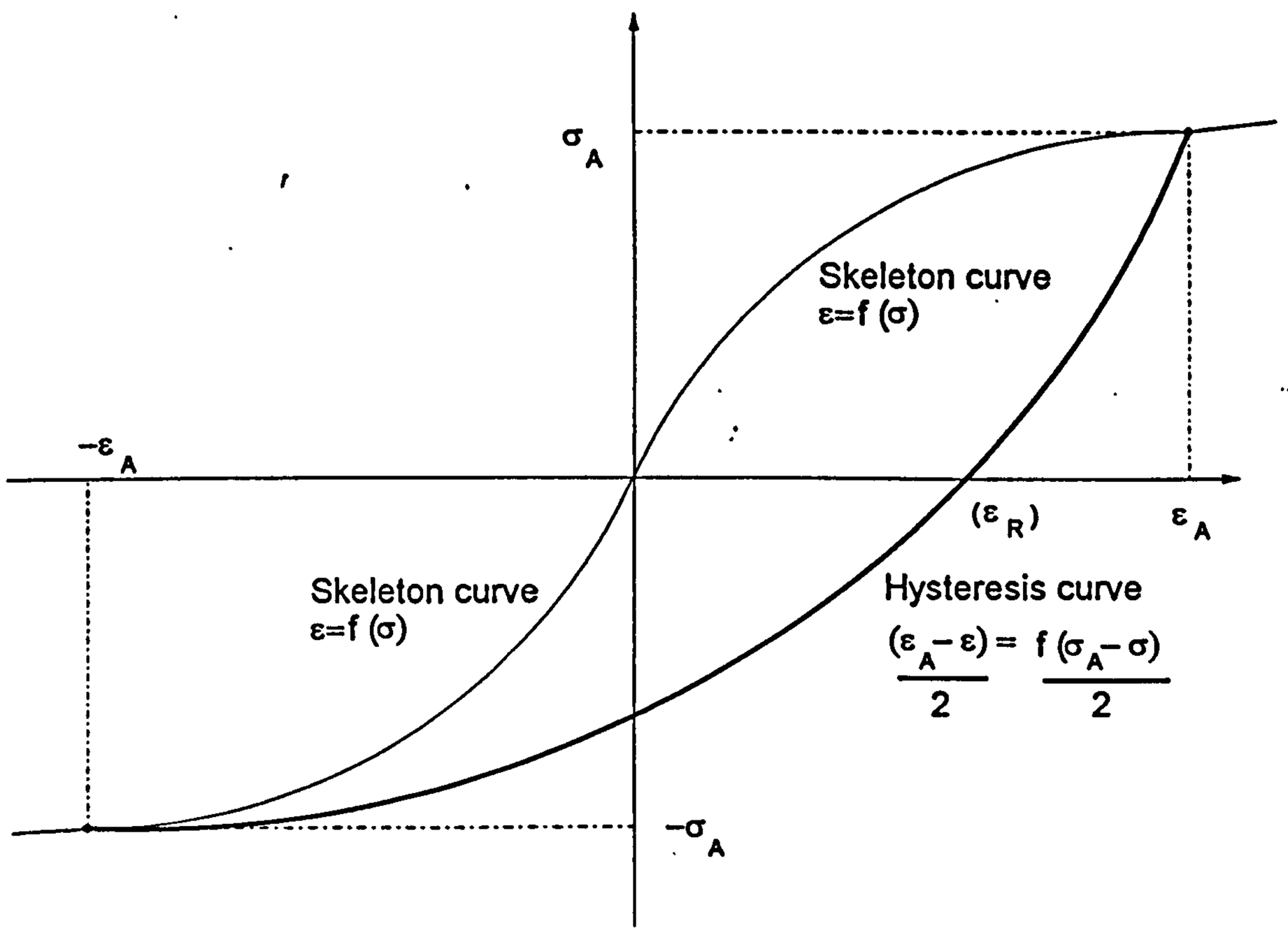

Fig. 7.02: Definition of loading and unloading curves.

7.03: IDENTIFYING UNLOADING DURING THE ANALYSIS.

As discussed in Chapter 2, the state of displacement, strain and stress is defined through the cross-section at integration (Gauss) Points. Due to the limitation of placing external loads at nodal points only, the element is automatically split into three sub-elements along its length as shown in Fig. 7.03. Each of these sub-elements has

four Gauss points at which the displacements, strains and stresses are defined at thirteen points on the cross-section as shown in Fig. 7.04. The automatic sub-division of elements allows Gauss points to be clustered near to the nodal positions so that the onset of inelastic behaviour will be incorporated within the analysis as it occurs. A static condensation scheme is applied to form an element stiffness matrix, by eliminating internal degrees of freedom created by this sub-division.

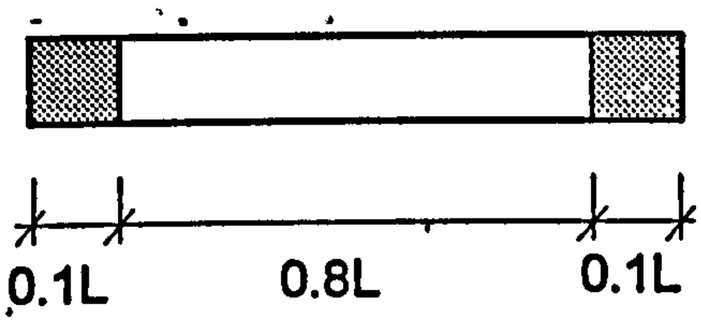

Fig. 7.03: Sub-division of elements

The mechanics of splitting the element into three sub-elements, each with four Gauss points, creates a total of 156 specific points per element at which displacements, and thus strain and stress, are defined. Due to the large number of strain values calculated per element it is imperative, due to limits on computer memory, that a method is adopted which records the loading/unloading history at each calculated strain point efficiently.

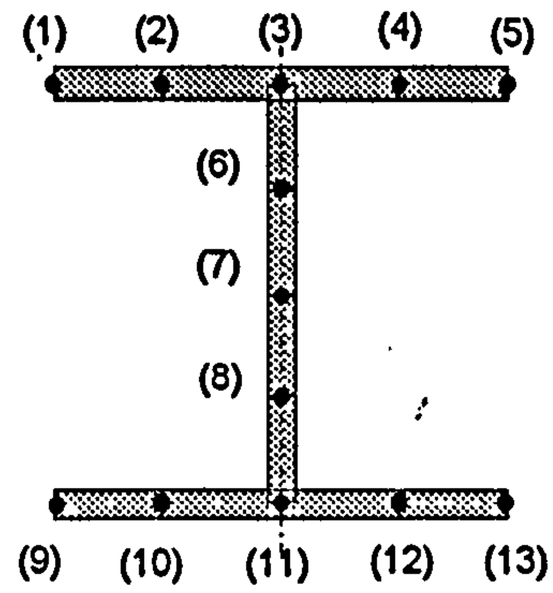

Fig. 7.04: Position on the cross-section at which displacements, strains and stresses are defined.

Within the bounds of the research presented here the generalised stress-strain history can be simplified by assuming that cyclic loading will not be encountered during the heating/cooling phase of the fire. Therefore the variables required to identify a unique stress-strain relationship for a specific temperature are greatly reduced. The procedure for defining this relationship is explained below:

Referring to Fig. 7.05, at temperature T_1 only 'loading' is encountered and equilibrium is reached at, $\sigma = \sigma_{AT1}$ and $\varepsilon = \varepsilon_{AT1}$. If a hysteresis loop is drawn from this equilibrium position it will cut the strain axis at a position which will, for ease of

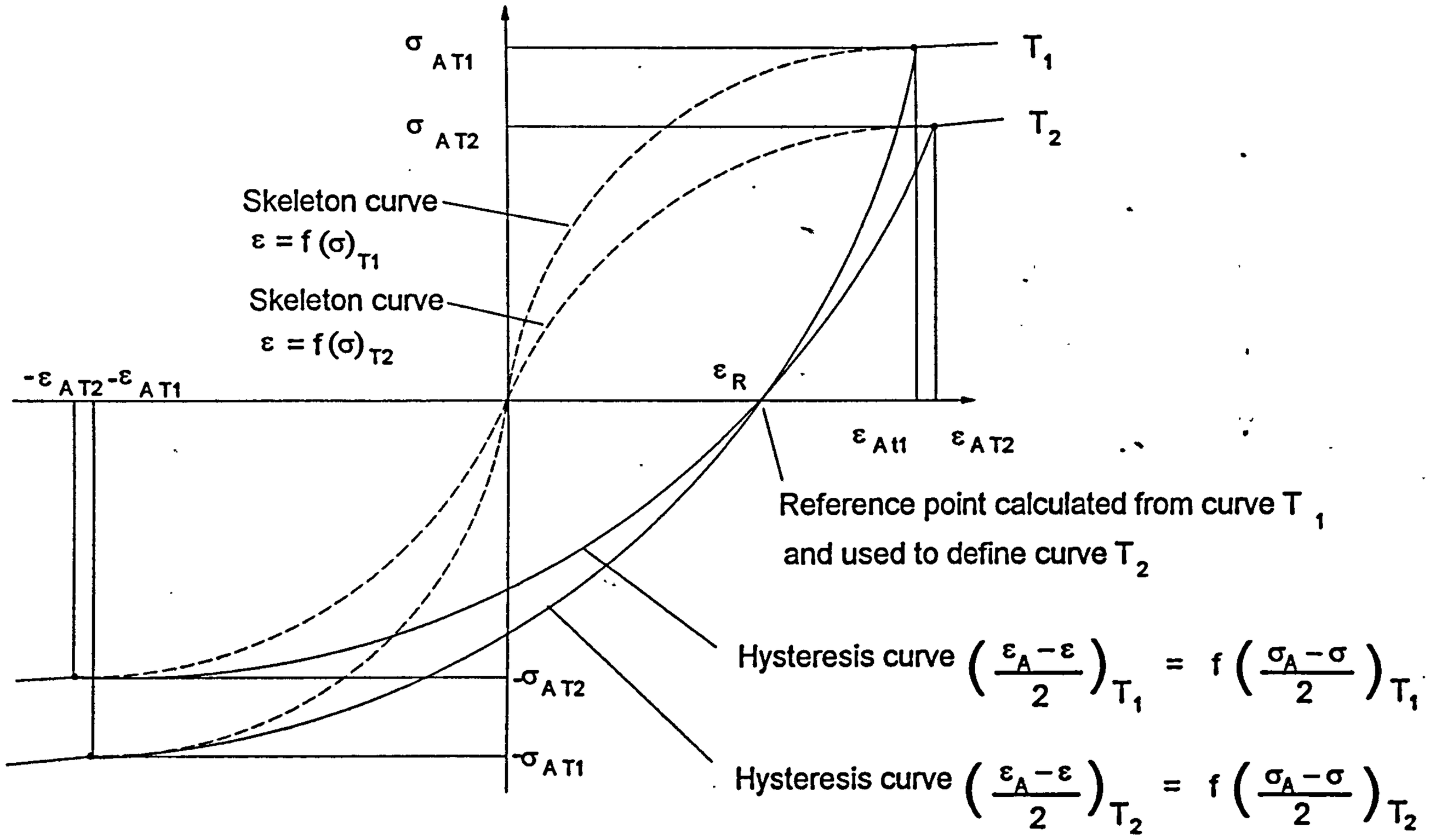

Fig. 7.05: Definition of the stress-strain model incorporating unloading for changes in temperature.

explanation, be termed the reference point. This reference point (ε_R) is stored and used to define the stress-strain model for the next temperature step T_2. This is achieved by positioning the hysteresis curve for temperature T_2 so that it intersects the strain axis at the reference point. Considering the analysis at temperature T_2 if the strain values are greater than ε_{AT2} then the skeleton curve is used and a new reference point is calculated from the equilibrium position. This indicates that loading has occurred and the absolute value of the reference point will increase. If the strain values are less than ε_{AT2} and greater than $-\varepsilon_{AT2}$ then the hysteresis curve is followed. When equilibrium is reached on the hysteresis curve the reference point remains unchanged for the next temperature step. Should the strains be less than $-\varepsilon_{AT2}$ then the skeleton curve is rejoined and the reference point re-calculated. The process of calculating the reference point is repeated for each temperature step during the analysis and used to define the stress-strain characteristics for the next temperature step.

For the mathematical process of defining the relationship shown in Fig. 7.05 consider first the equation of the hysteresis curve, given by

$$\left(\frac{\varepsilon_A - \varepsilon}{2}\right) = f\left(\frac{\sigma_A - \sigma}{2}\right) \tag{7.02}$$

where

ε_A = strain value at equilibrium when loading,

σ_A = stress value at equilibrium when loading.

Now at the reference point, $\varepsilon = \varepsilon_R$ and $\sigma = 0$

therefore

$$\left(\frac{\varepsilon_A - \varepsilon_R}{2}\right) = f\left(\frac{\sigma_A}{2}\right) \tag{7.03}$$

Expanding the function gives,

$$\frac{\varepsilon_A - \varepsilon_R}{2} = \frac{\sigma_A}{2A} + 0.01\left(\frac{\sigma_A}{2B}\right)^n \tag{7.04}$$

therefore,

$$\varepsilon_R = \varepsilon_A - \frac{\sigma_A}{A} - 0.02\left(\frac{\sigma_A}{2B}\right)^n \tag{7.05}$$

The reference point is calculated and stored when equilibrium is achieved for each analysis, so that it can be used to form a unique stress-strain relationship for the next temperature step. Therefore considering Fig. 7.05, for a new temperature step the reference point and the equations of both the loading and unloading curves are known. To allow the bounds of the unloading curve to be defined the intersection of the loading and unloading curves is required.

At the reference point, $\varepsilon = \varepsilon_R$ and $\sigma = 0$

therefore,

$$\left(\frac{\varepsilon_A - \varepsilon_R}{2}\right) = f\left(\frac{\sigma_A}{2}\right) \tag{7.06}$$

expanding the function gives,

$$\left(\frac{\varepsilon_A - \varepsilon_R}{2}\right) = \frac{\sigma_A}{2A} + 0.01\left(\frac{\sigma_A}{2B}\right)^n \tag{7.07}$$

$$\varepsilon_A = \frac{\sigma_A}{A} + 0.02\left(\frac{\sigma_A}{2B}\right)^n + \varepsilon_R \tag{7.08}$$

From the skeleton curve, when $\varepsilon = \varepsilon_A$ then $\sigma = \sigma_A$ and therefore,

$$\varepsilon_A = f(\sigma_A) \tag{7.09}$$

Expanding the function gives,

$$\varepsilon_A = \left(\frac{\sigma_A}{A}\right) + 0.01\left(\frac{\sigma_A}{B}\right)^n \tag{7.10}$$

Substituting equation (7.10) into equation (7.08) produces

$$0.02\left(\frac{\sigma_A}{2B}\right)^n - 0.01\left(\frac{\sigma_A}{B}\right) + \varepsilon_R = 0 \tag{7.11}$$

An iterative method is required to solve equation (7.11), for σ_A (the intersection of the loading and unloading curves) and the Newton-Raphson method was adopted, where

$$\sigma_{A_{n+1}} = \sigma_{A_n} - \frac{f(\sigma_A)_n}{f'(\sigma_A)_n} \tag{7.12}$$

in which,

$$f(\sigma_A)_n = 0.02\left(\frac{\sigma_A}{2B}\right)^n - 0.01\left(\frac{\sigma_A}{B}\right)^n + \varepsilon_R \qquad (7.13)$$

and

$$f'(\sigma_A)_n = 0.02n\left(\frac{\sigma_A}{2B}\right)^{n-1}\frac{1}{2B} - 0.01n\left(\frac{\sigma_A}{B}\right)^{n-1}\frac{1}{B} \qquad (7.14)$$

Once σ_A is obtained ε_A can be calculated from,

$$\varepsilon_A = \frac{\sigma_A}{A} + 0.01\left(\frac{\sigma_A}{B}\right)^n \qquad (7.15)$$

7.1: INDICATIVE STUDY OF THE BEHAVIOUR OF STEEL MEMBERS AND SUB-FRAMES DURING THE COOLING PHASE OF A FIRE.

7.11: SIMPLE BEAMS.

The simply supported beam shown in Fig. 7.06, with a load ratio of 0.5 (as defined in BS5950 Part 8[5]), was uniformly heated up to 630°C and then uniformly cooled down to 20°C, with only two-dimensional behaviour considered. At 630°C a vertical displacement at mid-span of 294 mm was calculated, which corresponds closely to span/20. This temperature is higher than the failure temperature specified in BS5950 Part 8. This was shown to be the general case for this type of loading condition in Chapter 5, Fig. 5.12. These results concluded that the BS5950 failure temperatures are conservative when considering uniform heating of simple two-dimensional restrained beams with a point load at mid-span.

As shown in Fig. 7.07, a permanent displacement of 259 mm was predicted at ambient temperature. Since no experimental data exists at the present time for the cooling behaviour of steel members it is impossible to validate the computer analysis in predicting this type of behaviour. However the results produced for this simple beam appear plausible, within the context of elementary structural theory.

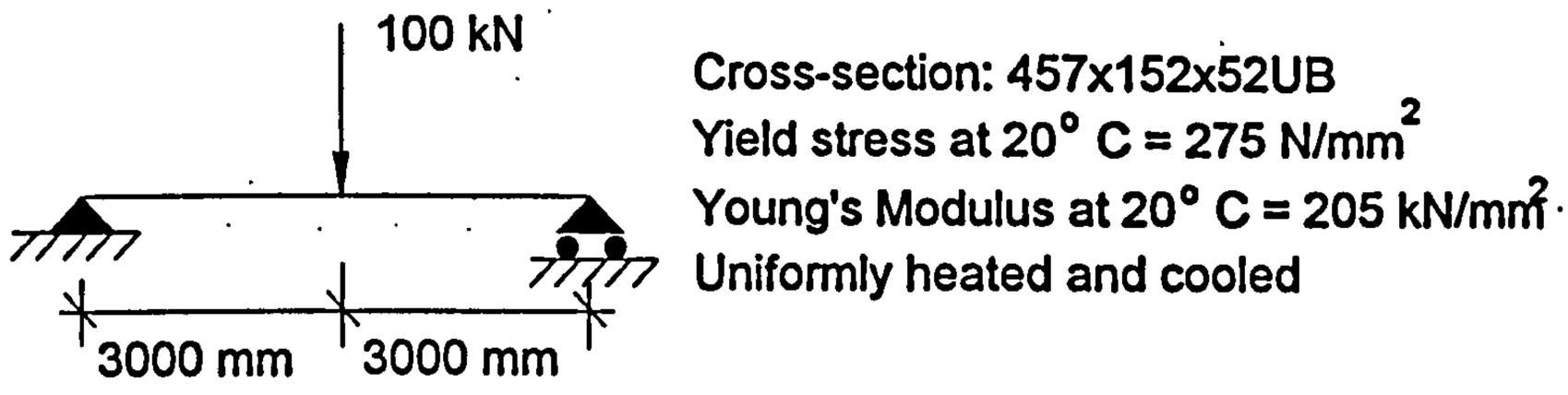

Fig. 7.06: Simply-supported beam used to investigate permanent deformation after a fire.

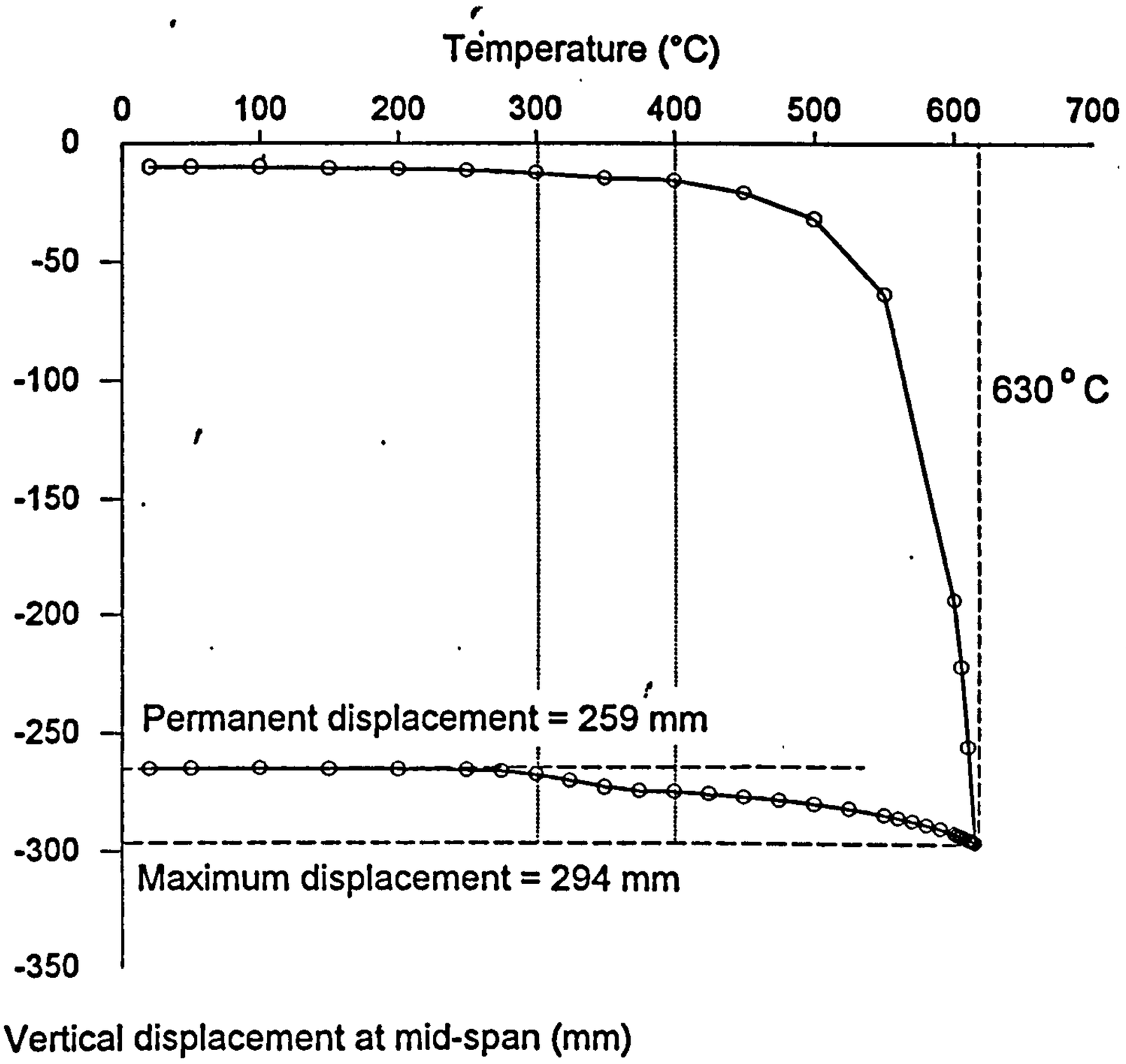

Fig. 7.07: Vertical displacement at mid-span of the simply-supported beam shown in Fig. 7.06 during the heating and cooling phases of a fire.

From Fig. 7.07 it can be seen that a very slight discontinuity in the smoothness of the unloading displacement curve occurs between 400°C and 300°C. To investigate this behaviour the mechanical strain values, together with the maximum reference point (strain), were recorded from the analysis at the centre of the bottom flange of the beam beneath the position of the point load (or more accurately the nearest Gauss point to the node at which the load is applied). The reference strain was recorded as 0.05 at this specific point at the maximum temperature. The unique stress-strain

relationship for this location within the steel beam is shown in Fig. 7.09 together with the actual recorded strain values at temperatures of 500, 400, 300 and 200°C. It can be seen that the change in stiffness between 500 and 400°C and also between 300 and 200°C is small compared to the change in stiffness between 400 and 300°C. This increase in the rate of change of stiffness between 400 and 300°C will cause the discontinuity highlighted in the temperature-displacement relationship during the cooling phase.

7.12: GOAL-POST FRAMES.

When all the members in the two-dimensional frame shown in Fig. 7.08 were uniformly heated the analysis predicts failure at 684.8°C by in-plane buckling of the columns. Therefore to investigate both the heating and cooling phases of the frame the temperature was increased to 680°C and then cooled uniformly to 20°C.

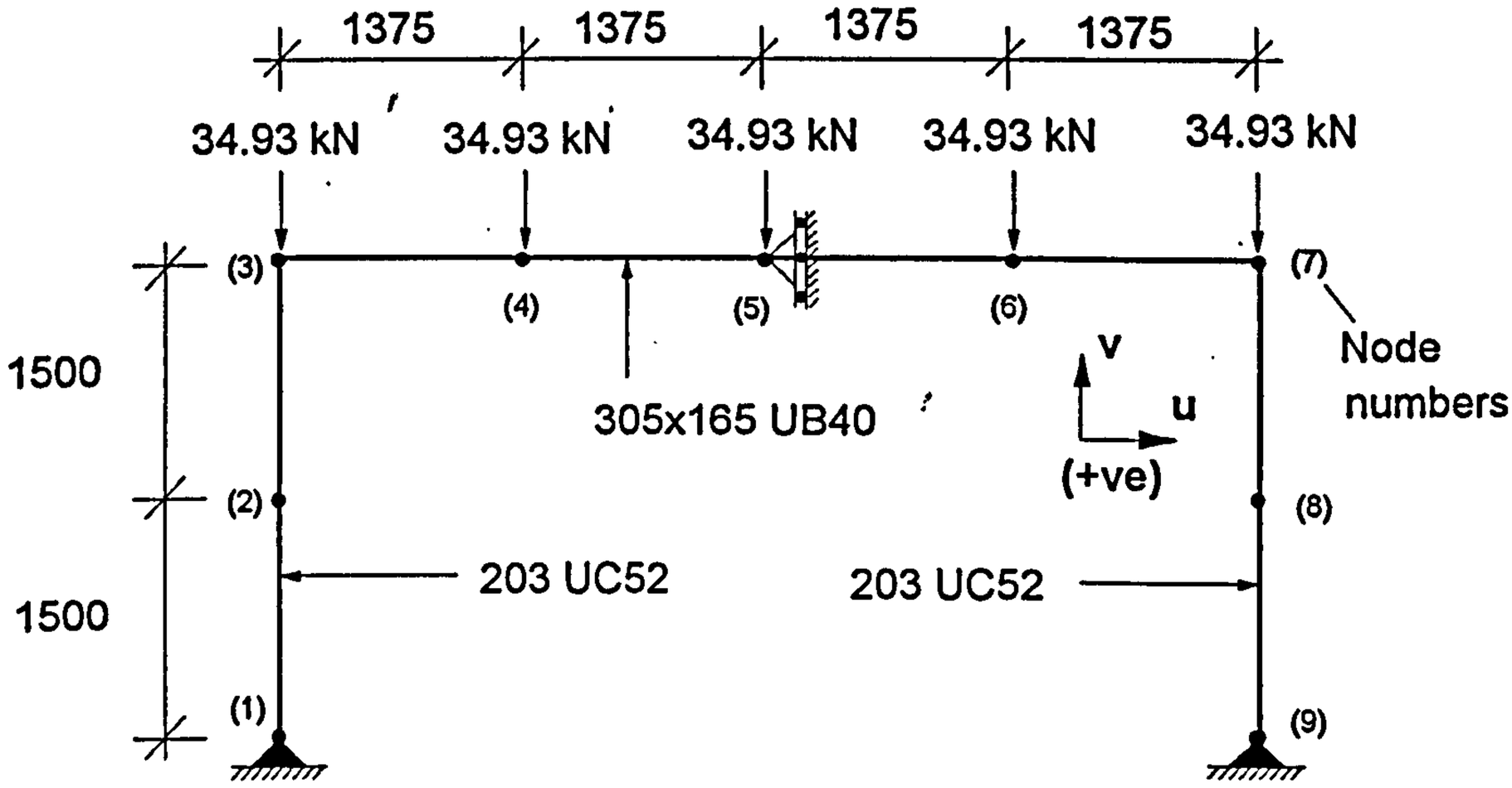

All dimensions are in mm
All members are uniformly heated
Out-of-plane displacements are restrained.
Load ratio of the beam = 0.56

Cross-section: 457x152x52UB
Yield stress at 20° C = 275 N/mm^2
Young's Modulus at 20° C = 205 kN/mm^2
Uniformly heated and cooled

Fig. 7.08: Goal-post frame used to investigate cooling behaviour.

Permanent strain values at the centre of bottom flange at point load position

Temperature (°C)	Strain value
500	0.052787
400	0.052329
300	0.051012
200	0.050651

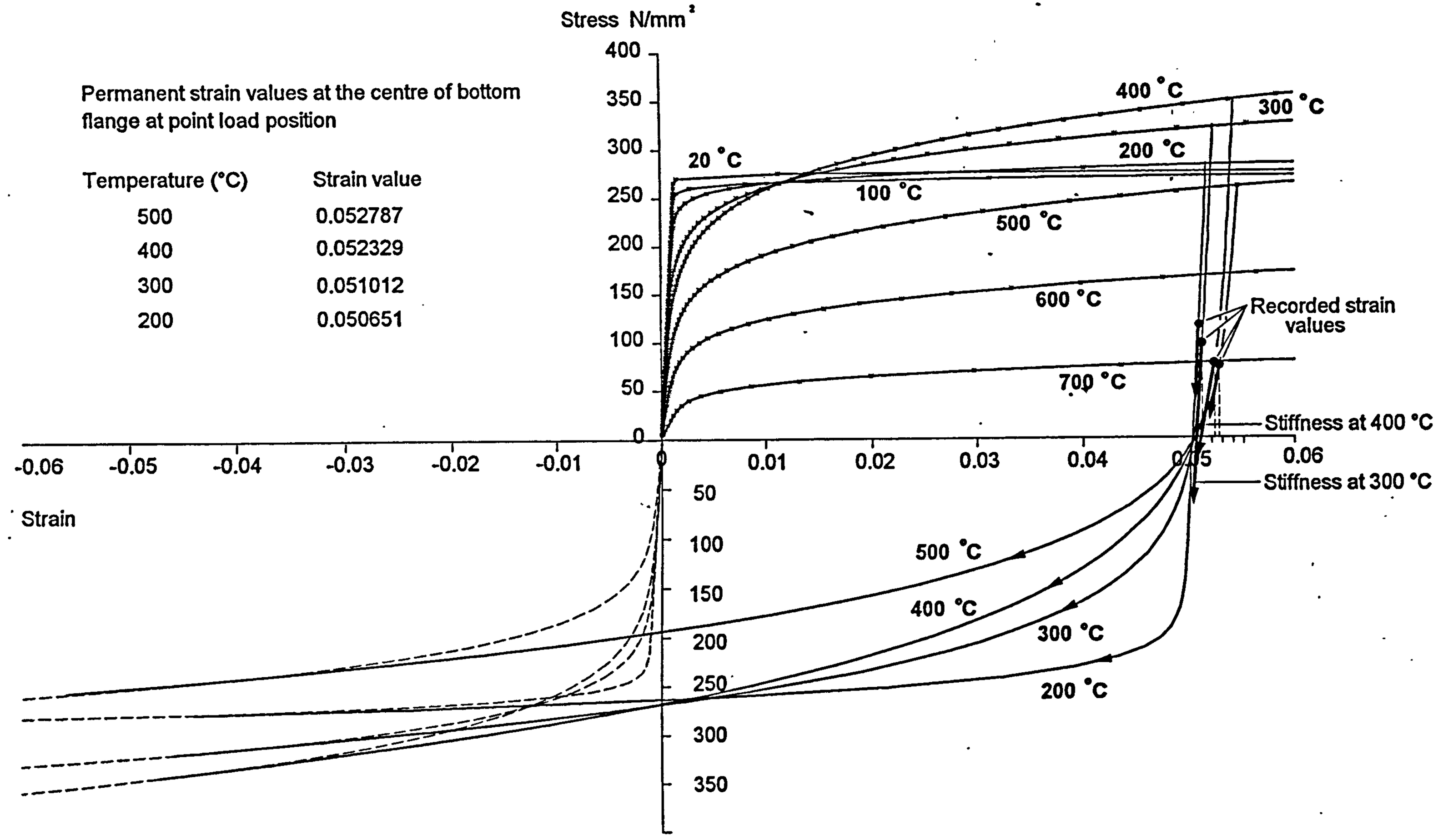

Fig. 7.09: Unique stress-strain relationship for one point (centre of bottom flange at load position) within the beam element.

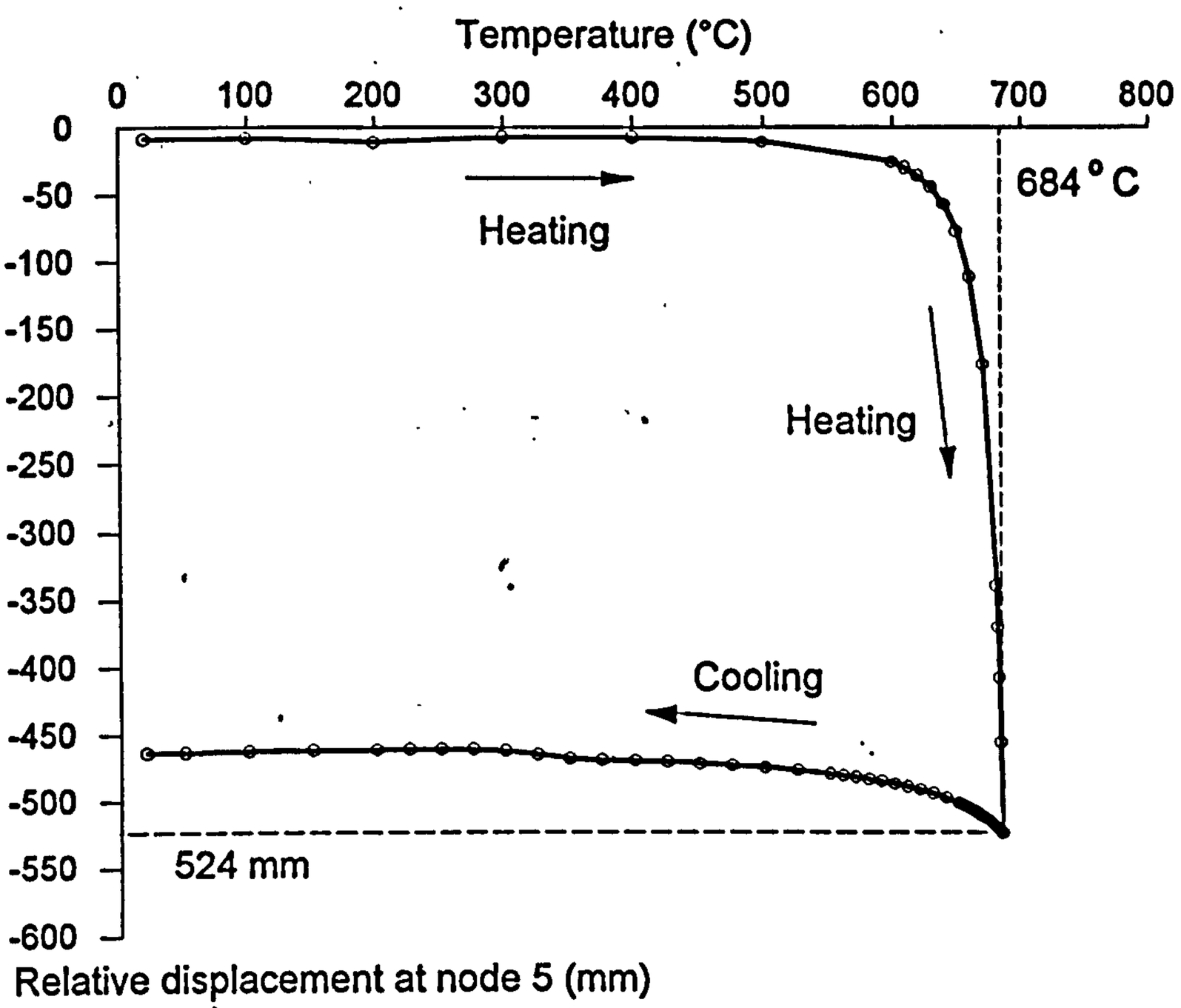

Fig. 7.10: Relative displacement at node 5.

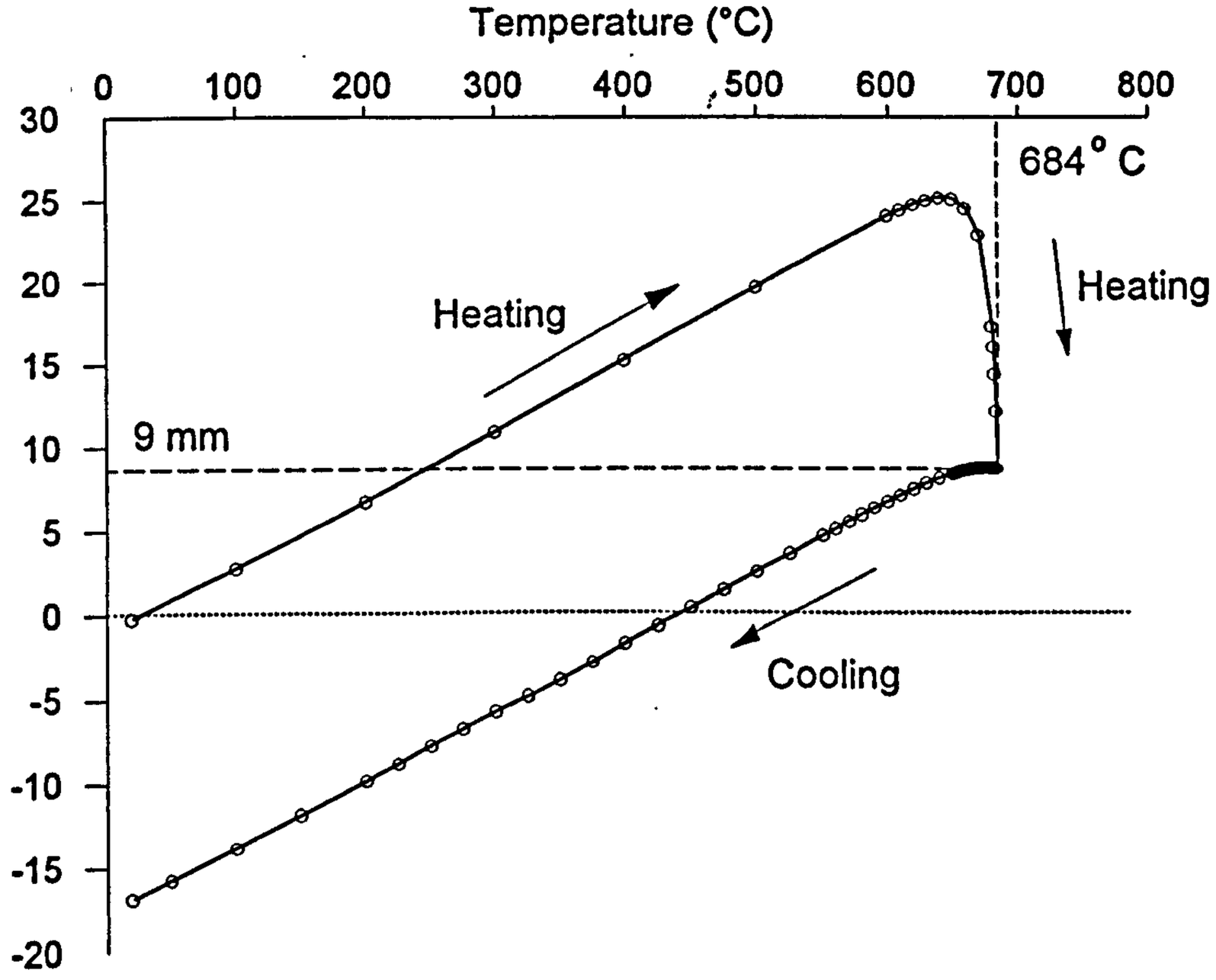

Fig. 7.11: Vertical displacement at node 3.

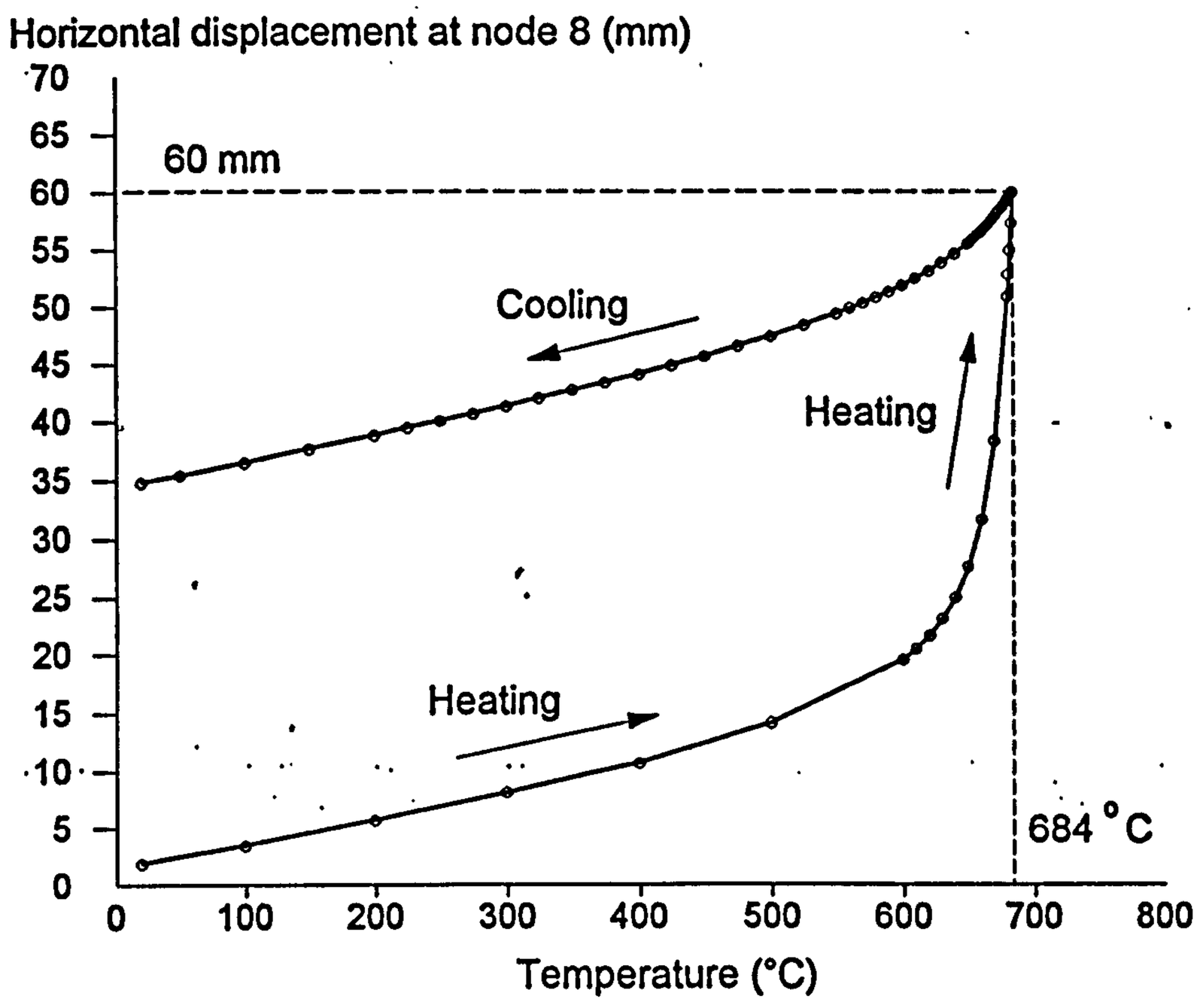

Fig. 7.12: Horizontal displacement at node 8.

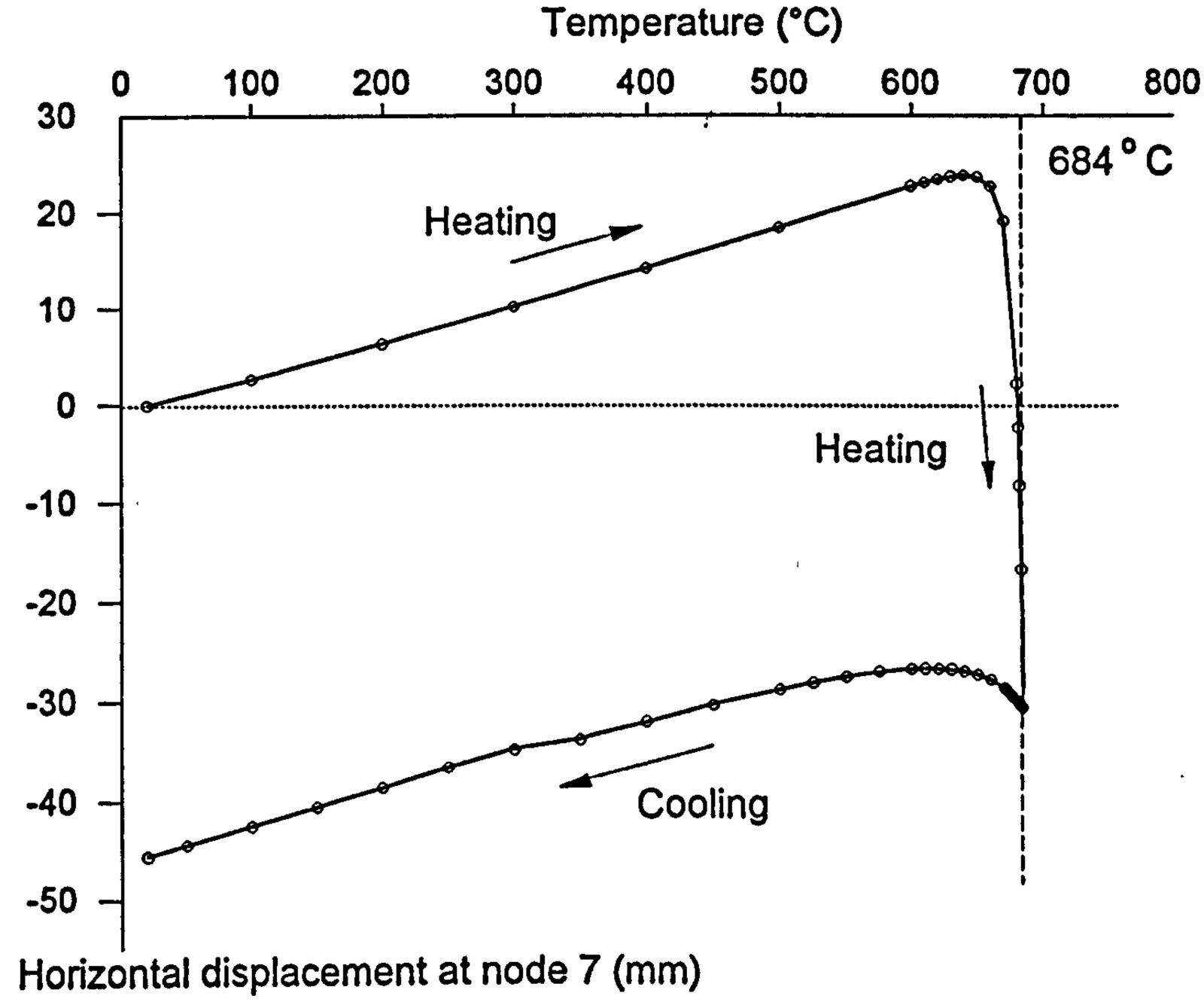

Fig. 7.13: Horizontal displacement at node 7

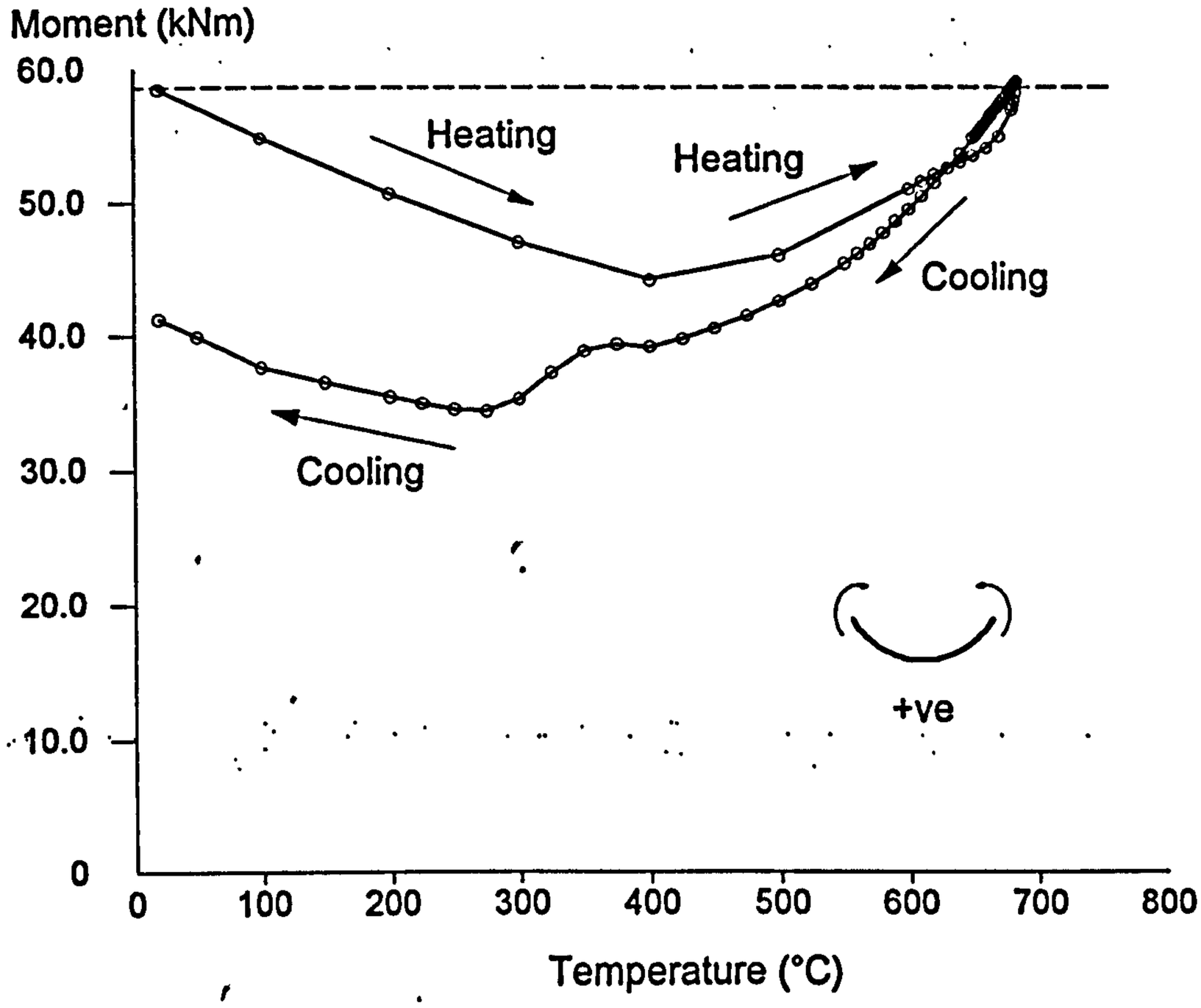

Fig. 7.14: Bending moment at centre of beam (node 5).

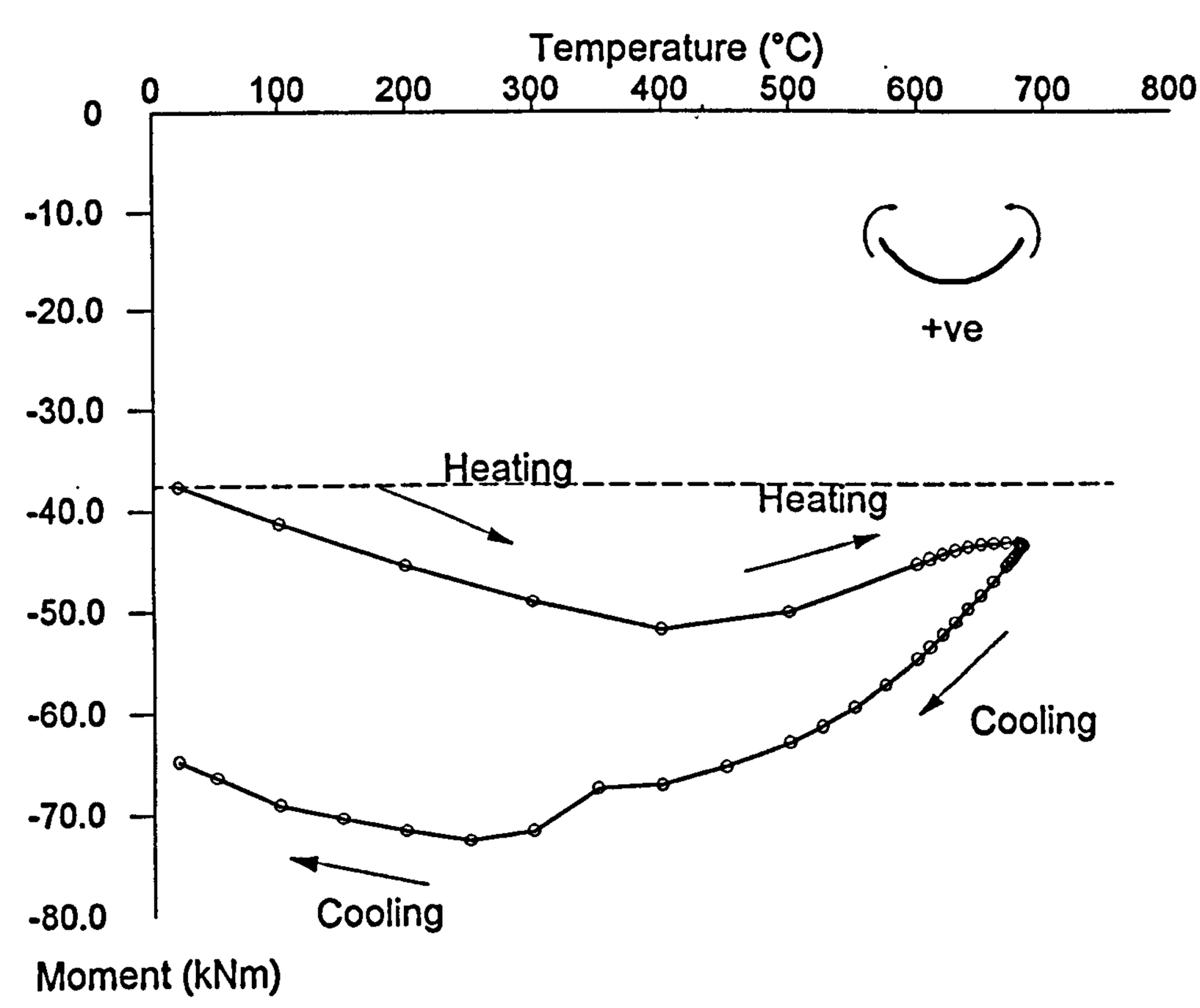

Fig. 7.15: Bending moment just to the left of node 7.

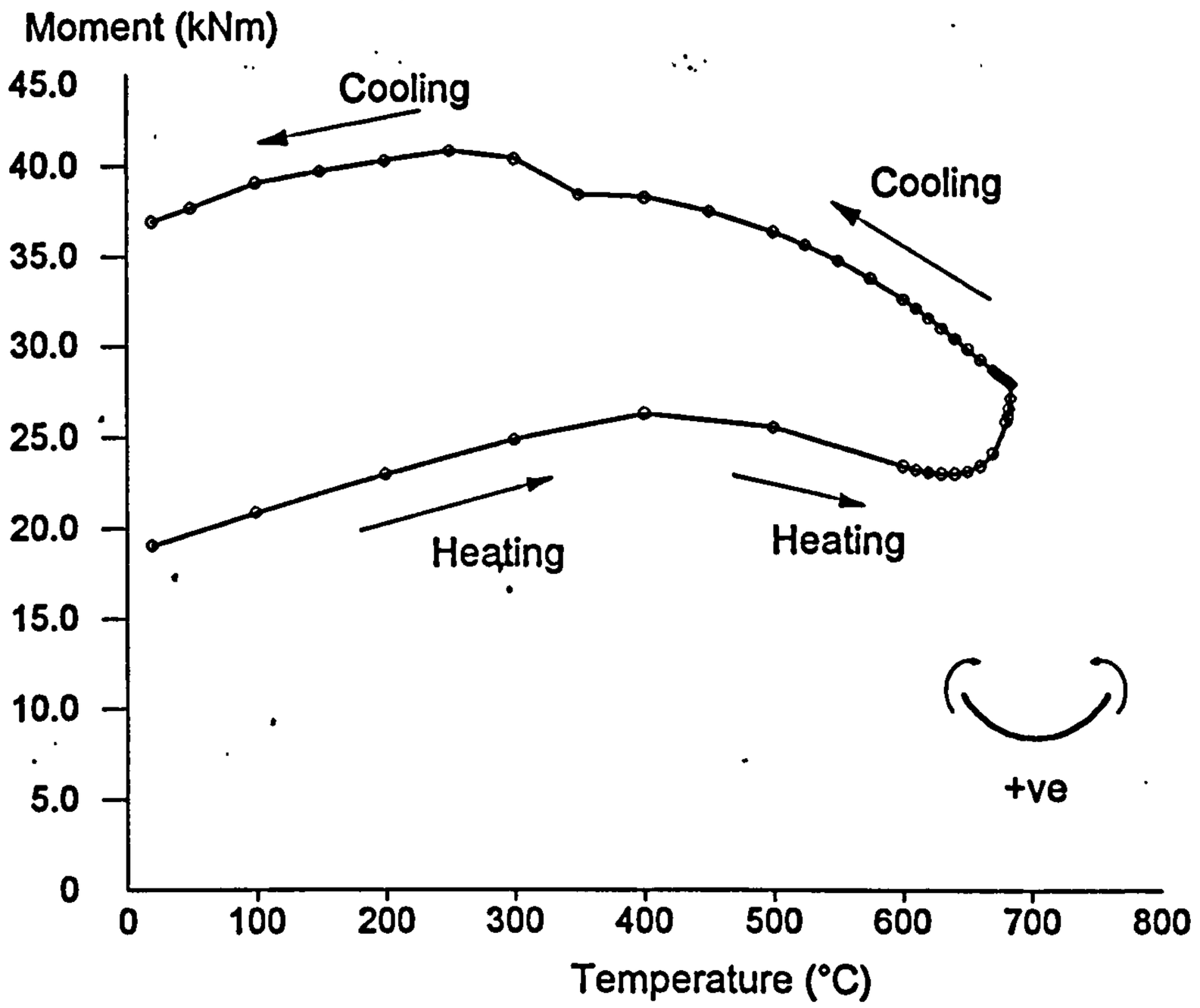

Fig. 7.16: Bending moment at mid-span of the column (node 8).

Shown in Figs. 7.10 to 7.13 are temperature-displacement relationships for the frame during the heating and cooling phases. From Figs. 7.12 and 7.13 it can be seen that at a temperature of 684°C failure is imminent, with a positive displacement of node 8 and a negative displacement of node 7, indicating that the frame is collapsing inwards. The permanent deformations when the frame is cooled down to 20°C are fairly large indicating areas of high plasticity (as expected) and seem reasonable.

Figs. 7.14 to 7.16 show temperature-bending moment relationships of the frame, with the moments being measured at the reference axis which is at the section's centroid at ambient temperature (since uniform heating is adopted the position of the centroid remains constant during the rise in temperature). Before the heating and cooling phases the mid-span moment in the beam was 58.5 kNm, with the beam end-moment being -37.6 kNm, which gives a free-moment of 96.1 kNm. As the beam is heated the mid-span moment is re-distributed to the column until a temperature of 400°C is reached. Above this temperature, due to the continuing degradation of strength and stiffness in the column, which can no longer support this re-distributed moment, the hogging moment in the beam decreases causing the mid-span moment to increase. After cooling the bending moment at mid-span of the beam is 41.3 kNm, with the beam end bending moment being -64.9 kNm, which gives an extra 10.2 kNm above the beam's free-moment. This is due to the P-δ effect in the beam. At the end of the

analysis a permanent axial force of 22.6 kN was predicted in the beam with a permanent vertical deformation at mid-span of 480.1mm. This will produce a secondary moment of 10.85 kNm, which compares well with the extra 10.2 kNm in the beam's free-moment.

7.13: EXTENSIVE TWO-DIMENSIONAL FRAMES.

Shown in Fig. 7.17 is a large two-dimensional frame with a simulated local fire. The example is fictitious since it is highly unlikely that a fire will be contained to such a small area. However the purpose of the example is to investigate the restraining effect on the heated members from the surrounding cold structure during the heating and cooling phases of the fire. If the members indicated were heated continuously then failure would occur by in-plane buckling of the columns at 606.7°C. Therefore the sequence of heating and cooling phases was defined as 20°C to 606°C to 20°C, with all elements heated uniformly and at the same rate.

Figs. 7.18 to 7.21 show temperature-displacement relationships during the heating and cooling phases for both the heated beam and columns. Fig. 7.20, which shows the horizontal displacement at the mid-height of the column, indicates that at 606°C failure is imminent due to in-plane buckling of the columns. During the heating phase, between 500°C and 580°C, the mid-height column displacements reverse direction, and this can be explained by considering the horizontal displacement at the heated beam-to-column connection (Fig. 7.21). Up to 400°C thermal expansion of the beam is the main component contributing to the horizontal displacement at the top of each of the heated columns. Above this temperature the vertical displacement of the heated beam begins to pull the top of the heated column inwards, and this influences the displacement at the mid-height of the column. Beyond 580°C, until cooling commences, the column's in-plane buckling behaviour becomes the dominant effect, as can be seen by the large increase in absolute horizontal mid-span displacements.

The axial forces induced in the heated beam during the heating and cooling phases are shown in Fig. 7.22. From Fig. 7.21 it can be seen that thermal expansion of the beam causes it to push outwards during the heating phase, with the restraint of the cold surrounding structure inducing a compressive axial force in the beam which increases until 500°C. Above this temperature, until 606°C, the compressive axial force decreases due to the sudden increase in vertical displacement of the beam (Fig. 7.18) caused by the continuing degradation of its strength and stiffness. Once cooling commences the heated members begin to regain strength and stiffness (from

an inelastic state), together with a reduction in thermal strains. This causes the axial force in the beam to become tensile due to the cooling beam pulling on the surrounding structure. After complete cooling the beam has a residual tensile force of 101.5 kN, which could be significant when considering localised tensile failure of the connections. This type of failure was found in flexible end connections following the Broadgate Phase 8 fire[81] and was also witnessed by the author following cooling in the first fire test conducted on the full-scale test frame at Cardington. However it should be appreciated that this is not necessarily catastrophic, since failure of all the bolts in the connection is not instantaneous. As each bolt fails (the order being dependent on the individual strength) the tensile force in the beam is partly relieved, due to strain relief caused by deformation of the end-plate, until the remaining bolts can withstand and equilibrate the induced tensile force. In some cases the bolts may not necessarily be the weak link, with failure of the welds, or the heat affected zone of the plate, occurring first as witnessed at the Cardington fire test. In the investigation following the Broadgate fire it was found that other connections, which consisted of double angle-cleats bolted through the beam web and to supporting members, accommodated axial movement by deforming the connecting cleats. This leads to the conclusion that the most favourable connection in fire conditions will be seating cleats, so that on cooling either the locating bolts will shear or the cleat material deform, allowing axial movement but still retaining vertical support.

The axial force in the heated columns is shown in Fig. 7.23. During the heating phase this force increases due to the vertical restraint from the structure above the fire compartment. As the temperature of 606°C is approached the column's axial force reduces, due to the squashing and in-plane buckling of the column, which will relieve the induced axial force caused by the restraint to thermal expansion. At the end of the heating phase the axial force approaches a value similar to that calculated at the start of the analysis, which corresponds to the applied load. On cooling the axial force continues to reduce, due to the relaxation of thermal stresses coupled with an increase in the strength and stiffness of the column.

During the analysis the steel members which became inelastic were identified and are shown in Fig. 7.17. It is hoped that future work on localised fires can be conducted using sub-frames with elastic restraints at the boundary conditions which represent the surrounding structure. This will require two analyses, the first consisting of calculating the elastic restraint from the surrounding structure and the second consisting of an elevated temperature analysis on the sub-frame. This method will typically reduce the computer run-time required for the full-frame analysis.

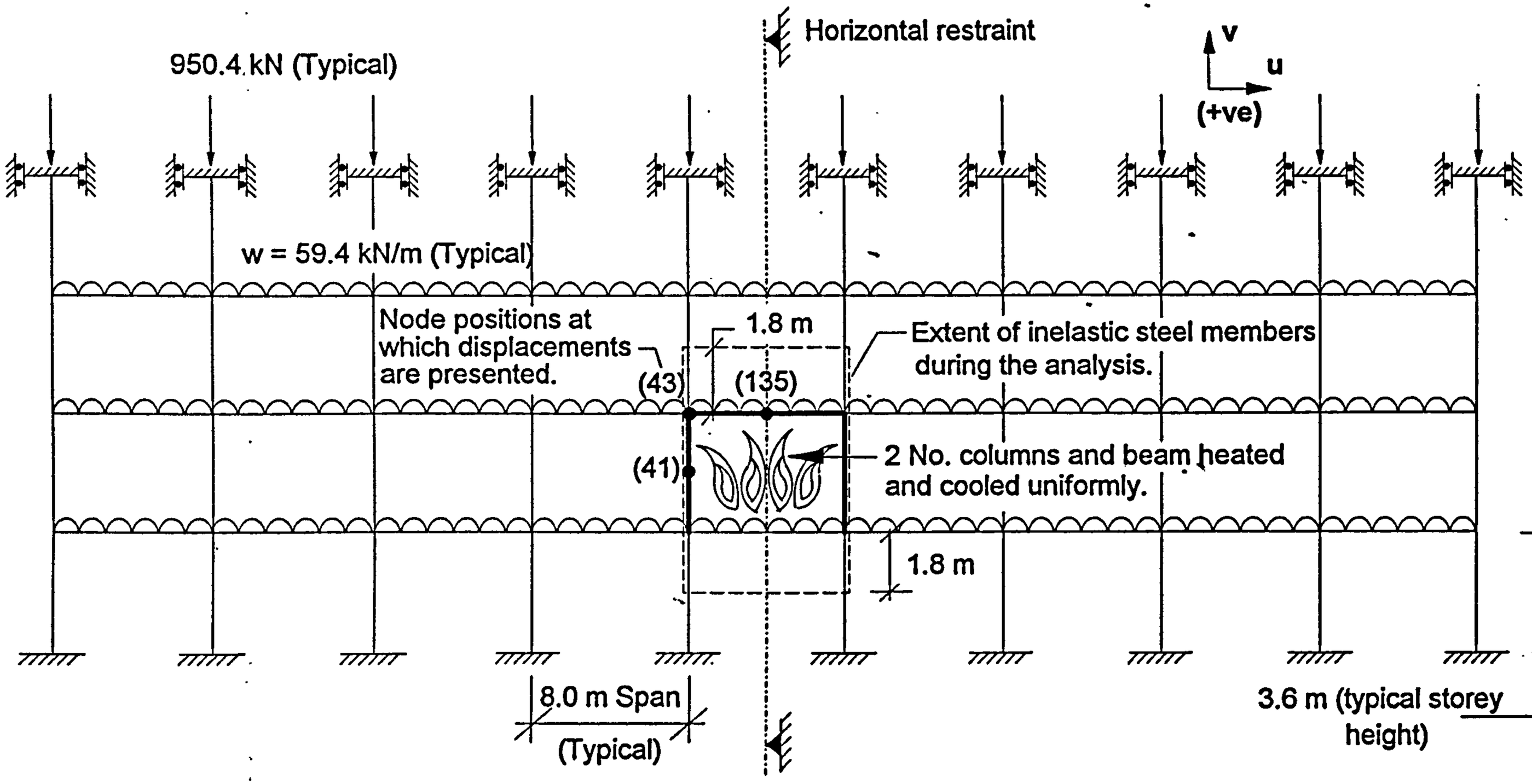

All beams 610x229x101UB : Load ratio =0.6
All columns 254x254x132UC : Load ratio = 0.45 (internal)

Yield stress at 20° C = 275 N/mm^2
Young's Modulus at 20° C = 205 kN/mm^2

Fig. 7.17: Two-dimensional frame used to investigate restraint to localised fires during the heating and cooling phase.

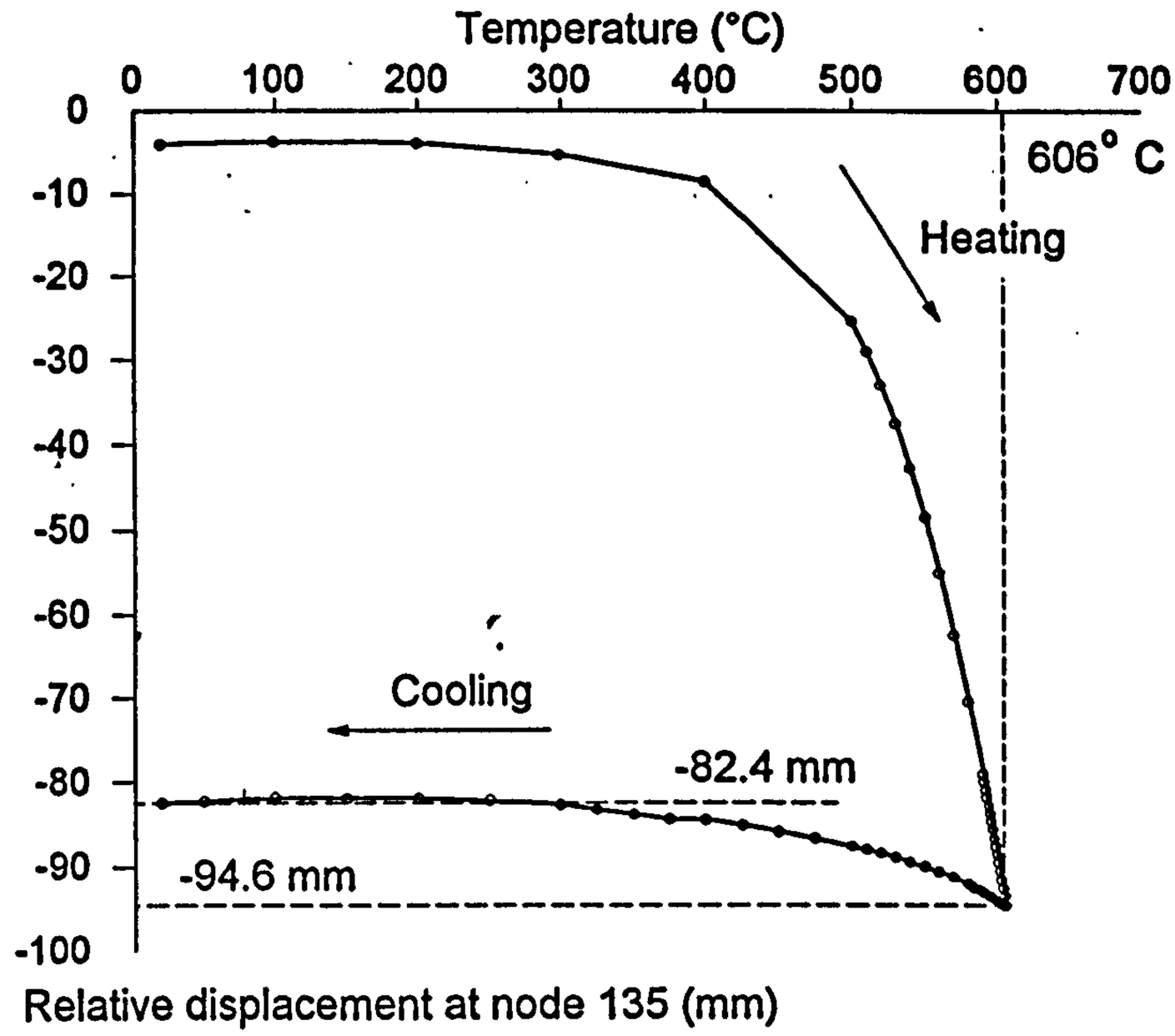

Fig. 7.18: Relative displacement at node 135 (mid-span of heated beam)

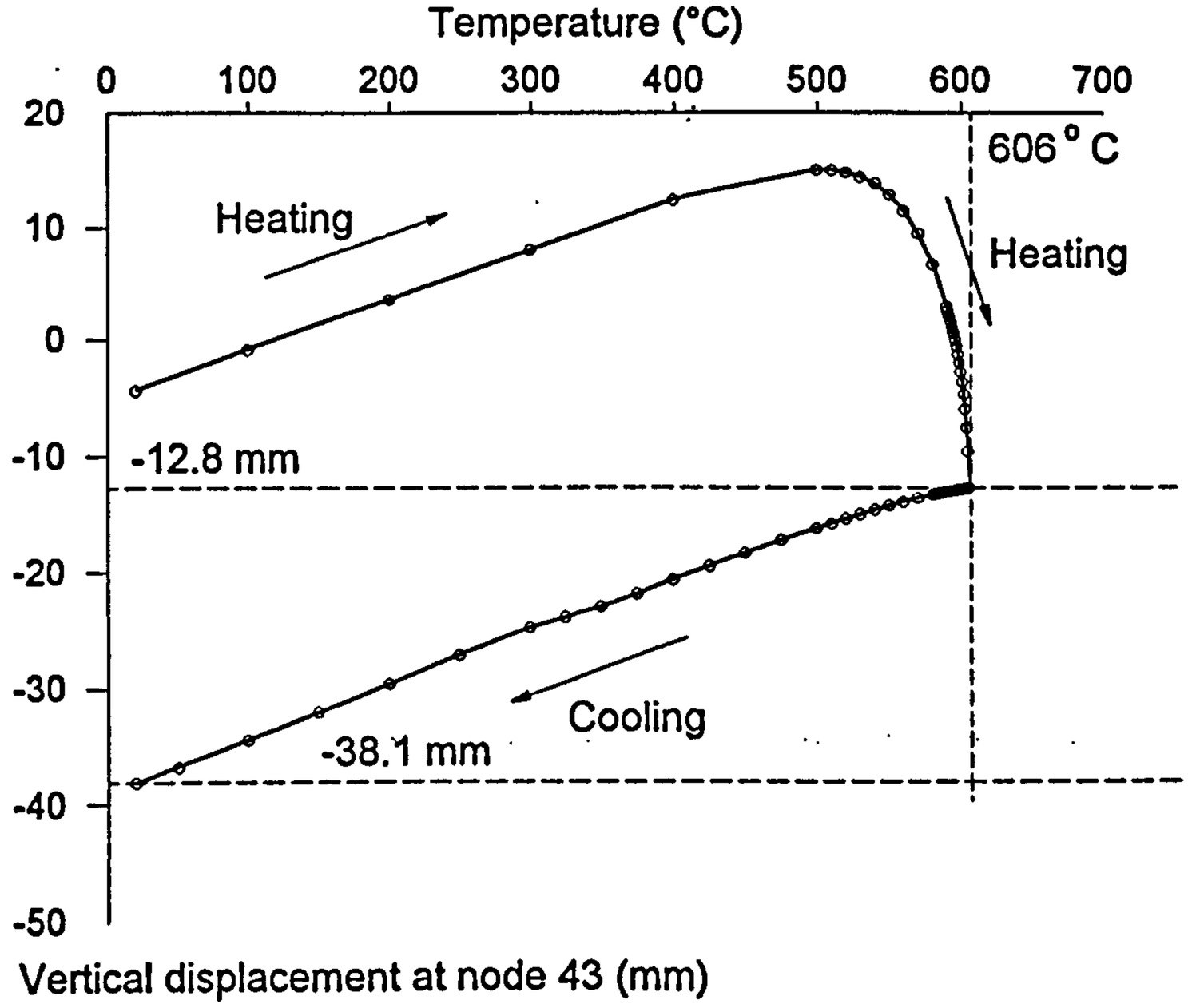

Fig. 7.19: Vertical displacement at node 43

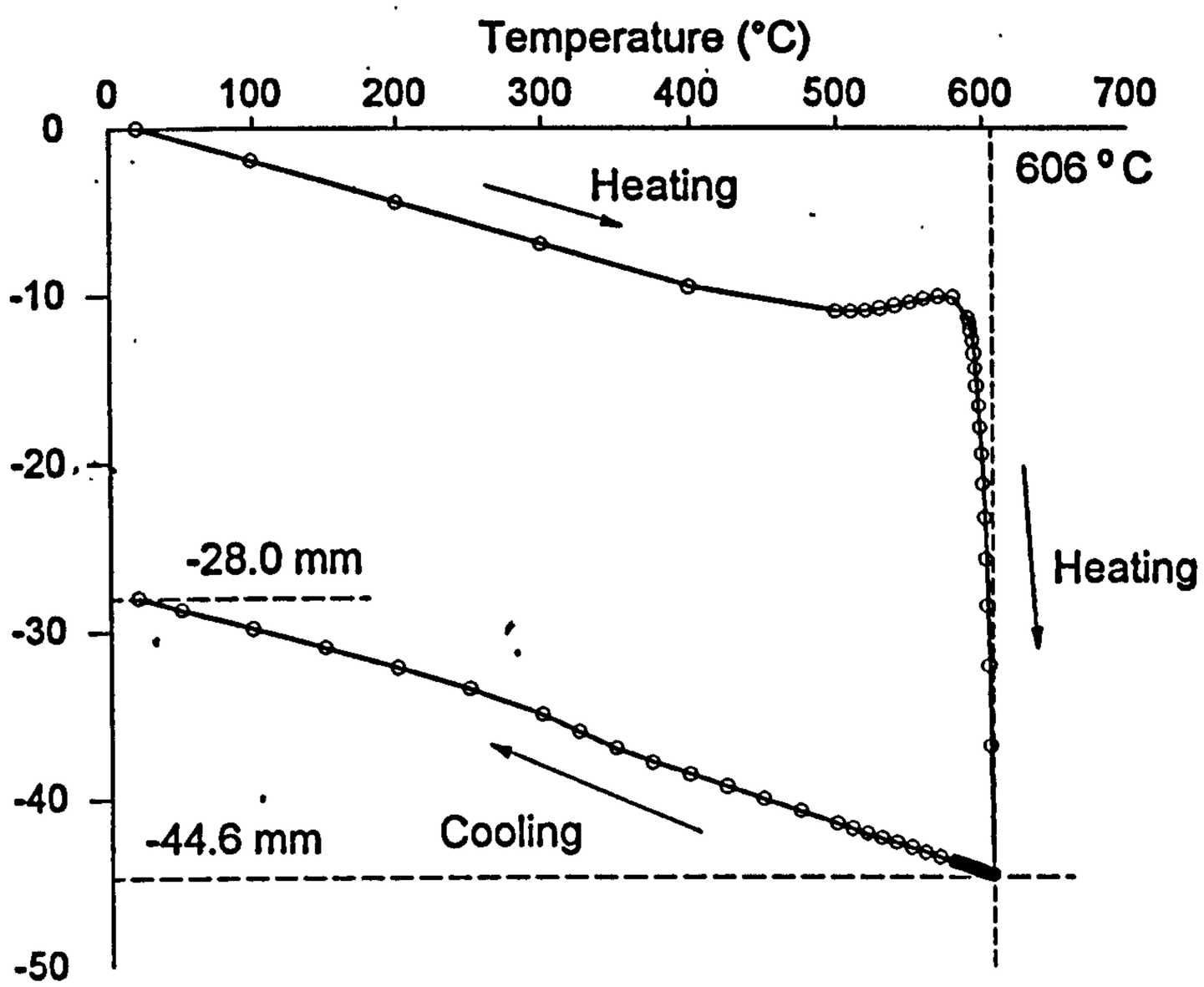

Fig. 7.20: Horizontal displacement at node 41.

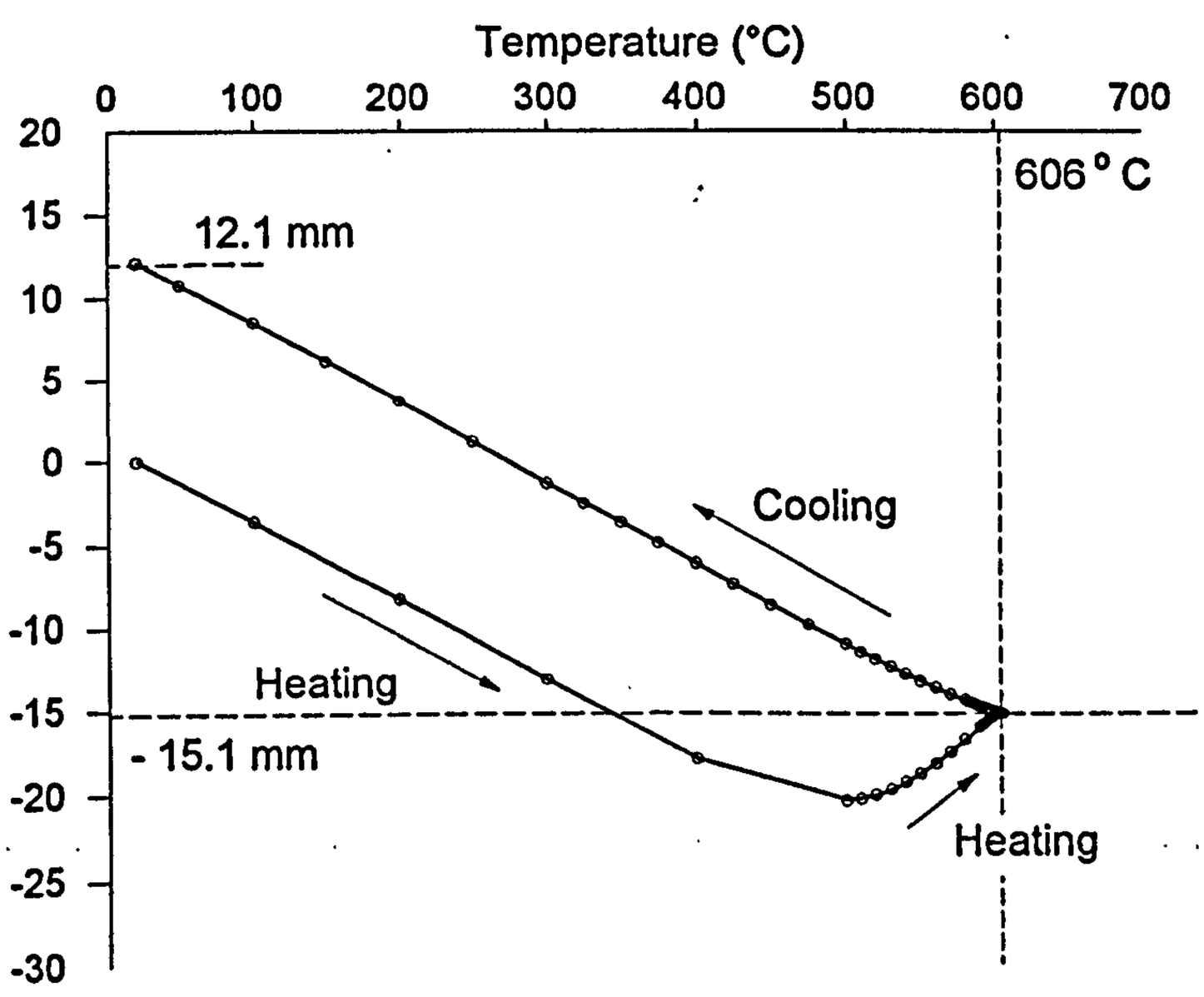

Fig. 7.21: Horizontal displacement at node 43.

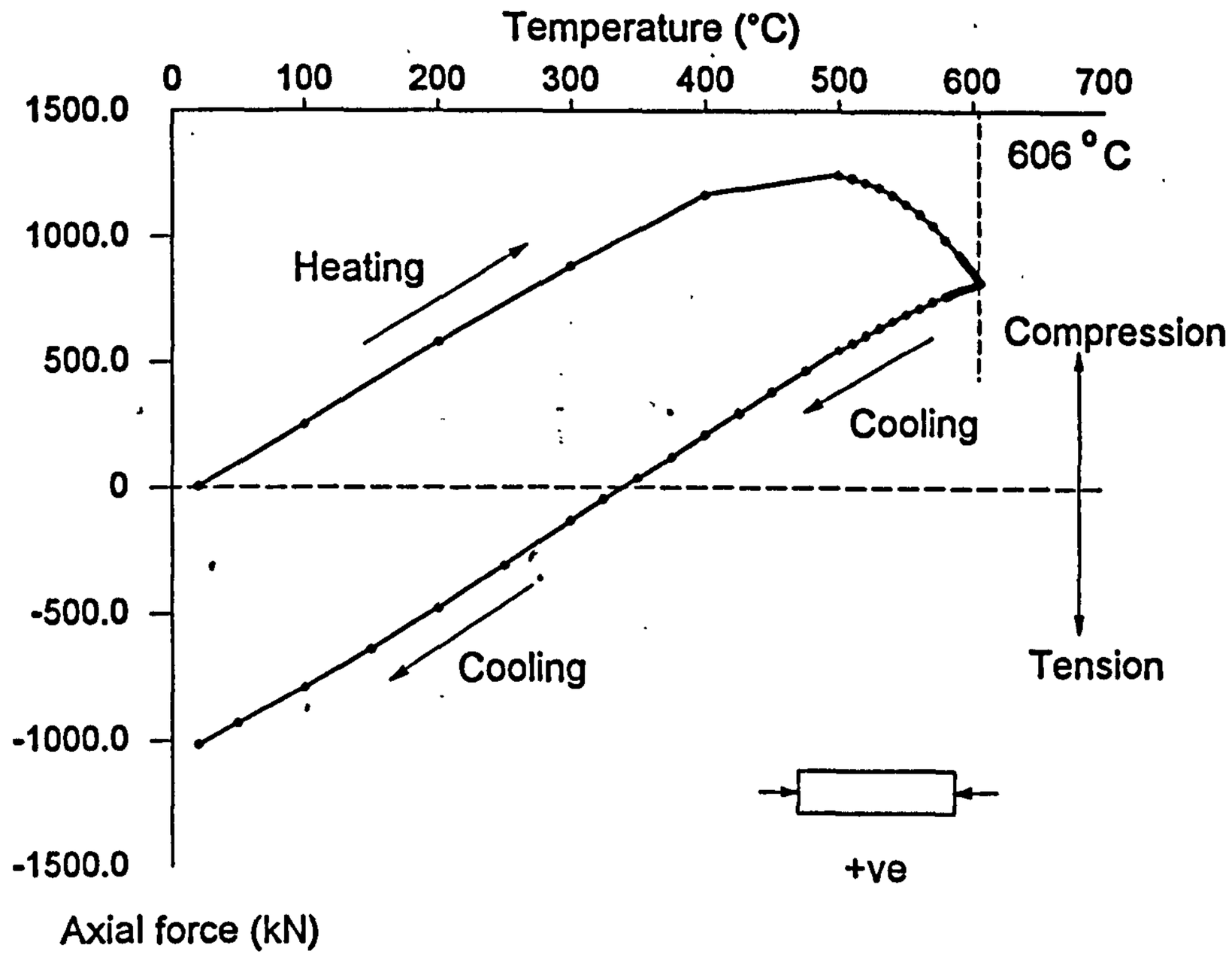

Fig. 7.22: Axial force in heated beam.

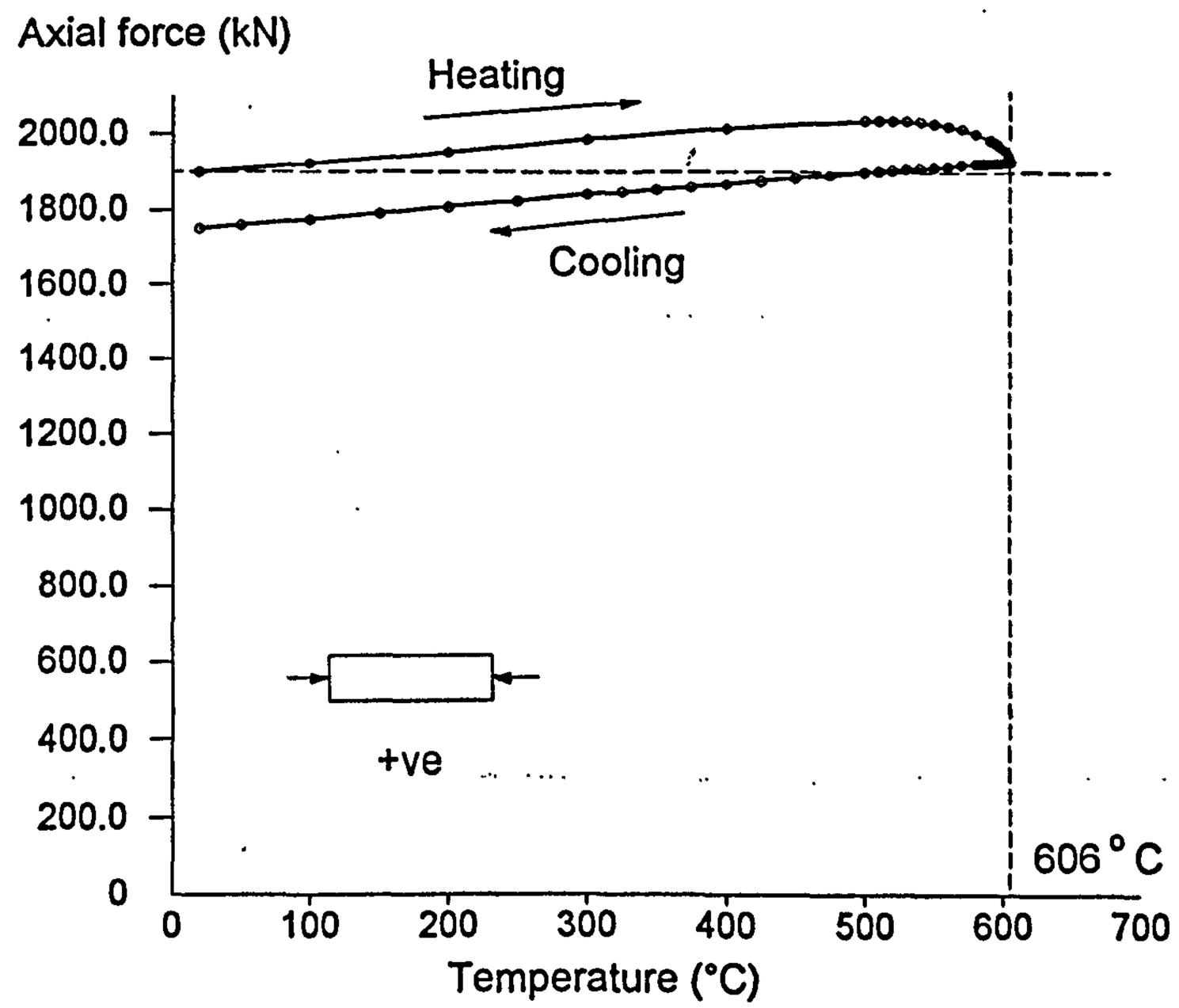

Fig. 7.23: Axial force in heated columns.

8.0: COMPUTER SIMULATION OF THE FIRE TESTS ON THE CARDINGTON TEST FRAME.

8.01: FULL-SCALE TEST FRAME CONSTRUCTED AT CARDINGTON.

A full-scale steel-framed composite structure, representing a medium-sized office block, was constructed at the Building Research Establishment laboratory at Cardington[82] during 1993. The structure is eight storeys in height and has a rectangular footprint of approximately 945m², as shown in Fig. 8.01. The structural design assumed a non-sway frame of simple construction with core areas providing restraint against lateral wind loads. The floor system, which also acts compositely with the supporting beams, consists of a steel deck and in-situ concrete.

A two year test programme is under way encompassing vertical loading, serviceability, vibration, blast, fire and smoke tests. The main purpose of these tests is to allow comparison between design procedures, which consider isolated members or sub-frames, and the actual test results on the full-scale building which has an inherently high degree of redundancy, and has been fabricated and erected under normal commercial conditions.

Considering the fire tests comparison with full frame building behaviour is of particular importance since recent design Codes BS5950 Part 8[5] and EC3 part 1.2[6] consider isolated member design only. The tests should represent fairly realistically the behaviour of buildings subjected to localised fires, which in reality are likely to occur due to the safety requirement of compartmentation. This will typically have a two-fold effect on the heated members. Firstly the restraint to thermal expansion provided by the surrounding cold structure will increase the axial force in the heated members. In the case of columns this may cause instability at lower temperatures compared with predictions based on isolated members. For beams higher vertical displacements will be experienced. However the second effect is mainly beneficial and relates to the support provided by the continuous cool structure around and above the heated area, which can allow load paths to be diverted away from the weakening members. Previously tests have been performed on single-members[9] or simple structures such as goal-post frames[13]. The step from these tests to full-scale real three-dimensional building behaviour is a large one, introducing numerous new variables which may contribute to the behaviour of the heated steel members.

There are five types of fire tests planned on the frame, and these are listed below.

1. A restrained beam test in which a secondary beam on the seventh floor is heated over a length of 8.0 metres.
2. A two-dimensional cross-frame test in which the columns and beams across the building between third and fourth floors are heated.
3. A corner test in which the structure within a corner-bay between the third and fourth floors is heated.
4. A demonstration test which consists of placing standard office furniture in half the floor area in one storey height and then starting a fire from an ignition point. The development of the fire together with steel temperatures will be recorded.
5. Column tests where portable furnaces[83] which can open and wrap around steel columns are used.

The tests which are most relevant to the present work are the first three and these will be considered individually. The corner test will be considered first, to highlight the development stages of the model (in particular the method of representing the continuous floor slabs). This will be followed by the restrained beam test and finally the two-dimensional cross-frame test.

8.1 CORNER TEST.

This test involves heating the corner bay, as shown in Fig 8.01. The finite element mesh layout used to model the structural response is shown in Fig. 8.02, together with the assumed heating profiles, with temperatures given relative to the beam lower-flange temperature T. The four columns bounding the compartment are heated at a lower rate compared to the beams, which will be achieved in the test by protecting the columns with insulating material. For the first examples, in which cracking and thermal strains in the concrete slab are ignored, the following assumptions apply,

1. The yield stress of steel is 308 N/mm^2 for Grade 43 and 390 N/mm^2 for Grade 50.
2. The steel elastic modulus is 210000 N/mm^2.
3. All steel-to-steel joints are rigidly connected.
4. The slab remains at 20°C.
5. The thickness of the slab remains constant at 130mm and the metal decking is ignored.
6. The concrete is isotropic and linear-elastic, with an elastic modulus of 21,000 N/mm^2.
7. The slab has the same properties in compression and tension.
8. A uniform floor load of 5.48 kN/m^2 was applied.

The results of the analysis are shown in the form of slab deflection profiles in Fig. 8.03, with more detailed representation of selected displacements and forces shown in Figs. 8.04 to 8.07.

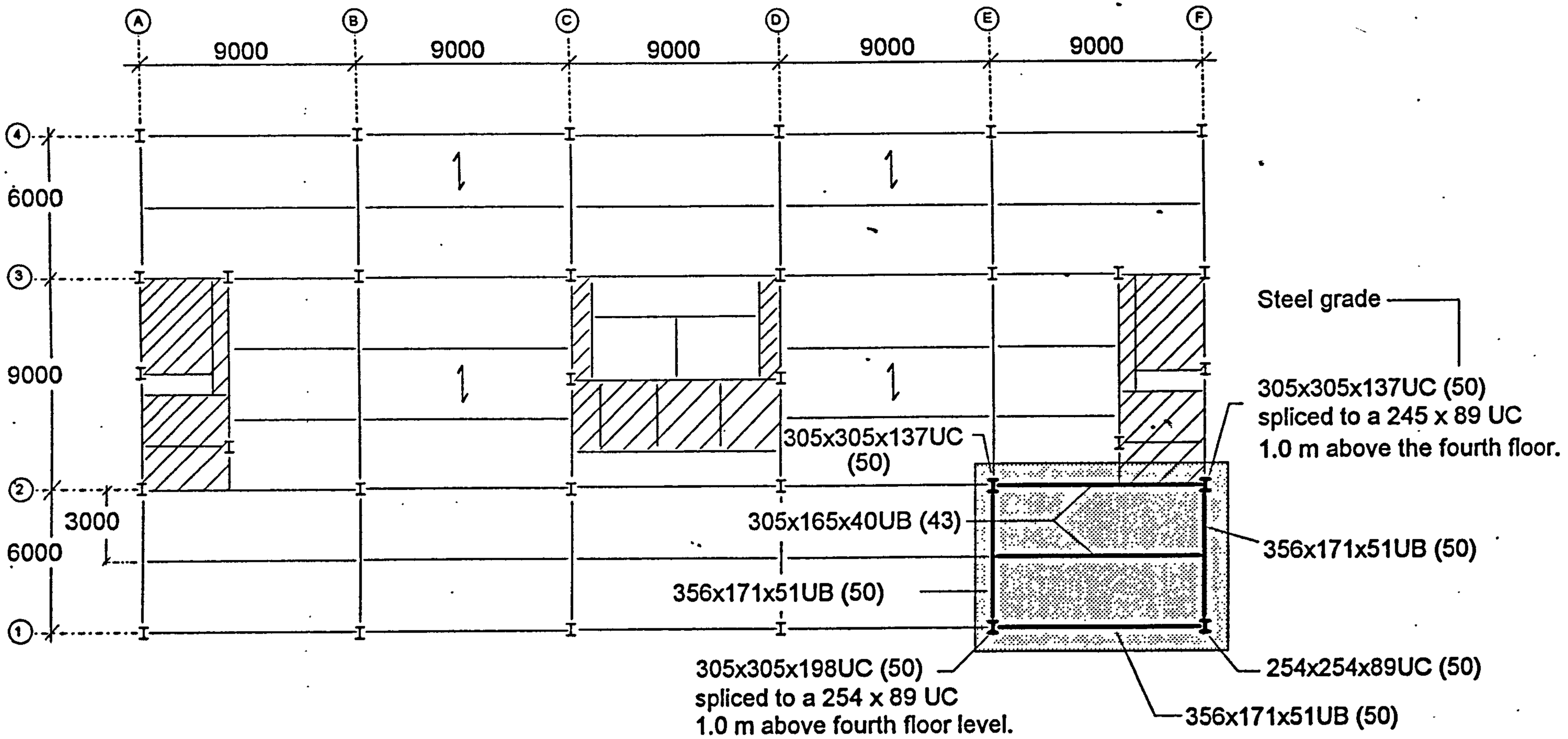

Fig. 8.01: Positioning of the corner-bay fire test.

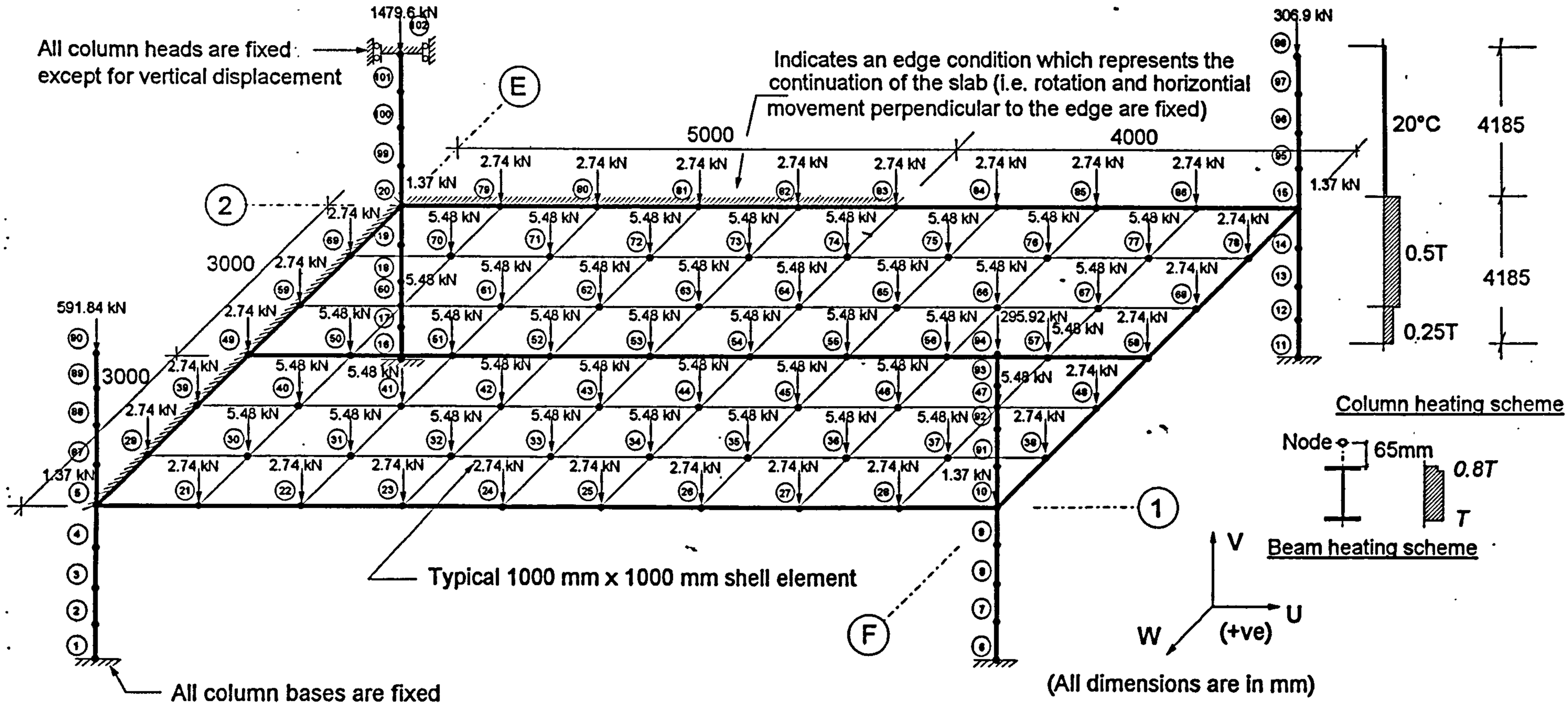

Fig. 8.02: Mesh layout adopted to represent the corner-bay.

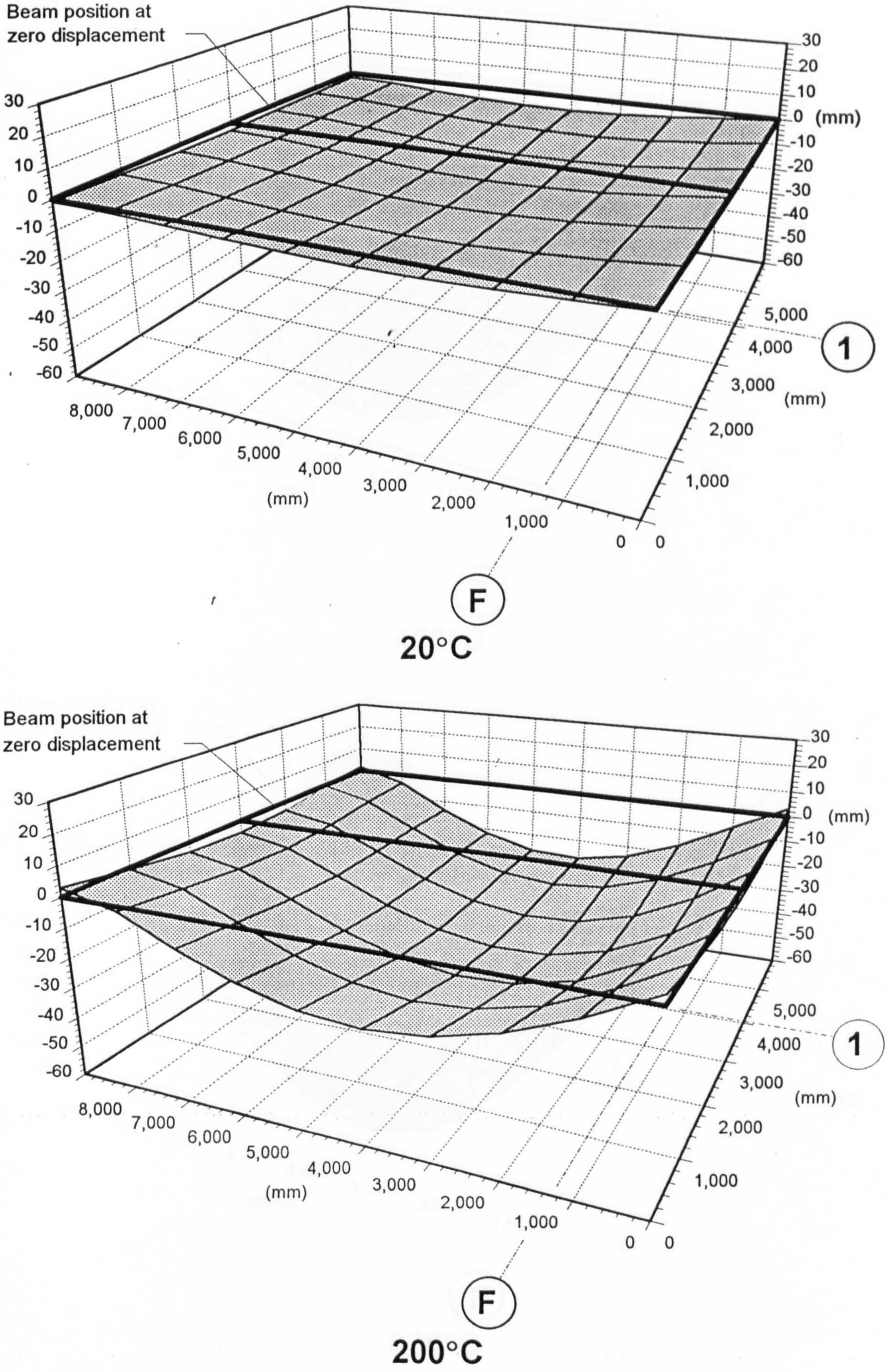

Fig. 8.03: Structural slab profile during rise in temperature:

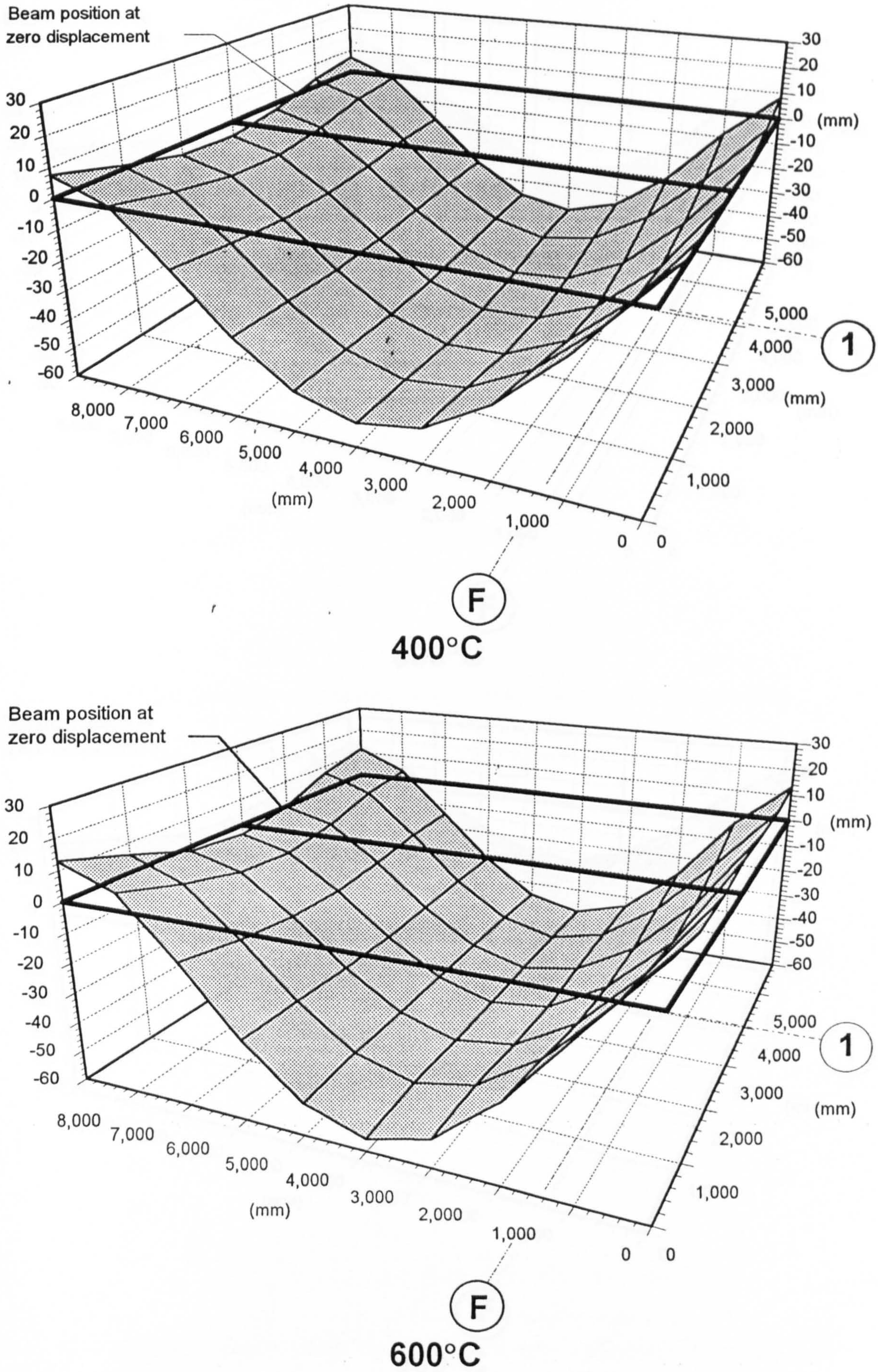

Fig. 8.03: (continued)Structural slab profile during rise in temperature:

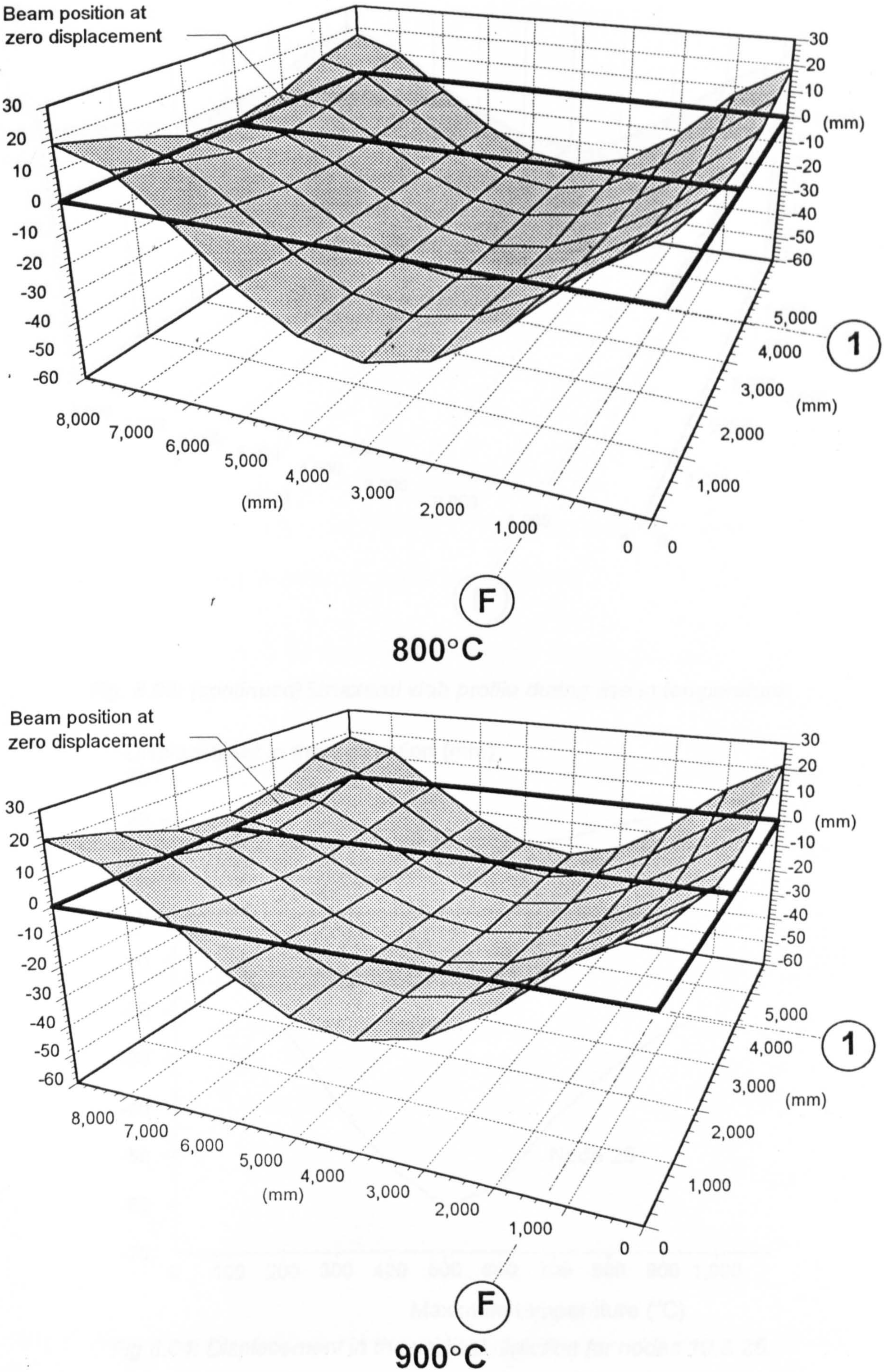

Fig. 8.03: (continued) Structural slab profile during rise in temperature:

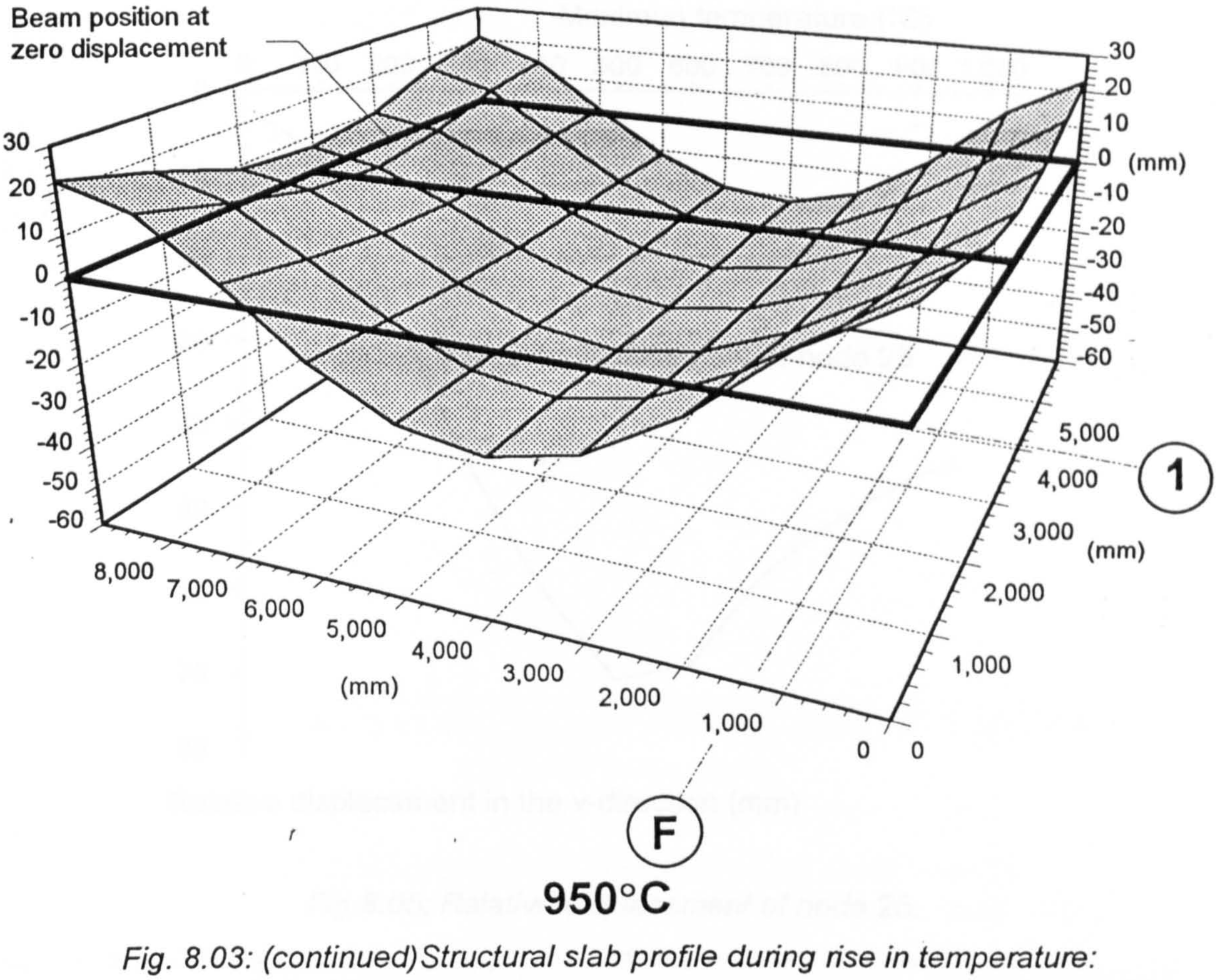

Fig. 8.03: (continued)Structural slab profile during rise in temperature:

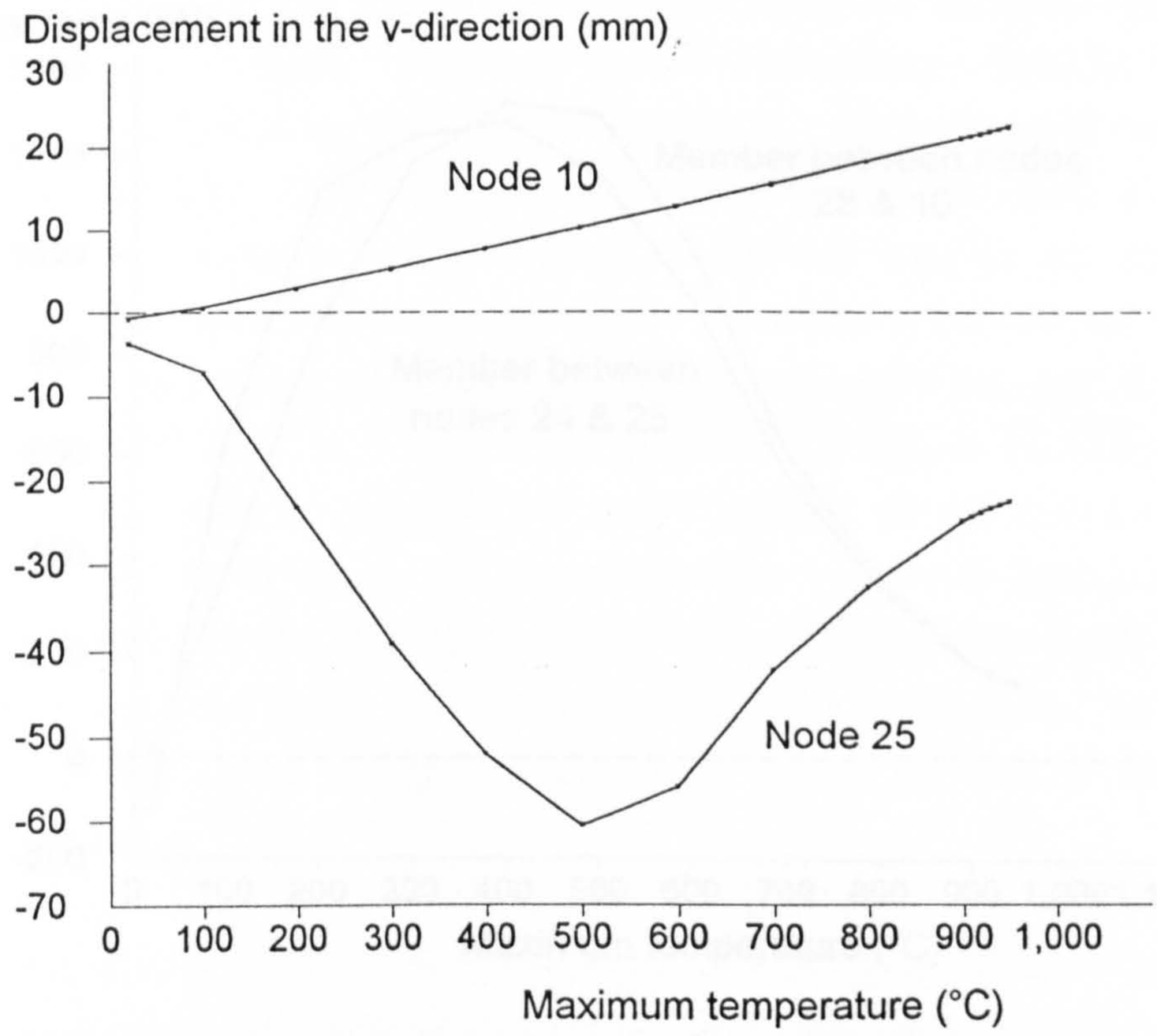

Fig 8.04: Displacement in the vertical direction for nodes 10 & 25.

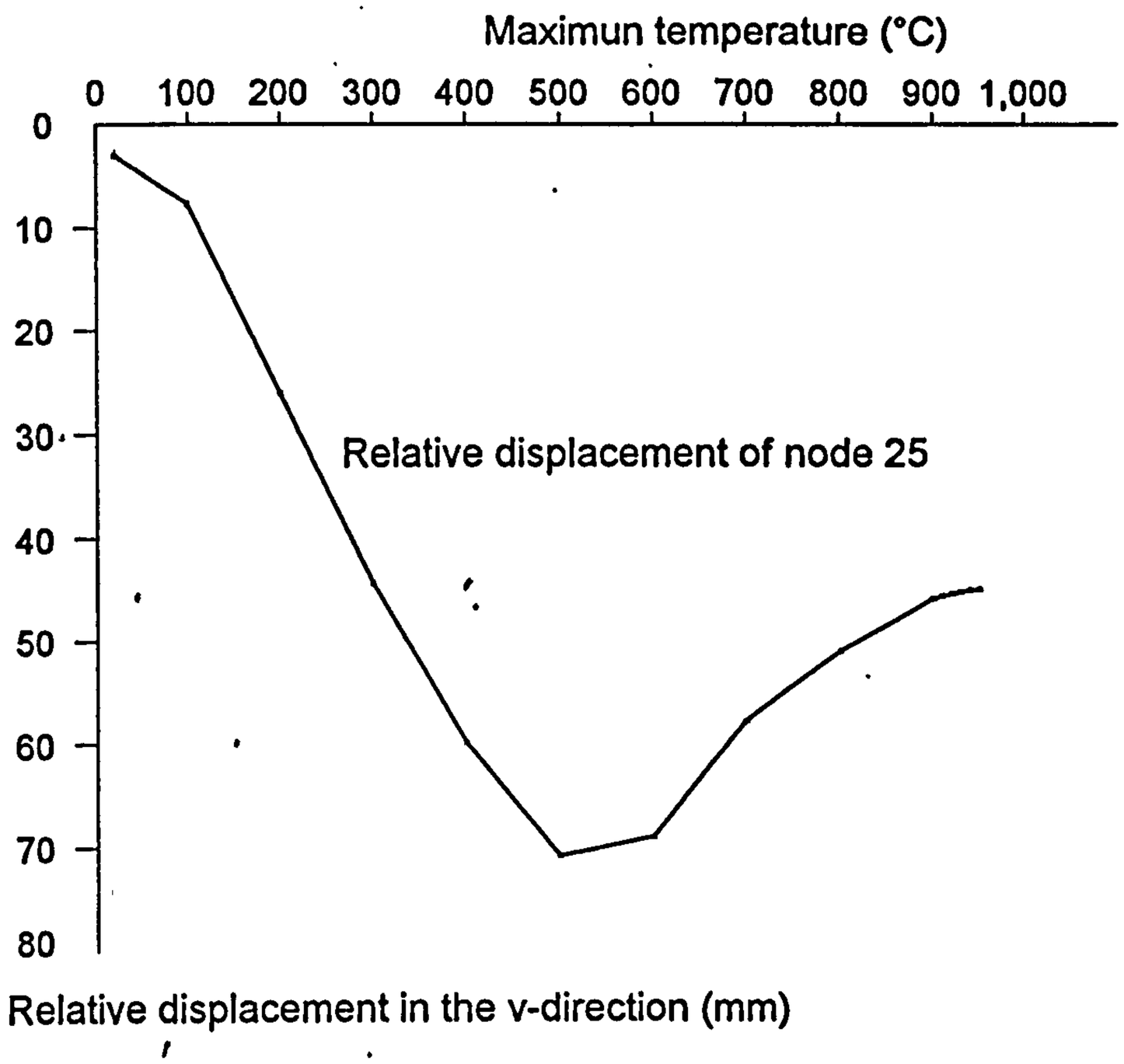

Fig 8.05: Relative displacement of node 25.

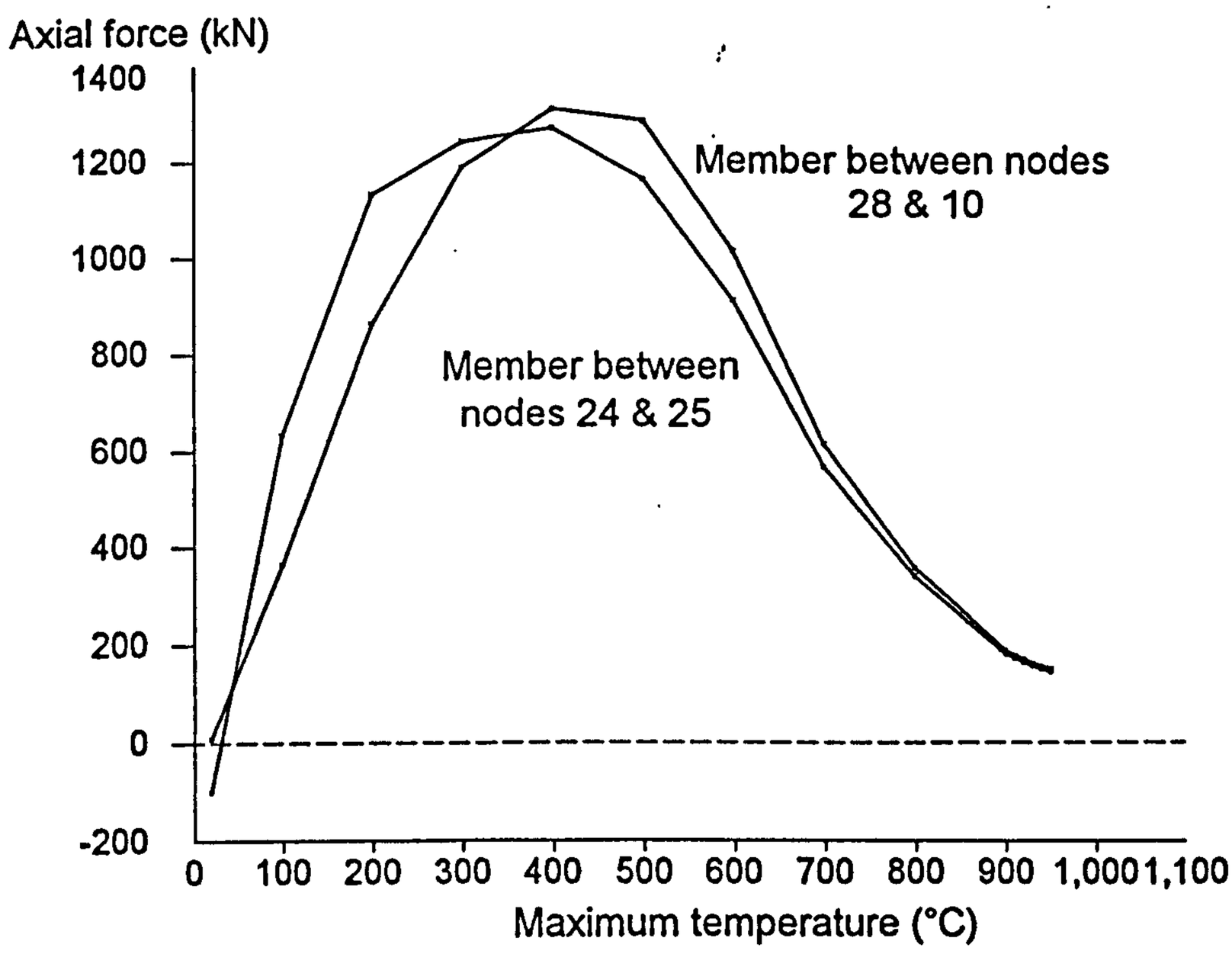

Fig 8.06: Internal axial force in steel member between nodes 24 & 25 and between nodes 28 & 10.

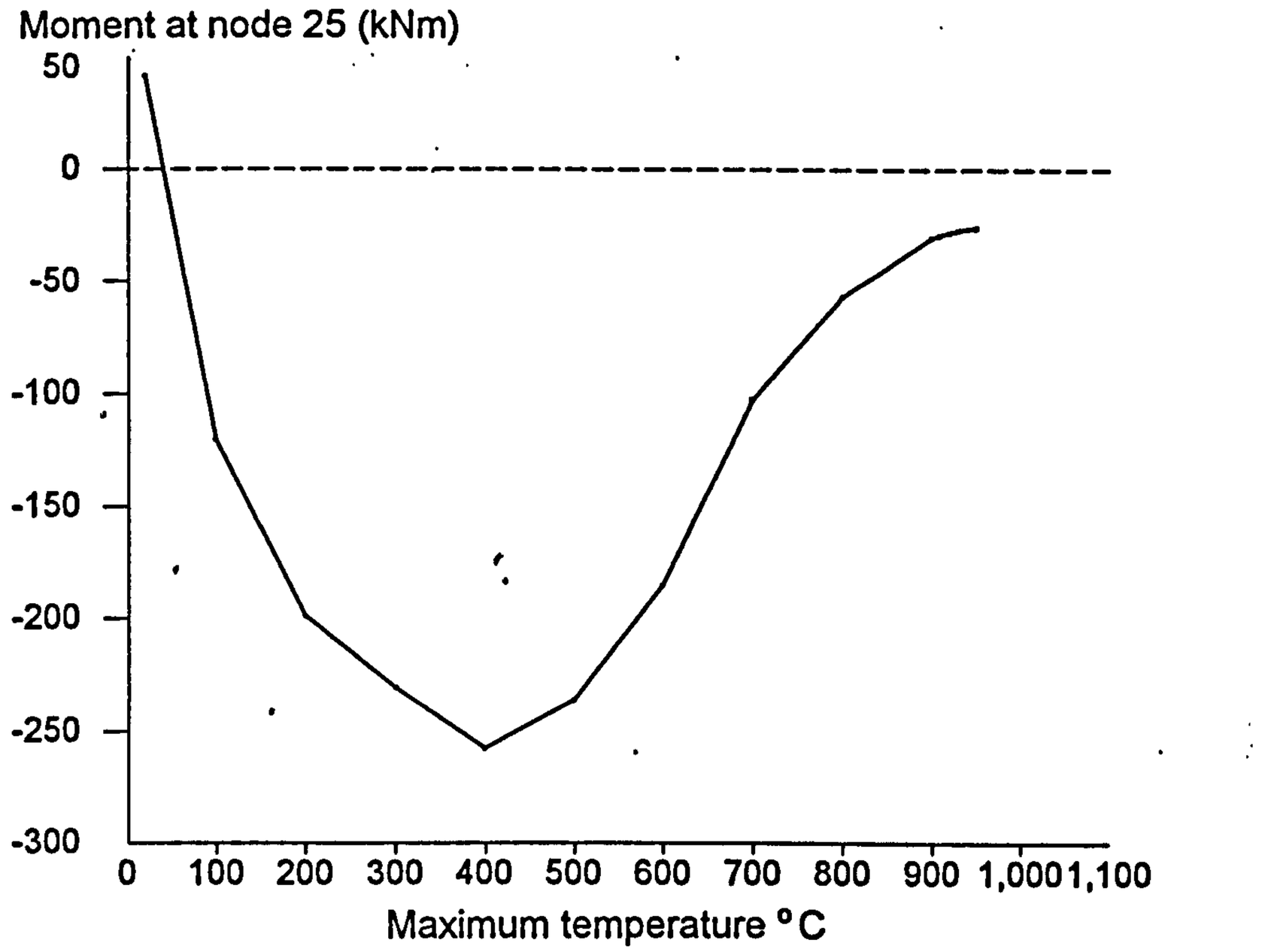

Fig 8.07: Internal moment of the steel beam about node 25.

Structural failure was not identified during the analysis, and the run was terminated at 950°C due to lack of further data for the Ramberg-Osgood representation[11] of the stress-strain curves of steel. Fig. 8.06 shows the variation of axial force with temperature at locations along the beam on gridline 1. Interpretation of these results requires extreme care. Connection of the beam-column and shell elements at common node points causes the modelled beam and slab to act compositely. However, from the calculated displacements at equilibrium, the internal forces are calculated about the nodal points using the stress distribution in the steel only. This is shown in Fig. 8.08 in which an elastic stress distribution is assumed for pure bending. Since concrete stresses are ignored an axial force will be calculated at ambient temperature as shown in Fig. 8.06. However during the rise in temperature these results do give an indication of the change of axial force in the steel beam due to the restraint against thermal expansion. This increases for temperatures up to about 400°C but then decreases at higher temperatures due to the loss of strength and stiffness of the beam.

Similarly to the axial force, the internal moments referred to in Fig. 8.07 relate to the steel beam only and are measured about the node position (which in this example is 65mm above the top flange of the beam). As the temperatures rise these moments will take into account the induced axial force in the beam, due to the restraint against

thermal expansion. Since the beam is subjected to a thermal gradient the position of the resultant internal axial force in the steel beam will continually move towards the cooler and thus stronger areas of the cross-section. Therefore it is difficult to draw general conclusions from Fig. 8.07, except that the moment reduces above 400°C, which is mainly due to the reduction in strength of the beam with rise in temperature.

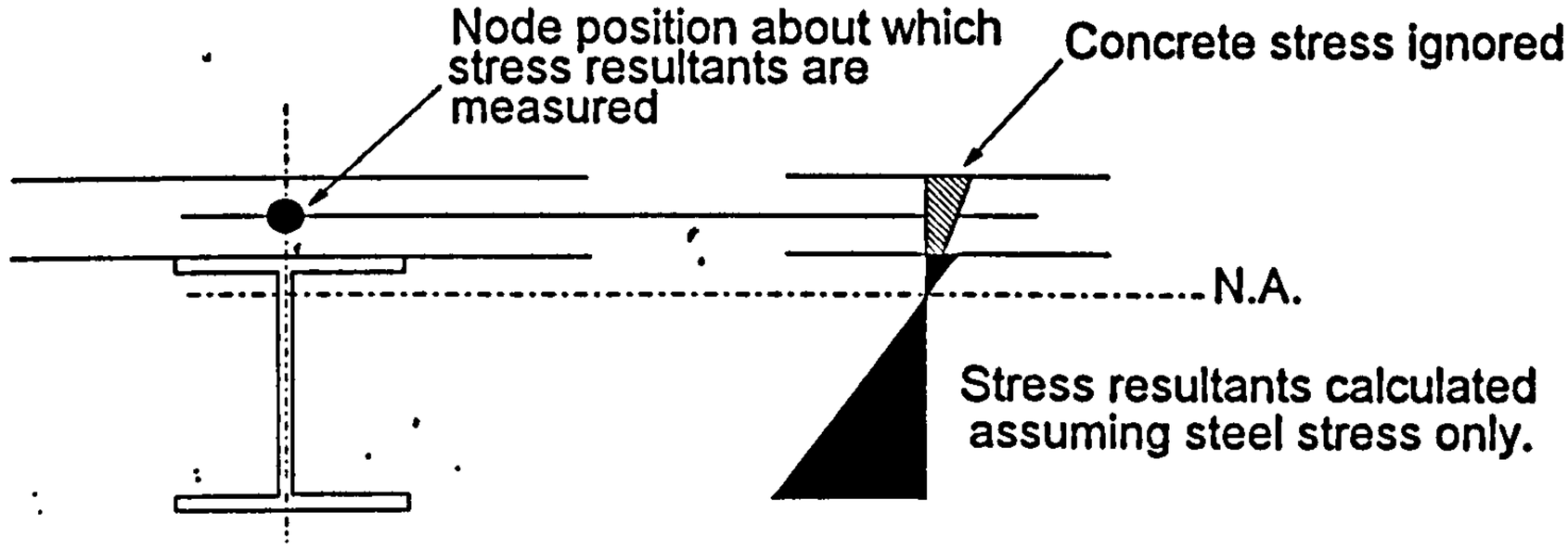

Fig. 8.08: Calculating steel stress resultants about the nodal point.

It can be seen from Fig. 8.05 that the predicted relative displacements of the beam on gridline 1 reduce beyond 500°C. The slab profiles shown in Fig. 8.03 indicate that all the beams behave in this manner. This phenomenon, of the structure beginning to recover from its maximum displacement as temperatures rise seems to be due to the extreme softening of the steel beams beyond 500°C assuming greater importance than their thermal expansion. To support this theory a highly simplified model of the corner-bay, as shown in Fig. 8.09, was analysed. The bay size remains as before, but the internal beam and all the columns (together with the edge condition which represents slab continuity) are excluded. The heating scheme for the perimeter beams and the general assumptions are the same.

The strain value at the bottom flange at node position 5 (shown in Fig. 8.09) is plotted in Fig. 8.10, together with the displacement of the beam at this position. It can be seen that the strain in the bottom flange starts to reduce at the same temperature as the change in direction of the vertical displacement, showing that the decrease in relative displacement of the beam is due to "squashing".

To investigate the effect of continuity of the floor slab into the region surrounding the test area, the previous model was extended to include an extra half-bay of structure in both directions, as shown in Fig. 8.11. The heating scheme remains the same, with all the additional structural elements remaining at ambient temperature. The results of this analysis are shown, in the form of slab deflection plots, in Fig. 8.12 and once again the decrease in relative displacement of the beams is highlighted. The slab

profiles have a slightly different shape during the rise in temperature, caused mainly by the support of the column positioned near the service ducts and stairwell. The positions of the columns can be identified clearly from the profiles, together with the hogging areas where in reality cracking is to be expected. The deflected shape of the slab outside the test area is also indicated.

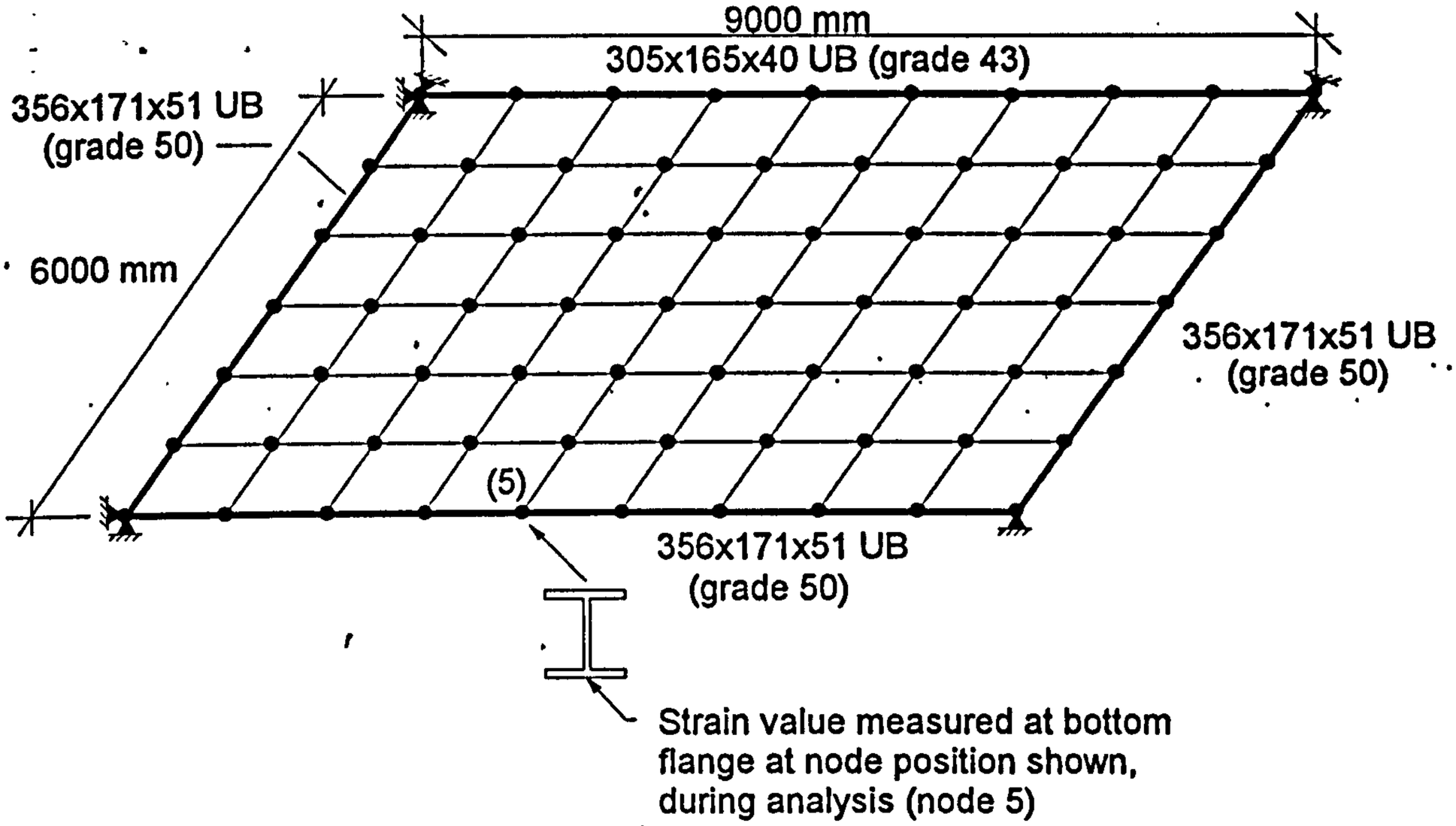

Fig. 8.09: Simplified corner bay model.

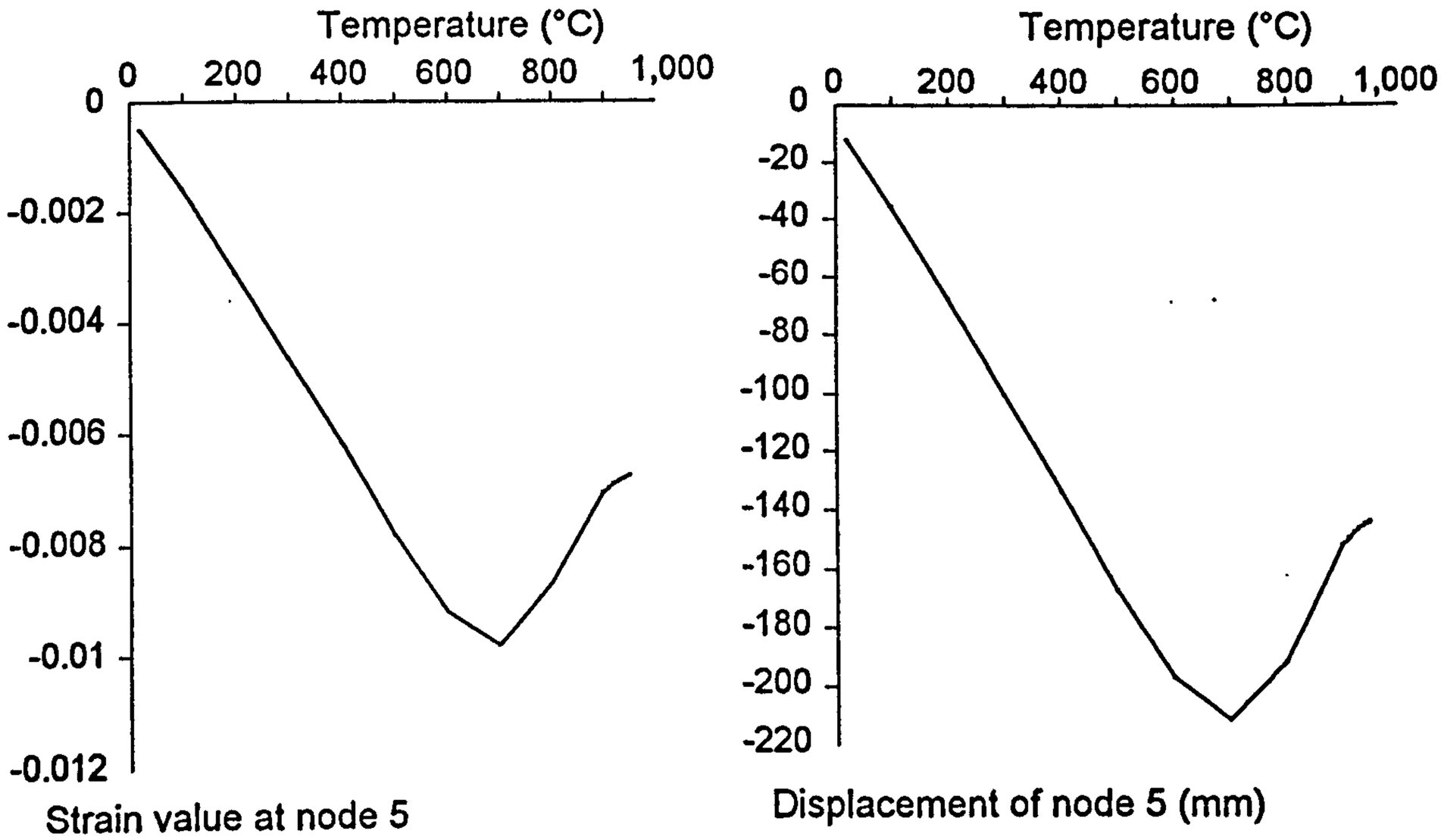

Fig 8.10: Strain and displacement values in bottom flange at node 5.

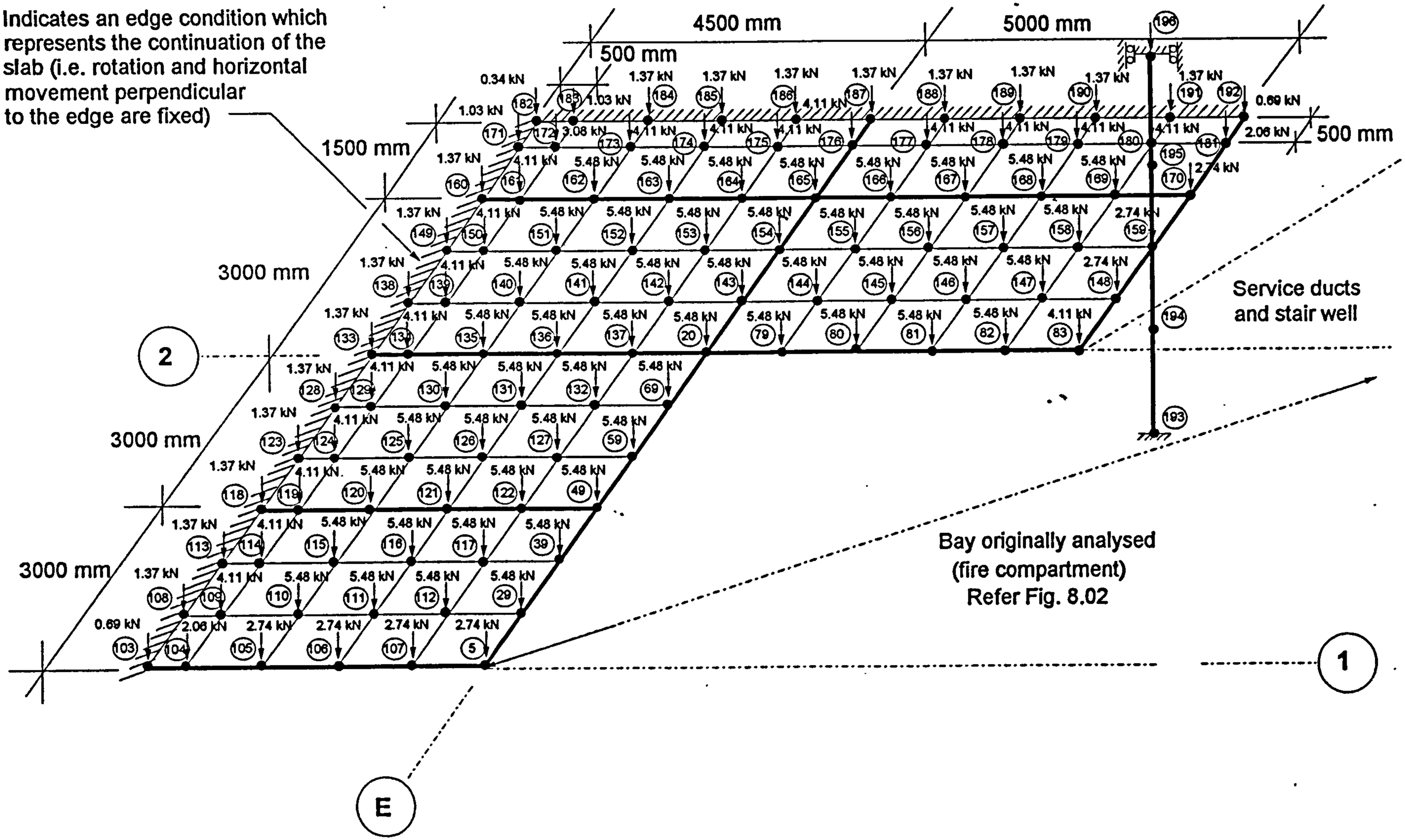

Fig. 8.11: Extra structure added to the corner-bay layout shown in Fig. 8.02

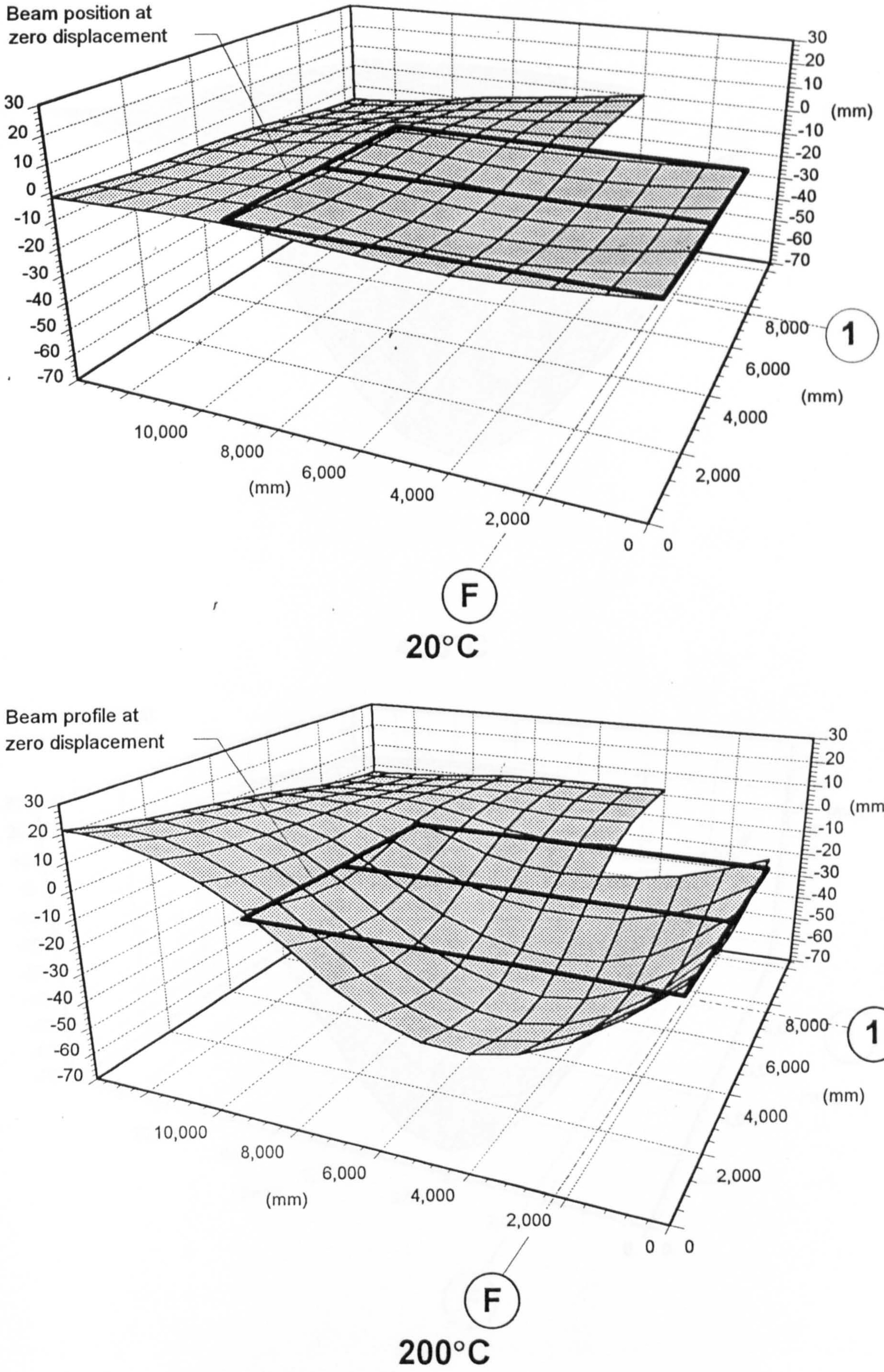

Fig. 8.12: Structural profile during the rise in temperature.

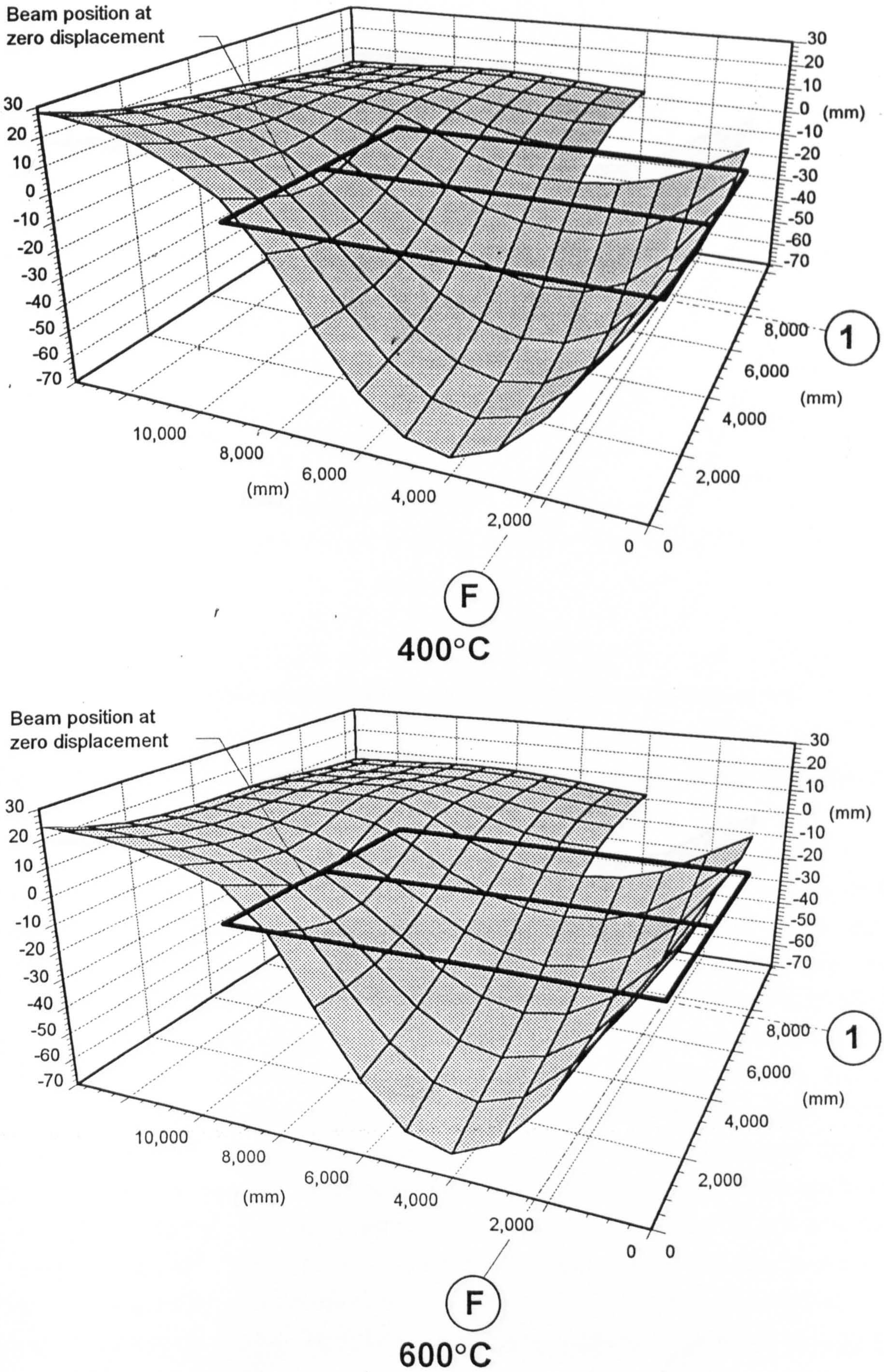

Fig. 8.12: (continued) Structural profile during the rise in temperature.

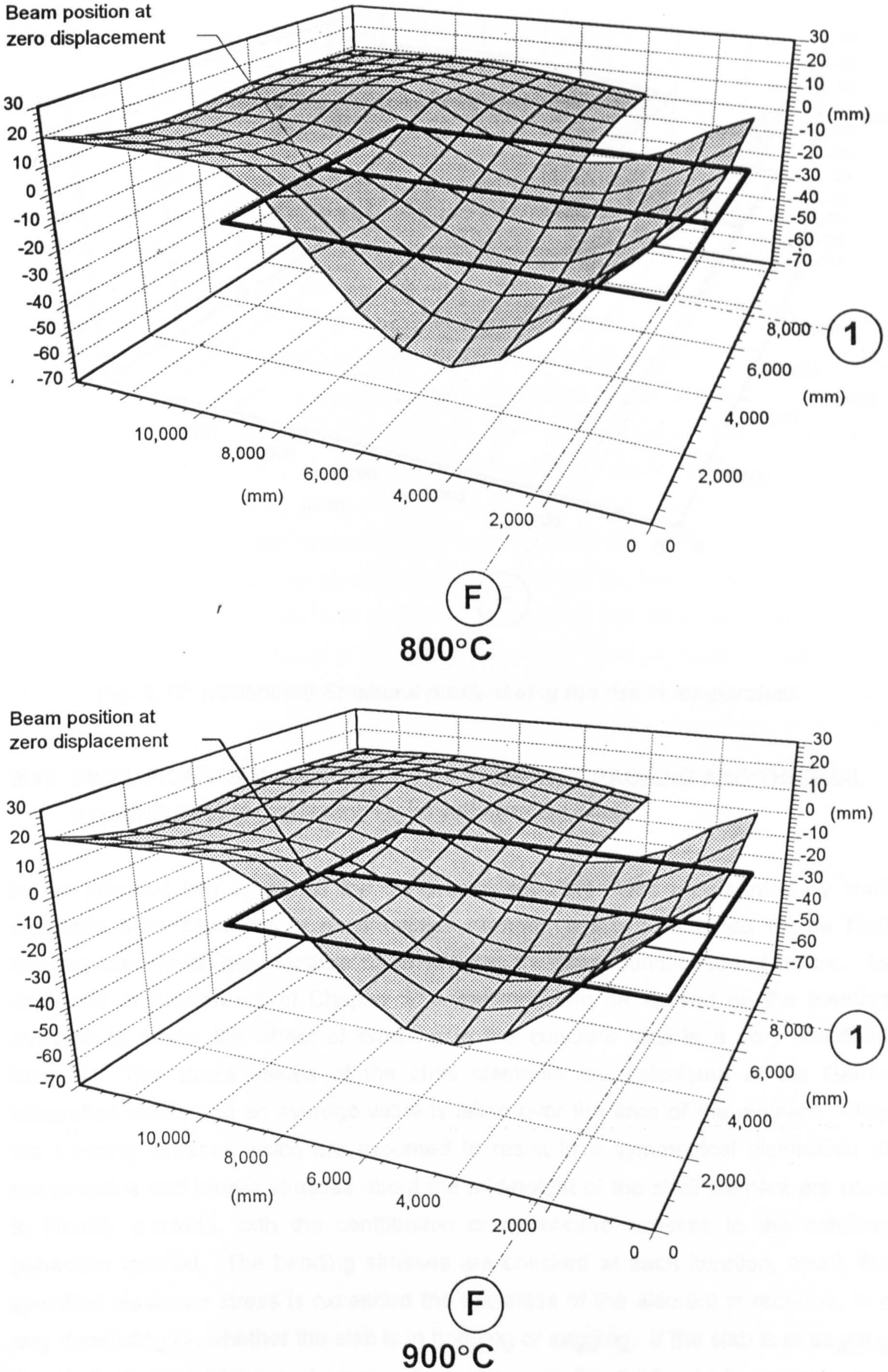

Fig. 8.12: (continued) Structural profile during the rise in temperature.

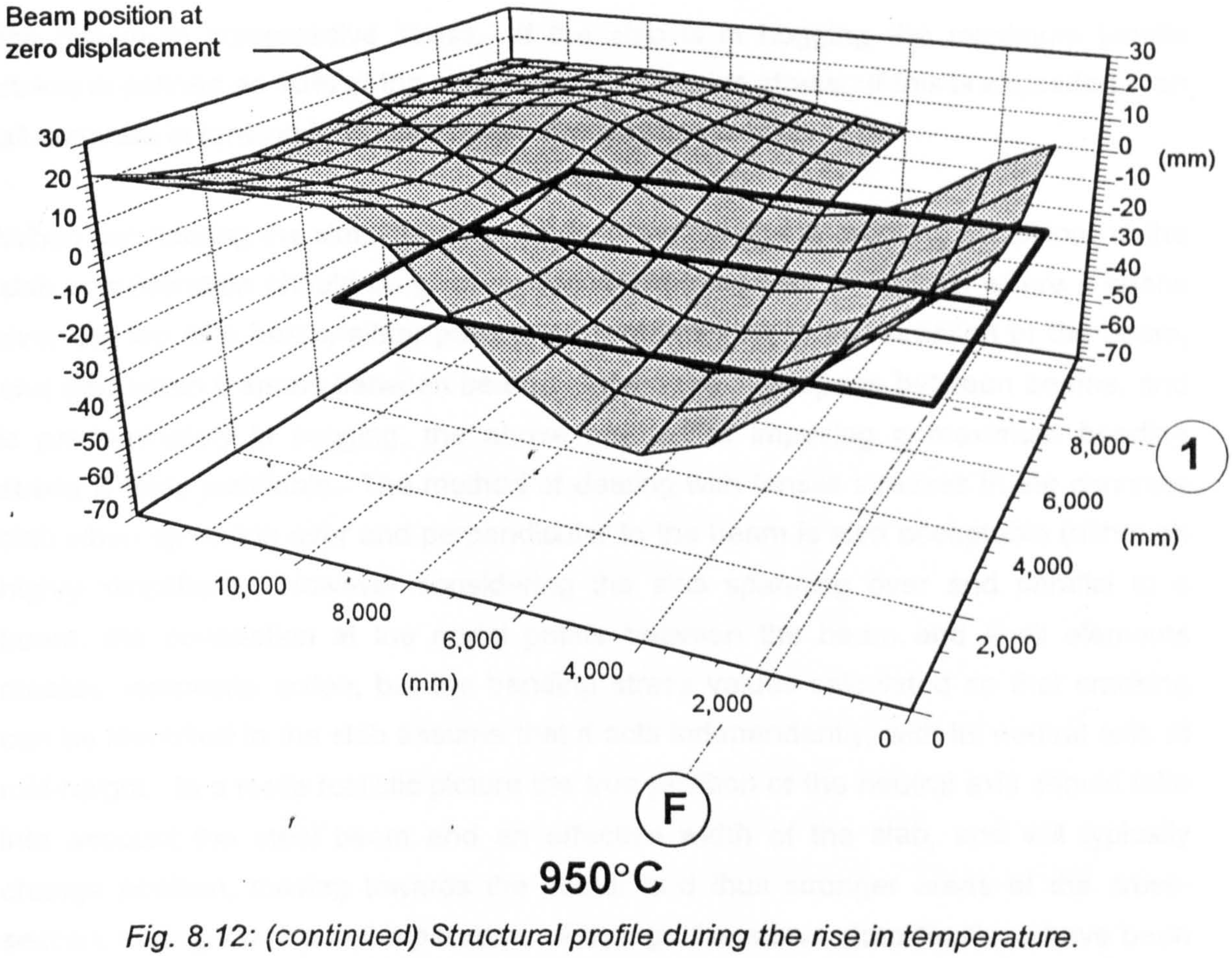

Fig. 8.12: (continued) Structural profile during the rise in temperature.

8.12: SIMPLIFICATIONS ADOPTED TO REPRESENT CRACKING AND THERMAL STRAINS IN THE CONTINUOUS CONCRETE SLABS

In the previous two examples the continuous concrete slabs represented by shell elements were assumed to have infinite strength, which contributed to the high temperatures which the structure could withstand without identification of failure. As explained in Section 6.5 of Chapter 6, a limitation can be applied on the bending stresses to model the effect of cracking in the concrete slab in a very simplified manner. The stress values of the shell elements are calculated at the Gauss integration points and an average value is taken over the area of the element. Only the bending stresses which are assumed to result in a symmetrical distribution of compressive and tensile stresses about the mid-height of the shell element are used to identify cracking, with the contribution of membrane stresses to the cracking behaviour ignored. The bending stresses are checked at each iteration, and if the specified maximum stress is exceeded the thickness of the element is reduced, in a way depending on whether the slab is in hogging or sagging. If the slab is in sagging the shell element thickness is reduced as shown in Fig 6.18, which assumes that there is sufficient reinforcement in the slab that the maximum tensile stress is equal to

the maximum compressive stress. If the slab is in hogging the maximum tensile stress is defined as 10% of the maximum compressive stress. If this is exceeded then all concrete in tension is ignored.

When considering the simplifications made in modelling the cracking behaviour of the slab consideration should be given to the slab's behaviour in regions where it spans over the top of a beam, either parallel or perpendicular to the direction of the beam, and also when it spans between beams. When the slab spans between beams, and is predominately in sagging, the above method of imposing a maximum bending stress is fairly justifiable. The method of dealing with tensile stresses in the concrete slab when spanning over and perpendicular to the beam is also acceptable (although highly simplified). However considering the slab spanning over and parallel to a beam, the connection at the nodal points between the beam and shell elements creates composite action, but the bending stress values calculated so that cracking can be identified in the slab assume that it acts independently, with its neutral axis at mid-height. In a more realistic picture the true position of the neutral axis should take into account the steel beam and an effective width of the slab, and will typically change position, moving towards the cooler and thus stronger areas of the cross-section, during the rise in temperature. Although the above simplifications have been adopted to represent cracking of the concrete slab, the model does give a partially correct indication of the importance of the continuous floor slab to the behaviour of steel-framed buildings at elevated temperatures.

Thermal strains in the concrete are represented by initial nodal forces, as explained in Section 6.6. However since flat shell elements are used the temperature distribution through the thickness of the slab must be assumed to be uniform.

The general assumptions relating to the steel material properties and proposed heating scheme remain the same as in the previous examples. To adopt a more realistic representation of the concrete slabs, the following assumptions apply,

1. A steel:concrete modular ratio of 15 is adopted, which is reduced by 30% if the slab is heated.
2. The temperature of the concrete is 20% of the hottest part of the steel, and is uniform through the thickness of the slab.
3. Only the top 70 mm of the slab is considered, as shown in Fig. 8.13. This represents the concrete thickness above the top of the trapezoidal steel deck.

4. The limiting stress when the slab is in sagging is 25 N/mm^2. This was obtained by taking an average of the measured cube strengths, multiplying by 0.67 and dividing by a material partial safety factor of 1.3 (as stated in BS5950 part 8).
5. The limiting stress when the slab is in hogging is 2.5 N/mm^2.
6. A thermal expansion coefficient of 14.0 x10^{-6} /°C and a Poisson's' ratio of 0.2 is taken for the concrete.
7. Slab elements above steel-to-column connections are reduced to 6mm thick, which corresponds to the thickness of the mesh in the slab.

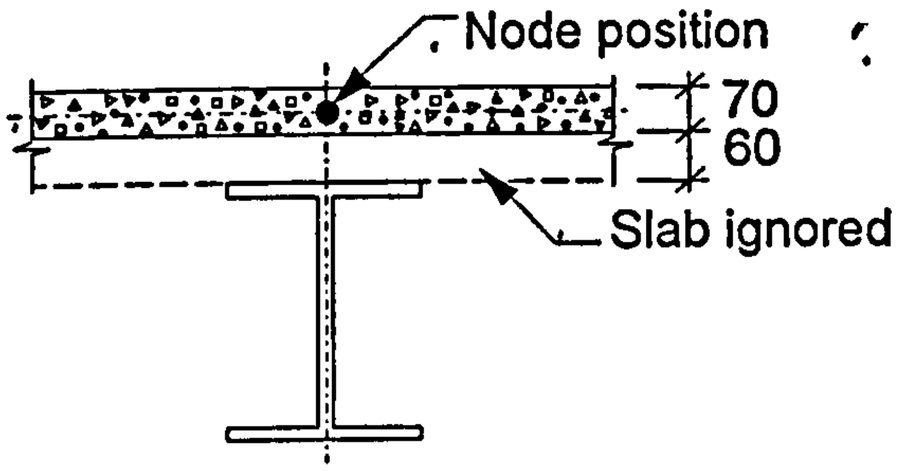

Fig. 8.13: Section through the slab and beam.

Steel-to-steel semi-rigid connections can be modelled, as explained in Chapter 4. However since actual moment-rotation characteristics of the joints are not available at the present time it was decided in the case of the corner test to represent beam-to-beam connections, which consist of fin-plates, by pins. Steel beam-to-column connections were considered fixed.

Both of the previous examples were re-analysed using the above assumptions. Considering first the mesh layout shown in Fig. 8.02, the recorded slab deflection profiles during the rise in temperature are shown in Fig 8.14 , with convergence failure occurring at 742°C.

Investigation of the slab profiles shows that the magnitudes of displacements are much higher than are given by the previous analysis. No reversal of direction of vertical displacement was recorded, due to the strength and stiffness of the slab reducing as the temperature rises. It is of interest to consider the slab elements above the beam on gridline E, for both analyses. In the first example where the slab remains at a constant thickness of 130mm throughout the analysis, the slab profiles shown in Fig. 8.03 indicate hogging behaviour perpendicular to the beam, due to the imposed boundary conditions. In the slab profiles shown in Fig. 8.14 it can be seen that hogging behaviour still occurs causing the slab to reduce in thickness in this area. This will also reduce the strength of the slab spanning in the other direction, thus reducing the strength of the composite beam on gridline E. This highlights one of the limitations of the model in that isotropic properties are assumed which means that reducing the strength of the slab in one direction also reduces its strength in the other direction.

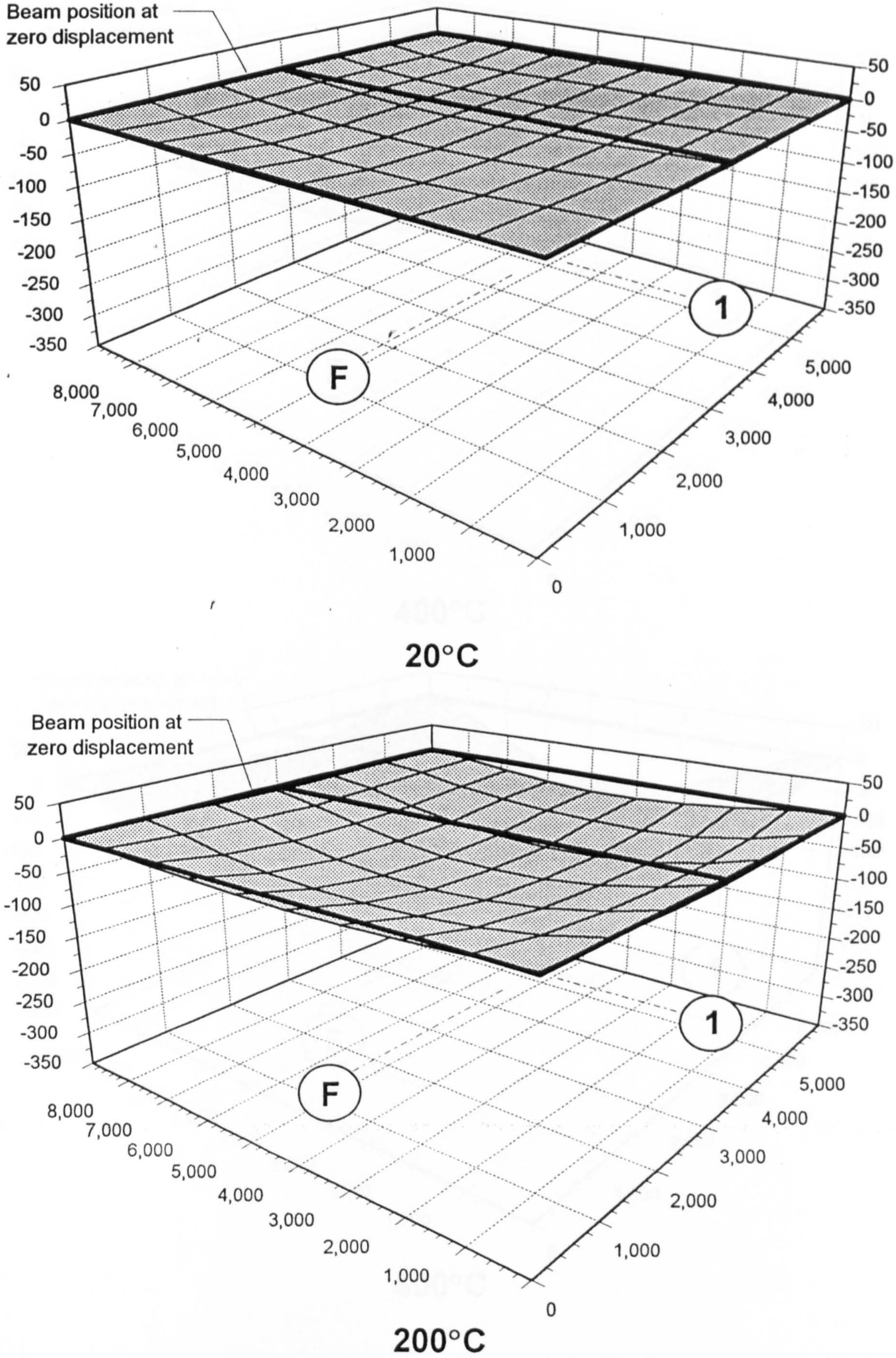

Fig. 8.14: Structural profile during the rise in temperature

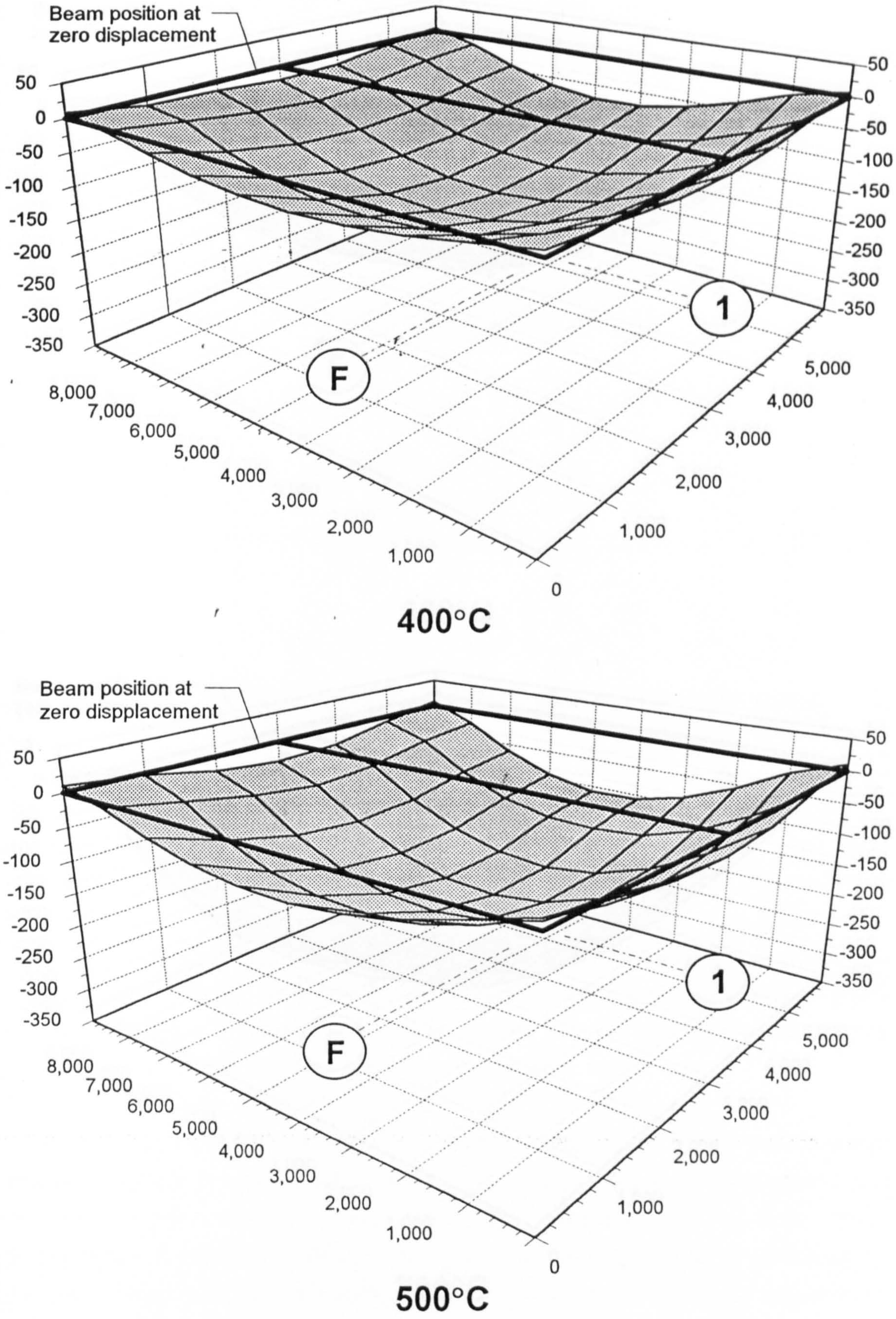

Fig. 8.14: (continued) Structural profile during the rise in temperature

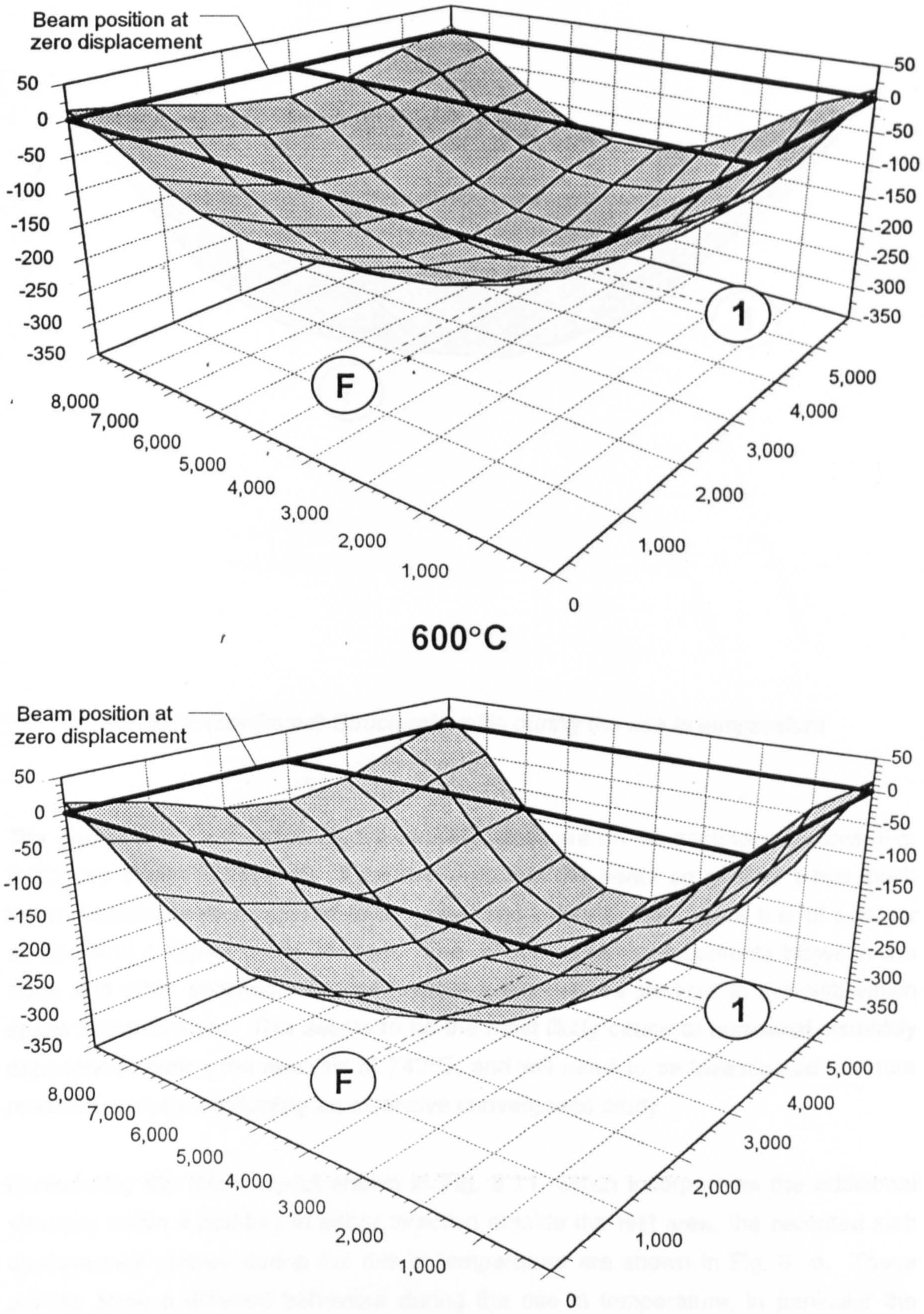

Fig. 8.14: (continued) Structural profile during the rise in temperature

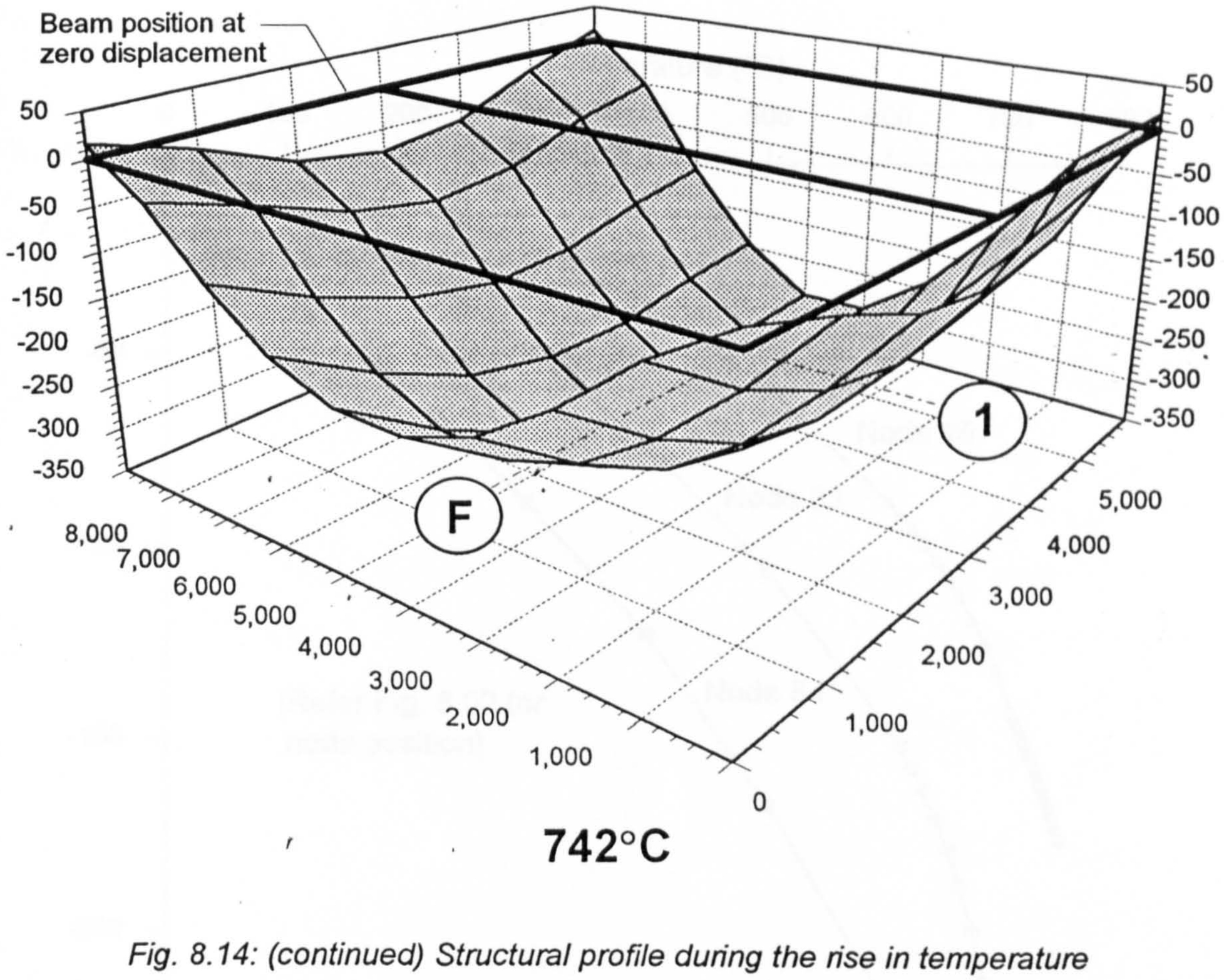

Fig. 8.14: (continued) Structural profile during the rise in temperature

The displacements at nodes 25, 54, and 83, which are on the secondary beams (Fig. 8.02), are shown in Fig 8.15. It can be seen that the beam on gridline 1 has much lower displacements compared to the other secondary beams, since it is of a larger section and a higher grade of steel. The difference in displacements between the edge and other secondary beams creates a high stress-gradient in the slab which spans between them. This seems to be the most likely cause of numerical instability experienced during the analysis at 742°C, and will need to be investigated in future research work by conducting an extensive convergence study.

Considering the mesh layout shown in Fig. 8.11, which incorporates the additional structure within a half-bay in either direction outside the test area, the recorded slab displacement profiles during the rise in temperature are shown in Fig. 8.16. These profiles show a different behaviour during the rise in temperature, in particular the displacements of the beam on gridline 2 which are much lower, due to the effect of the cold surrounding structure. Once again a high stress-gradient in the slab as it spans across the secondary beams was experienced, which may be the cause of the numerical instability experienced at 711°C.

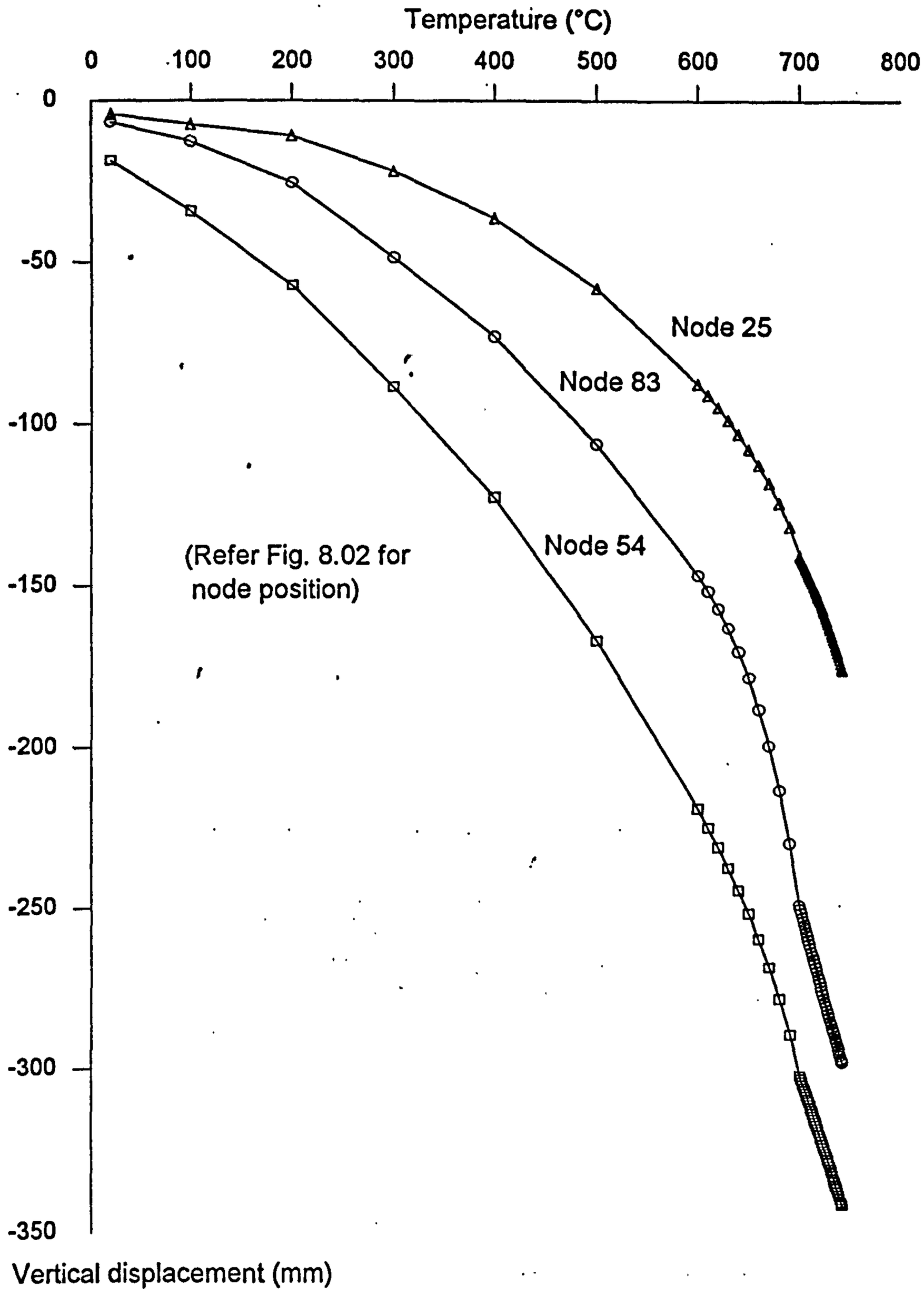

Fig. 8.15 : Vertical displacements at nodes 25, 54 and 83 relating to the slab profiles shown in Fig. 8.14.

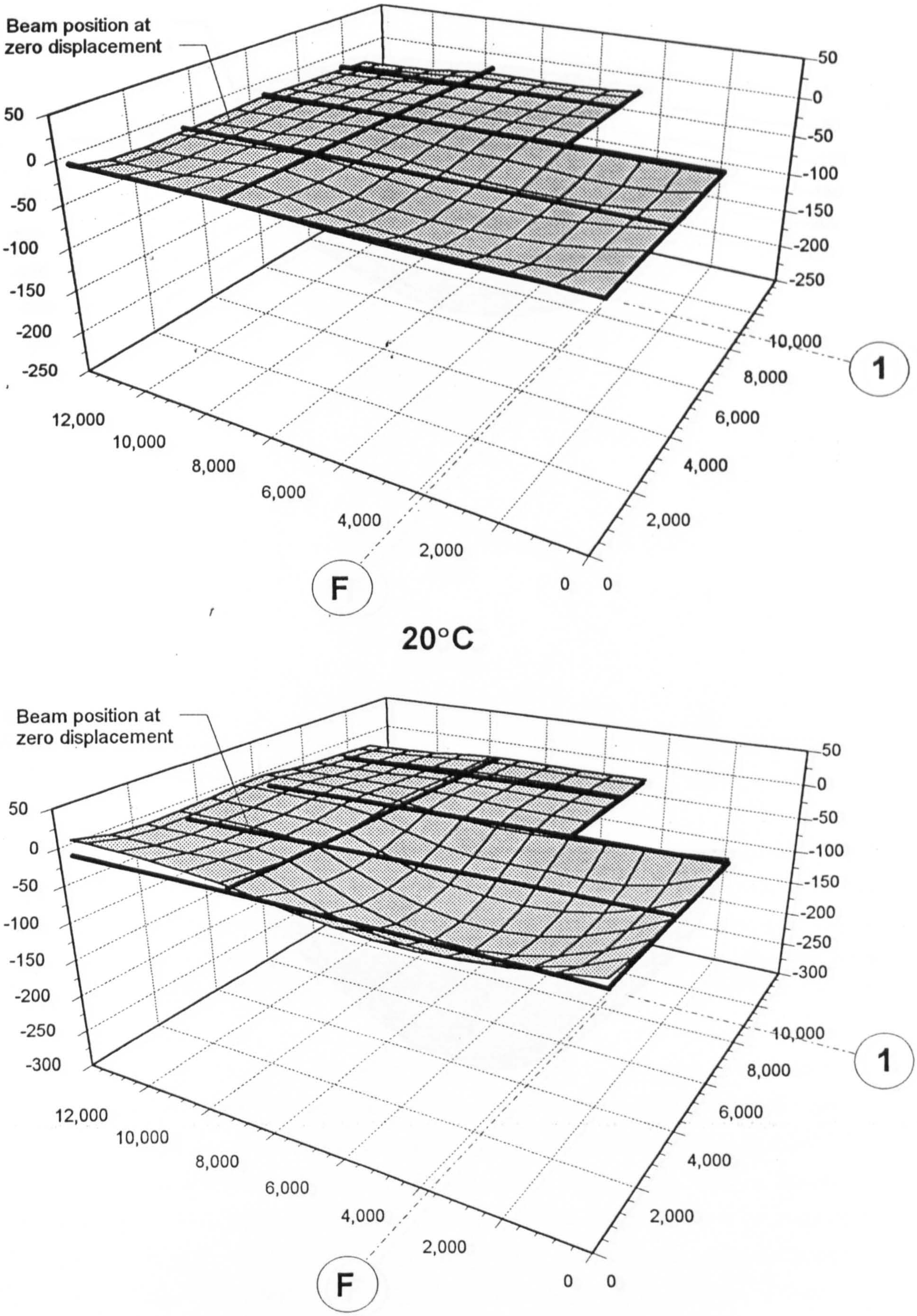

Fig. 8.16: Structural profile during the rise in temperature

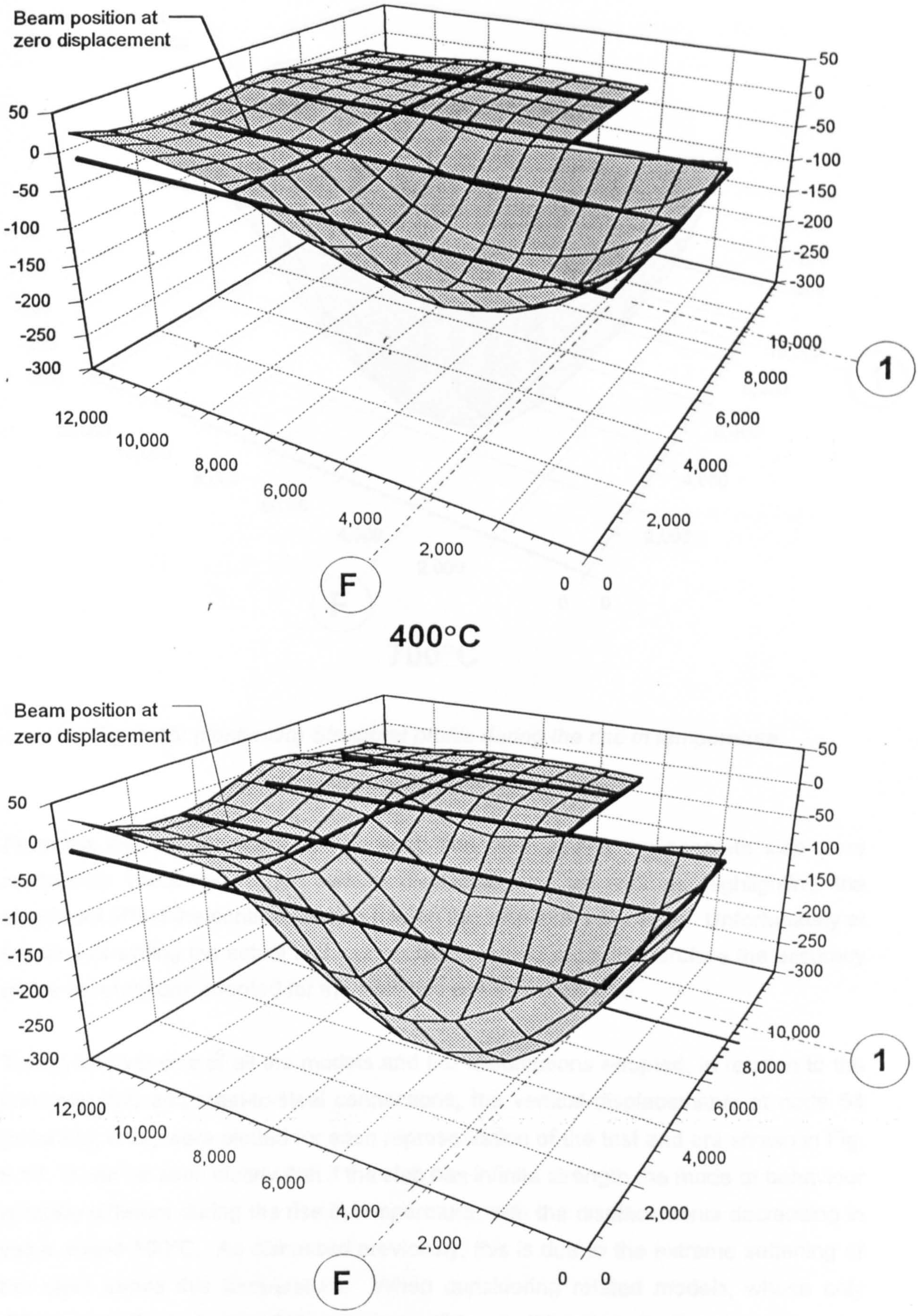

Fig. 8.16: (continued) Structural profile during the rise in temperature

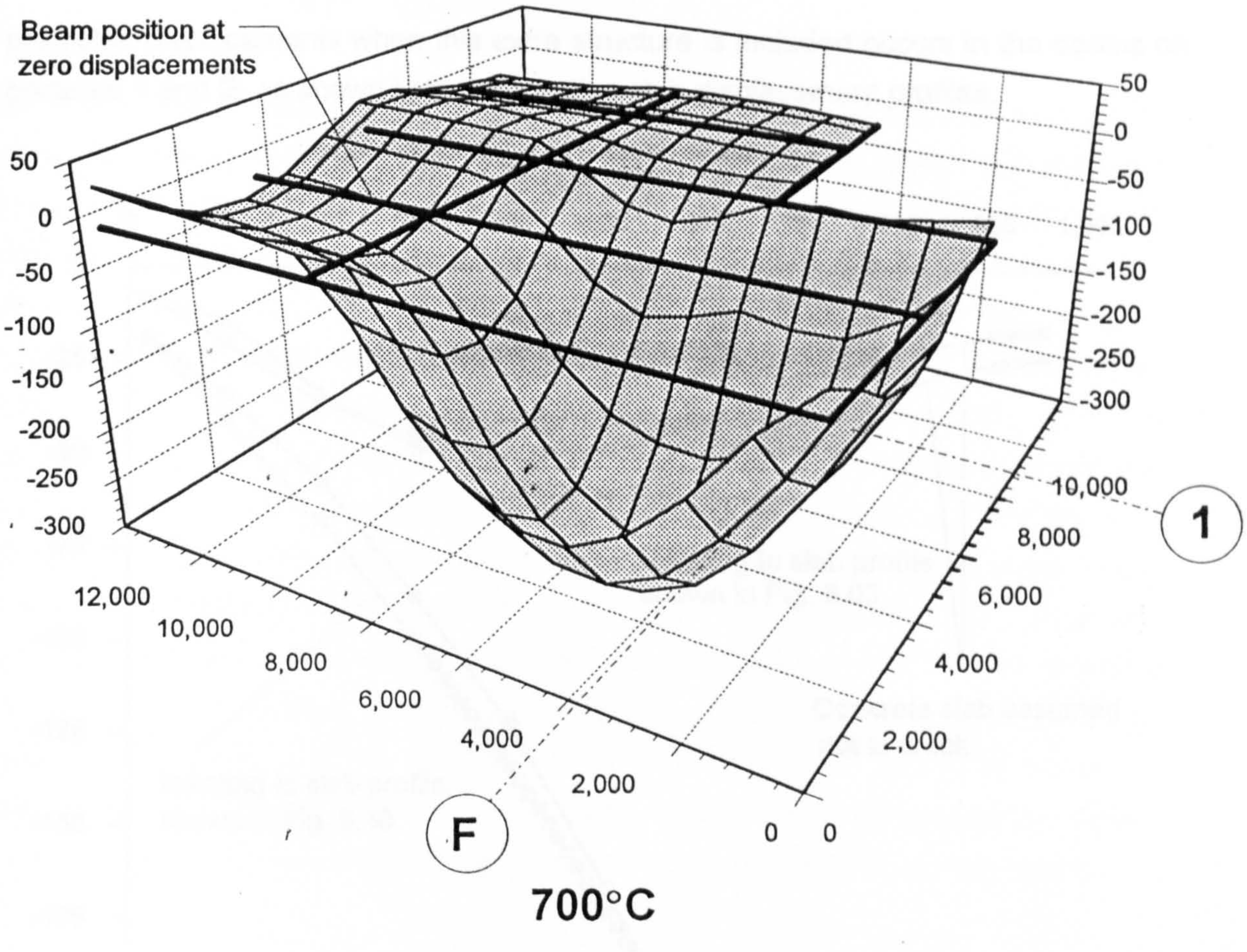

Fig. 8.16: (continued) Structural profile during the rise in temperature

From the last two models it can be seen that representing the concrete slab more realistically produces higher vertical displacements, as well as highlighting the significant effect the continuous slab has on the structural behaviour. Unfortunately at the time of writing the actual test has not been carried out and therefore the accuracy of the assumptions adopted for the slab cannot be investigated.

Taking an overview of all the models and the assumptions adopted, in relation to the concrete slab and steel-to-steel connections, the vertical displacements at node 54 (refer Fig. 8.02) were plotted for each representation of the test and are shown in Fig. 8.17. It can be seen clearly that if the slab has infinite strength the mode of behaviour is totally different during the rise in temperature, with the displacements decreasing in value above 500°C. As discussed previously, this is due to the extreme softening of the steel above this temperature. When considering related models, whose only difference is the inclusion of the structure within a half-bay in both directions, it can be seen that the vertical displacements are very similar. The major difference in the

predicted displacements when this extra structure is included occurs in the beams on gridlines 1 and E, as shown in the respective slab displacement profiles.

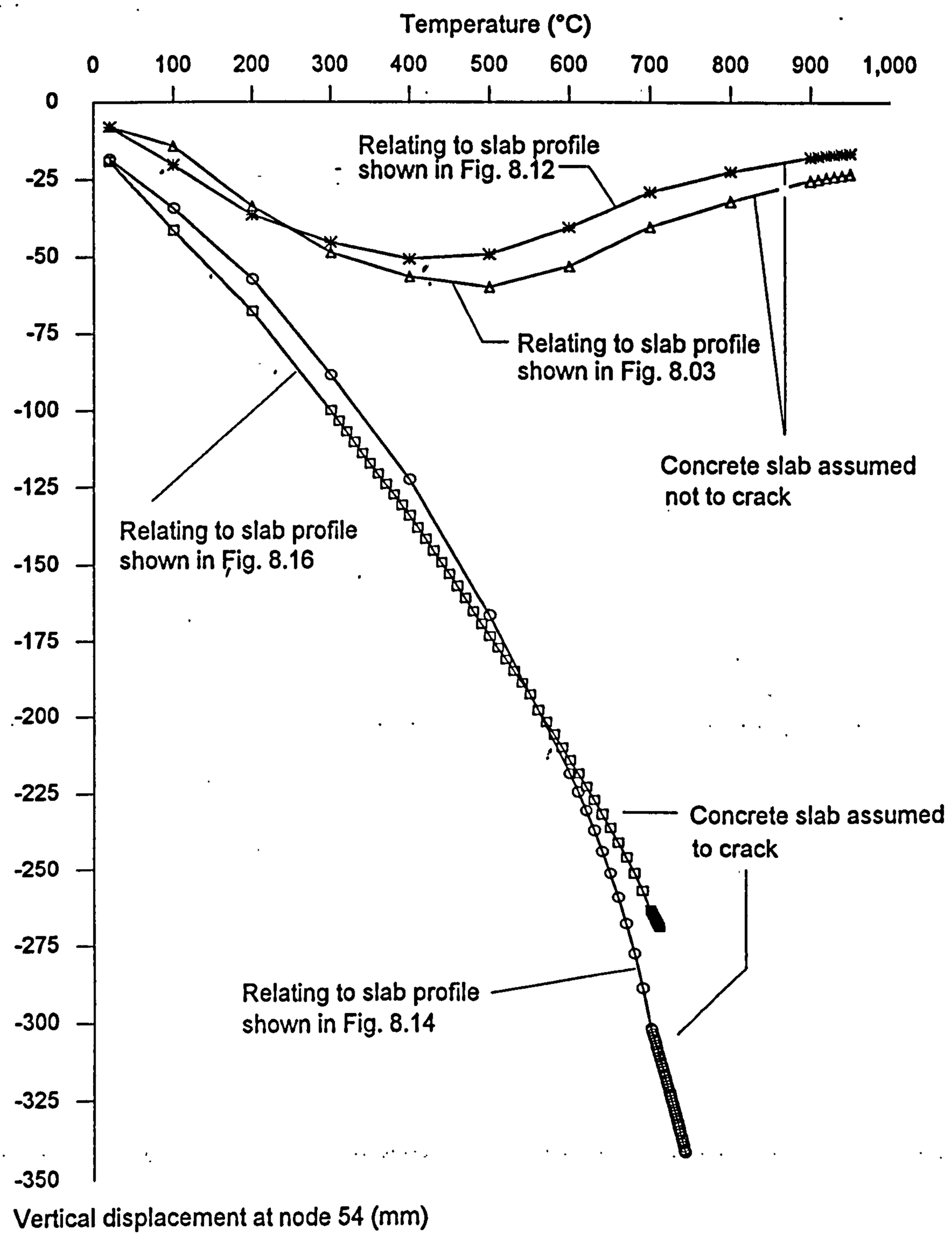

Fig. 8.17: Vertical displacements at node 54 for all four examples considered for the corner test.

8.2: RESTRAINED BEAM FIRE TEST.

The investigation following the Broadgate Phase 8 fire[81] showed that local buckling of the bottom flange occurred near to the supports of beams which had sufficient restraint against thermal expansion. Buckling occurred in the lower flange due to large induced thermal compressive forces combined with the hogging moment at the support. To investigate this type of behaviour on the Cardington test frame a secondary beam on the seventh floor was heated over a length of 8.0 metres as shown in Fig. 8.19. The test was carried out on the 19th January 1995, whilst this research project was in progress, and displacement values at average temperatures were available for comparison with the computer model predictions. The test was conducted by constructing a gas-heated furnace beneath the middle 8.0 metre length of the beam. Heating was carried out slowly over a two-and-a-half hour period, and was concluded when the bottom-flange steel temperature was 832°C. On removing the furnace local buckling similar to that which had been seen at Broadgate was apparent at the edges of the furnace, as shown in Fig. 8.18. It can of course be argued that local buckling of the bottom flange would not constitute member failure since formation of a hinge at this location would create a simply-supported beam.

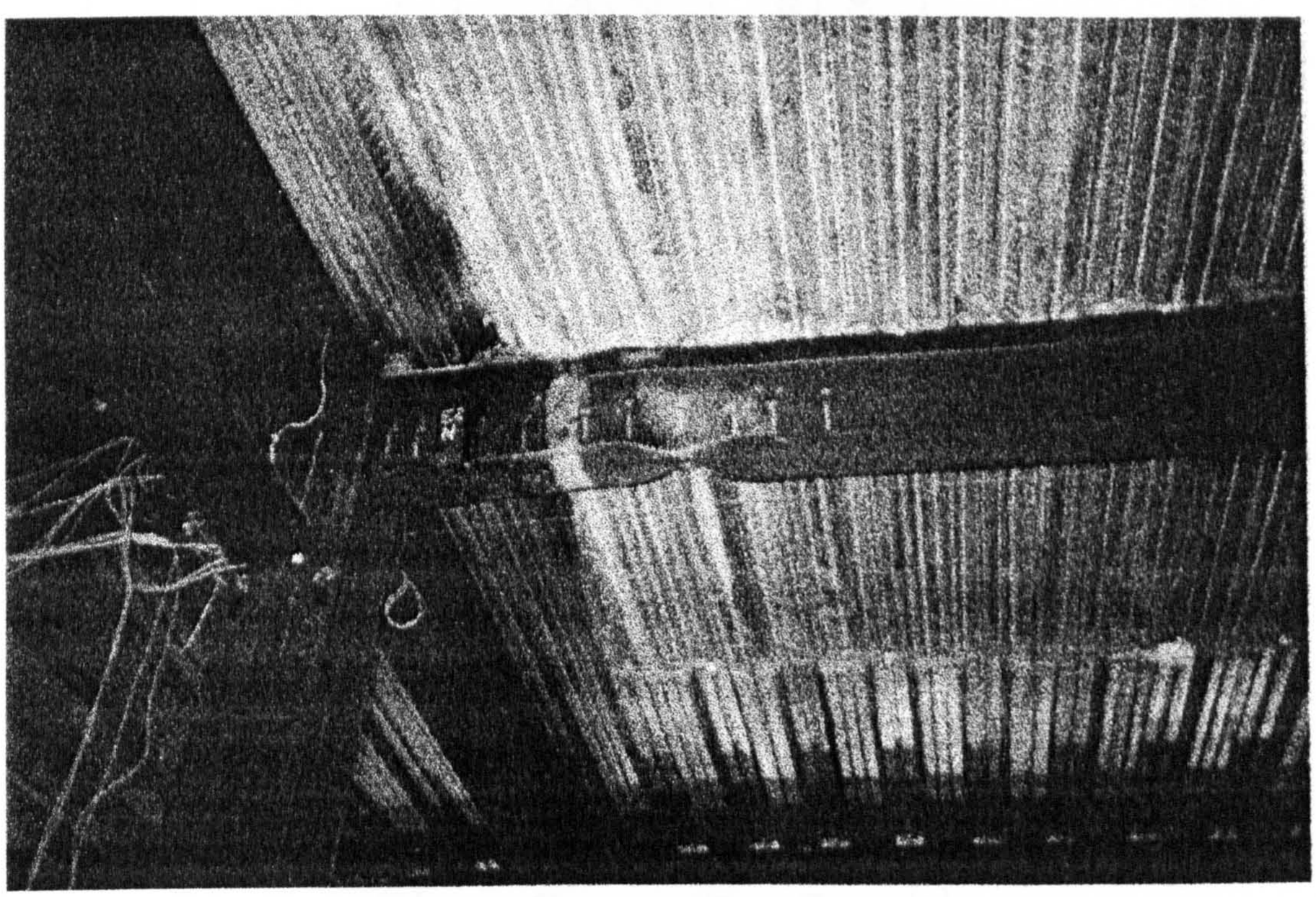

Fig. 8.18: Local buckling of the bottom flange after removal of the furnace for the restrained beam fire test conducted at Cardington.

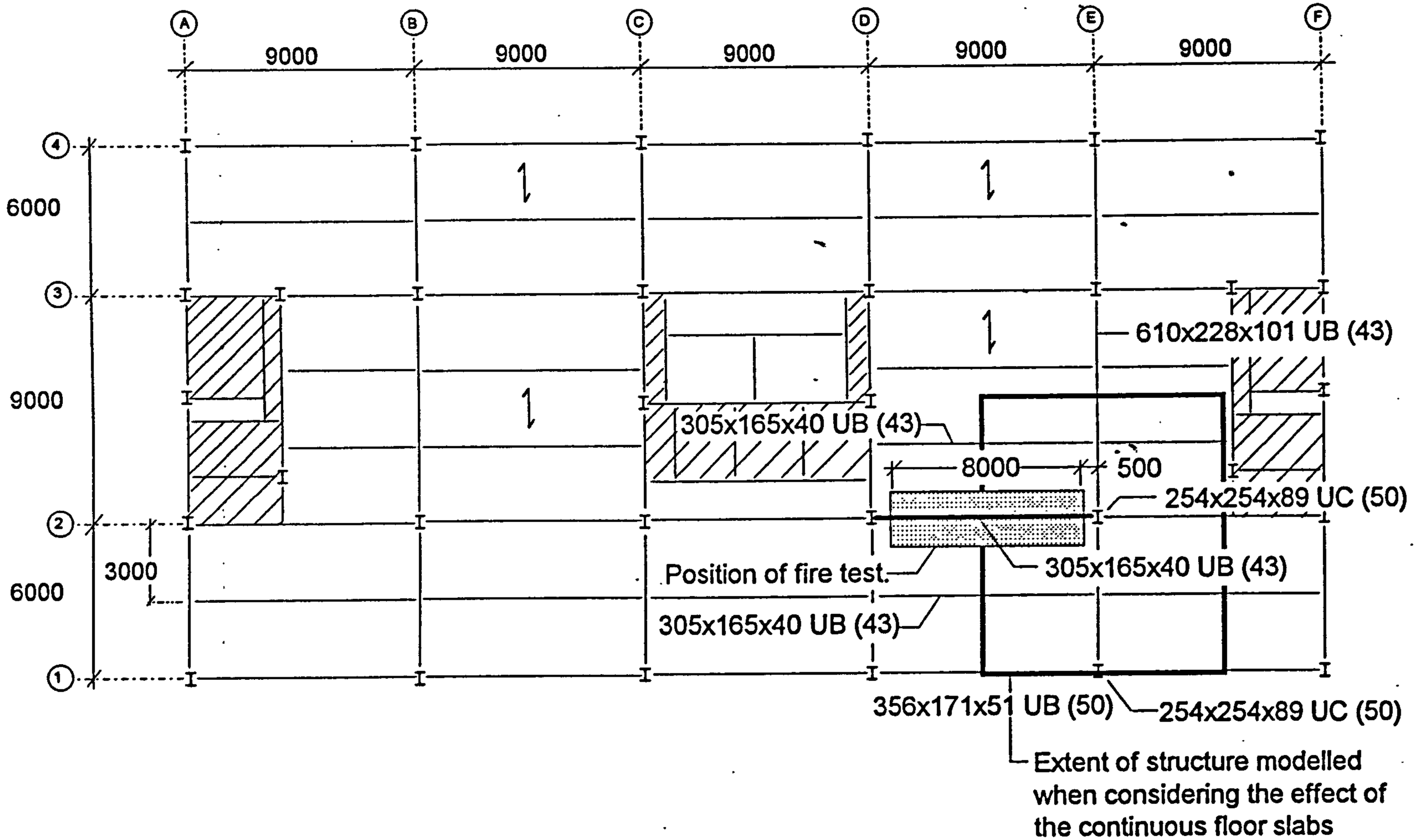

Fig. 8.19: Position of the restrained beam fire test at Cardington.

Since one-dimensional line elements are adopted to represent beam-columns, local buckling cannot be modelled. However the model was used to allow a comparison with the mid-span displacements recorded during the test. At the present time this is the only recorded information available from the test, and therefore the latest assumptions specified for modelling the frame apply, which may be revised later.

The extent of the structure incorporated within the model is shown in Fig. 8.19, with a more detailed representation, together with the finite element mesh layout adopted, shown in Fig. 8.21. Also indicated are the assumed temperature profiles of the heated steel, whose stress-strain data is represented by a Ramberg-Osgood type of equation[11]. Steel-to-steel semi-rigid connection characteristics were introduced as shown in Fig. 8.20. Since actual connection relationships are unavailable at the time of writing these characteristics are used only to allow comparison between ideal and semi-rigid joints.

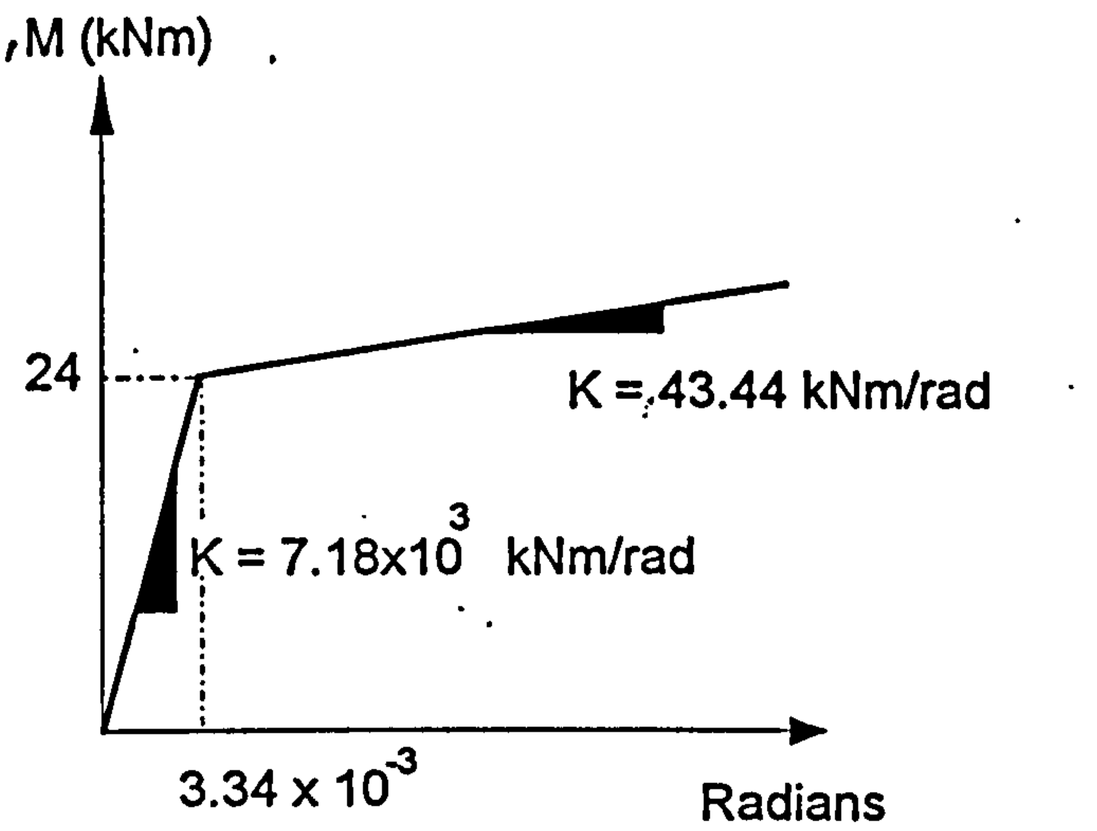

Fig. 8.20: Assumed moment-rotation relationship for semi-rigid joints.

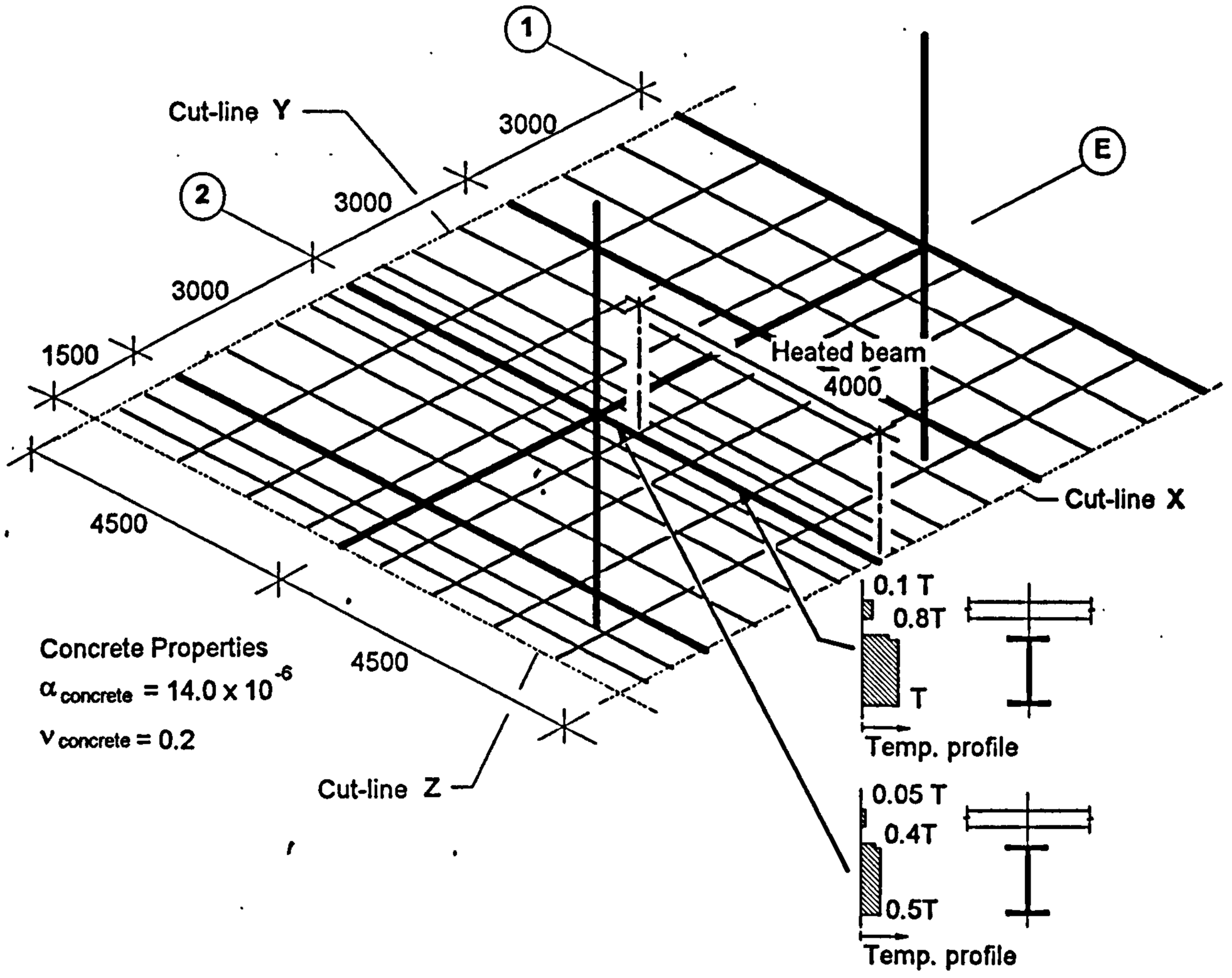

Fig. 8.21: Finite element layout for the restrained beam fire test.

When considering the analysis of the model shown in Fig. 8.21 at elevated temperatures the problem arises of how to represent the continuation of the structure on the three sides *X*, *Y*, and *Z*. Side *Z* has continuity into the depth of the building and is given restraint against both rotation and horizontal displacement perpendicular to the side. Cut-lines *X* and *Y* are restrained in rotation about the sides, since the slabs are continuous, but the effect of horizontal restraint from membrane action in the slabs is worth considering. If full lateral restraint is provided to both edges, then this restraint to thermal expansion will cause higher axial forces in the heated beam and thus higher displacements. If cut-lines *X* and *Y* represent the boundaries between the model and large areas of continuous cold slab then the extreme case of lateral restraint at these sides would be realistic. However considering the floor plan shown in Fig. 8.19, it can be seen that the adjoining bays are either external or have large cut-outs within them, thus reducing the amount of restraint to thermal expansion. The other extreme case which consists of allowing free horizontal lateral movement

across these edges could be adopted, although any tendency to differential horizontal movement makes the continuity of the slabs across these edges hard to envisage.

It was therefore decided to conduct three analyses by varying the conditions of horizontal restraint perpendicular to cut-lines *X* and *Y*.

(a) Horizontal movement perpendicular to cut-lines X and Y free.

The model shown in Fig. 8.21 is free to move laterally across cut-lines *X* and *Y*. The additional mid-span displacement of the heated beam as the temperature increases is shown in Fig. 8.22. Since the results for the semi-rigid connection did not lie between the bounds formed by the ideal connections additional analyses were conducted varying the connection stiffness and strength by scaling the characteristics shown in Fig. 8.20. To allow an appreciation of the structural behaviour the slab profiles at various temperatures during the analysis, incorporating semi-rigid connections, are shown in Fig. 8.23.

From the mid-span displacements (Fig. 8.22) it can be seen that the model compares very well with the test results until 500°C where divergence occurs. This is almost certainly due to the model's assumptions used to represent the cracking behaviour of the concrete slab in both the hogging and sagging regions. For the analysis where simple connections are adopted very little (if any) cracking is experienced in the hogging regions of the slab above and parallel to the heated beam. Therefore in this model (which represents cracking by reducing whole elements in thickness) the thickness of the slab is greater and thus stiffer when simple connections are adopted. This causes squashing of the beam to become the most prominent behaviour, causing reversal in its vertical displacement. This phenomenon was very apparent in the first analyses on the corner fire test, in which the slab was assumed not to crack.

For the rigid connections, and semi-rigid connections above 80% of the strength and stiffness of the connection characteristics, a change in gradient of the displacement:temperature relationship occurs between 700 and 800°C. Within the computer analysis the thermal expansion of steel between 750°C and 860°C remains constant due to the phase-change in steel at about 730°C. However the concrete which is at a much lower temperature (10% of the beam's lower flange temperature) and the upper flange of the beam (80% of the beam's lower flange temperature), will continue to expand. This will induce negative moments at the supports whose magnitude will depend on the rigidity of the connection.

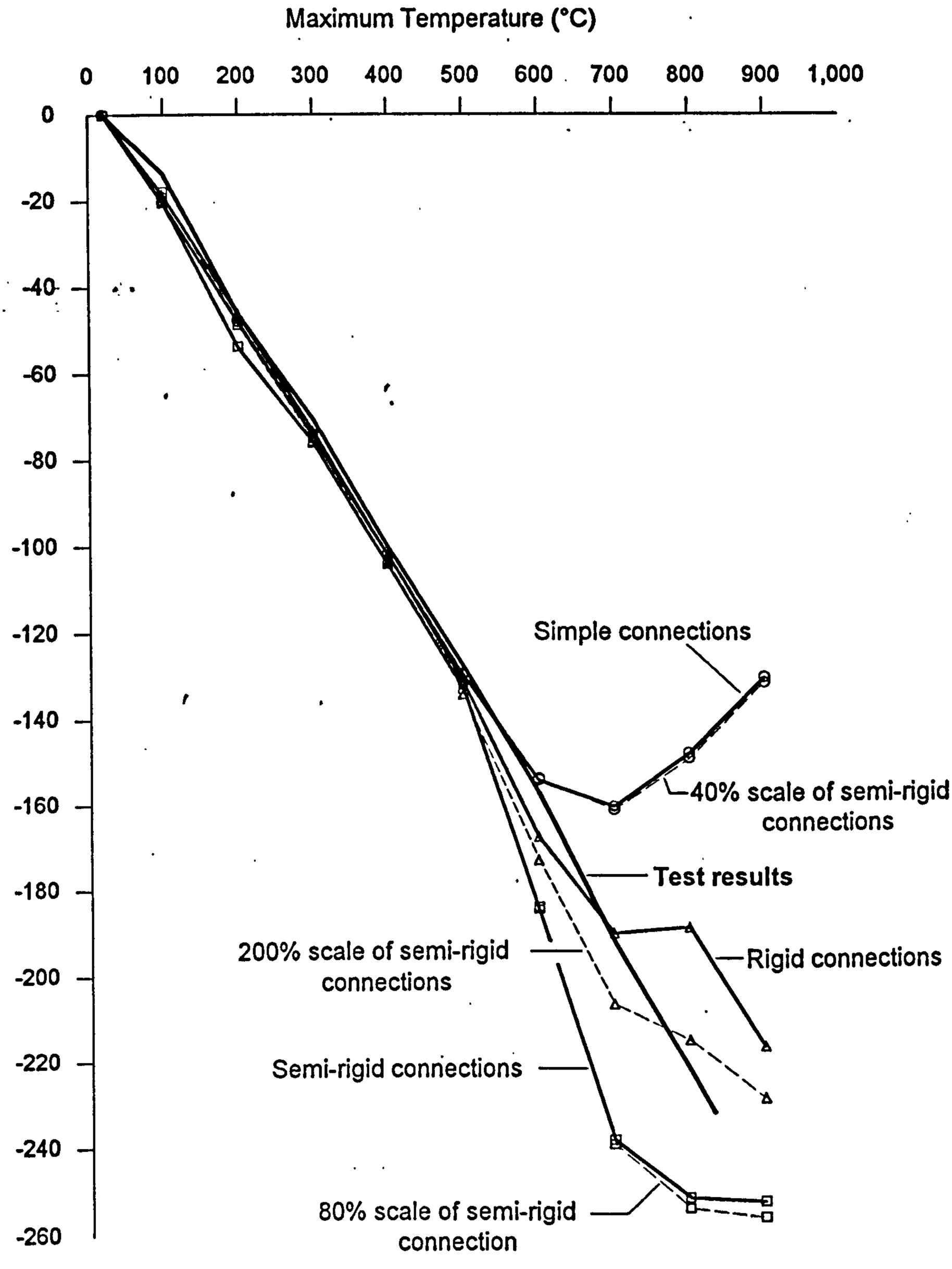

Fig. 8.22: Comparison between model analyses and test results when horizontal movement perpendicular to cut-lines X and Y is free.

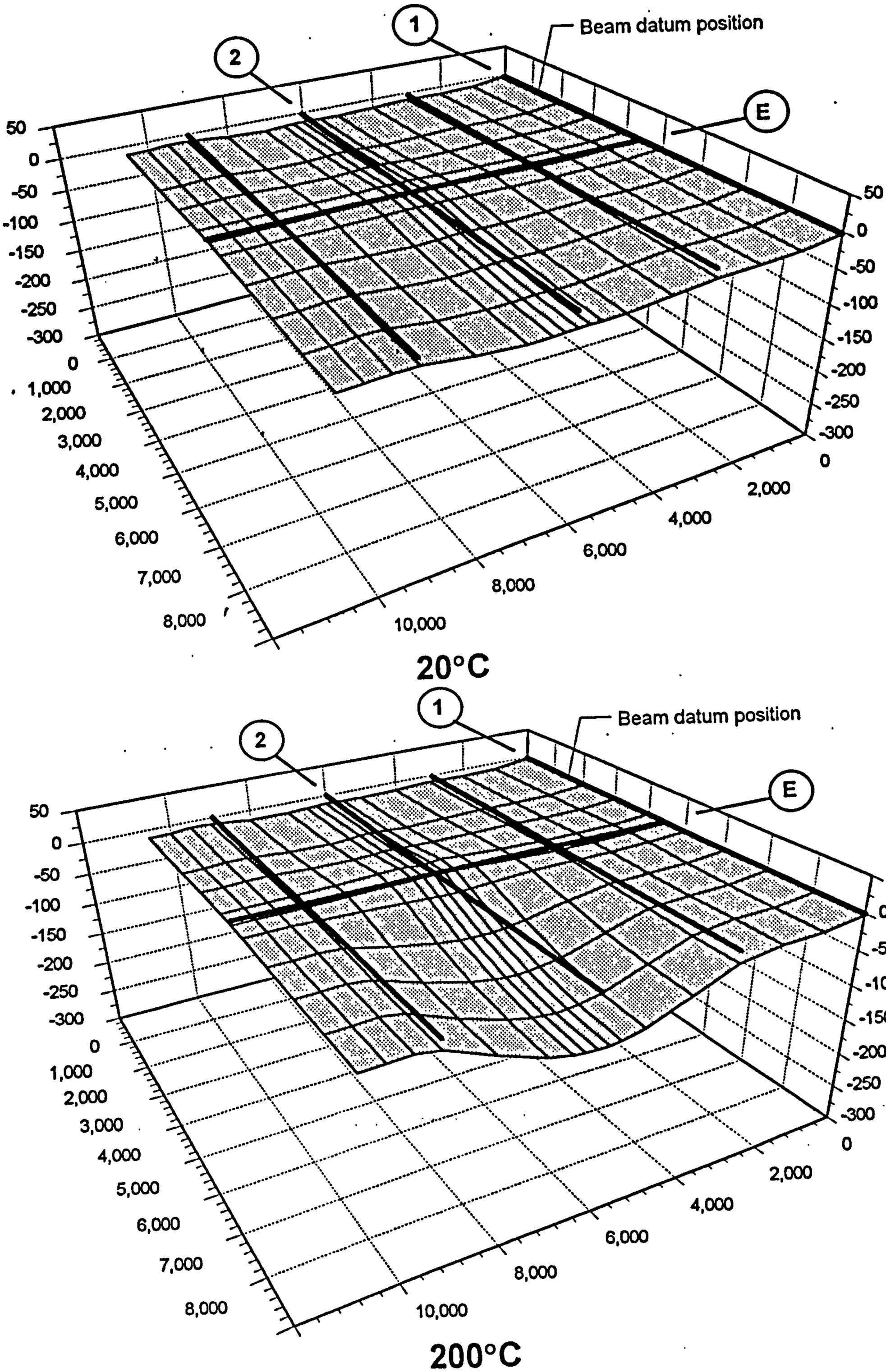

Fig. 8.23: Structural profile during rise in temperature.

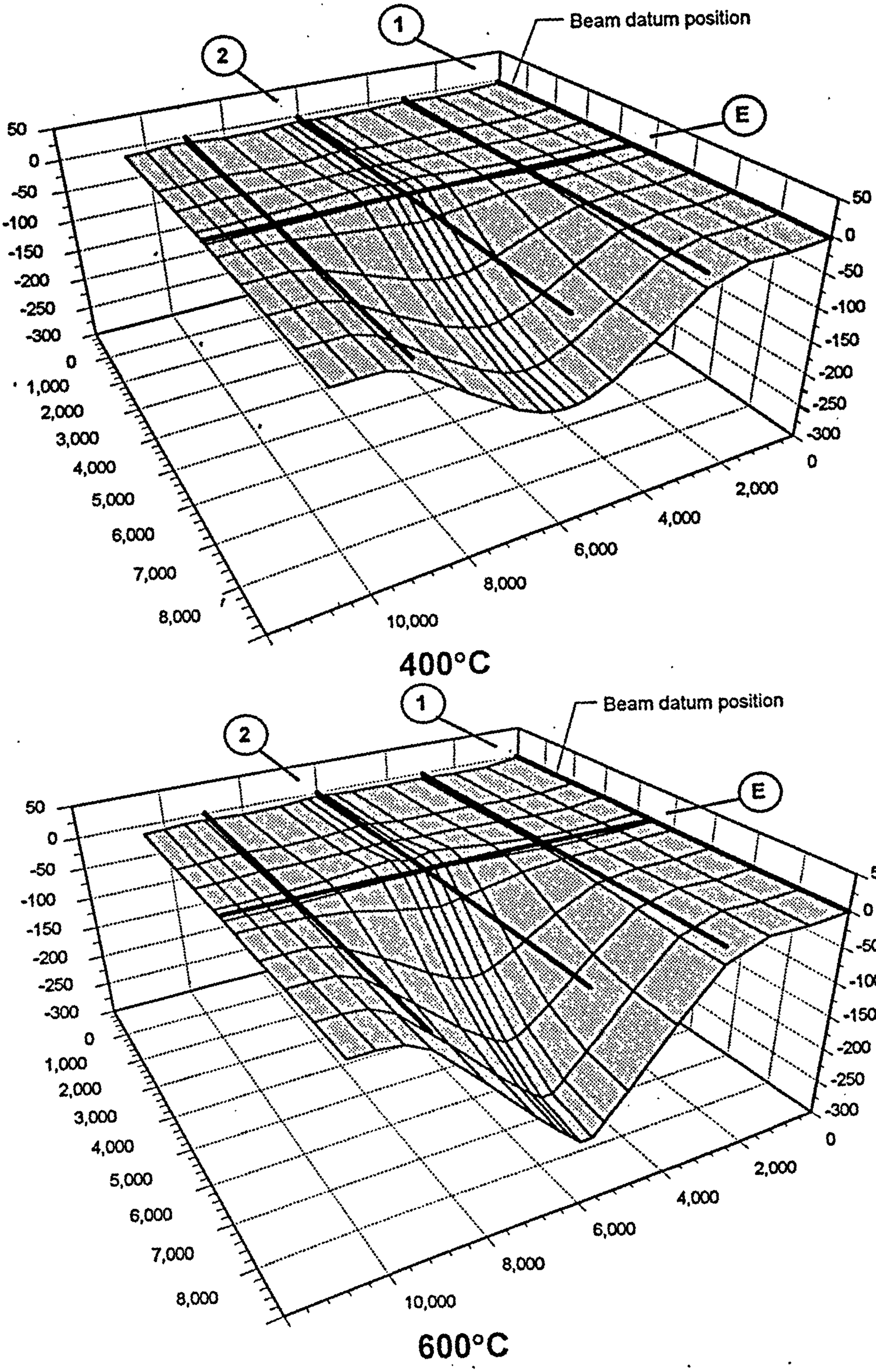

Fig. 8.23: (continued): Structural profile during rise in temperature.

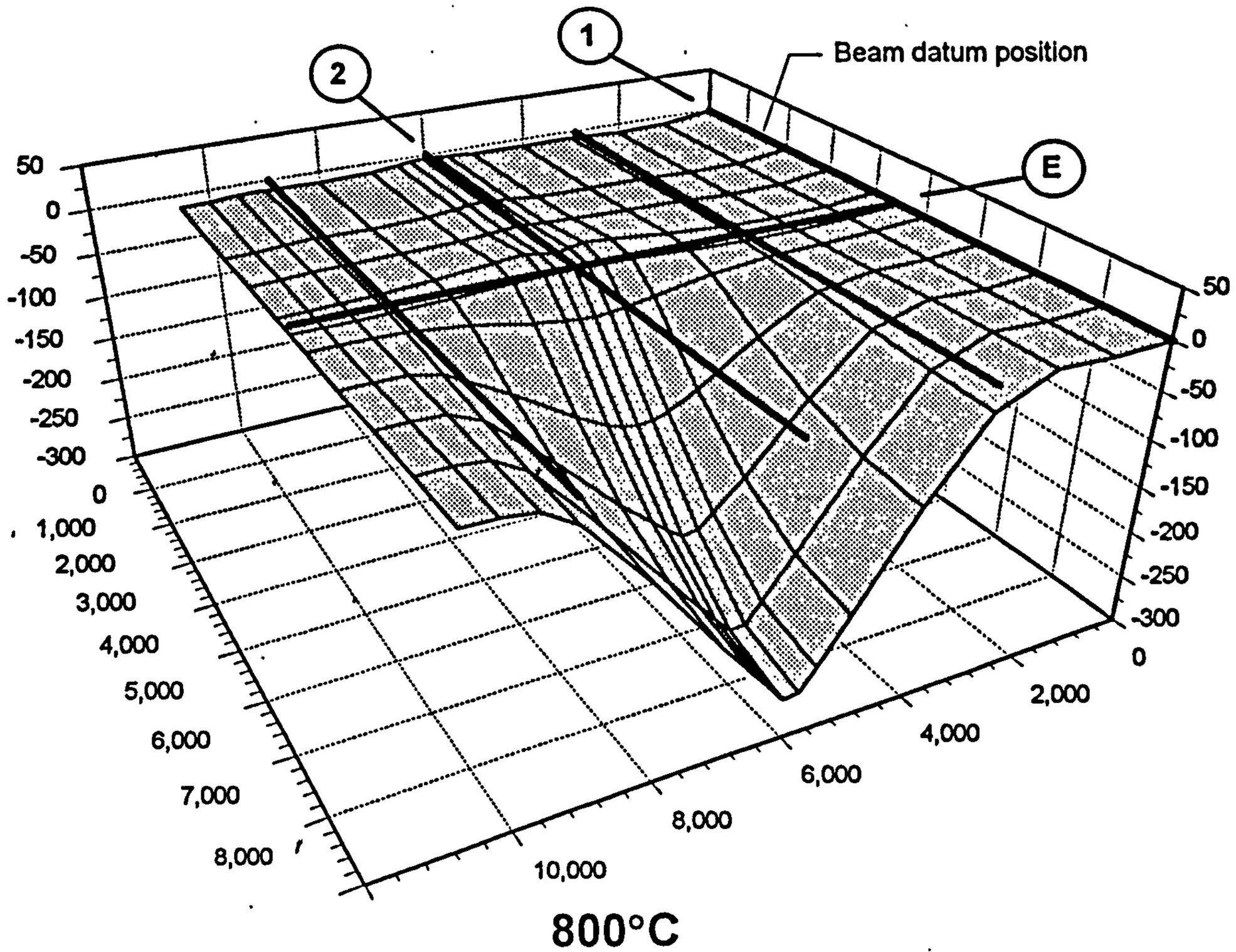

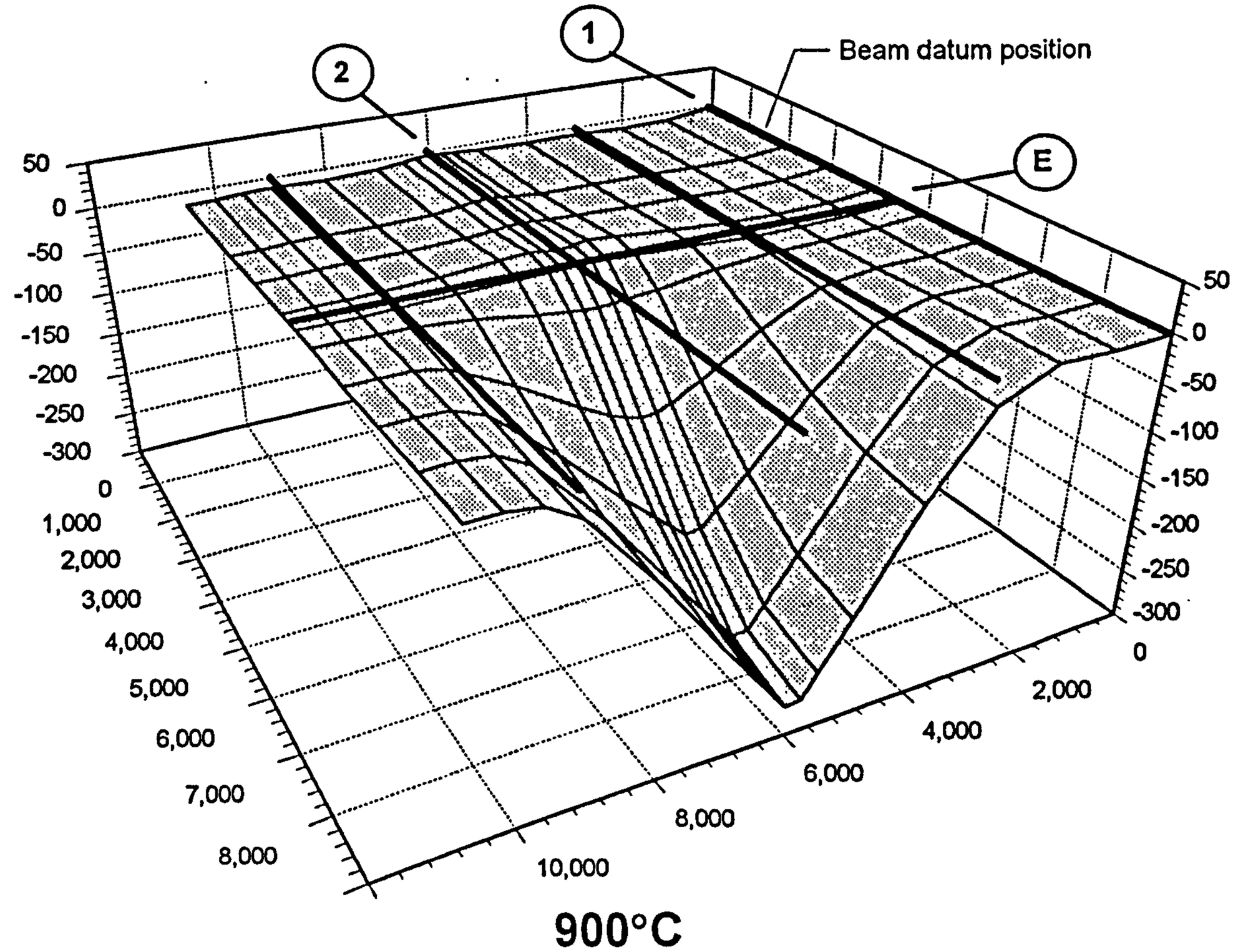

Fig. 8.23 (continued): Structural profile during rise in temperature.

Since the cut-lines *X* and *Y* have not been restrained horizontally the differential horizontal movement of the slab needs to be considered. In the example where semi-rigid connections are used the difference between the transverse horizontal displacement at the mid-span of the heated beam at 900°C and the two ends of cut-line *X* is 3.1mm and 1.6 mm.

(b) Horizontal movement perpendicular to cut-lines X and Y fully fixed.

In these analyses the cut-lines *X* and *Y* have transverse lateral movement restrained. The additional mid-span displacement of the heated beam, with rise in temperature, is shown in Fig. 8.24. It can clearly be seen that the imposed lateral restraint results in higher vertical displacements. In these analyses the semi-rigid case lies between the ideal joints, due to the thickness of slab in the sagging areas being smaller (since the vertical displacements are greater) than in the previous analyses. This causes the stiffness and strength of the slab to reduce, and thus squashing of the beam is not encountered.

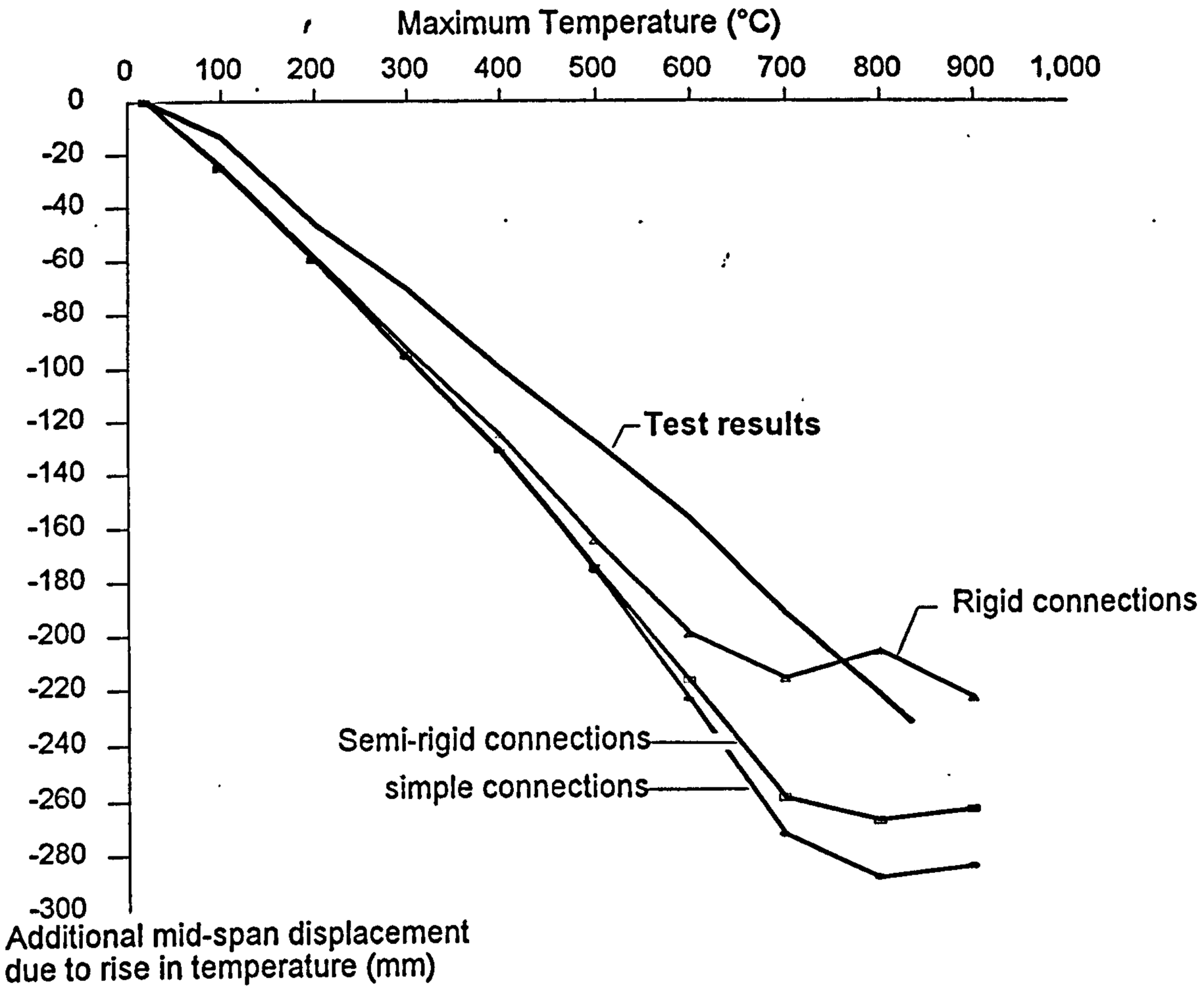

Fig. 8 24: Comparison between model analyses and test results when horizontal movement perpendicular to cut-lines X and Y is fully restrained.

(c) Horizontal movement perpendicular to cut-line X fully fixed whilst cut-line Y is free to move.

In these analyses nodes on cut-line *Y* are allowed to move laterally, with nodes on cut-line *X* (which is in the area of the heated members) remaining restrained against transverse movement. The results produced are shown in Fig. 8.25 and are very similar to the analysis where both cut-lines are fixed laterally, although vertical displacements are slightly less. For the semi-rigid case the horizontal shear of the slab at 900°C creates a difference of horizontal displacement between gridline 2 and the ends of cut-line *Y* of 1.7mm and 0.4mm.

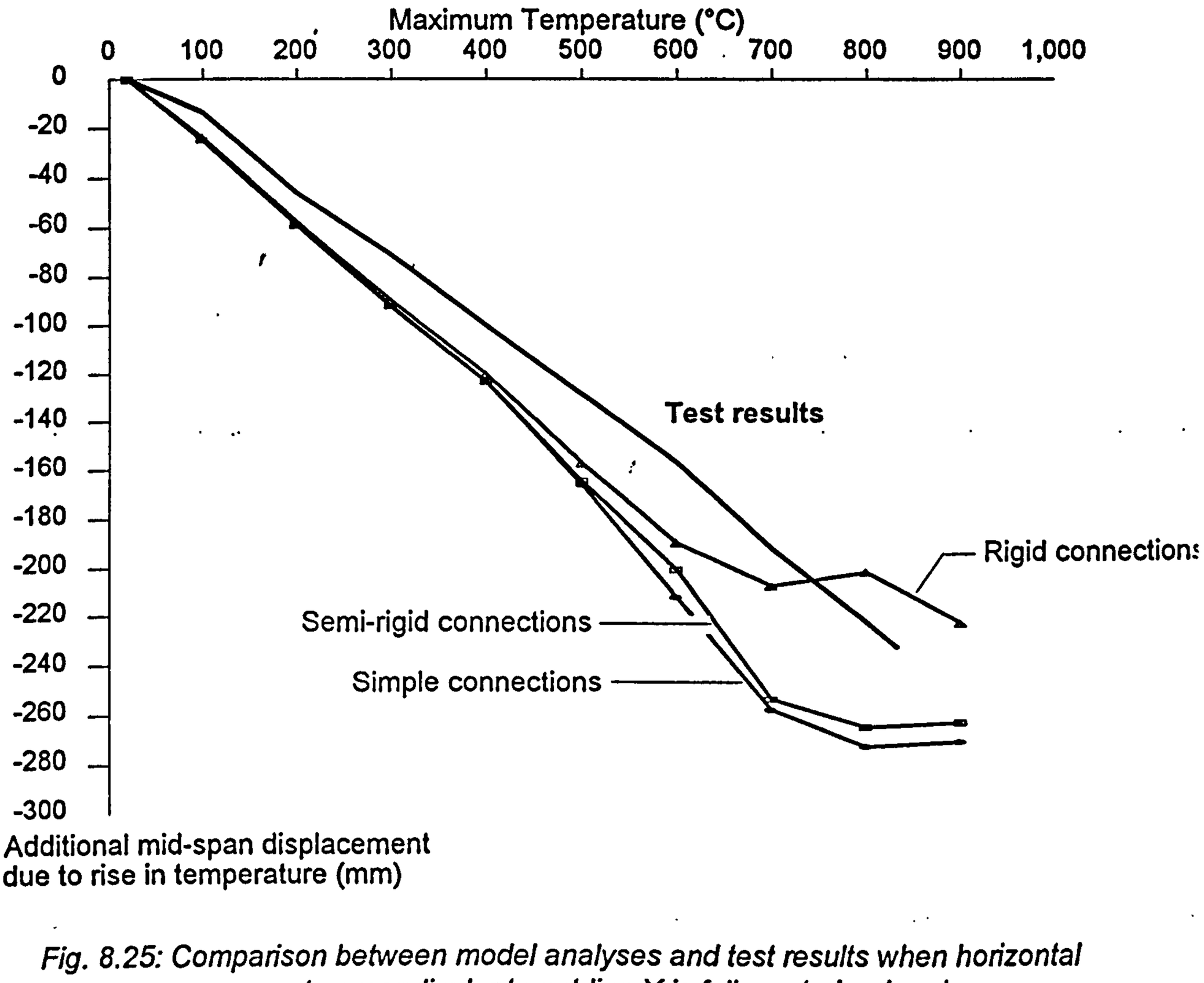

Fig. 8.25: Comparison between model analyses and test results when horizontal movement perpendicular to cut-line X is fully restrained and cut-line Y is free to move.

To set the above analyses into context the beam was also modelled as an isolated composite beam with an effective flange width of span/4, as shown in Fig. 8.26. The mesh of finite elements was similar to the layout in the proximity of the beam in the previous model in which continuous floor slabs were considered. Both semi-rigid and

ideal connections were considered, and free horizontal movement was allowed at the supports. The additional displacements at mid-span of the beam during the rise in temperature are shown in Fig. 8.27. Using the Limiting Temperature method from BS5950 Part 8[5], a load ratio of 0.44 gives a failure temperature of 668°C. The "failure" criterion[7] used for beams consists of a maximum in-plane deflection of span/20, or a maximum rate of deflection when span/30 is exceeded. Since time is not incorporated explicitly within the analysis it is impossible to use this second criterion. However both span/30 and span/20 are indicated on Fig. 8.27, together with the failure temperature specified in BS5950 Part 8.

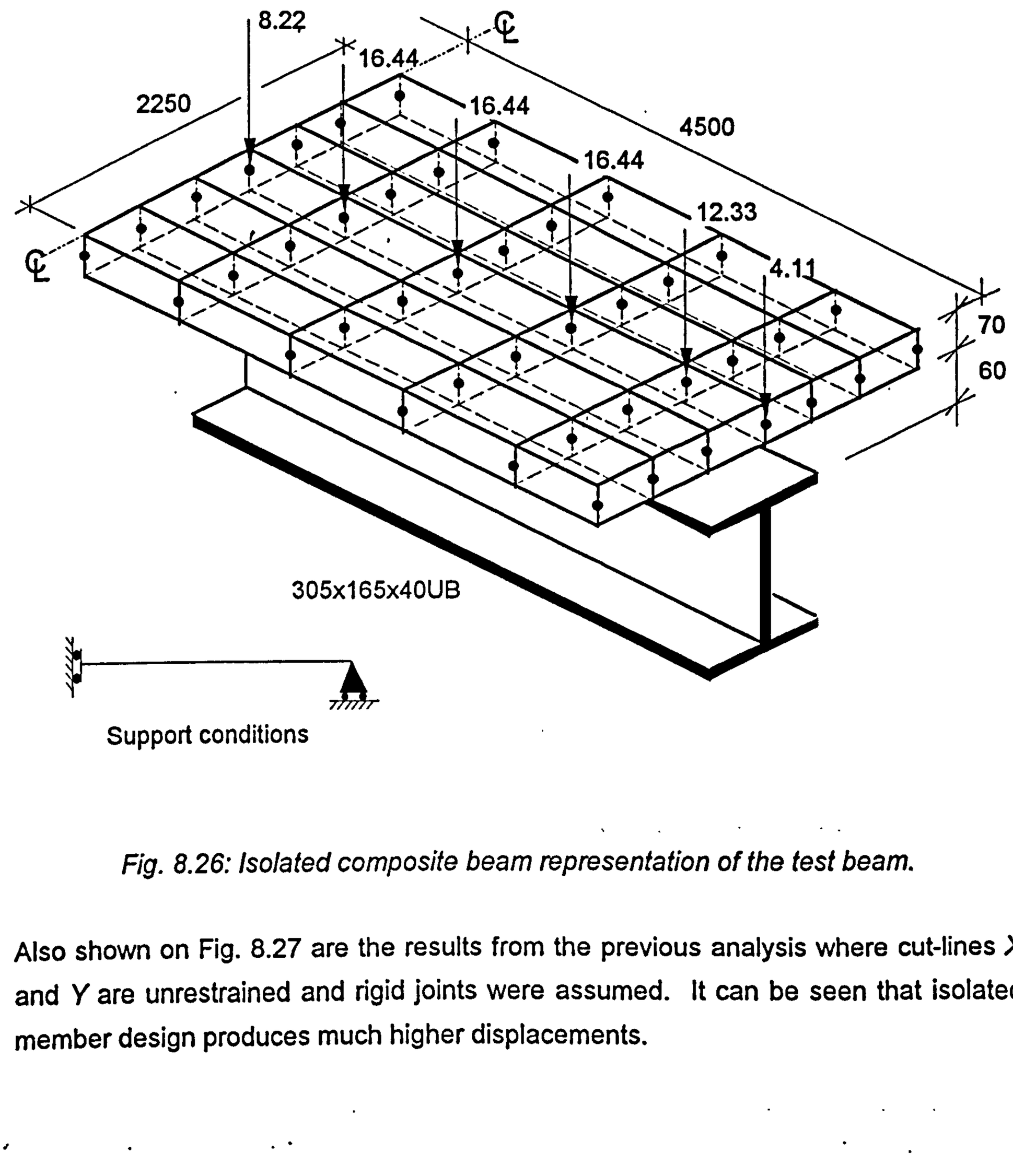

Fig. 8.26: Isolated composite beam representation of the test beam.

Also shown on Fig. 8.27 are the results from the previous analysis where cut-lines *X* and *Y* are unrestrained and rigid joints were assumed. It can be seen that isolated member design produces much higher displacements.

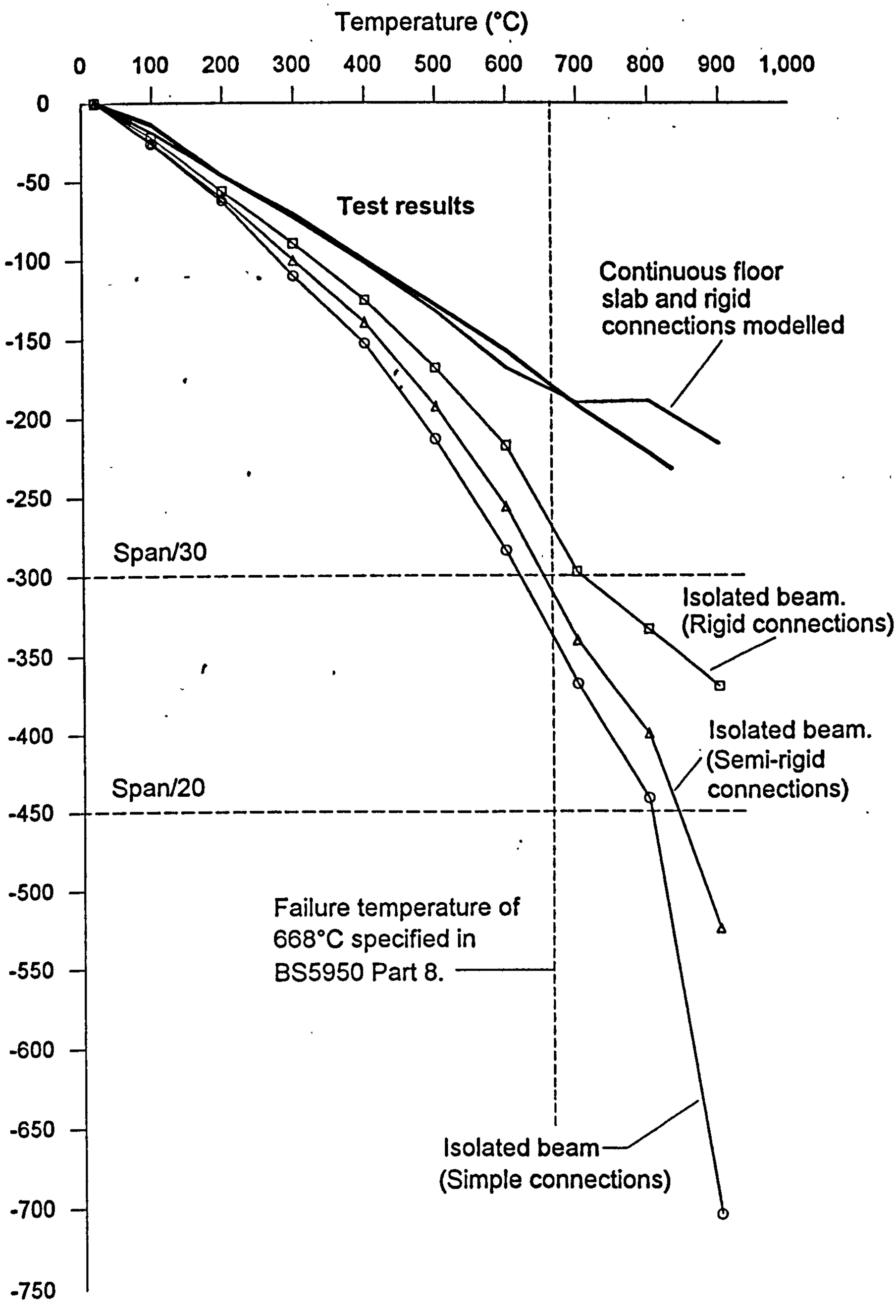

Fig. 8.27: Comparison between model analyses when considering an isolated composite beam and the test results.

8.21: CONSIDERATION OF LOCAL BUCKLING EFFECTS.

Since one-dimensional finite elements are used to represent beam-column members, local and distortional buckling cannot be identified. However since local buckling was experienced at the ends of the heated zone of the beam in the actual test it was decided to repeat the analysis for the case where horizontal movement perpendicular to cut-line *X* is fully fixed and cut-line *Y* is free to move (which are probably the most realistic boundary conditions), and to attempt to model the effect of local buckling. This was done by considering simple connections, with the spring element representing the connection between the heated beam and column displaced to the position where local buckling was experienced, as shown in Fig. 8.28. Since the beam acts compositely with the slab it is possible for the whole steel section to buckle locally if the neutral axis is within the slab, with the top flange buckling at a position between the troughs in the metal decking. Therefore the insertion of a pin in the steel section is realistic, except that it is placed in position at the start of the analysis since the temperature at which buckling occurred is not known. Removal of axial stiffness in the compressive areas of the steel was impossible to model. This was not considered significant, since in reality the axial force would be re-directed through the slab.

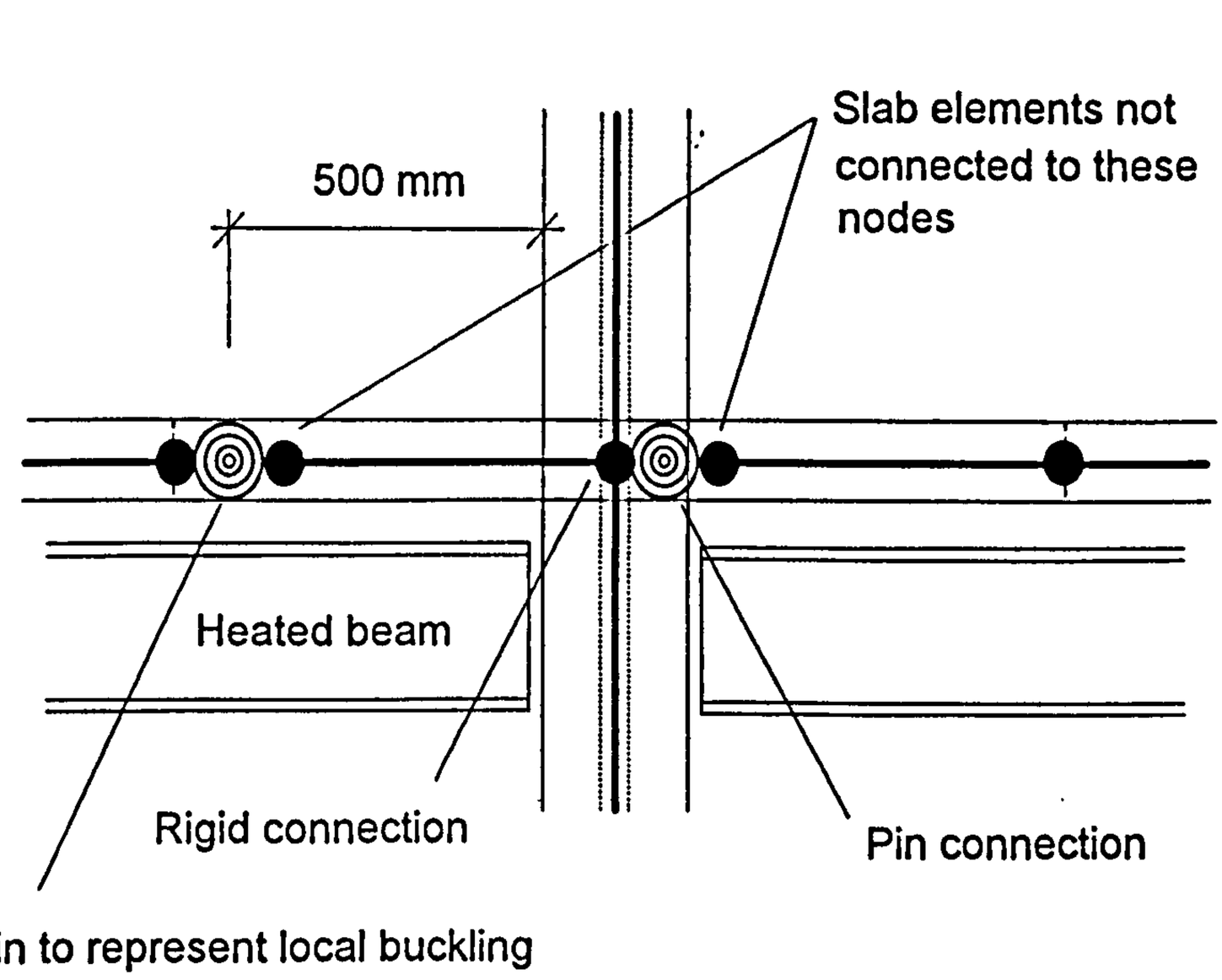

Fig. 8.28: Insertion of a 'pin' to represent local buckling.

The results of the analysis are shown in Fig. 8.29, and comparison with the previous analyses shown in Fig. 8.25, which are also superimposed on Fig. 8.29, indicates the

significant effect of local buckling with the vertical displacements being smaller. This is due to the beam behaving as approximately simply supported between the points of local buckling, causing less concrete to go into tension and thus less cracking in these areas.

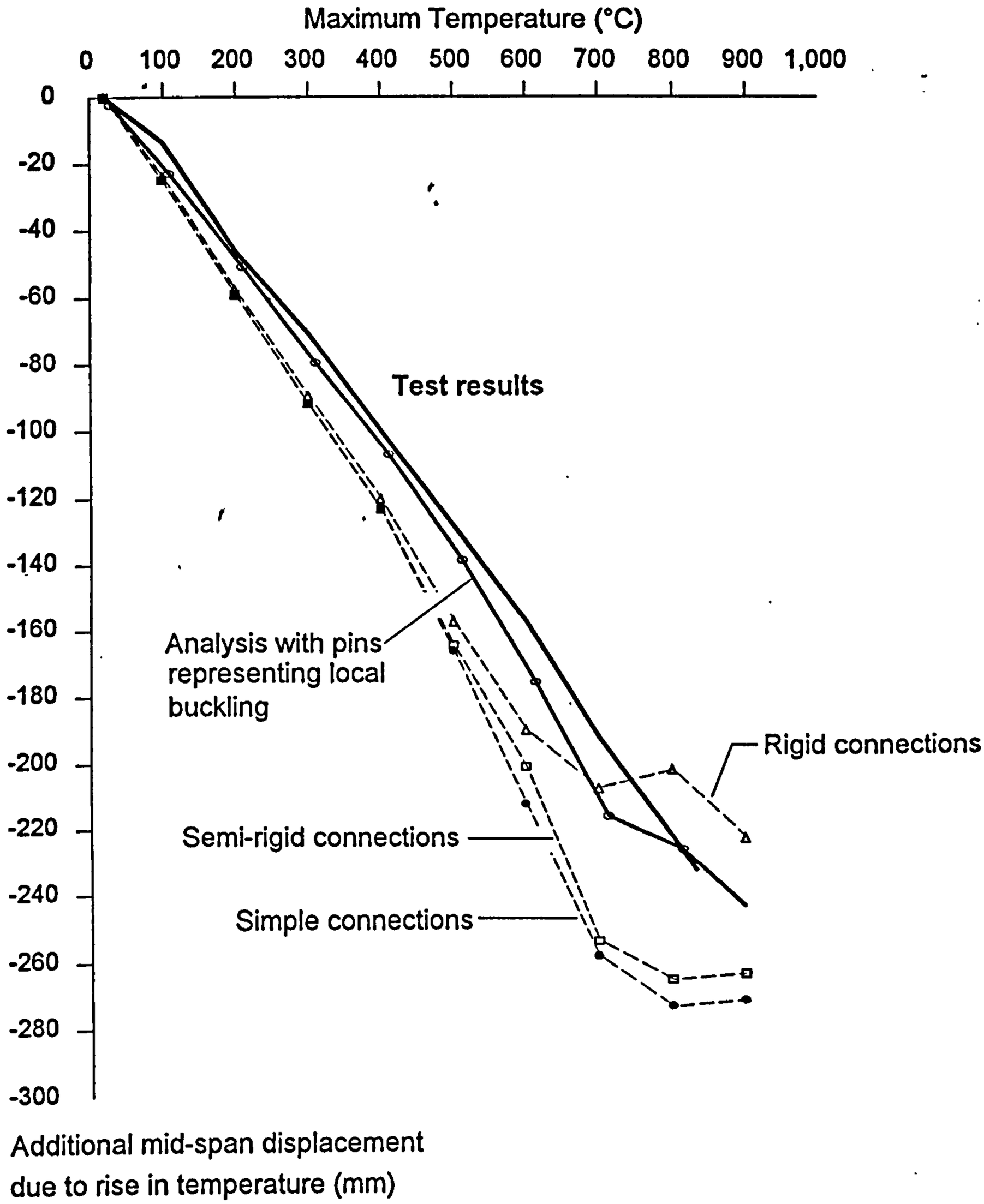

Fig. 8.29: Model predictions when assuming pins at the location of local buckling experienced at some point during the test.

To model local buckling effects a mesh of shell elements would be needed to represent the steel beam-column cross-sections. This would greatly reduce the size

of structural area which could practically and economically be modelled. Since it has been shown, in the examples presented on the Cardington frame, that a significant amount of structure surrounding the test area must be considered to obtain realistic predictions the use of such a mesh to represent the steel sections is clearly not feasible.

However, to be conservative when modelling design cases with one-dimensional elements, steel-to-steel connections can legitimately be considered as pinned. In this test local buckling occurred slightly away from the beam ends, since only the middle 8.0 metres was heated. In a real fire the whole beam will typically be heated and local buckling will usually occur much nearer to the connection.

8.3: TWO-DIMENSIONAL CROSS-FRAME FIRE TEST.

This test consists of heating the columns and beams on gridline B, between the third and fourth floors. The position of the test together with the extent of the structure incorporated within the analysis is indicated in Fig. 8.30, with a more detailed representation shown in Fig. 8.31. The assumptions adopted for the previous test remain the same, except for the heating scheme which is shown in Fig. 8.32, and the assumptions which represent steel-to-steel connections. Three analyses were conducted in which the assumptions for the steel-to-steel connections were varied.

(a) Fin plates connecting beam-to-beam considered as pinned, with beam-to-column connections considered as rigid.

In this analysis the steel beam-to-beam connections (fin-plates) were represented as pins. The steel beam connection to the major and minor axes of the column were considered as rigid.

The vertical displacements of the main beam on gridline B during the rise in temperature are shown in Fig. 8.33, with the horizontal displacements shown in Fig. 8.34. To allow an overall appreciation of the structural behaviour the slab deflection profiles during the rise in temperature are shown in Fig. 8.35.

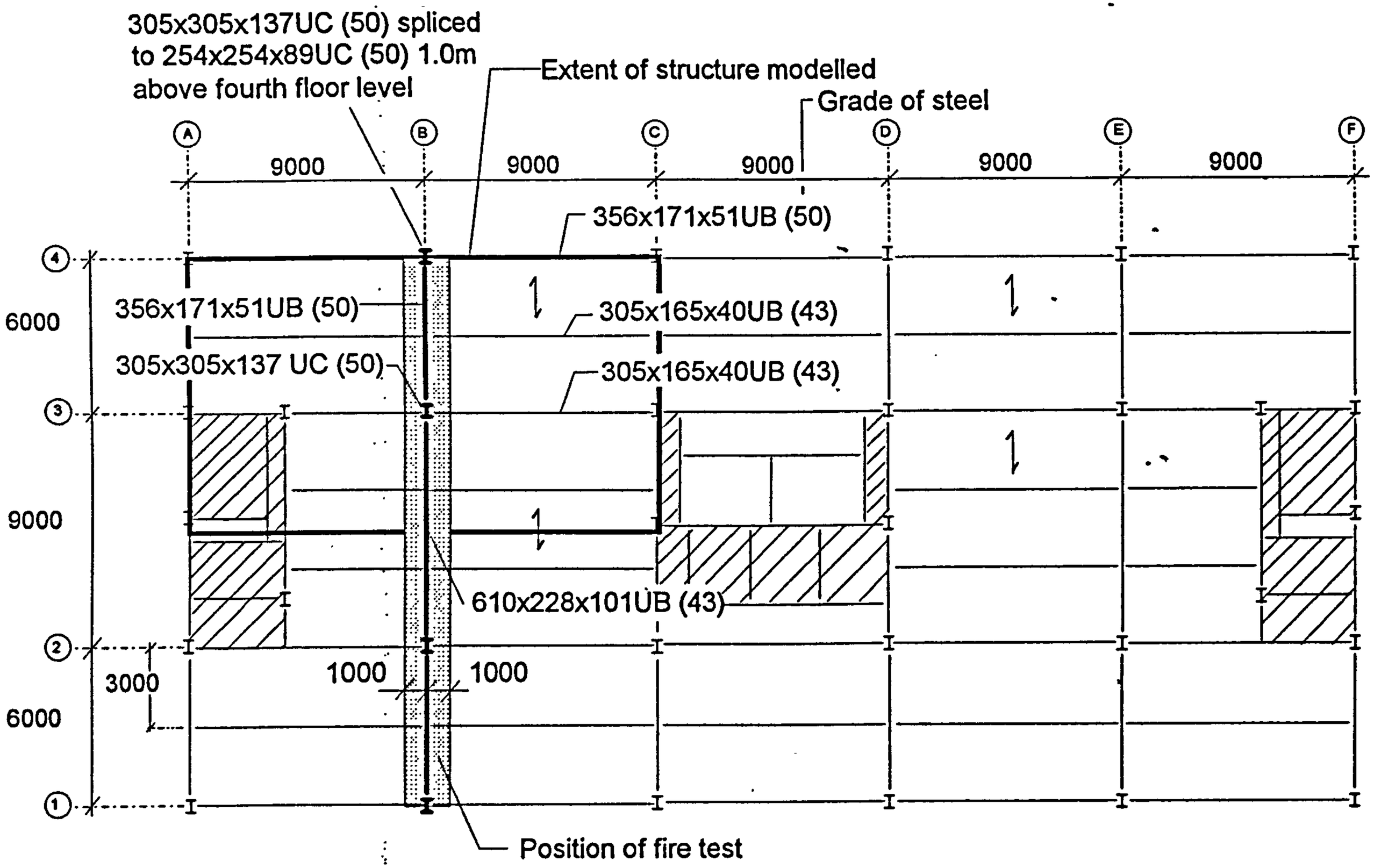

Fig. 8.30: Position of two-dimensional cross-frame fire test on the Cardington frame (conducted between third and fourth floors)

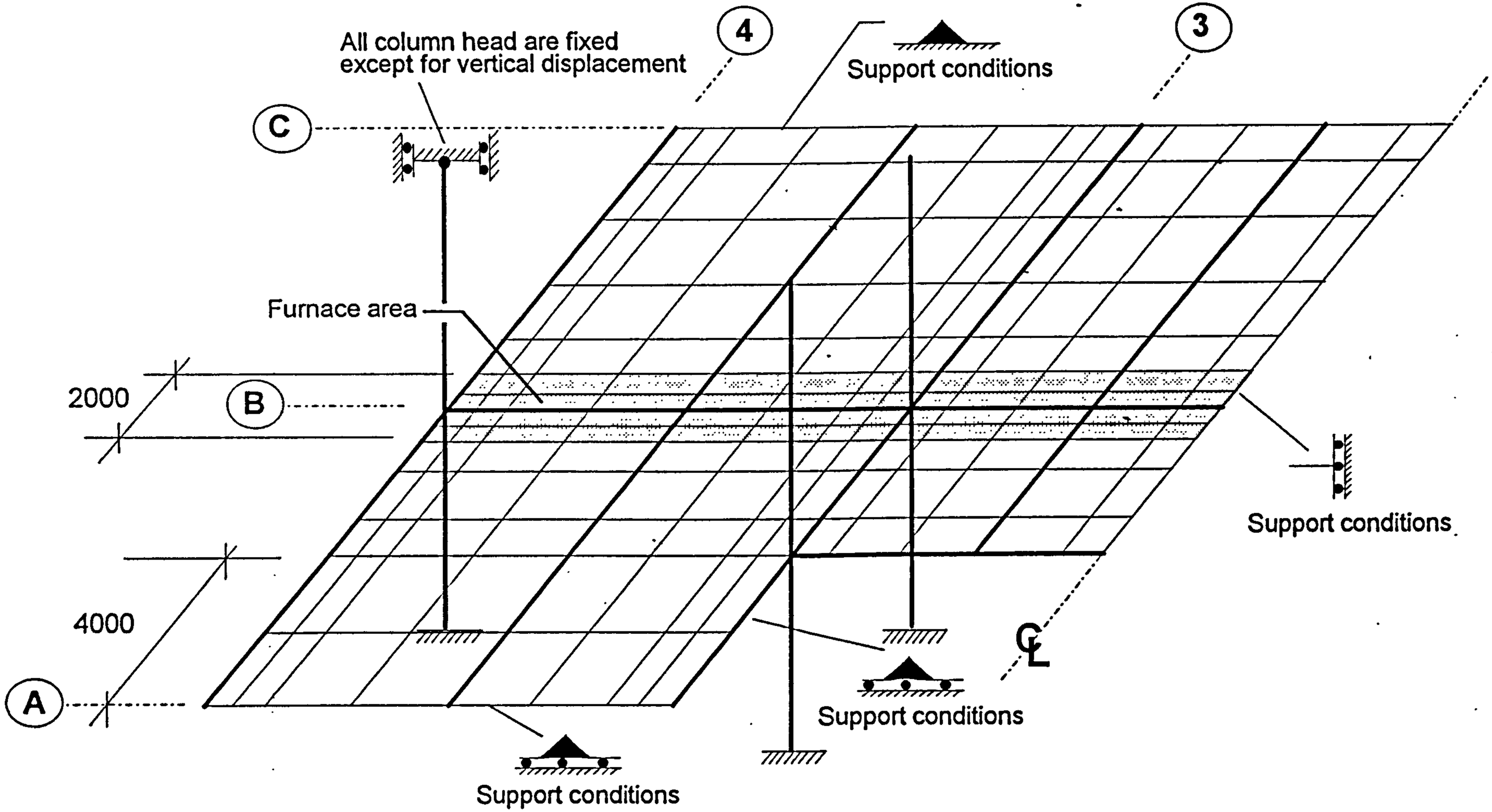

Fig. 8.31: Finite element layout for the two-dimensional frame fire test.

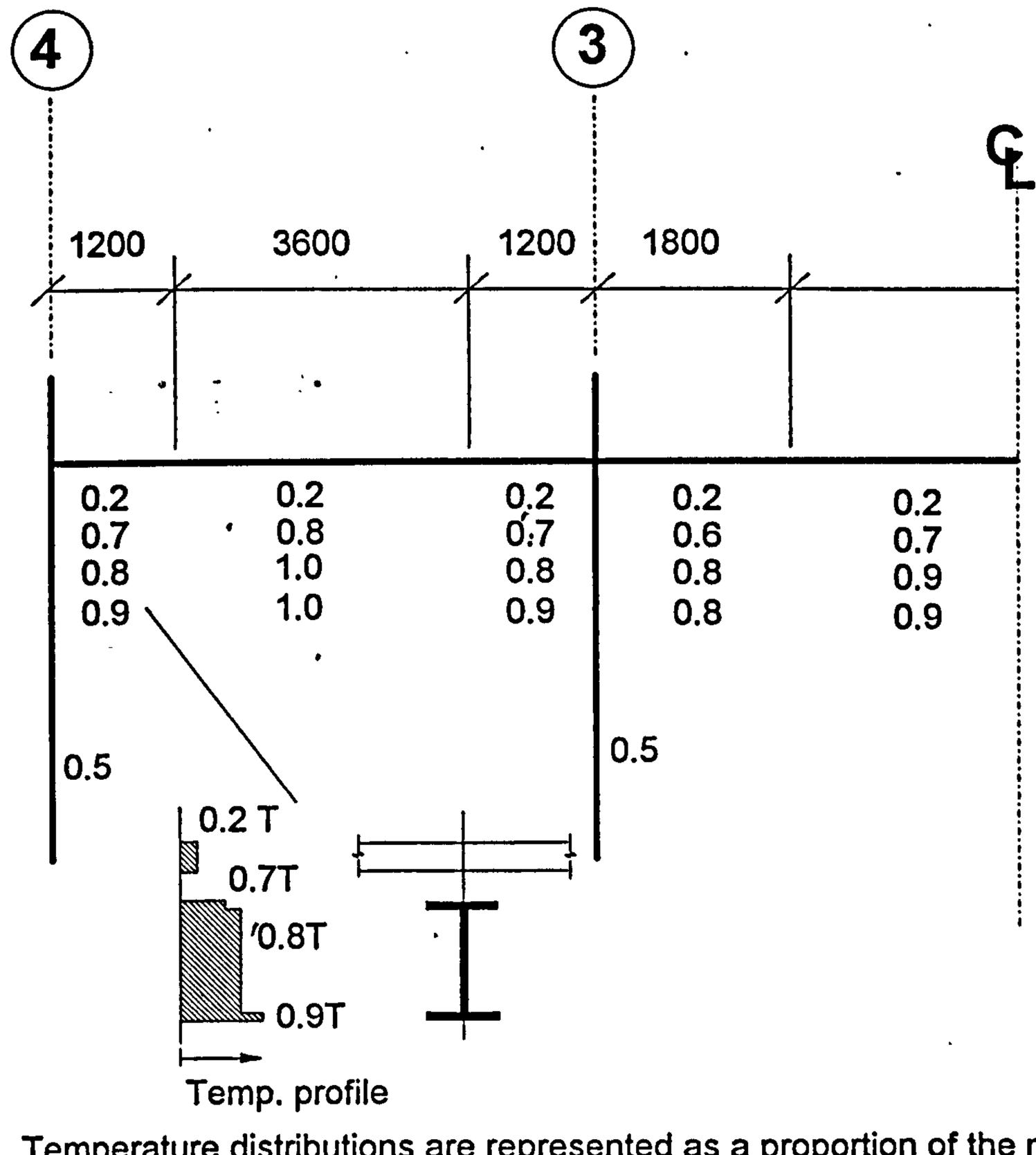

Temperature distributions are represented as a proportion of the maximum temperature and are defined in terms of slab, top flange, web and bottom flange temperatures. Column temperatures are uniform and at 0.5T.

Fig. 8.32: Temperature distributions adopted for the analyses of the two-dimensional cross frame.

From Fig. 8.33 it can be seen that the vertical displacement of both beams reverses direction during the analysis. For the beam between gridlines 4 and 3 this reversal occurs when the maximum temperature is 600°C, with a temperature distribution through the beam at mid-span of 480°C in the top flange and 600°C in both the web and lower flange. Considering the beam between gridlines 3 and 2 the vertical displacement reverses direction at a maximum temperature of 700°C, with a temperature distribution through the beam at mid-span of 490°C in the top flange and 630°C in both the web and lower flange. It can be seen that reversal of vertical deflection occurs at approximately the same temperature in each beam. This is due to squashing of the beam being the prominent behaviour, and has been investigated previously when considering the first examples analysed on the corner fire test.

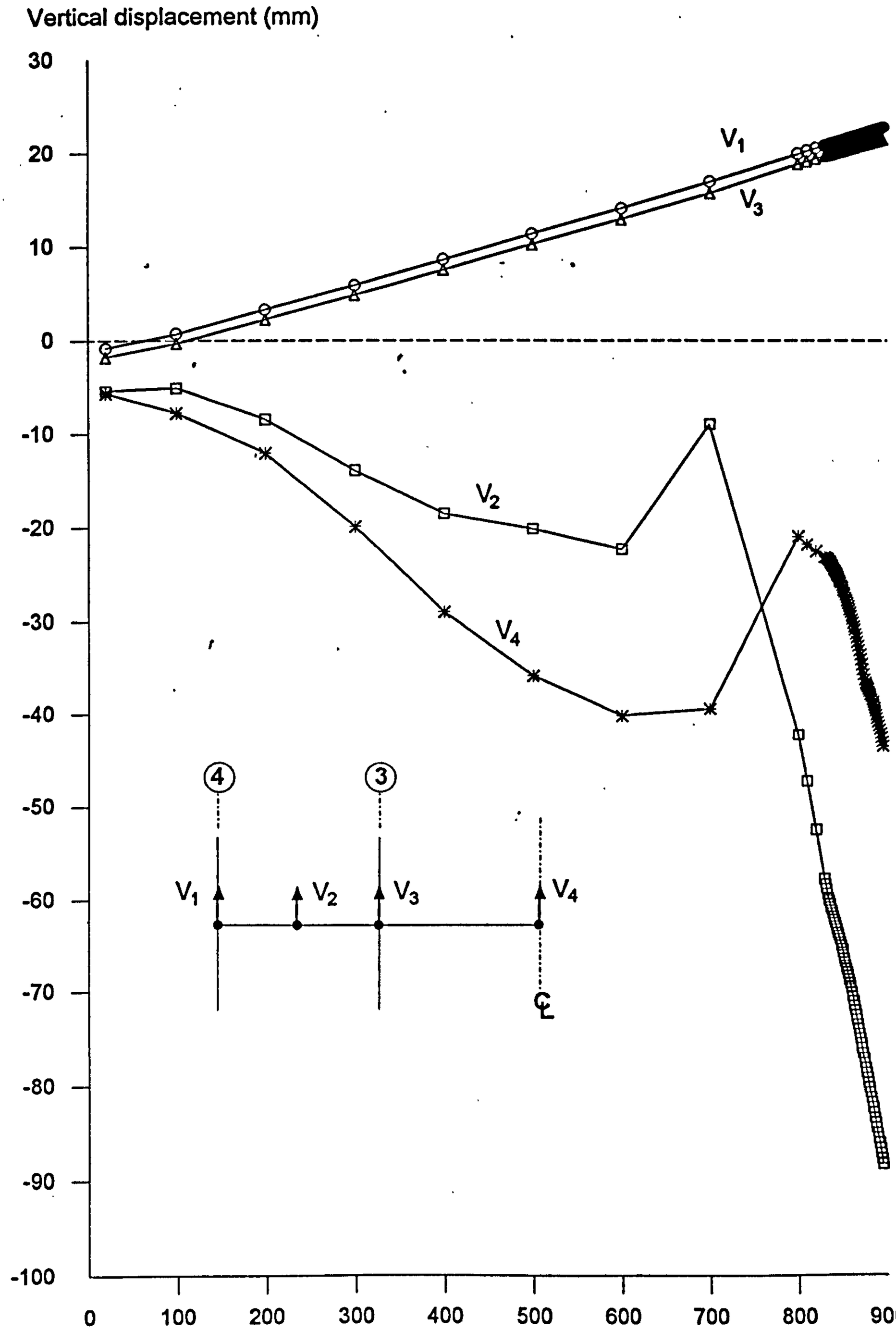

Fig. 8.33: Vertical displacement of beams on gridline B during the rise in temperature.

The horizontal displacements of the beams on gridline B are shown in Fig. 8.34. This displacement is mainly due to thermal expansion of the beams. As the temperature increases, causing the strength and stiffness of the steel beams to reduce, the rate of increase in horizontal displacement becomes smaller, due to the vertical displacements of the beams becoming greater.

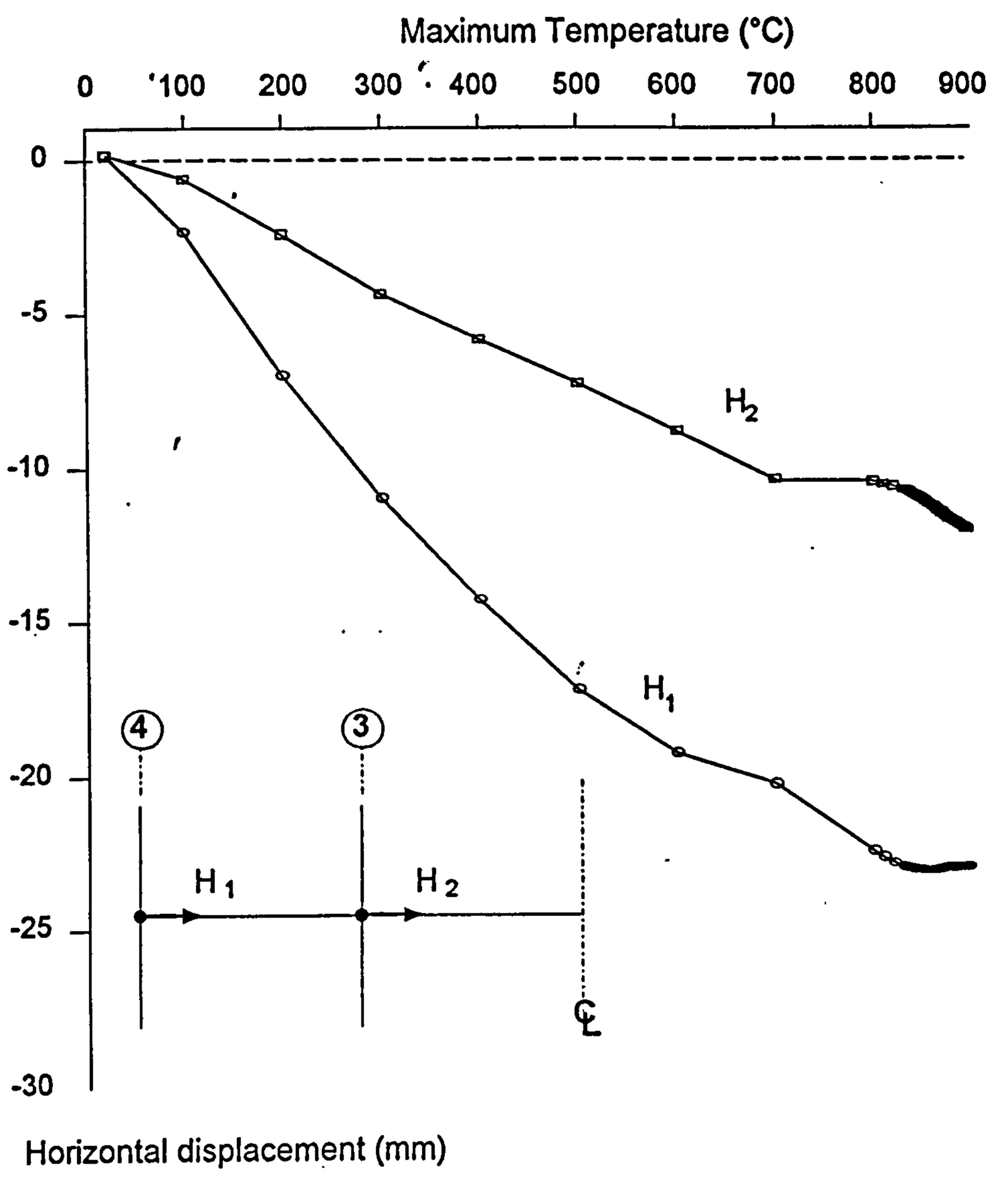

Fig. 8.34: Horizontal displacement of beam on gridline B.

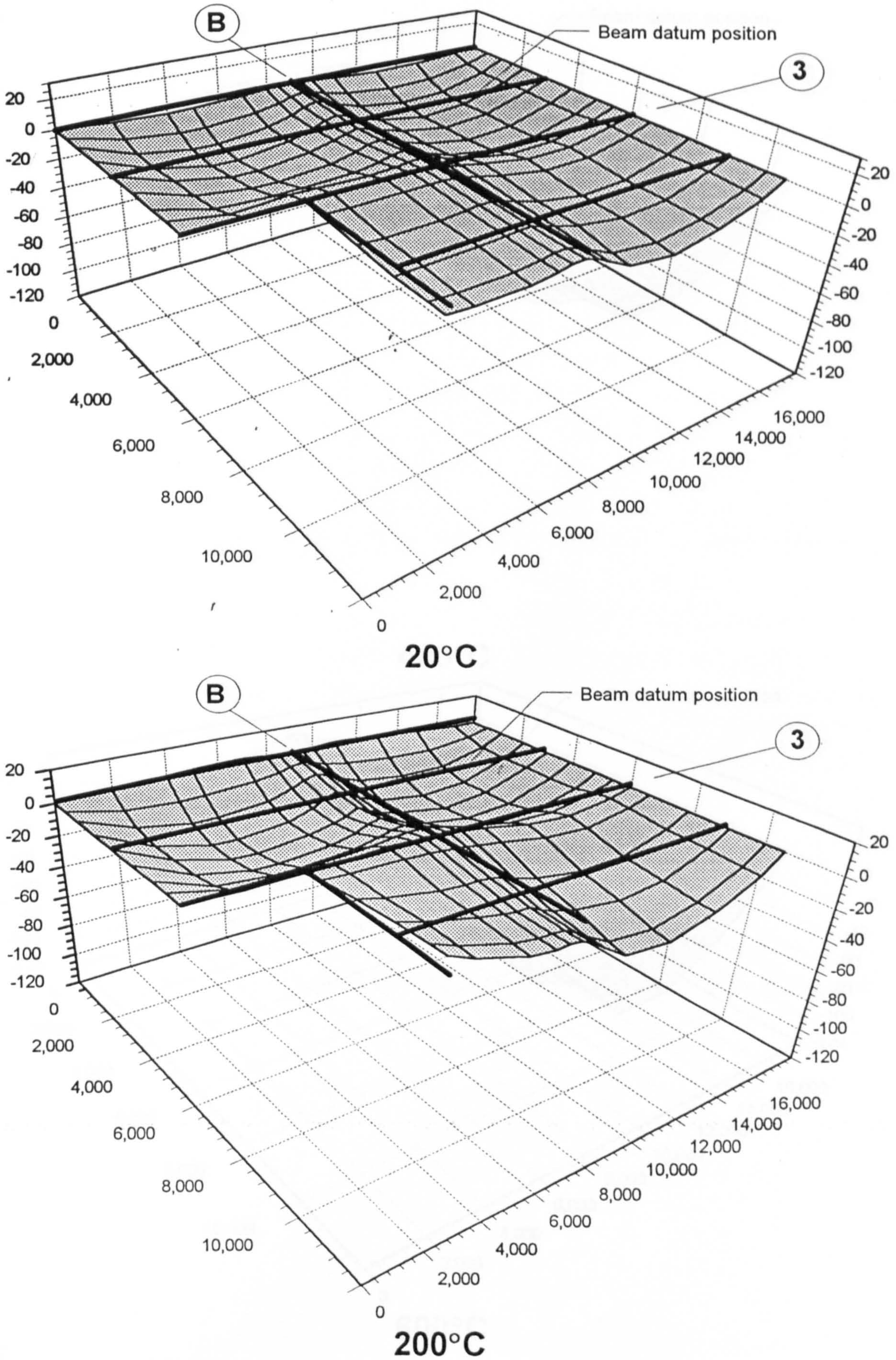

Fig. 8.35: Structural slab profile during the rise in temperature.

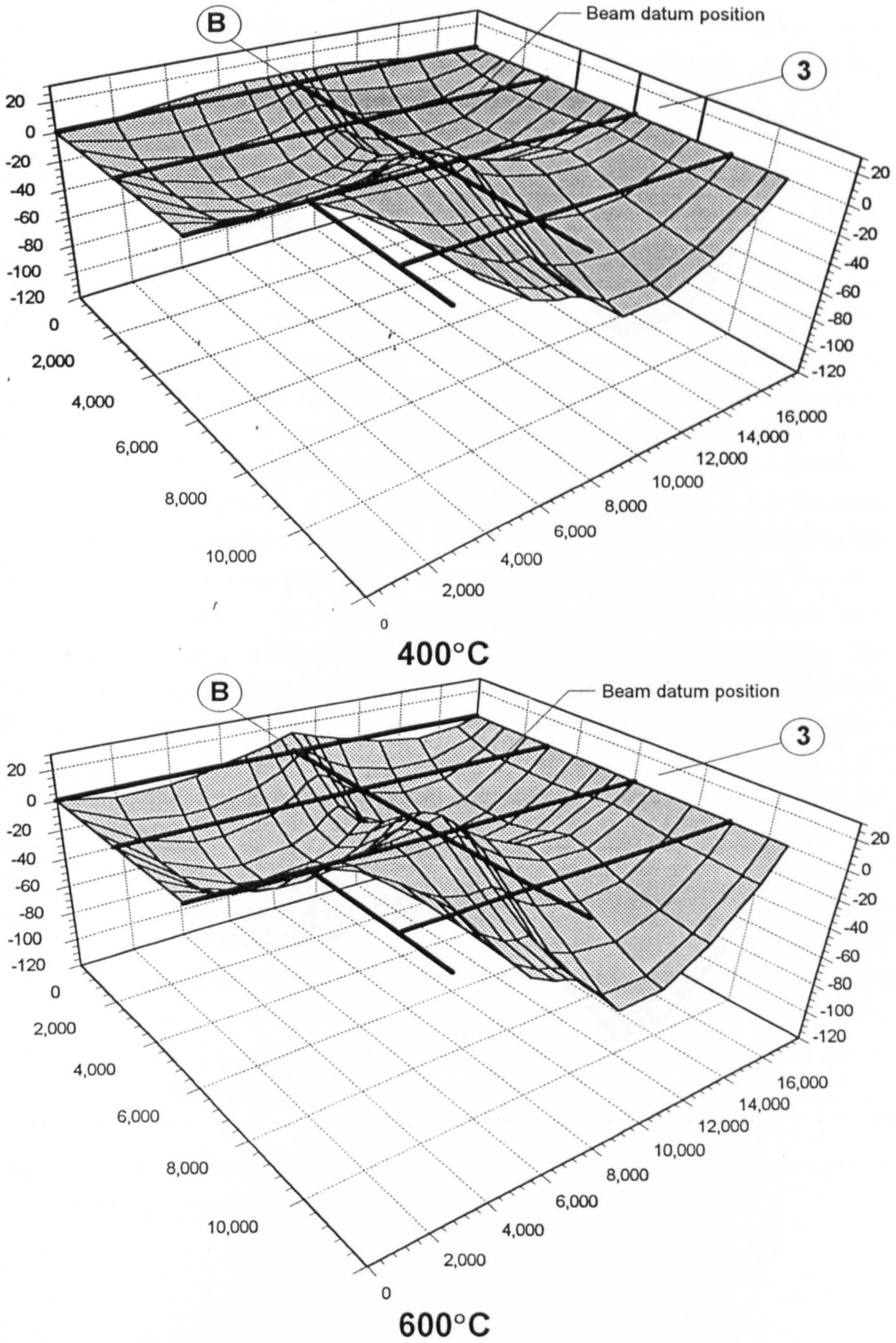

Fig. 8.35: (continued) Structural slab profile during the rise in temperature.

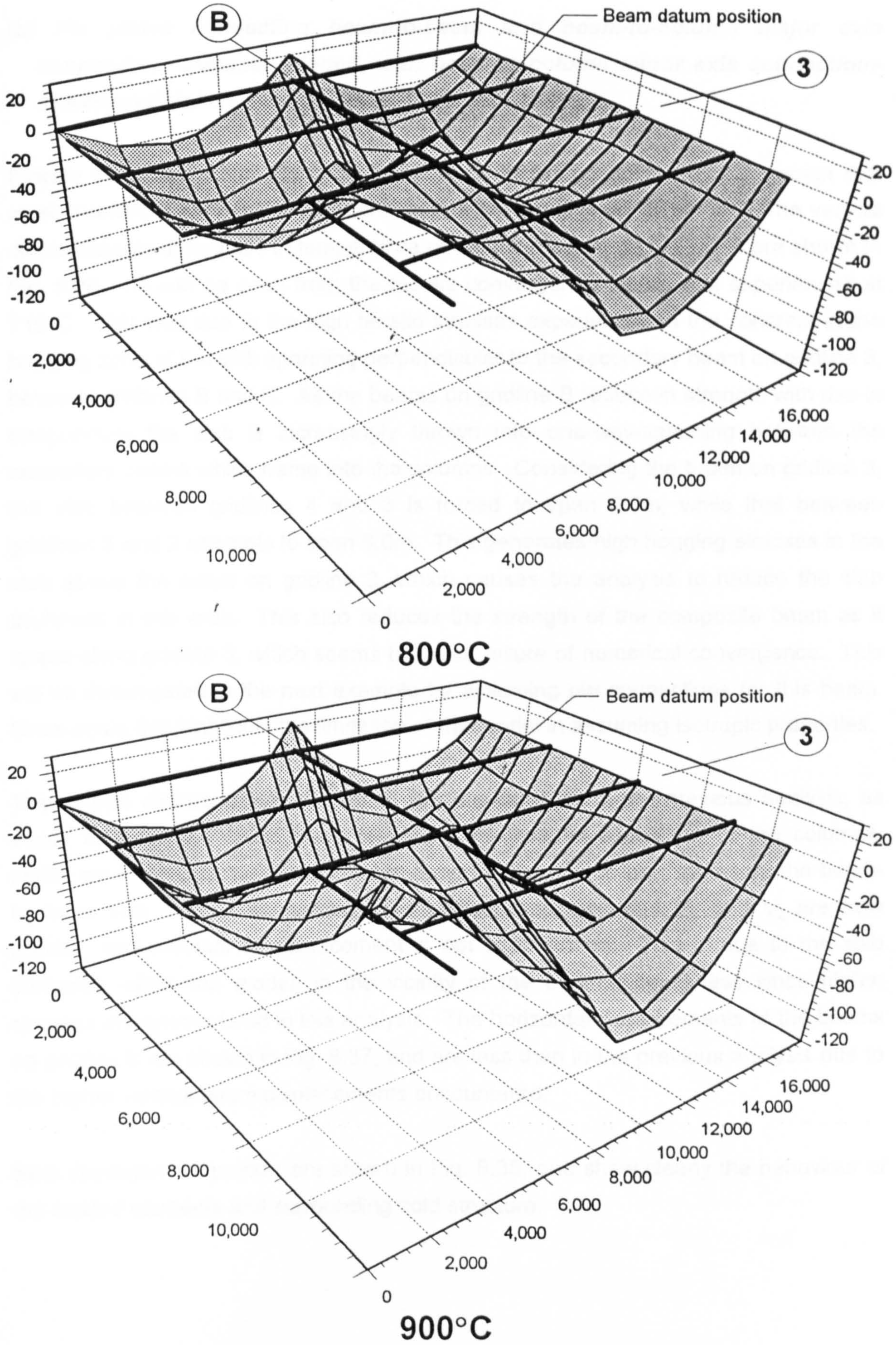

Fig. 8.35: (continued) Structural slab profile during the rise in temperature.

(b) Fin plates connecting beam-to-beam and beam-to-column major axis connections assumed pinned, with beam-to-column minor axis connections considered rigid.

Exactly the same assumptions are adopted as in the previous analysis, except that steel beam-to-column major axis connections are considered as pinned. The vertical displacements during rise in temperature of the main beam on gridline B are shown in Fig. 8.36. As can be seen from the results convergence failure was experienced at 715°C. This was due to the high tensile stresses experienced in the concrete in the hogging zone of the slab spanning perpendicular to the secondary beam on gridline 3, between gridlines B and C. As the beams on gridline B reduce in strength with rise in temperature the slab is increasingly thrown into one-way-spanning between the secondary beams which frame into the columns. Considering the beam on gridline 3, the slab between gridlines 4 and 3 is forced to span 6.0m, while that between gridlines 3 and 2 attempts to span 9.0m. This generates high hogging stresses in the slab above the beam on gridline 3, which causes the analysis to reduce the slab thickness in this area. This also reduces the strength of the composite beam as it spans along gridline 3, which seems to cause failure of numerical convergence. This will be investigated in the next example by assuming pin connections for this beam. Once again this highlights the limitation of the model in assuming isotropic properties.

The vertical displacements V_1 and V_3 are the same as in the previous analysis, as would be expected since these represent the thermal expansion of the columns, which are heated at half the maximum temperature. Since pins represent the beam-to-major axis column connections the vertical displacements V_2 and V_4 are now greater, and reversal of displacement is not experienced. This is due to the slab thickness within the model, in the vicinity of the beams, being less since higher stresses are encountered in this analysis. The horizontal displacements of the beams on gridline B are shown in Fig. 8.37, and are less than in the previous analysis due to the higher vertical beam displacements encountered.

Slab displacement profiles are shown in Fig. 8.38, and show clearly the behaviour of the heated elements and surrounding cold structure.

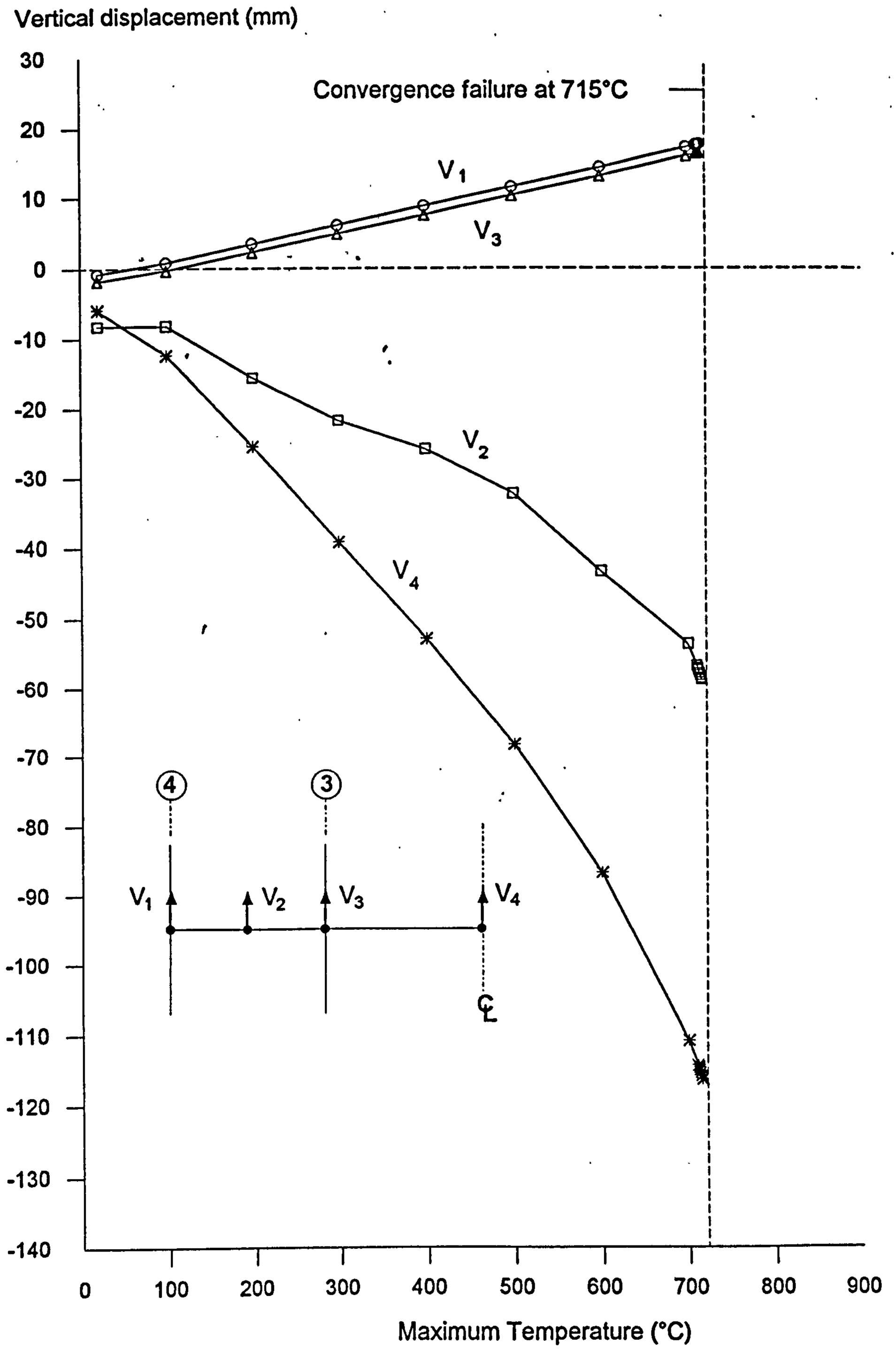

Fig. 8.36: Vertical displacement of beams on gridline B during the rise in temperature.

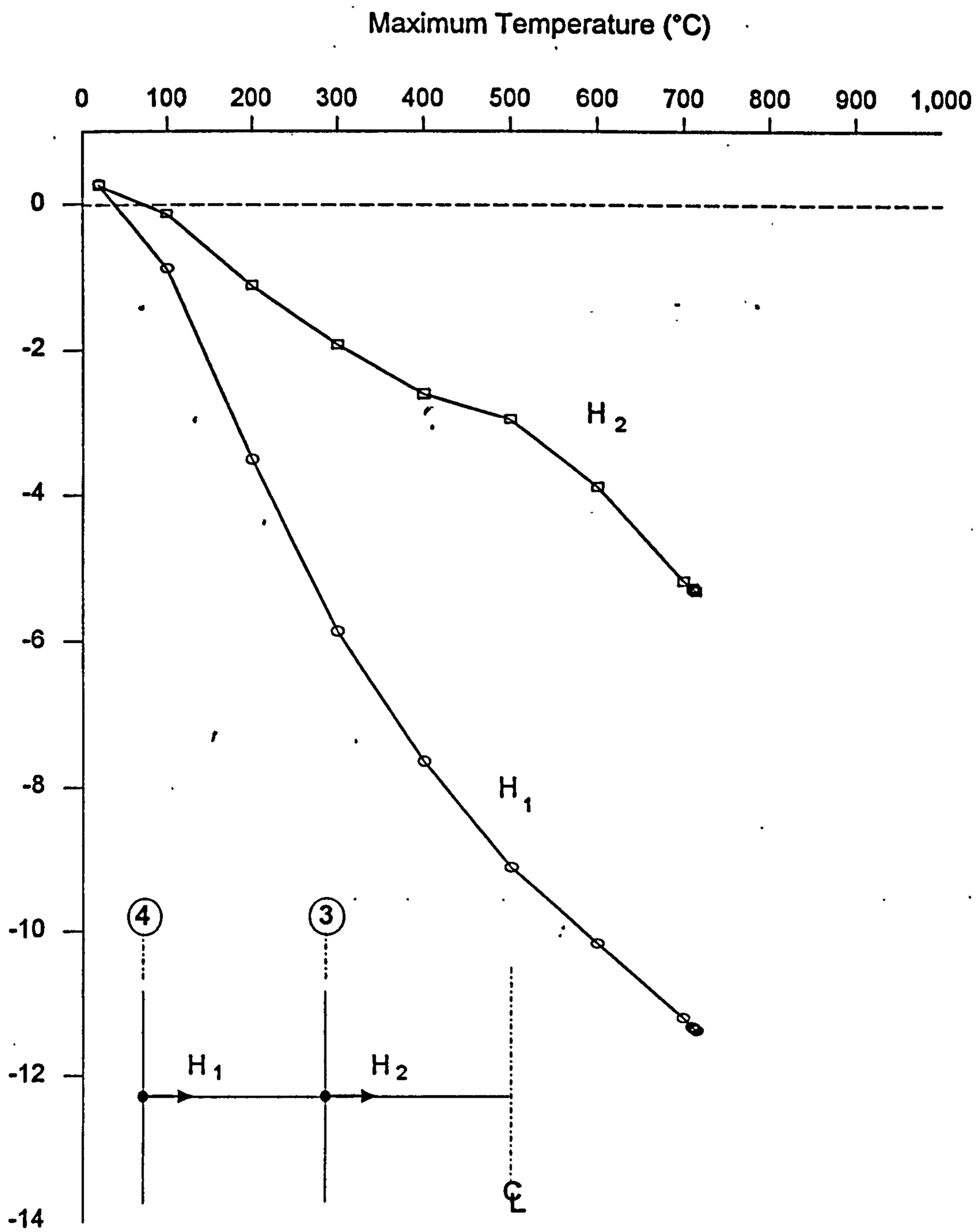

Fig. 8.37: Horizontal displacement of beam on gridline B.

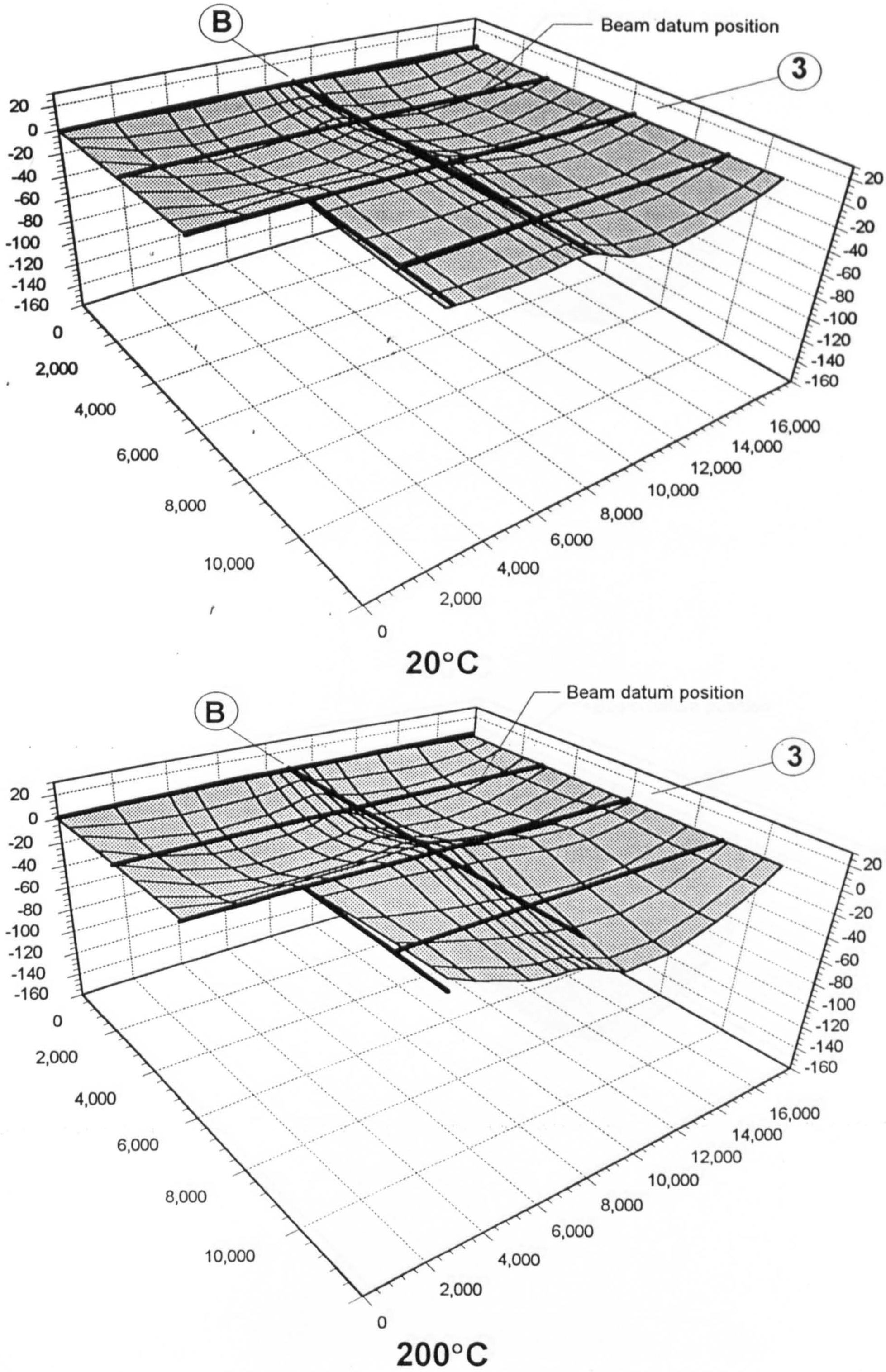

Fig. 8.38: Structural profile during rise in temperature.

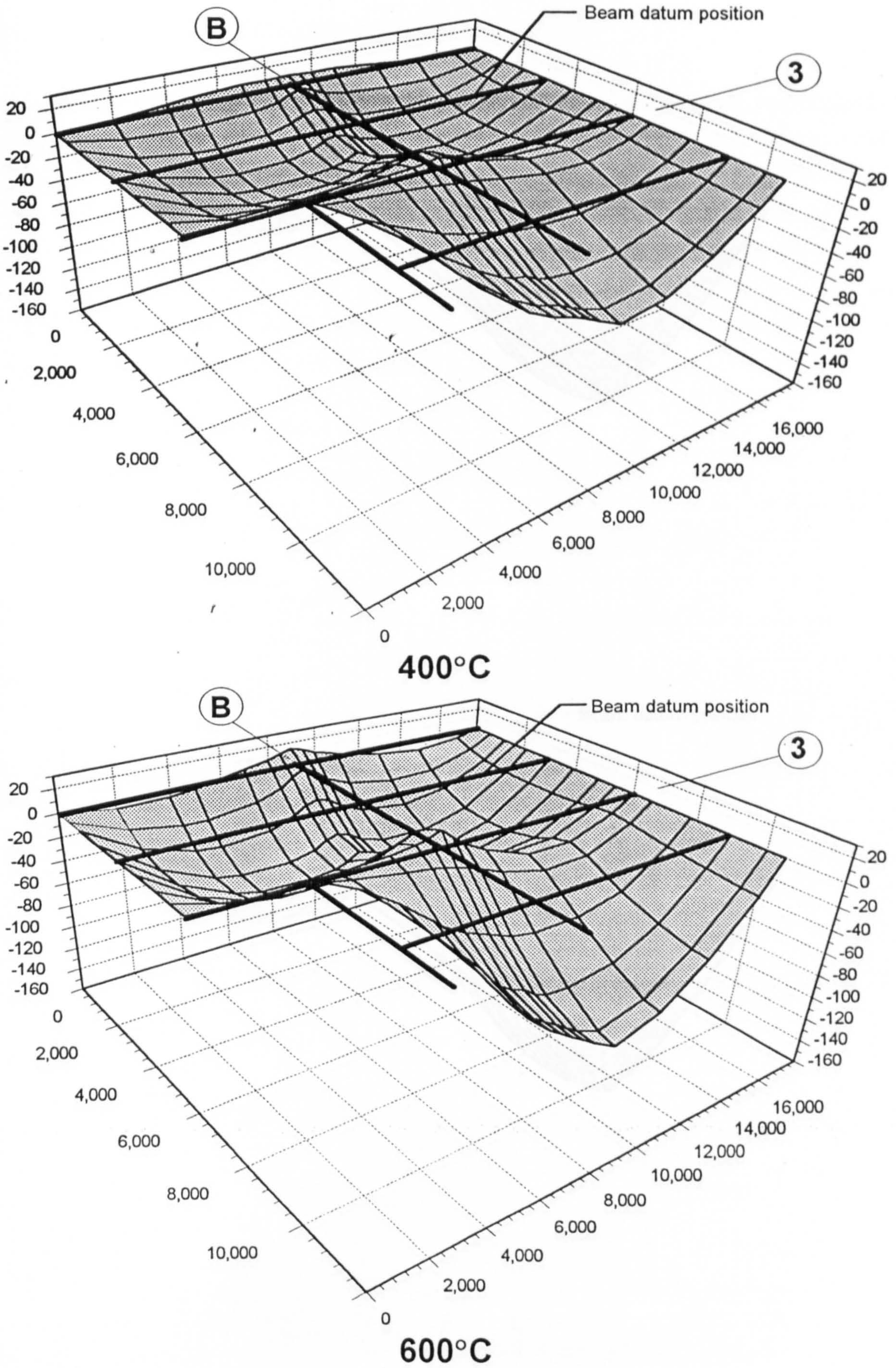

Fig. 8.38: (continued) Structural profile during rise in temperature.

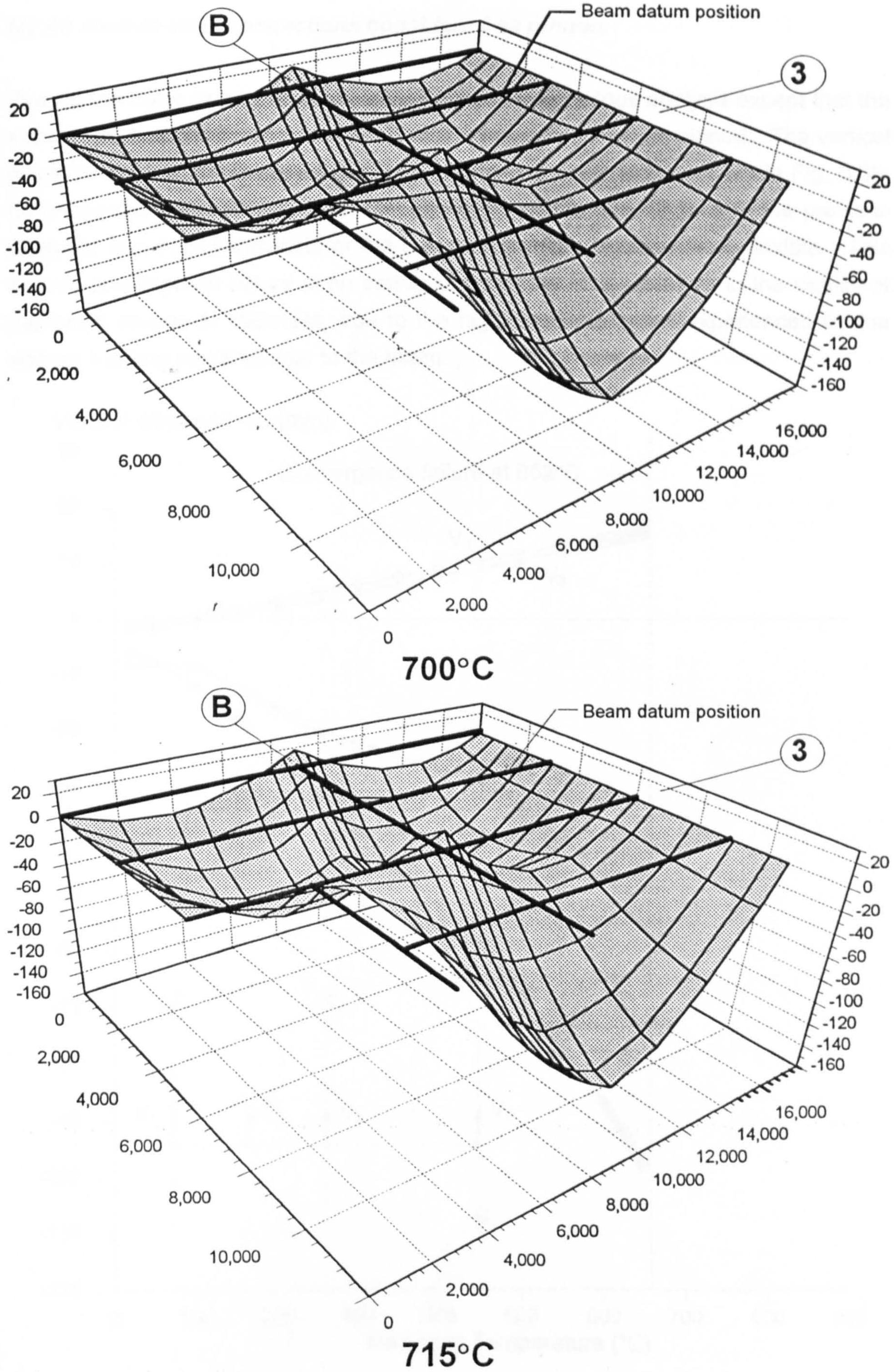

Fig. 8.38: (continued) Structural profile during rise in temperature.

(c) All steel-to-steel connections considered as pinned.

Exactly the same assumptions are adopted as in the previous analysis except that the steel beam-to-column minor axis connections are considered as pinned. The vertical displacements of the beam on gridline B during the analysis are shown in Fig. 8.39. Convergence failure was experienced at 652°C, which is lower than in the previous analysis, due the connections of the beam on gridline 3 being more flexible. This causes convergence failure at an earlier stage as the slab elements in the vicinity of the beam reduce in thickness, due to the high tensile stresses experienced by the slab as it spans perpendicular to the beam.

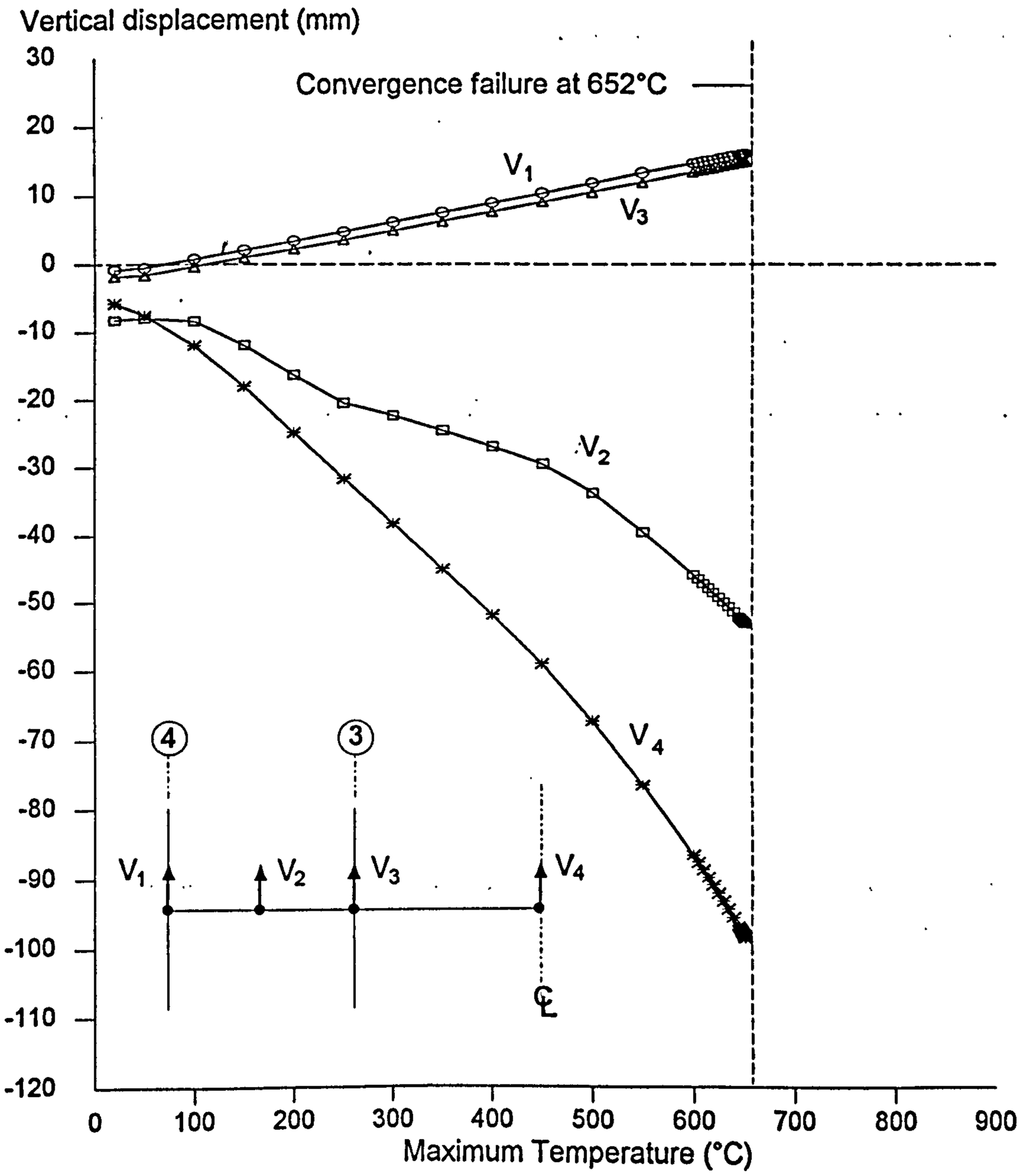

Fig. 8.39: Vertical displacement of beams on gridline B during the rise in temperature.

8.4: THE BEHAVIOUR OF THE RESTRAINED BEAM TEST DURING THE COOLING PHASE OF THE TEST.

As explained in Chapter 7 the computer analysis has been developed in part to investigate the behaviour of steel frames during the cooling phase of a fire. The structural model adopted to investigate the behaviour of the restrained beam test in its cooling phase was the case in which horizontal movement perpendicular to cut-lines *X* and *Y* (shown in Fig. 8.21) is unrestrained, and steel-to-steel connections were represented by the characteristics shown in Fig. 8.20. The additional mid-span displacements of the heated beam during the heating and cooling phases of the test are shown in Fig. 8.40.

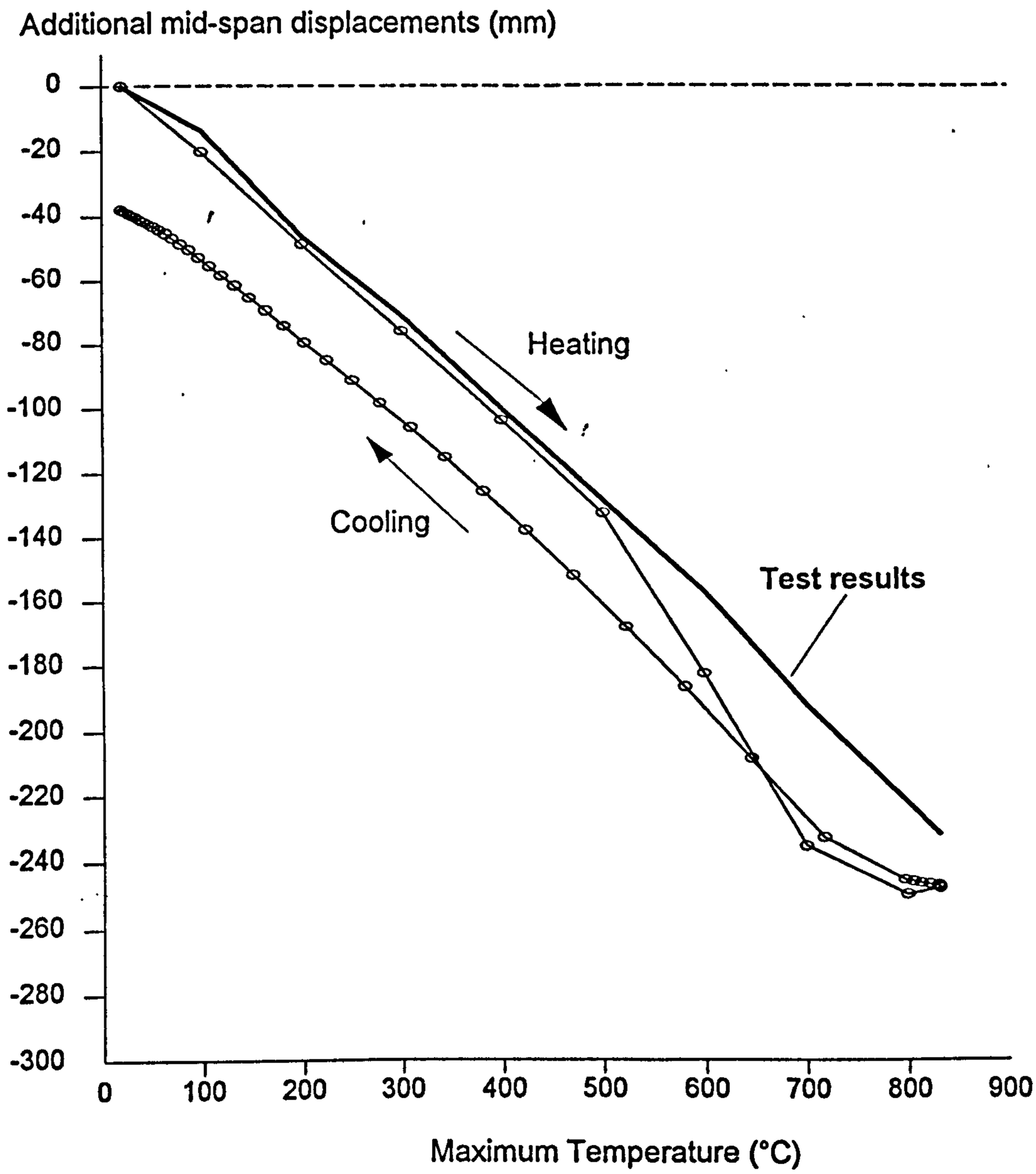

Fig. 8.40: Mid-span displacements during the heating and cooling phases of the restrained beam fire test.

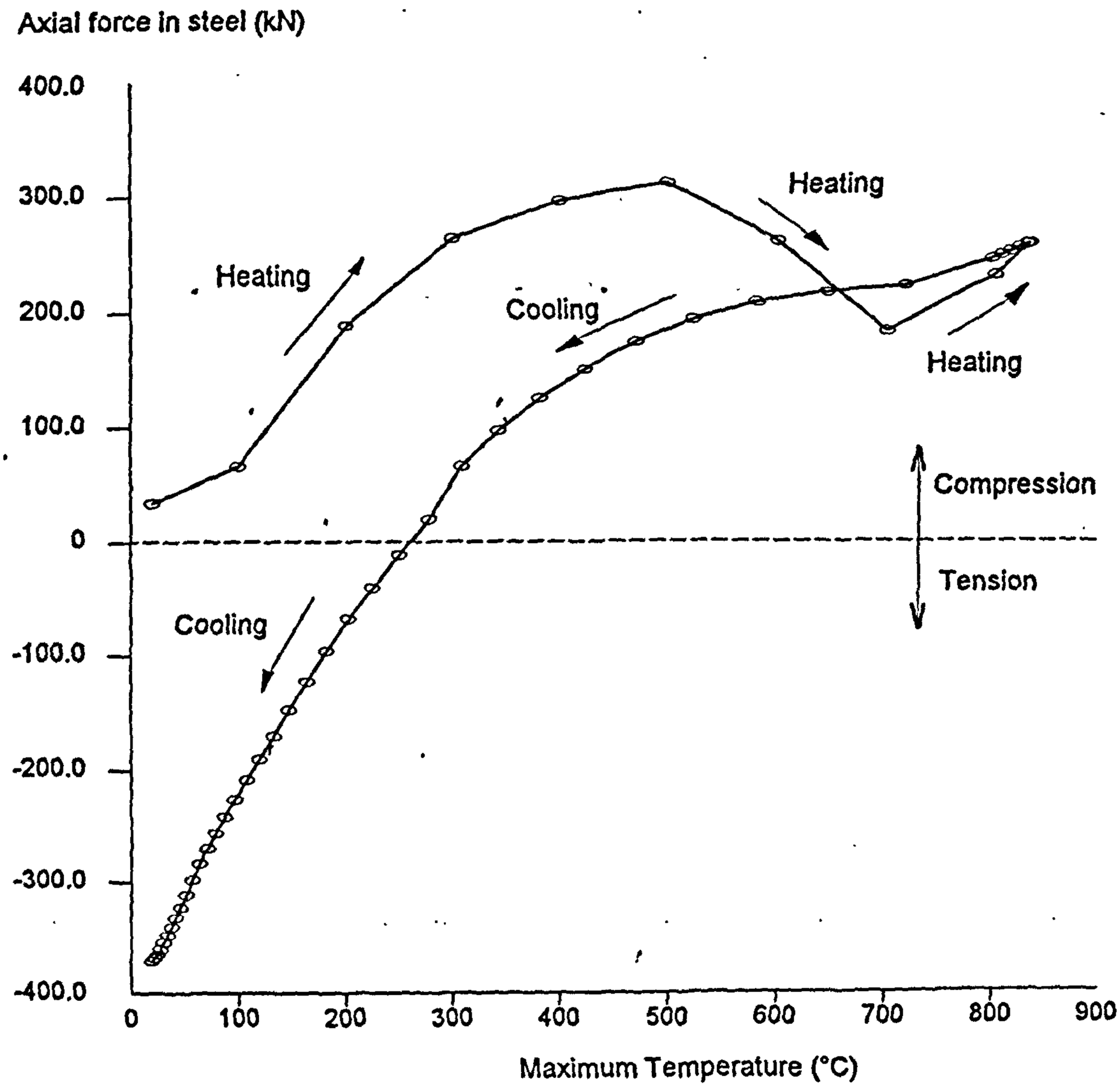

Fig. 8.41: Axial force in the steel member at the node connecting the test beam to the column.

The predicted permanent additional mid-span displacement of the beam after cooling was 38mm, and since the ambient-temperature displacement at the start of the analysis was 23.5mm this creates a total permanent displacement of 61.5mm. However the analysis takes no account of possible tensile fracture of the connections, which was experienced in the test and is discussed in Chapter 7. The axial force recorded during the analysis, at the nodal position which connects the test beam to the column, is shown in Fig. 8.41. As previously explained, extreme care is required in interpreting these results since only the axial force in the steel beam is considered. At the start of the analysis a compressive force is recorded due to the balancing tensile force in the slab being ignored. Between temperatures 700°C and 832°C during the heating phase the axial force begins to increase again due to the increase

of hogging moment in this location. As can be seen from Fig. 8.41 the rate of increase in displacement decreases in this temperature range. This is due to the steel exhibiting constant thermal expansion between 750°C and 860°C as explained earlier.

Only a limited study of the behaviour of the Cardington frame during the proposed and completed fire tests has been presented. These computer simulations have incorporated the full developments presented within this research project. Before comprehensive conclusions can be gained from these tests and computer analyses, which will aid the development of design codes, more studies will be needed. However the results presented here indicate that future research needs to be steered away from consideration of isolated members, towards analyses which incorporate continuity, both in the heated zone and with the surrounding cold structure.

9.0: DISCUSSION AND CONCLUSIONS.

Due to both its associated material cost and its effect on construction programmes considerable research has been conducted into the possibilities of reducing the required fire protection on steel-framed buildings. One of the main areas of this research consists of studies of the actual behaviour of steel members and frames at elevated temperatures. To obtain an understanding of this behaviour experiments have been conducted on steel members, and more recently on full-scale test frames. However it is recognised that these tests are very expensive and there is thus a need for accurate computer modelling. If confidence in software can be generated by validation against test results, the response of any frame to any fire scenario can be investigated very cheaply. It has been shown from recent full-scale fire tests that previous computer simulations, which have almost all been on planar frames together with some three-dimensional skeletal frames, are not accurate enough in modelling the true building behaviour. Therefore the research presented here has focused on the continuing development of computer modelling, with the aim of representing steel-framed building behaviour during fire conditions in a more justifiable manner.

The fully developed model, which is capable of analysing three-dimensional semi-rigid frames including their supported continuous floor slabs, has been validated against test results throughout the development stage. This has shown that the model is accurate in its prediction of member and building behaviour. The steel frame can be modelled during both the heating and cooling phases of the fire, which allows possible repairability to be assessed. The capability of predicting failure by lateral-torsional buckling has also been included within the model. It can be argued that this is of secondary importance in multi-storey buildings since most beams have full lateral restraint to their top flange from the supported floor. However in some situations such as plant areas, industrial buildings and office construction using the 'Parallel Beam Approach[64]', beams may fail by lateral-torsional buckling in a fire situation. The main development stages are discussed below.

9.01: REPRESENTATION OF SEMI-RIGID CONNECTIONS USING SPRING ELEMENTS.

Most multi-storey steel-framed buildings are designed simply, with the assumption that steel-to-steel connections resist shear and axial forces only. In a fire the restraint that even 'simple' connections can provide to the connected members can be beneficial. From the examples presented it has been concluded that the limiting (failure)

temperatures of beams are increased due to the rigidity of the connections, which were represented by spring elements of zero length. However, depending on the amount of restraint to thermal expansion that continuity provides, the beneficial effect of connection rigidity can also be reduced by the possibility of local buckling. This is caused by the combination of the support moment and induced axial force, which may cause buckling of the compressive zones of the cross-section near the support. This type of behaviour was discovered following the Broadgate fire[81], and also after the first fire test conducted on the Cardington full-scale test frame. Computer modelling of localised buckling behaviour is impossible using the one-dimensional beam-column finite elements which are adopted within the model. In fact the only conservative and credible method, within the bounds of this research, of taking account of local buckling effects near supports is to insert a pin at this location (or simply to assume pinned connections). Alternatively it may be argued that beams should be modelled using a mesh of two-dimensional shell elements. This would however greatly increase the time required for analysis, and also reduce the area of structure which can be modelled, due to the large number of elements required.

Ignoring the possibility of local buckling occurring in heated beams near to supports the true behaviour of steel-to-steel connections at elevated temperatures needs to be considered. This includes the possibility of unloading from an inelastic state. The model is capable of including this behaviour, so that if connection unloading during a fire occurs then an unloading stress-strain path is followed in which the stiffness is higher than the localised tangent stiffness. A simple goal-post frame, whose connections experienced reversal of rotation during a simulated fire, showed the increase of failure temperature which can be achieved by considering the true unloading connection behaviour. Although the model can accept any moment-rotation-temperature characteristics, and can also include unloading behaviour based on this relationship, very little experimental data exists for different joint configurations at elevated temperatures. If the true analytical behaviour of semi-rigid frames is to be investigated, then experimental work is required to obtain joint moment-rotation-temperature characteristics.

9.02: LATERAL-TORSIONAL BUCKLING OF SIMPLE BEAMS AT ELEVATED TEMPERATURES.

In order to set the findings for unrestrained beams into context the prescribed limiting temperatures (failure temperatures), specified in BS5950 Part 8[5], were first compared with analytical results for beams with the compression flange continuously restrained

against lateral deflection. Uniform heating was assumed to allow comparison with unrestrained beams, which would typically be engulfed in fire.

For restrained beams it was found that failure temperatures defined at a maximum vertical deflection of span/20[7], were dependent on the span:depth ratio and the pattern of load. Considering the span:depth parameter, for a given load ratio defined as:

$$R = \frac{M_f}{M_c}$$ where M_f = applied moment at the fire limit state, M_c = moment capacity about major axis.

sections with lower span:depth will develop higher strains for a given deflection. Therefore their failure temperatures will be greater. This can be explained by considering a schematic representation (Fig 9.01) of stress-strain-temperature characteristics for a localised point on the cross-section of two beams with the same load ratio, but different span:depth ratios. It can be seen that, to achieve the local stress level required for equilibrium, for a specific maximum deflection, the beam with the lower span:depth ratio fails at the higher temperature. Since the failure criterion[7] for beams is based mainly on deflection the loading pattern will also have an effect on failure temperatures.

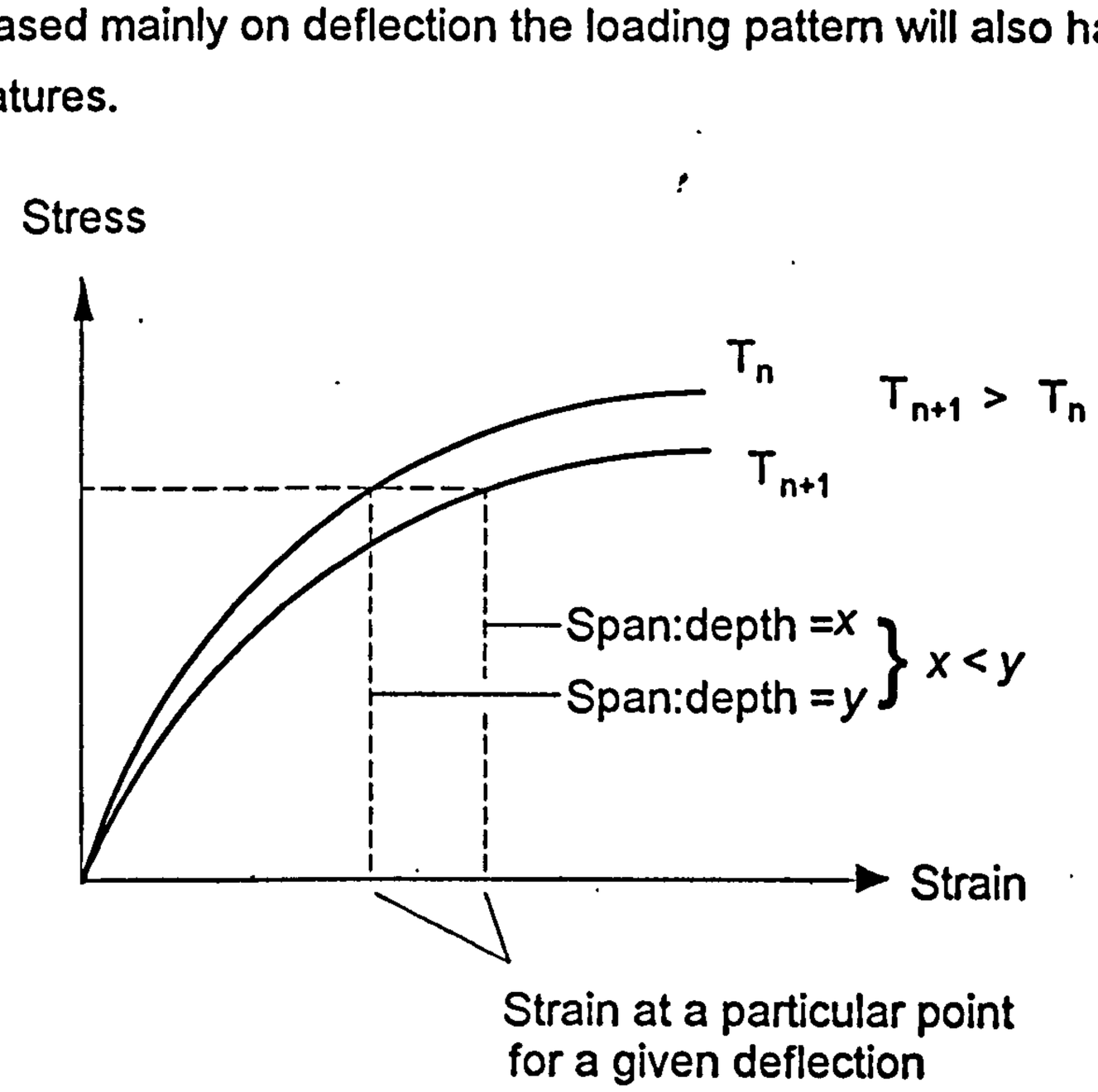

Fig. 9.01: Illustration showing variation of strain values for a particular point on two beams with identical load ratios but different span:depth ratios.

For uniformly heated restrained beams the limiting temperatures specified in BS5950 Part 8 are based on strength reduction factors. These factors are basically the strength recorded at a specific strain value (1.5% strain for BS5950) for various temperatures from tests conducted on tensile specimens. If the steel were to exhibit a sharp yield point at this strain, and failure of beams was defined as the completion of a central plastic hinge, then simple beams would fail at the same temperature for any given load ratio, irrespective of span:depth ratio and loading pattern.

A study of simple unrestrained beams, uniformly heated and subjected to typical loading patterns, was conducted over a range of load ratios at elevated temperatures. From these analytical results it was concluded that the limiting temperatures in BS5950 Part 8 were generally unconservative. This is in contrast to the restrained case for which analytical predictions have shown that the limiting temperatures of BS5950 are very accurate. For uniformly heated unrestrained beams it was found that the least conservative predictions were for those load cases which have high moment over the longest portions of the beam in the mid-span region. Thus a moment profile which changes sign at mid-span produces the best prediction and uniform moment the worst.

Further research work will be required before an all-embracing approach to the design of unrestrained beams can be proposed. However at present the results produced highlight a relationship between failure temperature and the ambient temperature ratio of lateral-torsional buckling resistance moment (M_b) to moment capacity (M_{cr}). It was shown that as this ratio increases the failure temperature decreases for any given load ratio, which is defined as:

$$R = \frac{mM_f}{M_b}, \qquad \text{where,}$$

m = equivalent uniform moment factor (=1.0 if the slenderness correction factor n is used in the calculation of M_b),

M_f = applied moment at the fire limit state,

M_b = buckling resistance moment (lateral torsional)

It may be argued that the ratio M_b/M_{cr} is a controlling parameter because inelastic buckling loads (and buckling loads in general) are controlled by tangent modulus values on the local stress-strain curves of the members affected, just prior to instability occurring. As previously explained the stress-strain curves of steel at elevated temperatures are continuously curvilinear, tending towards zero slope at ultimate stress levels which degrade with rise in temperature. At any given load ratio

a beam with a higher value of M_b/M_{cr} will be more highly stressed than one with a lower value. Its compression flange is therefore subject to a lower tangent modulus in resisting any infinitesimal disturbance, and as the temperature rises the tangent modulus rapidly declines. This is shown schematically in Fig. 9.02

As the load ratio decreases it has been shown that the failure temperatures of all beams converge to a single value depending only on the load ratio. Since the strain values on these sections are much lower, failure is essentially by elastic buckling, which occurs when the increase in temperature has reduced the initial (Young's) modulus to a proportion of its original value approximately equal to the load ratio.

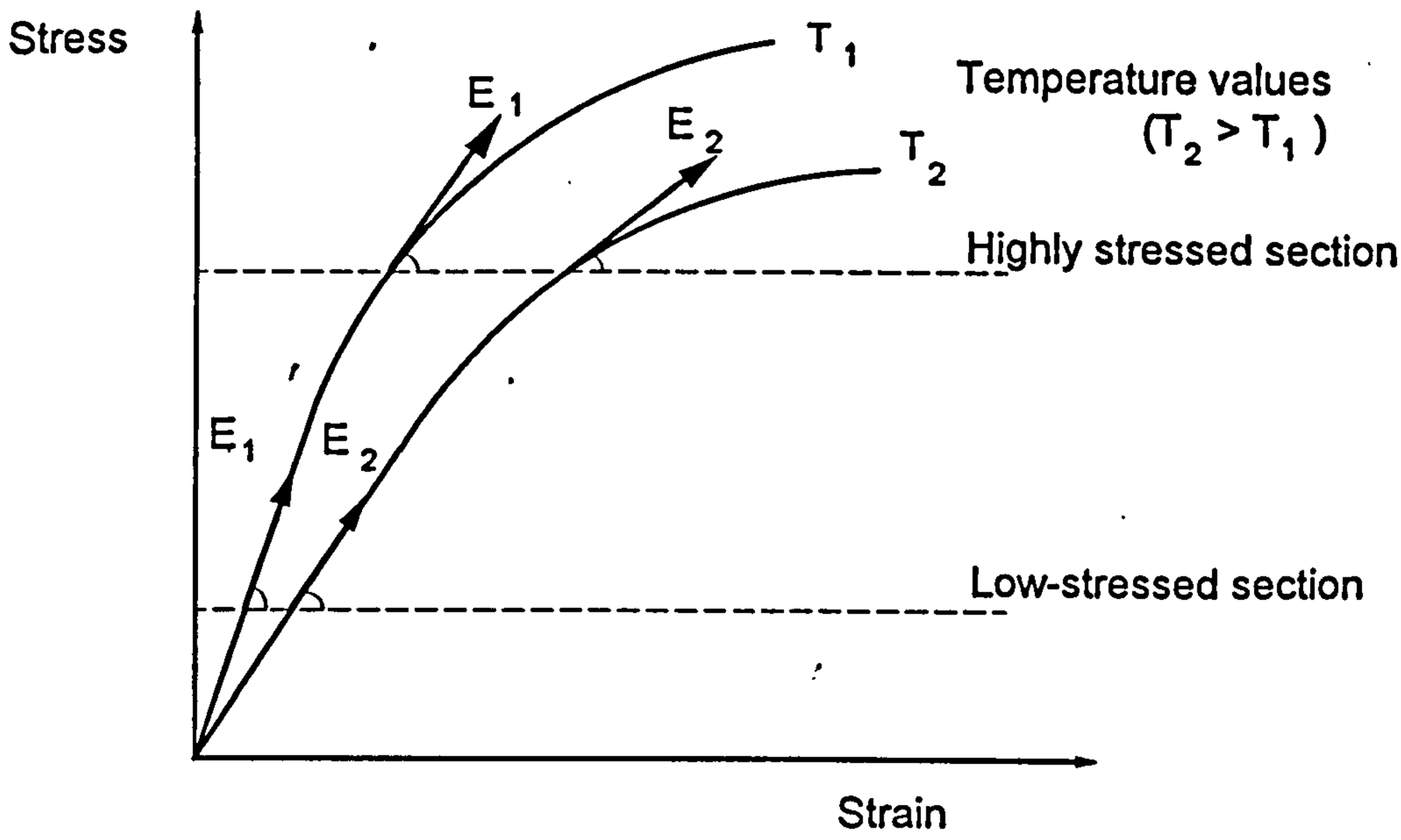

Fig. 9.02: Illustration of the different rates of degradation of tangent modulus with temperature for members at high and low load levels.

9.03: MODELLING CONTINUOUS FLOORS.

The structural effect of the flooring system, if it acts compositely with the supporting frame, will have a significant effect on the behaviour of a building during a fire. Most previous analytical modelling has only included the floor as a flange of the composite beam using an effective width concept. This approach ignores the membrane action of the slab, which can be considered as having two significant effects. The first consists of the restraint against thermal expansion provided by the continuous slab. This generally increases displacements in heated members due to the P-δ effect of the induced axial forces. The second effect is beneficial, and consists of a bridging action by the slab which may be able to divert load-paths away from the weakening

members. In the final stages it is possible that structural collapse could be avoided by catenary action of the slab. This will depend on its support conditions and the strength of its reinforcement or mesh. Future research work could be steered towards investigating this type of behaviour.

To investigate the structural effects of a flooring system which acts compositely with the supporting frame, shell finite elements have been introduced into the model. The connection of the one-dimensional beam-column elements to the two-dimensional shell elements is at common nodal points located at the mid-height of the shell element. The concrete slab is assumed to be linear-elastic with cracking behaviour crudely modelled by reducing the thickness of the shell element, so that a maximum bending component of stress is not exceeded. The stresses in the slab are calculated, once equilibrium is obtained, at the Gauss points and then averaged over the element. Connection of the beam elements at a common node point causes the floor and beams to act compositely. However the calculation of the concrete stresses for ultimate strength purposes considers the slab only, with its neutral axis at mid-height. This method is clearly incorrect when considering the cracking behaviour of the slab when it spans over and parallel to the beam. For this case the stress distribution should be calculated about a neutral axis whose position is based on the steel and slab. This is difficult since during a fire the neutral axis will continuously move towards the cooler, and thus stronger, areas of the section. Future research work should concentrate on modelling more realistically the cracking behaviour of the concrete over beams, and should also include the true behaviour of the reinforcement, together with methods of modelling localised cracking. Extension to include non-linear material properties of the concrete at elevated temperatures should also be considered.

Thermal strains for the concrete slab have been included in the model. However the temperature distribution must be assumed to be uniform since flat shell elements have been adopted at this stage. If material non-linearity were to be included in the model then an integration through the slab thickness will be required which will allow a temperature gradient to be specified. However even with these simplifications it has been found that comparison with test results on isolated composite sections indicate that the model's displacement predictions are very accurate. It was therefore decided to use the model to simulate the fire tests on the full-scale test frame at Cardington. Generally it can be concluded from these analyses that the structure, especially the concrete slab, surrounding a fire zone has a major influence on the performance of the directly heated members. During the course of these studies the mid-span

displacements and the corresponding average temperatures became available for the first Cardington fire test, in which a 9.0 metre secondary beam was heated over most of its length. A Comparison was made between the test results and the computer analysis, assuming both an isolated member and full three-dimensional subframes including slabs. It was shown that the treatment of members in isolation was highly unrealistic, with the three-dimensional model correlating far better with the test results. This indicates that future research should concentrate on fire scenarios in building structures rather than on isolated members. Although an inevitable complication of the analysis occurs when the whole building behaviour is incorporated, it is considered justifiable since a realistic prediction of building behaviour is required. The final objective of this continuing research is to simplify the knowledge gained into design rules which allow manual calculations to be conducted by practising engineers.

9.04: THE COOLING BEHAVIOUR OF STEEL FRAMES.

In reality, due to the regulatory requirement of compartmentation (which creates localised fires) together with the inherently high degree of redundancy in most buildings complete structural collapse due to a fire is highly unlikely. Research is therefore required into the permanent deformations, internal forces and residual strength once a frame has cooled so that repairability can be assessed. The model has been extended to include extensive strain reversal in the steel members, which will allow their behaviour to be investigated during the cooling phase.

Only a limited study has been presented here, but one effect of interest is the high tensile force predicted in a beam subjected to restraint from the surrounding frame and cooled from the inelastic state. This tensile force can cause 'failure' of the connections, as was observed in the flexible end-plate connections after the Broadgate fire and following cooling of the first fire test on the Cardington frame. It can be argued that this failure is not necessarily catastrophic. Tensile failure of the bolts is not instantaneous, since as each bolt fails (the order being dependent on their individual strengths) the tensile force in the beam is partly relieved due to deformation of the end-plate, until the remaining bolts can withstand and equilibrate the induced tensile force. In some cases the bolts may not necessarily be the weak link, with failure of the welds or the heat affected zone of the end-plate occurring first, as was witnessed after the fire test at Cardington. In the investigation following the Broadgate fire it was found that other connections, which consisted of double angle-cleats bolted through the beam web to supporting members, accommodated axial movement by deforming the connecting cleats. This could lead to the conclusion that

the most favourable type of connection in fire conditions could be seating cleats, for which cooling would either cause the locating bolts to shear or the cleat material to deform, allowing axial movement but still retaining vertical support.

Further research is required into the behaviour of frames during the cooling phase of the fire. These studies should focus on frames since it has been shown that restraint to thermal expansion significantly influences member behaviour during both the heating and cooling phases of a fire.

9.05: CONCLUDING REMARK.

It can be argued that since a fire is an accidental occurrence, design methods for fire safety of structures should only consider strength. This could be extended further by permitting localised failure (buckling) and even member failure, provided that disproportional collapse is avoided. Based on the findings presented here it has been shown that future work should be steered towards considering the building structure as an entity, with the aim of avoiding complete collapse. This may conclude by requiring protection of vertical structural elements and possibly increasing the tensile reinforcement in the concrete slab (or ensuring continuity if precast slabs are adopted). However extensive further evidence is needed to support these concepts and the results from the Cardington frame, together with the continuing development of sophisticated computer models, could possibly provide this.

REFERENCES.

1. Latter, R., The European Market for Constructional Steelwork, *New Steel Construction,* **2** (5). October 1994.
2. *The Building Regulations, Approved Document B: Fire safety,* Department of the Environment and the Welsh Office, HMSO 1991.
3. *Fire Protection of Structural Steel in Buildings, 2nd Edition.* Association of Structural Fire Protection Contractors and Manufacturers Limited and The Steel Construction Institute, UK, 1989.
4. *BS449: 1969, The Use of Structural Steel in Building.* BSI, London, 1969.
5. *BS5950: 1990, Structural use of steelwork in building. Part 8: Code of Practice for Fire Resistant Design,* BSI, London, 1990.
6. *Eurocode 3: Design of Steel Structures. Part 1.2: Structural Fire Design (Draft),* European Committee for Standardisation, 1993.
7. *BS476: 1987, Fire tests on building materials and structures. part 20: method of determination of the fire resistance of elements of construction (general principles),* BSI, London 1987.
8. *ISO834: 1985, Fire resistance tests - Elements of building construction.*
9. Wainman, D.E. and Kirby, B.R.,*Compendium of UK Standard Fire Test Data on Unprotected Structural Steel.* British Steel Report (Swindon Labs), 1987.
10. Lawson, R.M., and Newman, G.M., *Fire Resistant Design of Steel Structures - A Handbook to BS5950 Part 8;* The Steel Construction Institute, 1991.
11. Burgess I.W., El-Rimawi, J. and Plank, R.J., Studies of the behaviour of steel beams in fire., *J. Constr. Steel Research,* **19** 1991 pp. 285-312.
12. Kirby, B.R. and Preston, R.R., High temperature properties of hot rolled structural steels for use in fire engineering studies. *Fire Safety Journal,* **13** 1988.
13. Cooke G.M.E., and Latham D.J., The inherent fire resistance of a loaded steel framework. *Steel Construction Today.* **1** (2) April 1987.
14. Witteveen J. Some aspects with regard to the behaviour of the calculation of steel structures in fire. *Symposium No.2 - Behaviour of Structural Steel in Fire.* Fire Research Station, Borehamwood Herts. 24th Jan. 1967.
15. Marchant E., *A Complete Guide to Fire and Buildings.* Medical and Technical Publishing Co. London. 1972.
16. Knight D. The Behaviour of Steel Structures in Fire. *BHP Technical Bull,.***16** (2) Nov. 1972.
17. Culver C., Steel column buckling under thermal gradients. *ASCE J. Struct. Div.,* 1972, 98 (ST8) pp. 1853-1865
18. Ossenbruggen, P.J., Aggarwal, V., and Culver, C.G., Steel column failure under thermal gradients. *ASCE J. Struct. Div.,* 1973, 99 (ST4) pp. 727-739

19. Culver, C.G., Aggarwal, V., and Ossenbruggen, P.J., Buckling of steel columns at elevated temperature. *ASCE J. Struct. Div.,* 1973, 99 (ST4)
20. Brockenbrough, R., Theoretical stresses and strains from heat curving. *ASCE J. Struct. Div.,* 1970, 96 (ST7) pp. 1421-1444.
21. Cheng, W., and Mak, K., Computer analysis of steel frames in fire. *ASCE J. Struct. Div.,* 1970, 101 (ST4) pp. 855-867.
22. Furumura, F., and Shinohara, Y., *Inelastic behaviour of protected steel beams and frames in fire.* Report of the Research Laboratory of Engineering Materials, No.3 1978 pp. 1-14.
23. Kruppa, J., Collapse temperature of steel structures. *ASCE J. Struct. Div.,* 1979, 105 (ST9) pp. 1769-1787.
24. Iding, R., and Bresler, B., *Effect of fire exposure on steel frame buildings.* Final report, WJE No. 78124 Janney Elstner and Associates Inc. Sept. 1981.
25. Jain, P., and Rao, R., Analysis of steel frames under fire environment. *Int. Journal for Numerical Methods in Engineering.* 19. 1983 pp 1467-1478
26. Baba, S., and Nagura, H., Effect of material properties on the deformation of steel frames in fire. *Proc. of JSCE Structural Eng./Earthquake Eng.,* 2, (1) 1985 pp. 47-57.
27. Dotreppe, J., Franssen, J., and Schleich, J., Numerical simulation of fire resistance tests on steel and composite structural elements or frames. *Fire Safety Sci. - Proceedings of the First International Symposium.* Oct. 1985.
28. Sharples, J.R., *The Strength of Partially Exposed Steel Columns in Fire.* M.Phil Thesis, University of Sheffield. 1987.
29. El-Zanaty, M.H., and Murray, D.W., Non-linear finite element analysis of steel frames, *ASCE J. Struct. Div.,* 1983, 109 (ST2) pp. 353-368.
30. Olawale, A.O., *Collapse behaviour of steel columns in fire.* Ph.D Thesis, University of Sheffield, 1988.
31. Olawale, A.O. and Plank, R.J., The collapse analysis of steel columns in fire using a finite strip method. *Int. J. Num. Methods Eng.* 26 1983. pp 2755-2764.
32. El-Rimawi, J., *The behaviour of flexural members under fire conditions.* Ph.D Thesis, University of Sheffield. 1989.
33. Burgess, I.W., El-Rimawi, J. and Plank, R.J., A secant stiffness approach to the fire analysis of steel beams. *J. Constr. Steel Research,* 11 1988, pp.105-120.
34. Saab, H.A., *Nonlinear finite element analysis of steel frames in fire.* Ph.D Thesis, University of Sheffield. 1990.
35. Saab, H.A., and Nethercot, D.A., Modelling steel frame behaviour under fire conditions. *Engineering Structures.* 13, (4). 1991 pp. 371-382.

36. Jeyarupalingam, N., and Virdi, K.S., *Steel beams and columns exposed to fire hazard. Structural design for Hazardous loads.* Edited by J.L. Clarke, F.K. Garas and G,S,T Armer. E&FN Spon, 1992.
37. Virdi, K.S., and Dowling, P.J., *The ultimate strength of composite columns in biaxial bending.* Proceedings of the Institution of Civil Engineers, Mar. 1973, Part2.
38. Wang, J.C., and Moore, D.B., *Fire resistance of steel beams.* Int. Seminar on Structural Design for Hazard Loads, Brighton U.K. 17-19 April 1991.
39. Najjar, S.R., *Three-Dimensional Analysis of Steel Frames and Subframes in Fire.* Ph.D Thesis. 1994.
40. Najjar, S.R. and Burgess, I.W., A non-linear analysis for three-dimensional steel frames in fire conditions. *Engng. Struct.,* (In Press).
41. Bathe, K., *Finite Element Procedures in Engineering Analysis,* Prentice-Hall Inc., 1982.
42. Zienkiewicz, O.C. and Taylor, R.L. *The Finite Element Method. Fourth Edition, Volume 1: Basic Formulation and Linear Problems.* McGraw-Hill Book Company.
43. Zienkiewicz, O.C., and Taylor, R.L., *The Finite Element Method. Fourth Edition, Volume 2: Solid and Fluid Mechanics Dynamics and Non-linearity.* McGraw-Hill Book Company, 1991.
44. Griffiths, D.V., and Smith, I.M., *Numerical Methods for Engineers.* Blackwell Scientific Publications. 1991.
45. Chen, W., and Atsuta, T., *Theory of Beam-Columns. Volume 2: Space Behaviour and Design.* McGraw-Hill Book Company. 1977
46. Zbirohowski-Koscia, K. *Thinned Walled Beams. From theory to practice.* Crosby Lockwood & Son Ltd. 1967.
47. Rajasekaran, S., and Murray, D.W., Finite Element Solution Of Inelastic Beam Equations. *ASCE J. Struct. Div.,* 1973, 99 (ST6) pp. 1025-1041
48. Meek, J.L., *Computer Methods in structural Analysis.* Chapman & Hall. 1991.
49. *BS5950: 1990, Structural Use of Steelwork in Building: Part 1. Code of practice for design in simple and continuous construction: hot rolled sections,* BSI, London 1990.
50. Crisfield, M.A., A fast incremental/iterative solution procedure that handles snap-through. *Computers and Structures,* **13.** pp. 55-62. 1981.
51. Chen, W.F., and Lui. E.M., Semi-rigid steel beam-to-column connections: data base and modelling., *ASCE J. Struct. Div.,* 1989, **115** (1), pp.105-119.
52. Jones, S.W., Kirby, P.A. and Nethercot, D.A. Columns with semi-rigid joints, *ASCE J. Struct. Div.,* 1982, **108** (ST2), pp. 361-372.
53. Chen, W.F., and Lui, E.M., *Stability Design of Steel Frames,* CRC Press Inc., 1991.

54. Lui, E.M., and Chen, W.F., Analysis and behaviour of flexibly-jointed frames. *Engng Struct.*, 8, 1986. pp.107-118.
55. Sibai, W.A., and Frey, F., New Semi-Rigid Joint Elements for Non-linear Analysis of Flexibly Connected Frames. *J. Construct. Steel Research.* 1993, **25** pp.185-199.
56. Lawson, R.M., Behaviour of steel beam-to-column connections in fire. *The Structural Engineer*, 1990 **68** (14). pp. 263-271.
57. Lawson, R.M., *Enhancement of Fire Resistance of Beams by Beam to Column Connections.* Technical Report SCI. Publication 086. 1990.
58. Kishi, N., and Chen, W.F., *Data Base of Steel Beam-to-Column Connections.* Structural Engineering Report No. CE-STR-86-26, School of Civil Engineering, Purdue University, West Lafayette, IN, 653.
59. Nethercot, D.A., *Steel Beam-to-Column Connections-A Review of Test Data and its Applicability to the Evaluation of Joint Behaviour in the Performance of Steel Frames*, CIRIA Project Record, RP338.
60. El-Rimawi, J.A., Burgess, I.W., and Plank, R.J., *Modelling the behaviour of steel frames and subframes with semi-rigid connections in fire.* 1993 University of Sheffield, Dept. of Civil and Structural Engineering, Research Report DCSE/93/S/02.
61. Gerstle, K.H., Effect of Connections on Frames. *J. Construct. Steel Research.* **10** (1988) pp. 241-267.
62. Moncarz. D.P., and Gerstle, K.H., Steel Frames with Nonlinear Connections. *ASCE J. Struct. Div.,* 1981, **107** (ST8), pp. 1427-1441.
63. Vlasov, V.Z., *Thin-Walled Elastic Beams.* English translation, Israel Program for Scientific Translations Jerusalem, Israel. 1961.
64. Brett, P., and Rushton, J., *Parallel Beam Approach-A Design Guide.* The Steel Construction Institute, Publication 074., 1990.
65. Trahair, N.S., and Bradford, M.A., *The Behaviour and Design of Steel Structures.* Chapman & Hall. 1988.
66. Timoshenko, S.P., and Gere, J.M., *Theory of Elastic Stability.* McGraw-Hill. 1963.
67. Kirby, P.A., and Nethercot, D.A., *Design for Structural Stability.* Constrado Monographs, Collins. 1979.
68. Kitipornchai, S. and Trahair, N.S., Inelastic buckling of simply supported steel I-beams, *ASCE J. Struct. Div.,* 1975 **101** (ST7), pp. 1333-1347.
69. Kitipornchai, S. and Trahair, N.S., Buckling of inelastic I-beams under moment gradient, *ASCE J. Struct. Div.,* 1975 **101** (ST5), pp. 991-1004.
70. Burgess, I.W., El-Rimawai, J. and Plank, R.j., Studies of the behaviour of steel beams in fire, *J. Constr. Steel Research,* **19**, (1991) pp. 285-312.

71. *Eurocode 3: Design of Steel Structures Part 1.1: General rules and rules for buildings (Draft),* Commission of the European Communities, 1993.
72. Steelwork Design Guide to BS5950: Part 1: 1990, Volume 1, *Section Properties, Member Capacities:* 3rd Edition, Steel Construction Institute 1993.
73. Owens, G.W. and Knowles, P.R, *Steel Designers Manual,* 5th Edition, Steel Construction Institute, 1994.
74. Onate, E, Zienkiewicz, O.C., Suarez, B., and Taylor, R.L:, A General Methodology for Deriving Shear Constrained Reissner-Mindlin Plate Elements. *International Journal for Numerical Methods in Engineering,.* 1992 **33.** pp. 345-367.
75. Bathe, K. and Dvorkin, E.N, Short Communication: A Four-node plate bending element based on Mindlin/Reissner plate theory and a mixed interpolation, *International Journal for Numerical Methods in Engineering,* 1985, **21,** pp. 367-383.
76. Timoshenko, S., and Woinowsky-Krieger, S., *Theory of Plates and Shells.* McGraw-Hill, 1959.
77. Fenner, D.A., *Engineering Stress analysis. A finite element approach with FORTRAN 77 software.* Ellis Horwood. 1987.
78. Barlow, J. Optimal Stress locations in Finite Element Models. *International Journal for Numerical Methods in Engineering,* **3,** pp. 243-251.
79. CP117: 1965, *Composite Construction in Structural Steel and Concrete,* BSI, London, 1965.
80. Ishihara, K., Yoshida, N., and Tsujino, S., Modelling of stress-strain relations of soils in cyclic loading. *Fifth International Conference on Numerical Methods in Geomechanics / Nagoya.* 1-5 April 1985.
81. *Structural Fire Engineering. Investigation of Broadgate Phase 8 Fire.* The Steel Construction Institute. 1991.
82. Armer, G.S.T, and Moore, D.B., Full-scale testing on complete multi-storey structures. *The Structural Engineer.* 18th Jan. 1994, **72** (2), pp.30-31.
83. Lennon, T., Portable Furnaces. *New Steel Construction.* 1995 **3** (1), pp 21-24.
84. Dvorkin, E.N., and Bathe, K., A continuum mechanics based four-node shell element for general non-linear analysis. *Eng. Comput.,* 1984, **77.** pp. 77-88.